MECO Superconducting Solenoid System Conceptual Design Report

Prepared by the Massachusetts Institute of Technology
Plasma Science and Fusion Center

June 6, 2002

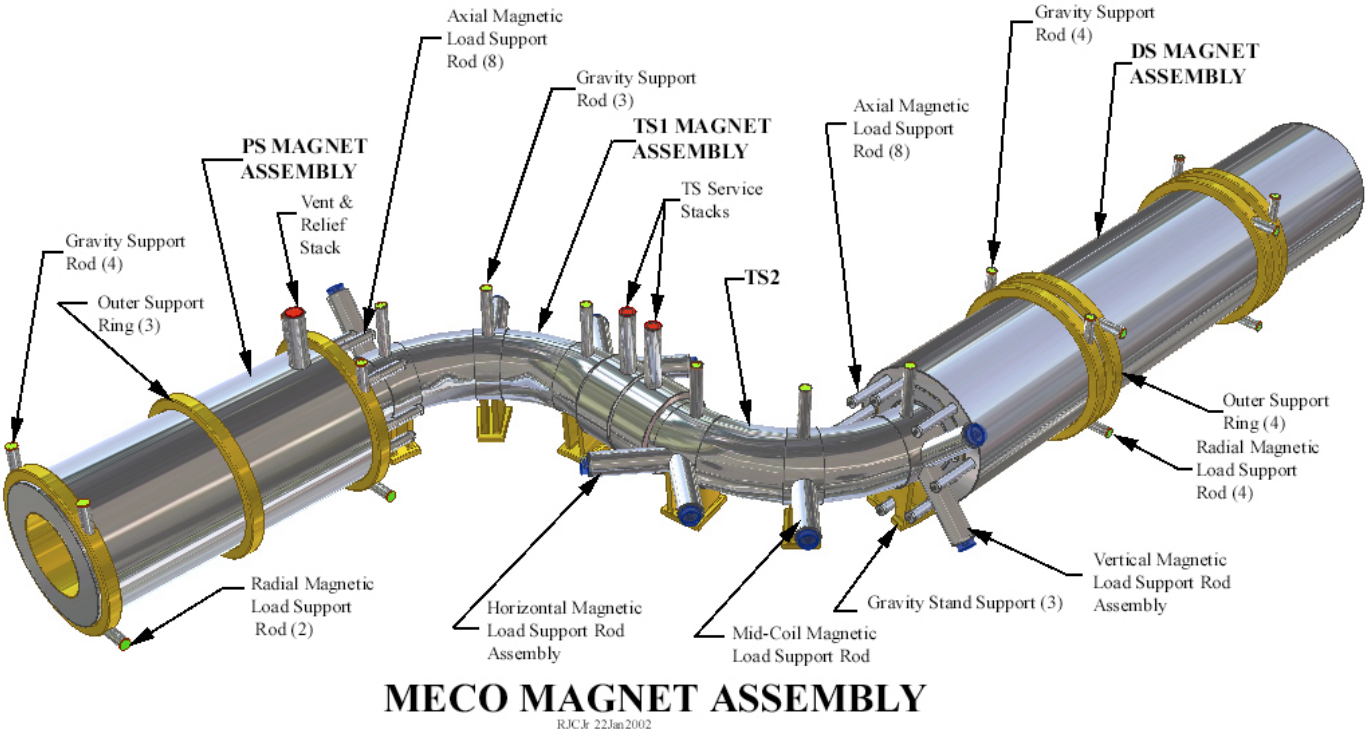

Table of Contents

Section 1 - Introduction and Summary 1
Section 2 - Interfaces 6
PS Shield and Clear Bore Vacuum 6
Incoming Proton Beam 6
Outgoing Proton Beam and Required Clear Bore Access 7
Heat and Radiation Load on the Production Solenoid 7
Service Ports for the Production Solenoid 8
Service Ports for the Transport Solenoid 8
Beryllium Window for Vacuum Isolation 8
Service Ports for the Detector Solenoid and Vacuum Interface 8
Use of Cryostat as Vacuum Vessel for Transport and Detector Solenoids 9
Support of Collimators Off the Transport Solenoid 9
Support of Experimental Equipment Off Detector Solenoid 9
Steel Cosmic Ray Shield and Muon Beam Dump 9
Electrical Noise Environment 10
Gravity Supports 10
Procedure for Transportation to and Installation at BNL 10
Section 3 - Field Specifications and Field Matching 11
Models and Methods of Analyses 13
Coil Definitions 17
General Characteristics of Magnet Systems 21
Field-Quality-Related Recommendations for Coil Manufacturing and Assembly 22
B-H Curve for the Detector Solenoid Iron Shield Box 24
Section 4 - Conductor Design 26
Requirements 26
Design 27
Production Solenoid Conductor 30
Transport Solenoid Conductor 31
Detector Solenoid Conductor 32
Section 5 - Coil Insulation Design 35
Section 6 - Conductor Joint Design 39
Section 7 - Current Lead and Bus Bar Design 43
Current Bus 43
PS Current Bus 44
PS Current Leads 44
TS and DS Current Buses 44
TS and DS Current Leads 45
Section 8 - Quench Detection System 46
Overview 46
Voltage Taps and Wire Routing 47
Analog Signals and DAS Protection 48
Signal conditioning 48
Master Controller with Digital Quench Detector 50
Digital Quench Detection 50

Consecutive Quenches 51
Digital Quench Detection in Transient Voltages 51
Speed and Reliability of Digital Quench Detection 52
Optional Backup Analog Quench Detector (AQD) 52
Data Acquisition System (DAS) 53
Section 9 - Quench Protection 55
Details of the Quench Analysis 56
PS Quench 57
TS1 quench 63
T3u with cable only quench 65
DS Quench 69
Section 10 - Power Supplies, Dump Resistors, and Switches 75
Requirements 75
Preliminary power supply design 76
Section 11 - Structural Design Criteria 78
Typical Materials Properties 78
Tensile Strain Allowable Normal to Plane 80
References 82
Section 12 - Production Solenoid Coil, Cryostat, and Support Stress Analysis 83
Introduction 83
Coil Stress Summary 87
Mandrel Stress -External Shell/Mandrel 95
Mandrel Bolting 97
Displacements - Axisymmetric Model with External Mandrel/Shells 99
Warm and Cold Mass Supports 101
Supports for the Production Solenoid Cold Mass 102
Cryostat Stresses 104
Helium Can 108
Addendum to Section 12 112
Model with Internal Mandrel/Shells 115
References 116
Section 13 - Structural Analysis of the Transport Solenoid Mandrel, Winding and Supports 117
Introduction 117
Summary of Results 121
TS Coil Displacements 122
TS Coil Displacement Summary 122
Structural Models 129
Evolution of the Structural Concepts 136
Coil and Conductor Stress 144
Supports 150
Strut Stresses and Design 153
Vertical Support Rods 159
Mandrels 161
Other Analyses Using the Large 3D Model 165
Support Cases/Cryostat and Collimator 166

References 174
Section 14 - Analysis of the Detector Solenoid Mandrel, Winding and Supports 175
Introduction 175
Lorentz Forces are Not Strongly Effected by The Iron Shield 176
Axisymmetric Model 179
Detector Solenoid Coil Stresses with Local Stress Multipliers Applied 181
3D Gravity Load Model 182
Force and Magnetic Stiffness Interactions with the Iron Box 184
Axial Support Struts 186
Vertical and Horizontal Hanger Rods 187
End Pole Analysis 188
Field Decay on the Downstream End of the DS 193
Cryostat 194
References 199
Section 15 - Cryogenic System Design 200
Overview 200
Helium system 200
Thermal Design for the MECO Detector and Transport Solenoids 204
Thermal Design for the MECO Production Solenoid 210
Flow in the channels between the Coil and the Mandrel 213
The PS safety vent line 213
Cool-down system 216
Estimate of Cooldown Times 217
Quench of a solenoid 219
Re-cooling after a quench 219
Component accessibility 219
Section 16 - Magnet Assembly 229
Introduction 229
Production Solenoid Assembly 231
Transport Solenoid Assembly 243
Detector Solenoid Assembly 256
Section 17 - Installation 258
Introduction 258
Installation of the Detector Solenoid 266
Installation of the Transport Solenoid 267
Production Solenoid Installation 270
Field Mapping and Final Positioning 271
Insertion of the Production Target/Heat and Radiation Shield Assembly 271
Cryogenic System Installation 273
Section 18 - Draft MECO Test Plan 278
Introduction 278
1 — SUPERCONDUCTOR ACCEPTANCE 280
2 — COIL VERIFICATION AND ACCEPTANCE 282
3 — LOW POWER SYSTEM TEST 284
4 — SYSTEM ACCEPTANCE TEST 285
5 — FINAL ACCEPTANCE MAGNETIC VERIFICATION TEST 294

Master Fabrication and Test Sequence..... 295

List of Figures

Figure 1.1 – The layout of the MECO Magnet system 4
Figure 1.2 – Persepective view of the assembled MECO Magnet System 5
Figure 2.1 – Proton beam interface 6
Figure 3.1 – The MECO Magnet System Layout and Field Specification 12
Figure 3.2 – The TOSCA three-dimensional model 14
Figure 3.3 – Field Specification Paths 15
Figure 3.4 – Magnetic Field, B(T), along the Paths vs. Z-coordinate (m) 16
Figure 3.5 – Magnetic Field Derivative, dB/dZ(T/m), along the Paths vs. Z-coordinate (m). Relative magnet positions are given by zmin and zmax in Table 3.1. 16
Figure 3.6 – B-H curve for the 1010 iron used in the analyses 24
Figure 4.1 – Peak azimuthal nuclear heat load to the Production Solenoid [new7coldmassb.xls] 26
Figure 4.2 – Plot of SSC inner strand and cable data at 4.2 K with J_c fit from Table 4.2. 29
Figure 4.3 – Plot of SSC outer strand and cable data at 4.2 K with J_c fit from Table 4.2. 29
Figure 4.4 –The Production Solenoid coil conductor. 30
Figure 4.5 – Contours of constant temperature margin in the first PS coil. 31
Figure 4.6 – TS coil conductor, except in coils next to the Be window (see text). 32
Figure 4.7 – DS coil conductor. 32
Figure 5.1 – Compressive strength degradation in epoxy systems as a function of neutron fluence (see footnote 4 for credit). 37
Figure 5.2 – Compressive strength degradation in epoxy systems as a function of radiation dose. Note 1 Gy = 100 Rads (see footnote 4 for credit). 38
Figure 6.1 – Typical joint configuration. 39
Figure 8.1 – Voltage taps and wires for quench detection 47
Figure 8.2 – Coil voltage signals and quench detection / protection system; single line: sequential signal stream, double line: array of signal streams, thick single line: power line. 49
Figure 9.1 – Generic quench protection circuit using a dump resistor 55
Figure 9.2 – PS1 coil current decay. 58
Figure 9.3 – PS1 normal zone resistance. 58
Figure 9.4 – PS1 normal zone voltage. 59
Figure 9.5 – PS1 total resistive ($R_{coil} + R_{dump}$) voltage. 59
Figure 9.6 – PS Aluminum mandrel currents. 60
Figure 9.7 – PS1 hot spot temperature. 60
Figure 9.8 – PS mandrel temperatures. 61
Figure 9.9 – PS1 maximum axial compression at 2 s is 10.2 MPa. 61
Figure 9.10 – Coil axial stress after 38 s, showing 45.5 MPa relative to the cold state with no Lorentz load. 62
Figure 9.11 – TS1 current. 63
Figure 9.12 – TS1 normal zone resistance. 64
Figure 9.13 – TS1 normal zone voltage. 64
Figure 9.14 – TS1 total resistive ($R_{coil} + R_{dump}$) voltage. 65
Figure 9.15 – TS1 hot spot temperature. 65
Figure 9.16 – TS3u coil with cable only, current vs. time. 66

Figure 9.17 – TS3u coil with cable only, normal zone resistance. 67
Figure 9.18 – TS3u coil with cable only, normal zone voltage. 67
Figure 9.19 – TS3u coil with cable only, total resistive ($R_{coil} + R_{dump}$) voltage. 68
Figure 9.20 – TS3u coil with cable only, hot spot temperature. 68
Figure 9.21 – DS current. 70
Figure 9.22 – DS normal zone resistance. 70
Figure 9.23 – DS normal zone voltage. 71
Figure 9.24 – DS total resistive ($R_{coil} + R_{dump}$) voltage. 71
Figure 9.25 – DS hot spot temperature. 72
Figure 9.26 – DS temperature distribution in first DS coil 40 s after quench. 73
Figure 9.27 – Shear stress in first DS coil at 40 s following quench. 74
Figure 11.1 – NIST Data - Oxygen Free Copper Tensile Properties (4-300K)- C10100 - C10700 Cold Worked 79
Figure 12.1 – The MECO Coil system. The Production Solenoid is at the left. 83
Figure 12.2 – Cutaway drawing of the PS as viewed from above. 84
Figure 12.3 – Production solenoid 3D model showing structural supports. 84
Figure 12.4 – Expanded Assembly View Showing Shell Stack-up for Vertical Assembly. The yellow "skirt" is an axisymmetric representation of flexure cold mass supports that were not used. 85
Figure 12.5 – Detail drawing of flange bolting. 86
Figure 12.6 – Local conductor Von Mises stress. Aluminum mandrels 1/2 coil build thick, No axial gap and 0.5mm radial gap, Run #prod14 87
Figure 12.7 – Final PS conductor cross-section chosen. The conductor is 32.3% of the volume. 88
Figure 12.8 – Conductor cross-section used in the structural calculations. The conductor is 28.6% of the volume. 88
Figure 12.9 – Conductor array model, showing coupling (at top) and load for vertical loading (radial winding pack direction). Vertical constraints (not shown) are applied to the lower edge. Two other cases of loads and constraints were modeled, three total, one for each direction of loading. 89
Figure 12.10 – Copper SX or axial winding pack direction. The "unit" load is 10^6 Newton on a 19.6×1 mm cross-section for a 51020 Pa average loading. The "primary" SX stress is about 66000Pa for a multiplier of 66000/51020=1.3. The multiplier for the peak SX stress is 103/51=2.02 90
Figure 12.11 – Copper SY or winding pack radial stress. The "unit" load is 10^6 N on a $2*37.9 \times 1$ mm area, for a 13192 Pa average stress. 90
Figure 12.12 – "Smeared" Coil SZ or hoop stress, model with aluminum external mandrel/support. Aluminum Mandrels are 1/2 coil build thick, No axial gap and 0.5mm radial gap, Run# prod14, Normal operating loads. 93
Figure 12.13 – "Smeared" coil SY or axial stress - Model with aluminum external mandrel/support. Aluminum mandrels are 1/2 coil build thick, No axial gap and 0.5mm radial gap, Run #prod14, Normal operating loads 94
Figure 12.14 – "Smeared" Coil Von Mises Stress - Model with aluminum external mandrel/support. The maximum Von Mises stress in this plot is 139. Aluminum mandrels are 1/2 coil build thick, No axial gap and 0.5mm radial gap, Run #prod14 94

Figure 12.15 – Aluminum Outer Shell/Mandrel Von Mises Stress - Aluminum Mandrels are 1/2 coil build thick, No axial gap and 0.5mm radial gap, Run #prod14 - Peak stress is 141 MPa. The allowable for 6061-T6 at 4K is 165 MPa 95
Figure 12.16 – Production Solenoid Mandrel showing He bubble vent grooves, and flange bolting. This is an aluminum 6061T6 forging with all surfaces machined. 96
Figure 12.17 – An earlier model of the outer shell Von Mises stress. 97
Figure 12.18 – Radial Displacements for the latest axisymmetric model. Mandrel Thickness = 1/2 Coil Build 99
Figure 12.19 – Axial Displacements for the latest axisymmetric model. Mandrel Thickness = 1/2 Coil Build 99
Figure 12.20 – The three dimensional Production Solenoid model. 100
Figure 12.21 – Reverse view of the three dimensional model. 100
Figure 12.22 – Present design for supporting PS axial loads toward the TS 101
Figure 12.23 – An adjustable axial support strut used in the production solenoid. The bellows allows final position adjustment when the magnet is cold, and when the cryostat is evacuated. Eight 2" schedule 40 pipes would be adequate. 102
Figure 12.24 – For a 2.5 inch schedule 40 pipe that is 30 inches long with pinned ends, the kL/r is around 30. For this kL/r loaded with 40,000 lbs the ratio of the applied stress to the AISC allowed buckling stress is 0.36 and the ratio of the applied stress to the membrane allowable is 23.5/62.2=0.38. A 2 inch schedule 40 pipe would also be OK with a ratio of applied stress to AISC allowable of about 0.65 103
Figure 12.25 – Temperature distribution in the cold mass support strut. 103
Figure 12.26 – Thermal stresses due to the temperature gradient along the strut and at the heat station. 104
Figure 12.27 – Cryostat Von Mises stress with five atmospheres external pressure, solved with a large displacement analysis to demonstrate structural stability at five times the nominal vacuum loading. 105
Figure 12.28 – First mode buckled shape with a multiplier of 9.03. The next two modes have multipliers of 9.36, and 9.457. 106
Figure 12.29 – Vertical Displacement of the assembly under pressure, cold mass and shield deadweight, Run#grav01. The end drops 1.7mm, probably too large a deflection to satisfy field quality requirement. Additional vertically oriented radius rods have been added at both ends of the production solenoid. 106
Figure 12.30 – Displacement of the cryostat shells under pressure and shield deadweight. The maximum displacement is mid span on the inner shell which supports the deadweight of the shield. , Run#grav01 107
Figure 12.31 – Von Mises stress in the cryostat shells. Vacuum and shield DW. The left-right variation results from a different gap density. The stresses are quite low. - Displacements may govern. 107
Figure 12.32 – Annular helium can shell model with pressure vectors. 109
Figure 12.33 – Vertical displacements of the Production Solenoid Helium can under Helium hydrostatic head. These are X displacements which is positive downward. The inner shell "floats" upward, and the lower shell is weighed down by the helium. These are trivial displacements, and the stresses to support the helium are also trivial, but this loading is imposed in addition to the quench pressure to see if there is any interaction with buckling modes. 109

Figure 12.34 – Production solenoid Helium can pressurized to three times the design pressure off five atmospheres plus the Helium hydrostatic head. A large displacement solution is used. The response of the 2cm thick inner shell is bounded – It does not buckle. 110
Figure 12.35 – Outer Helium Can Shell 10 inch Quench Vent Line. 3 inch wide reinforcement ring , Membrane Von Mises in psi. Smaller penetrations are also needed, and similar reinforcements will be needed at these locations as well..... 110
Figure 12.36 – Results of linear buckling analysis of the production solenoid helium can -Mode 1 111
Figure 12.37 – Lorenz Forces in the Axisymmetric model – TS energized 112
Figure 12.38 – Axisymmetric Model - 9 coils of the production solenoid are modeled. An additional 14 coils in the transport solenoid are included in the field and force calculation. These are “turned off” for the second load case. Plots of the models based on the use of internal mandrels are included with the discussion of the early results that used internal mandrels. 112
Figure 12.39 – Force distribution used in the 3D model..... 113
Figure 12.40 - Field vectors from the axisymmetric analysis. 113
Figure 12.41 – Inner shells in this model are all 5mm thick. Flanges are 1cm thick. Constraints were applied just to the right of P1 to model the cold mass support. .. 115
Figure 12.42 – Second Generation of Internal Mandrel Model, with reinforcements added to P1 and the thin coils , p2 and p8, Used in Run # prod02. 115
Figure 13.1 – TS structural model with mid-span radial support heavy shells/frames carry the net loads to the foundation. The model shows the horizontal Vee support at the beryllium window end of the TS and the vertical Vee support that clears the proton beam at the production solenoid end. The model includes one of the collimators and associated cryostat components, but most of the cryostat shells are not modeled.. 118
Figure 13.2 – Model with channel showing mandrel and cold mass support arrangement. This support rod configuration allows stress free cool-down. Support rods take compression as well as tension aid..... 119
Figure 13.3 – Horizontal “Vee” (below) and mid-span tension-only support (above).. 120
Figure 13.4 –Model coordinate system. 122
Figure 13.5 – UX Displacement at the Be Window end - Normal operating CD and deadweight (DW), Run#6, set,4. Displacements range from -.0056 to -.000455 m123
Figure 13.6 – UZ Displacement at the Be Window end - Normal operating CD and DW, Run#6, set,4 Displacements range from -.0035 to +.0024 m..... 124
Figure 13.7 – Displacements from Run#10 - "Final": Support Arrangement (Not Yet Tabulated)..... 125
Figure 13.8 – UZ displacements at cool-down. At the end nearest the angled rods, the axial contraction is 7 mm, Run#5..... 127
Figure 13.9 – Displacements from Run#10 - "Final": Support Arrangement (Not Tabulated)..... 128
Figure 13.10 – Single mandrel and coil. Gap elements are used at the interface between the coil and mandrel 130
Figure 13.11 – Crescent vs. wedge spacers. Both concepts were explored, but the final choice was to incorporate the wedge shapes into the side flanges of the bent sections 131

Figure 13.12 – Case and support rod model segment before reflection. 132
Figure 13.13 – Normal operating loads on the 3D model, looking down. Load vectors near the ends rotate toward the center of the elbow when the neighboring coil systems are turned off. 133
Figure 13.14 – TS Lorentz forces near Production Solenoid (left) and beryllium window (right). 135
Figure 13.15 – Single coil module (cryostat section shown removed) radius rods are assumed as a cold mass support. 137
Figure 13.16 – Von Mises stresses, for normal operating loads, with the early "one-sided" flange bolting which allowed prying of the flanges, and the compound curvature channels. 139
Figure 13.17 – A sequential bolted assembly scheme was required for a pool-cooled design. Access with a hex key through the neighboring flange was necessary. The present conduction-cooled design eliminates the tight fitting He can and allows for a much simpler assembly with full access to the bolting in the bore. 141
Figure 13.18 – Coil Von Mises stress with the early "one-sided" flange bolting that allowed prying of the flanges. 141
Figure 13.19 – Cooldown displacements of the "Over-Constrained" configuration with a rod pair at each end of the elbow - Note the vertical tower deflections indicating the coil contraction effects 142
Figure 13.20 – An early "over-constrained" support concept, with a pair of angled support rods in the middle of the elbow and channels with compound curvature .. 143
Figure 13.21 – The conductor cross-section used as a basis for stress calculations. The conductor is 28.6% of the volume. 144
Figure 13.22 – Final TS conductor cross-section chosen. The conductor is 48.4 % of the volume. 144
Figure 13.23 – Single coil axisymmetric analysis shown with axisymmetric and XZ plane reflection symmetry expansions. The maximum "smeared" Von Mises stress is 39.2 MPa. 145
Figure 13.24 – Results of post-processing the axisymmetric model of a single coil based on multipliers from [3]. 146
Figure 13.25 – TS coil stresses in straight section coils near the Production Solenoid - local conductor Von Mises stress. 147
Figure 13.26 – Axisymmetric analysis of the coils near the Be Window. -"smeared" Von Mises stress (no conductor multipliers). 148
Figure 13.27 – Coil "smeared" Von Mises stress Run#6, no channel reinforcement. 149
Figure 13.28 – Coil Von Mises stress with the tension-only mid span support. Local coil stresses are less than 113 MPa, peaking where the vertical pair of struts is connected to only one mandrel flange. Stresses are better than for the model below, which does not have the mid-span support. 149
Figure 13.29 – Coil Von Mises stresses - No channel reinforcement Run#6. Note higher stress where the rod pair connects to the mandrel. The red contour ranges from 152 to 170 MPa. This local effect will have to be improved with local gussets, using the channel, or with an additional mid-span support as used in the model on top of the page. 149

Figure 13.30 – Transport Solenoid structural model shown with some cryostat shells removed, and the "Final" conceptual design for the supports. The horizontal "Vee" is at the beryllium window end of the coil. 150
Figure 13.31 – Six struts restrain the six DOF of a rigid body [4] 151
Figure 13.32 – Horizontal "Vee" and clevis support plate. 151
Figure 13.33 – A view of the vertical “vee” support that clears the proton beam. The structural model shown in Figure 13.30 does not include the cryostat outer shell. 152
Figure 13.34 – Tension and compression strut concept used in horizontal and vertical "Vee" supports. 152
Figure 13.35 – Tension-Only Design - This is the concept proposed for the mid-span support. 153
Figure 13.36 – Von Mises Stress in the early model of the strut. Note that the variations in the stress are due to bending. The design of the strut employs spherical rod ends and spherical washers to ensure only direct tension or compression is taken by the rods. 153
Figure 13.37 – For comparison, C-Mod's Drawbar holds 500,000 lbs - 2000 PSFC web photo. 154
Figure 13.38 – Gap produced in mid-span support strut on cool-down. 155
Figure 13.39 – Stresses in the "horizontal Vee" support during normal operating loads. 155
Figure 13.40 – Note that the centerline of the ¾” attachment bolts has been shifted ½ of a mandrel width to eliminate the bolt access problems under the clevis. Also under this plate is a copper plate that serves as the 4K shunt to the LHe piping on top of the coil assembly. 156
Figure 13.41 – Stresses in the mid-span support rod and clevis details. 157
Figure 13.42 – Thermal conduction solution. The concern was that the thickness of the rod was such that the nitrogen temperature would not get beyond the skin and the 2-inch diameter portion of the rod would have higher temperatures than 80 K. 158
Figure 13.43 – Von Mises stress near the nitrogen intercept. This result includes the effects of the thermal gradient. The brown contour is 200 MPa. 159
Figure 13.44 – The Vertical Rod is stressed to an average of no more that 40 MPa. The vertical rod load is then $40\times 10^6 \times 0.001197 \times 0.2248$ =10780 lbs 160
Figure 13.45 – Bolted mandrel design 161
Figure 13.46 - For sizing the bolts, the direct mandrel tension resulting from bending of the TS is assumed to be transmitted directly into the lower flange bolt. For the bolts, this is conservative, The upper flange bolt will contribute some, and will carry the offset moment. This sketch shows the elbow inner radius equatorial plane tensile load. 162
Figure 13.47 - Installing inner copper shells prior to winding. This is a mandrel at the curve/straight transition 162
Figure 13.48 – The bolts have been removed from this model to show the prying action - the large gap in the flange-to-flange "contact" results from an interference used to preload the bolts. 164
Figure 13.49 – Maximum principal tensile stress - Bolting on the "blue side" can have twice the spacing. 164
Figure 13.50 – Mandrel stresses, deadweight only 165

Figure 13.51 – Cooldown Von Mises Stresses in the Mandrel. Some of the mandrel stress shown here results from an interference artificially imposed between the coil and mandrel to numerically stabilize the model. 166
Figure 13.52 – Vertical displacements of the collimator. Sag at the collimator end is about 1/3 mm. This appears to be small but the inner cryostat shell will have to carry it's own deadweight and that of the collimator, with only support at it's ends. The model with the full bore tube and collimators at each end produced sag of 1.4 mm 168
Figure 13.53 – Von Mises in the cryostat with the collimator loading ~200 MPa peak, and results from strain compatible stresses from the frame (Figure 13.54). The outer shell is modeled as 1 cm thick, or twice as thick as those sections of the outer cryostat that connect the support frames. The annular end plate at the right in this plot is 5 cm thick, and even though it is lightly stressed, it needs to be stiff to resist the collimator rotations..... 169
Figure 13.54 – TS support frame stress, normal operating loading. In this plot, the red contour is 360 MPa, the yellow contour is 240 MPa. The plate thickness used in this model is 2 cm. Rigidity is required of these frames as much as adequate stress. The lower support baseplate is 1 m below the beam centerline. 170
Figure 13.55 – Model of inner bore tube and collimators, supported by the outer cryostat extensions – lower half of model with pressure vectors. 171
Figure 13.56 – Model of inner bore tube and collimators, supported by the outer cryostat extensions – lower half of model. 171
Figure 13.57 - Von Mises stress in the 1 cm thick cryostat end cap at the Be window end. The model is evaluating the impact of the collimator loads on the end cap with the effect of the curved bore tube included. 172
Figure 13.58 – Vertical displacements of the inner bore tube under its own deadweight and that of the collimators at each end. The collimators are shown removed for clarity..... 172
Figure 13.59 – The first buckling mode shape. TS outer cryostat sections. 173
Figure 13.60 – Von Mises Stress, large displacement solution. Five atmospheres external pressure. 5mm shell. 174
Figure 14.1 - Detector Solenoid in its Iron Return Frame 175
Figure 14.2 – Lorentz Forces from axisymmetric model, fields computed without iron. 175
Figure 14.3 – Coarse mesh magnetic model 177
Figure 14.4 – Current density..... 178
Figure 14.5 – Axisymmetric field plot..... 178
Figure 14.6 – Magnet Lorentz forces from the non-linear model with iron. Non-axisymetry is small and not evident in this plot, nor is it significant structurally... 179
Figure 14.7 – Axial stress from the axisymmetric model - A symmetry expansion is used to visualize the half section of the coil. Maximum compression is 41 MPa. 180
Figure 14.8 – Hoop stress in the axisymmetric model. The maximum value is 50.2 MPa. 180
Figure 14.9 – Conductor cross-section used in the stress analysis. The final conductor cross section differs from this. The conductor is 28.6% of the volume. 181

Figure 14.10 – Final DS conductor cross-section chosen. The conductor is 48.4% of the volume. 181
Figure 14.11 – Conductor stress with original multipliers, first five coils from the high field end. Note that the coil at left has been split into two coils to mitigate the quench behavior. A hot spot in the middle of this coil produced a non-uniform radial expansion that then caused axial bending stresses. 182
Figure 14.12 – Vertical displacement under gravity load. Maximum sag is at the bottom and is -0.8 mm. 1/2 Vol = 0.927 m^3 183
Figure 14.13 – In Radovinsky's model [7] X points down from the symmetry plane of the MECO magnet system, Y is along the axis of the DS, and Y complements XZ. dZ is the offset between the axis of the iron box, and the axis the coils of the DS in the equatorial plane. 184
Figure 14.14 – Detector solenoid vertical hanger rod connected via a clevis to extensions of the mandrel flanges. The other end (not shown) is supported by a tower that is integral with the cryostat. 185
Figure 14.15 – Buckling evaluation of strut. Black curve shows the ratio of actual axial stress divided by AISC allowable, giving ~0.15, implying a factor of safety of 6.6. 186
Figure 14.16 – Adjustable axial support strut used in both the production and detector solenoid. 187
Figure 14.17 – Vertical support rod attachments to the DS mandrels from the CDR drawingsl. 188
Figure 14.18 – Model end pole. The model assumes symmetry at mid-length of the detector solenoid, and about horizontal and vertical planes. Shown is an up-down symmetry expansion. 189
Figure 14.19 – End pole field. MECO has not decided if the addition of the end pole is needed. 190
Figure 14.20 – Field Contours at 1 m upstream from the end of the bore of the solenoid. Without increasing the current in the end coils, the field drops off to 0.65 T at the end of the solenoid 191
Figure 14.21 – Field contours at 1 m from the end of the bore of the solenoid. 192
Figure 14.22 – Von Mises Stress in the DS with a 1% square lobed load variation 193
Figure 14.23 – Fields near the end pole piece/shield. 194
Figure 14.24 – Inner vessel wall, first mode buckling shape, deadweight load vector. The load multiplier in this linear Eigenvalue solution is 387. The second mode is similar, and has a similar multiplier. The third mode has a multiplier of 432. The linear analysis shows a large margin against buckling, but relies on end circular constraint. 195
Figure 14.25 – Non-Converged Large displacement solution with ends held circular but free to displace axially. Greater than 150 times the gravity load. 196
Figure 14.26 – Mode 3 Shape 197
Figure 14.27 – Von Mises stress and deflected shape for the DS inner cryostat shell. .. 198
Figure 15.1 – A schematic cross section of the conduction cooling method proposed for the DS and TS. The drawing is not to scale. 205
Figure 15.2 – A conceptual top view of a TS or DS coil segment. The 4 K cooling loop is shown brazed in position to the thermal bridge. The drawing is not to scale. 206

Figure 15.3 – Mounting scheme for the helium cooling tubes to the thermal bridge. The copper cooling tube is brazed to the copper saddle that is brazed to the copper bridge. (Not to scale.) 207
Figure 15.4 – Contour plot of the expected temperature distribution for the worst case coil in the DS. 208
Figure 15.5 – Conceptual drawing for cooling of short sections of the TS coil. Do not scale. 209
Figure 15.6 – Configuration of the 2D model used to calculate the temperature distribution in the coil windings and the aluminum mandrel. The vertical direction corresponds to the axial direction in the PS coil, the horizontal corresponds to the radial direction. The bore of the magnet is in the right hand direction. Do not scale. 210
Figure 15.7 – Temperature distribution in the PS 1 coil with the radiation heat load. Violet corresponds to a temperature 4.5 K and red to 4.57 K. Labels on the temperature contours are in degrees Kelvin. 211
Figure 15.8 – Contour plot of the change in the temperature distribution in the PS 1 solenoid due to the presence of a 15 cm wide bubble on the inner surface of the coil. Temperature labels are in degrees Kelvin. 212
Figure 15.9 – The proposed vent line for the PS cryostat. 214
Figure 15.10 – Pressure versus time for an "all coil" quench in the PS solenoid for three different diameter safety pipes. 215
Figure 15.11 – Helium flow sheet for TSu, TSd, and DS cryostats and valve box 220
Figure 15.12 – Helium flow sheet for control dewar and valve box 221
Figure 15.13 – Helium flow sheet for PS cryostat and dewar 222
Figure 15.14 – Helium flow sheet for liquefier/Refrigerator and Cool-Down Heat Exchanger. 223
Figure 15.15 – Normal steady operation: Helium flow sheet for TSu, TSd, and DS cryostats and valve box. 224
Figure 15.16 – Normal steady operation: Helium flow sheet for control dewar and valve box. 225
Figure 15.17 – Normal steady operation: Helium flow sheet for PS cryostat and dewar. 226
Figure 15.18 – Normal steady operation: Helium flow sheet for liquefier/Refrigerator and Cool-Down Heat Exchange. 228
Figure 16.1 – Production Solenoid and it's cryostat; the transport solenoids - the break in the TS assemblies is in the middle of the "S", at the Berylium window, and the detector solenoid. 229
Figure 16.2 – Mid-plane section of the magnet assembly 230
Figure 16.3 – The Production Solenoid assembly. 230
Figure 16.4 – Winding the LDX Floating Coil. The pancake on the left has been wound and is being held with the wooden clamp. This leaves both terminations at the coil OD. The remaining turns are layer wound. 231
Figure 16.5 – The LDX floating coil taping head 232
Figure 16.6 – Stainless steel coil form being machined on the King Vertical Boring Mill 62" Table (internet photo from an unknown project) http://www.metweld.com/machine.html 232

Figure 16.7 – Production Solenoid mandrel showing He bubble vent grooves, and flange bolting. This is an aluminum 6061T6 forging with all surfaces machined. 233
Figure 16.8 – Production Solenoid axial support concept using eight axial columns. ... 234
Figure 16.9 – The coil lead end break-outs fit a slot in the flanges, and allow access from the outer helium can volume. 235
Figure 16.10 – Bolted mandrel assembly detail. Waffle cooling channels and helium vent grooves are not shown. 236
Figure 16.11 – Expanded Assembly View - Yellow "skirt" is an axisymmetric representation of flexure cold mass supports. 237
Figure 16.12 – Illustrates the support and compression struts for the PS. 238
Figure 16.13 – Vertical section of the PS assembly. 239
Figure 16.14 – Production Solenoid Support Strut 240
Figure 16.15 – Detail of the spherical ball-end connection. 240
Figure 16.16 – JDB-1 strong brass bearing (http://www.sf-bearing.com/e-jdb.htm). Made in China. 241
Figure 16.17 – DuPont TriLok™ metallic supported composites fiberglass PTFE cloth-lined metal. 241
Figure 16.18 – Radiation resistance of Aurum (http://www.mitsuichemicals.com/spep/aurum/ch10.htm) 242
Figure 16.19 – TS mandrel inner shell - 1/4 inch plate. 243
Figure 16.20 – Adding the flat flange that mates up with the straight section of coil segments. 243
Figure 16.21 – Adding the wedge plate that begins the curved array of coils. 244
Figure 16.22 – Installing inner copper shells prior to winding 244
Figure 16.23 – Winding of the LDX Floating Coil. Very similar to winding the MECO TS coils. The winding mandrel becomes part of the TS structure. 245
Figure 16.24 – Installing the outer copper shells. 246
Figure 16.25 – Installing the copper conduction bars. These thermally connect the winding through the inner and outer shells with the closed loop Helium cooling pipes. 246
Figure 16.26 – TS bolted assembly scheme. 247
Figure 16.27 – Elbow dimensioning. 248
Figure 16.28 – Installation of the bore tube in the TS bend sections. 249
Figure 16.29 – A conceptual top view of a TS or DS coil segment. The 4 K cooling loop is shown brazed in position to the thermal bridge. The drawing is not to scale. 250
Figure 16.30 – Split cryostat concept. 251
Figure 16.31 – Horizontal "Vee" and Clevis support plate 251
Figure 16.32 – Vertical "Vee" near PS. 252
Figure 16.33 – Split casing with pins and lip seal. This can be nibbled or sheared off for disassembly. 253
Figure 16.34 – TS interface at the Be Window. The magnets are not shown. 253
Figure 16.35 – Support strut end. 254
Figure 16.36 – Adjustment detail at the end of the strut. Bellows maintains vacuum during adjustment. 254
Figure 16.37 – Inserting the collimator into the TS straight sections. 255
Figure 16.38 – Sketch of a handling frame to support the collimator during rigging. 255

Figure 16.39 – Arrangement of Detector Solenoid support rods. 256
Figure 16.40 – Niles Vertical Lathe 240" dia x 198" (http://www.demmercorp.com/equpment/evt0001.htm) 257
Figure 16.41 – Vertical support attachment detail. 257
Figure 17.1 – An overview of the MECO experiment. 258
Figure 17.2 – Production Solenoid and it's cryostat, the transport solenoids (the break in the TS assemblies is in the middle of the "S", at the Berylium window), and the detector solenoid. The TS and DS are shown without their cryostats. 259
Figure 17.3 – Mid-plane section of the magnet assembly 260
Figure 17.4 – General Arrangement of the MECO Experimental area. Grid lines are on 200-inch centers. Receipt overhead doors are at the right. 261
Figure 17.5 - Envelope dimensions of the individual cryostats 263
Figure 17.6 – The base pedestal for the magnet system 264
Figure 17.7 – Forces and Moments Sum to Zero Production Solenoid Net Axial Load is 1.49 MN, or 334,755.8 Lbs Detector Solenoid Net Axial Load .5076 MN, or 114,120 Lbs 265
Figure 17.8 – Axial view of the Detector Solenoid, its cryostat, and the iron cosmic ray shielding. 266
Figure 17.9 – Transport Solenoid embedment loads 267
Figure 17.10 – Coordinate system used for the TS bend sections. 267
Figure 17.11 – Arrangement of the support pads for the TS bend sections. 268
Figure 17.12 – Collimators are slid in the TS bore at each end of each TS, at the Be window ends. 269
Figure 17.13 – Collimator handling frame. 269
Figure 17.14 – Use of Hillman rollers is one way of solving the 40 Ton crane limit. These rollers are for moving from 1 to 200 tons on hard level floor surfaces without a track (http://www.hilmanrollers.com/C1.htm). 270
Figure 17.15 – PS external support structure. 270
Figure 17.16 – Vertical Displacement of the cryostat shells under pressure and shield deadweight. The maximum displacement is mid span on the inner shell which supports the deadweight of the shield. Run#grav01 271
Figure 17.17 – Alternative Target/Shield installation procedure. 272
Figure 17.18 – Vacuum boundary between PS bore and TS bore. 272
Figure 17.19 – PS power lead and helium transfer line assembly, dewar, and valve box. 273
Figure 17.20 – PS quench vent assembly 273
Figure 17.21 – Cryogenic control dewar and valve box. 274
Figure 17.22 – TS cryogenic system components. 274
Figure 17.23 – Typical cryogenic conduit joint. The LN2 shield includes a supply line (not shown). 275
Figure 17.24 – 1/2 in Helium line with 2 inch vacuum jacket can be factory fabricated with 6 inch bends. Smaller radii are achieved with a mitered cut on the vacuum jacket. 276

List of Tables

Table 1.1 – Component Mass Summary 2
Table 1.2 – MECO memoranda referenced by CDR section. 3
Table 2.1 – Production Solenoid nuclear heating loads to 4.5K cold mass 8
Table 3.1 – Field specification characteristics 13
Table 3.2 – Coil parameter definitions 18
Table 3.3 – The inductance matrix by power supplies 21
Table 3.4 – Coils grouped by power supplies 21
Table 3.5 – B-H values for the 1010 iron used in the analyses 25
Table 4.1 – SSC Inner and Outer Cable properties. 28
Table 4.2 – $T_c(B)$ and $J_c(B,T)$ fit parameters for SSC Inner and Outer Cable 28
Table 4.3 – Average non-copper area 30
Table 4.4 – Conductor parameter summary 34
Table 5.1 – Turn to turn voltages in MECO Coils 35
Table 5.2 – Comparative gas evolution rates of epoxy resins with anhydride and amine curing agents (see footnote 5 for credit) (cm^3g^{-1} MGy^{-1}). 38
Table 6.1 – Best and worst case assumptions used in the calculations 40
Table 6.2 – Joint analysis model. 41
Table 7.1 – Coil operating currents 43
Table 8.1 – Number of voltage taps and pin connection for quench detection 48
Table 9.1 – Quench parameters for all coil sets 56
Table 9.2 – Quench protection analysis results for all coils evaluated 57
Table 10.1 – Coil Set Inductance, Operating Current and Minimum Charging Rate. 76
Table 10.2 – Nominal dump resistors, L/R time constants and stored energy including coupling. 76
Table 10.3 – 6-pulse power supply design calculations. 77
Table 10.4 – 12-pulse power supply design calculations. 77
Table 11.1 – Properties of Variants of Copper 79
Table 11.2 – Insulating Material Strengths. 80
Table 11.3 – Modulus of Elasticity for G-10 at several temperatures. 80
Table 11.4 – Tensile Properties for Stainless Steels and Aluminum. 81
Table 11.5 – Coil structure cryogenic (292 K) maximum allowable stresses, Sm = lesser of 1/3 ultimate or 2/3 yield, and bending allowable=1.5*Sm 81
Table 11.6 – Coil Structure cryogenic (80 K) maximum allowable stresses, Sm = lesser of 1/3 ultimate or 2/3 yield, and bending allowable=1.5*Sm 81
Table 11.7 – Coil Structure Cryogenic (4 K) Maximum Allowable Stresses, Sm = lesser of 1/3 ultimate or 2/3 yield, and bending allowable=1.5*Sm 82
Table 11.8 – Inconel 718 Tensile data (hardening for 1 hr. at the most favorable temperature, either 1750 or 1950 F from [3]) 82
Table 12.1 – G-10 Temperature Dependent Moduli 89
Table 12.2 – Modulus calculations based on the conductor array calculations 90
Table 12.3 – Conductor multipliers 91
Table 12.4 – Estimates of Coil and Mandrel Hoop Stresses for zero initial assembly gap between the coil and mandrel. Mandrel thickness is 1/2 the coil build. 92

Table 12.5 – Estimates of Coil and Mandrel Stresses for .5mm initial assembly gap between the coil and mandrel. Mandrel thickness is 1/2 the coil build. 92
Table 12.6 – Production solenoid coil segment stresses, Run #prod14, Conductor E=110 GPa, TS On , Net axial load = 194630 N/rad or 137 ton total for the Coil, Normal operating loads. 93
Table 12.7 – Mandrel Bending, and Bolt tensile stress, Mandrels are ½ the coil thickness 98
Table 12.8 – Cold mass support summary. 102
Table 12.9 – Production solenoid cryostat stess and displacement summary..... 105
Table 12.10 – Production solenoid model weights 108
Table 12.11 – Helium can buckled mode load multipliers 111
Table 12.12 – Model run log..... 114
Table 12.13 – Model Outer Mandrel Thicknesses (cm)..... 114
Table 12.14 – Coil Build and Currents [4]..... 115
Table 13.1 – Summary of stress analysis results for the TS magnet..... 121
Table 13.2 – Summary of TS system displacements for various load cases. Normal loading is with all systems, PS, TS, and DS energized. 123
Table 13.3 – Displacements of center of TS Elbow..... 123
Table 13.4 – TS dimensions. 132
Table 13.5 – Run log for the large 3D model..... 133
Table 13.6 – Run log for the axisymmetric models. 134
Table 13.7 – Axisymmetric model build and currents near the Be window. 134
Table 13.8 - Possible Bolting Options and Stresses..... 163
Table 14.1 – Forces on the DS as a function of the lateral offset, dZ from [7]. Coordinates are defined in Figure 14.13 above. 184
Table 14.2 – Outer Shell Load Multipliers from the Linear Buckling Analysis..... 196
Table 15.1 – State properties for steady operation of the cryogenic system..... 203
Table 15.2 – Heat loads for the 4.5 K system for steady state operation with the beam on 204
Table 15.3 – Worst case dimensions for conduction cooling in the DS and TS solenoids. 207
Table 15.4 – Heat loads for the liquid nitrogen system for steady operation 216
Table 15.5 – Estimate of cooldown times for three different cases. 218
Table 16.1 – Properties of candidate bearing materials. 241
Table 16.2 – Elbow dimensions for each bend pipe section in the TS. 248
Table 16.3 – Elbow pipe availability information from the Shaw Group Inc..... 248
Table 16.4 – Additional pipe information from The Shaw Group, Inc..... 249
Table 17.1 – Approximate dimensions of installation assemblies. Figure 17.5 shows the dimensions to which the tabulations correspond.) 262
Table 17.2 – Normal operating reaction forces. The coordinate system is shown in Figure 17.10, and the pad arrangement is illustrated in Figure 17.11. 268
Table 18.1 -MECO furnished services..... 279
Table 18.2 – MECO furnished hardware 279
Table 18.3 - SMS Ramp and Quench Test Currents and other parameters. 287
Table 18.4 – Nominal operating currents for each coil set. 288
Table 18.5 – List of tests to perform during subsystem fabrication and assembly. 295

Table 18.6 – List of tests to conduct during system assembly. 296

Section 1 - Introduction and Summary

The Muon-Electron Conversion Experiment (MECO) seeks to detect direct muon to electron conversion, and thus provide evidence for a process that violates muon and electron lepton number conservation and that cannot be explained by the Standard Model of particle physics. The experiment is to be installed at Brookhaven National Laboratory (BNL). A high energy proton beam is directed onto a heavy target inside the 4 m active field length by 1.5 m diameter bore of the Production Solenoid (PS), producing pions. A fraction of the muons resulting from pion decay are captured in the PS and in a 0.5 m bore diameter Transport Solenoid (TS), which is S-shaped with an axial length of about 13 m and which provides sign and momentum selection with collimators. The muons are brought to rest in a stopping target inside the 10 m long by 1.9 m bore Detector Solenoid (DS). The magnetic field on the axis of the system is carefully designed to monotonically decrease in a specified profile from 5 T at the high end of the PS to 1 T in the detector region of the DS. In addition to a monotonic field gradient on axis, deviation of the field from the specified profile is also controlled to within 5% in the PS, 1% in the TS and to within 0.2% in the detector region of the DS. This report summarizes the conceptual design for the PS, TS, and DS magnet systems.

The magnet system is contained in four cryostats—PS, TS1, TS2, and DS. A scale drawing of the magnet system is included as Figure 1.1, and a labeled, 3-D rendering of the system is shown in Figure 1.2. The two TS cryostats are divided by a Beryllium window which serves to separate the upstream and downstream bore vacuum systems. The upstream TS cryostat (TS1) contains the series- connected TS1 and TS3u (TS3 upstream) coil sets, together labeled TS13u, located in the straight sections and the TS2 coil set located in the 90° bend. Similarly, the downstream TS cryostat (TS2) contains the series-connected TS3d (TS3 downstream) and TS5 straight-section coil sets, together labeled TS3d5, and the TS4 coil set in the second 90° bend. The PS coils are subjected to a nuclear heat load that could approach 190 W at 4.5 K, depending on the final proton beam target shield design chosen by the MECO project. The PS coils, therefore, are cooled with a combination of natural-convection and/or forced flow helium that is in direct contact with the ID and OD of the windings. The TS and DS coils are conduction cooled using thermal heat drains connected to helium tubing. The cryogenic system has been designed to facilitate the cooling of any cryostat while any of the others are either warm or cold.

Field matching is achieved in the conceptual design with a series of 94 individual solenoid windings each having a different number of ampere turns. Inner or outer NbTi cable inventory from the SSC project is planned for use in all magnets, with most conductor configurations requiring the cable be soldered into a half-hard copper channel to provide necessary quench protection. The conductor has been designed to a minimum temperature margin of 1.5 K in all coils. This criterion actually sets (limits) the PS operating current at 3500 A. The TS and DS operating currents are set either at 1500 or 4000 A based on the results of a current-placement-tolerance study described in more detail in the field matching section of this report. Soldered lap joints have been designed to interconnect the windings within each coil group, and still operate a temperature margin of at least 4.5 K.

Table 1.1 – Component Mass Summary

Component	PS (kg)	TSu (kg)	TSd (kg)	DS (kg)
SSC cable	4,844	1,034	782	1,700
Conductor including cable	18,409	3,756	2,839	7,980
Mandrels[1]	5,398	10,532	10,418	5,470
Copper shields, ribs + bridges	N/A	1,147	1,147	520
He can	8,760	N/A	N/A	N/A
LN shield	1,209	666	666	5,720
Vacuum can[2]	13,539	9,977	9,977	28,123
Gravity supports[2]	3,245			3,245
Support rods	2,063	2,760	2,760	1,869
Total	52,624	28,838	27,807	52,926

Notes:
1. Al shells for PS, stainless steel mandrels for TS + DS
2. Gravity support masses are included in the TSu and TSd vacuum can masses

Total stored energy in the magnet system is approximately 150 MJ, with the PS magnet comprising 109 MJ of the total. A quench detection and protection system is required for all coils and is described in detail in this report. When a quench is detected, associated magnet energy is dumped through an external dump resistor sized to remove the stored energy, limit the coil hot-spot temperature to 150 K, and limit dump voltages to less than 2 kV. To prevent over-current in the TS coils when either the PS or DS is dumped, the TS must be simultaneously dumped. Simultaneous dumping of the PS or DS with the dumping of another quenching coil is not required. The PS cryostat contains about 6700 liters of helium, which will all be lost to atmosphere if the PS quenches. Because the TS and DS are conduction-cooled, a quench in either of these results in the loss of a minimum amount of helium.

The MECO magnet system will operate with six power supplies, one for each of the six coil sets: PS, TS13u, TS2, TS3d5, TS4, and DS. The power supplies are designed to ramp the coils to full current in one hour. In this conceptual design, the supplies are also required to provide a reverse voltage capability, which enables a slow discharge of each of the six coil sets in under one hour.

Structural designs have been completed for all magnet systems. The PS coils employ aluminum shells to contain the hoop and axial loads of the winding. The TS and DS coils are self-supporting to their Lorentz loads, but have internal mandrels to facilitate gravity and overall axial support. Axial and gravity loads are carried in all cryostats by spherical rod-end rods that serve as cold to warm supports and also accommodate the motions associated with cooldown. The PS and DS coils are designed to contract axially toward the TS, and the two TS cryostats are designed such that their coils contract axially toward the central Be window. Final adjustment of the rod nuts when the coils are cold, and following magnetic surveying during installation, will ensure that the coils are properly positioned for operation. The magnet system has been designed structurally to enable any or all coil systems to be powered at once.

The magnet system has been designed with several interface constraints in mind. Some of these require further definition or finalization by the MECO project. Magnet interfaces are described in more detail in that section of the report.

The contents of this report are intended to stand-alone and are self-contained. However, in some cases, MECO memoranda are referenced for further details. These memoranda are listed in Table 1.2 by the sections in which they are referenced. The referenced memoranda are included as Appendices with the CDR for completeness.

Table 1.2 – MECO memoranda referenced by CDR section.

	Section	References
1	Introduction	
2	Interfaces	[mm040]
3	Field Specifications and Field Matching	[mm005] [mm030] [mm032] [mm040]
4	Conductor Design	[mm038]
5	Insulation Design	
6	Conductor Joint Design	[mm048]
7	Current Lead and Bus Bar Design	
8	Quench Detection	
9	Quench Protection	[mm043]
10	Power Supplies and Dump Resistors	
11	Structural Design Criteria	
12	Production Solenoid Structural Design	
13	Transport Solenoid Structural Design	
14	Detector Solenoid Structural Design	
15	Cryogenic System Design	[mm038] [mm039]
16	Assembly Plan	
17	Installation Plan	
18	Draft Test Plan	

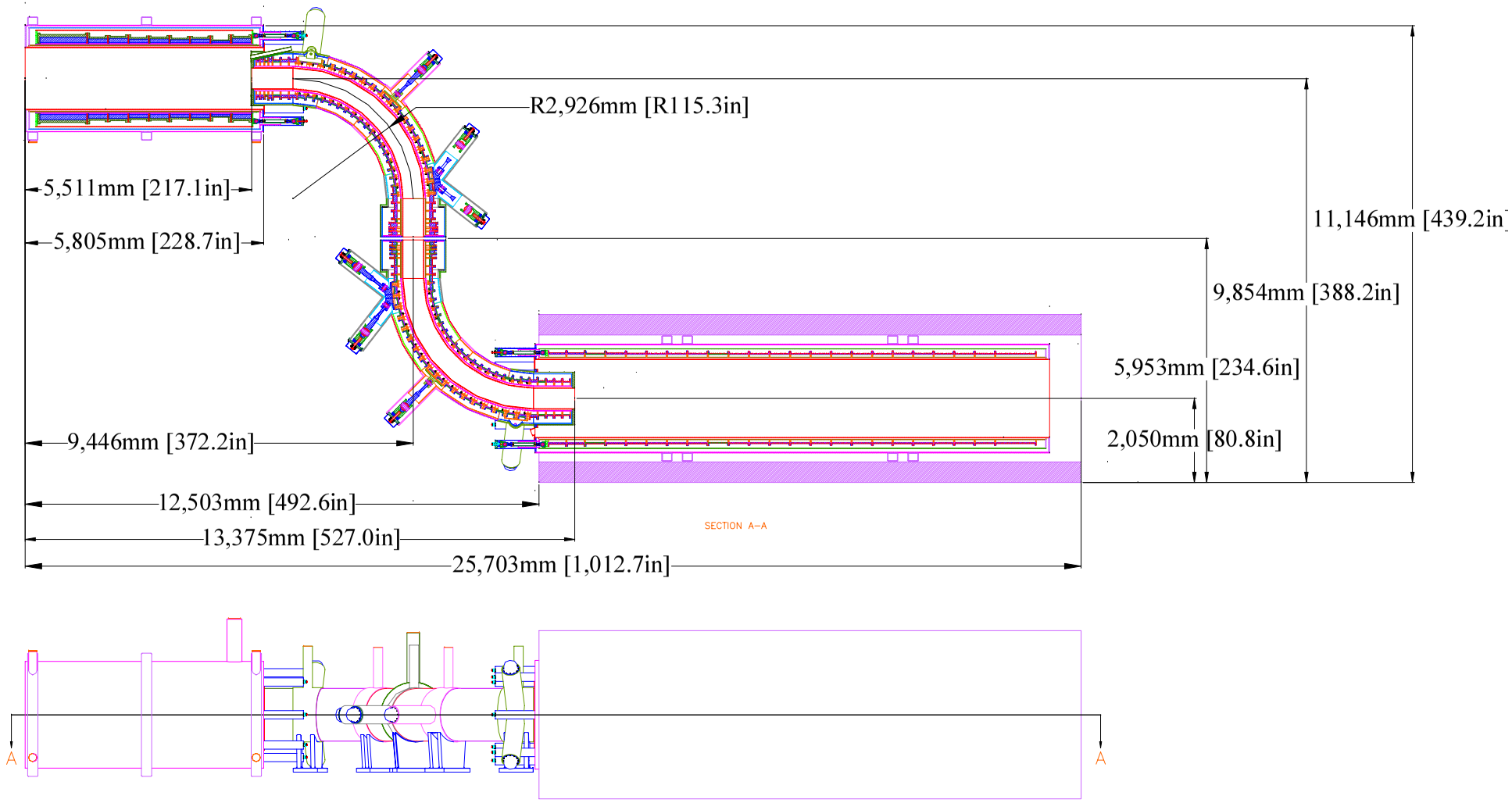

Figure 1.1 – The layout of the MECO Magnet system

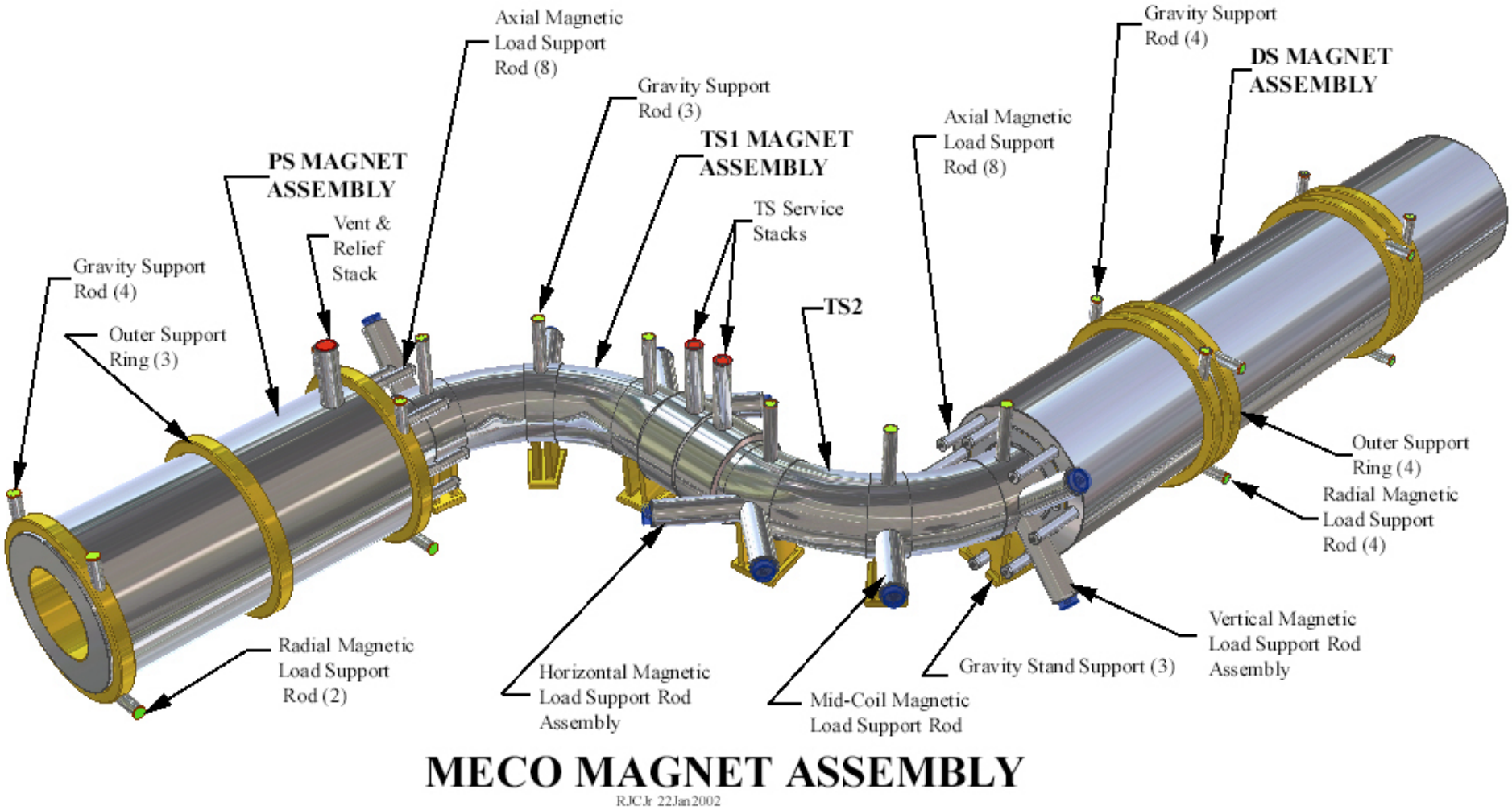

Figure 1.2 – Persepective view of the assembled MECO Magnet System

Section 2 - Interfaces

At the time of writing this CDR, several of the project interfaces are in the process of further definition. Interfaces to the MECO magnets are discussed here to the extent they are currently known.

PS Shield and Clear Bore Vacuum

The bore of the production solenoid will have a vacuum vessel containing the production target and a massive heat and radiation shield, neither of which are part of the magnet CDR effort. These will be supported off a non-magnetic strongback with an outer diameter of 150 cm. Preliminary analysis indicates that the shield may be supported off the PS cryostat itself, if there are operational or maintenance advantages to this arrangement. The strongback will also serve as a vacuum vessel for the bore of the PS. This vacuum vessel will mate to the transport solenoid cryostat, the inner wall of which will serve as the vacuum vessel in the transport solenoid bore. The TS design has made provisions for mating of the cryostat end wall to the PS bore vacuum to provide a continuous vacuum vessel connecting the bores of the PS and TS. The PS surrounds the strongback, but is provided with its own gravity support system, independent of the strongback. Based on the UCI spreadsheet *new7coldmassb.xls*, the maximum nuclear heat load density to the PS is about 20 μW/g during a 0.5 s beam pulse or half of that averaged over the 50% beam duty cycle. The UCI spreadsheet has been used for all calculations of nuclear heating in this document, although the final design of the shield is still underway within the MECO project.

Incoming Proton Beam

Provisions have been made in the conceptual design to accommodate the proton beam tube that enters the magnet region in the zone between the TS and PS. These details are visible in the conceptual design drawings, a portion of which is shown below for convenience.

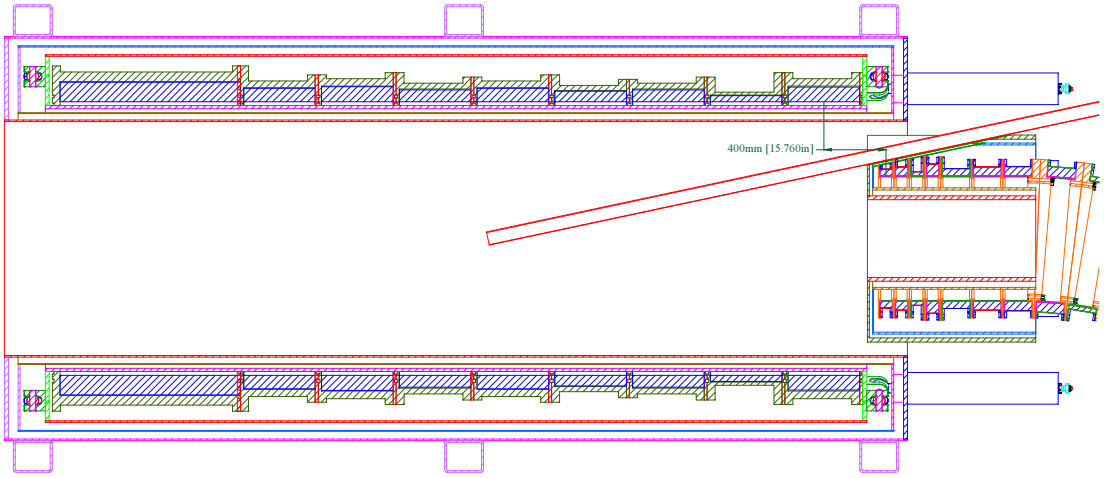

Figure 2.1 – Proton beam interface

The proton beam enters the PS in a horizontal plane. The tube is shown with an 80 mm ID and a 3.2 mm wall thickness. The centerline of the port projects to a point that is approximately 1590 mm to the right of z=0 relative to the field specification coordinates. The beam tube is presently shown at an angle of 210 mrad with respect to the PS axis. The MECO project has indicated that small changes in the approach angle of the beam tube relative to the PS axis are both acceptable and perhaps desirable so as to move the projected extension of the beam tube slightly further to the left relative to Figure 2.1, in an attempt to further reduce the nuclear heating effects in the PS. The beam tube approach angle may be reduced (and thereby moving the outlet further to the left in Figure 2.1) without changing the details of the intersection of the TS cryostat if the rotation point is taken as the right-most point (relative to Figure 2.1) at which the beam pipe intersects the TS cryostat. Details of this revised beam geometry must be coordinated with the MECO project during the final design activity.
Provisions have been made in the design of the TSu cryostat and TSu magnet design for the proton beam tube to penetrate the TSu cryostat and enter the experimental beam-line vacuum space within the bore of the PS cryostat.

Outgoing Proton Beam and Required Clear Bore Access

The outgoing proton beam will exit through a port interior to the strongback, which is outside the scope of the magnet CDR activity. The effect of the outgoing proton beam on the heat load is reflected in the UCI spreadsheet, new7coldmassb.xls, which has been taken as the reference heating condition for the CDR work. The PS cryostat and service ports shall not and do not extend inside the radius of the strongback, thus avoiding interference with the proton beam exit and access to the interior of the production solenoid clear bore.

Heat and Radiation Load on the Production Solenoid

Interactions of the proton beam with the production target will heat the target to approximately 2200 K; it will radiate about 5 kW of thermal radiation. Most of this will be absorbed by the cylindrical thermal shield consisting of some combination of copper, tungsten and/or depleted uranium. The heat shield will be maintained at ambient temperature by a special cooling system. At the time of writing the CDR, this shield is still under design by the MECO project.

Particle radiation is also produced, most of which is also absorbed in the thermal shield; the thickness of this shield is chosen to reduce to an acceptable level the heat and radiation load on the cold mass. This heat load has been calculated as part of the conceptual design activity based on the UCI new7coldmassb.xls spreadsheet. Heat loads are summarized in Table 2.1. There are two total nuclear heating columns, one based on the maximum heat load at any azimuth in the associated axial interval, and the other based on the average azimuthal heat load in the associated axial interval. The total impact on the 4.5 K refrigeration load is 186 W, and 100 W by the two methods, respectively. At the time of the CDR writing, UCI is in the process of iterating on the shield design and resulting heating calculations with indication that 186 W could be confidently taken as an upper limit.

Table 2.1 – Production Solenoid nuclear heating loads to 4.5K cold mass

Axial Interval	Coil Mass (kg)	Al Shell Mass (kg)	Inner He can Mass (kg)	Outer He can Mass (kg)	He can end flange (kg)	Total 4.2 K mass in axial interval (kg)	Max Nuclear Heating (μW/g)	Avg Nuclear Heating (μW/g)	Total nuclear heating in axial interval-max (W)	Total nuclear heating in axial interval-avg (W)
1	6850	1314	1039	724	412	10339	7.31	2.65	75.6	27.4
2	1842	362	414	288		2906	8.34	4.11	24.2	11.9
3	2058	407	414	288		3167	9.88	5.36	31.3	17.0
4	1629	318	414	288		2649	7.34	4.78	19.4	12.7
5	1842	362	414	288		2906	3.67	3.01	10.7	8.7
6	1418	274	414	288		2395	3.90	3.51	9.3	8.4
7	1629	318	414	288		2649	3.41	2.92	9.0	7.7
8	798	151	414	288		1651	1.93	1.68	3.2	2.8
9	2058	407	435	303	412	3615	0.92	0.84	3.3	3.1
	20123	3911	4371	3046	825	32277			186.0	99.7

Service Ports for the Production Solenoid

The service ports for the production solenoid have been located in the area where the radiation is minimum, at the end closest to the TS. One port is a vertical stack, integral with the PS cryostat, which includes the helium quench vent. A separate penetration of the PS cryostat at the TS end includes superconducting buses, cryogenic lines and wires carrying coil voltage signals for external quench detection circuitry, both of which are brought outside the shield blocks for the experiment.

Service Ports for the Transport Solenoid

Transport solenoid service ports are located at the ends of the two TS cryostats closest to the Beryllium window. Motion at these ends of the TS cryostats is limited during cooldown and operation by the support structure, thus also facilitating cryogenic line, magnet bus, and instrumentation wiring egress at these locations.

Beryllium Window for Vacuum Isolation

A beryllium window is placed between the two TS cryostats to isolate the upstream and downstream portion of the beam vacuum. This window is outside the scope of the magnet CDR and is under design by the MECO project at the time of the CDR writing. The specified interface to the magnet design for the conceptual design activity is to retain a 7.5 cm distance between the room temperature end flanges of the up- and down-stream TS cryostats. This dimension is largely preserved via the horizontal TS radius rods which limit cooldown and operating motions of the TS cryostats at their Be window ends.

Service Ports for the Detector Solenoid and Vacuum Interface

The cryostat bore for the DS mates with the cryostat bore for the TS on one end and with a vacuum vessel on the other end that extends the bore vacuum beyond the DS. The bore vacuum vessel beyond the DS is not part of the magnet CDR work scope. The detector solenoid cryostat serves as the bore vacuum vessel in the region of the DS. Service ports are located at near the TS

end of the DS cryostat, away from the downstream end that is busy with detector instrumentation.

Use of Cryostat as Vacuum Vessel for Transport and Detector Solenoids

As has been mentioned, the TS and DS inner cryostat cans serve as bore vacuum in these regions of the experiment. The TS and DS bores will therefore be evacuated during data taking. At other times, for example during possible installation testing, these bore regions may be at atmospheric pressure. Thus, the TS and DS cryostats must be designed for either pressure condition. The design of mating flanges which interface with the DS vacuum extending spool piece and with the PS vacuum vessel, both of which are the outside the scope of the magnet conceptual design activity, must be coordinated with the project.

Support of Collimators Off the Transport Solenoid

Each of the straight sections of the transport solenoid has a collimator installed in it during the magnet assembly. Design of the collimators is not part of the magnet conceptual design activity. The collimators are cylindrical shells with an outer diameter designed to fit inside the TS cryostat bore. They have an inner bore that varies from 15 cm radius for the two end straight section collimators to about 20 cm for each of the two central straight section collimators. Each collimator is approximately 1 m in length and has a mass of about 1200 kg. The TS cryostat has been designed with sufficient strength to carry these dead loads, although details of the attachment are left for final design when precise values for the masses and dimensions will be available from the project.

Support of Experimental Equipment Off Detector Solenoid

The detector solenoid cryostat supports experimental equipment and particle absorbers. The most massive of these is an electron calorimeter of mass about 2400 kg. The inner wall of the DS cryostat has been designed to support the mass of the detector, as discussed in the DS structural analysis section.

Steel Cosmic Ray Shield and Muon Beam Dump

A massive shield surrounds the DS to absorb cosmic ray particles that are a source of background in the experiment. The design of the shield is not part of the magnet conceptual design activity, but its magnetic effects have been included in the design of the magnet system. The steel shield has been included in the magnetic analysis [mm040] as a 13.2 m long square box with a 0.5 m wall thickness, coaxial with the DS coil, and having an inner square aperture 3.1 m on a side. The steel is assumed to be 1010 carbon steel, as designated by BNL personnel. The box will be closed at the ends by non-magnetic material. It is desired that the field beyond the end of the DS fall below 0.05 T as quickly as possible to improve the performance of the beam dump. The field analysis with the iron has been submitted to the MDMG. There should be no flux return or pole piece material at a radius smaller than 45 cm at any axial position. For axial positions more than 1 m beyond the end of the coil, there should be no flux return or pole piece material at a radius smaller than the cryostat OD. The current design meets these criteria.

Penetrations through the shield for bus and cryogenic service have been coordinated with the MDMG. These will come horizontally out of the top of the DS cryostat at the TS end.

Electrical Noise Environment

The solenoids will be operated in a large experimental hall with many other high current magnets and power supplies. The nature of the electrical noise environment is yet to be quantified by the MECO project. Nevertheless, the quench detection/protection system has been designed to trip when the resistive voltage within the coils of each circuit exceeds 0.1 V for 1 second. The combination of the 0.1 V signal and the 1 second delay time are regarded as sufficient to provide protection against false trips for many environments. Safe quench behavior with either higher detection thresholds or longer delay times may be possible with additional analysis if shown necessary during final design.

Gravity Supports

All coils have internal cold rods that support the cold mass out to the cryostat shells, and room temperature supports from the cryostat shells to the building floor.

Procedure for Transportation to and Installation at BNL

The magnets will be installed at an experimental area at BNL that is serviced by a 40-ton crane. The crane is capable of making vertical lifts to above 31 feet as limited by the bottom of the bridge, but permanent structures should not exceed 24’ 6”, which represents the bottom of the crane cab. The individual cryostats for the MECO magnet system have weights that exceed this crane limit, so temporary rigging and moving equipment will be required for magnet installation in the experimental facility.

Section 3 - Field Specifications and Field Matching

The design of the MECO magnet system is driven by the field specifications defined in [mm005], and on which Figure 3.1 and Table 3.1 are based. The specification is a set of rules specifying fields in a volume limited by a surface formed by a circle of a variable radius, R_{fs}, normal to the S-shaped axis of the magnet system.

Figure 3.1 and Table 3.1 summarize these field specifications. The global axial coordinate, Z, is measured along the axis of the magnet system with zero point at the upstream, 5 T, end of the PS. Field specifications apply limitations on deviations of the field from the field spec, as well as on the values of field derivatives, dB/ds. Here B is the axial component of the magnetic field, and 's' is measured along lines, equidistant from the axis of the magnet system in any fixed azimuthal axial plane. Field specs are different in different sections along the global axial coordinate. In [mm005] and in Table 3.1 these sections are associated with respective magnets, Production Solenoid (PS), Transport Solenoid (TS), and Detector Solenoid (DS). Some magnets are subdivided into subsets to conform to changes in the field specifications. In particular, the TS is subdivided into five parts, TS1-TS5. TS1, TS3, and TS5 are straight and contain collimators with strict limitations on dB/ds, and TS2 and TS4 are toroidal sections with relaxed requirements for field quality. The tightest tolerances on the field quality are imposed in the central part, DS2, of the DS.

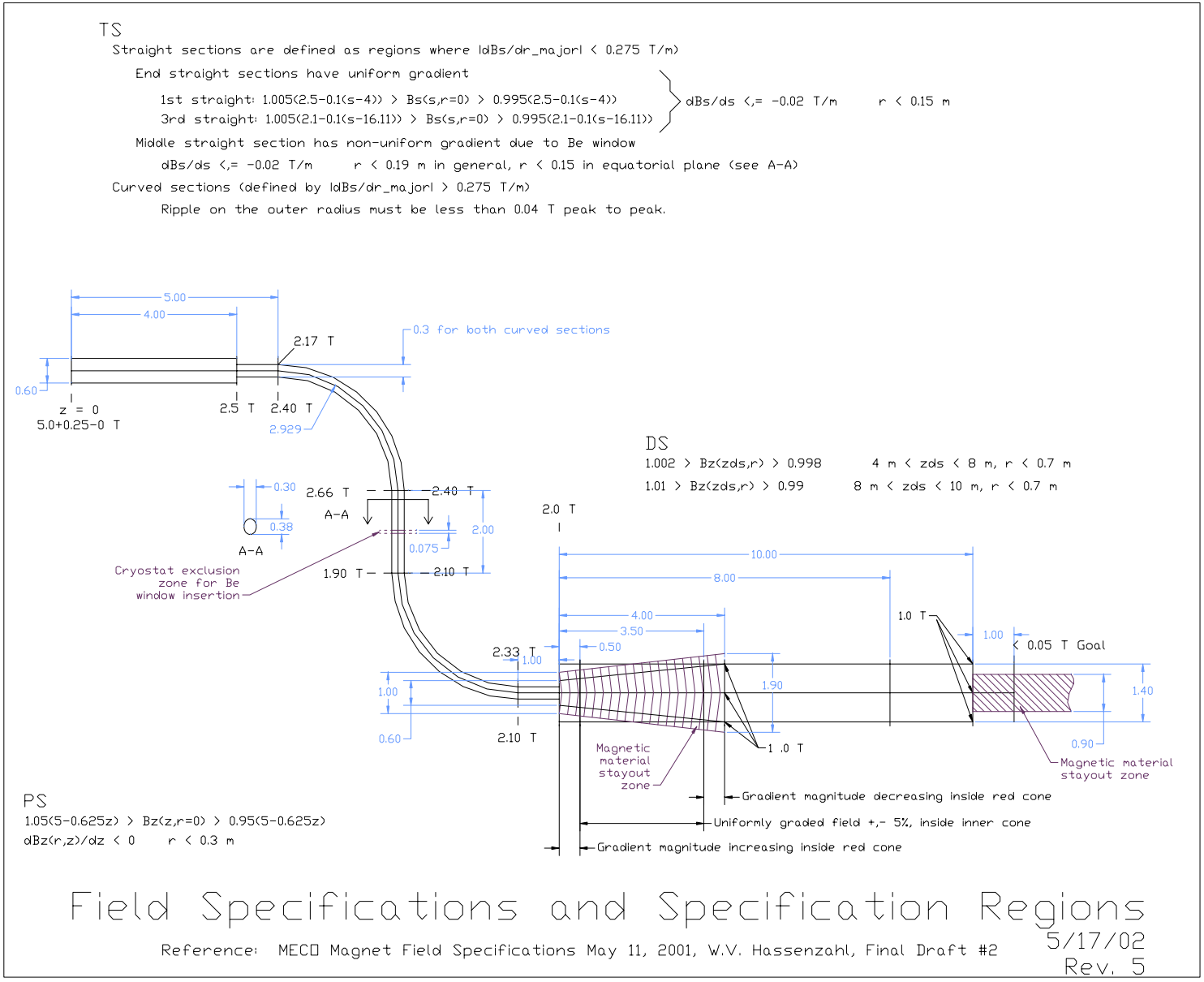

Figure 3.1 – The MECO Magnet System Layout and Field Specification

Table 3.1 – Field specification characteristics

Coil	L (m)	Zmin (m)	Zmax (m)	R_{fs} (m)	|ΔB/B| max	|ΔB/B| where	dB/ds** (T/m)
PS0	4.00	0.00	4.00	0.30	0.050	r=0	< 0
TS1	1.00	4.00	5.00	0.15	0.005	r=0	< -0.02
TS2	4.60*	5.00	9.60	0.15	0.010	$r<R_{fs}$	na
TS3	1.95	9.60	11.55	0.19	na	na	< -0.02
TS4	4.60*	11.55	16.15	0.15	0.010	$r<R_{fs}$	na
TS5	1.00	16.15	17.15	0.15	0.005	r=0	< -0.02
DS1	4.00	17.15	21.15	0.30-0.70	na	na	var< 5%
DS2	4.00	21.15	25.15	0.70	0.002	$r<R_{fs}$	na
DS3	2.00	25.15	27.15	0.70	0.010	$r<R_{fs}$	na

* Corresponds to $R_{major} = 2.929$ m

** where $r<R_{fs}$

Models and Methods of Analyses

The analytical procedure used to design the magnet system, and to verify the compliance of the fields with the field specifications is described in detail below, based on [mm040]. This procedure consists of several stages performed using the following analytical tools.

MECOSOLOP2D

MECOSOLOP2D is a FORTRAN90 program. It operates in a 2D coordinate space corresponding to the equatorial plane of the MECO magnet system. The magnets are modeled as real-size solenoidal windings with currents uniformly smeared over the rectangular cross section of each individual coil. Magnetic field can be calculated, and matched at any point of the equatorial plane shown in the plan view in Figure 3.1. Since the program assumes that the number of points at which the field is matched vs. specs is equal to the number of coils in the model, there are 94 coils, and 94 points in this model.

TOSCA by Vector Fields

A three dimensional TOSCA model of the MECO coil system shown in Figure 3.2 was developed for the analyses. It includes the DS iron shield as well as a predefined set of solenoids. This model can be used for direct calculations of the EM fields at any point in space with account of magnetic fields from nonlinear iron. The DS iron shield is modeled as a 13.2-m long square box coaxial with the DS. The wall thickness of the box is 0.5 m, and the inner square aperture opening is 3.1 m on a side. In the coordinate system with the origin at the 5 T spec point on the axis of the PS, Y-axis indicating the downstream direction of the PS, and X-axis supplementing it in the equatorial plane of the magnet system, the iron shield box extends from Y=11 m to Y=24.2 m. Magnetic properties of the iron are modeled using a standard BH curve for C1010 provided by Vector Fields, and reproduced at the end of this section.

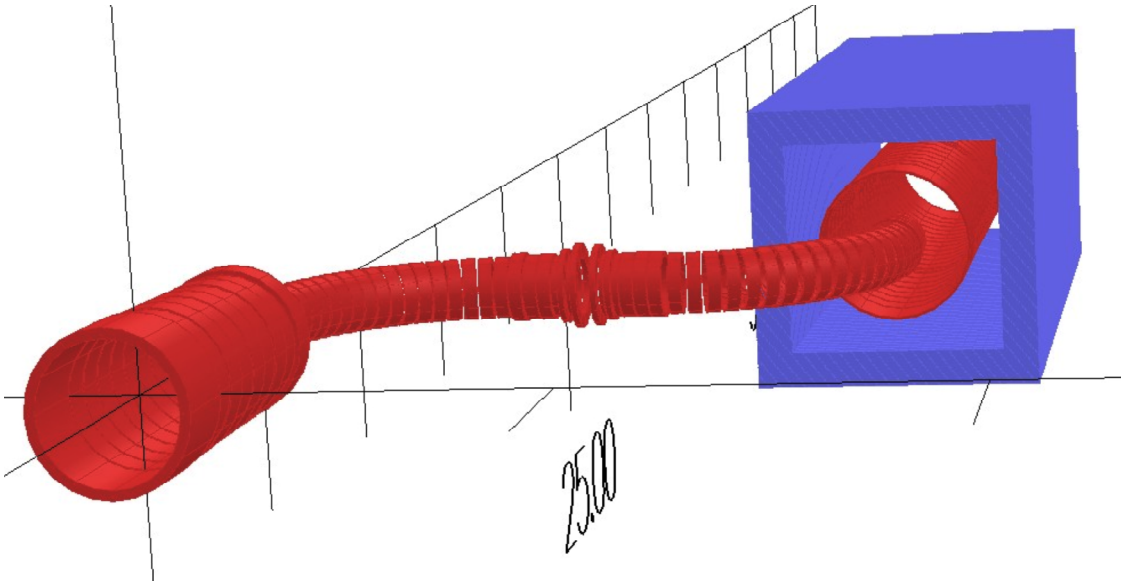

Figure 3.2 – The TOSCA three-dimensional model

Analytical Design Procedure

The following procedure is used in the analyses:

Step 1. MECOSOLOP2D is used to generate a 94-coil set, S_0, matching fields [mm005], B_0, at 94 field-matching points.

Step 2. TOSCA model with coil set S_0, and the iron is used to calculate the field, B_{n+1} (n=0 in the first loop) at the same 94 field matching points. The new field requirement from the coils is imposed at these points as $B_{n+2} = B_0 - (B_{n+1} - B_0)$.

Step 3. MECOSOLOP2D is used to generate a 94-coil set, S_{n+1}, matching fields, B_{n+2}, at the same field matching points as in Step 1.

Step 4. TOSCA model with coil set S_{n+1}, and the iron is used to calculate the compliance of the field to the field specifications.

Step 5. If the field does not comply with the specifications, steps 2-4 are repeated (with n = 1,2…) until they do

Step 6. If the field does comply with the specifications, coils of the last set are adjusted for an integer number of turns, chosen operating currents, and actual radial builds. This set is checked for compliance with the field specifications and, if necessary, adjusted manually.

More details on the optimization process are given in the next section.

Verification of Field Quality

Verification of field quality was limited to three paths specified below. Figure 3.3 shows the limits of the trace of the Field Specification area on the equatorial plane. It is a corridor between the left path shown in blue, and the right path shown in green, each equidistant from the axis shown in red. The width of this corridor is variable, as is the field spec radius, Rfs, defined in Table 3.1. The length, L, of each of the parts of the system, as well as the axial coordinates of the beginning and the end of each part, field spec radius, R_{fs}, and the spec on the relative magnetic field error, $(\Delta B/B)_{spec}$, is specified in Table 3.1. Fields calculated at points along the left, and the right paths are tied to the global axial coordinate, Z.

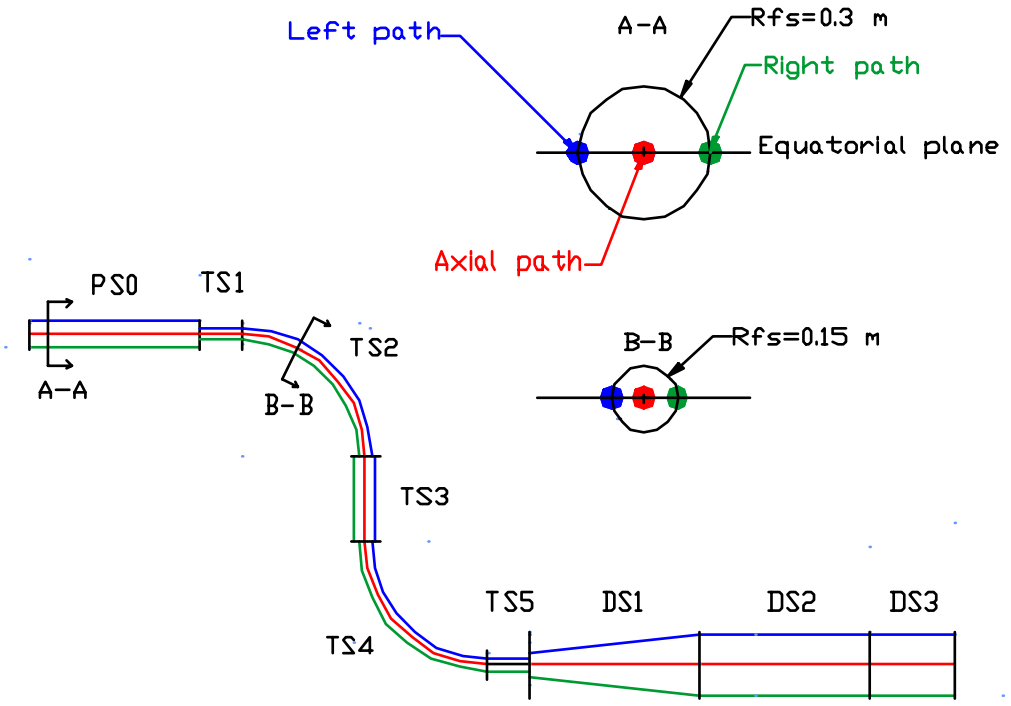

Figure 3.3 – Field Specification Paths

Figure 3.4 shows B as a function of Z for all three paths. Figure 3.5 shows dB/dZ, or to be more precise dB/ds in the bends, along all three paths. Field derivatives are calculated at every point by dividing the difference between the field at this, and the previous point by the actual distance between these points. Note that since the left and the right paths have break points, at which the radial position changes discretely the field derivative at such points assumes the value at the previous point on this path along Z. Evaluation points are spaced at 1 cm along Z, so that there are 2716 such points along each path.

The analyses of the field quality have shown its compliance with the field specifications. The field quality provided by the designed magnet system was reviewed, and accepted by the MECO Magnet System Interim Design Review Committee [mm037] as appropriate for conceptual design. Any changes in the field solution during final design must be approved by the MECO project.

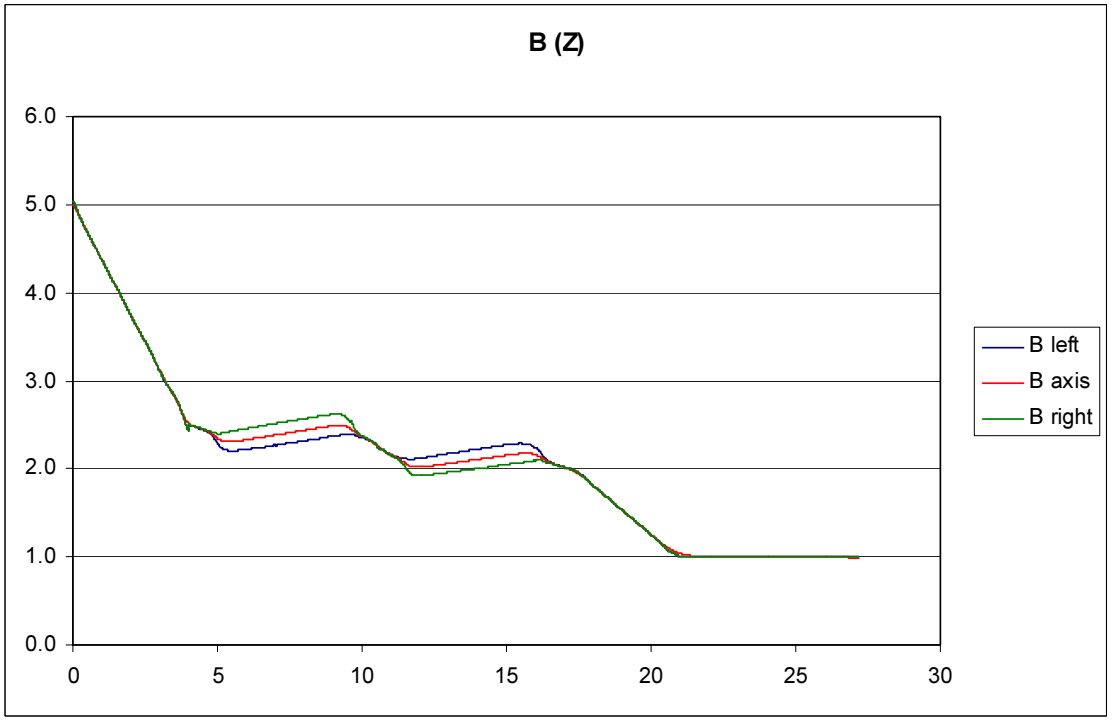

Figure 3.4 – Magnetic Field, B(T), along the Paths vs. Z-coordinate (m)

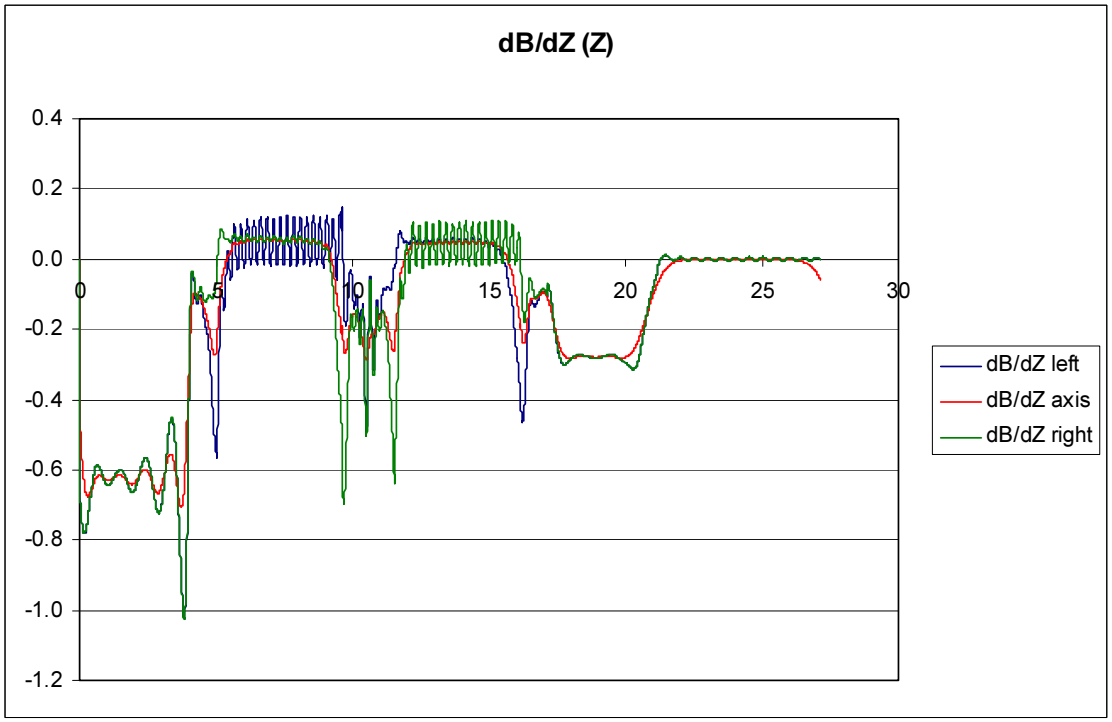

Figure 3.5 – Magnetic Field Derivative, dB/dZ(T/m), along the Paths vs. Z-coordinate (m). Relative magnet positions are given by zmin and zmax in Table 3.1.

Coil Definitions

Table 3.2 summarizes parameters of the windings of the MECO magnet system designed as described above to satisfy the field specifications. The columns in the table indicate:

(1) The coil number;
(2) The name of the magnet this coil belongs to;
(3) X-coordinate of the centroid of the coil in the equatorial plane;
(4) Y-coordinate of the centroid of the coil in the equatorial plane;
(5) Alpha, the angle between the axis of the coil, and the X-axis;
(6) R_{in}, the inner radius of the coil winding;
(7) dR, the radial build of the winding;
(8) dZ, the axial build of the winding,;
(9) NI, the total ampere-turns in the coil as defined by the analytical procedure;
(10) I_{op}, operating current in the coil associated with the magnet it belongs to;
(11) w_{ic}, the width of the conductor with insulation;
(12) h_{ic}, the height of the conductor with insulation;
(13) Number of layers including layers with incomplete numbers of turns;
(14) Number of full turns in the coil;
(15) Length of the conductor in the coil.

The turn count assumes the following winding scheme. A 1-mm thick ground insulation of fiberglass is wrapped over the mandrel OD, and a 1-mm thick ground insulation of G11CR is placed inside each of the mandrel side flanges. Coil winding starts, and ends at the OD of the winding. In order to achieve it winding begins at the ID of the winding, and goes in two directions. First, a single pancake along one of the sidewalls of the mandrel is wound. This pancake is isolated from the remainder of the winding by an insulating plane of 1 mm of G11CR. The other end of the conductor is used for layer winding the rest of the coil between the pancake winding, and the other sidewall of the mandrel. A 1 mm thick layer of insulation is introduced between the pancake, and the rest of the winding for voltage isolation.

The calculation of the number of layers in Table 3.2 takes in account that each layer-to-layer transition is accompanied by a loss of a half of a turn. There are two transitions in each layer, which results in a loss of a full turn per layer. The number of layers in the TS, and in the DS can be either even or odd. The number of turns in the PS can be only even, which is preconditioned by the cooling scheme of the magnet. Turns in all layers are wound tight to the mandrel flange or single pancake insulation barrier. As a result, layers will be wound with a non-integer number of turns. Nevertheless, each coil must be wound with the specified integer number of turns in all. Thus, the final layer will complete its last turn at the same azimuthal location at which the first turn of the layer winding was started. The same alignment requirement holds for the start and end of the single pancake. Thus, the single pancake, layer windings as a group, and the entire coil winding will each have an integral number of turns.

Table 3.2 – Coil parameter definitions

Coil # (1)	Magnet Name (2)	X_c (m) (3)	Y_c (m) (4)	Alpha (deg) (5)	R_{in} (m) (6)	dR (m) (7)	dZ (m) (8)	NI (kA-t) (9)	I_{op} (kA) (10)	w_{ic} (mm) (11)	h_{ic} (mm) (12)	N Layers (13)	N Turns (14)	Conductor Length (m) (15)
1	PS0	0.0000	-0.6000	90.000	0.880	0.1248	1.16	6786.5	3.5	14.93	4.80	26	1939	11481
2	PS0	0.0000	0.2500	90.000	0.880	0.0864	0.46	1802.5	3.5	14.93	4.80	18	515	2987
3	PS0	0.0000	0.7500	90.000	0.880	0.0960	0.46	1998.5	3.5	14.93	4.80	20	571	3329
4	PS0	0.0000	1.2500	90.000	0.880	0.0768	0.46	1634.5	3.5	14.93	4.80	16	467	2695
5	PS0	0.0000	1.7500	90.000	0.880	0.0864	0.46	1708.0	3.5	14.93	4.80	18	488	2831
6	PS0	0.0000	2.2500	90.000	0.880	0.0672	0.46	1326.5	3.5	14.93	4.80	14	379	2176
7	PS0	0.0000	2.7500	90.000	0.880	0.0768	0.46	1554.0	3.5	14.93	4.80	16	444	2562
8	PS0	0.0000	3.2500	90.000	0.880	0.0384	0.46	815.5	3.5	14.93	4.80	8	233	1316
9	PS0	0.0000	3.7500	90.000	0.880	0.0960	0.46	1963.5	3.5	14.93	4.80	20	561	3271
10	TS1	0.0000	4.1500	90.000	0.405	0.0336	0.08	75.0	1.5	14.00	2.80	12	50	133
11	TS1	0.0000	4.2500	90.000	0.405	0.0644	0.08	150.0	1.5	14.00	2.80	23	100	275
12	TS1	0.0000	4.3500	90.000	0.405	0.0140	0.08	30.0	1.5	14.00	2.80	5	20	52
13	TS1	0.0000	4.4500	90.000	0.405	0.0840	0.08	201.0	1.5	14.00	2.80	30	134	376
14	TS1	0.0000	4.6000	90.000	0.405	0.0392	0.18	240.0	1.5	14.00	2.80	14	160	427
15	TS1	0.0000	4.8000	90.000	0.405	0.0532	0.18	330.0	1.5	14.00	2.80	19	220	597
16	TS1	0.0000	5.0000	90.000	0.405	0.0504	0.18	313.5	1.5	14.00	2.80	18	209	565
17	TS1	0.0100	5.2420	85.263	0.405	0.0728	0.18	438.0	1.5	14.00	2.80	26	292	810
18	TS2	0.0400	5.4820	80.526	0.405	0.0224	0.18	372.0	4.0	14.00	2.80	8	93	243
19	TS2	0.0900	5.7190	75.789	0.405	0.0252	0.18	416.0	4.0	14.00	2.80	9	104	273
20	TS2	0.1590	5.9510	71.053	0.405	0.0280	0.18	424.0	4.0	14.00	2.80	10	106	279
21	TS2	0.2470	6.1770	66.316	0.405	0.0280	0.18	432.0	4.0	14.00	2.80	10	108	284
22	TS2	0.3530	6.3940	61.579	0.405	0.0280	0.18	436.0	4.0	14.00	2.80	10	109	287
23	TS2	0.4770	6.6020	56.842	0.405	0.0280	0.18	444.0	4.0	14.00	2.80	10	111	292
24	TS2	0.6180	6.7990	52.105	0.405	0.0280	0.18	448.0	4.0	14.00	2.80	10	112	295
25	TS2	0.7740	6.9840	47.368	0.405	0.0280	0.18	452.0	4.0	14.00	2.80	10	113	297
26	TS2	0.9450	7.1550	42.632	0.405	0.0280	0.18	456.0	4.0	14.00	2.80	10	114	300
27	TS2	1.1300	7.3110	37.895	0.405	0.0280	0.18	460.0	4.0	14.00	2.80	10	115	303
28	TS2	1.3270	7.4520	33.158	0.405	0.0280	0.18	464.0	4.0	14.00	2.80	10	116	305
29	TS2	1.5350	7.5760	28.421	0.405	0.0280	0.18	464.0	4.0	14.00	2.80	10	116	305
30	TS2	1.7520	7.6820	23.684	0.405	0.0308	0.18	472.0	4.0	14.00	2.80	11	118	312
31	TS2	1.9780	7.7700	18.947	0.405	0.0308	0.18	468.0	4.0	14.00	2.80	11	117	309
32	TS2	2.2100	7.8390	14.211	0.405	0.0308	0.18	472.0	4.0	14.00	2.80	11	118	312

Coil #	Magnet Name	X_c (m)	Y_c (m)	Alpha (deg)	R_{in} (m)	dR (m)	dZ (m)	NI (kA-t)	I_{op} (kA)	w_{ic} (mm)	h_{ic} (mm)	N Layers	N Turns	Conductor Length (m)
(1)	(2)	(3)	(4)	(5)	(6)	(7)	(8)	(9)	(10)	(11)	(12)	(13)	(14)	(15)
33	TS2	2.4470	7.8890	9.474	0.405	0.0280	0.18	444.0	4.0	14.00	2.80	10	111	292
34	TS3	2.6870	7.9190	4.737	0.405	0.0868	0.18	540.0	1.5	14.00	2.80	31	360	1014
35	TS3	2.9290	7.9290	0.000	0.405	0.0784	0.18	481.5	1.5	14.00	2.80	28	321	896
36	TS3	3.1290	7.9290	0.000	0.405	0.0504	0.18	307.5	1.5	14.00	2.80	18	205	554
37	TS3	3.3290	7.9290	0.000	0.405	0.0672	0.18	417.0	1.5	14.00	2.80	24	278	766
38	TS3	3.4790	7.9290	0.000	0.405	0.0448	0.08	105.0	1.5	14.00	2.80	16	70	188
39	TS3	3.5790	7.9290	0.000	0.405	0.0612	0.08	313.5	1.5	12.10	1.57	39	209	572
40	TS3	3.6740	7.9290	0.000	0.415	0.0267	0.05	-70.5	1.5	12.10	1.57	17	47	126
41	TS3	3.7690	7.9290	0.000	0.405	0.1021	0.08	522.0	1.5	12.10	1.57	65	348	997
42	TS3	4.0390	7.9290	0.000	0.405	0.0942	0.08	481.5	1.5	12.10	1.57	60	321	912
43	TS3	4.1340	7.9290	0.000	0.415	0.0236	0.05	-63.0	1.5	12.10	1.57	15	42	113
44	TS3	4.2290	7.9290	0.000	0.405	0.0534	0.08	265.5	1.5	12.10	1.57	34	177	480
45	TS3	4.3290	7.9290	0.000	0.405	0.0532	0.08	123.0	1.5	14.00	2.80	19	82	222
46	TS3	4.4790	7.9290	0.000	0.405	0.0560	0.18	339.0	1.5	14.00	2.80	20	226	615
47	TS3	4.6790	7.9290	0.000	0.405	0.0560	0.18	337.5	1.5	14.00	2.80	20	225	612
48	TS3	4.8790	7.9290	0.000	0.405	0.0532	0.18	328.5	1.5	14.00	2.80	19	219	594
49	TS3	5.1210	7.9390	4.737	0.405	0.0672	0.18	417.0	1.5	14.00	2.80	24	278	766
50	TS4	5.3610	7.9690	9.474	0.405	0.0224	0.18	352.0	4.0	14.00	2.80	8	88	230
51	TS4	5.5980	8.0190	14.211	0.405	0.0252	0.18	384.0	4.0	14.00	2.80	9	96	252
52	TS4	5.8300	8.0880	18.947	0.405	0.0252	0.18	384.0	4.0	14.00	2.80	9	96	252
53	TS4	6.0560	8.1760	23.684	0.405	0.0252	0.18	388.0	4.0	14.00	2.80	9	97	255
54	TS4	6.2730	8.2820	28.421	0.405	0.0252	0.18	388.0	4.0	14.00	2.80	9	97	255
55	TS4	6.4810	8.4060	33.158	0.405	0.0252	0.18	392.0	4.0	14.00	2.80	9	98	257
56	TS4	6.6780	8.5470	37.895	0.405	0.0252	0.18	396.0	4.0	14.00	2.80	9	99	260
57	TS4	6.8630	8.7030	42.632	0.405	0.0252	0.18	396.0	4.0	14.00	2.80	9	99	260
58	TS4	7.0340	8.8740	47.368	0.405	0.0252	0.18	396.0	4.0	14.00	2.80	9	99	260
59	TS4	7.1900	9.0590	52.105	0.405	0.0252	0.18	396.0	4.0	14.00	2.80	9	99	260
60	TS4	7.3310	9.2560	56.842	0.405	0.0252	0.18	400.0	4.0	14.00	2.80	9	100	262
61	TS4	7.4550	9.4640	61.579	0.405	0.0252	0.18	396.0	4.0	14.00	2.80	9	99	260
62	TS4	7.5610	9.6810	66.316	0.405	0.0252	0.18	392.0	4.0	14.00	2.80	9	98	257
63	TS4	7.6490	9.9070	71.053	0.405	0.0252	0.18	388.0	4.0	14.00	2.80	9	97	255
64	TS4	7.7180	10.1390	75.789	0.405	0.0252	0.18	380.0	4.0	14.00	2.80	9	95	249
65	TS4	7.7680	10.3760	80.526	0.405	0.0224	0.18	344.0	4.0	14.00	2.80	8	86	225
66	TS5	7.7980	10.6160	85.263	0.405	0.0588	0.18	352.5	1.5	14.00	2.80	21	235	641

Coil # (1)	Magnet Name (2)	X_c (m) (3)	Y_c (m) (4)	Alpha (deg) (5)	R_{in} (m) (6)	dR (m) (7)	dZ (m) (8)	NI (kA-t) (9)	I_{op} (kA) (10)	w_{ic} (mm) (11)	h_{ic} (mm) (12)	N Layers (13)	N Turns (14)	Conductor Length (m) (15)
67	TS5	7.8080	10.8580	90.000	0.405	0.0448	0.18	276.0	1.5	14.00	2.80	16	184	494
68	TS5	7.8080	11.0580	90.000	0.405	0.0196	0.18	115.5	1.5	14.00	2.80	7	77	201
69	TS5	7.8080	11.2580	90.000	0.405	0.0196	0.18	112.5	1.5	14.00	2.80	7	75	195
70	TS5	7.8080	11.4580	90.000	0.405	0.0084	0.18	43.5	1.5	14.00	2.80	3	29	75
71	TS5	7.8080	11.6580	90.000	0.405	0.0028	0.18	13.5	1.5	14.00	2.80	1	9	23
72	DS1	7.8080	11.4330	90.000	1.080	0.0352	0.43	1100.0	4.0	15.40	3.20	11	275	1897
73	DS1	7.8080	11.8830	90.000	1.080	0.0352	0.43	1100.0	4.0	15.40	3.20	11	275	1897
74	DS1	7.8080	12.3580	90.000	1.080	0.0192	0.48	688.0	4.0	15.40	3.20	6	172	1178
75	DS1	7.8080	12.8580	90.000	1.080	0.0192	0.48	708.0	4.0	15.40	3.20	6	177	1212
76	DS1	7.8080	13.3580	90.000	1.080	0.0192	0.48	660.0	4.0	15.40	3.20	6	165	1130
77	DS1	7.8080	13.8580	90.000	1.080	0.0160	0.48	580.0	4.0	15.40	3.20	5	145	991
78	DS1	7.8080	14.3580	90.000	1.080	0.0160	0.48	548.0	4.0	15.40	3.20	5	137	937
79	DS1	7.8080	14.8580	90.000	1.080	0.0160	0.48	488.0	4.0	15.40	3.20	5	122	834
80	DS1	7.8080	15.3580	90.000	1.080	0.0096	0.48	340.0	4.0	15.40	3.20	3	85	579
81	DS2	7.8080	15.8580	90.000	1.080	0.0128	0.48	376.0	4.0	15.40	3.20	4	94	642
82	DS2	7.8080	16.3580	90.000	1.080	0.0128	0.48	392.0	4.0	15.40	3.20	4	98	669
83	DS2	7.8080	16.8580	90.000	1.080	0.0128	0.48	400.0	4.0	15.40	3.20	4	100	683
84	DS2	7.8080	17.3580	90.000	1.080	0.0128	0.48	396.0	4.0	15.40	3.20	4	99	676
85	DS2	7.8080	17.8580	90.000	1.080	0.0128	0.48	400.0	4.0	15.40	3.20	4	100	683
86	DS2	7.8080	18.3580	90.000	1.080	0.0128	0.48	396.0	4.0	15.40	3.20	4	99	676
87	DS2	7.8080	18.8580	90.000	1.080	0.0128	0.48	400.0	4.0	15.40	3.20	4	100	683
88	DS2	7.8080	19.3580	90.000	1.080	0.0128	0.48	396.0	4.0	15.40	3.20	4	99	676
89	DS2	7.8080	19.8580	90.000	1.080	0.0128	0.48	400.0	4.0	15.40	3.20	4	100	683
90	DS3	7.8080	20.3580	90.000	1.080	0.0128	0.48	400.0	4.0	15.40	3.20	4	100	683
91	DS3	7.8080	20.8580	90.000	1.080	0.0128	0.48	400.0	4.0	15.40	3.20	4	100	683
92	DS3	7.8080	21.3580	90.000	1.080	0.0128	0.48	400.0	4.0	15.40	3.20	4	100	683
93	DS3	7.8080	21.8580	90.000	1.080	0.0128	0.48	408.0	4.0	15.40	3.20	4	102	696
94	DS3	7.8080	22.6080	90.000	1.080	0.0128	0.98	984.0	4.0	15.40	3.20	4	246	1679

General Characteristics of Magnet Systems

Table 3.3 shows the inductance matrix calculated for the coil system divided into six groups as in Table 3.4, each driven by an individual power supply. The last column of Table 3.4 shows the maximum energy stored in each of the coil groups driven by the respective power supply. The energy in the i^{th} coil is calculated by the following formula.

$$E_i = \frac{1}{2}\sum_{i,j=1}^{6} M_{ij} I_i I_j$$

Table 3.3 – The inductance matrix by power supplies

i	j	M_{ij} (H)
1	1	17.73
1	2	0.1503
1	3	2.481×10^{-2}
1	4	3.385×10^{-3}
1	5	1.380×10^{-3}
1	6	5.128×10^{-3}
2	2	2.045
2	3	0.1085
2	4	0.1831
2	5	6.034×10^{-3}
2	6	3.544×10^{-3}
3	3	0.5228
3	4	5.959×10^{-3}
3	5	9.074×10^{-4}
3	6	1.258×10^{-3}
4	4	1.192
4	5	6.704×10^{-2}
4	6	7.983×10^{-2}
5	5	0.3862
5	6	2.744×10^{-2}
6	6	3.780

Table 3.4 – Coils grouped by power supplies

Magnet #	Name	Coils #	Iop (kA)	Energy (MJ)
1	PS	1-9	3.50	109.20
2	TS1,3u	10-17, 34-41	1.50	3.26
3	TS2	18-33	4.00	4.72
4	TS3d,5	42-49, 66-71	1.50	2.01
5	TS4	50-65	4.00	3.55
6	DS	72-94	4.00	30.76
Total		1-94		153.50

Note: These results were calculated in the same way as in [mm032]. In particular, the whole magnet system was assumed to be straight along the centerline of the solenoids. Our estimates

show that such changes should not result in significant errors in the estimates of the EM energy of the whole system or its components.

Field-Quality-Related Recommendations for Coil Manufacturing and Assembly

The following are recommendations regarding design, manufacturing, and assembly of the magnets based on the results of the tolerances study [mm030]. It is highly recommended that a reader requiring more details on the tolerance study refer to [mm030] for clarification.

Current Placement Constraints — All Coils

Part of the tolerance study was to evaluate, for each magnet, the maximum current that could be placed as a loop at any random location within the side flanges of any coil without violating the field specification. These currents, which were determined in the work outlined in [mm030], are one constraint on choosing a maximum operating current in any magnet. In addition to meeting this constraint, the conductor must still satisfy the fraction of critical current limit of 0.65 and the temperature margin on the conductor of 1.5 K, both of which are project-imposed limits. In the PS, the temperature margin is more limiting, and the operating current must be limited to 3500 A in SSC inner cable to satisfy the temperature margin requirement. In the TS and the DS, the current placement constraint is more limiting than the temperature margin constraint. The resulting maximum operating currents imposed by the current constraint are 1500 A for the straight sections of the TS, and in the end TS coils of the 90° bends, and 4000 A in the remainder of the TS bends and in the DS. Note that with the integral-turn-count requirement and the tight layer-winding scheme, single turn placement will only be an issue in practice on the outermost layer where the layer may be incomplete.

PS Coil Manufacturing

The analysis determines the maximum value of a random deviation of the centroids of individual coils from nominal that will not cause a violation of the field specification. These can be up to 10 mm in the axial direction in most of the magnet, and 2 mm in the axial direction in the last coil, next to the interface with TS1. Although determination of the complete testing requirements for field verification is part of the final design activity, measurement of the magnetic field from each coil at low current (room temperature) is expected to provide confirmation of the axial centroid locations. Incomplete layers must be wound by turns evenly spaced or grouped so that the total current in conductors of a group should not exceed 170 kAT. These groups must be evenly spaced along the coil. In the last coil, next to the TS, incomplete layers must be wound with evenly spaced turns. Lateral tolerances (center line offsets) of coil assembly up to at most twice the axial tolerances are acceptable. Angular tolerances of the coil assembly are acceptable as long as Rin*dAlpha is at most equal to the axial tolerance.

TS Coil Manufacturing

There will be two magnets, TS1+TS2+TS3u (TS123u for short) and TS3d+TS4+TS5 (TS3d45 for short), made according to the same scheme. TS3u is a portion of TS3 upstream from the Be window, and TS3d is a portion of TS3 downstream from the Be window. The

requirements for TS13u and TS3d5 vs. TS2 and TS4 are so different, that it makes sense to use different strategies for their manufacturing.

TS2, TS4

These can be designed and built with up to 2-mm axial tolerances. Incomplete layers must be wound with evenly spaced turns. Lateral tolerances of coil assembly are acceptable as long as they are up to twice the axial tolerances. Angular tolerances of the coil assembly are acceptable as long as Rin*dAlpha is at most equal to the axial tolerance.

TS13u, TS3d5

TS13u refers to the combined series cold connection of TS1 and TS3u. TS3d5 nomenclature is similar. To accomplish this, a cold superconducting bus must be connected from the downstream end of TS1 to the upstream end of TS3u; likewise for TS3d5. TS13u and TS3d5 can be designed and built with up to 1-mm axial tolerances, which are essential. Incomplete layers must be wound with evenly spaced turns. Lateral tolerances of coil assembly are acceptable as long as they are in up to twice the axial tolerances. Angular tolerances of the coil assembly are acceptable as long as Rin*dAlpha is at most equal to the axial tolerance.

DS Coil Manufacturing

DS consists of three sub-magnets, DS1, DS2, and DS3. They all reside in the same cryostat. However, tolerances applied to the central part, DS2 are much tighter than tolerances required in DS1, and DS3. To simplify the design, and to avoid additional power supplies the following compromise is suggested. All three parts of the magnet can be connected in series. Incomplete layers must be wound with evenly spaced turns. In DS2 it is essential, and in DS1 and DS3 conductors can be grouped into evenly spaced groups of no more than two conductors. Axial tolerances are 1 mm in DS2, and up to 2-3 mm in DS1, and DS3. Lateral tolerances of coil assembly are irrelevant as long as they are in line with at most twice the axial tolerances. Angular tolerances of the coil assembly are irrelevant as long as Rin*dAlpha is at most equal to the axial tolerance.

All magnets

In all coils of all magnets, exact turn count should be controlled.

Assembly of the Magnets

Assembly procedures of the PS, TS123u, TS3d45, and DS are straightforward, as long as the individual coils comply with the above specifications. At assembly, the coil manufacturer may be required to make field measurements on the individual coils, and on the assembled magnets, PS, TS123u, TS3d45, and DS. Actual measurement requirements must be integrated with the overall plan for magnetic field confirmation, which must be addressed in more detail in final design.

Installation of the Magnets

Once the magnets are assembled and tested for the 'internal' field quality, the only thing left will be to adjust the gaps on the interfaces between the magnets under working conditions, i.e. after cooldown, and in presence of the real EM loads. We must be prepared to make small adjustments to the positions of the coils, as a set, within individual cryostats after initial installation, if necessary. The means for accomplishing this adjustment is discussed further in the assembly section.

B-H Curve for the Detector Solenoid Iron Shield Box

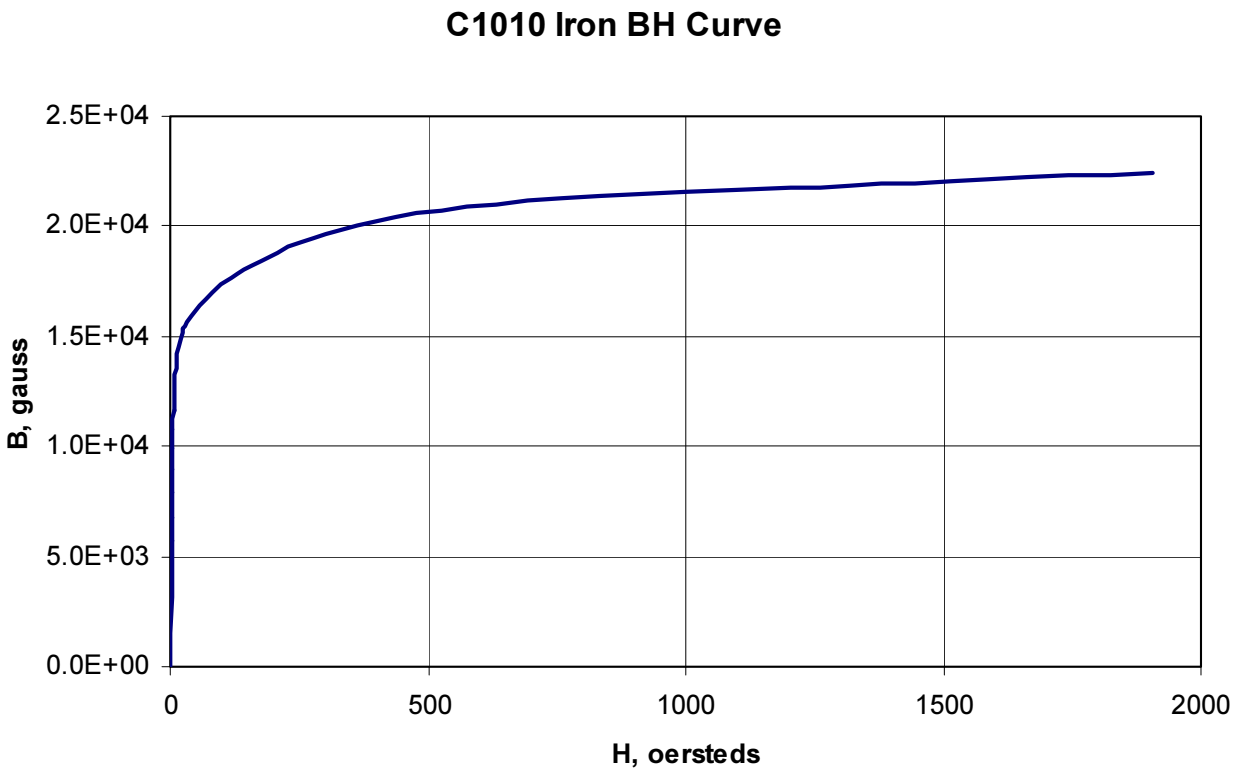

Figure 3.6 – B-H curve for the 1010 iron used in the analyses

Table 3.5 – B-H values for the 1010 iron used in the analyses

H (oersteds)	B (gauss)	H (oersteds)	B (gauss)
0.00	0	83.18	17019
2.09	5757	120.23	17679
2.50	6800	144.50	18045
3.02	7918	173.80	18432
3.63	8949	208.90	18831
4.37	9921	251.20	19236
5.25	10821	301.99	19636
6.31	11640	363.08	20022
7.59	12373	436.50	20384
9.12	13021	524.80	20713
10.96	13586	630.95	21003
13.18	14074	758.70	21251
15.85	14494	912.00	21461
22.91	15171	1096.50	21646
27.54	15451	1318.30	21869
39.80	15955	1584.90	22137
57.54	16455	1905.00	22458

Section 4 - Conductor Design

Requirements

The MECO conductor configurations are closely coupled with the magnetic field solution, protection requirements, heating and cooling environment, structural design, and margin constraints. A modification to the overall design solution in any of these areas imposes a need to reaffirm the conductor solution.

The MECO project originally required that the conductor must satisfy the simultaneous constraints that the fraction of critical (f_c) current be less than 0.65, and that the temperature margin be greater than 0.75 K. These constraints were reevaluated following a literature survey [mm038], and the more restrictive temperature margin of 1.5 K was adopted by the project as both more conservative and more in keeping with other previously-designed, conduction cooled coils having significant stored energy. Thus, the MECO conductor must now meet both

1) Fraction of critical (f_c) shall be less than or equal to 0.75 and
2) Temperature margin shall be greater than or equal to 1.5 K.

The Production Solenoid (PS) is exposed to nuclear heating. The nuclear heating has been quantified in a spreadsheet new7coldmassb.xls provided by UCI. This spreadsheet shows the nuclear heating to be a function of both azimuth and axial position within the winding. The spreadsheet results have assumed the use of tungsten as a shield material everywhere inside the PS bore. A new shield design is currently underway to replace tungsten with copper in those locations where the nuclear heating does not drive the design. In particular, this is expected to result in less of an azimuthal variation in the nuclear heating, since the locations with currently lower heating will sustain greater heating as the tungsten is replaced with copper. The assumption made for the current design, therefore, is that the peak azimuthal heat load from the spreadsheet is taken as the average heat load in azimuth at each axial location; i.e. the assumed azimuthal variation in nuclear heating is zero. A plot of this assumed axial distribution of nuclear heating is given in Figure 4.1.

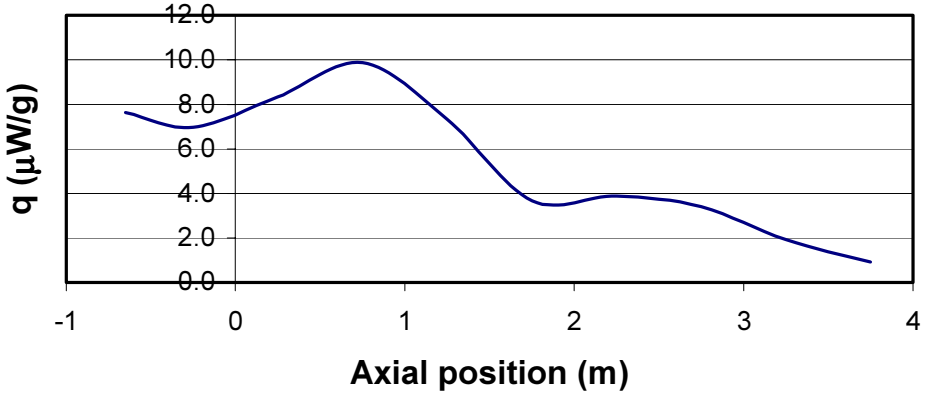

Figure 4.1 – Peak azimuthal nuclear heat load to the Production Solenoid [new7coldmassb.xls]

The requirement for the final design is that the conductor margin requirements specified above must be met in the PS in the presence of the nuclear heating as it is finally specified by the MECO project.

Protection constraints have also been imposed by the project. These require

1) Coil maximum temperature following quench shall be less than or equal to 150 K
2) Coil voltage following detection of a quench and initiation of protection shall be less than 2.0 kV.

Merely meeting the above requirements does not necessarily result in a satisfactory design. Quench analyses shall be performed on each type of conductor and coil combination to ensure that the structural design criteria are satisfied during a quench event.

Design

The MECO project has been offered the use of sufficient quantities of existing inventories of SSC inner and outer cable. Characteristics of these conductors were provided by the MECO Magnet Design Management Group (MDMG) and are summarized in Table 4.1. Although the use of this conductor is not mandated by the project, alternative conductors would have to provide clear advantages in the cost-performance space. Once it was shown that conductor designs using the SSC cables met the project requirements, alternative solutions using other conductor configurations were never seriously considered during the limited scope and period of performance of the conceptual design activity. The conceptual design has chosen to use SSC inner cable for the Production Solenoid (PS), and SSC outer cable for the Transport (TS) and Detector Solenoids (DS) where the field requirements are lower. Except in the case of the low current TS coils, which will be described below, all conductors require additional copper for quench protection. The additional copper is provided as a copper channel (one for each coil type) into which the cables are soldered. The individual designs for the PS, TS, and DS will now be discussed in more detail.

Table 4.1 – SSC Inner and Outer Cable properties.

Parameter	Unit	SSC Inner	SSC Outer
Strand Diameter	(mm)	0.81	0.65
Cu:SC		1.3	1.8
Filament Diameter	(microns)	6	6
Strand Twist pitch	(mm)	12.8	12.8
Number of strands		30	36
Cable Twist Pitch	(mm)	94	86
Cable area	(mm^2)	15.5	11.9
SC area	(mm^2)	6.7	4.3
Width	(mm)	12.13	11.7
Average thickness	(mm)	1.46	1.17
Keystone angle	(degrees)	1.23	1.0
Availability*	(km)	120	300

*Note: Availabilities need to be confirmed.

Strand data from Lawrence Berkeley Lab and the University of Wisconsin and cable data from Brookhaven National Lab have been analyzed and conservative fits applied using a simple model.[1] The model and the fit parameters used are given below with the resulting fits plotted with the data in Figures 2 and 3 for inner and outer cable respectively.

$$J_c(B,T) = J_{c0}(B)\left[1 - \frac{T}{T_c(B)}\right]$$

$$T_c(B) = T_{c0}\left(1 - \frac{B}{B_{c20}}\right)^a$$

$$J_{c0}(B) = J_{c00}\left(1 - \frac{B}{B_{c20}}\right)$$

Table 4.2 – $T_c(B)$ and $J_c(B,T)$ fit parameters for SSC Inner and Outer Cable

Parameter	Units	Inner	Outer
B_{c20}	T	15	15
T_{c0}	K	9.05	9.3
J_{c00}	A/mm^2	9330	9400
a		0.59	0.66

[1] *M.S. Lubell, IEEE Trans. on Mag, MAG-19 (1983), 754

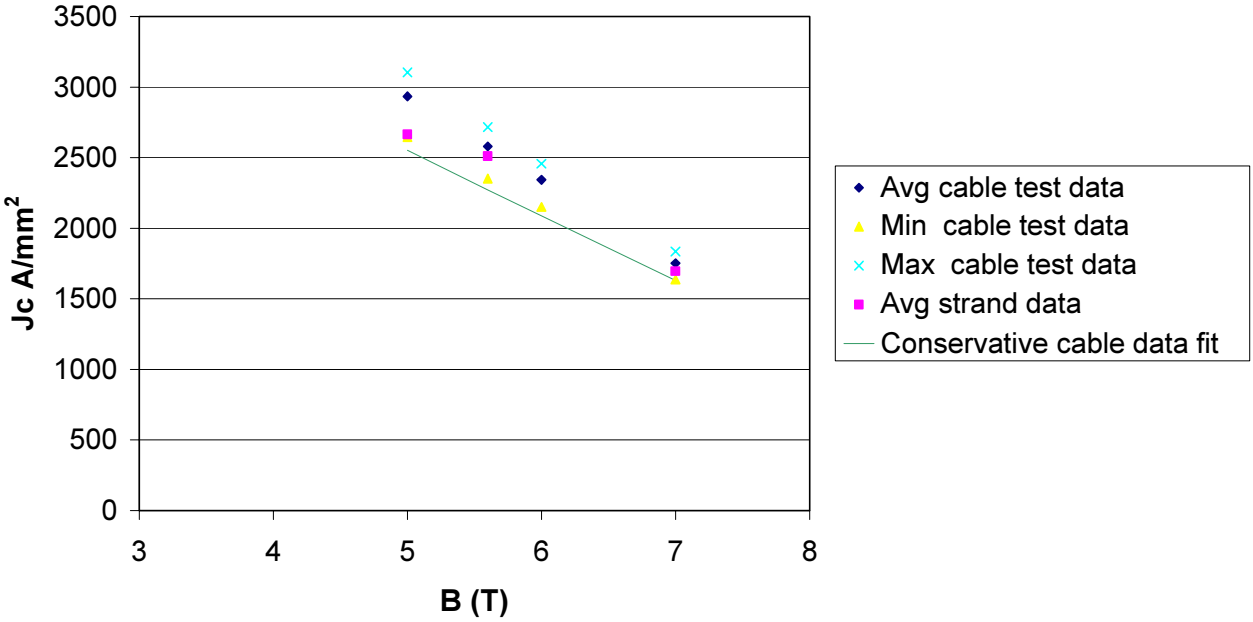

Figure 4.2 – Plot of SSC inner strand and cable data at 4.2 K with J_c fit from Table 4.2

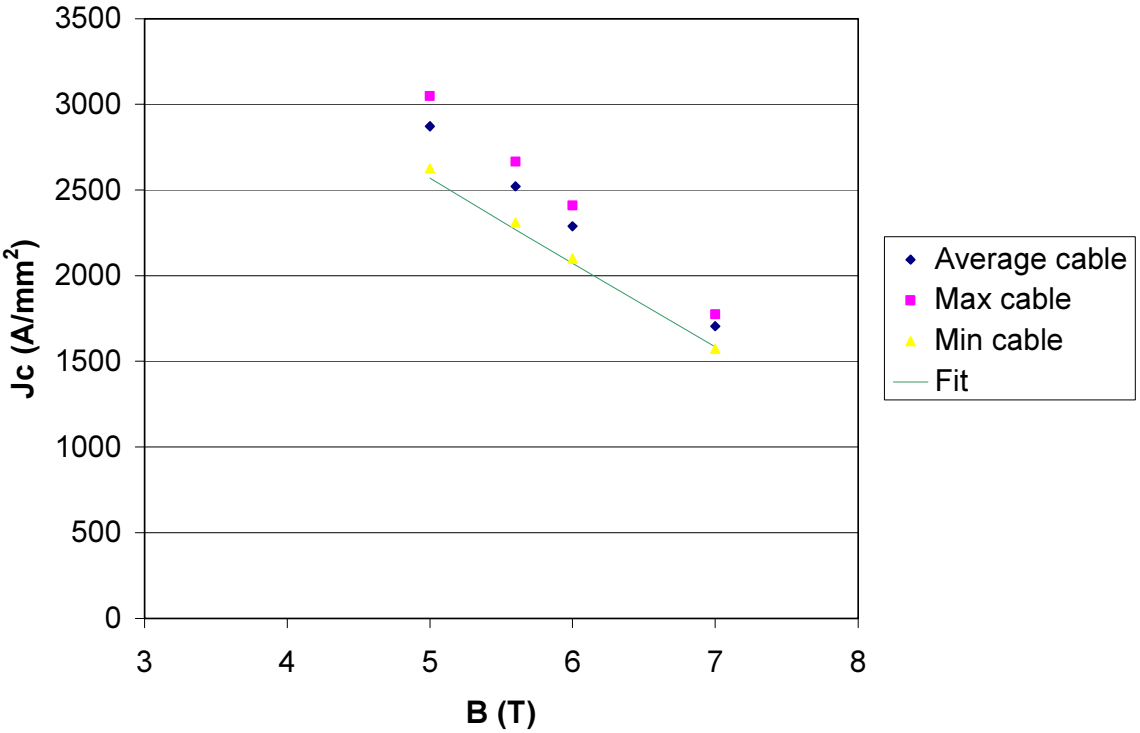

Figure 4.3 – Plot of SSC outer strand and cable data at 4.2 K with J_c fit from Table 4.2

Cable data was also used to establish the average non-copper cross sectional area in the cables, and this data is given in Table 4.3. Since these values are based on actual measurement, they take precedence over the SC area values listed in Table 4.1.

Table 4.3 – Average non-copper area

Area non-copper	Units	Value
Inner	mm^2	6.21
Outer	mm^2	4.286

The general coil configuration to meet the field requirements, as well as the peak fields on the conductors and nominal stored energies, are determined as part of the field solution, which is discussed elsewhere. Turn insulation for all conductors has the same design consisting of a half lap of 1 mil Kapton tape followed by a half lap of 3 mil fiberglass tape, for a total turn overwrap thickness of 8 mils. Aspects of the conductors chosen individually for the PS, TS, and DS will now be discussed.

Production Solenoid Conductor

The PS conductor operates in the highest field environment and with the most stored energy of all the MECO conductors. In addition, it is the only coil set operating in the presence of significant nuclear heating, whose magnitude (μW/g) is summarized by the graph in Figure 1. In addition, the PS is the only coil whose operating current is limited by the temperature margin constraint, and this current limit is 3500 A.

The conductor configuration chosen for the PS coil is shown in Figure 4.4. The conductor has SSC inner cable soft soldered into the copper channel whose dimensions have been chosen to meet both the protection requirements and to minimize the turn width (14.93 mm with insulation). Minimizing the turn width enables placing the maximum number of turns in a layer, and thus minimizes the number of layers, and limits the temperature rise in the radial middle of the winding.

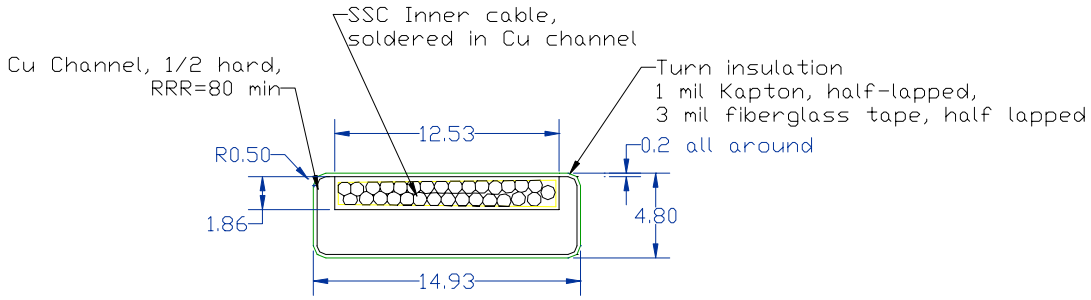

Figure 4.4 –The Production Solenoid coil conductor.

When the PS conductor is wound into coil builds required by the field solution, the coil builds, and conductor lengths given in Table 3.2 of the Field Specification and Field Matching Section result.

All PS coils are cooled at their ID and OD by 2-phase Helium at about 4.5 K. In addition to the turn insulation on the conductor shown in Figure 4.4, each coil will have 1 mm of ground insulation, which is assumed to be a combination of G11 and an over-wrap of epoxy impregnated fiberglass tape. The turn insulation and the ground insulation offer the major thermal resistance to heat removal from the winding to the helium. A combined thermal analysis that includes the effects of the nuclear heating together with cooling arrangement shows that the first PS coil (coil 1 in) has the lowest temperature margin, and that this margin is minimum at the location of the

peak field in the winding. A plot of the temperature margin in the first PS coil from this analysis is provided in Figure 4.5. The contours account for the variation of both operating temperature and magnetic field at each location.

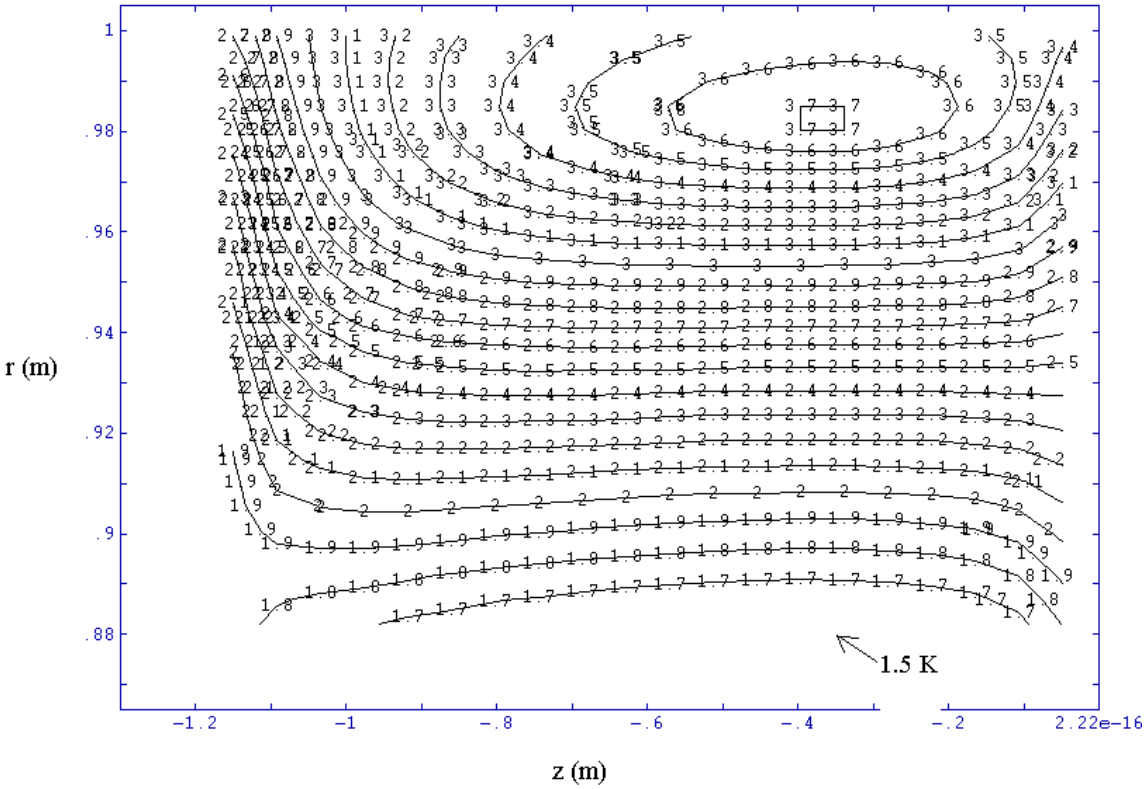

Figure 4.5 – Contours of constant temperature margin in the first PS coil.

Minimum temperature margin is at the point labeled 1.5 K, which is at the winding ID and at the location of the peak field.

Transport Solenoid Conductor

The Transport Solenoid currents are limited more by the allowable current placement tolerances relative to meeting the field specification than by the temperature margin requirement. See the field matching section of this report for more information. These tolerance limits set the current in the straight sections of the Transport Solenoid at 1500 A and for the most part in the 90 ° bend sections at 4000 A, although the first and last coils in the 90 ° bend sections are set at 1500 A as an added conservatism.

The TS conductor design is shown in Figure 4.6. This design is common for coils operating both at 1500 A and at 4000 A. The quench analysis shows that there is sufficient copper in the outer cable alone, without the copper channels, to satisfy the protection requirements. The use of a common conductor with the copper channel shown in Figure 4.6, however, is considered beneficial from the perspectives both of manufacturing ease and robustness of the design for the 1500 A TS coils, except in the coils immediately adjacent to the Be window. Here, to maintain the field specifications throughout the window region, the coils require more layers than the other TS coils. See Table 3.2.

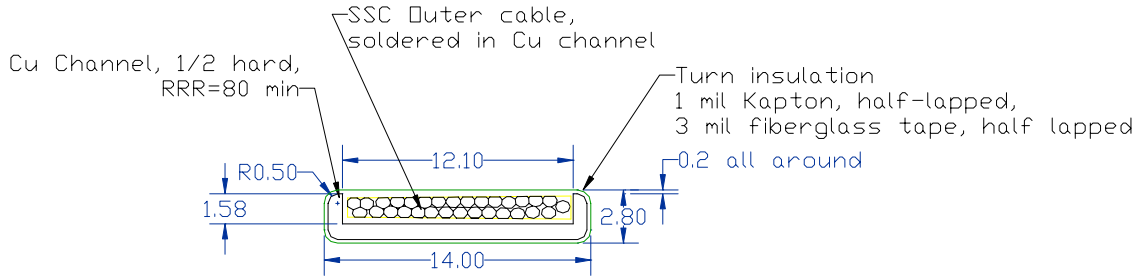

Figure 4.6 – TS coil conductor, except in coils next to the Be window (see text).

The TS coils immediately adjacent to the beryllium window have 71 and 62 layers and are wound with SSC outer cable without the copper channel. This exception to the winding scheme is used in these two coils only to facilitate access to the window, which may require servicing from time to time.

Detector Solenoid Conductor

As in the Transport Solenoid, the Detector Solenoid currents are limited more by allowable current placement tolerance relative to meeting the field specification than by the temperature margin requirement. These tolerance limits set the current in all DS coils at 4000 A. Due to the larger stored energy in the DS, however, the DS conductor requires more copper for protection. The DS conductor design is shown in Figure 4.7 and coil builds are given in Table 3.2.

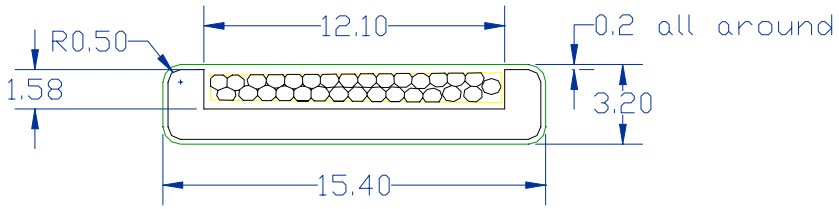

Figure 4.7 – DS coil conductor.

A summary of the conductor parameters for all coils is given in Table 4.4. In this table, the following definitions apply (units are given in the table):

Energy	stored energy in the coil set
I_{op}	operating current
τ	calculated time constant based on the stored energy, the operating current and setting V_{dump} = 1800 V
A_{sc}	non-copper area in the cable
J_{sc}	current density in the non-copper area
A_{Cu_cable}	Area of the copper in the cable
w_{cond}	overall width of the copper channel
h_{cond}	overall height of the copper channel
w_{slot}	width of the slot in the channel
h_{slot}	height of the slot in the channel

r_{chan}	corner radius of outer corners in the channel
t_{ins}	totol overwrap thickness of turn insulation
w_{turn}	width of the insulated conductor
h_{turn}	height of the insulated turn
A_{ch_actual}	area of the copper in the channel
A_{Cu_actual}	sum of channel copper area + cable copper area
$A_{inscond}$	cross-sectional area of the insulated conductor
$J_{inscond}$	current density over the cross-sectional area of the insulated conductor
J_{cu}	current density when all current flows in the Acu_actual
B_{max}	peak field on the conductor in the coil set
T_{op}	operating temperature of the conductor at the peak field location
J_c	critical current at Top, Bmax
f_c	J_{op}/J_c
TempMar	$T_{cs} - T_{op}$, where T_{cs} is the current sharing temperature

Table 4.4 – Conductor parameter summary

	Units	PS	TS1+TS3u +TS2 end coils	TS2 w/o end coils	TS3d+TS5 +TS4 end coils	TS4 w/o end coils	DS
SSC Cable Type		Inner	Outer	Outer	Outer	Outer	Outer
Energy	MJ	109	3.26	4.72	2.01	3.55	30.8
I_{op}	A	3500	1500	4000	1500	4000	4000
τ	s	34.67	2.41	1.31	1.49	0.99	8.54
A_{sc}	mm^2	6.21	4.29	4.29	4.29	4.29	4.29
J_{sc}	A/mm^2	564	350	933	350	933	933
A_{Cu_cable}	mm^2	8.07	7.71	7.71	7.71	7.71	7.71
w_{cond}	mm	14.53	13.60	13.60	13.60	13.60	15.00
h_{cond}	mm	4.40	2.40	2.40	2.40	2.40	2.80
w_{slot}	mm	12.53	12.10	12.10	12.10	12.10	12.10
h_{slot}	mm	1.86	1.58	1.58	1.58	1.58	1.58
r_{chan}	mm	0.5	0.5	0.5	0.5	0.5	0.5
t_{ins}	mm	0.2	0.2	0.2	0.2	0.2	0.2
w_{turn}	mm	14.93	14	14	14	14	15.4
h_{turn}	mm	4.8	2.8	2.8	2.8	2.8	3.2
A_{ch_actual}	mm^2	40.41	13.32	13.32	13.32	13.32	22.68
A_{Cu_actual}	mm^2	48.48	21.03	21.03	21.03	21.03	30.39
$A_{inscond}$	mm^2	71.664	39.2	39.2	39.2	39.2	49.28
$J_{inscond}$	A/mm^2	48.84	38.27	102.04	38.27	102.04	81.17
J_{Cu}	A/mm^2	72.2	71.3	190.2	71.3	190.2	131.6
B_{max}	T	5.9	3.54	2.85	3.37	2.49	2.03
T_{op}	K	4.58	5.04	5.04	5.04	5.04	5.04
$J_c(T_{op}, B_{max})$	A/mm^2	1832	2881	3207	2961	3379	3599
f_c		0.308	0.122	0.291	0.118	0.276	0.259
Temp. Margin	K	1.5	2.30	1.97	2.37	2.12	2.30

Notes:

1) Actual operating temperature varies with location. The values given in the table correspond to the peak-field location where the margin is minimum.
2) Operating temperature for the TS and DS coils are chosen consistent with the discussions in the Cryogenic section of this report.

Section 5 - Coil Insulation Design

The maximum coil voltage in all MECO coils is seen at the beginning of a quench protective dump, and all of the MECO coil/power supply sets are designed to operate with a maximum dump voltage of 2 kV to ground. In addition, the PS coils are subject to a maximum nuclear heat load of 20 μW/g during a 0.5 second beam pulse. The experiment is designed for 3×10^7 pulses, so the total integrated radiation dose over the lifetime of the experiment is 22.5 Mrad. Using a conversion factor of 4×10^{21} n/m^2 = 10^9 rads of gamma radiation[2] gives an equivalent fluence of 9×10^{19} n/m^2 or approximately 1×10^{20} n/m^2 for the PS system. These dose and fluence levels will be useful in the discussions that follow regarding the insulation system's tolerance to nuclear radiation damage.

All of the MECO coils will be wound with a single pancake winding at one end with the balance of the coil layer wound. This approach is needed to extract the coil leads at the coil OD where double pancake windings are not used. Double pancake windings are less desirable and do not form the baseline approach, since this would result in the need for additional conductor joints and lead to lower reliability. The pancake must have a layer of insulation between itself and the adjacent layer-wound portion of the coil. This insulation will see nearly the full coil potential on quench, so it should be designed with the same thickness as the ground insulation.

Table 5.1 gives the approximate number of total turns in each of the six MECO coil sets, as well as the maximum number of turns per layer, enabling a calculation in the same table of the maximum turn-to-turn voltage for a layer wound coil. The maximum turn-to-turn voltage is simply the single turn voltage multiplied by the number of turns per layer times two.

Table 5.1 – Turn to turn voltages in MECO Coils

Coil Set	Coils	Approx. total turns	Volts/turn at dump	Approx. max turns/ layer	Max voltage between turns
1	PS	5595	0.36	77	55
2	TS13u	2975	0.67	12	16
3	TS2	1796	1.11	12	27
4	TS3d5	2106	0.95	12	23
5	TS4	1543	1.3	12	31
6	DS	3118	0.64	63	81

Turn insulation for all coils is specified as two half-laps of 1 mil Kapton tape (2 mils total), followed by 2 half laps of 3 mil fiberglass tape (6 mils total). Table 1 shows the maximum turn-to-turn voltage to be 81 V for the DS. If we conservatively assume that all the voltage might be across one or the other of the materials, the worst-case turn-to-turn electric field is about 20 V/mil in the Kapton or about 9 V/mil in the epoxy impregnated fiberglass tape. These compare very favorably with handbook[3] published breakdown voltages in the range of 500 V/mil for Kapton and 300 V/mil in epoxy impregnated fiberglass tape. Johnson[4] found a lower scatter band

[2] Reed et al, "US/ITER Insulation Irradiation Program—Update III, Aug 4, 1994

[3] *Electronic Designers Handbook*, Second Edition, L.J. Giacoletto, Editor, McGraw-Hill Book Company, 1977

[4] H.G. Hohnson, M.W. Liberi, and T.G. Meighan, "Electrical Insulation Development Esperiences and Test Results for TFTR Magnetic Field Coils", Proceedings of the 8th Symposium on Engineering Problems in Fusion Research, San Francisco, 1979

for the breakdown limit in a 0.375" thick epoxy fiberglass insulation system for TFTR to be greater than 100 V/mil all the way out to greater than 10^6 half cycles of 60 Hz.

Ground insulation and the pancake-to-layer-wound insulator is designed to be 1 mm of epoxy impregnated fiberglass tape or G11CR. With a maximum voltage of 2000 V to ground, the maximum voltage gradient in the epoxy-impregnated fiberglass tape is 2000/46 = 43.5 V/mil, which is again safely below the breakdown limit for these materials.

Insulation testing was done as part of the ITER program to assess the degradation of mechanical properties with radiation dose and neutron fluence. Compressive and shear strengths were evaluated. Results, together with the MECO operating lines, are shown in the figures below[5]. The MECO neutron fluence level of 10^{20} n/m^2 is clearly low enough to have negligible effect on the insulation compressive strength of the epoxy impregnated fiberglass.

Figure 5.2 shows the percent of initial shear strength retained by the insulation system as a function of the irradiation dose. At the MECO integrated dose level, the data imply no damage due to radiation at 4 K and only a 5% reduction for room temperature irradiation, using the relatively small number of data points. Kapton, which is a polyimide, is far more tolerant to irradiation than epoxy-based systems.

Finally, the issue of gas evolution was evaluated by Evans[6] in 1995, with results provided in Table 2. If a rate of 1 cm^{3}g^{-1} MGy^{-1} is taken as representative, together with an assumed density of 1.2 g/cc, and a dose of 0.22 MGy, the evolved gas over the MECO lifetime will be 0.26 cc/cc. Of all the effects, this one is simultaneously of greatest concern and most difficult to assess. Acceptable thresholds for gas evolution were never satisfactorily defined for ITER. This is a mechanism, however, which is thought to have destroyed the DESY magnet[7]. The ITER study also found that the gas evolution could be lowered by the addition of small amounts of accelerator to the resin. Both the hardener and the accelerator affect the pot life of the resin, once it is mixed for impregnation. Thus, for the potted winding which is recommended for MECO, the solution would appear to be to pick the combination of resin, hardener and accelerator that will provide the required mechanical properties and pot life, while minimizing the expected gas evolution under irradiation. This tradeoff would best be done by experts in the field, those who produced the ITER report being an example. At the same time, further reduction of the maximum radiation dose from the assumed peak value of 20 μW/g[8] will directly reduce the expected net gas evolution.

[5] P.E. Fabian and J.B. Schutz, "US ITER Insulation Irradiation Program", 31 August 1995
[6] D. Evans and R.P. Reed, "Gas Evolution from Potential ITER Insulating Materials, 15 November 1995
[7] H. Becker and J. Schultz, "Magnet Design and Material Requirements", in Proceedings of Meeting, Electrical Insulators for Fusion Magnets, Dec 1980, Germantown, MD
[8] UCI spreadsheet "newcoldmass7b.xls"

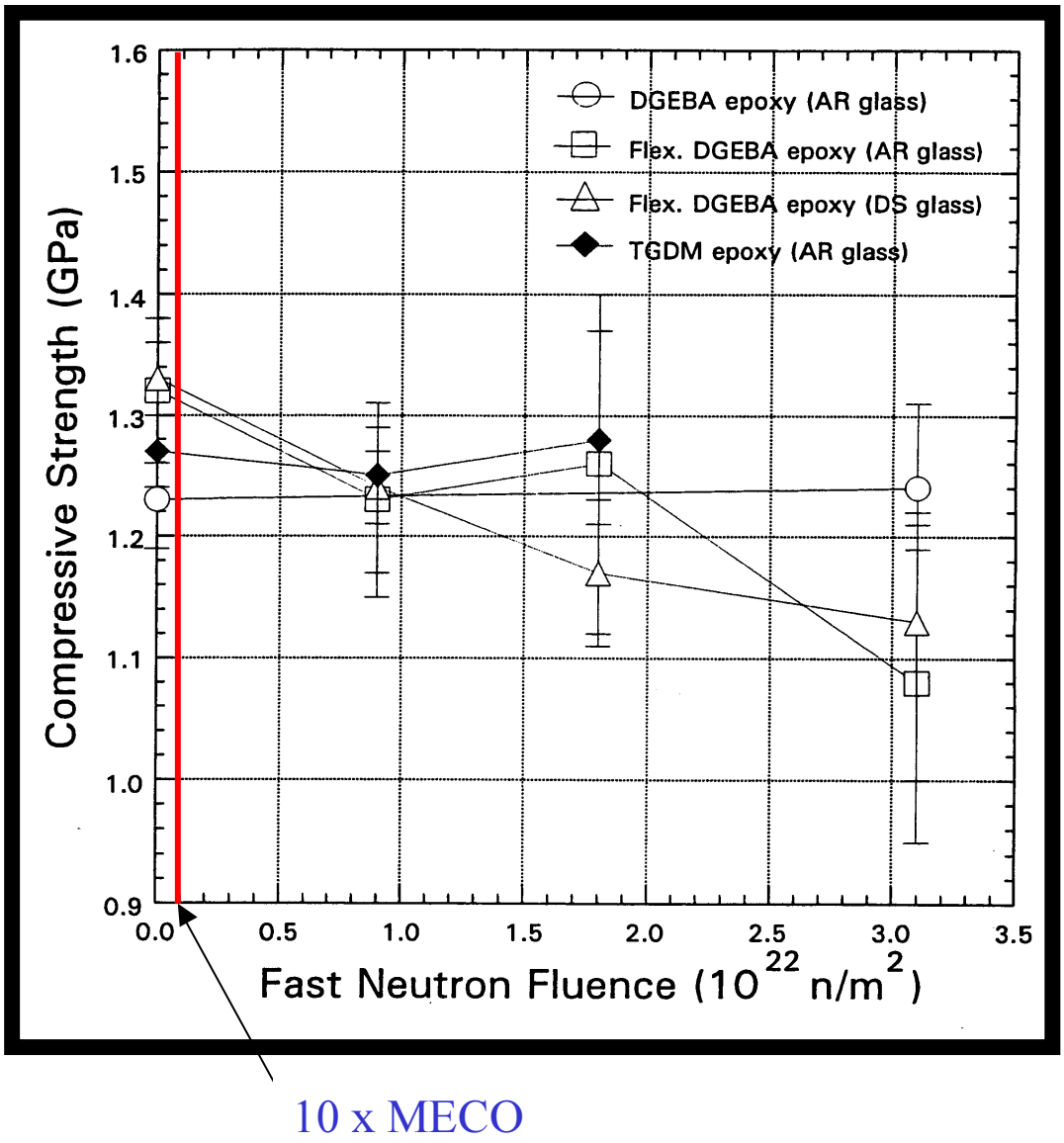

Figure 5.1 – Compressive strength degradation in epoxy systems as a function of neutron fluence (see footnote 4 for credit).

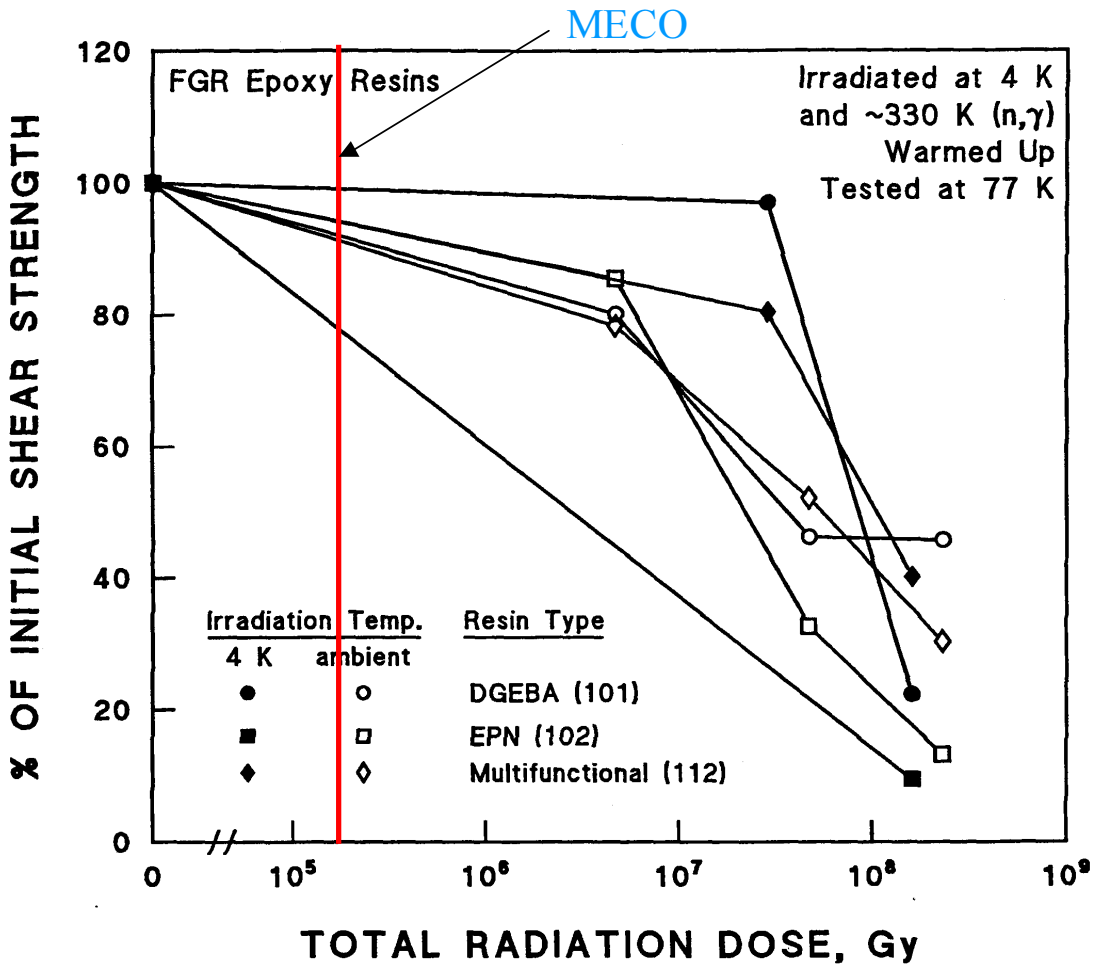

Figure 5.2 – Compressive strength degradation in epoxy systems as a function of radiation dose. Note 1 Gy = 100 Rads (see footnote 4 for credit).

Table 5.2 – Comparative gas evolution rates of epoxy resins with anhydride and amine curing agents (see footnote 5 for credit) (cm^3g^{-1} MGy^{-1}).

Resin	Hardener			
	MNA (anhydride)	MTHPA (anhydride)	DDM (aromatic amine)	DETD (aromatic amine)
DGEBA	1.35 1.23	1.38 1.27	0.32	0.57
DGEBF		1.08 1.03		0.58
TGPAP		1.19 1.1		0.58
TGDM	1.4 0.77		0.38	

Section 6 - Conductor Joint Design

Joint design and analysis is discussed in more detail in [mm048]. A summary of the key points is presented here. Regardless of the differences in conductor details between coil types, all MECO joints are designed to be soft-soldered lap joints with a recommended minimum overlap length of two cable twist pitch lengths, or 188 mm for the PS (SSC inner cable) and 172 mm for the TS and DS (SSC outer cable). Most joints will be formed in the "shaking hands" rather than the "praying hands" arrangement, although the analysis and results apply to either type, should special conditions require the latter in certain cases. Figure 6.1 shows a typical joint cross-section and soldering arrangement.

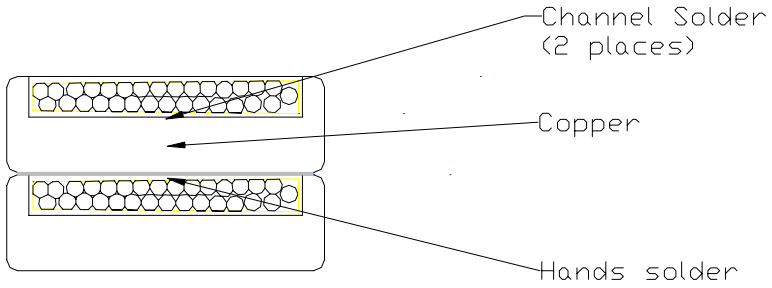

Figure 6.1 – Typical joint configuration.

Joint resistance is expected to range from about 1 nΩ to about 11 nΩ depending on the magnitude of the local magnetic field, the quality of the solder bonds and also on the types of solder used. The analysis assumed that the cable will be soldered into the copper channel with 60Sn-40Pb solder (liquidus 188 °C, solidus 188 °C), and that the two hands will be bonded with 44In-42Sn-14Cd (Indalloy #8) with a liquidus/solidus temperature of 93 °C. Because most of the joint resistance comes from the solders in the current path (see Figure 6.1), turning the top conductor over so the cables of the conductors face each other is not particularly effective in reducing the joint resistance, and is considered not worth the bother.

All joints are assumed to be insulated with the nominal turn insulation (half lap of 1 mil Kapton plus a half lap of 3 mil epoxy impregnated or wet fiberglass tape), plus a 1 mm thick ground wrap consisting of an additional half of 1 mil Kapton with the balance one or more layers of half lapped epoxy impregnated or wet fiberglass tape. In the PS, the insulated joints will be immersed in the 2-phase, 4.5 K helium bath. In the TS and DS, because the windings are in vacuum and conduction cooled, the joints will be clamped to cooling plates, which are assumed to be at a maximum temperature of 4.6 K. Heat flux from the joint Joule heating must pass through the insulation layers to the cooled outside joint surface, and this raises the joint internal temperature above the surface temperature. The peak joint temperature is required to remain below the current-sharing temperature by the project temperature margin amount of 1.5 K. The model shows that the joints described above meet this requirement, although some development activity should be included in the final design/fabrication phase to ensure that the joints can be soldered to reliably achieve minimal resistance.

The parameter ranges used in the analysis are summarized in Table 6.1, and the tabulated results from the model are given in Table 6.2, with the key values of the joint resistance and the joint temperature margin highlighted in yellow.

In all cases, the calculated joule heating in the joint is under 0.2 W in the worse case. With the present design, there will be 90 – 100 joints in the entire MECO magnet, so the joint losses will contribute a maximum of 20 watts of heat load to the cryogenic system.

The preferred approach for the joints would be to have joints only between individual coils within a coil group and not inside the winding. Whether this can be achieved in practice, will require verification of the SSC cable lengths in inventory, which has not been done during conceptual design. If the individual cable piece lengths are too short to enable the winding of all coils without internal joints, then the detailed design of a joint internal to the coil must be evaluated. Placing an internal joint at the end of a coil layer, where the joule heat can be conducted out to the helium cooled end flanges (PS) or to the copper conduction sheets (TS and DS) may be sufficient to keep the joint temperature at T_{cs} – 1.5 K, but this will need to be analyzed for the specific field and configuration as part of final design.

Table 6.1 – Best and worst case assumptions used in the calculations

Parameter	Best	Worst
B(T)	B_{min}	B_{max}
RRR_{Cu}	80	50
Ts1 (m)	0	hslot - hcable
Ts2 (m)	0	hslot - hcable
Ts3 (mils)	0.001	0.005
f	1.0	0.5
Number of cable twist pitches in joint length	1	1.5

Table 6.2 – Joint analysis model.

			PS		TS1,3,5		TS2,4		DS	
	Units	Notes	Rjoint_min	Rjoint_max	Rjoint_min	Rjoint_max	Rjoint_min	Rjoint_max	Rjoint_min	Rjoint_max
I	A		3500	3500	1500	1500	4000	4000	4000	4000
B	T	1	0.016	2.310	0.030	2.440	0.032	0.727	0.008	1.680
Twist pitch	m		0.094	0.094	0.086	0.086	0.086	0.086	0.086	0.086
Ws	m		0.01253	0.01253	0.0121	0.0121	0.0121	0.0121	0.0121	0.0121
ρsolder1	Ohm-m	2	6.52E-09	6.67E-09	6.52E-09	6.68E-09	6.52E-09	6.57E-09	6.52E-09	6.63E-09
ρsolder2	Ohm-m	3	3.63E-08	4.30E-08	3.64E-08	4.34E-08	3.64E-08	3.84E-08	3.63E-08	4.12E-08
RRRCu			80	50	80	50	80	50	80	50
ρCu			1.98E-10	4.26E-10	1.98E-10	4.32E-10	1.99E-10	3.52E-10	1.97E-10	3.97E-10
hslot	m		1.86E-03	1.86E-03	1.58E-03	1.58E-03	1.58E-03	1.58E-03	1.58E-03	1.58E-03
hcable	m		1.46E-03	1.46E-03	1.17E-03	1.17E-03	1.17E-03	1.17E-03	1.17E-03	1.17E-03
hchannel	m		4.40E-03	4.40E-03	2.40E-03	2.40E-03	2.40E-03	2.40E-03	2.80E-03	2.80E-03
Ts1	m		0.00E+00	4.00E-04	0.00E+00	4.10E-04	0.00E+00	4.10E-04	0.00E+00	4.10E-04
Ts2	m		0.00E+00	4.00E-04	0.00E+00	4.10E-04	0.00E+00	4.10E-04	0.00E+00	4.10E-04
Ts3	m		2.54E-05	1.27E-04	0.0000254	1.27E-04	0.0000254	1.27E-04	2.54E-05	1.27E-04
Tcu	m		2.54E-03	2.54E-03	8.20E-04	8.20E-04	8.20E-04	8.20E-04	1.22E-03	1.22E-03
f			1	0.5	1	0.5	1	0.5	1	0.5
k_kap	W/mK		0.01	0.01	0.01	0.01	0.01	0.01	0.01	0.01
t_kap	m		1.02E-04	1.02E-04	1.02E-04	1.02E-04	1.02E-04	1.02E-04	1.02E-04	1.02E-04
k_G10	W/mK		0.062	0.062	0.062	0.062	0.062	0.062	0.062	0.062
t_G10	m		1.12E-03	1.12E-03	1.12E-03	1.12E-03	1.12E-03	1.12E-03	1.12E-03	1.12E-03
keff	W/mK		4.33E-02	4.33E-02	4.33E-02	4.33E-02	4.33E-02	4.33E-02	4.33E-02	4.33E-02
Tins	m		1.22E-03	1.22E-03	1.22E-03	1.22E-03	1.22E-03	1.22E-03	1.22E-03	1.22E-03
ntp			1.00	1.50	1.00	1.50	1.00	1.50	1.00	1.50
L	m		0.094	0.141	0.086	0.129	0.086	0.129	0.086	0.129
Rs1			0.00E+00	3.02E-09	0.00E+00	3.51E-09	0.00E+00	3.45E-09	0.00E+00	3.48E-09
Rs2			0.00E+00	3.02E-09	0.00E+00	3.51E-09	0.00E+00	3.45E-09	0.00E+00	3.48E-09
Rs3			7.83E-10	6.19E-09	8.88E-10	7.07E-09	8.88E-10	6.25E-09	8.86E-10	6.70E-09
Rcu			4.26E-10	1.22E-09	1.56E-10	4.54E-10	1.56E-10	3.70E-10	2.31E-10	6.20E-10
Rjoint	Ohm		1.21E-09	1.35E-08	1.04E-09	1.45E-08	1.04E-09	1.35E-08	1.12E-09	1.43E-08

Joint power	W		1.48E-02	1.65E-01	2.35E-03	3.27E-02	1.67E-02	2.16E-01	1.79E-02	2.29E-01
QA	W/m^2		5.63E+00	4.18E+01	1.03E+00	9.55E+00	7.32E+00	6.32E+01	7.83E+00	6.68E+01
ΔT_actual	K		1.59E-01	1.18E+00	2.90E-02	2.69E-01	2.06E-01	1.78E+00	2.21E-01	1.88E+00
Tbath	K		4.50	4.60	4.50	4.60	4.50	4.60	4.50	4.60
Top	K		4.66	5.78	4.53	4.87	4.71	6.38	4.72	6.48
Tcs	K		8.47	7.61	8.70	7.79	8.13	7.87	8.14	7.49
Tcs-Top	K		3.81	1.84	4.17	2.92	3.43	1.48	3.42	1.00
	Notes:	1	Fields are from MECO-MIT- ALRadovinsky-110501-01.							
		2	60Sn-40Pb, R.W. Fast, W.W. Craddock, M. Kobayashi and M.T. Mruzek, "Electrical and							
			mechanical properties of lead/tin solders and splices for superconducting cables", Cryogenics,							
			Vol. 28, January 1988, pp. 7-9.							
		3	44In-42Sn-14Cd, Solder resistivities.xls from T. Painter, NHMFL, via S. Pourrahimi							
			Fractional contribution to Rjoint							
		Rs1	0%	22%	0%	24%	0%	26%	0%	24%
		Rs2	0%	22%	0%	24%	0%	26%	0%	24%
		Rs3	65%	46%	85%	49%	85%	46%	79%	47%
		Rcu	35%	9%	15%	3%	15%	3%	21%	4%

Section 7 - Current Lead and Bus Bar Design

The MECO magnet system requires six (6) separate power circuits with current ratings as shown in Table 7.1. The nine coils of the PS are connected in series and energized by a single power supply. All coils of the DS are also connected in series and energized by a single power supply. The TS magnet system is separated into four individual circuits each with an independent power supply.

Table 7.1 – Coil operating currents

Coil Set	Location	Operating Current (A)
1	PS	3500
2	TS13u	1500
3	TS2	4000
4	TS3d5	1500
5	TS4	4000
6	DS	4000

Separation of the coils into these six circuits allows the PS, TS, and DS magnets to be energized independently. This is useful for start-up operation and other types of off-normal operation. The TS is subdivided first into two halves contained in separate cryostats on either side of the beryllium window. Each TS half is then further subdivided electrically into two circuits of different currents. Although each coil set in the upstream TS cryostat has the same operating current as a coil set in the downstream cryostat, they are not connected in series from a common power supply. That could be done but it would either require cold bus interconnects bridging the beryllium window, or separate current leads and room temperature jumper buses. In either case, this would prevent independent energization of the upper and lower TS magnet halves. The option selected here is to bring all TS circuits to room temperature via four separate current lead pairs. Each of these circuits then would have their own, independent quench detection and protection circuits.

Current Bus

For safety and reliability, all components that could potentially require service or maintenance are located outside the radiation shielding. Since current leads are defined as such components, they require superconducting bus bars to connect the magnets from their respective cryostats to the current leads where the transition occurs between nominal 4.5 K superconducting operation and room-temperature normal resistive current busbars. In all cases, the superconducting bus will be made from the same superconductor that is used for the respective magnet it is servicing. The lengths and routing of each current bus have not been determined yet. This can be done after determination of the final location of the coils and the definitive radiation shielding block placement. All bus bars should be routed to minimize total length and directional changes. Since the PS coil's cryogenic cooling scheme is different from that of the TS and DS coils, there are slight differences in the bus bar details.

PS Current Bus

The PS coil is forced-convection-cooled by two-phase helium. The busbars serve as the helium transfer tubes from the external PS control dewar to the PS magnet cryostat. Since the bus bars will be contained within the equivalent of a liquid helium transfer tube the bus bars must be contained inside the helium space, and the transfer line thermally shielded and vacuum insulated.

The PS current bus will use the same 3500 A conductor used to wind the nine PS sub-coils. The current to and from the PS will be brought to the bottom of the cryostat where a low resistance joint will be made to the bus bar conductor. Bus bars will be individually insulated along their lengths. They will be clamped together with insulating supports periodically along their length. If the clamps are bolted, the bolts will also be insulated. The insulation system should be rated for full terminal-to-terminal and terminal-to-ground voltage levels. Both current buses will be contained within a single helium transfer tube.

Since it is likely that the bus bar/transfer line will make several turns along it's route between the control dewar and the magnet cryostat, it is envisioned that the current/helium transfer system must be at least partially assembled in the field. The bus bar, however, must be fabricated from a single length of conductor for each lead, having only a single termination at the magnet and current lead ends. No intermediate electrical splices should be required.

PS Current Leads

The PS current bus will terminate near, but not inside, the PS control dewar located outside the radiation shielding wall, in a location accessible for maintenance. The bus bar will end in a low resistance splice to the bottom of a standard vapor-cooled current lead of the proper current rating. The vapor-cooled leads will receive their supply of helium from a separately valved and controlled helium branch from the PS control dewar. These tubes supplying helium to the vapor-cooled current leads will require a helium-tight, cold, electrical insulating break to isolate the cryogenic piping system from the magnet system potential. An appropriate vacuum and thermal radiation insulated container will hold the vapor cooled current lead.

TS and DS Current Buses

Although there are four pairs of TS current leads and a single DS current lead pair, they are geometrically and topologically similar because all the coils they serve are conduction-cooled by forced flow, two-phase helium. Here the bus bars are made, respectively, from the same conductor as used for the coils they service. The current to and from the coils will be brought to the final lead-out pairs where a low resistance joint will be made to the bus bar conductor. Bus bars will be individually insulated along their lengths. They will be clamped together with insulating supports periodically along their length. If the clamps are bolted, the bolts will also be insulated. The insulation system should be rated for full terminal-to-terminal and terminal-to-ground voltage levels.

Both current bus leads for each electrical circuit will be traced by helium tubes and conduction cooled (through the electrical insulation layer) by the same helium stream which cools the magnet they are servicing. The conduction-cooled busbars will be contained and supported within a thermally shielded, vacuum-insulated tube.

Since it is likely that the bus bar/transfer line will make several turns along it's route between the magnet cryostat and the vapor-cooled lead location outside the radiation shielding, it is envisioned that the current/helium transfer system must be at least partially assembled in the field. The bus bar, however, must be fabricated from a single length of conductor for each lead, having only a single termination at the magnet and current lead ends. No intermediate electrical splices should be required.

TS and DS Current Leads

The TS and DS current buses will terminate near, but not inside, the TS and DS control dewars, respectively, located outside the radiation shielding wall, in a location accessible for maintenance. The bus bars will end in a low resistance splice to the bottom of a standard vapor-cooled current lead of the proper current rating. The vapor-cooled leads will receive their supply of helium from a separately valved and controlled helium branch from the helium stream exiting the individual magnets and busbars. An appropriate vacuum and thermal radiation insulated container will hold the vapor cooled current leads.

Section 8 - Quench Detection System

Overview

A preliminary design of the quench detection (QD) and data acquisition system (DAS) for monitoring MECO magnet system is presented. A conventional voltage measurement method is adopted for quench detection. The locations of voltage taps and the routing of the signal wires are described. This is followed by signal conditioning circuit, which is designed to protect the data acquisition system, prevent the high background noise from saturating the DA channels, and reduce error in the analog to digital conversion by using anti-aliasing low-pass filters.

Quench detection using voltage method measures the resistive component in the coil voltage. The quench detector triggers the quench protection system when the resistive voltage exceeds a pre-selected threshold voltage $V_{threshold}$ over a duration t_{delay}. The resistive component (signal) is in general a few orders of magnitude less than the inductive component (noise). To improve the signal to noise ratio, an often-used practice is to wind an inductive-cancellation pick up coil following the magnet winding. An attendant risk of using a co-wound pickup coil is that the pick up coil wires themselves can cause shorts and reduce reliability. An alternative is to process voltage signals from two neighboring coils through a bridge to reduce the inductive component. In the case of the MECO magnet system, which has a large number (94) of coils with various numbers of turns and layers, it is impractical to use either of the above cancellation methods in the primary quench detector.

A digital quench detection (DQD) system is proposed as the primary quench detector for the complicated MECO magnet system. The DQD uses six programmable DA cards. Each DA card has the $V_{threshold}$ and the virtual inductances and joint resistances built in the DA program. Once the coil voltages, joint voltages, and the equivalent charging currents are scanned at each sampling time, the DA program calculates both self and mutual inductive voltages in each coil, and the resistive voltage in each joint. The resistive voltage in a coil is obtained by subtracting the virtual inductive voltage from the measured coil voltage. The additional resistive voltage in the joint is similarly obtained. The feasibility of the DQD for the present MECO quench protection plan is evaluated. The speed and the reliability of the DQD are discussed.

An optional analog quench detector (AQD) is proposed as a backup detection system. This is used to prevent coil damage caused by any failure mode in the DQD, which has not been included in the present design. The AQD detects quenches in each coil system instead of a single coil. A larger threshold voltage is used to avoid interference with the primary DQD. An AQD dump signal in any power supply circuit overrides the lack of a DQD dump signal for that circuit. Though there are large differences in inductance in the various coils, a balancing circuit can be used in the AQD to make comparisons among various coils in the same circuit.

The quench detection system operates in conjunction with a data acquisition system (DAS) to help with quench isolation and troubleshooting. Both the DQD and the AQD shall be powered with a backup Uninterruptible Power Supply (UPS). When power is lost, the DQD/AQD shall begin to slowly discharge the magnets through their power supplies and the normal power bus resistance, but without the presence of reverse voltage from the power supply. Should any coil quench during the power loss sequence or subsequent slow discharge, the magnets shall be fast dumped using the same guidelines as specified here for quench protection during normal operation.

Voltage Taps and Wire Routing

Figure 8.1 shows that each of the 94 MECO coils is designed to have two voltage taps. Each is located at the coil termination close to the near end of the coil joint. In each of the six magnet systems, the last coil at each end of the magnet system has an extended bus connected to the external current lead. A pair of voltage taps, respectively located at the outer end of the coil winding and beyond the bus joint, is used to monitor the bus connection.

For reliability of signal delivery and reduction of induced voltage, each voltage tap is soldered with two voltage signal wires. As shown in Figure 8.1, all the voltage wire pairs are twisted. Not shown in the figure, although recommended, are current limiting resistors that should be placed between the cold wire end and the soldered connection. These can go a long way in eliminating the effect of shorts due to wire insulation failures. The exact value of the resistor should be chosen during final design. For internal joints and coil system leads, one voltage wire will be routed along the lead and twisted with the mating wire after passing the other tap.

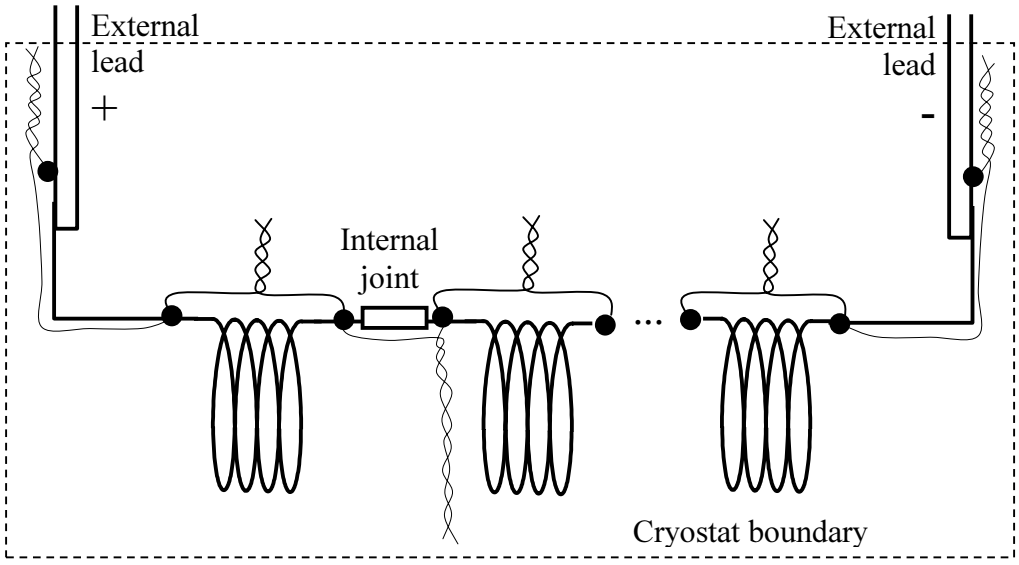

Figure 8.1 – Voltage taps and wires for quench detection

Table 8.1 shows the number of voltage taps on the conductor and the number of pins in the feed through across the cryostat boundary for each coil system. A total of 202 voltage taps and 390 pins are needed to monitor the voltage development over the full length of the superconducting cable and joints.

During normal operation, charging all six coil systems to operating currents in 60 mins, the largest voltage induced in a PS coil from the TS coils is roughly on the order of 2 V. When a coil is quenched and the current is quickly discharged to a dump resistor, the peak resistive voltage can be on the order of 10^2 Volts. It is crucial to protect all the DA channels from such transient voltage spikes.

Table 8.1 – Number of voltage taps and pin connection for quench detection

Coil System	Coil	Internal Joint	Bus Joint	Voltage Tap	Pin in Cryostat Feedthrough
PS	9	8	2	20	38
TS1	8	7	2	18	34
TS2	16	15	2	34	66
TS3	16	15	2	34	66
TS4	16	15	2	34	66
TS5	6	5	2	14	26
DS	23	22	2	48	94

Analog Signals and DAS Protection

As shown in Figure 8.2, a current limiting resistor is used in series with the isolation amplifier in order to reduce the input current to a nondestructive level. A transient voltage suppressor (TVS) taps off the voltage spike before the signal entering the isolation amplifier, which clamps the voltage to an acceptable level (10 V ~ 15 V) for all the downstream DA instrumentation.

As a practical example, the PTF DA channel at MIT uses a BURR-BROWN INA118P preamplifier, which has an input protection to ± 40 V and a safety input current rating of 1.5 mA - 5 mA. The peak voltage resulting from current dumping at a quench is expected to be less than 200 V. The quench detection DA channel is protected by a resistor of 50 kΩ and 0.6 W, and a capacitor type DIODES P6KE20 TVS, which has a 600 W peak pulse power dissipation, a voltage range of 6.8 V – 400 V, and a bi-directional break down voltage of ~ 20 V. The RC circuit preserves signals below 1 KHz, which is consistent with the sampling rate of the DAS in previous applications.

Also shown in Figure 8.2, a voltage divider is installed between the feed through and the current limiting resistor. The voltage divider is used to prevent the mutual inductive voltage, which is induced by quenching in other coil systems, from saturating the DA channel. This will keep the quench detections of non-quenched coils functioning during a transient voltage spike caused by the fast discharge of a quenched coil system, which will be described in detail in a later section.

Signal conditioning

In order to prevent higher frequency noise from introducing distortion into the digitized signal, an anti-aliasing filter is used between the output of each isolation amplifier and the analog-to-digital converter in the data acquisition / quench detection systems.

Based on preliminary quench protection analysis for the MECO magnet system, the quench detection system is required to trigger the quench protection system when the resistive voltage consistently exceeds $V_{threshold}$ = 0.1 V for more than t_{delay} = 1 s. Tentatively, it is sufficient to set the sampling interval to 10 ms – 100 ms for completion of scanning and processing 200 channels of data. The filtering will be set accordingly without significantly attenuating the lower frequency signal. The array of conditioned analog signals are streamed to the master controller with digital quench detector (DQD), the DAS, and the backup analog quench detector (AQD).

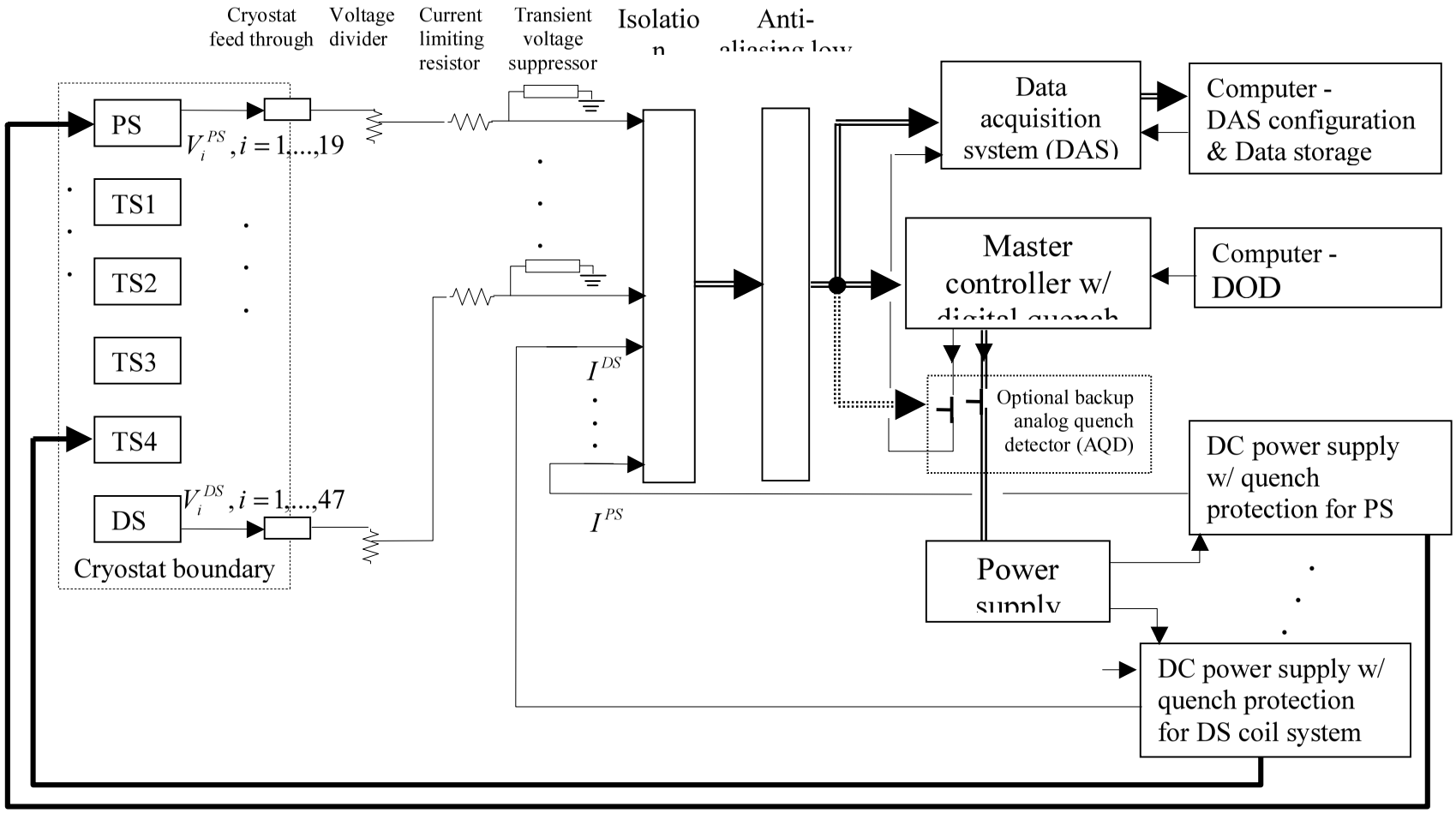

Figure 8.2 – Coil voltage signals and quench detection / protection system; single line: sequential signal stream, double line: array of signal streams, thick single line: power line.

Master Controller with Digital Quench Detector

The major functions of the master controller with digital quench detector are 1) to detect quenching in any of the 94 coils and 101 joints / leads; 2) to clear the default 'dump' command to the power supply controller before current up ramp; 3) to trigger the DAS at quench, 4) to trip all six power supplies if a quench is detected, and 5) to trigger a fast current dump of the quenched coil systems and slow dump in the non-quenched systems. To prevent an over-current condition in the TS coils, however, all TS coils must be fast discharged whenever a quench is detected in any PS, TS or DS coil.

The slow dumping is designed to lower the AC loss heating to the coil system, which is especially important in preserving liquid helium in the PS coil system, which resides in several thousand liters of liquid helium.

The master controller has 12 analog voltage outputs for activating quench protection systems, 6 for controlling power supplies and the DAS, and the other 6 for fast dump switches. All will be at 10 V to 15 V during coil charging and steady state operation. When a quench is detected, the control voltage of the quench circuit power supply, the TS power supplies, and the DAS are stepped down to 0 V, while the non-quenching coil (PS and DS, as appropriate) power supplies are reversed, initiating slow discharge. Meanwhile, the DQD steps down the fast dump switch voltages of the quenched coil systems to 0 V.

Digital Quench Detection

The digital quench detector consists of an array of computer (preferably PC) based programmable data acquisition cards such as National Instrument cards. A computer is linked to the sub-system for configuring the instrument cards into 195 quench detectors. A matrix of virtual coil inductances $L_{i,j}$ and joint resistances $R_{k,k+1}$ are stored in the computer, which are pre-calculated and then measured as part of the initial magnet setup procedure. These virtual parts are built into the DA program.

At each sampling, the DAS will scan 195 coil / joint voltages and six scaled current values (from power supplies or shunt voltages) effectively at once. With known currents and current changing rates, the virtual inductive voltages in the coils

$$V_{VC,i} = \sum_j L_{i,j} \frac{dI_i}{dt}, i, j = 1,...,94$$

and the virtual resistive voltages of the joints / leads

$$V_{VR,k} = I_k R_{k,k+1}, k = 1,...,100$$

are calculated and subtracted from the analog signals taken at the same sampling time. The voltage difference ΔV between the analog and the virtual voltage is considered as the resistive component of the coil voltage.

All the virtual resistive voltages are compared with the $V_{threshold}$ preset in the DA program each time a new set of data is sampled. Individual channel with $\Delta V > V_{threshold}$, will be counted

and registered with the channel number. The count will be restarted from zero if a $\Delta V < V_{threshold}$ occurs in the same channel before the count reaches the total number of samples per channel in t_{delay}. Recall that for MECO, $t_{delay} = 1$ second.

A coil is considered as quenched if its quench count exceeds the number of samples per channel in t_{delay}. The master controller / DQD will then respond to the quench as described above. If multiple coil systems reach the quench count at the same time, the DQD will open the fast dump switches of the corresponding coil systems.

Consecutive Quenches

It is possible that some coil systems may have already accumulated a significant fraction of quench count (say 90%) when a fast dump is initiated by another coil system. If quenches are activated in those coils by the preceding fast dumping, they may not be detected until the first transient voltage is over. This is especially critical if one of the PS or DS coils is first quenched and the other follows closely after. To assure protection in such a quench scenario, one may consider, as an option, to activate fast dumping of both already-quenched and nearly-quenched coils simultaneously. The modification can easily be done by re-programming the DA cards.

Digital Quench Detection in Transient Voltages

When a fast dump is initiated, all the non-quenched coil systems are affected by mutual inductive voltages with peak values 1 ~ 400 V. The maximum transient mutual inductive voltage in individual coil can be 20 V – 50 V. Precise values can be determined when the coil system design and the quench protection scheme are finalized.

As mentioned previously, the voltage divider for each signal path shown in Figure 8.2 is used to prevent the mutual inductive voltage (noise) from saturating the DA channel and shadowing the quench voltage (signal) detection in the non-quenched coil system. They are not used to detect or condition the fast dump voltage of a quenched coil system, which is on the order of 100 – 200 V per coil. The transient voltage suppressors are used for protecting DA channels from damage by the voltage generated in the dump resistor during a full current fast dump.

As a preliminary estimation, the divider that reduces the peak mutual inductive voltage by 50% - 60% is possibly sufficient to avoid saturating the DA channels. It is clear that the voltage divider reduces not only the background mutual inductive voltage, but also the quench signal by the same ratio. Therefore, the setting of the $V_{threshold}$ must be adjusted accordingly. With the present rough estimation, the $V_{threshold}$ can be set to ~ 50 mV, which remains a reasonable signal level.

Since the transient mutual inductive voltage in each coil system is unique, one may consider using different voltage dividers in order to keep the quench signal as large as possible. In order to use consistent quench protection criteria, multiple values of $V_{threshold}$ must be used in the master controller / DQD program. Selection of proper voltage divider and adjustment to the $V_{threshold}$ will be determined in the final design.

During the transient time of the first fast discharge, the DQD uses the same digital cancellation of the inductive voltage technique to detect further quenching in the slowly discharging coil systems. Since all the power supplies are freewheeling at a quench, the currents for calculating inductive voltages need to be extracted from a different source such as a shunt resistor in series in the closed loop of the coils and the dump resistor.

Speed and Reliability of Digital Quench Detection

The real coil voltages, and the equivalent coil current for calculating the virtual mutual inductive voltage are scanned from different DA channels. With the present technology, a DA board is capable to scan 200 channels in less than a millisecond at each sampling time. The phase difference in one sampling of ~ 200 scans is expected to be insignificant.

All scanned data will be processed only within the DA cards in the DQD system. This includes calculation of the mutual inductive and the resistive voltages, subtraction of virtual inductive voltage from the real coil voltage, comparison of the resistive component of the coil voltage with the $V_{threshold}$, and recording of quench counts in all channels. Since data does not have to pass between the DA cards and the computer for computation, the quench judgment is reached very quickly. If a quench is detected, the DA cards initiate a triggering command through the analog output channels. All processes are expected to be completed within one sampling interval, which is a small fraction of $t_{delay} = 1$ s. This is sufficiently fast for quench detection both in normal operation and during a quench event.

Since the processing speeds of commercialized DA cards are affected by the number of channels at different levels, it is important to evaluate the candidate DA instrumentation using the design number of DA channels before the final decision is made.

During the first fast discharge of the quenched coil, the error in the mutual inductive voltage calculation is magnified by two to three orders of magnitude due to the large current discharging rate in the quenched system. If the error exceeds the $V_{threshold}$, a fast dump will be faultily triggered. It is important to calibrate the virtual inductances at equivalent fast current discharging rates.

As previously mentioned, the master controller / DQD system sends out high-to-low step signal to trip the power supplies and open the dump switches. In case of power failure and computer / DQD failure, all the output control voltages are dropped to zero. All fast dump switches will be opened and all coil currents will be discharged. The coils are therefore protected. In general applications, both QDS and DAS are typically serviced by a UPS.

Optional Backup Analog Quench Detector (AQD)

To prevent destruction of the coils due to unexpected failures of the master controller/DQD, an optional backup analog quench detector (AQD) included in Figure 8.2 is proposed. As a backup setup, the AQD monitors the balanced voltage of each coil system, and detects quenches in coil systems instead of individual coils.

As a preliminary approach, to balance the inductive voltage in a coil system, the voltages from respectively odd and the even number coils are added. These two voltages are balanced with a traditional bridge circuit. Since most of the 94 coils have unique number of turns and layers, a better combination of the summations and cancellation will be refined in the final design.

The quench detection criteria in the AQD are tentatively set at $2 \times V_{threshold}$ with t_{delay} the same as that used in the DQD. This is to avoid interference with the primary digital quench detector. The final setting for the AQD threshold voltage depends heavily on the balancing of the inductive voltages.

An adjustable RC circuit is used to accumulate the resistive voltage consistently higher than 2 $V_{threshold}$. Similar to DQD, if there is a voltage lower than 2 $V_{threshold}$ before the capacitor is saturated, the capacitor is discharged to 0 V. All the threshold voltage and delay time settings and the tripping / dumping signal circuits are electronic and independent from those of DQD.

As shown in Figure 8.2, the AQD controls the downstream of the DQD analog outputs with internal electronic switches. All internal switches have default open position. For charging the coils, the AQD will activate a high voltage (5 V ~ 10 V) to close the switches. When a quench is detected by the AQD ($V > 2\ V_{threshold}$ for $t > t_{delay}$) and the DQD ($V > V_{threshold}$ for $t > t_{delay}$) is not responding, the AQD will step down the activation voltages to 0 V to open the internal switches. This interrupts (or steps down) the analog signals from the DQD to the power supplies, dump switches, and the DAS.

The optional backup AQD is to be used as the second line of quench detection / protection. Once a quench is detected, output signals in the AQD are driven with the same logic as in the DQD.

A manual dump switch can be included in the AQD system as an additional quench protection. In case both DQD and AQD are not responding to a quench event, which may have been detected by abnormal pressure or temperature rise, the manual dump switch briefly disrupts the DC power supply in the AQD to open all the internal electronic switches.

If the optional AQD is not used, the internal switches in Figure 8.2 should be removed, and the analog signal lines should be shorted.

Data Acquisition System (DAS)

The presently proposed DAS tends to be used during the magnet system testing and debugging phase. It is crucial to collect detailed information of individual coils, joints, and leads. Once the overall magnet system is fully operating, the DAS might be simplified to monitor the total voltage of each magnet sub system.

For quench detection purpose, the DAS requires a minimum of 195 channels for detecting coil and joint / lead voltages, and 6 channels for currents in the coils. Additional DA channels for helium level, pressure, temperature, vacuum condition, and other sensors need to be included after the in-vessel instrumentation design is finalized. Two CAMAC A/D converters controlled by DA card such as PC based National Instrument board should be sufficient for the present application.

The first CAMAC is set to pre-triggering mode and at a higher frequency (~100 Hz) data acquisition, which is used to record the quench events. The second CAMAC, with slower clocking (~10 Hz), is set to post-triggering mode, which is used to record data during the full time of the magnet operation. Considering the large quantity of data collected by the low frequency CAMAC over a long magnet operation, the data may have to be streamed into a computer file for direct storage if the CAMAC buffer is limited.

Both CAMAC's will be software initiated by the DAS computer. The low frequency CAMAC starts to collect and record data once initiated. The high frequency CAMAC is waiting for a triggering signal for data storage, which is a high-to-low hardware voltage controlled by the DQD and the AQD in the event of a quench. The waiting time for triggering is programmed to cover the whole duration while the magnets are operated.

For diagnosis of the sources of the initial quench, the duration of pre-triggering data is set to 1~2 mins. In order to record possible additional quench events occurring in the slow discharges

of coils, the high frequency CAMAC is required to continue collecting data until all slow discharge processes are completed. During the magnet testing phase, the overall discharging time of the non-quenched systems after the first quench event could be from 30 seconds (all quenched) to 1 hour (all slowly discharged). A better setting for the post-triggering DA duration is longer than 1 hour with manual disruption to end the data acquisition. The same manual disruption is also used to end the low frequency CAMAC.

Section 9 - Quench Protection

A quench protection system is required to protect the MECO coils from overheating or being overstressed in the unlikely event of a quench. A generic quench protection circuit is shown in Figure 9.1. Other arrangements are possible, but the requirements for quench protection are to remove as much energy from the coil as possible without exceeding the voltage limit of 2 kV, to limit the hot spot temperature in the coil to under 150 K, a limit set by the MECO project with MIT concurrence, and to ensure that coil stresses remain within design allowables.

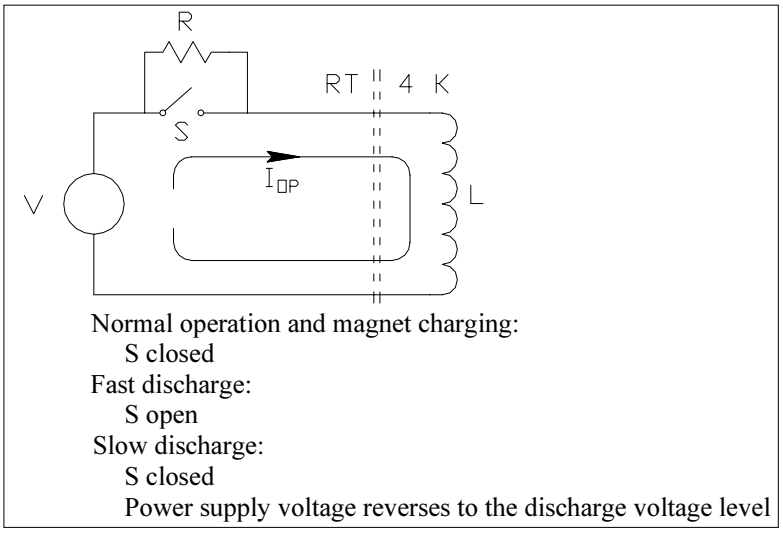

Figure 9.1 – Generic quench protection circuit using a dump resistor

In the circuit of Figure 9.1, a quench detection signal is generated by the quench detection circuitry (see separate section of this document), and this initiates the fast discharge sequence in the coil set where the quench is detected. Simultaneously, the quench circuitry should initiate a slow discharge in the remaining MECO coil systems as a rule. The exception, however, is that all TS coils must be fast discharged whenever a quench is detected in any (PS, TS or DS) coil. Fast discharge of all four TS coil circuits on any quench detection is required to prevent an over-current condition in the TS coils. The PS and DS systems, which have much greater self inductances than do the TS coils, are required to be dumped only when a quench is detected in the PS or DS, respectively, and otherwise they would be slow-discharged. Slow discharge of the PS, when any other coil set but itself has quenched, will preserve helium which will otherwise be released in large volumes with a PS fast dump. Slow rather than fast discharge of the DS when any other coil set but itself has quenched, will facilitate a much more rapid DS cool-down following the slow discharge. The quench detection circuitry should be designed so that should a quench subsequently occur in a coil set (PS or DS) that is slow discharging, the slow discharge will be superceded by a fast discharge in the coil set where the quench is newly detected.

Both the digital quench detector (DQD) and the optional analog quench detector (AQD) are powered with a backup Uninterruptable Power Supply (UPS). When power is lost, the DQD/AQD will begin to slowly discharge the magnets through their power supplies and the normal power bus resistance but without the presence of reverse voltage from the power supply. Should any coil quench during the power loss sequence or subsequent slow discharge, the

magnets are to be fast dumped using the same guidelines as specified for quench protection during normal operation.

Quench parameters for all coil sets are given in Table 9.1. Note that the inductance matrix for the six coil sets is given in the section of this report on field specification matching.

Table 9.1 – Quench parameters for all coil sets

Parameter	Units	PS	TS13u	TS2	TS3d5	TS4	DS
Maximum voltage spec	kV	2	2	2	2	2	2
Maximum temperature spec	K	150	150	150	150	150	150
Operating current	A	3500	1500	4000	1500	4000	4000
Stored energy	MJ	109	3.26	4.72	2.01	3.55	30.8
Dump resistor	Ω	0.529	1.23	0.463	1.23	0.463	0.463

Details of the Quench Analysis

The quench program used for analyzing the MECO coils is a three dimensional, transient finite element calculation written in FORTRAN 90. Temperature rise in each element is calculated for each time step based on an energy balance between joule heating in the normal zone (if applicable), energy stored as heat capacity, and conduction. Joule heating is initiated within the element if the local value of $T_c(B)$ is exceeded. Coupled currents (if any) are also solved in each time step using the circuit equations. Quench program data (element and node geometry and property data and temperature of each element vs. time) are passed as inputs for structural analysis in ANSYS, as necessary.

Quench analyses have been competed on the PS, TS and DS coil sets. The PS results are reported in detail in [mm043], and the analytical methods for the other coil sets are similar, although less complex, since only the PS has electromagnetically-coupled aluminum shells that participate in the quench event. Each coil set (six total) requires its own quench protection circuit, similar to that in Figure 9.1. Other common assumptions in the quench analysis are that the quench detection voltage threshold is 0.1 V, and that the 0.1 V signal must be present for at least 1 second before protective action is initiated. The combination of the threshold and the delay act to prevent spurious trips from being generated which, in turn, would cause unnecessary experimental down time. In all analyses, the quench was assumed to initiate in the coil with the highest field, at the peak field location.

Quench protection analysis results in four of the six MECO coil sets are summarized in Table 9.2 and discussed individually below. Separate analytical results are included in the table for the TS3u adjacent to the Be window which will be wound with SSC outer cable only to conserve space. Separate quench analyses of quench in the downstream TS coil sets (TS3d5 and TS4) were not run. They are sufficiently similar to TS13u and TS2, with lower stored energy, respectively, to not warrant a separate analysis in the conceptual design phase.

Table 9.2 – Quench protection analysis results for all coils evaluated

Parameter	Units	PS	TS1	TS2	TS3u Cable	DS
I_{op}	A	3500	1500	4000	1500	4000
Coil set stored energy	MJ	109	3.26	4.72	3.26	30.8
R_{dump}	Ohm	0.529	1.23	0.463	1.23	0.463
L/R_{dump} time constant (excludes time varying effect of Rcoil)	s	33.64	2.36	1.27	2.36	8.32
Vmax for coil	V	1900	1853	1876	1862	1863
Vmax for normal zone	V	532	4.6	41.4	27.4	145
Maximum normal resistance	Ohm	0.427	0.0053	0.0179	.0708	0.118
Maximum hot spot temperature	K	88.5	33	74.5	65.8	123
Maximum Al shell temperature	K	53	na	na	na	na
Energy dissipated in coil	MJ	27.2	9.6e-3	175e-3	56e-3	2.69
Energy dissipated in all Al shells	MJ	6.6	na	na	na	na

From the table, it is clear that all coils satisfy the minimum criteria that the hot spot temperature remain below 150 K following quench, and that the maximum resistive voltage for the coil (Vmax) is below 2 kV. Additional results for each coil are given below.

PS Quench

The high field point is located in the first PS coil, at the ID, and at about 0.35 m from the downstream end of the winding. PS quench transient results are given in a set of figures, in [mm043]. The plots are repeated here as Figure 9.2 through Figure 9.10 for convenience and comparison with quench results for other coils.

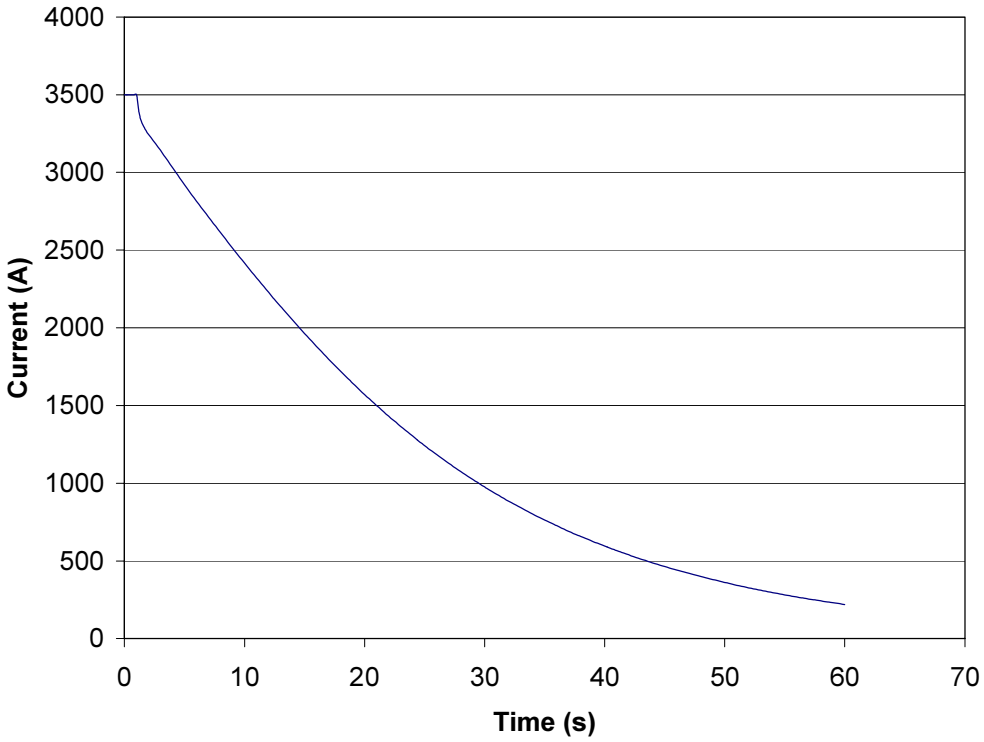

Figure 9.2 – PS1 coil current decay.

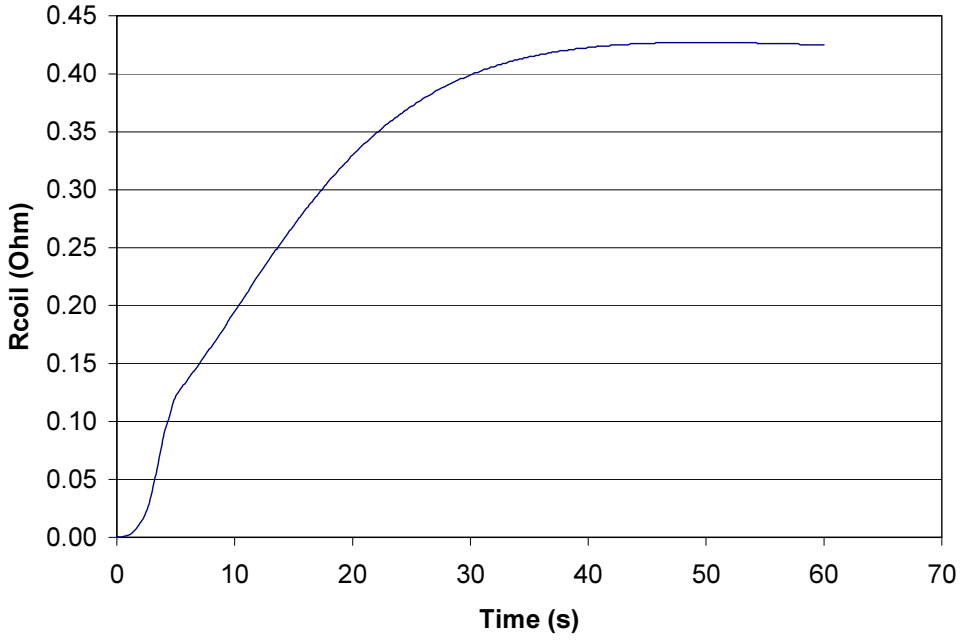

Figure 9.3 – PS1 normal zone resistance.

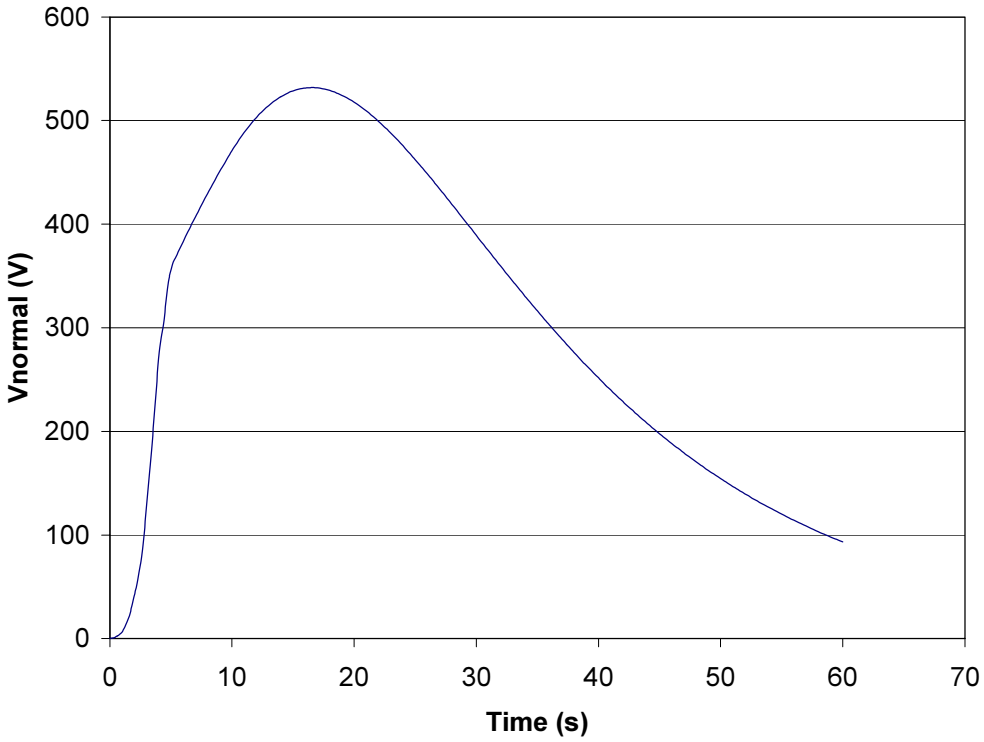

Figure 9.4 – PS1 normal zone voltage.

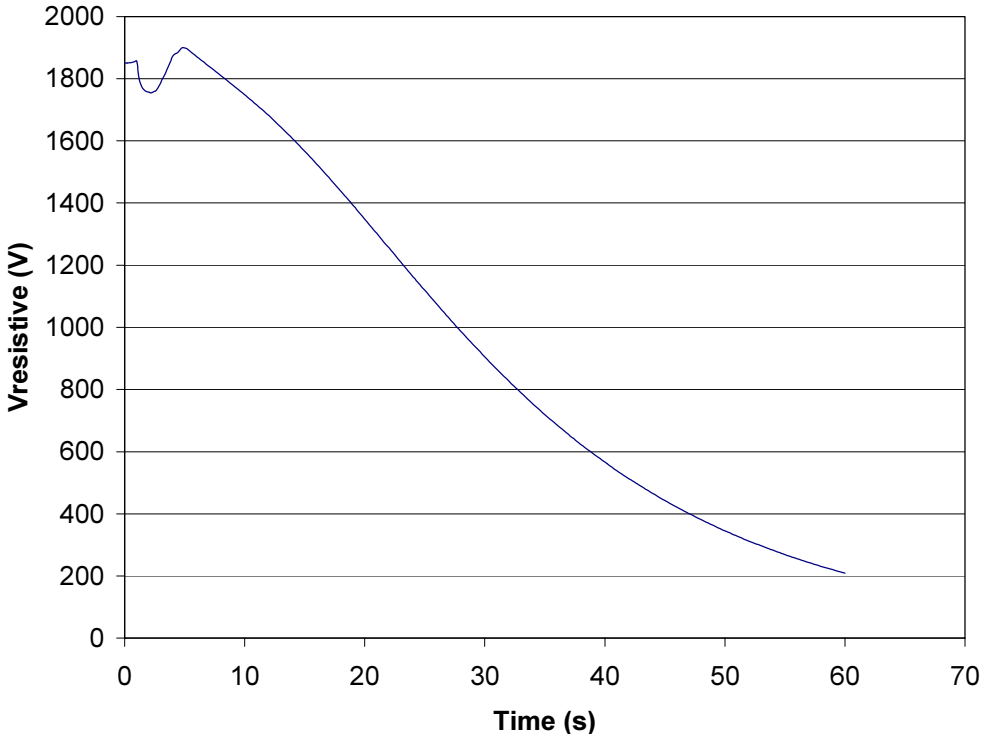

Figure 9.5 – PS1 total resistive (R_{coil} + R_{dump}) voltage.

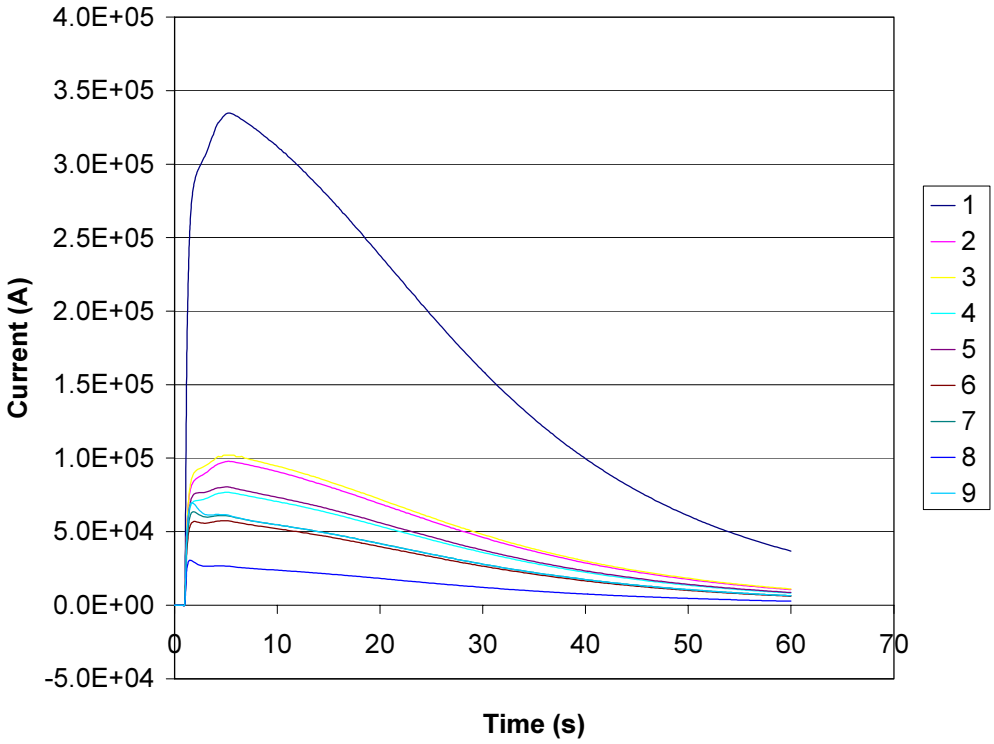

Figure 9.6 – PS Aluminum mandrel currents.

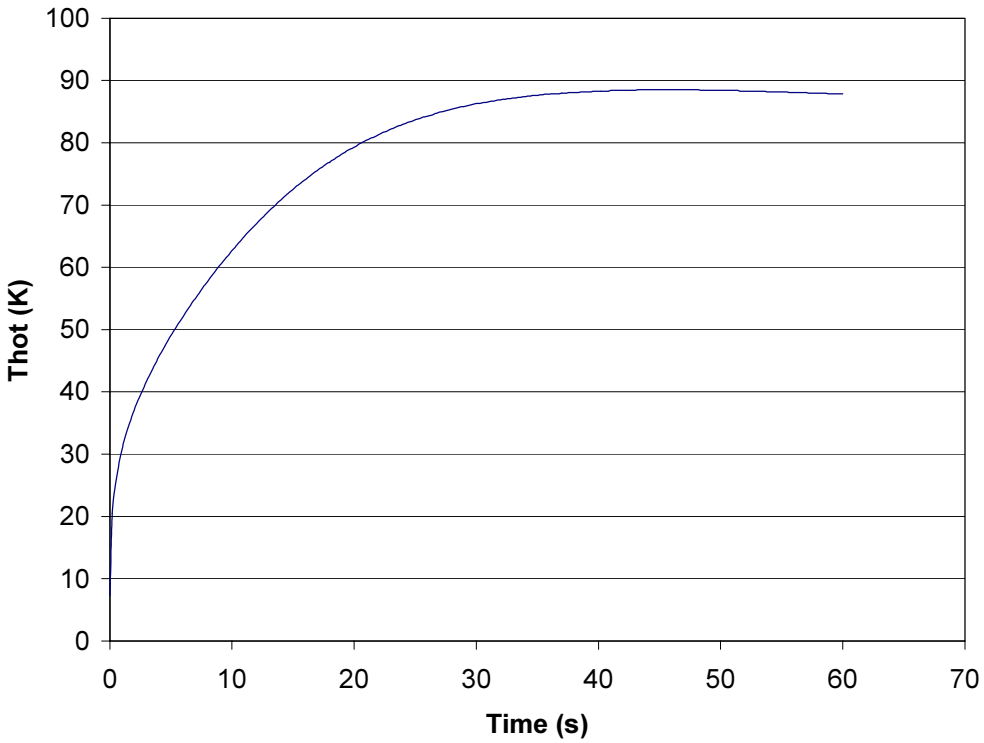

Figure 9.7 – PS1 hot spot temperature.

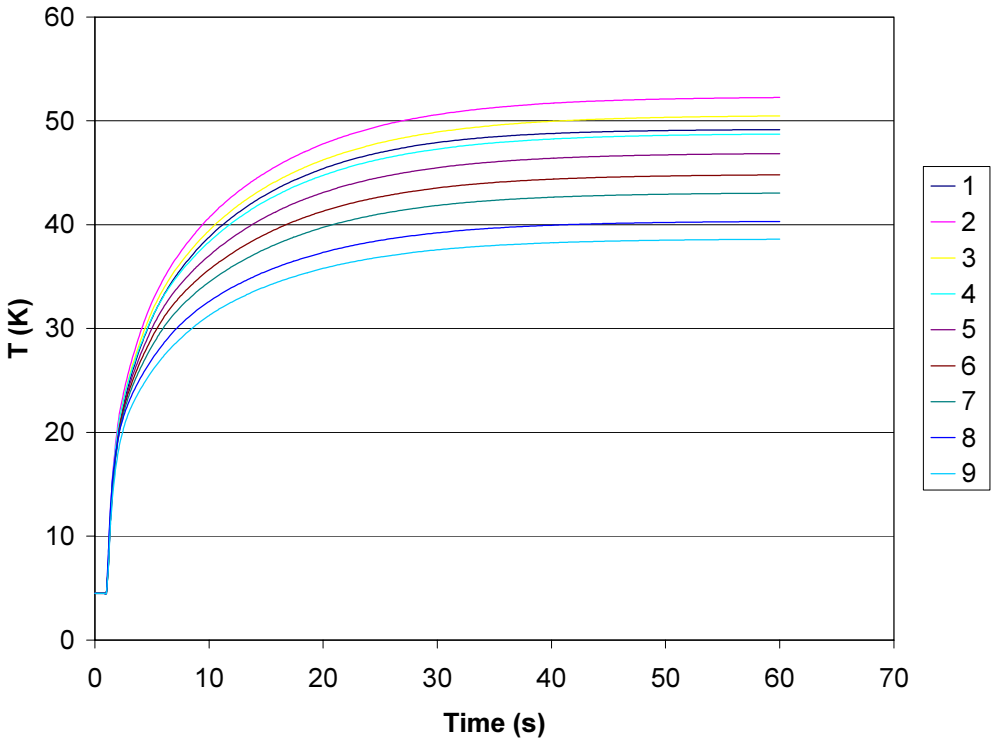

Figure 9.8 – PS mandrel temperatures.

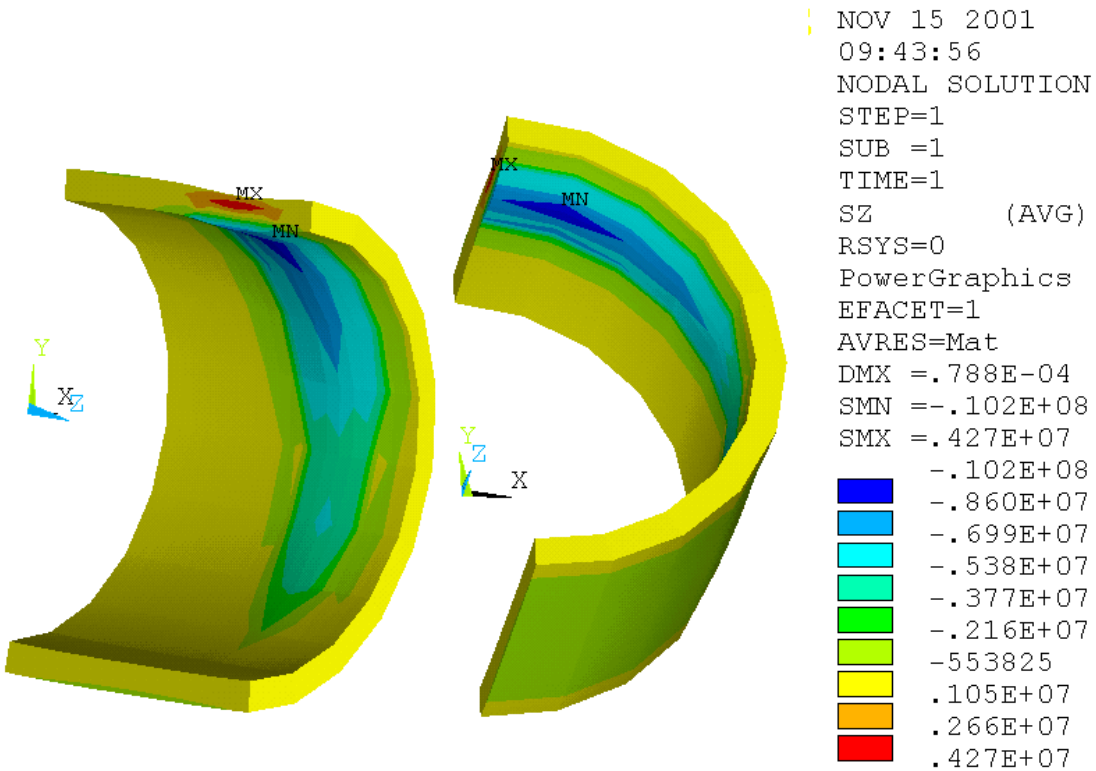

Figure 9.9 – PS1 maximum axial compression at 2 s is 10.2 MPa.

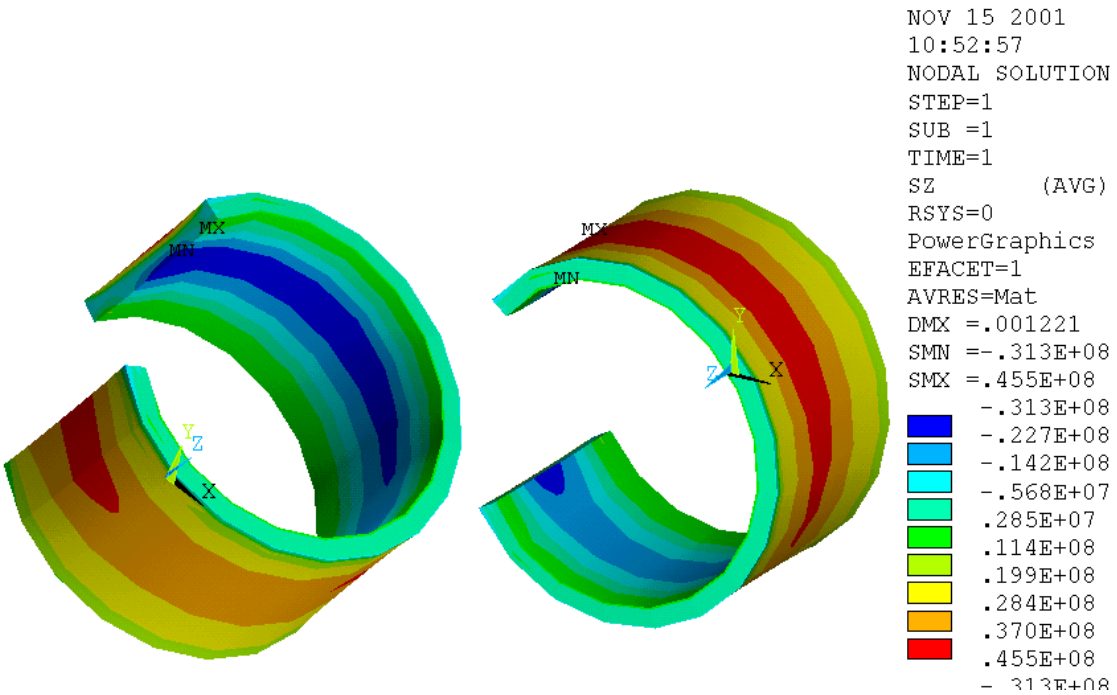

Figure 9.10 – Coil axial stress after 38 s, showing 45.5 MPa relative to the cold state with no Lorentz load.

The maximum difference between the coil hot spot temperature at the coil ID, where the quench initiates, and the cooler coil OD occurs early in the transient. Since the bulk of the winding is still relatively cold, the small hot spot region is placed in 10.2 MPa of axial compression (Figure 9.9). This stress level is low and easily accommodated by the winding. As the quench event evolves, the entire coil eventually goes normal, with the last element reaching its critical temperature at just after 5 seconds. Beyond this time, all parts of the coil are joule heating, and the coil temperature is increasing everywhere. Joule heating in the mandrels, although initially zero, rises rapidly with the rapid rise of the shell eddy currents (Figure 9.6).

The difference between the PS1-coil hot spot temperature and its mandrel temperature reaches a maximum at about 38 seconds. At this time, the coil axial stress reaches a level that is 45.5 MPa more tensile than it was when all components were at about 4.5 K (Figure 9.10). Thus, if the axial compressive preload is set at 45.5 MPa or higher at 4.5 K, an axial tensile stress state will be avoided on quench. This stress condition will be used to set the axial preload on the PS coils.

Note that 45.5 MPa is based on an effective winding modulus of 75 GPa. This value will need to be confirmed by a test during final design. A modulus of 100 GPa in the structural analysis produced a 60 MPa tension. The effective winding modulus with the Kapton wrap is expected to be closer to the 75 GPa modulus value assumed.

TS1 quench

The TS13u coil set, as well as the TS3d5 coil set operates at only 1500 A. Except for the conductor which is used in the two TS3 coils immediately adjacent to the beryllium window, and which is discussed separately below (TS3u cable only), the conductor for the TS13u and TS3d5 coils is the same as the conductor for TS2 and TS4, which operate at 4000 A. Thus, it is not unexpected that the hot spot temperature in the case of TS1 quench is limited to only 33 K. As such, a separate stress analysis of the quench condition is not warranted.

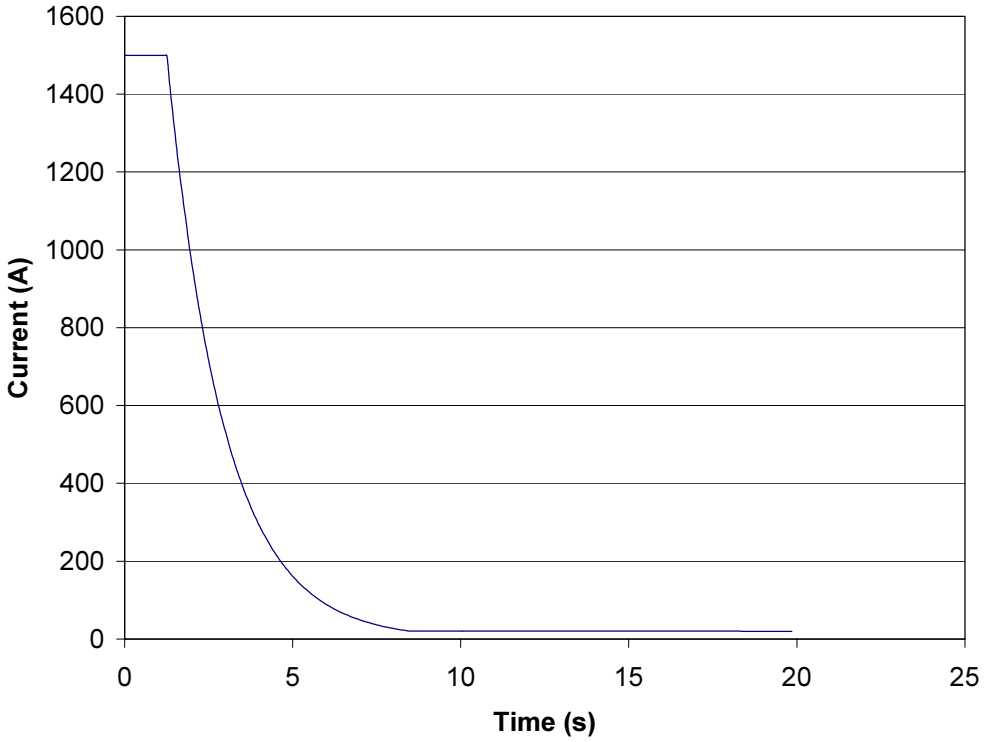

Figure 9.11 – TS1 current.

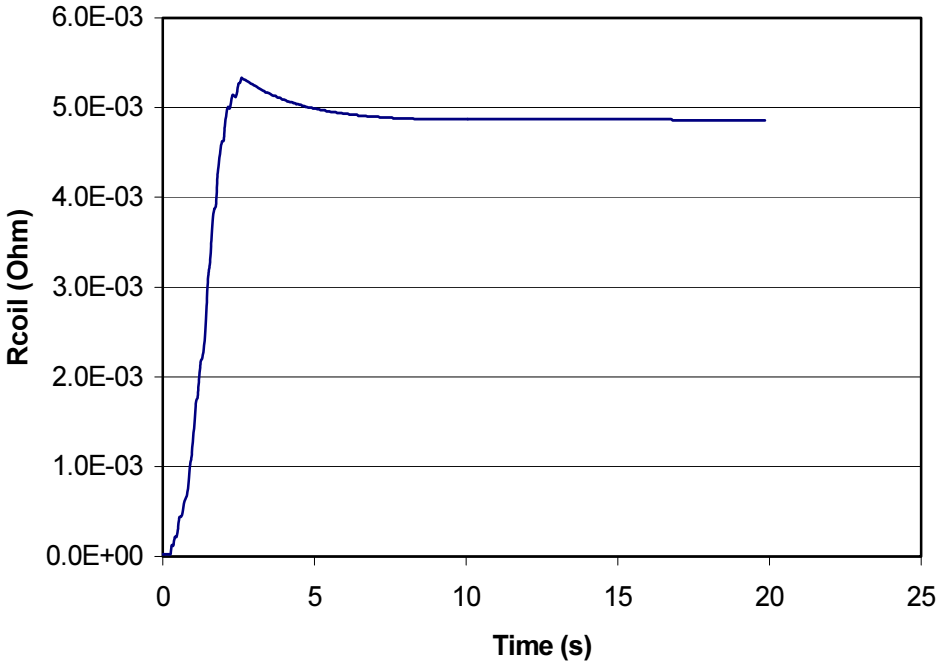

Figure 9.12 – TS1 normal zone resistance.

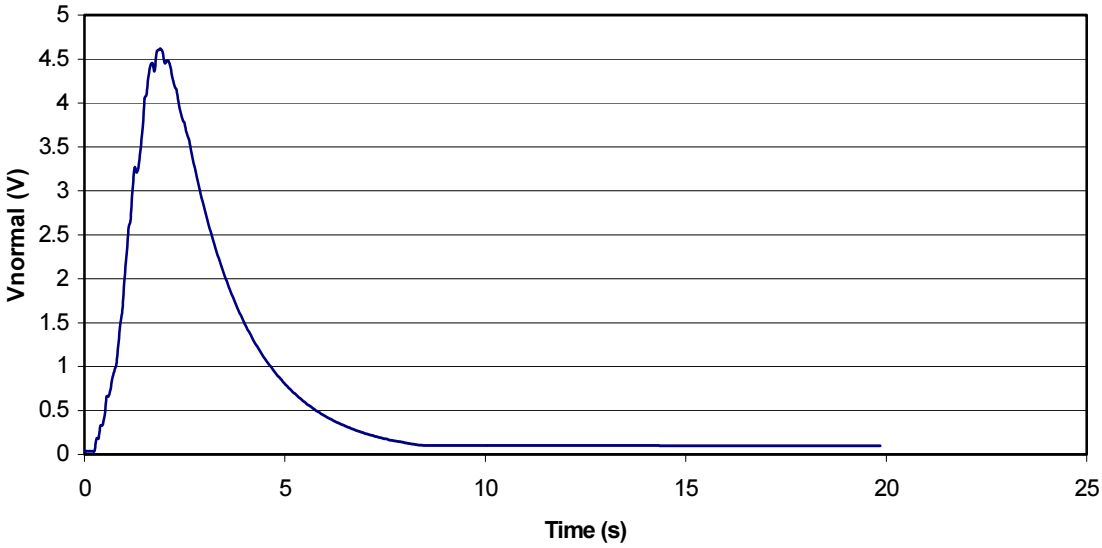

Figure 9.13 – TS1 normal zone voltage.

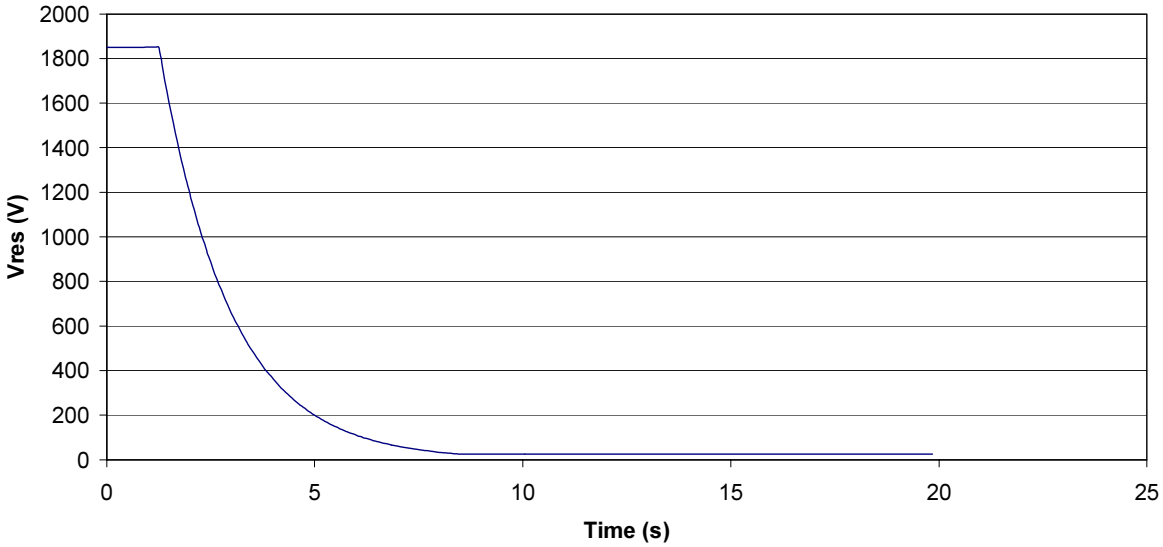

Figure 9.14 – TS1 total resistive (R_{coil} + R_{dump}) voltage.

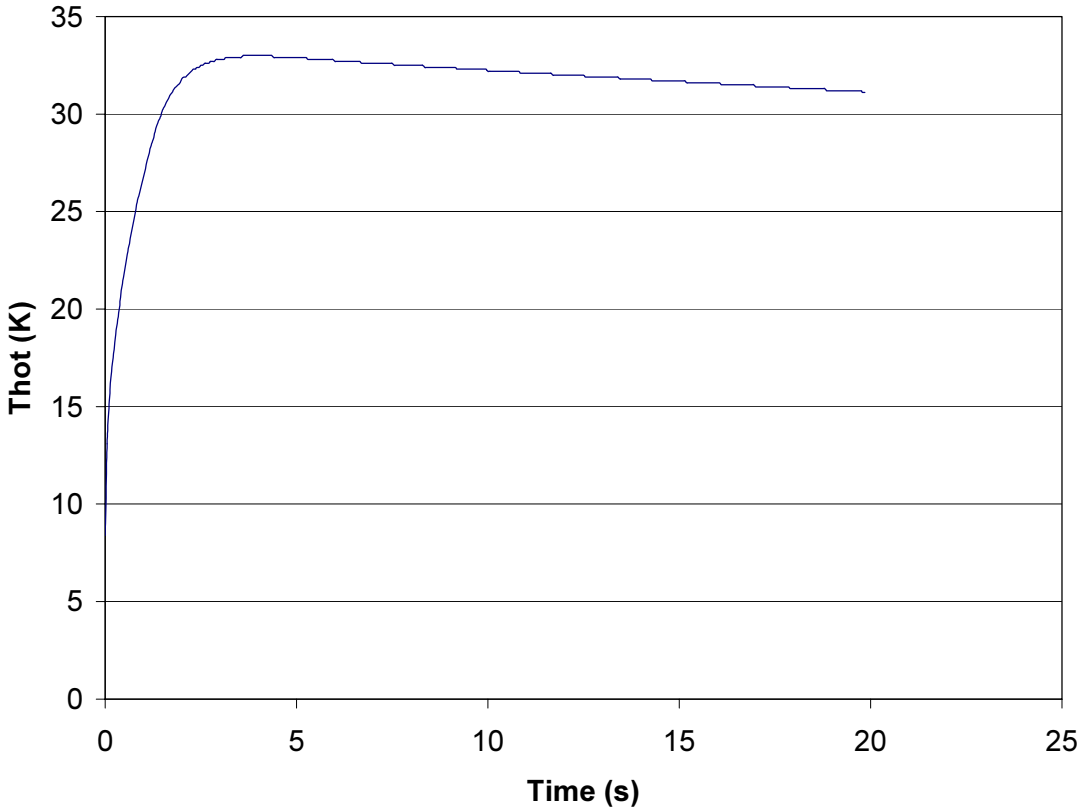

Figure 9.15 – TS1 hot spot temperature.

T3u with cable only quench

The coils in TS3u and TS3d immediately adjacent to the beryllium window have more ampere turns than the other TS coils in order to provide the correct magnetic field profile across

the gap at the beryllium window. This gap is nominally 7.5 cm between the TS3u cryostat and the TS3d cryostat, although the gap between the coil ends is even larger. Because these coils do not strictly need the copper channel for protection during quench, they are designed to be wound with SSC outer cable alone to minimize the coil builds and maximize access to the window. To ensure safe quench behavior, a quench analysis was conducted on the coil in TS3u immediately adjacent to the beryllium window with SSC outer cable alone. This coil has an axial extent of only 8 cm, but has a radial build of over 11 cm.

The system resistive voltage peaks at 1862 V, and the coil hot spot temperature is a relatively modest 65.8 K. Axial stresses were evaluated throughout the post-quench event, and are plotted at 2.5 seconds after the quench initiation in the figure below. Tensile stresses are only 5.5 MPa, and compressive stresses are 13.6 MPa. Both stresses are low.

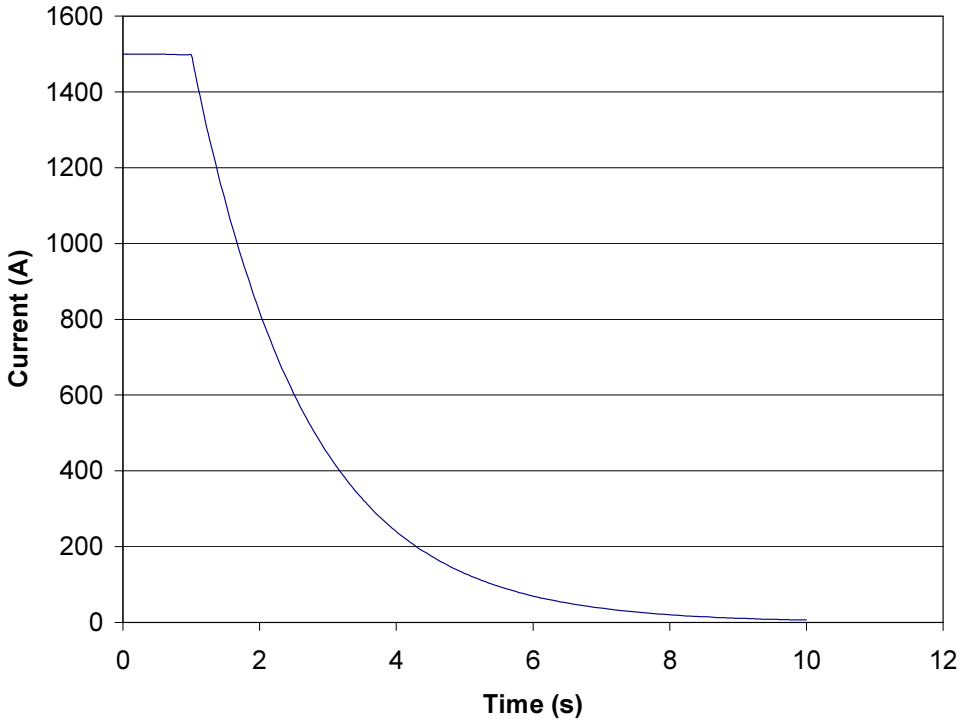

Figure 9.16 – TS3u coil with cable only, current vs. time.

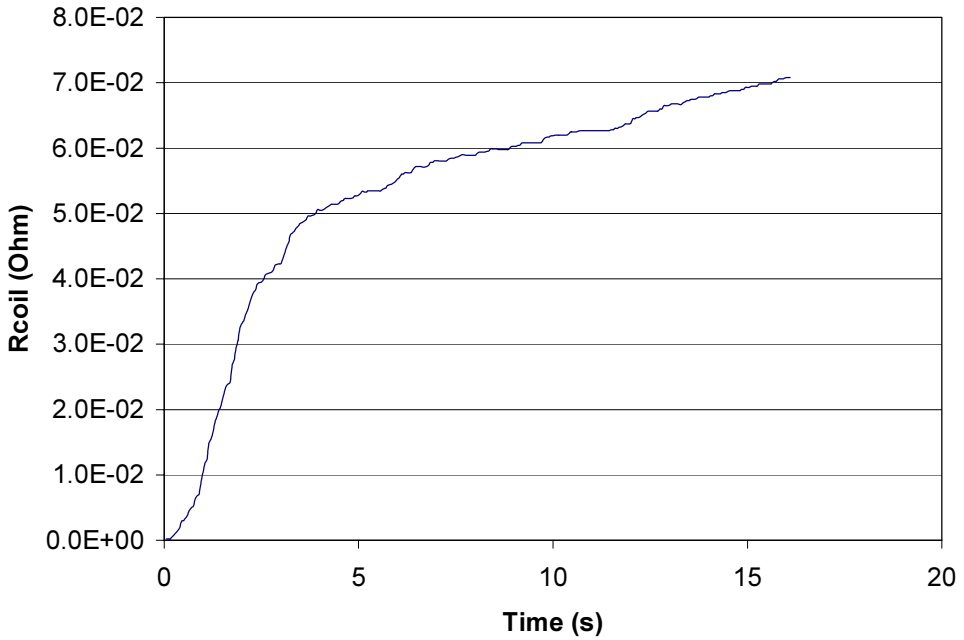

Figure 9.17 – TS3u coil with cable only, normal zone resistance.

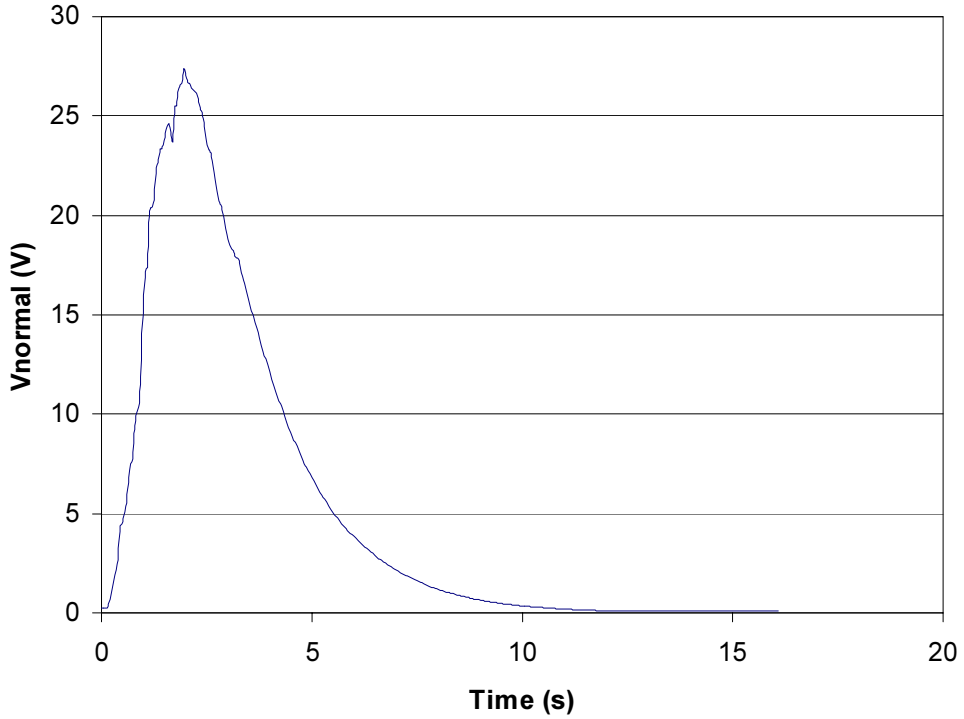

Figure 9.18 – TS3u coil with cable only, normal zone voltage.

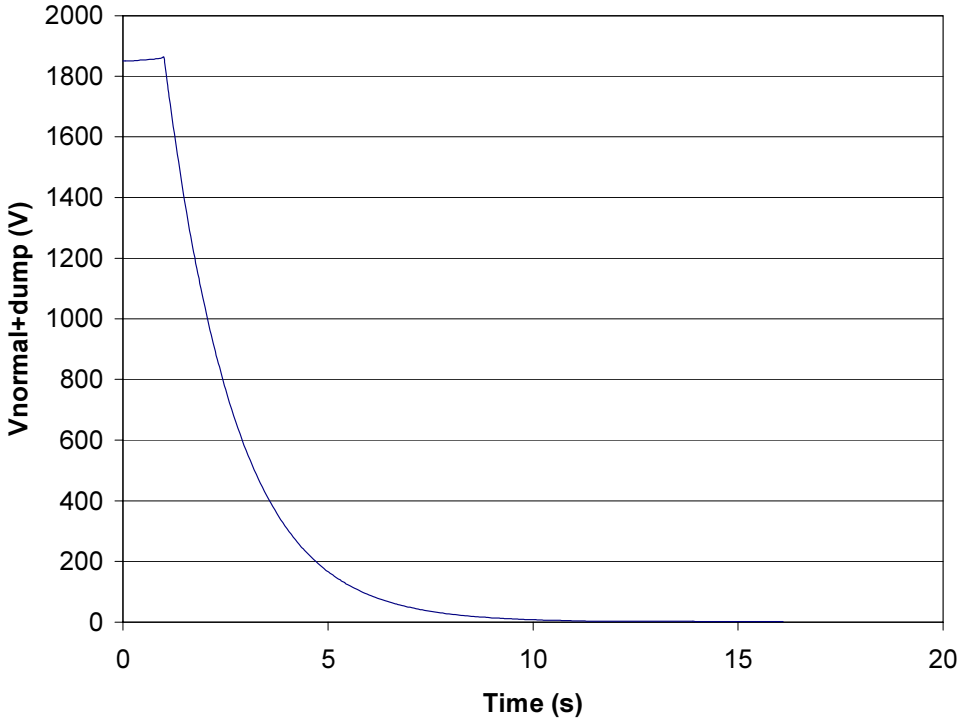

Figure 9.19 – TS3u coil with cable only, total resistive (R_{coil} + R_{dump}) voltage.

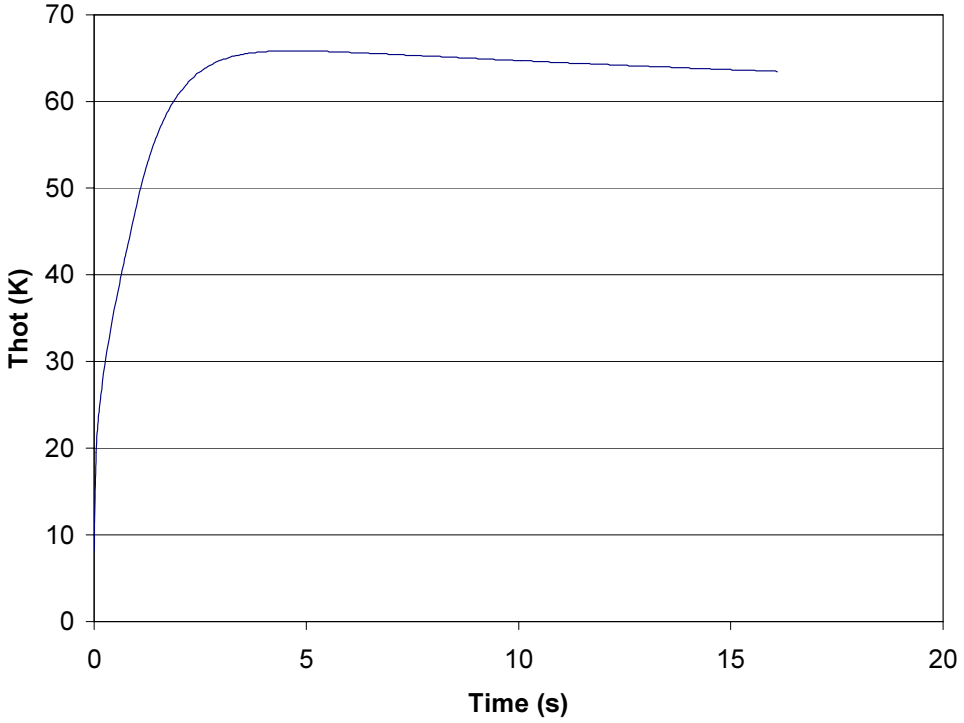

Figure 9.20 – TS3u coil with cable only, hot spot temperature.

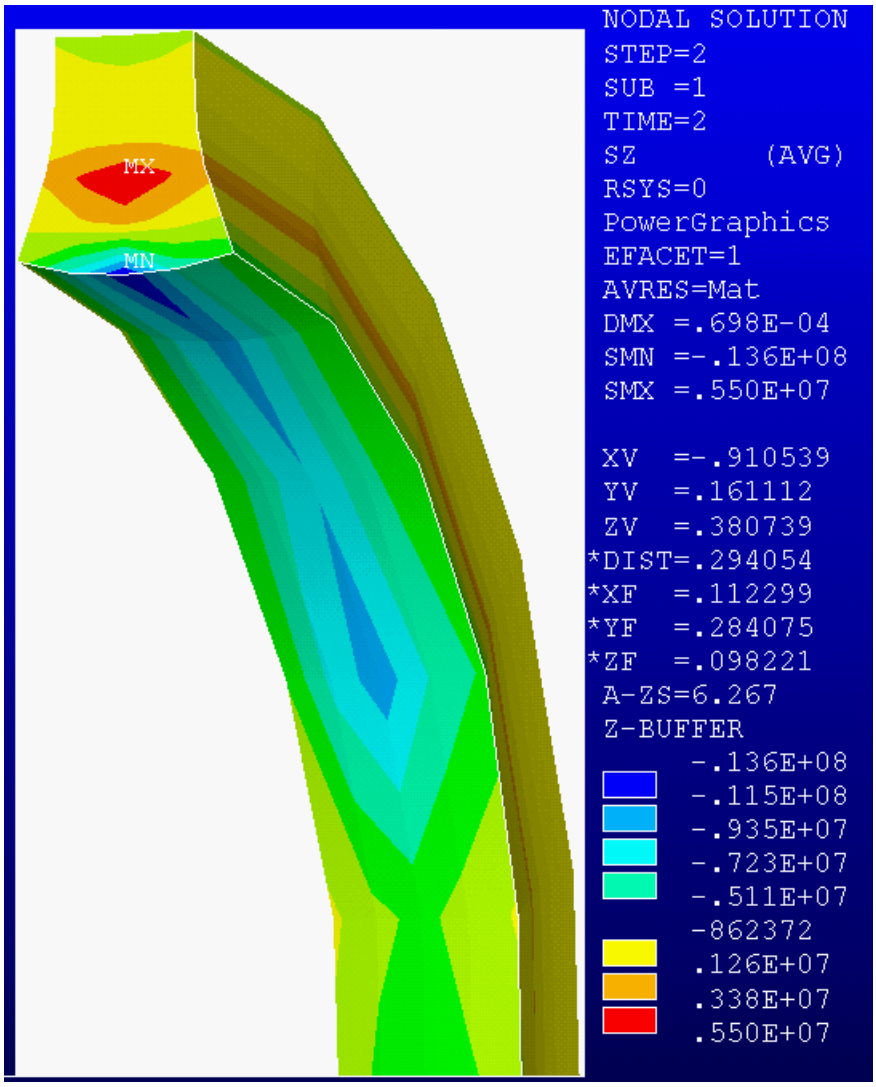

Figure 9.22 – Axial stress distribution at 2.5 s after quench initiation.

DS Quench

Prior to running the initial DS quench analysis, the first DS coil had an axial length of 0.88 m. A quench analysis of this coil showed that an r-z plane bending stress occurred during quench and this added to the axial tensile stress created from the localized heating in the normal zone. The bending condition produces an attendant shear stress. These stresses were excessive, but breaking the coil lengthwise into two coils could relieve them. When the quench analysis was run on the shorter coils, the stresses were acceptable. The maximum hot spot temperature for the shorter coils is 123 K, which is hotter than the other coils, but still well under the project-allowable 150 K. Results for the DS are provided in the following figures.

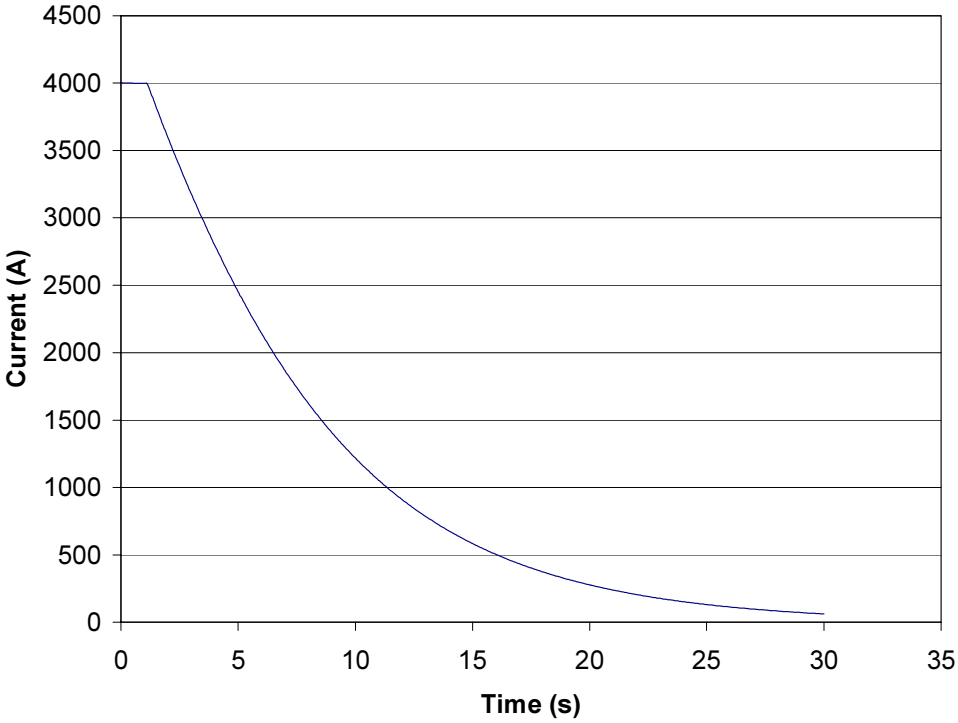

Figure 9.21 – DS current.

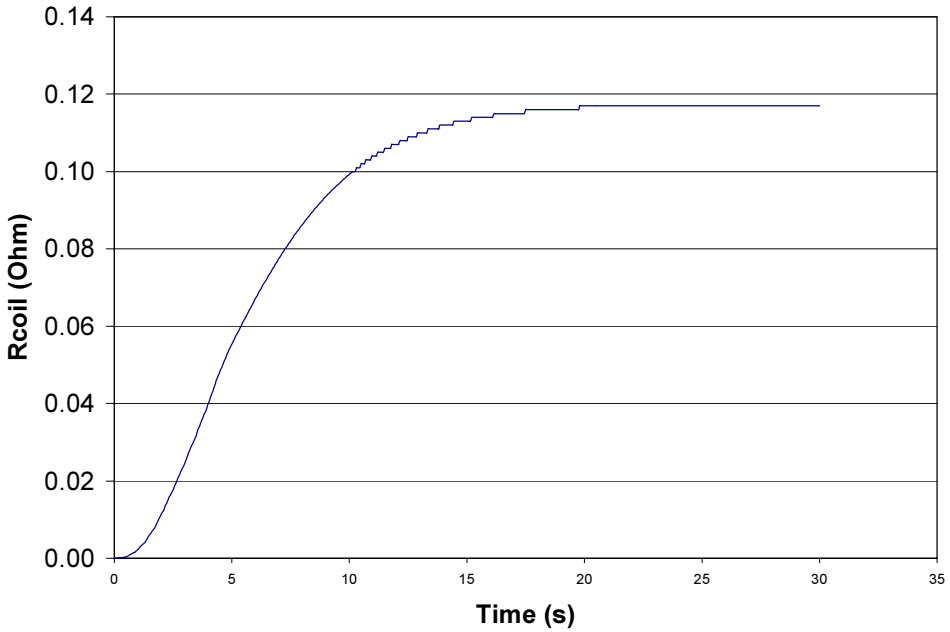

Figure 9.22 – DS normal zone resistance.

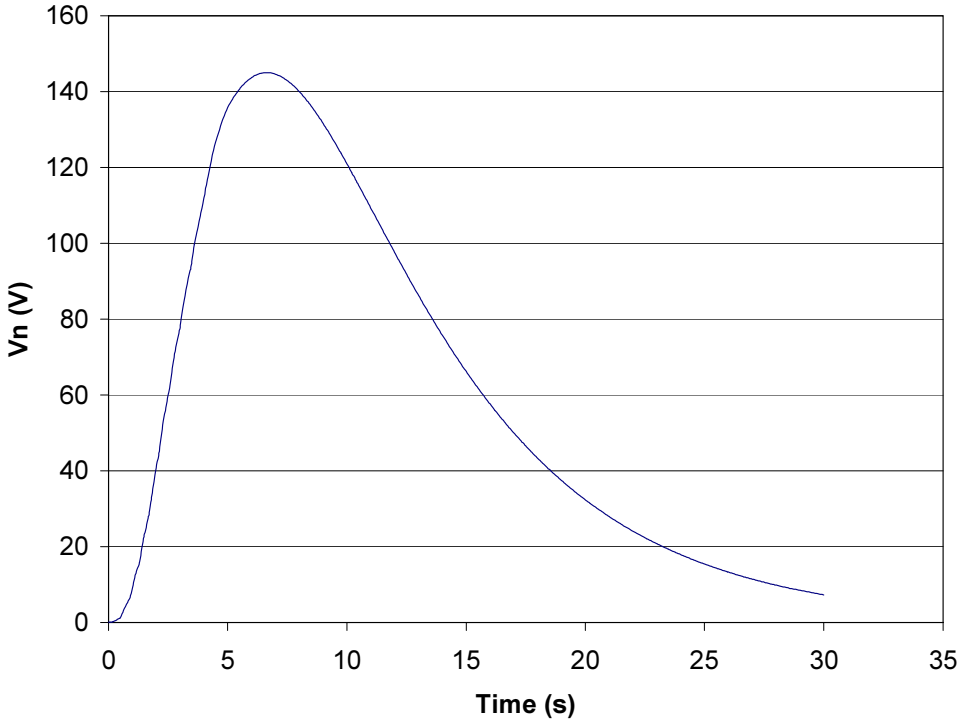

Figure 9.23 – DS normal zone voltage.

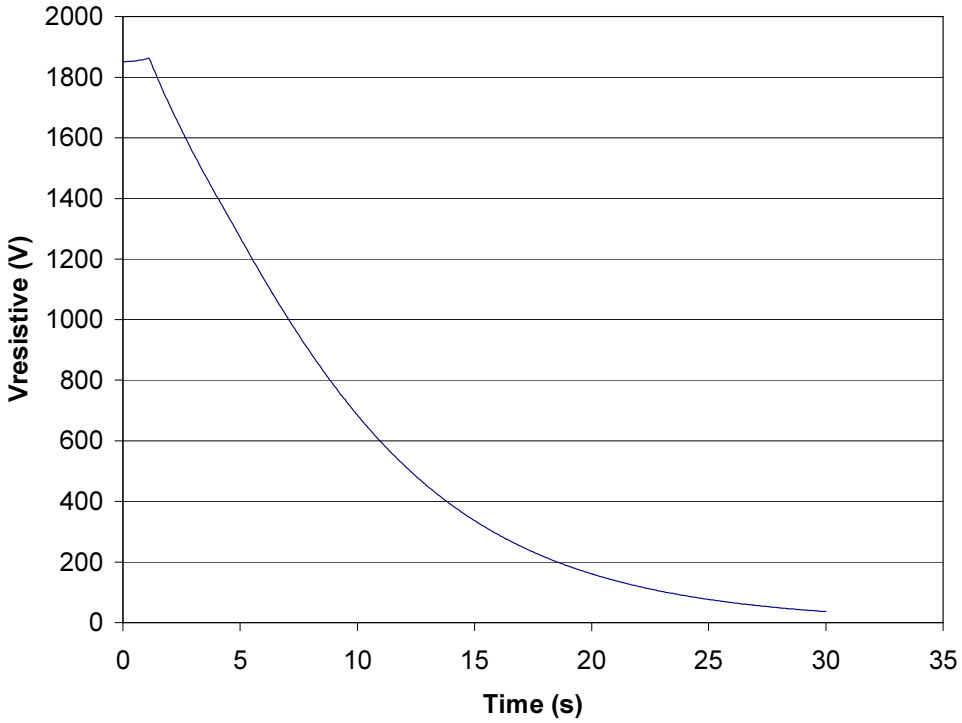

Figure 9.24 – DS total resistive (R_{coil} + R_{dump}) voltage.

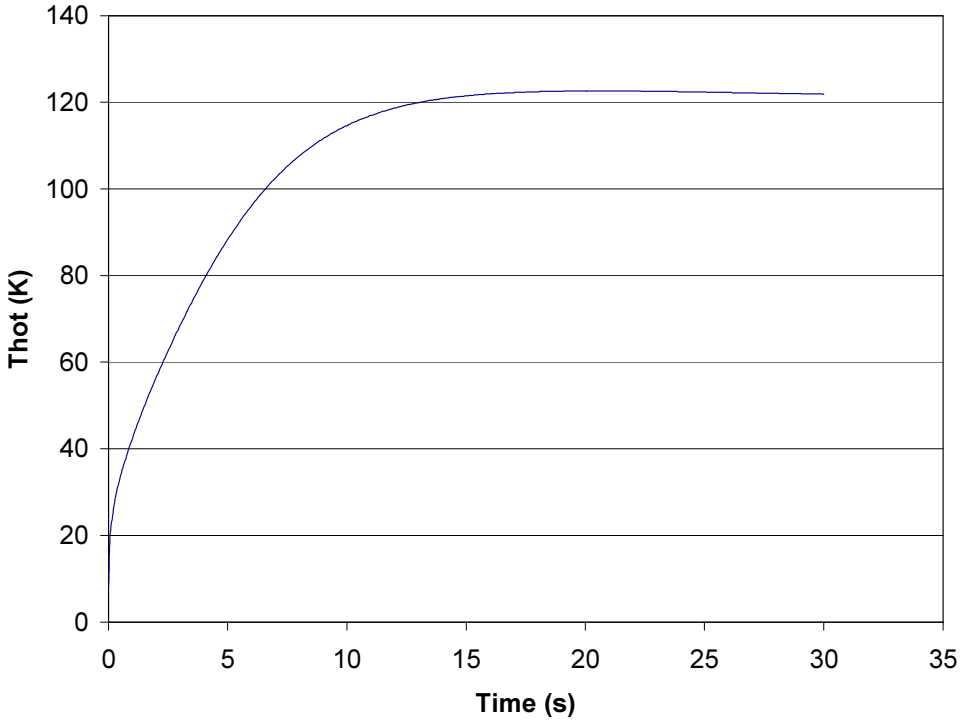

Figure 9.25 – DS hot spot temperature.

The quench was initiated from the end of the coil at the peak field location. Figure 9.26 shows the temperature distribution after 40 s. Note that although the entire coil is normal the hot spot is still rather localized. This is a large coil, and the thermal diffusion takes a long time. Even after 3 minutes, the hot spot has only dropped to 113 K while the coolest section of the winding has only come up to 47 K—not a lot different than the temperature extremes at shown in the figure for the 40 s time point. With the reduced axial length of the first DS coil, stresses have now been brought under control. The winding shear stress is now a benign 0.67 MPa, as shown in Figure 9.27.

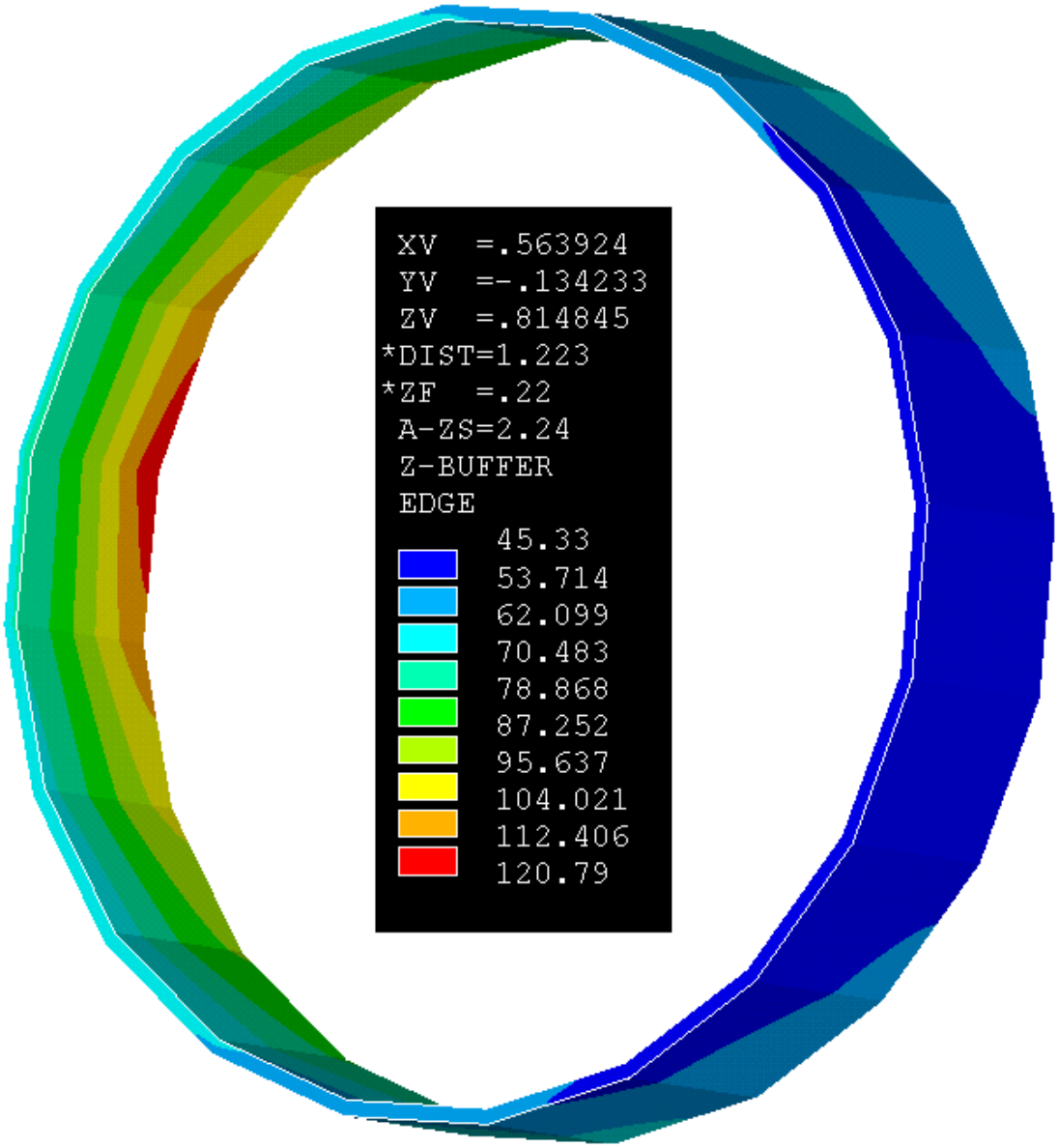

Figure 9.26 – DS temperature distribution in first DS coil 40 s after quench.

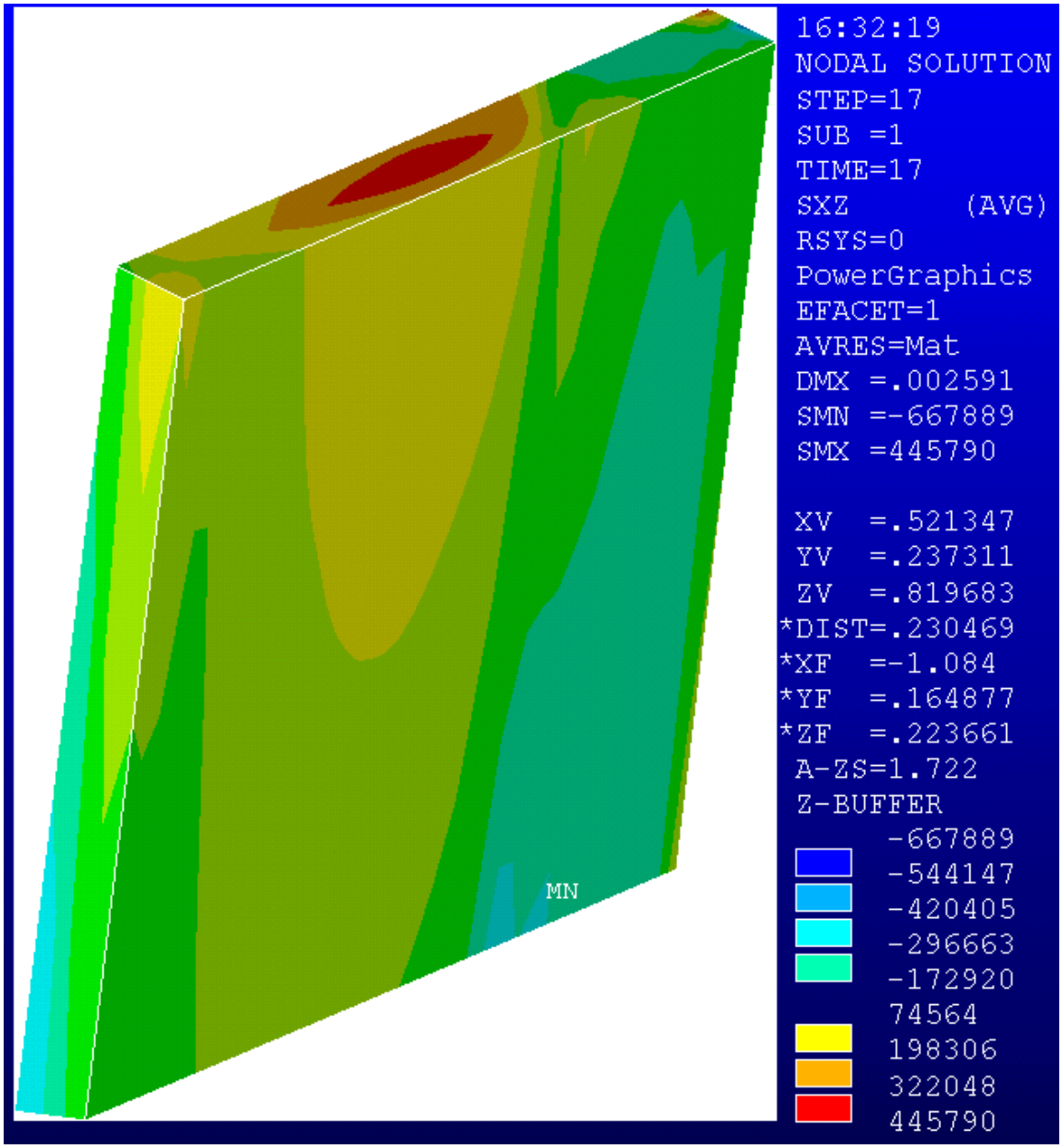

Figure 9.27 – Shear stress in first DS coil at 40 s following quench.

Section 10 - Power Supplies, Dump Resistors, and Switches

There are six power supplies for the MECO magnet system, one for each coil set consisting of PS, TS13u, TS2, TS3d5, TS4, and DS. The supplies share several common requirements, but also have unique requirements based on matching the characteristics of each coil set.

Requirements

Each power supply system shall provide a 0–10 V output signal proportional to the power supply voltage and another 0–10 V output signal proportional to power supply current. Both signals shall be accurate to 0.5 % or better. The frequency response of these output signals shall be sufficiently high to read the time rate of change of current and voltage to 0.5 % accuracy or better while the associated coil is being charged, slow discharged or dumped.

Each power supply shall accept a 0–10 V signal from the quench detection circuitry which shall cause the power supply voltage to drop to 0, while maintaining a low resistance current conducting (freewheeling) path through the power supply.

Each power supply shall be equipped with a bypass rectifier set that will be fired should on conditions that suggest loss of control of the power supply, such as logic or control circuit failure, commutation failure, AC power loss, excessive bus voltage, etc. This bypass rectifier set shall be placed as close to the magnet as practical, and shall, in any event, be placed in a separate enclosure from the power supply itself.

Each power supply shall be capable of meeting all requirements herein with up to 0.001 Ohm of series power cable resistance in the associated coil circuit.

The forward voltage requirement of each power supply shall be sufficiently large to charge its respective coil set, with the inductance specified, to full operating current at the charging rate specified in Table 10.1. The minimum charging voltage requirement given in the table shall also be met. This specification will result in the capability to charge each coil set to its full operating current in 1 hour. These relatively slow charging rates are necessary to limit eddy current and hysteresis heating of the windings to sufficiently low levels relative to the 1.5 K temperature margin of the superconductor.

Each power supply shall be capable of electronically reversing its voltage polarity from full current, thus enabling the reduction of the operating current to zero at a controlled rate. Reverse voltage capability shall be at least sufficient to drive the current of the associated coil set to 0 V in the times specified in Table 10.1.

Each power supply and dump resistor circuit shall have a switch which is placed across the dump resistor as described in the quench protection section of this report. The switch shall be closed for normal charging and discharging, but shall open upon receipt of a dump command from the quench detection circuits. During a loss of power, the quench detection circuits are kept alive by an uninterruptible power supply (UPS). Should a quench occur subsequent to a loss of power, the quench detection circuits will command the appropriate dumps. The dump switches shall therefore be capable of being operated for proper magnet protection even with loss of ac power. Whether backup power for the dump switches is provided during loss of ac power by batteries or a UPS will be better determined by final design.

Table 10.1 – Coil Set Inductance, Operating Current and Minimum Charging Rate.

Coil Set	Inductance (H)	Operating current (A)	Minimum charging rate (A/s)	Minimum charging voltage (V)	Maximum time to zero current (A/s)
PS	17.73	3500	0.972	20.0	3100
TS13u	2.045	1500	0.417	1.0	650
TS2	0.523	4000	1.11	1.0	270
TS3d5	1.19	1500	0.417	1.0	400
TS4	0.386	4000	1.11	1.0	200
DS	3.78	4000	1.11	5.0	1450

Each power supply shall have a ripple current no greater than 0.1 % of full current. Each coil set and power supply shall be provided with an associated dump resistor for fast discharge of the coil current to zero. Each dump resistor shall be designed to stay below its maximum design operating temperature for the worse case quench condition. The design of the dump resistor shall be fully consistent with the final design and fabrication vendor's quench analysis.

Table 10.2 – Nominal dump resistors, L/R time constants and stored energy including coupling.

Coil Set	Inductance (H)	Rdump (Ω)	L/R time constant (s)	Energy (MJ)
PS	17.73	0.529	33.5	109
TS13u	2.045	1.23	1.66	3.26
TS2	0.523	0.463	1.13	4.72
TS3d5	1.19	1.23	0.967	2.01
TS4	0.386	0.463	0.83	3.55
DS	3.78	0.463	8.16	30.8

Preliminary power supply design

Preliminary power supply designs have been created using the above requirements. These analyses indicate that either a 6- or 12- pulse power supply will meet the requirements, although this conclusion needs the approval of the MECO project. A 3-pulse supply would also meet the ripple requirement, but would not be acceptable for voltage inversion. Open circuit voltage, and percent ripple have been calculated for 6- and 12 pulse designs and are summarized in Table 10.3 and Table 10.4, respectively. Other assumptions for the preliminary design are:

- Impedance of power supply and bus: 0.001 Ohm
- Commutating reactance (per-unit): 0.06
- Power supply internal voltage drop: 1.5 V

Table 10.3 – 6-pulse power supply design calculations.

Coil set	Open-circuit voltage (V)	Ripple current (A)	% Ripple current
PS	24.361	4.6×10^{-4}	1.3×10^{-5}
TS13u	5.532	8.8×10^{-4}	5.9×10^{-5}
TS2	7.802	0.005	1.3×10^{-4}
TS3d5	5.161	0.0014	9.4×10^{-5}
TS4	7.644	0.0068	1.7×10^{-4}
DS	11.662	9.9×10^{-4}	2.5×10^{-5}

Table 10.4 – 12-pulse power supply design calculations.

Coil set	Open-circuit voltage (V)	Ripple current (A)	% Ripple current*
PS	24.003	1.1×10^{-4}	3.2×10^{-6}
TS13u	5.451	2.2×10^{-4}	1.4×10^{-5}
TS2	7.688	0.0012	3.1×10^{-5}
TS3d5	5.085	3.5×10^{-4}	2.3×10^{-5}
TS4	7.531	0.0017	4.2×10^{-5}
DS	11.491	2.4×10^{-4}	6.1×10^{-6}

*Note: Since there is a single operating point for each magnet (see Table 10.1), the percent ripple refers to percent of that operating current.

Section 11 - Structural Design Criteria

Lacking a specific design code jurisdiction, fusion project criteria are used for guidance in coil design [1]. The referenced FIRE design document allows the primary membrane stress to be based on the lesser of 2/3 of the Yield Strength (Sy) or 1/2 of the Ultimate Strength (Su). The ASME Code bases the primary stress on 1/3 ultimate. The fusion project based criteria is based on a distinction between coils that are supported by cases and those that are not. For MECO, this means that the PS coils, which are supported by their outer aluminum shells, need only meet the lesser of the 2/3 Sy or 1/2 Su, while the other windings, which are self-supporting, must meed the lesser of 2/3 Sy or 1/3 Su. For structural elements, ASME-like criteria are adopted with membrane stresses remaining below the maximum allowable stress, Sm, where Sm is the lesser of 2/3 of yield or 1/3 of ultimate. Bending discontinuity, and secondary stresses are treated in a manner similar to the ASME Code. Guidance for bolting and column buckling is taken from AISC, with average net section bolt stresses kept below $0.6 \times$ yield. Yield Strength and Tensile Strength properties are taken at the loaded temperature.

The cryostats are to be qualified in accordance with ASMEVIII. Qualification of all the weld details, shell thicknesses, nozzle reinforcements, and saddle or support details of these vessels will be done at the final design stage. The conceptual design sizing presented here is intended to ensure adequate space allocation and cold mass performance.

The magnets are to be seismically qualified in accordance with the Uniform Building Code.

Typical Materials Properties

Mechanical properties for some of MECO magnets structural materials and coil components are given in this section. Tensile yield strength for oxygen free copper is given in Figure 11.1 at 4 K, 76 K and at 296 K. Yield and Ultimate strength data is given for several variants of copper at RT and 77K in Table 11.1.

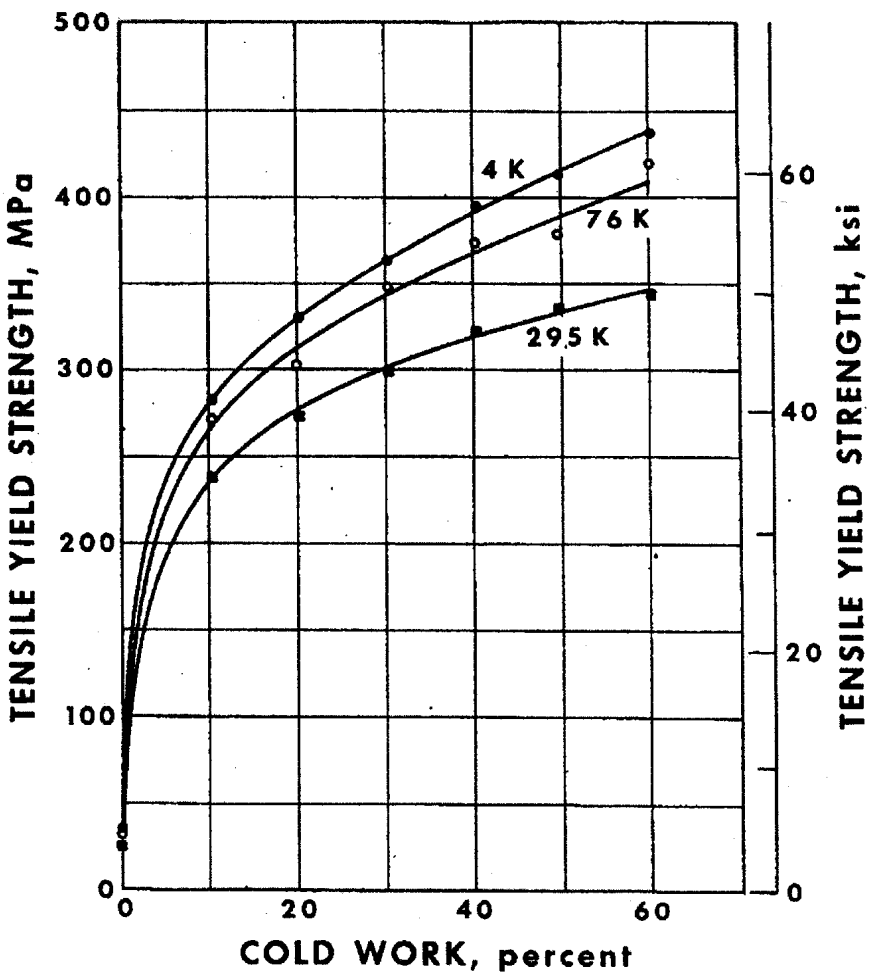

Figure 11.1 – NIST Data - Oxygen Free Copper Tensile Properties (4-300K)- C10100 - C10700 Cold Worked

Table 11.1 – Properties of Variants of Copper.

Variant	Yield at RT (MPa)	Yield at 77 K (MPa)	Ultimate at RT (MPa)	Ultimate at 77K (MPa)
C10100/C10700 80%CW	380		420	500
C10100 Becker/C-Mod 60%CW	308	373	350	474

Typical values of mechanical strength for several different types of composite insulating materials are given in Table 11.2. Warp and Fill tensile allowable with a Factor of Safety F.S.=3 or 1/3 ultimate is 167 MPa. Note that for tension normal to the reinforcement, there is no capacity listed. Normally primary tension in this direction is not allowed. Secondary or strain controlled tensile stresses are nearly unavoidable in bonded conductor arrays. Small cracks often develop near corners, and multi-layered insulations are used to limit the likelihood of through cracks. For MECO magnets, Kapton tape is specified to mitigate the effects of these cracks on electrical insulating integrity and this has the effect of reducing the tensile bond strength. It also

reduces the winding pack modulus in the direction normal to the Kapton tape. The interplay between modulus and secondary displacement controlled strains will be resolved with measured properties and strengths of a representative impregnated array of conductors.

Table 11.2 – Insulating Material Strengths.

Composite Material	Strength Normal to Fiber (MPa)		
	At 4K	At 77K	At 292K
G-10CR	749 [4]	693 [4]	420 [4]
G-11CR	776 [4]	799 [4] 900 [7]	461 [4]
CTD 101K AR irradiated	1260 (ave) [5]		
CTD-112P irradiated	1200 (ave) [5]	1150 [5]	
Polyimide/S2 Glass Laminate			1033 [6]
Tensile Strength (Warp)			
G-10CR	862 [4]	825 [4]	415 [4]
G-11CR	872 [4]	827 [4]	469 [4]
Tensile Strength (Fill)			
G-10CR	496 [4]	459 [4]	257 [4]
G-11CR	553 [4]	580 [4]	329 [4]

Tensile Strain Allowable Normal to Plane

No primary tensile strain is allowed in the direction normal to the adhesive bonds between metal and composite. Secondary strain will be limited to 1/5 of the ultimate tensile strain. In the absence of specific data, the allowable working tensile strain is 0.02% in the insulation adjacent to the bond. Table 11.3 provides modulus data for G-10 composite materials.

Table 11.3 – Modulus of Elasticity for G-10 at several temperatures.

Temperature (K)	G-10 Warp/Fill (GPa)	G-10 Normal (GPa)	Epoxy Only (GPa)
295	27.8	14.0	3.81
250	29.5	16.5	5.25
200	31.3	18.8	6.69
150	32.5	20.5	7.84
100	33.0	21.5	8.54
76	33.5	21.8	8.68

Additional properties for materials used in the MECO magnet system conceptual design are provided in Table 11.4 through Table 11.7.

Table 11.4 – Tensile Properties for Stainless Steels and Aluminum.

Material	Yield at 4 K (MPA)	Ultimate at 4 K (MPa)	Yield at 80 K (MPa)	Ultimate at 80 K (MPa)	Yield at 292 K (MPa)	Ultimate at 292 K (MPa)
316 LN SST	992	1379			275.8	613
316 LN SST Weld	724	1110			324	482
304 SST 50% CW			1344 (195 ksi)	1669	1089	1241
304 Stainless Steel (Bar, annealed)			282 (40.9 ksi)	1522	234	640
Aluminum 6061T6	362 (20K)	496 (20K)	275.8		275 (40ksi)	310 (45ksi)
Alum 6061 Weld	259	339				

Table 11.5 – Coil structure cryogenic (292 K) maximum allowable stresses, Sm = lesser of 1/3 ultimate or 2/3 yield, and bending allowable=1.5*Sm

Material	Sm (MPa)	1.5 Sm (MPa)
316 LN SST	183 (26.6 ksi)	275 (40ksi)
304 SST 50% CW		
304 Stainless Steel (Bar,annealed)	156 (22.6ksi)	234 (33.9ksi)
Aluminum 6061T6		

Table 11.6 – Coil Structure cryogenic (80 K) maximum allowable stresses, Sm = lesser of 1/3 ultimate or 2/3 yield, and bending allowable=1.5*Sm

Material	Sm (MPa)	1.5 Sm (MPa)
304 SST 50% CW	556 (80 ksi)	834 (120 ksi)
304 Stainless Steel (Bar, annealed)	188 (27ksi)	281 (40.9ksi)

Table 11.7 – Coil Structure Cryogenic (4 K) Maximum Allowable Stresses, Sm = lesser of 1/3 ultimate or 2/3 yield, and bending allowable=1.5*Sm

Material	Sm (MPa)	1.5 Sm (MPa)
316 LN SST	459.6 (66.7 ksi)	689 (100 ksi)
316 LN SST Weld	366 (53.2ksi)	550 (79.7ksi)
Alum 6061T6	165	248
Alum 6061T6 Weld	113	169.5

Inconel 718 was used in the C-Mod Drawbars and oblong Pins. Physical properties were measured from samples of the forgings used for these drawbars. This data is summarized in Table 11.8. These values are representative of strengths expected for the 718 bolting specified for MECO. Used as bolting, 718 would have a 0.6×173=100 ksi maximum allowable operating stress.

Table 11.8 – Inconel 718 Tensile data (hardening for 1 hr. at the most favorable temperature, either 1750 or 1950 F from [3])

	4 in. Bar	5/8 in Bar	5/8 in. Bar
Temperature (K)	292	292	77
Yield (ksi)	165	180	173
Ultimate (ksi)	195	208	237
Modulus of Elasticity (psi)	29.8×10^6	29.8×10^6	31.0×10^6
Density (lb/in^3)	0.296	0.296	0.296

References

[1] Fusion Ignition Research Experiment Structural Design Criteria; Doc. No. 11_FIRE_-DesCrit_IZ_022499.doc; February, 1999

[2] “General Electric Design and Manufacture of a Test Coil for the LCP”, 8th Symposium on Engineering Problems of Fusion Research, Vol III, Nov 1979

[3] Product Literature, Inco Alloys International, Inc Huntington West Virginia 25720, USA

[4] “Mechanical, Electrical and Thermal Characterization of G10CR and G11CR Glass Cloth/Epoxy Laminates Between Room Temperature and 4 deg. K”, M.B. Kasen et al, National Bureau of Standards, Boulder Colorado.

[5] “US ITER Insulation Irradiation Report Program Final Report” August 31 1995 Reed, Fabian, Shultz

[6] “Effect of Face Compression on Interlaminar Shear Strength of Polyimide/S2 Glass Laminate Insulators - Preliminary Report" H.Becker, T. Cookson (GDC) June 24 1985

[7] "Shear Compression Tests for ITER Magnet Insulation" Simon, Drexler, Reed, Advances in Cryogenic Engineering Materials Vol 40 (1994)

Section 12 - Production Solenoid Coil, Cryostat, and Support Stress Analysis

Introduction

The production solenoid (PS) is shown in the MECO magnet array in Figure 12.1. Stress analysis of the coil winding packs of the production solenoid indicates acceptable conductor stresses for a structural concept that employs external aluminum shells to contribute to the support of the coil hoop stresses. The use of external shells/mandrels as a support scheme results from the advantage in conductor stress, from the need to bridge axial loads around the thin coil sections, to provide axial compressive stresses to mitigate the effects of a quench, and the need to have reliable attachment points for the cold mass supports. The external shell/mandrel allows freedom in selecting higher conductor current density, while controlling the conductor hoop stress with adjustments in the shell thickness. Additional nuclear heat in the external shells may be removed separately from the winding pack A cold mass support scheme employing compressively loaded struts supports the axial attractive force between the production and transport solenoids. Vertical and lateral support rods are also provided. The cryostat inner shell was modeled as 2 cm thick and is capable of supporting the nuclear shield (up to 70 tons). This is intended to provide an alternative to the strongback support as an assembly and support option for the shield. If the cryostat bore is used for this purpose further, work is needed particularly to qualify the insertion loads on the shell. The analysis considered the shield in its assembled location in which the end caps of the cryostat stabilize the shell.

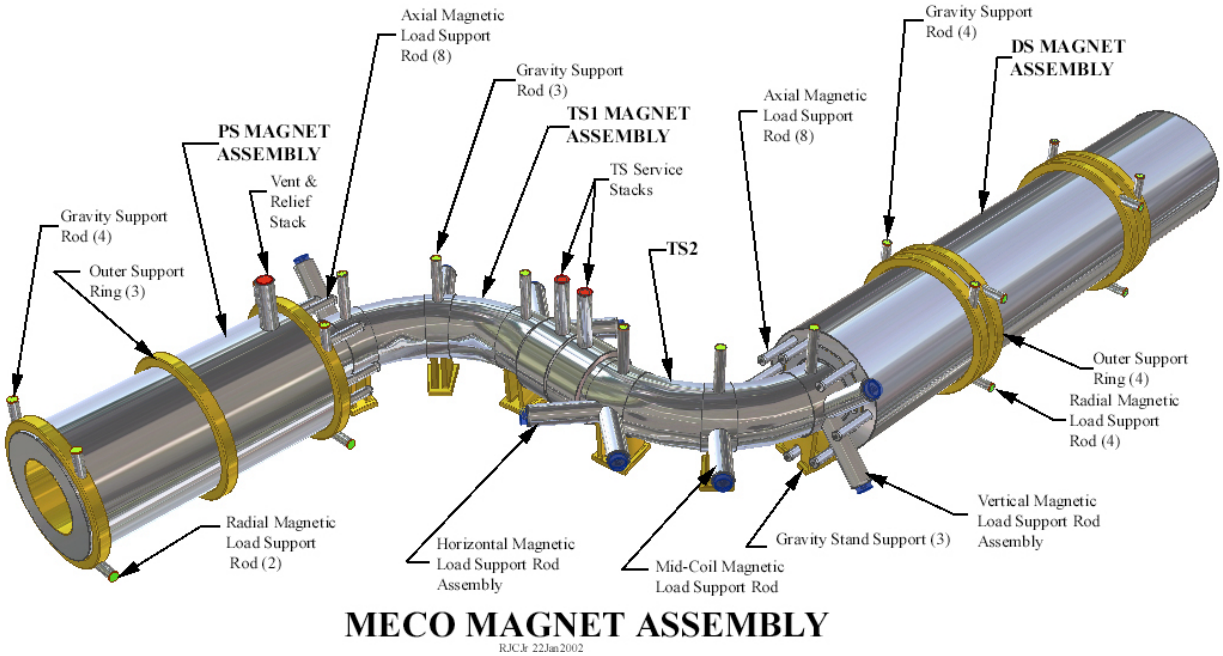

Figure 12.1 – The MECO Coil system. The Production Solenoid is at the left.

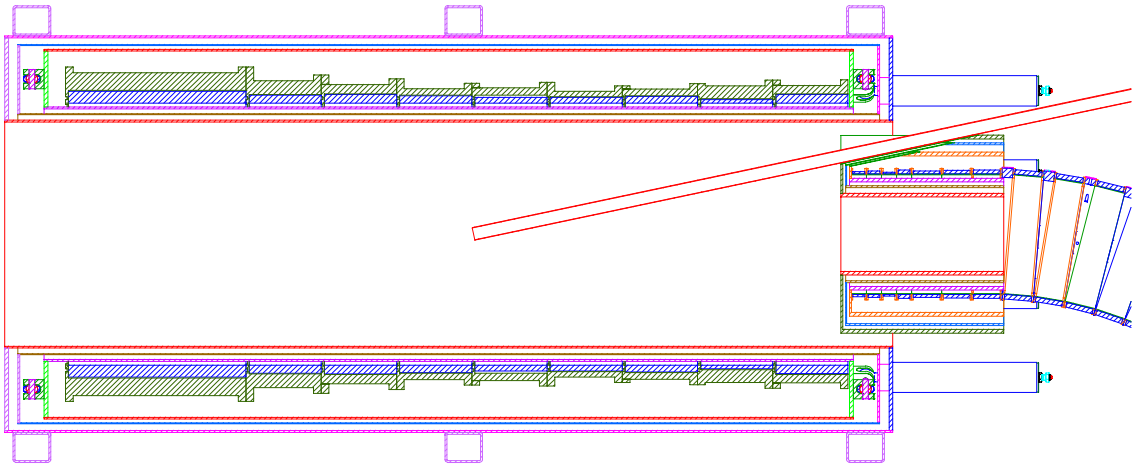

Figure 12.2 – Cutaway drawing of the PS as viewed from above.

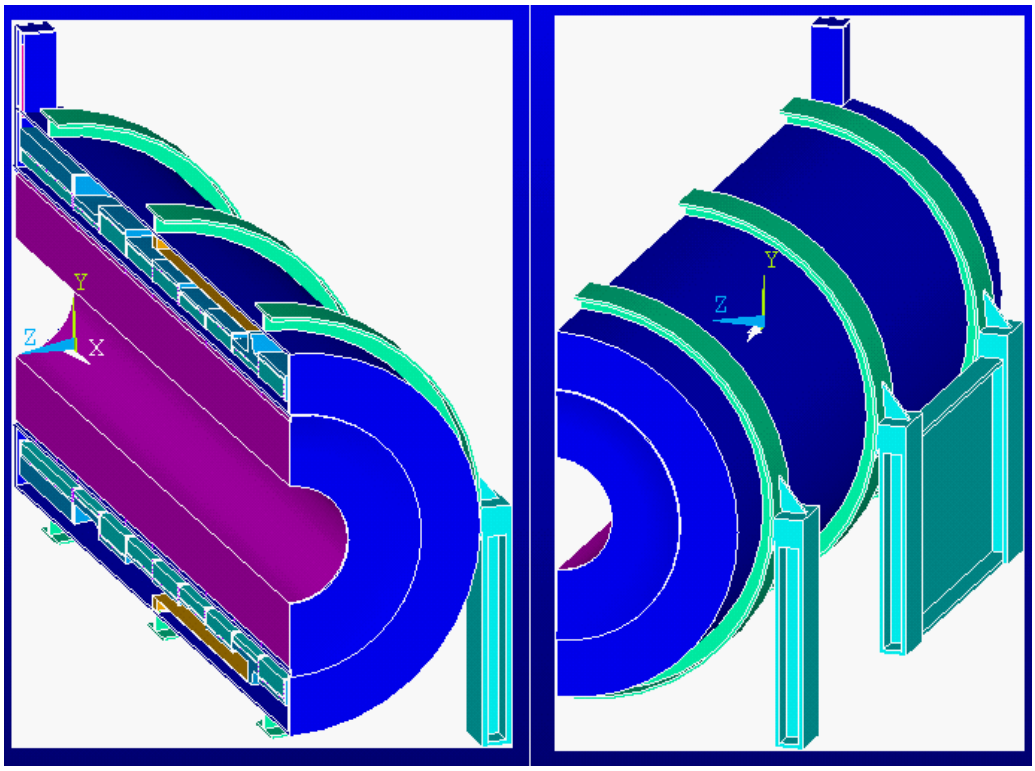

Figure 12.3 – Production solenoid 3D model showing structural supports.

A couple of different mandrel/support schemes have been modeled for the production solenoid. The most attractive arrangement uses external aluminum 6061 T6 shells for the structural support of the coils. Results for this arrangement are presented. External support eliminates the gap between an internal mandrel and coil when the coil is energized and reduces the coil stress. The coils could be wound on GRP shells mounted with fixtures on a turntable. The coolant channels on the OD of the coil are formed with rubber rings that are removed after impregnation. The outer surface is then machined to fit the ID of the mandrel shell. A more

detailed description of the winding and coil fabrication procedure is included in the assembly and manufacture section.

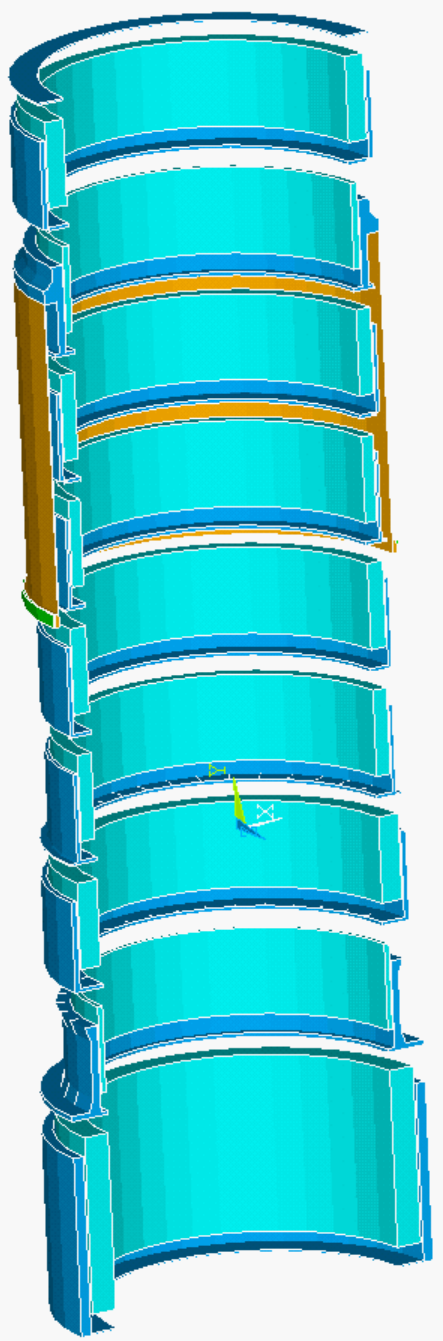

Figure 12.4 – Expanded Assembly View Showing Shell Stack-up for Vertical Assembly. The yellow "skirt" is an axisymmetric representation of flexure cold mass supports that were not used.

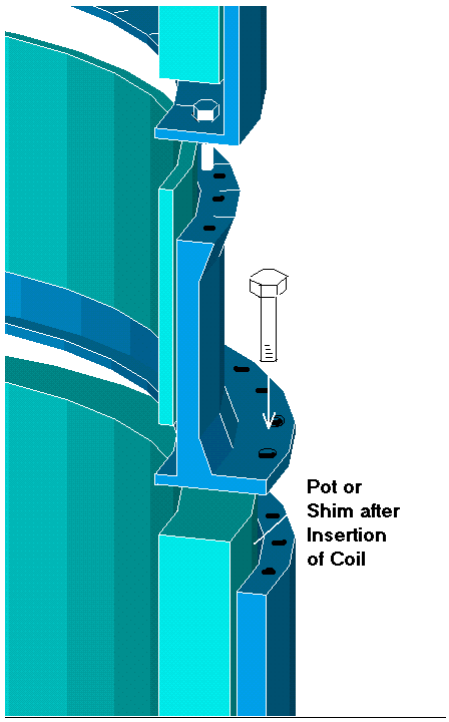

Figure 12.5 – Detail drawing of flange bolting.

The solenoid assembly is built from the large coil end (Z=0). Coil numbering begins with this coil, designated P1. Vertical assembly is probably preferred. Vertical assembly was attractive in the Neutrino factory solenoid study. Thin shells used for the cryostat, helium vessel, and LN2 shields can be slipped over the coil array with vertical lifts. The inner cryostat wall, and radiation shield would be erected. The thermal shield and inner Helium vessel would be slipped over that. Coil assembly would start with the outer structural shell for P1. The wound coils would be sequentially slipped into their outer structural shells. A 1 mm nominal diametral gap is specified for the radial fit of the coil and the mandrel. This is specified to moderate the thermal pre-compression provided by the interaction of the copper coil and aluminum mandrels. Grooves in the mandrel flanges allow connection of the joints. The shell for the next coil would be lowered onto the stack and bolted to the shell/mandrel below. In Figure 12.4 and Figure 12.5, the bolting is shown as being accessed from inside the coil cavity before insertion of the next coil. The present design uses bolting only on external flanges.

A number of iterations were used to arrive at the present shell geometry. P2 originally was quite thin and the shell for P2 had to be thickened, not because of hoop or direct axial stresses, but because the off-set in the axial load resulting from the centroid shift between P1 and P2 caused bending stresses in P2 and it's shell. In the present set of coil builds, P2 is thicker. The aluminum mandrels have been specified as one half the coil thickness, providing sufficient pre-compression, while avoiding excessive thermal stresses. The choice of mandrel thickness was a convenience, and during detailed design, mandrel shell thicknesses might optimize to some other fraction of the coil build. The mandrel for P8 appears thin because the coil is thin. It satisfies stress criteria but its thickness should probably be re-visited.

Coil Stress Summary

There were many iterations of coil builds, mandrel thicknesses and mandrel materials. All had conductor stresses at or below the 200 MPa allowable for half hard copper at 4 K (see the discussion in the criteria section for the derivation of the 200 MPa allowable). The local conductor stress as a post-processed result from the axisymmetric analysis is shown at below. These stresses include the effects of local conductor stress "multipliers" In these plots, the solenoid axis is "up" and only P1 to P4 are shown. The remaining coils are less severely loaded than P1. The external mandrel allows thicknesses and fits to be adjusted to accommodate variaties of builds and current densities. Note that the 200 MPa primary stress allowable should be applied to the average section stress, but the max coil stress is below 200 MPa, ensuring an adequate conceptual design.

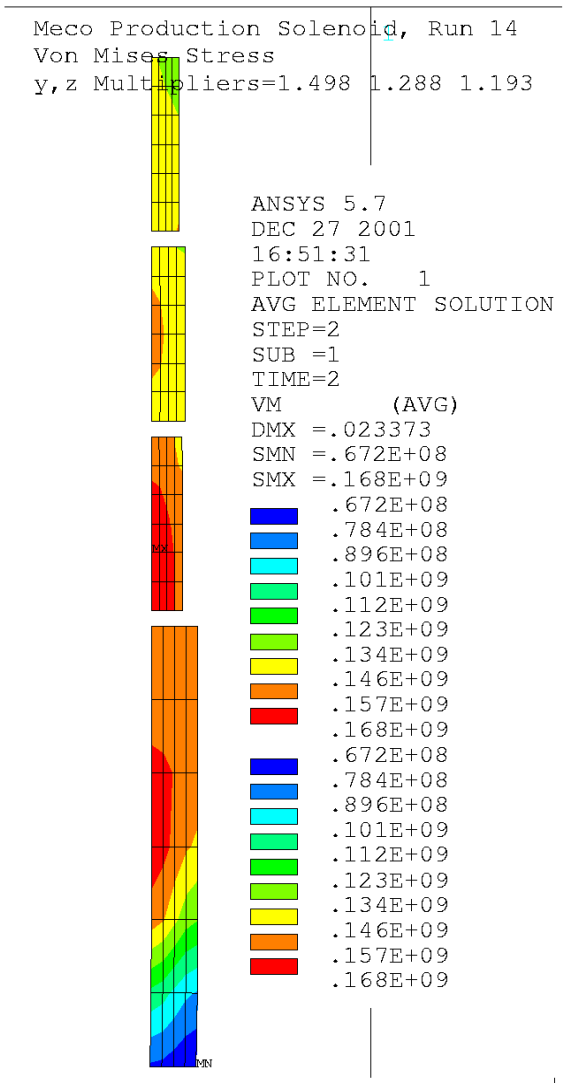

Figure 12.6 – Local conductor Von Mises stress. Aluminum mandrels 1/2 coil build thick, No axial gap and 0.5mm radial gap, Run #prod14

Conductor Allowable

The conductor is predominantly copper, and is approximately half hard. Hardness is assumed to correlate with percent cold work. Figure 11.1 in the preceding Section plots yield as a function of cold work. The conceptual design assumes that the copper will be cold worked to provide a primary membrane allowable (lesser of 2/3 Sy or 1/2 Su for externally supported coils) of about 200 MPa. At 4 K 30% CW reaches these levels. It would be wise to do a tension test of the full copper channel section before soldering the superconductor. Surface hardness may not be a reliable indicator of the full section strength.

Conductor Array Model

The present conceptual design for the PS coil conductor is shown in Figure 12.7, where the cable is 32.3% of the volume. Figure 12.8 shows an earlier conductor design that was used for much of the PS stress analysis, and where the cable is 28.6% of the volume. This change is a difference of about 5% and was considered insufficient at the conceptual level to rerun all the calculations. Thus, the results presented correlate with the conductor arrangement of Figure 12.8, even though the actual design is shown in Figure 12.7.

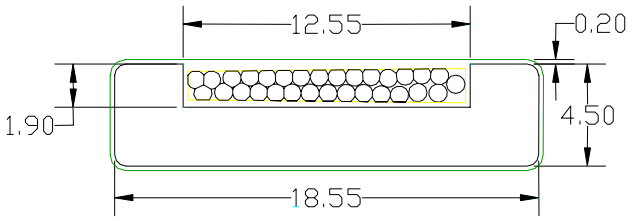

Figure 12.7 – Final PS conductor cross-section chosen. The conductor is 32.3% of the volume.

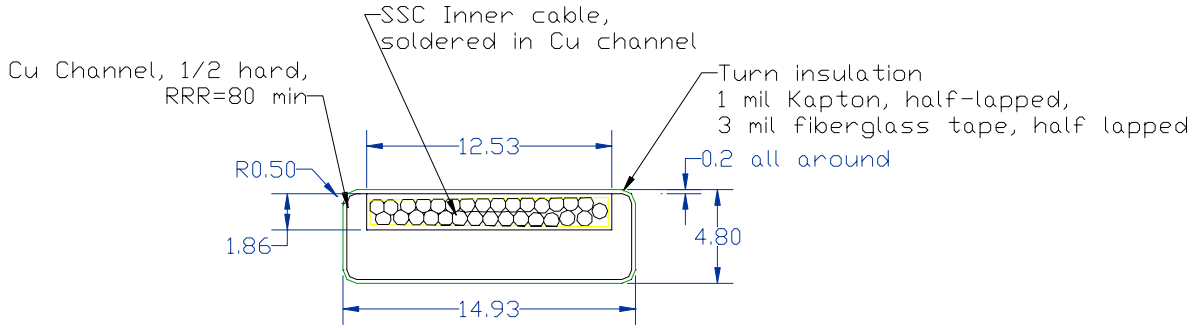

Figure 12.8 – Conductor cross-section used in the structural calculations. The conductor is 28.6% of the volume.

This analysis is used to calculate an equivalent modulus for the analyses in which "smeared" coil properties are employed. It is also used to calculate the multipliers to be applied to the "smeared" stress results. The multipliers are applied in a post-process of the coil analyses to obtain the local copper stress from the “smeared” stress, which is output directly from the model. The conductor finally chosen for the PS is different than that used in the stress calculations. The area of added copper estimates the change in stress. An approximate correction factor to be

applied to the postprocess results is then: (1-.286)/(1-.323) = 1.05, or a 5% error in the postprocess results.

Material Properties input in the Conductor Model

Young's modulus for Copper at 4 K: 1,138 GPa
Young's modulus assumed for solder: 2.25 GPa
Young's modulus assumed for insulation (see Table 12.1): 3.25 GPa

Table 12.1 – G-10 Temperature Dependent Moduli

Temp (K)	G-10 Warp/Fill (GPa)	G-10 Normal (GPa)	Epoxy Only (GPa)
295	27.8	14.0	3.81
250	29.5	16.5	5.25
200	31.3	18.8	6.69
150	32.5	20.5	7.84
100	33.0	21.5	8.54
76	33.5	21.8	8.68

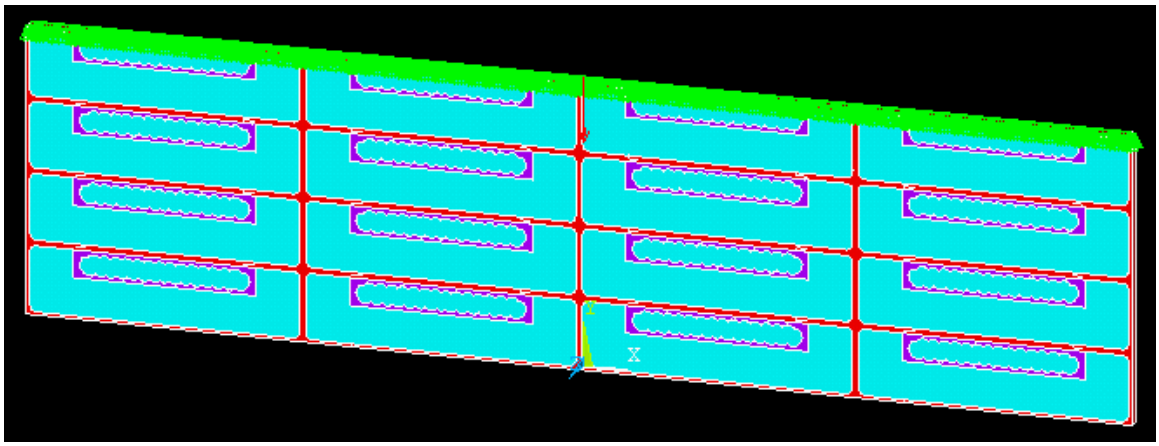

Figure 12.9 – Conductor array model, showing coupling (at top) and load for vertical loading (radial winding pack direction). Vertical constraints (not shown) are applied to the lower edge. Two other cases of loads and constraints were modeled, three total, one for each direction of loading.

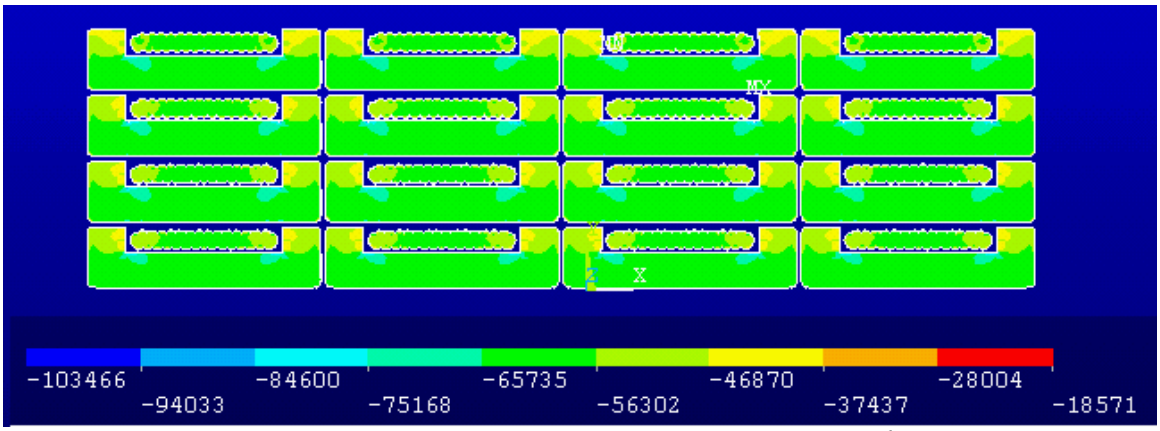

Figure 12.10 – Copper SX or axial winding pack direction. The "unit" load is 10^6 Newton on a 19.6×1 mm cross-section for a 51020 Pa average loading. The "primary" SX stress is about 66000Pa for a multiplier of 66000/51020=1.3. The multiplier for the peak SX stress is 103/51=2.02

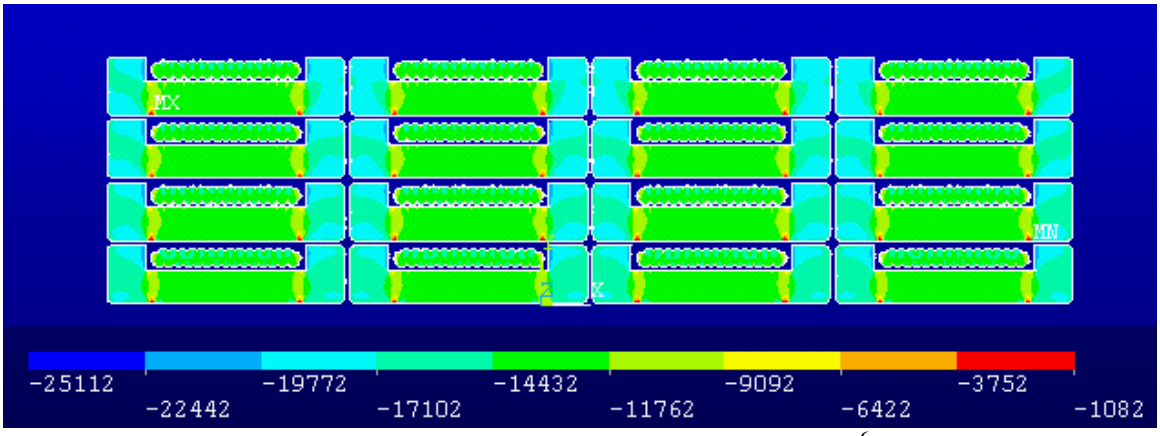

Figure 12.11 – Copper SY or winding pack radial stress. The "unit" load is 10^6 N on a $2*37.9 \times 1$ mm area, for a 13192 Pa average stress.

Table 12.2 – Modulus calculations based on the conductor array calculations

Direction with respect to winding pack	Unit Load (N)	Area (mm^2)	Ave. Stress (Pa)	Displace-ment (mm)	Length (mm)	Strain	E (GPa)
Axial (X)	10^6	19.6	51020	-3.68×10^{-5}	75.8	4.85×10^{-7}	105
Radial (Y)	10^6	75.8	13192	-3.01×10^{-6}	19.6	1.54×10^{-7}	85.8
Hoop (Z)	10^6	1485.68	673.09	-5.82×10^{-9}	1	5.82×10^{-9}	115.6

To simplify the analyses, an isotropic modulus of 110 GPa is used in the finite element analyses.

Table 12.3 – Conductor multipliers

Direction	Ave Stress (Pa)	"Primary" Directional Stress (Pa)	Multiplier
Axial (X)	51020	65735	1.288
Radial (Y)	13192	19772	1.498
Hoop (Z)	673.09	803	1.193

A conductor effective modulus of 110 GPa is used in the last of the axisymmetric runs. Orthotropic properties have been implemented in the latest analyses. The conductor stress multipliers are used in a post-process of the coils to recover local stresses from the "smeared" coil results.

The Composite Axial α of the Conductor

The analysis is based on 0.2mm thick G-10-like material wrapping the copper conductor which is 18.55 mm wide. The actual insulation system uses a wrap of 2 mils of Kapton and 6 mils of epoxy glass for each conductor, and the presence of Kapton will change the tensile modulus normal to the insulation planes. But lacking measured data on the proposed system, 0.2mm of G-10 is assumed. The normal direction α for G-10 is 24.3×10^{-6}, and 10.82×10^{-6} for copper. The effective α is $(24.3 \times 10^{-6} \times 0.4 + 10.82 \times 10^{-6} \times 18.55) / 18.95 = 11.10 \times 10^{-6}$. The differential α of alum-conductor is $13.88 \times 10^{-6} - 11.10 \times 10^{-6} = 2.78 \times 10^{-6}$. The conductor insulation is presently specified as 2 mil of Kapton with an overwrap of 6 mils of a G-10-like material. The presence of the Kapton tape brings into question the modulus calculations presented here, particularly for tensile stresses. In previous projects, tests were performed on a conductor array, and the structural performance was confirmed. This should be considered during detailed design.

Axisymmetric Model Results

There were many iterations of coil builds, mandrel thicknesses and mandrel materials. Quench behavior, and the higher field of the production solenoid led to a different support scheme than has been used in the transport and detector solenoids. An aluminum external mandrel has been chosen for the production solenoid. This has provided some stress control during a quench, and hoop load sharing during normal operation. The mandrel also constrains motion of the coil. Quench axial tensile stresses are in the range of up to 45.5 MPa [5] and it is desirable to fully offset these. This has been computed based on winding modulus of 75 GPa and with a realistic account of the effects of Kapton, the tensile modulus may be substantially below this. A lower tensile modulus reduces the quench tension that needs to be offset. There is a discussion of axial coil compression in the section that deals with the mandrel flange bolting. Large axial compressive stresses can be obtained using the thermal interactions between coil and mandrel, but the mandrel flange bolting must be sturdy enough to sustain the resulting axial tension loads. In the tables below, the hoop interaction between the coils and their outer mandrels is explored for different radial assembly clearances. Even with a 0.5 mm room

temperature gap, there is some thermal compression in the coils, and there is some freedom in selecting the assembly clearance between impregnated and OD machined coils and the machined ID of the aluminum mandrel.

Table 12.4 – Estimates of Coil and Mandrel Hoop Stresses for zero initial assembly gap between the coil and mandrel. Mandrel thickness is 1/2 the coil build.

	Coil Thermal Stress	Mandrel Thermal Stress	Coil Lorentz Stress	Mandrel Lorentz Stress	Coil Thermal+ Lorentz stress	Mandrel Thermal+ Lorentz Stress
P1	-29.9	65.9	164.4	90	134.5	155.9
P2	-28.1	60.1	153.1	86.6	125	146.7
P3	-28.5	61.3	143.1	80.4	114.6	141.7
P4	-27.8	59	132.6	75.4	104.8	134.4
P5	-27.9	59.3	122.4	69.5	94.5	128.8
P6	-27.1	56.8	111.9	64.4	84.8	121.2
P7	-27.6	58.4	101.8	58.1	74.2	116.5
P8	-25.9	53.2	91.1	53.4	65.2	106.6
P9	-28.5	61.2	81.7	45.9	53.2	107.1

Table 12.5 – Estimates of Coil and Mandrel Stresses for .5mm initial assembly gap between the coil and mandrel. Mandrel thickness is 1/2 the coil build.

	Coil Thermal Stress	Mandrel Thermal Stress	Coil Lorentz Stress	Mandrel Lorentz Stress	Coil Thermal+ Lorentz stress	Mandrel Thermal+ Lorentz Stress
P1	-16.5	36.3	164.4	90	147.9	126.3
P2	-13.5	28.8	153.1	86.6	139.6	115.4
P3	-14.2	30.4	143.1	80.4	128.9	110.8
P4	-13	27.5	132.6	75.4	119.6	102.9
P5	-13.2	27.9	122.4	69.5	109.2	97.4
P6	-11.8	24.7	111.9	64.4	100.1	89.1
P7	-12.7	26.7	101.8	58.1	89.1	84.8
P8	-9.9	20.2	91.1	53.4	81.2	73.6
P9	-14.1	30.2	81.7	45.9	67.6	76.1

Axisymmetric models were run in parallel with the local conductor analysis, and the initial "guess" for the conductor modulus was low. This was corrected, but because there is always some uncertainty in the effective modulus of impregnated coils, final design analyses should include some variation in moduli.

The following three tablulated stresses are all "smeared" results. The model is a non-linear model with gaps modeling frictional sliding and parting of interfaces. While finite friction was input, the path dependent cooldown was not rigorously simulated. Estimates of frictional energy deposition should be the subject of future work in the final design phase. At this point, care

should be taken to apply Teflon sheets especially on mandrel shell sidewalls to minimize frictional energy release.

Table 12.6 – Production solenoid coil segment stresses, Run #prod14, Conductor E=110 GPa, TS On , Net axial load = 194630 N/rad or 137 ton total for the Coil, Normal operating loads.

Coil#	1	2	3	4	5	6	7	8	9
Max SIGE (VM)	141	144	128	137	124	128	112	137	110
Min SY (Axial)	-84	-82.7	-75.9	-95.3	-80.6	-94.6	-74.6	-115	-85.2
Max SZ (Hoop)	149	88.5	79.4	76.7	71.1	64.4	61.2	59.7	61.1

Local stresses near the Helium groves in the mandrels are not included in the results tabulated above. The minimum axial stresses (or the max compressive stresses) tabulated above, typically appear as a bearing stress at the flange. This stress will interact with the grooves cut in the mandrel. The build of P8 is small, and the bearing stress is the largest. The local stress at this point in the winding pack should be investigated in greater detail during the final design phase.

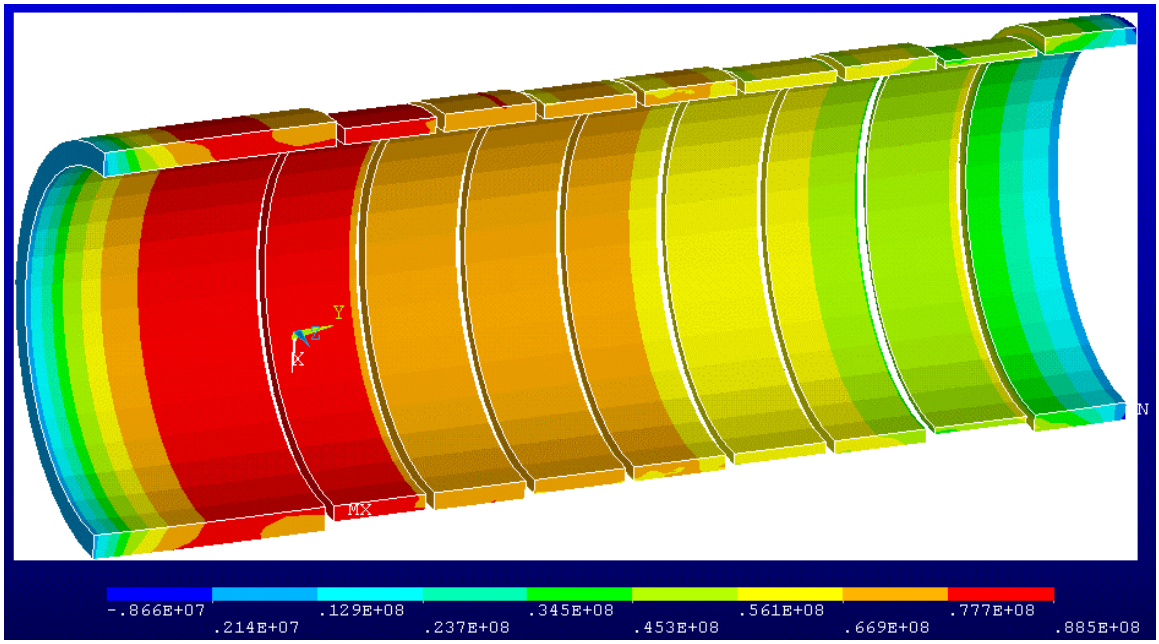

Figure 12.12 – "Smeared" Coil SZ or hoop stress, model with aluminum external mandrel/support. Aluminum Mandrels are 1/2 coil build thick, No axial gap and 0.5mm radial gap, Run# prod14, Normal operating loads.

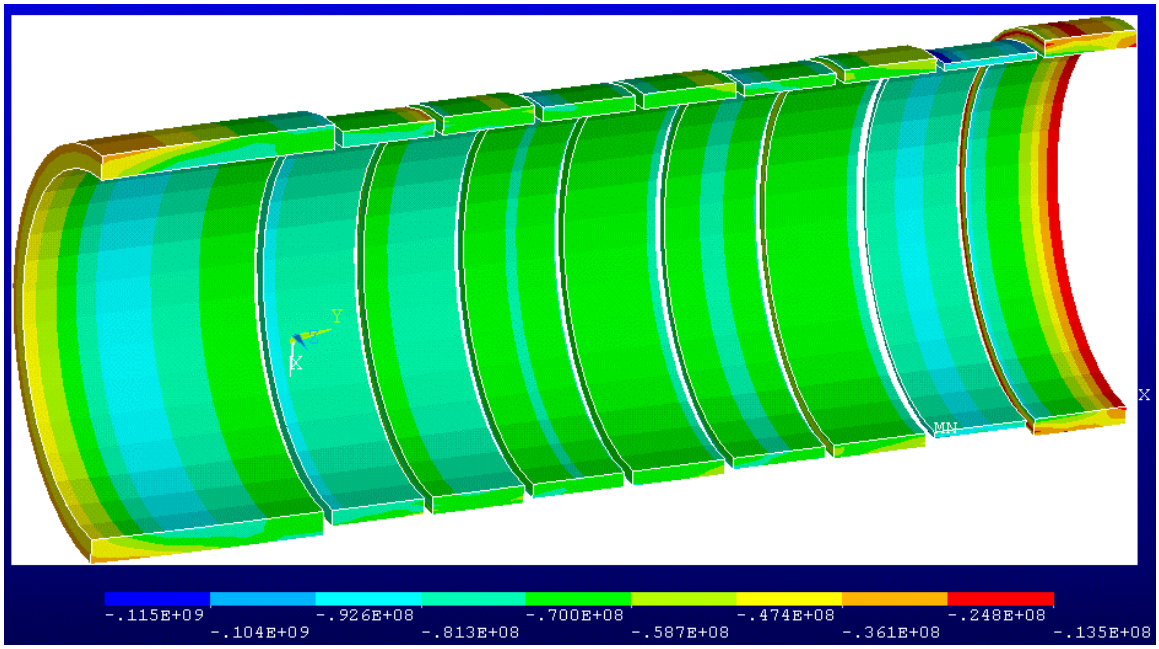

Figure 12.13 – "Smeared" coil SY or axial stress - Model with aluminum external mandrel/support. Aluminum mandrels are 1/2 coil build thick, No axial gap and 0.5mm radial gap, Run #prod14, Normal operating loads

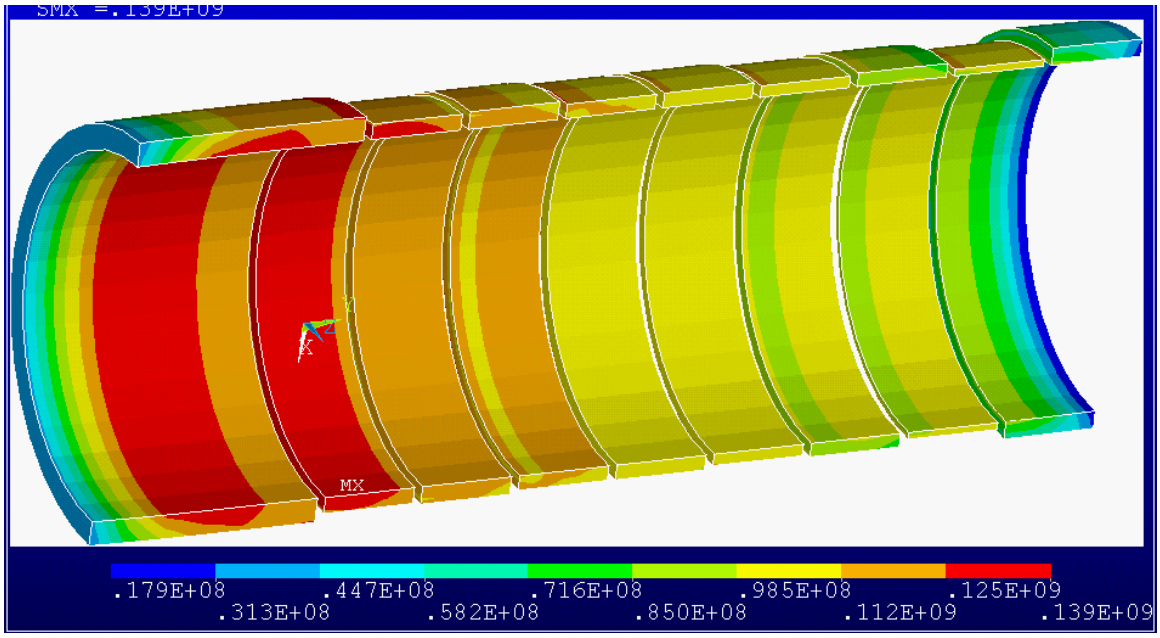

Figure 12.14 – "Smeared" Coil Von Mises Stress - Model with aluminum external mandrel/support. The maximum Von Mises stress in this plot is 139. Aluminum mandrels are 1/2 coil build thick, No axial gap and 0.5mm radial gap, Run #prod14

Mandrel Stress -External Shell/Mandrel

The mandrel was first modeled with stainless steel properties, with internal and external mandrels. Stresses in the external mandrel of about 180 MPa were obtained. This is is small compared with 316 stainless steel primary membrane allowable of 459.6 MPa (66.7 ksi) for the base metal and 366 MPa (53.2 ksi) for welds. Aluminum mandrels are not as strong, but they provide axial preload to offset the quench pressures. Also, importantly, they are easier to machine. A stress plot for the aluminum mandrels is shown in Figure 12.16, where the 141 MPa peak stress compares favorably with the 165 MPa 4 K allowable.

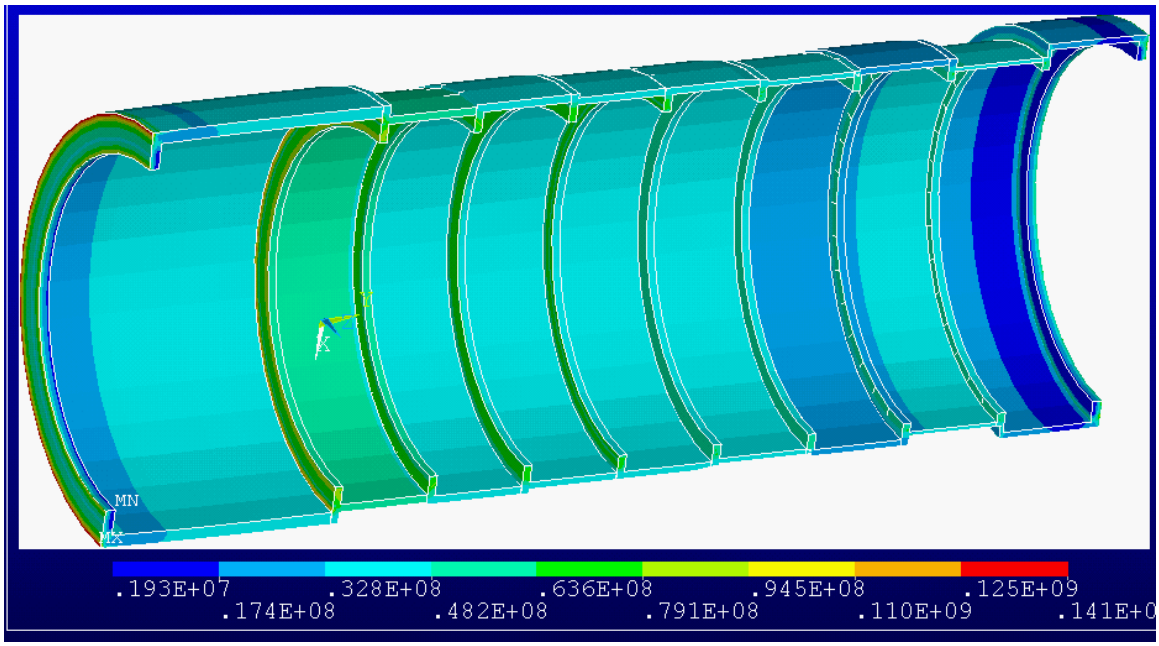

Figure 12.15 – Aluminum Outer Shell/Mandrel Von Mises Stress - Aluminum Mandrels are 1/2 coil build thick, No axial gap and 0.5mm radial gap, Run #prod14 - Peak stress is 141 MPa. The allowable for 6061-T6 at 4K is 165 MPa

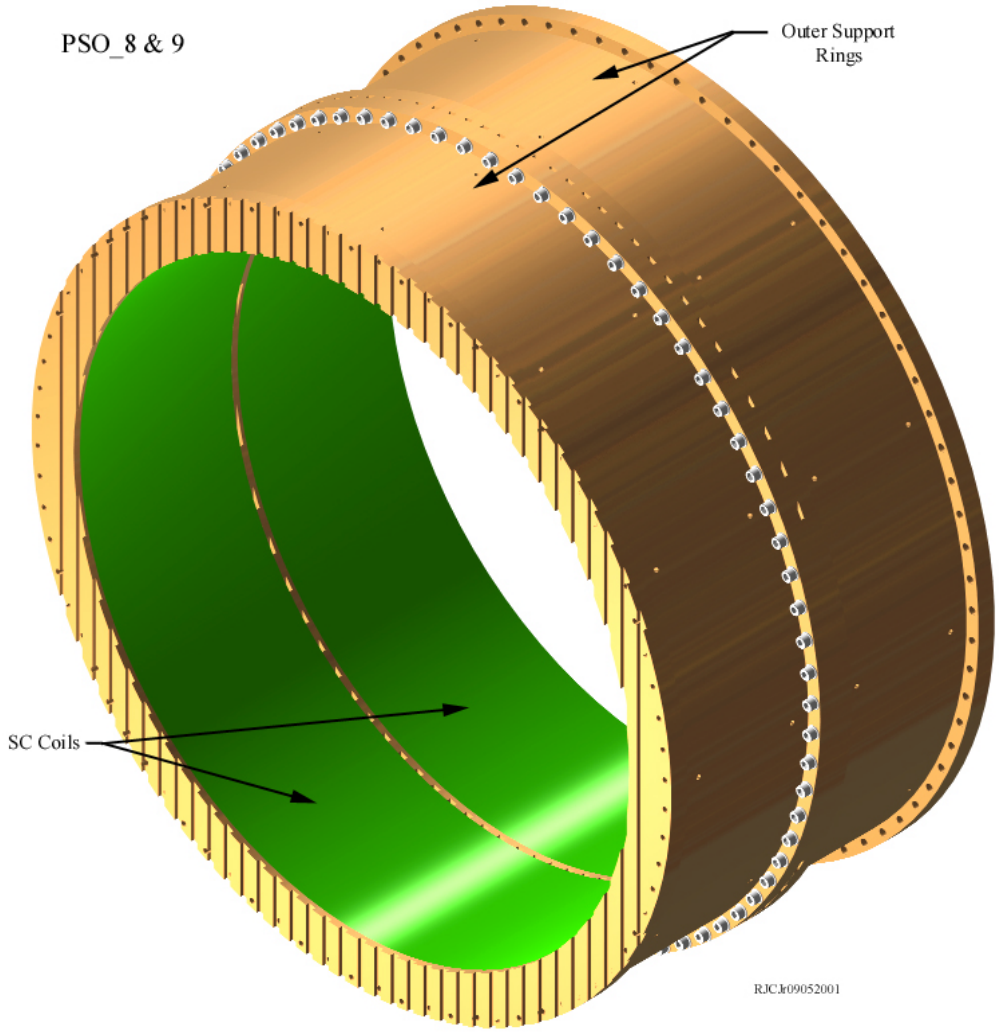

Figure 12.16 – Production Solenoid Mandrel showing He bubble vent grooves, and flange bolting. This is an aluminum 6061T6 forging with all surfaces machined.

The mandrels will have many grooves and holes for Helium passage. A drawing of some of these details is shown in Figure 12.16. The axisymmetric model includes some flange bending and some of the stresses due to the offset in the coil compressive loading with respect to the mandrel and bolt tension. In the mandrel bolting section, an attempt is made to estimate the bending component due to this offset, and about 100 MPa was obtained. Interactions between the bolt prying action, and Helium passage details should be modeled in greater detail. The thickness of the outer bolted flange can be increased to whatever is needed. The inner flange thickness is 2 cm and this is set by the magnet spacing and field specs. It too has the helium grooves. A more detailed analysis of this flange connection is warranted during final design.

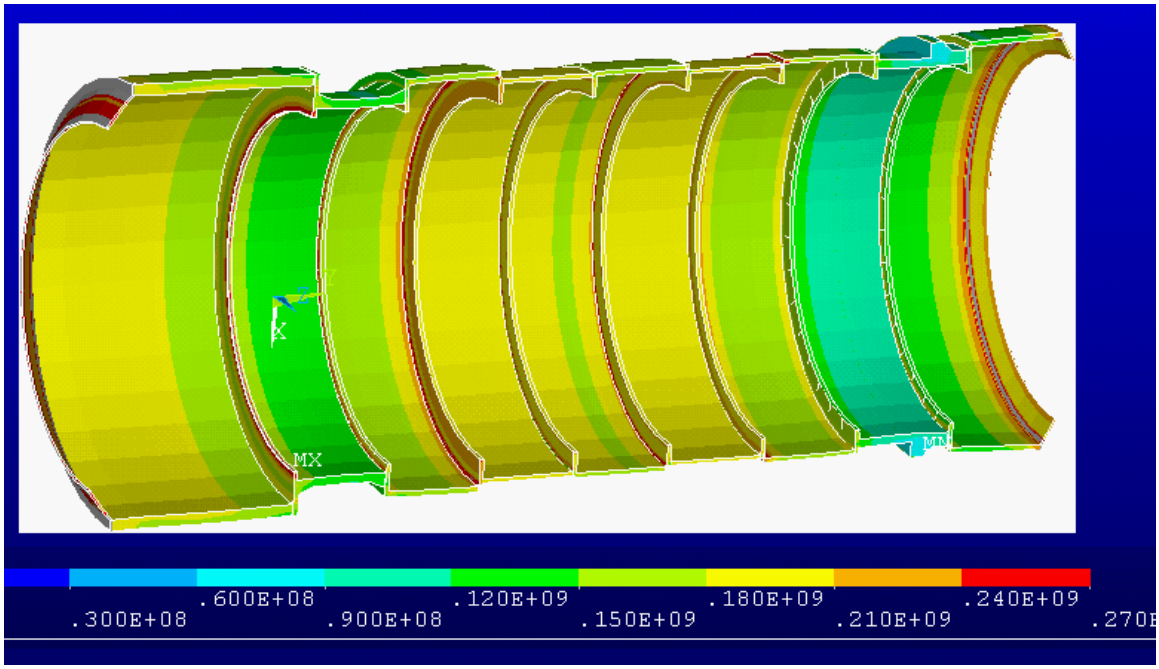

Figure 12.17 – An earlier model of the outer shell Von Mises stress.

An earlier model of the outer shell/aluminum mandrel Von Mises stress is shown in Figure 12.17. Note the bending of the 1cm thick end flange. This is a result of the axial relative contraction of the mandrel/shell with respect to the winding pack. The local stresses in the flanges were much higher than in the shells, and the contour range in this plot has been adjusted to show the shell stresses. If aluminum shells are used, the local structure of the flanges and their interconnections will have to be designed to accommodate the relative "expansion" of the coils. Certainly, the end flanges will have to be considerably thickened. 6061 T-6 has a cryogenic yield of 275 MPa. With an allowable of 2/3 of this, a primary stress of 180 MPa (the yellow contour areas) would be acceptable. The higher stresses are in the neighborhood of the flanges, which have been thickened in the final design as discussed below.

The present design uses the equivalent of 5 cm thick flanges at the extreme ends of the PS. On the high field end of the PS assembly, the flange is actually is 5 cm thick. On the low field end the combination of the aluminum flange thickness and the stainless steel helium can thickness add to 4.5 cm. Elsewhere in the PS assembly, the inner flange thickness is 2 cm. These design changes, which are depicted in the conceptual design drawing package, should relieve the issues with flange stresses in the above model.

Mandrel Bolting

Production Solenoid mandrel flange bolts have to equilibrate the coil compression with bolt tension. The differential contraction between aluminum and copper produces coil compression and is estimated to be 20 MPa, with no gaps at assembly. 600 MPa working stress is required in the bolts for this compression. Inconel 718 bolts stressed to 0.6*yield have a cryogenic working stress of 689 MPa. Sizing of the bolts is based on the no gap assembly. An interference at assembly will add to the axial compression obtained from the Aluminum-coil thermal

contraction differential, and is an option to increase the coil axial precompression beyond 20 MPa.

The composite axial α of the conductor is computed from the following: 0.4 mm thick G-10-like material, and 18.55 mm of copper are used in the conductor winding pack. The normal direction α for G-10 is 24.3×10^{-6}, and 10.82×10^{-6} for copper. The effective α is given by $(24.\ 3 \times 10^{-6} \times 0.4 + 10.82 \times 10^{-6} \times 18.55) / 18.95 = 11.10 \times 10^{-6}$. The differential α of alum-conductor is 13.88×10^{-6}-$11.10 \times 10^{-6} = 2.78 \times 10^{-6}$. The modulii of the alum is 70 GPa and the composite 85.8 GPa, hence we treat it all with an axial modulus of 77 GPa.

Table 12.7 – Mandrel Bending, and Bolt tensile stress, Mandrels are ½ the coil thickness

	Δr (m)	Estimate of Aluminum Mandrel Bending due to Bolt Offset, MPa	M20 Bolt stress, MPa Coil stress = 22 MPa
P1	.1228	108.997	609.592
P2	.0823	130.156	408.546
P3	.0908	124.15	450.741
P4	.0752	136.213	373.301
P5	.0773	134.305	383.725
P6	.0605	153.273	300.328
P7	.0709	140.471	351.955
P8	.0374	207.176	185.657
P9	.0898	124.797	445.776

For mandrels which are 1/2 the coil build, which is the present choice, the axial strain is twice that of the coils, and both must add up to $2.70 \times 10^{-6} \times 288 = 0.000777$ ($\alpha\ \Delta T$), so the strain in the aluminum mandrel would be $2 \times 0.000777/3 = 0.000518$, and the strain in the copper would be $0.000777/3 = 0.000259$. The tensile stress in the aluminum is 77 GPa $\times$ 0.000518 = 39.9 MPa. Suppose a typical mandrel is 4cm thick, and suppose the bolts can be stressed to 600 MPa, then for every 10cm of circumferential length of mandrel flange we would need $40 \times 39.9 / 600 = 2.66$ cm^2 of bolt cross section. M18 bolts have a cross section of 2.54 cm^2, so the bolt pitch would have to be 8 cm. That would be 78 bolts on a 1 meter radius. This would produce about a 20 MPa axial compression in the coil. This is not sufficient to offset the 45.5 MPa from the quench analysis, unless the effect of the Kapton reduces the tension. For the modulus of 77 GPa, the tensile stress in the aluminum is 45 MPa, slightly lower than for the thinner mandrel but because the mandrel is twice as thick, almost twice the bolt area is needed. Bolt stresses vary with mandrel thickness, and the results for simple calculations based on the various mandrel connections are shown in Table 12.7. Bolt loads should be extracted from a more detailed finite element model during final design.

It was hoped that an axial gap could be allowed at assembly. A radial gap of 0.5 mm is allowed, and that is expected to be sufficient to allow insertion of the coil in the mandrel. If a 0.001 m axial gap was allowed in the fit-up between coil and the next closure flange, the strain to be absorbed is $.001 / 1.156 = .000865$ (1.156 m is the axial coil build for the production solenoid). This is approximately all the thermal strain of .000875, so with this gap all the axial thermal compression would be lost. Conversely, introduction of an interference can increase the axial compressive preload to offset quench tensions.

Displacements - Axisymmetric Model with External Mandrel/Shells

These results are based on cooldown plus Lorentz forces, deadweight is not included. Based on the energized, cold displacements of the PS coil, the coils should be manufactured about 4 mm oversize in radius, and 2.25 cm longer than the required cold dimension.

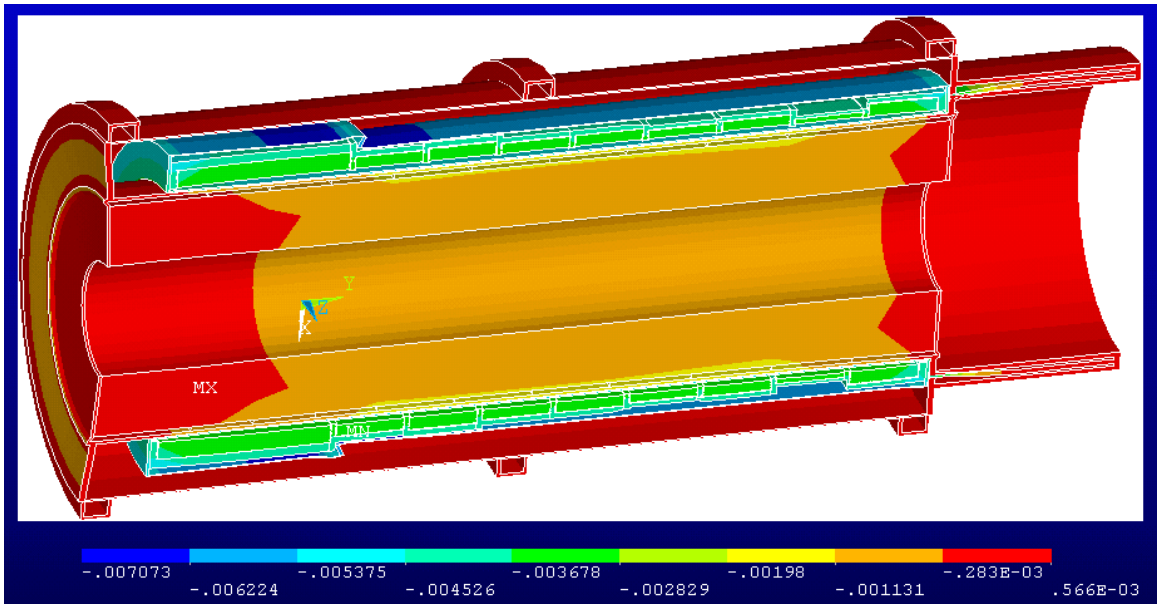

Figure 12.18 – Radial Displacements for the latest axisymmetric model. Mandrel Thickness = 1/2 Coil Build

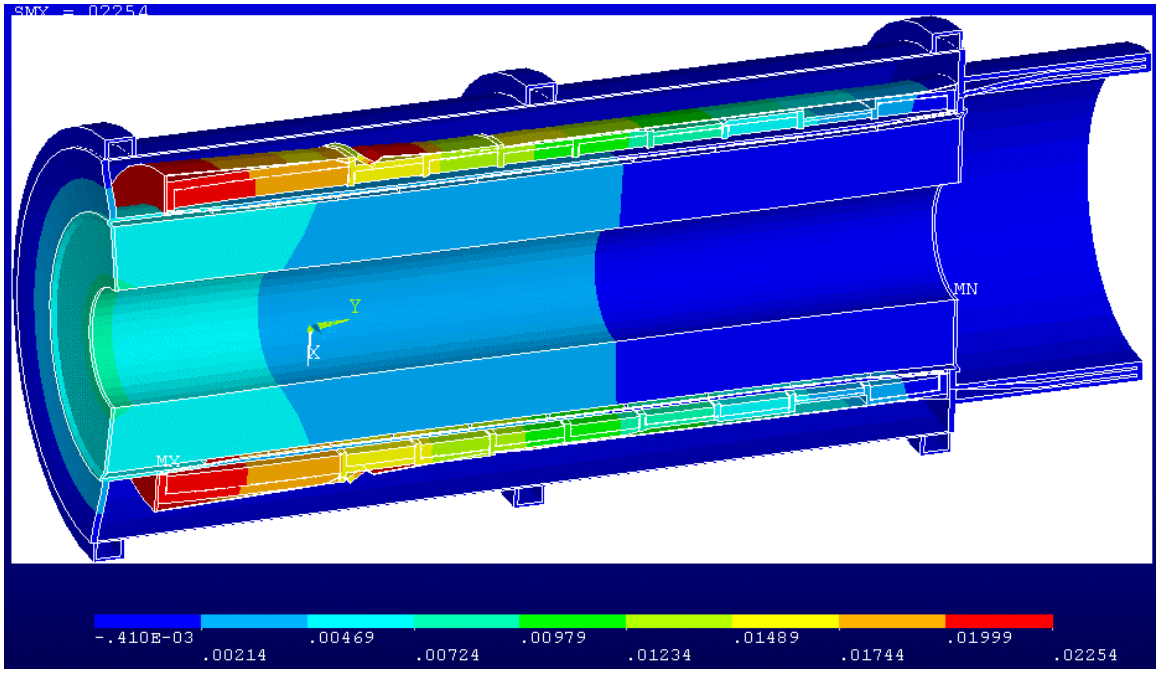

Figure 12.19 – Axial Displacements for the latest axisymmetric model. Mandrel Thickness = 1/2 Coil Build

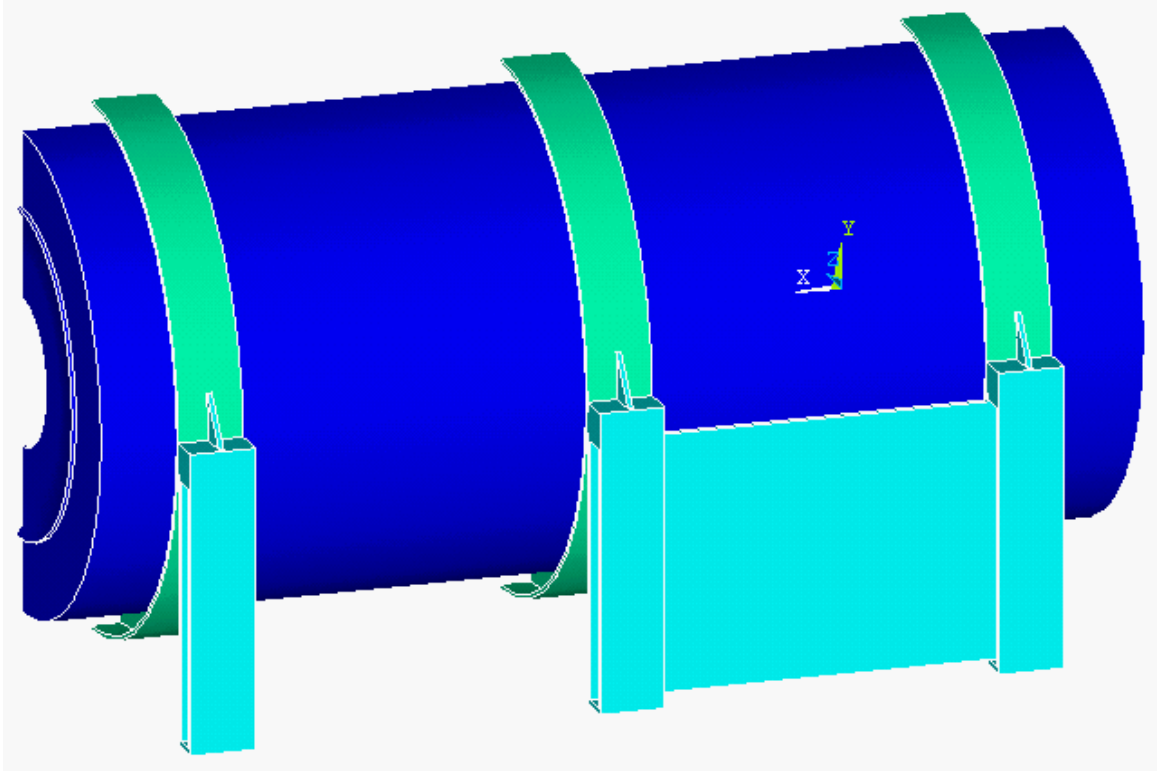

Figure 12.20 – The three dimensional Production Solenoid model.

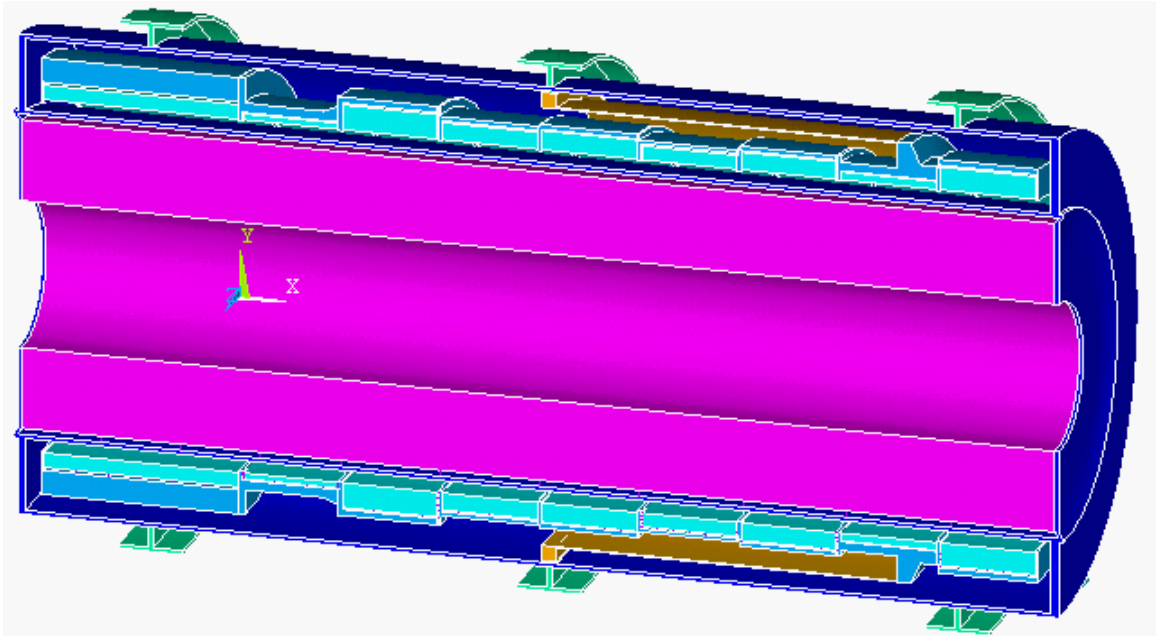

Figure 12.21 – Reverse view of the three dimensional model.

Warm and Cold Mass Supports

With the production and transport solenoids energized, the net lateral load in the production solenoid cold mass is 1.2 MN, or 140 Ton. It is a force exerted towards the transport solenoid. The current design employs the column loaded struts, and these are shown in Figure 12.22. The net magnetic loads are reacted by the support rods within the columns, which carry the load back to the stiffener ring on the outer PS cryostat can, near the TS end . The system is intended to provide the needed shear load capability to take the net lateral loading. The cryostat sees mostly the effects of the pressure loading, and the weight of the shield. The shield weight may be overestimated in this model. Current nuclear calculations are based on a shield that weighs 50 tons [2]. With only the axial flexure support of the previous design, the high field end of the cold mass deflected 1.7mm, which was too large a deflection to satisfy field quality requirement. Vertically oriented hanger rods are now used at both the high field end and low field end of the production solenoid.

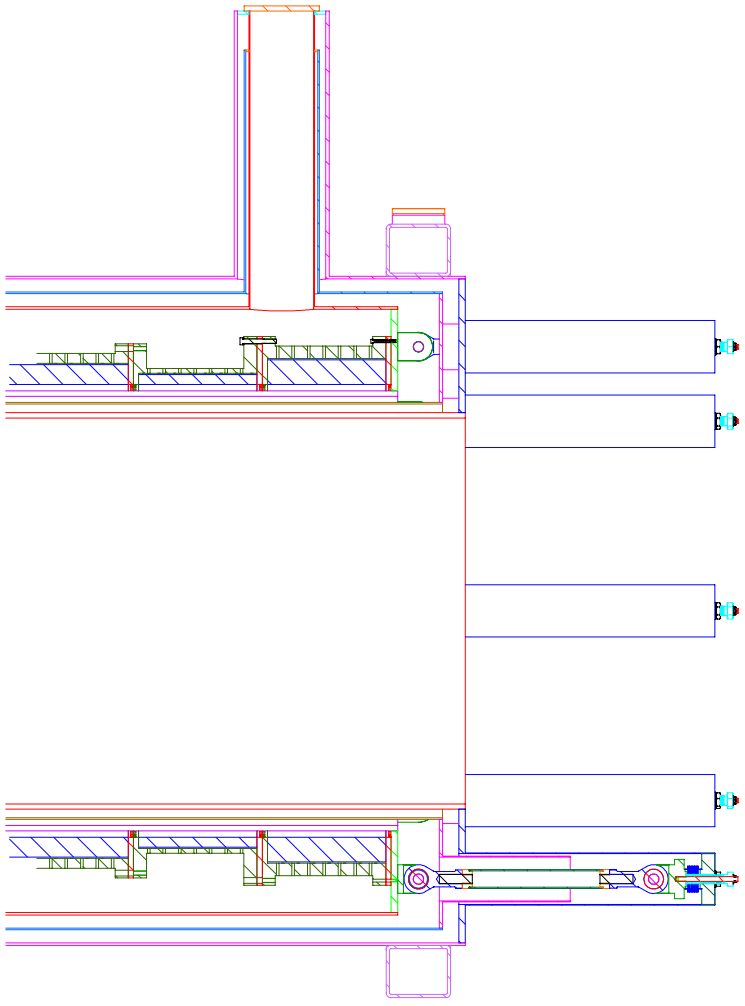

Figure 12.22 – Present design for supporting PS axial loads toward the TS (3 of 8 rods are not shown in the section view).

Supports for the Production Solenoid Cold Mass

Table 12.8 – Cold mass support summary.

	PS Axial Support Pipe Strut	PS Vertical Rods	PS Lateral Pipe Strut
Number	8	4	2[2]
Total Design Load	320 kips	80000 lb	[2]
Load per Support	40 kips	20000 lb	[2]
Material	2.5"sch 40 pipe 316 SST	316 SST rod	1."sch 40 pipe 316 SST
4K to 80K OD	2.875"	1.25"	1.315"
4K to 80K ID	2.469"	0	1.049"
4K to 80K Length	12"[3]	15"[1]	15"[1]
80K to RT ODr	2.875"	1.25"	1.315"
80K to RT ID	2.469"	0	1.049"
80K to RT Length	12"[3]	15"[1]	15"[1]

[1] These Struts have been qualified in buckling for 30 inch length. The intercept can be placed optimally along this length

[2] There is no significant side load on the coil - struts are provided for uncertain reactions with neighboring shielding, seismic and shipping loads. Only 2 are provided, relying on gravity loading the vertical supports for moment equilibrium.

[3] These Struts have been qualified in buckling for 24 inch length. The intercept can be placed optimally along this length.

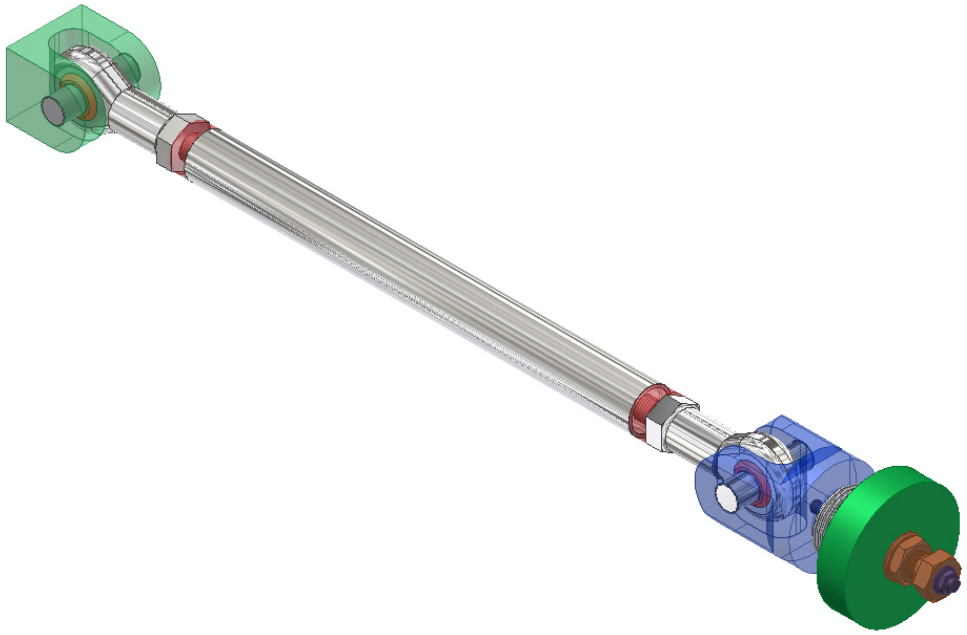

Figure 12.23 – An adjustable axial support strut used in the production solenoid. The bellows allows final position adjustment when the magnet is cold, and when the cryostat is evacuated. Eight 2" schedule 40 pipes would be adequate.

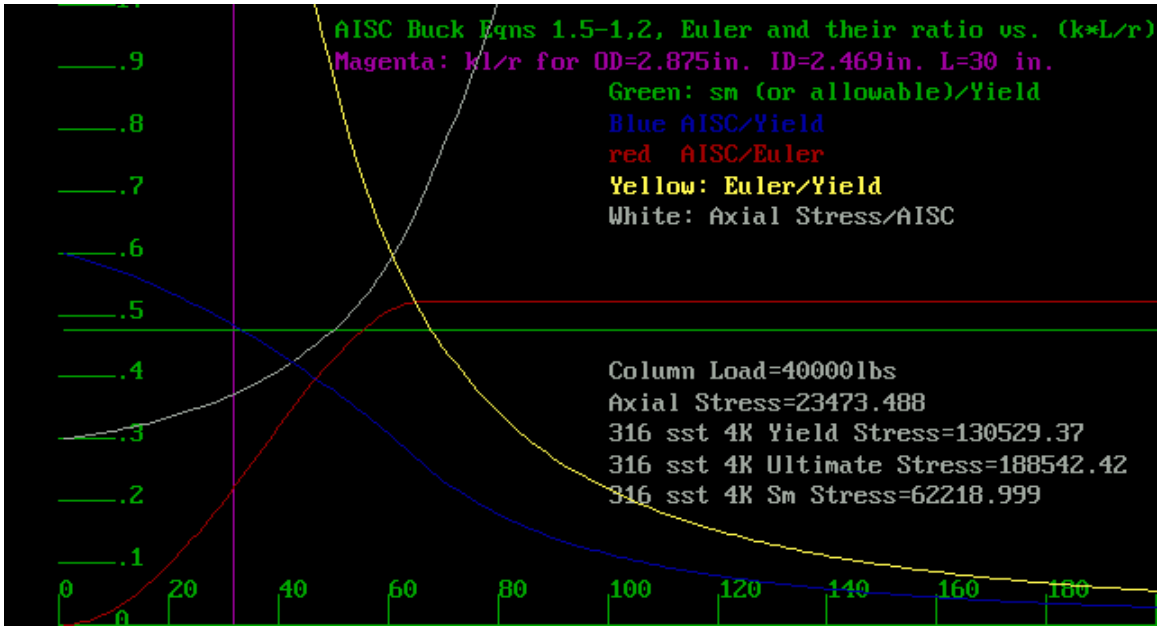

Figure 12.24 – For a 2.5 inch schedule 40 pipe that is 30 inches long with pinned ends, the kL/r is around 30. For this kL/r loaded with 40,000 lbs the ratio of the applied stress to the AISC allowed buckling stress is 0.36 and the ratio of the applied stress to the membrane allowable is 23.5/62.2=0.38. A 2 inch schedule 40 pipe would also be OK with a ratio of applied stress to AISC allowable of about 0.65

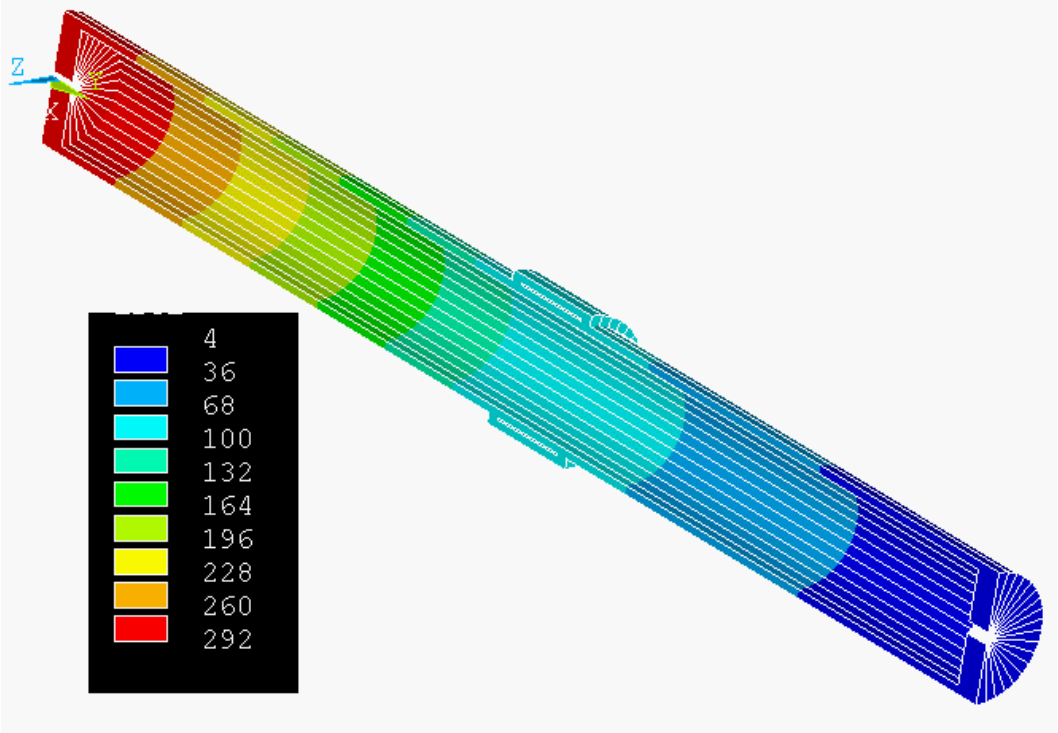

Figure 12.25 – Temperature distribution in the cold mass support strut.

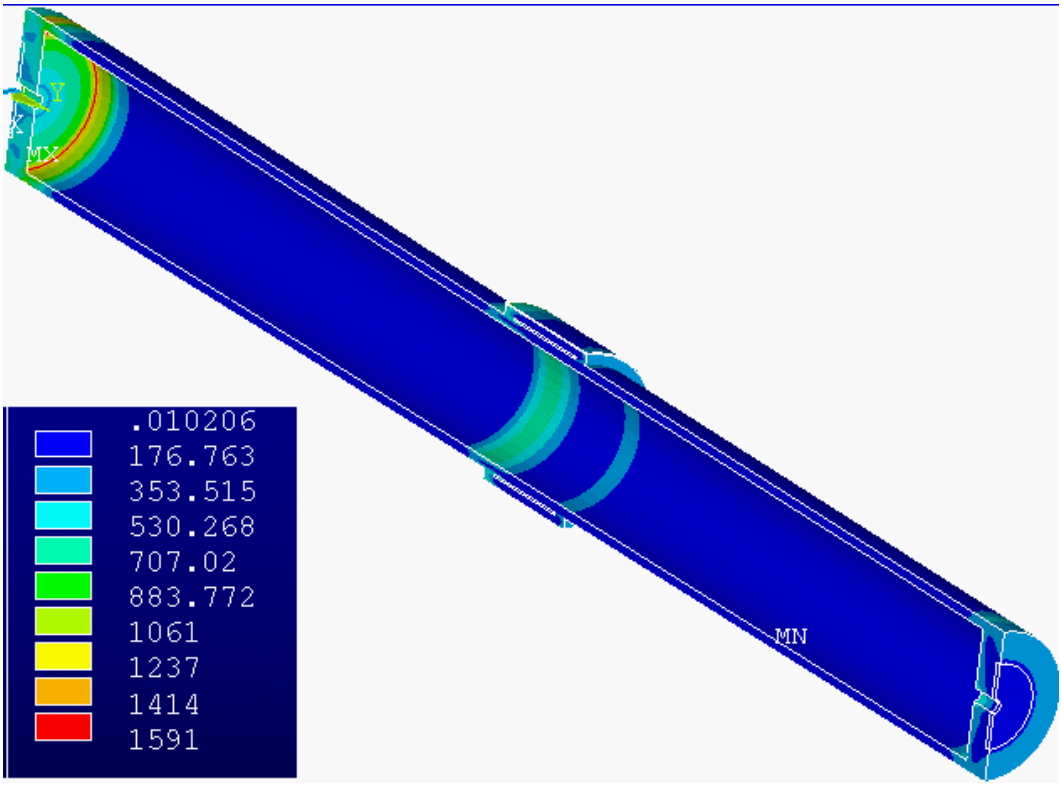

Figure 12.26 – Thermal stresses due to the temperature gradient along the strut and at the heat station.

Cryostat Stresses

The PS cryostat design pressure is nominally one atmosphere outside the cryostat with a vacuum inside. It is possible that with long-term use of the cryostat, gasses may condense in the multilayer insulation or shield, or on the helium can. These could potentially pressurize the cryostat when it is warmed to room temperature. This is assumed to be no more than one atmosphere, making the differential pressure zero. There is a possibility of a leak or rupture of the helium can, which could produce large pressures as the liquid helium contacts the room temperature cryostat. To provide adequate venting for this case, an O-ring sealed disk or flapper valve should be provided that would vent as soon as the cryostat differential pressure goes positive.

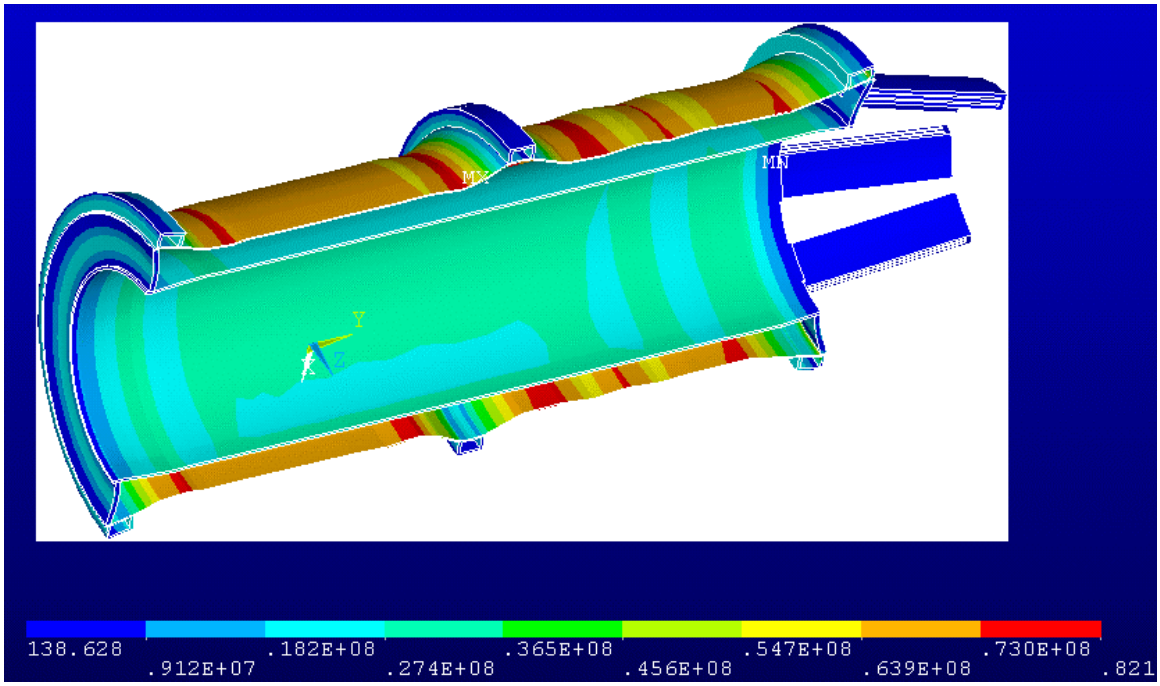

Figure 12.27 – Cryostat Von Mises stress with five atmospheres external pressure, solved with a large displacement analysis to demonstrate structural stability at five times the nominal vacuum loading.

The stresses in the cryostat are low. Two models address the stresses in the cryostat. An early model includes the shield weight, and a later model investigates cryostat shell stresses and buckling under vacuum. The use of the inner cryostat wall as a strongback to support the nuclear shield argues for retention of the 2 cm inner wall thickness. It is not needed for the pressure loading. The external shell thickness is 1.0 cm. The support box sections provide adequate buckling support for a 1 cm shell. The latest shell buckling calculations use this combination. These results are given in Figure 12.30, which shows that external pressures must reach about 9 atm to buckle the 1 cm thick outer shell. Thus, the 1 cm thick outer shell with the box support rings are adequate.The primary membrane allowable for 304 annealed (hot rolled plate) at room temperature is 156 MPa (22.6 ksi), so the stress levels given in Table 12.9 are all very low.

Table 12.9 – Production solenoid cryostat stess and displacement summary.

Cryostat Shell Component	Thickness (cm)	Shield/Magnet Deadweight Von Mises (MPa)	Vacuum Von Mises (MPa)	Max Static Vertical Displacement (mm)
Inner wall	2	18	3.5	-0.4
Outer Wall	2 (1 cm final design)	6 (2cm thick)	16 (1cm thick)	-0.2
End Caps	4	12	3.6	

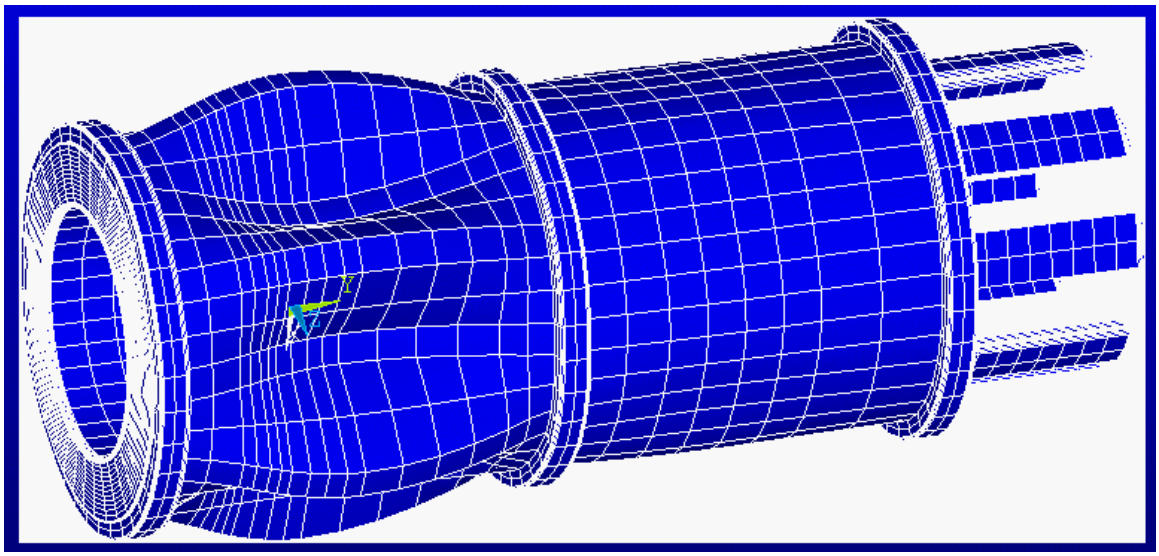

Figure 12.28 – First mode buckled shape with a multiplier of 9.03. The next two modes have multipliers of 9.36, and 9.457.

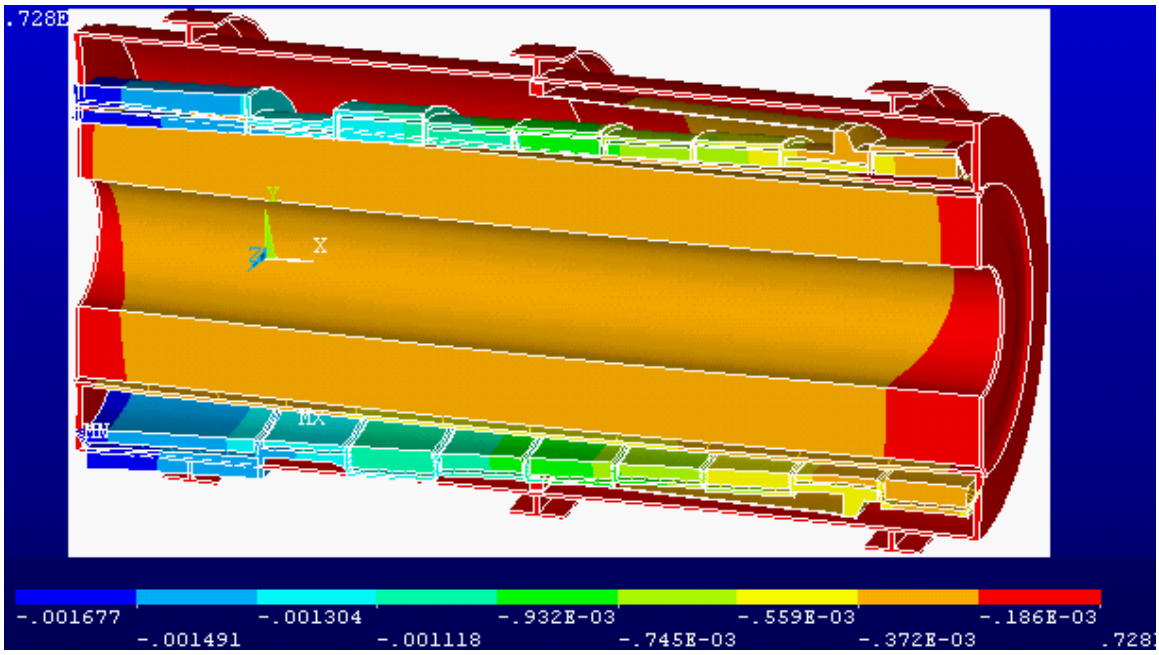

Figure 12.29 – Vertical Displacement of the assembly under pressure, cold mass and shield deadweight, Run#grav01. The end drops 1.7mm, probably too large a deflection to satisfy field quality requirement. Additional vertically oriented radius rods have been added at both ends of the production solenoid.

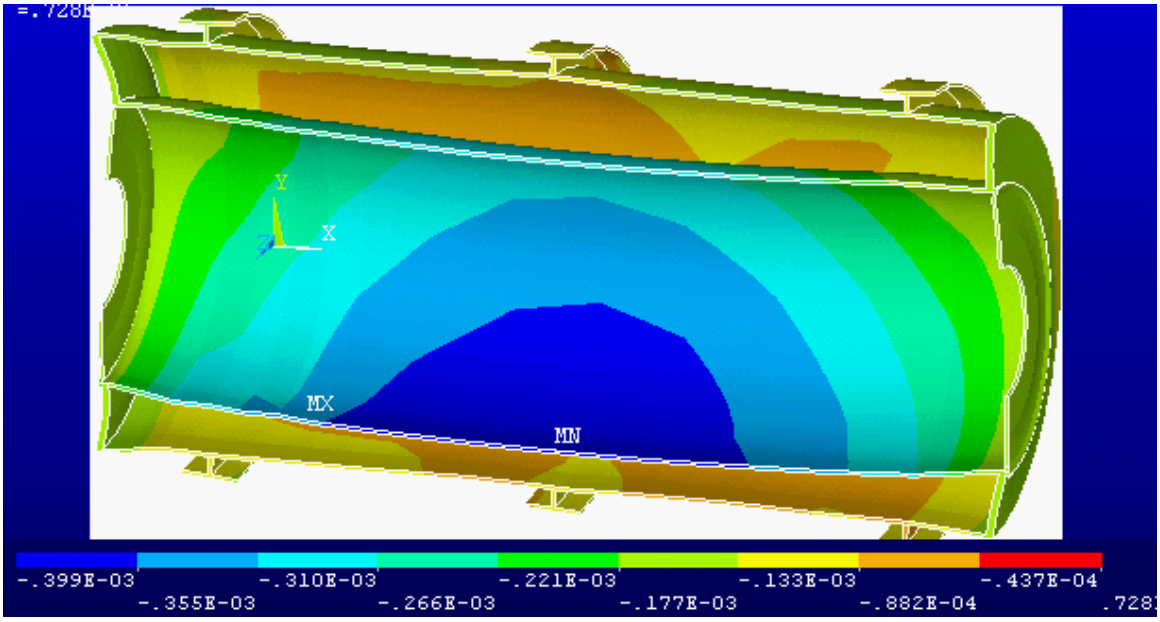

Figure 12.30 – Displacement of the cryostat shells under pressure and shield deadweight. The maximum displacement is mid span on the inner shell which supports the deadweight of the shield. , Run#grav01

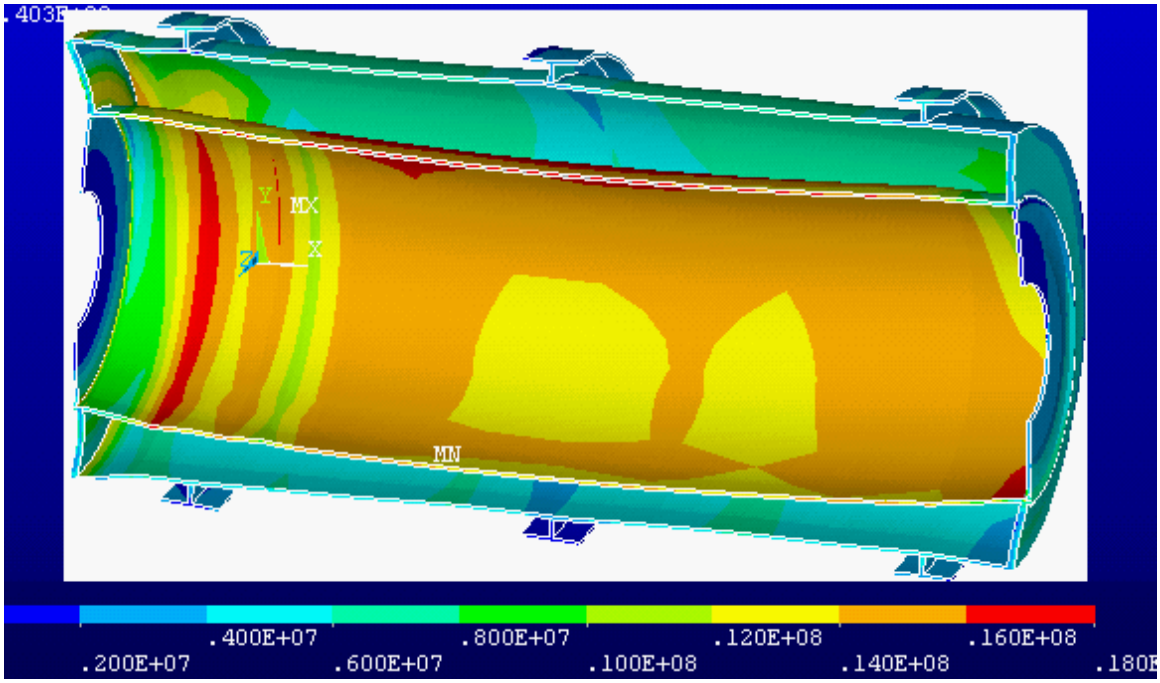

Figure 12.31 – Von Mises stress in the cryostat shells. Vacuum and shield DW. The left-right variation results from a different gap density. The stresses are quite low. -Displacements may govern.

Table 12.10 – Production solenoid model weights

Assembly	Source	Value	Unit	Weight Tons
Total	3D Model	57465	Reaction-Newton/Half Model	129
40cm Cu Shield	3D Model	-316508	Reaction-Newton/Half Model	71.1
Cold Mass (no He)	Axisym	4.654	M^3, 40500 kg at 8700 kg/m^3	40

Helium Can

The production solenoid is a bath cooled magnet. The helium is contained in an annular can that surrounds the coil/mandrel structure. The normal operating design pressure loading is the hydrostatic head of the Helium in the can. The specific gravity of liquid Helium is 0.124. During a quench, the pressure can reach five atmospheres. One atmosphere is 0.1014 MPa of pressure. The outer shell of the helium is specified as 1 cm thick. The can and is 1.1m in radius. It is loaded in hoop tension, and the $p \times r / t$ stress is only 55 MPa, or 8.1 ksi. During a quench, local nozzle stresses for the 10 inch vent are 17 ksi for this case. Nozzle stress and reinforcement details for this and the many other connections should be qualified during final design. The ID shell of the helium can has been specified as 2 cm thick and is at a 0.86 m radius. It is loaded with external pressure, and concerns over buckling of this shell dictated the 2-cm-thick shell specified. In addition to the quench pressure, the hydrostatic pressure from the Helium, as low as it is, adds a non-axisymmetric perturbation to the shell that could precipitate a buckling mode. To analyze this, three times the hydrostatic pressure plus three times the quench pressure were superimposed and the shell was analyzed with a large displacement solution. It did not buckle. The quench pressure was imposed as a uniform pressure. In fact, the pressures may not be uniform, and a large margin against buckling is appropriate. A linear buckling analysis was performed. In this analysis, the load vector used in the prestress pass was the vacuum pressure with the Helium hydrostatic pressure. Three buckled modes were extracted. The load multipliers were very large for this geometry.

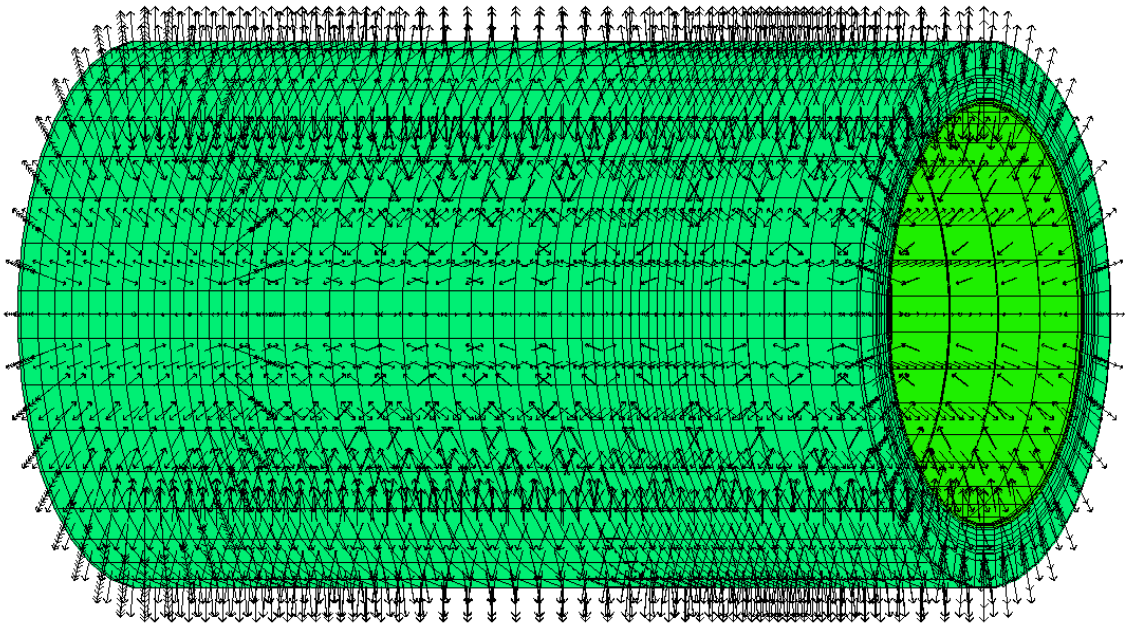

Figure 12.32 – Annular helium can shell model with pressure vectors.

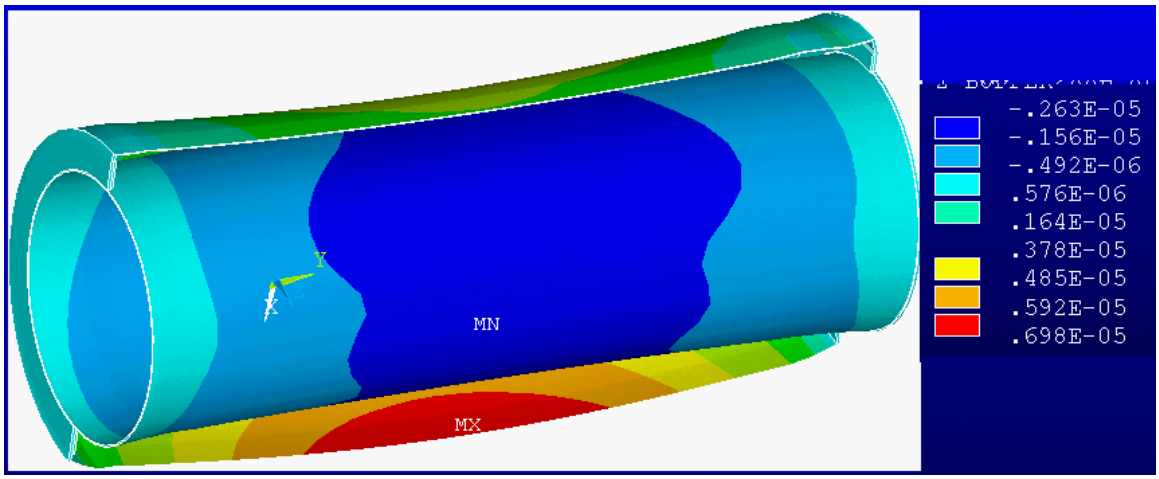

Figure 12.33 – Vertical displacements of the Production Solenoid Helium can under Helium hydrostatic head. These are X displacements which is positive downward. The inner shell "floats" upward, and the lower shell is weighed down by the helium. These are trivial displacements, and the stresses to support the helium are also trivial, but this loading is imposed in addition to the quench pressure to see if there is any interaction with buckling modes.

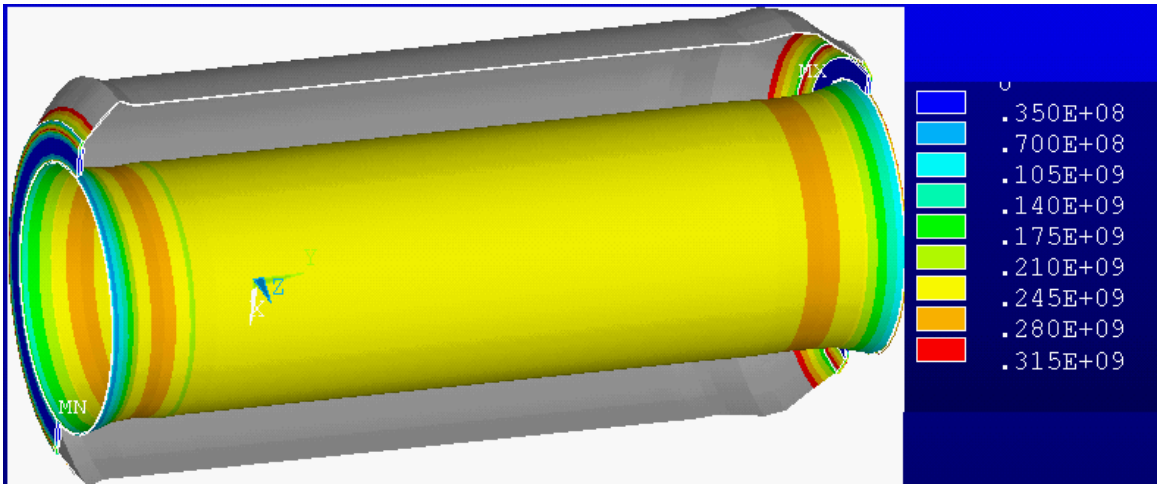

Figure 12.34 – Production solenoid Helium can pressurized to three times the design pressure off five atmospheres plus the Helium hydrostatic head. A large displacement solution is used. The response of the 2cm thick inner shell is bounded – It does not buckle.

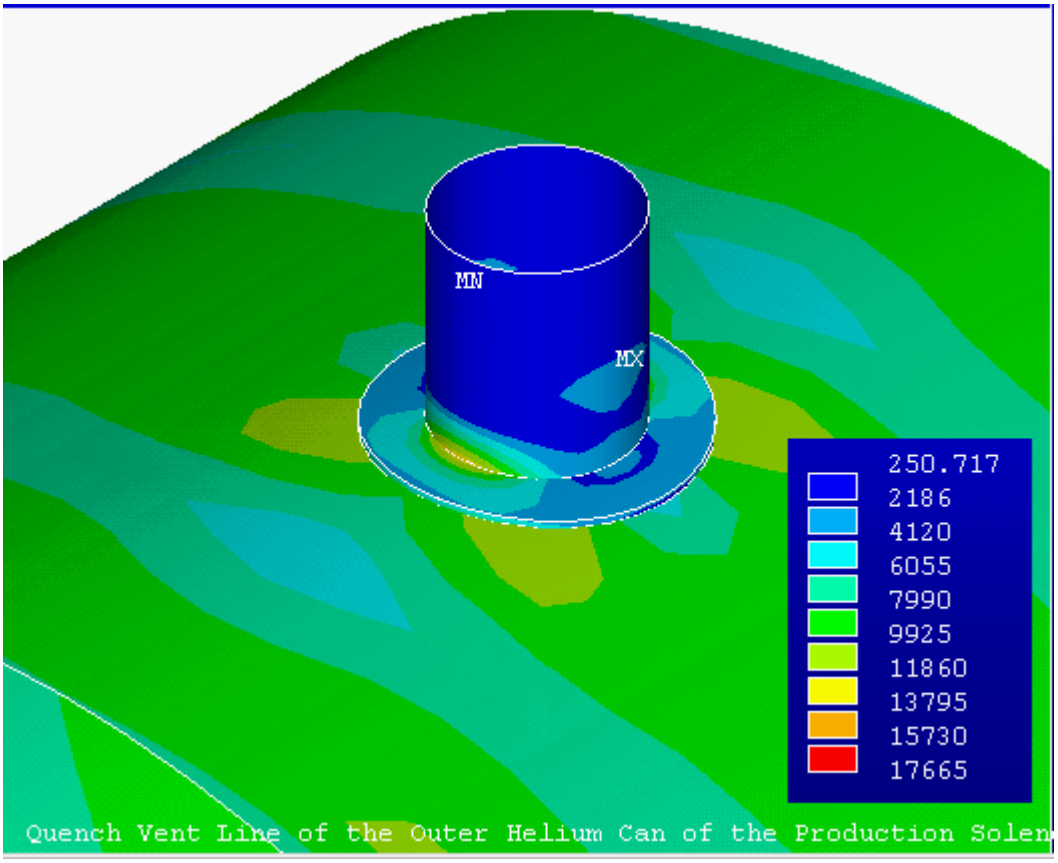

Figure 12.35 – Outer Helium Can Shell 10 inch Quench Vent Line. 3 inch wide reinforcement ring , Membrane Von Mises in psi. Smaller penetrations are also needed, and similar reinforcements will be needed at these locations as well.

Table 12.11 – Helium can buckled mode load multipliers

Shape Number	Load Multiplier
1	1110.1
2	1110.8
3	1794.2

The linear analysis procedure typically yields larger buckling margins. This coupled with the non-linear analysis confirms a large margin needed to address the uncertainty in how the quench pressure is applied. The first mode buckled shape is plotted in Figure 12.36. In this figure, a portion of the outer can is plotted with the inner shell. Appropriately, the outer shell shows no buckled shape because the load vector produces tensile stresses in the outer Helium can shell.

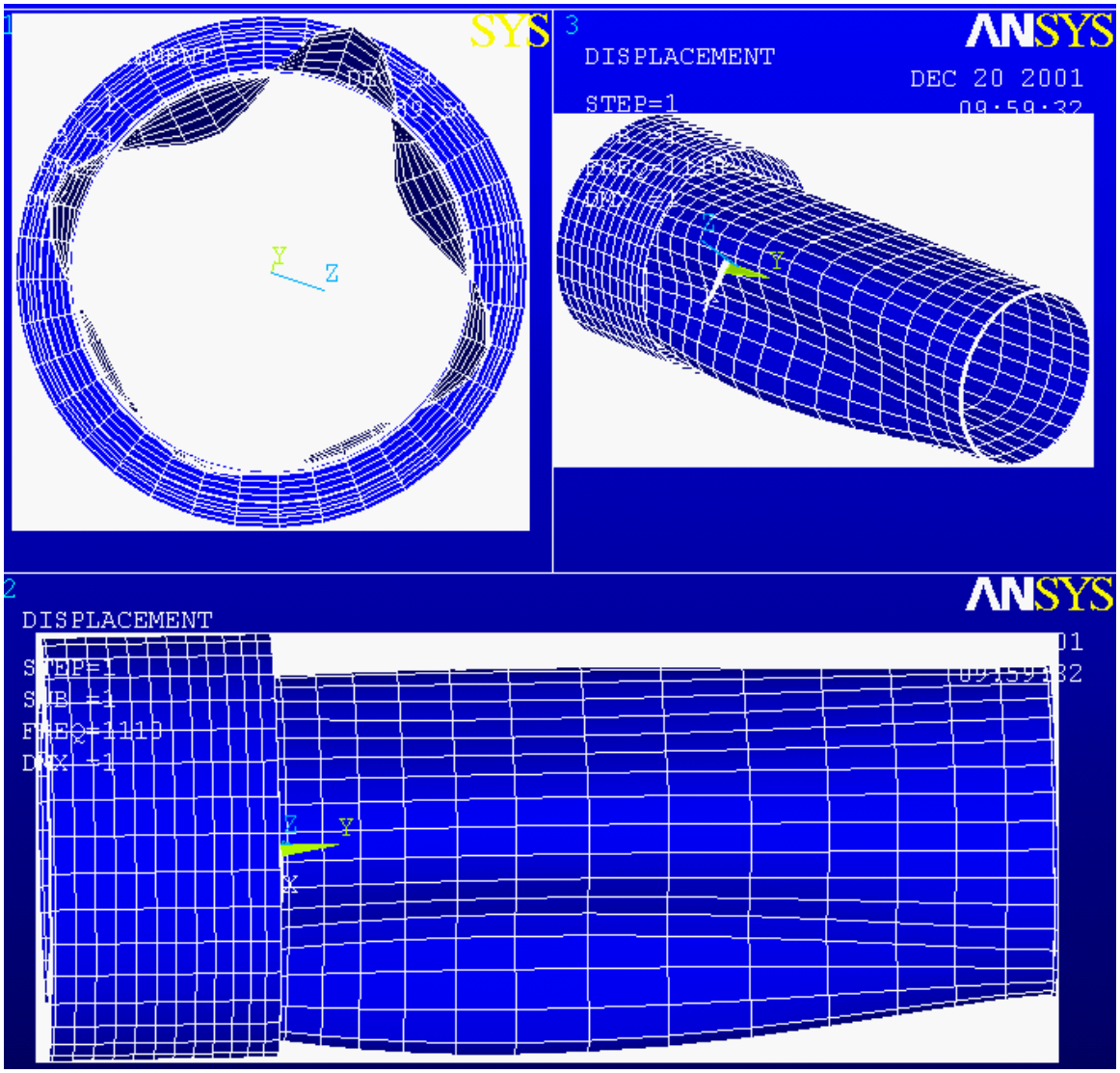

Figure 12.36 – Results of linear buckling analysis of the production solenoid helium can -Mode 1

Addendum to Section 12

Analysis Methods and Models

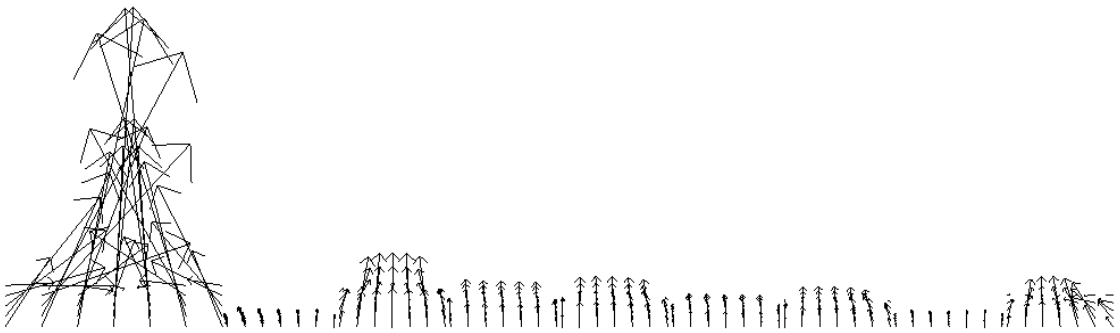

Figure 12.37 – Lorenz Forces in the Axisymmetric model – TS energized

A series of axisymmetric and 3D half symmetry and full symmetry models have been used to simulate the behavior of the production solenoid. The axisymmetric models are used to investigate coil stresses and their interaction with the coil structure, but these models do not include gravity loading. A 2D model of the conductor array, discussed previously, is used to calculate the effective properties of the winding pack. Loads used in both the axisymmetric and 3D models of the coil are calculated with a simple elliptic integral field calculation, and then applied to the ANSYS model. Gap elements are used between coil and shell/mandrel. These have the capability of modeling frictional energy deposition via the product of gap normal force and extent of slide.

Figure 12.38 – Axisymmetric Model - 9 coils of the production solenoid are modeled. An additional 14 coils in the transport solenoid are included in the field and force calculation. These are "turned off" for the second load case. Plots of the models based on the use of internal mandrels are included with the discussion of the early results that used internal mandrels.

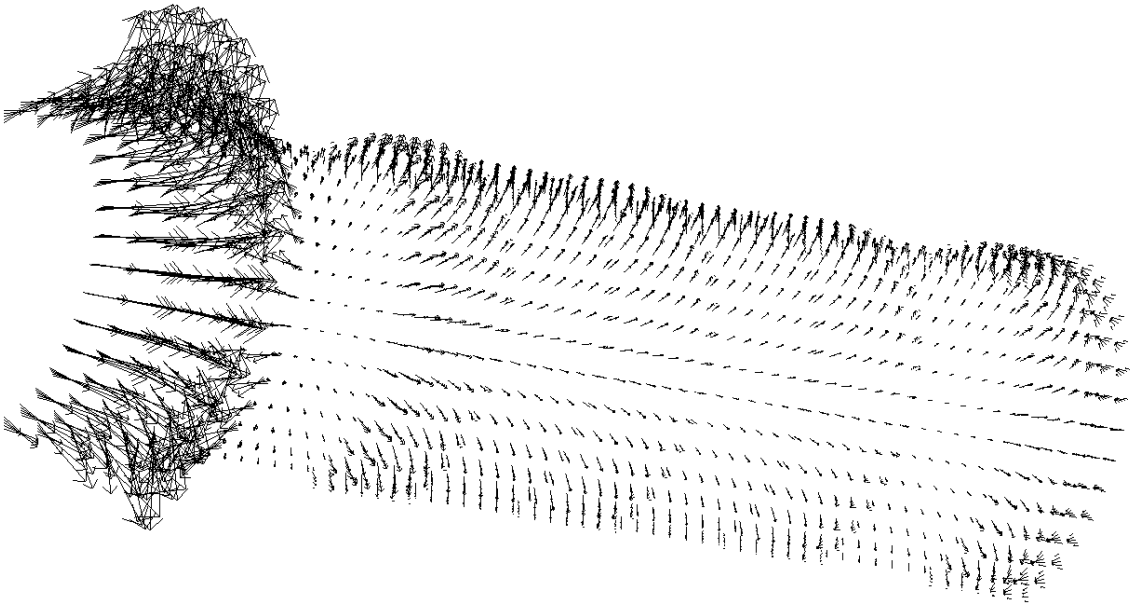

Figure 12.39 – Force distribution used in the 3D model.

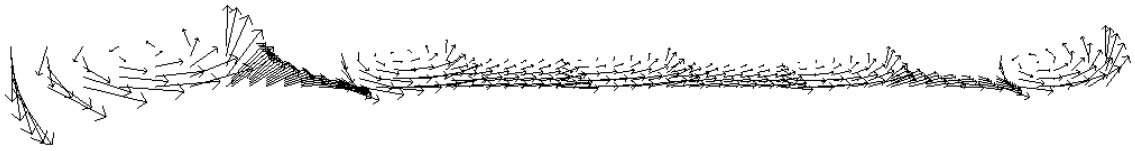

Figure 12.40 - Field vectors from the axisymmetric analysis.

Table 12.12 – Model run log

Run#	Model Type	Notes	Ext/Int Mandrel	Coil Model File	Mandrel Model File	Mandrel Mat	Conductor E	TS ON	TS OFF
Prod01	Axisym		Int	Coil	Mand	SST	75e9	Y	N
Prod02	Axisym	Outer shells added to P1, P3 and P8, and CM Flexure added	Int w Ext Sup at P1	Coil	Man2	SST	75e9	Y	
Prod03	Axisym		Ext	Coil	Man3	SST	75e9	Y	Y
Prod04	Axisym		Ext	Coil	Man3	ALUM	75e9	Y	
Prod05	Axisym	Decreased P1 build	Ext	Coil2	Man4	SST	75e9	Y	
Prod06	Axisym	Inc. P1 man thck	Ext	Coil2	Man5	SST	75e9	Y	
Prod07	Axisym	Cor. E	Ext	Coil	Man3	SST	110e9	Y	Y
Prod08	Axisym	Cor E	Ext	Coil2	Man5	SST	110e9	Y	N
Preod09	Axisym		Ext						
Prod10	Axisym		Ext		Man8	Alum	110e9		
Prod11	Axisym		Ext						
Prod12	Axisym		Ext	Coil5	Ma11	Alum			
Prod13	Axisym	Added assem gap	Ext	Coil5	Ma11				
Grav01	3D	No CD or Lorentz	Ext	grav	Man6	SST	75e9		
Grav02	3D	Added CD, Lorentz, and High Field end Gravity Sup. Nlgeo,on 1cm ext cryo shell	Ext	Gra2	Man6	SST	100 e9	Y	N
HeCn01	3D	Non-Linear Buckling							
HeCn02	3D	Linear Buckling							
Cryo01	3D	Non-Linear Buckling		cryo	Ma11				
Cryo01	3D	Linear Buckling		cryo	Ma11				

Table 12.13 – Model Outer Mandrel Thicknesses (cm)

	P1	P2	P3	P4	P5	P6	P7	P8	P9
Mandrel	.0594	.0391	.0434	.0356	.0366	.0282	.0167	.0334	.0429
Coil	.1188	0783	.0868	.0712	.0733	.0565	.0334	.0669	.0858
Ratio	.5	.5	.5	.5	.5	.5	.5	.5	.5

Table 12.14 – Coil Build and Currents [4]

Coil Number	R (m)	Z (m)	DR (m)	DZ (m)	MAT
1	.9414	-.6	.1188	1.156	6.783700
2	.92115	.25	.0783	.456	1.803300
3	.9254	.75	.0868	.456	1.989700
4	.9176	1.25	.0712	.456	1.648000
5	.91865	1.75	.0733	.456	1.694400
6	.91025	2.25	.0565	.456	1.326500
7	.91545	2.75	.0334	.456	1.552700
8	.8987	3.25	.0669	.456	.819190
9	.9249	3.75	.0858	.456	1.967300
10	.42125	4.15	.0285	.08	.088023
11	.42745	4.25	.0409	.08	.126070
12	.4153	4.35	.0166	.08	.051264
13	.435	4.45	.056	.08	.172830
14	.4256	4.6	.0372	.18	.258460
15	.43015	4.8	.0463	.18	.321840
16	.43195	5.0	.0499	.18	.346420
17	.4172	5.242	.0204	.18	.377970
18	.4178	5.482	.0216 ,	.18	.399320
19	.4182	5.951	.0224	.18	.414950
20	.41845	5.719	.0229	.18	.424120
21	.41865	6.177	.0233	.18	.431100
22	.4188	6.394	.0236	.18	.436200

Model with Internal Mandrel/Shells

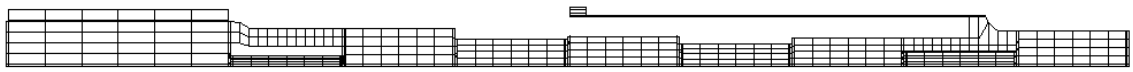

Figure 12.41 – Inner shells in this model are all 5mm thick. Flanges are 1cm thick. Constraints were applied just to the right of P1 to model the cold mass support.

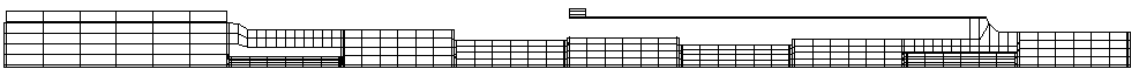

Figure 12.42 – Second Generation of Internal Mandrel Model, with reinforcements added to P1 and the thin coils , p2 and p8, Used in Run # prod02.

References

[1] Coil Sizing Preliminary Results A.L. Radovinsky MECO-MIT-ALRadovinsky-052501-01 May 25, 2001

[2] Email To: Bradford Smith From: W. Molzon, Monday, April 02, 2001 8:10 Subject: Heat and Radiation Loading

[3] Memo to Brad Smith from J.G. Brisson "Sizing of the Safety vent line in the Meco Production Solenoid" November 26 2001

[4] Coil builds from MECO-MIT- ALRadovinsky-101701-01

[5] Memo # MECO-MIT-BASmith-111401-01 "PS Coil Quench Analysis" B.A. Smith and P.H. Titus MECO#mm043

Section 13 - Structural Analysis of the Transport Solenoid Mandrel, Winding and Supports

Introduction

The transport solenoid (TS) is made up of two opposed quarter toroidal arrays of coils with straight end segments. Concepts for the structural support of the coils and their global assembly are presented. Coils are wound on mandrels that are retained as the primary structural elements of the TS. These mandrel spool pieces are bolted together at their flanges. A large number of bolts are used to obtain good bending resistance. A plate/channel strongback was investigated early in the design process to help with assembly and distribute the local cold mass support loads. This is shown in Figure 13.2.

In the proposed design, the strongback has been reduced to only a local reinforcement around the radial support rod attachment as shown in Figure 13.3. Analyses with and without the strongback/channel have been performed. The channel does not help with the inner radius of the elbow, which sees the tensile bending stress, and is not sufficient reinforcement for attachment points. It was omitted in the latest analysis. It may still be attractive as an assembly aid. Some of the early work with the channel is presented to show the evolution of the design. The system of three vertical support rods, and three lateral support points make-up the cold mass support. This configuration allows stress-free cool down while having the capacity to support the normal operating "centering" force along with off normal combinations of energized states of the remaining coil systems. Large frames, which are integral with the cryostat, transmit net loads to the foundations. Coil winding pack stresses are computed to be acceptable, but further work during the detailed design phase is recommended to optimize the structures and reinforce the local attachments of the cold mass supports. A 4 mm mandrel shell was initially analyzed and found to be undersized. It is recommended that this mandrel thickness should be increased to a 0.25 inch plate, which is shown in the CDR drawing package. Although not analyzed here, the thicker mandrel shell provides an appropriate match with the heavier wedge sections that make up the mandrel sidewalls. A summary of the stress analysis results is given in Table 13.1.

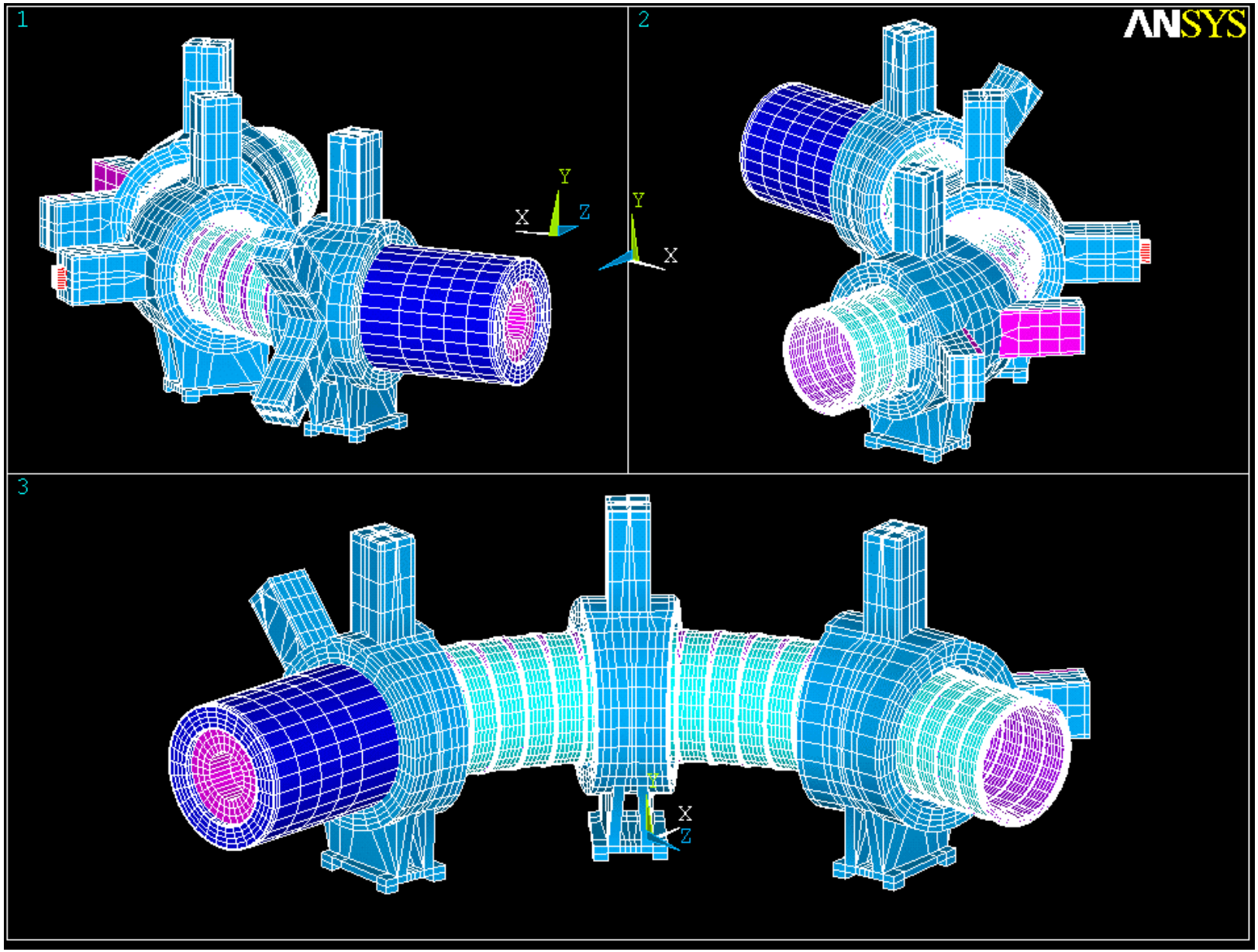

Figure 13.1 – TS structural model with mid-span radial support heavy shells/frames carry the net loads to the foundation. The model shows the horizontal Vee support at the beryllium window end of the TS and the vertical Vee support that clears the proton beam at the production solenoid end. The model includes one of the collimators and associated cryostat components, but most of the cryostat shells are not modeled.

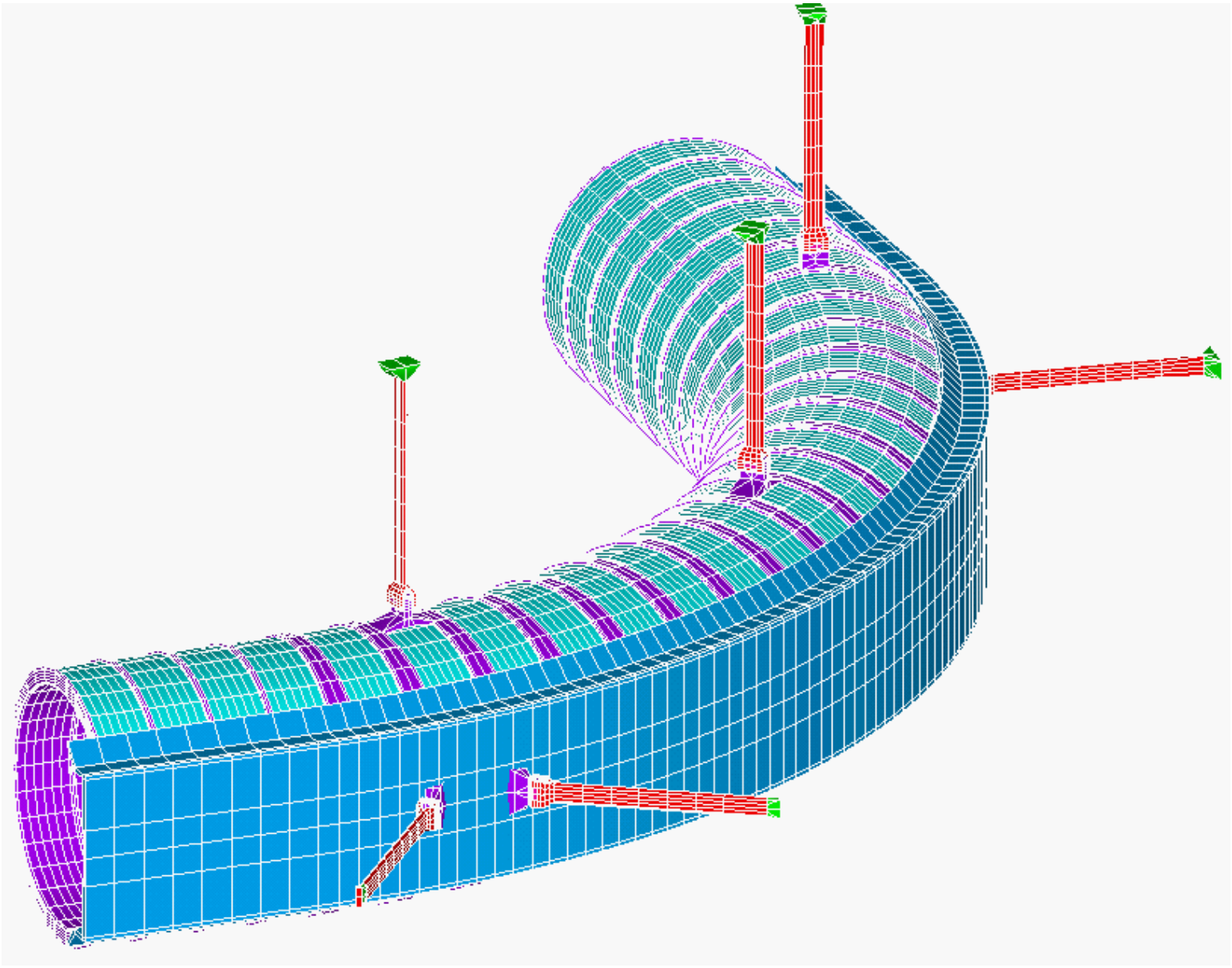

Figure 13.2 – Model with channel showing mandrel and cold mass support arrangement. This support rod configuration allows stress free cool-down. Support rods take compression as well as tension aid.

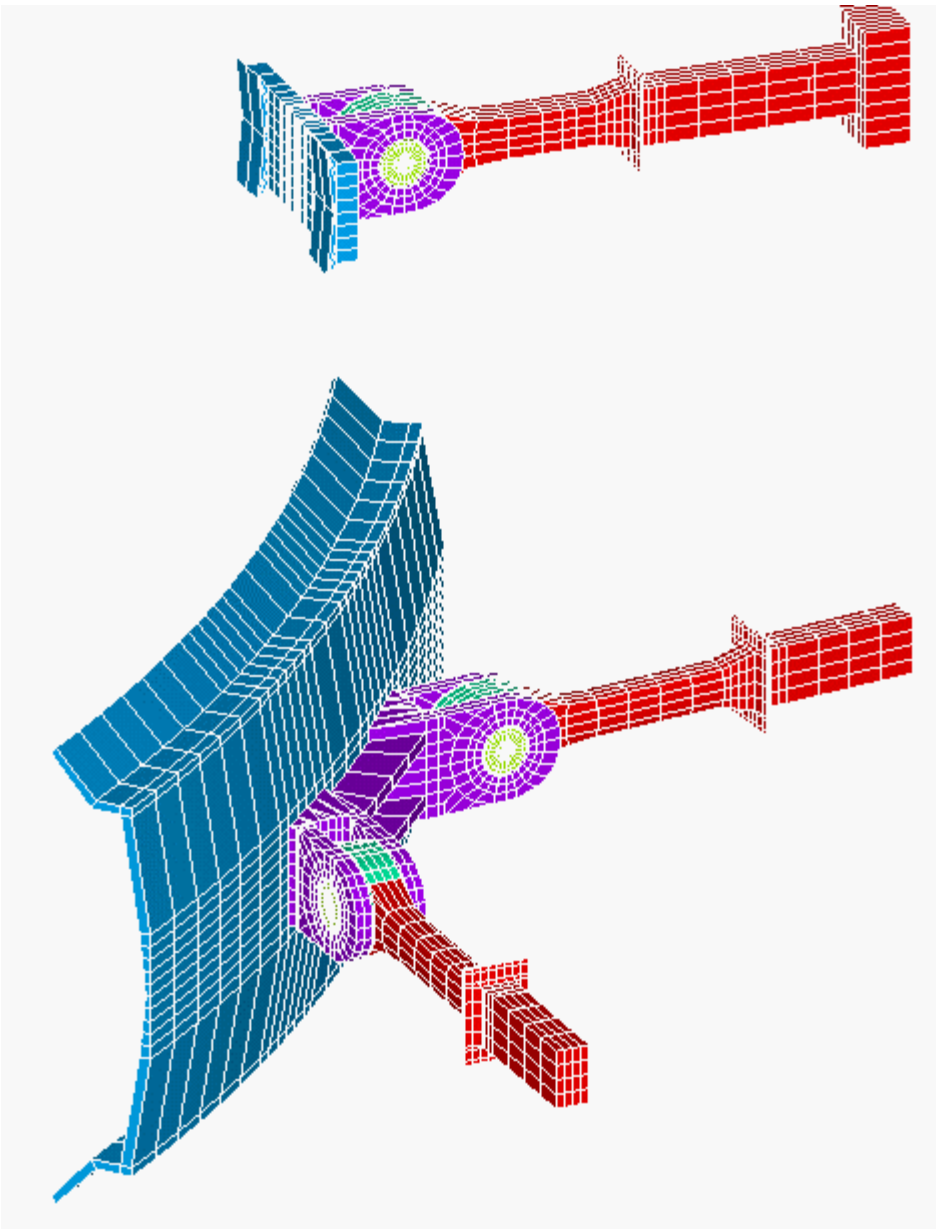

Figure 13.3 – Horizontal "Vee" (below) and mid-span tension-only support (above).

Summary of Results

The final conceptual structural design is best depicted by the MECO magnet drawing package delivered with the CDR, with materials, stresses and factors of safety as given in Table 13.1. As is often the case in conceptual design, the exact configuration of the final conceptual structural design was not analyzed in many cases. Instead, the last previous concept is often sufficient to provide final sizing estimates without the need to repeat all the analyses. The "stress from analysis" column of Table 13.1 therefore summarizes the last calculated stress results, while the factor of safety column represents the factor of safety expected to be achieved in the final conceptual design with the noted changes. The changes noted in the table are generally reflected in the conceptual design drawing package.

Table 13.1 – Summary of stress analysis results for the TS magnet.

	Material	Stress from Analysis (MPa)	Allowable (MPa)	Safety Factor
Winding Pack Metal Stress at Strut Attachment	Copper Channel 50% CW	149	150 (free standing coil allowable)	1.00
Mandrel Shell	316LN	300	459	1.53
Mandrel Bolting	Inc718	689	689	1.0 (sized to FS=1)
Support Case Stress	304	360	281 (1.5 Sm annealed)	1.0 if CW 304 is chosen
Cold Mass Strut 4K end	316LN	~300 (as modeled in FE Model)	495	1.0 (Re-sized to 2"OD FS=1)
Cold Mass Strut Clevis, 4K End.	316LN	700 Peak	3Sm=1485	2.1
Cold Mass Strut Clevis, 4K End.	316LN	~400 Net Section	Sm=459	1.14
Cold Mass Strut RT End	316LN	~200 (as modeled in FE Model)	Sm=165	1.0 (Resized to 4"OD, FS=1)
Cryostat 1cm thick end cap	316LN	53.6	1.5 Sm=247	4.6

TS Coil Displacements

A displacement summary is presented here, but it is primarily intended as an illustration of what will be need to be repeated during final design of the magnet systems. Only the upstream TS (TSu) is modeled because it is structurally limiting, but displacements will have to be quantified for both TS coil arrays. The precision of the analysis in predicting the final displacements is limited presently by the uncertainties resulting from bolted connections, coil moduli, and coil interactions with the mandrels. Added to this is the uncertainty in the final design details. The solution is to design the support struts with adjustments that can be made at cryogenic temperature and under vacuum. Bellows details and nested thread details have been developed to allow this adjustment. With this type of strut design all that is needed is to specify how large the adjustment capability must be. After final design, the displacements should be predictable within millimeters, while the strut adjusters accommodate a few centimeters of adjustment capability. Magnetic tolerance studies have shown there is a substantial ability to accept a reasonable amount of misalignment. The struts can be used to make final adjustments to the magnetic field profile by adjusting the magnet position.

TS Coil Displacement Summary

The displacement patterns under cool-down and Lorentz loads are complex and difficult to predict because of the uncertainties described above. The cooldown axial contraction at the PS or DS end is 2.4 cm, and 7mm at the beryllium window end. The assembly tends to contract toward the fixed point, or horizontal Vee support, i.e. in positive X and Z (Figure 13.4). When the whole MECO coil system is energized, there is a net centering force directed in -X and +Z.

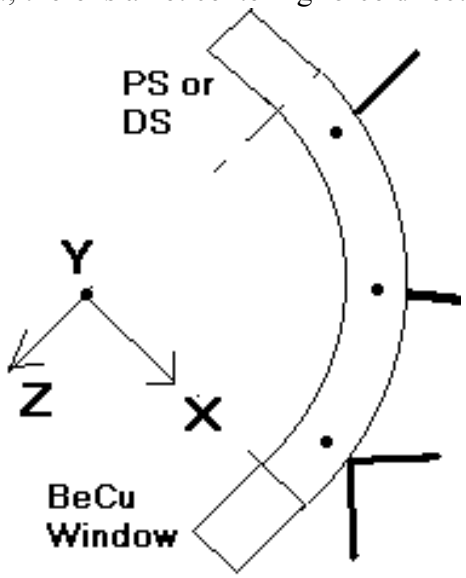

Figure 13.4 –Model coordinate system.

Displacements for these cases plus several other combinations of load cases are summarized in the following two tables.

Table 13.2 – Summary of TS system displacements for various load cases. Normal loading is with all systems, PS, TS, and DS energized.

	Be Window End		PS or DS End	
Load	**UX (mm)**	**UZ (mm)**	**UX (mm)**	**UZ (mm)**
Cooldown (CD)	+2, –3	–7	24.2	–9
CD + Normal	–3	–4	2.4	–6.7
CD + TSu Only (Self Load)	–0.7	–8.5	26.5	–9
CD + TSu + TSd	–2.55	6	33.7	–12

Table 13.3 – Displacements of center of TS Elbow

Load	UX (mm)	UZ (mm)
CD	13.3	1.7
CD+Normal	–13	8
CD+Self	11.3	1.8

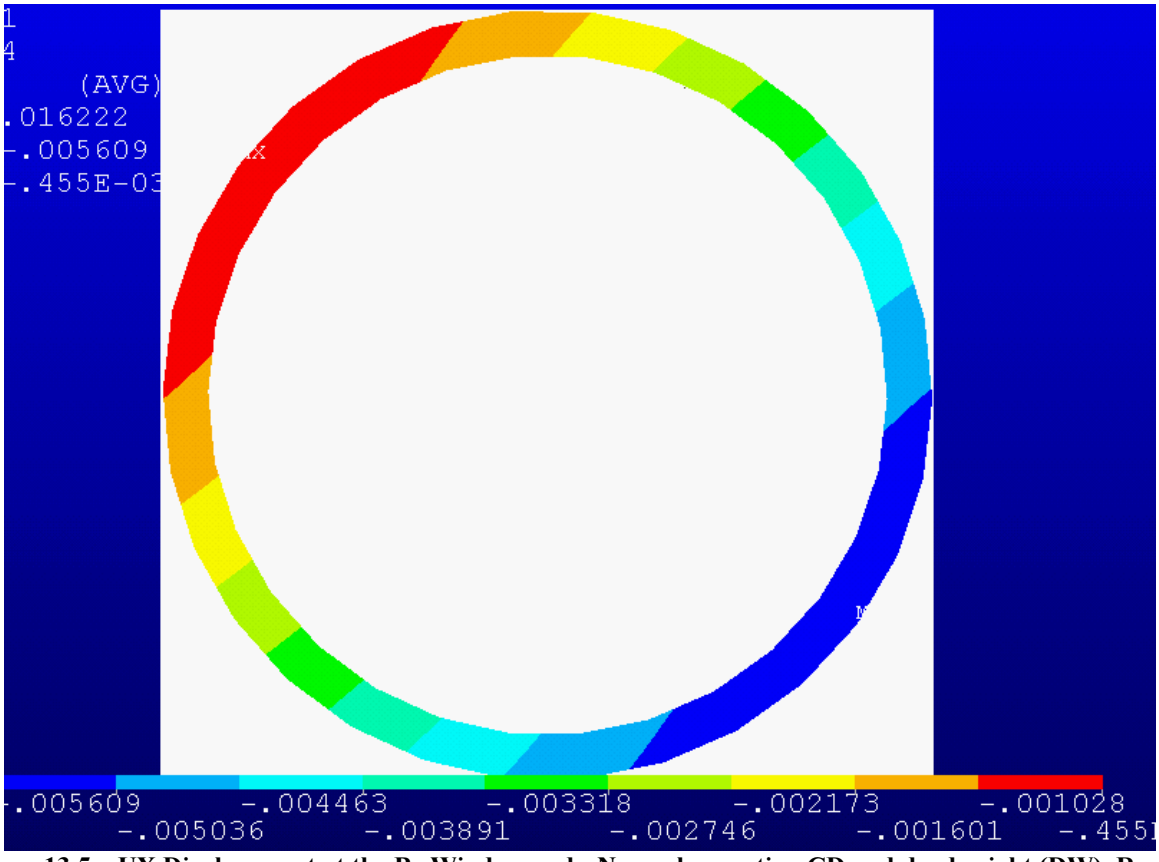

Figure 13.5 – UX Displacement at the Be Window end - Normal operating CD and deadweight (DW), Run#6, set,4. Displacements range from -.0056 to -.000455 m

More effort will be needed during final design to plot and tabulate the necessary information to guide "oversize" manufacture and initial placement at room temperature and then final

adjustment of the position when it is cold and loaded. Adjustable support struts will be essential if an accurate alignment is to be accomplished.

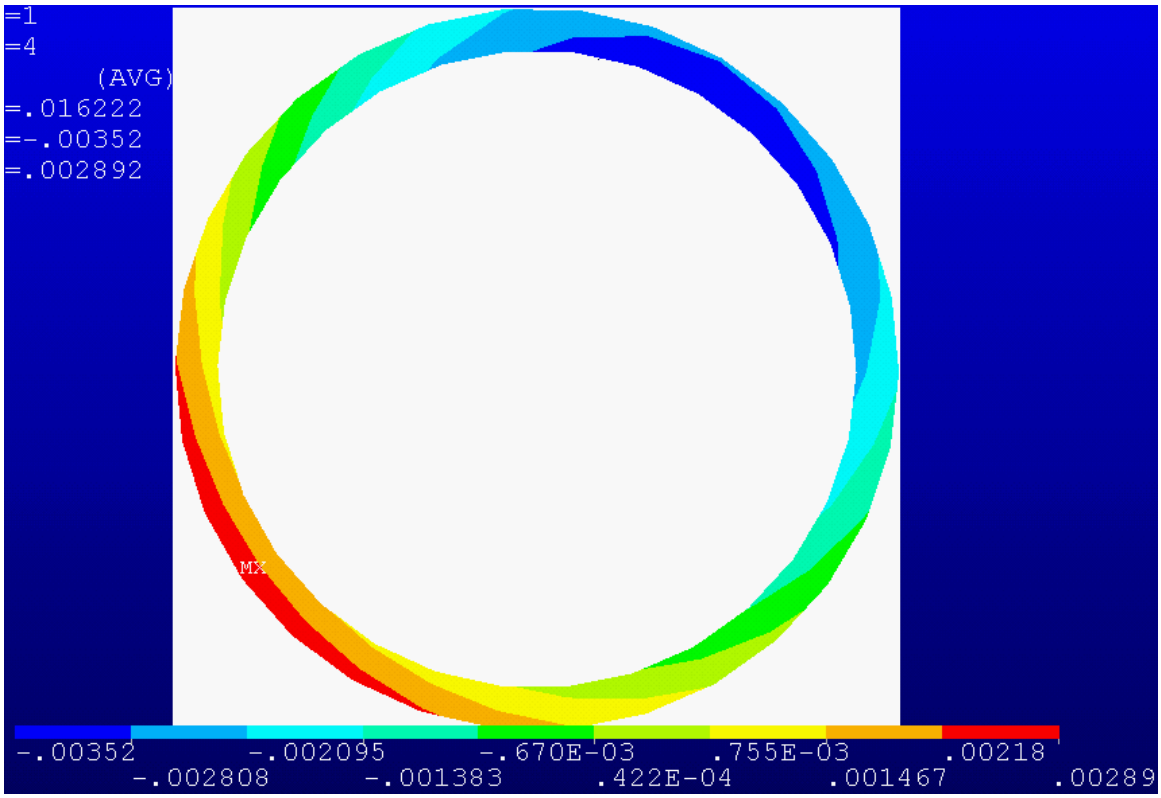

Figure 13.6 – UZ Displacement at the Be Window end - Normal operating CD and DW, Run#6, set,4 Displacements range from -.0035 to +.0024 m

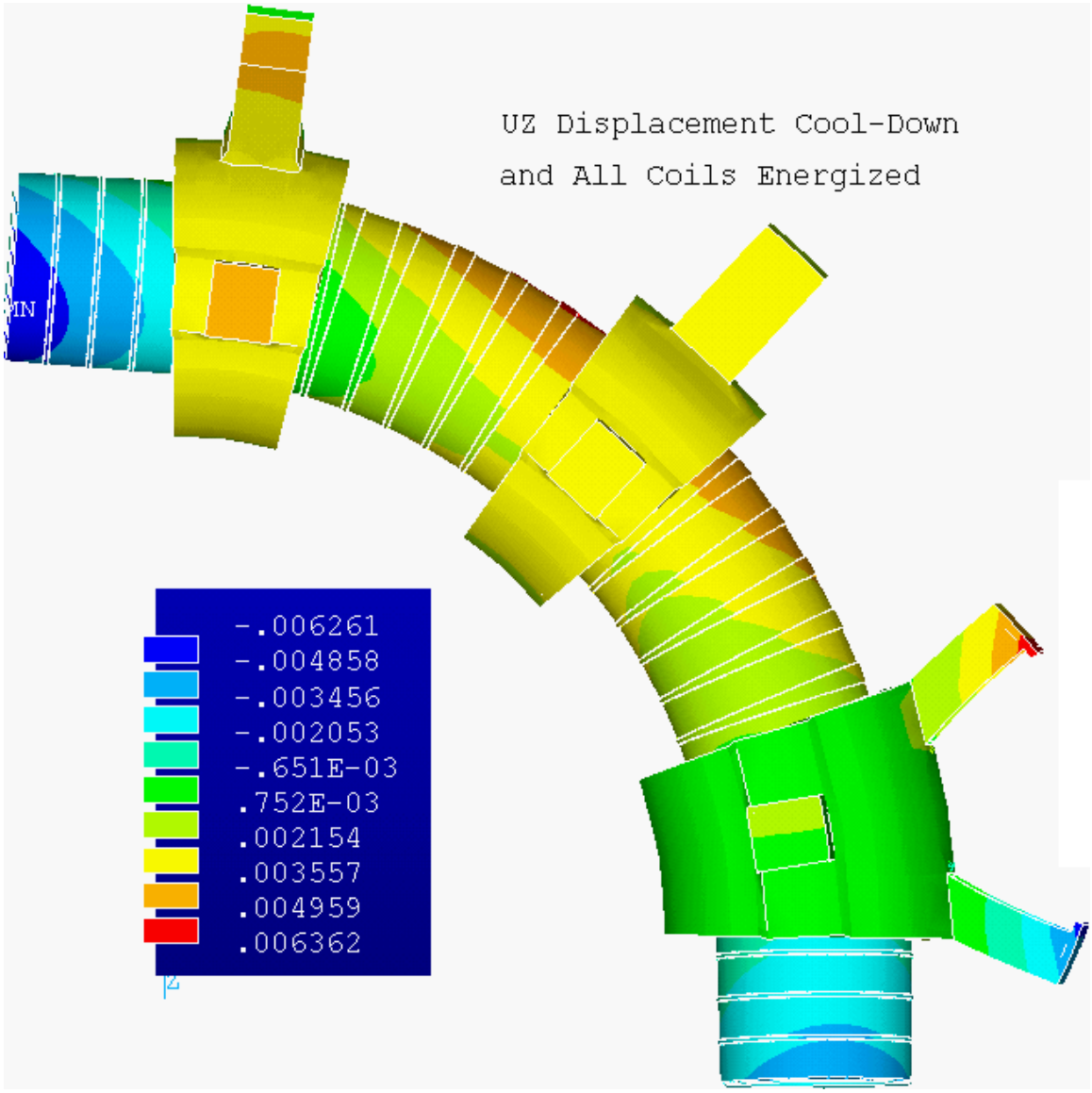

Figure 13.7 – Displacements from Run#10 - "Final": Support Arrangement (Not Yet Tabulated)

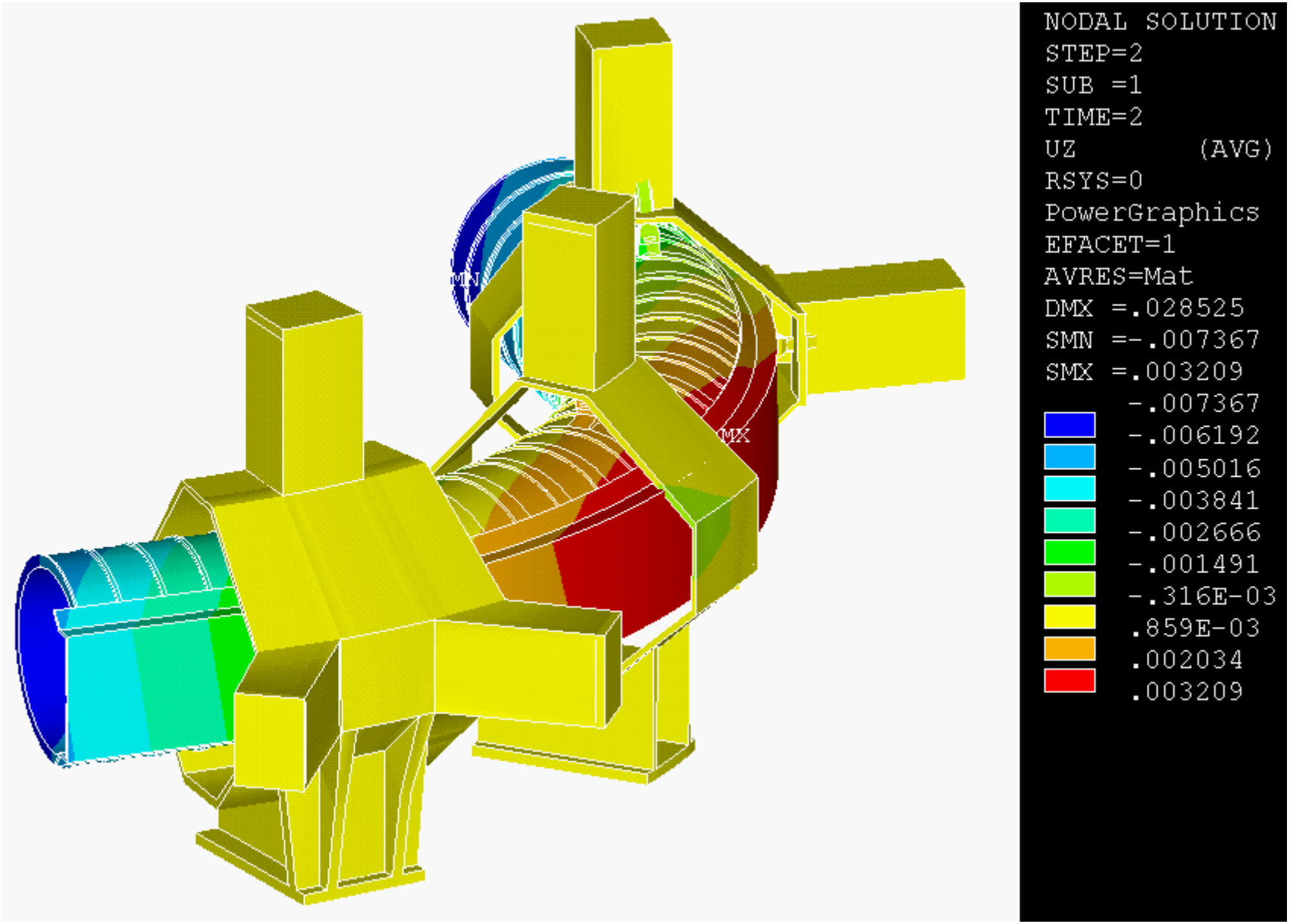

Figure 13.8 – UZ displacements at cool-down. At the end nearest the angled rods, the axial contraction is 7 mm, Run#5.

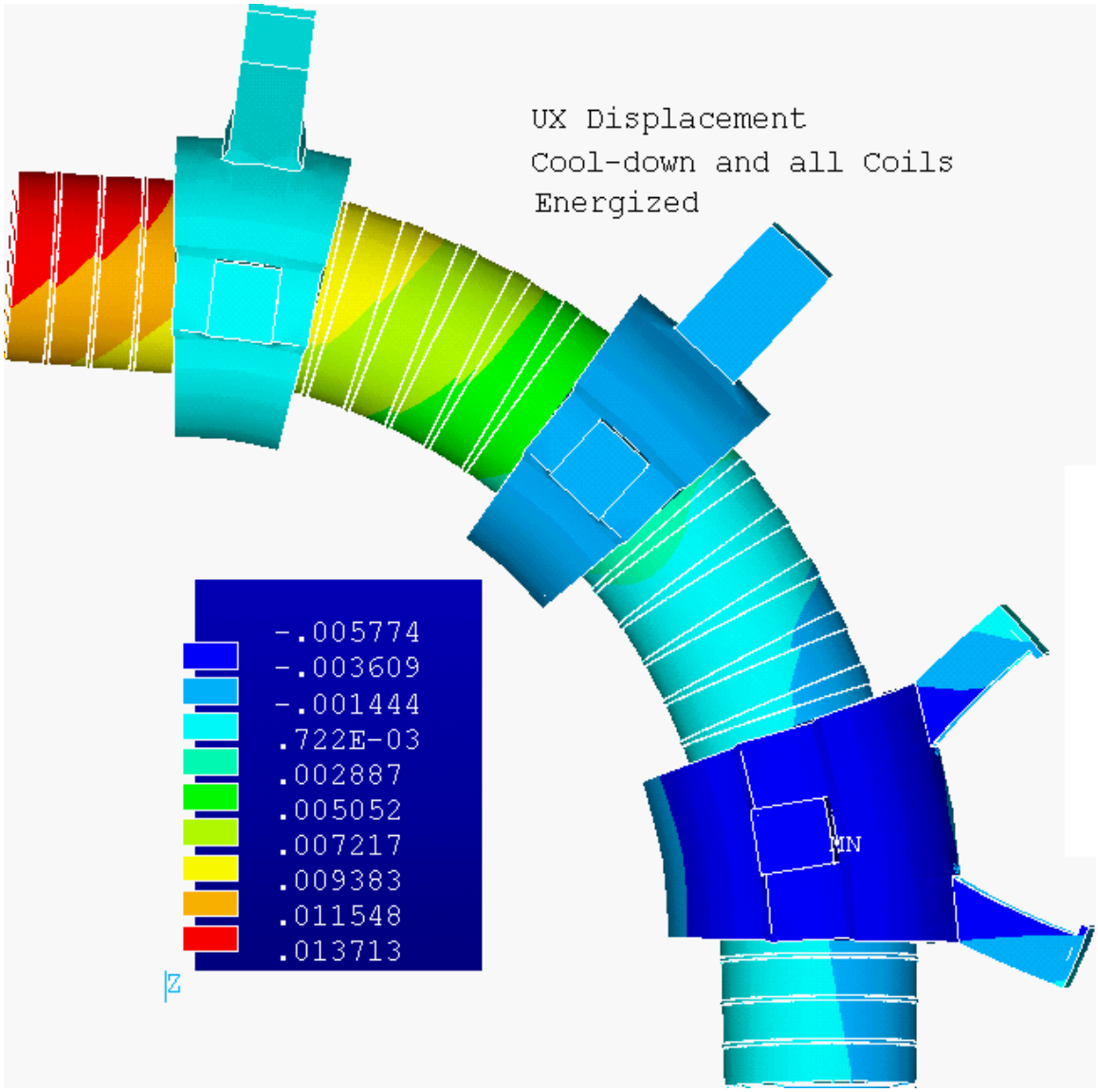

Figure 13.9 – Displacements from Run#10 - "Final": Support Arrangement (Not Tabulated).

Structural Models

The large 3D model of Figure 13.1 represents one half of the transport solenoid and consists of a 90° turn with straight sections at each end. The cooling tubes and thermal shields are not modeled. The cryostat vacuum boundary and bore tube are also omitted, but the heavy structures that take the coil net loads and would be a part of the cryostat vacuum boundary are included. The one 3D model of the TS is intended to envelope the structural response of both TSu – the upstream TS and TSd, the downstream TS. Currents from TSu are used in the model. The effects of the coil arrays at each end of the TS model are approximated with straight solenoid extensions. Five load steps have been used in the analysis:

- Deadweight
- Cool-down to 4 K
- Self load with only the elbow energized
- Normal operating load with coil systems at each end energized
- A side-load case in which coils at only one end are energized.

The model was built from model segments (Figure 13.10 through Figure 13.12) that could be read in separately and readily changed to investigate different mandrel and support concepts.A Biot-Savart solution external to ANSYS is used, and appropriate load files are read into the mechanical analysis. Force vectors plots (Figure 13.13 and Figure 13.14) are a visualization aid that is useful in the design process. The large 3D magnetic model predates the final field error calculations, and coil builds varied from that assumed in this model. To address these variations, axisymmetric analyses of the end regions of the TS were added.

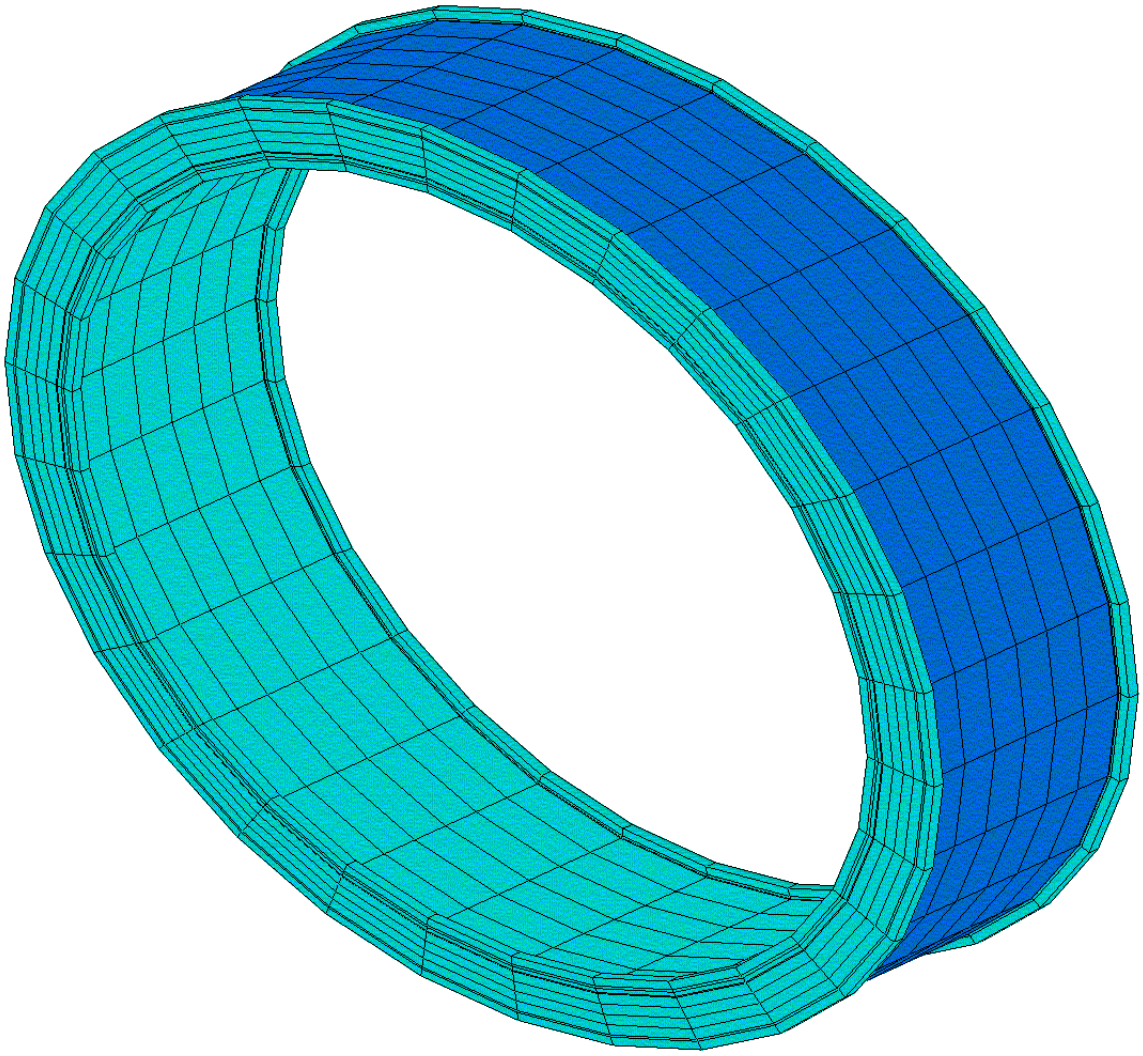

Figure 13.10 – Single mandrel and coil. Gap elements are used at the interface between the coil and mandrel

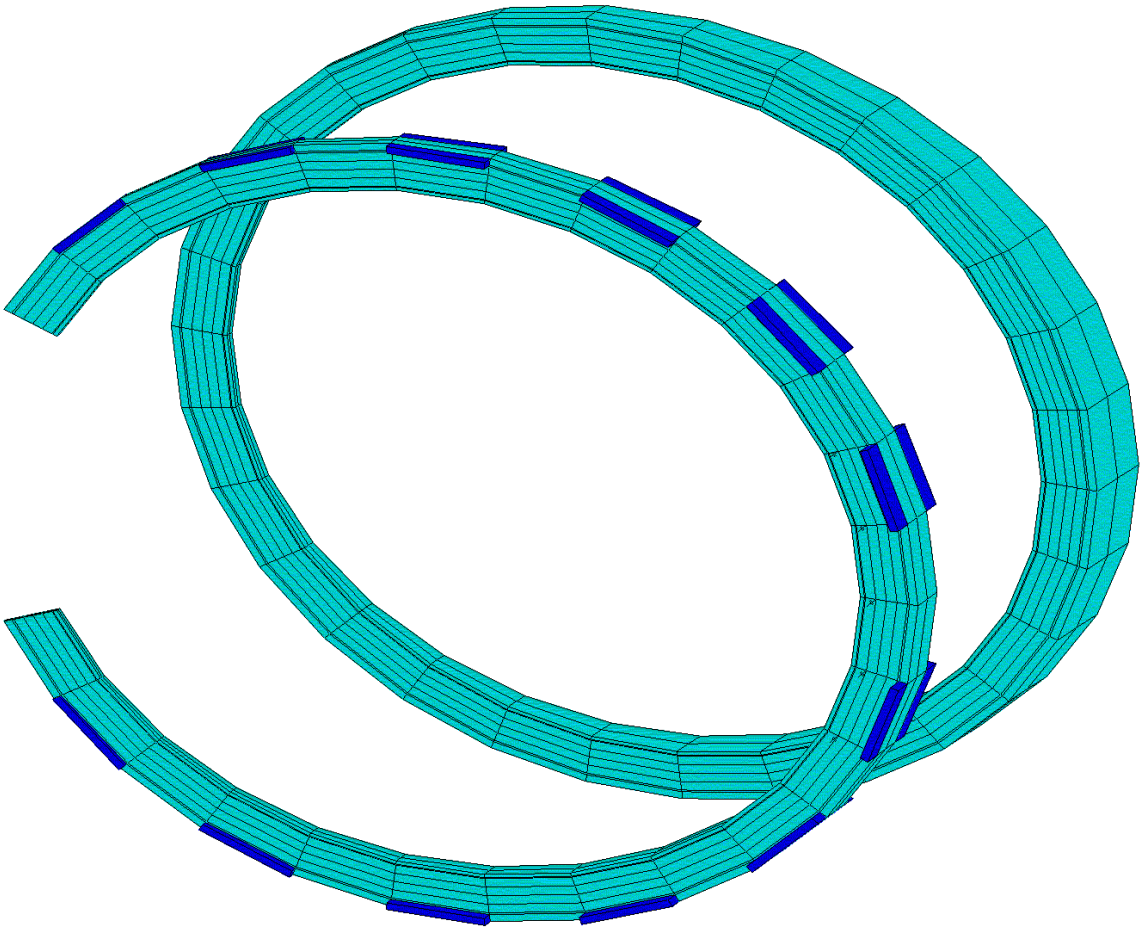

Figure 13.11 – Crescent vs. wedge spacers. Both concepts were explored, but the final choice was to incorporate the wedge shapes into the side flanges of the bent sections

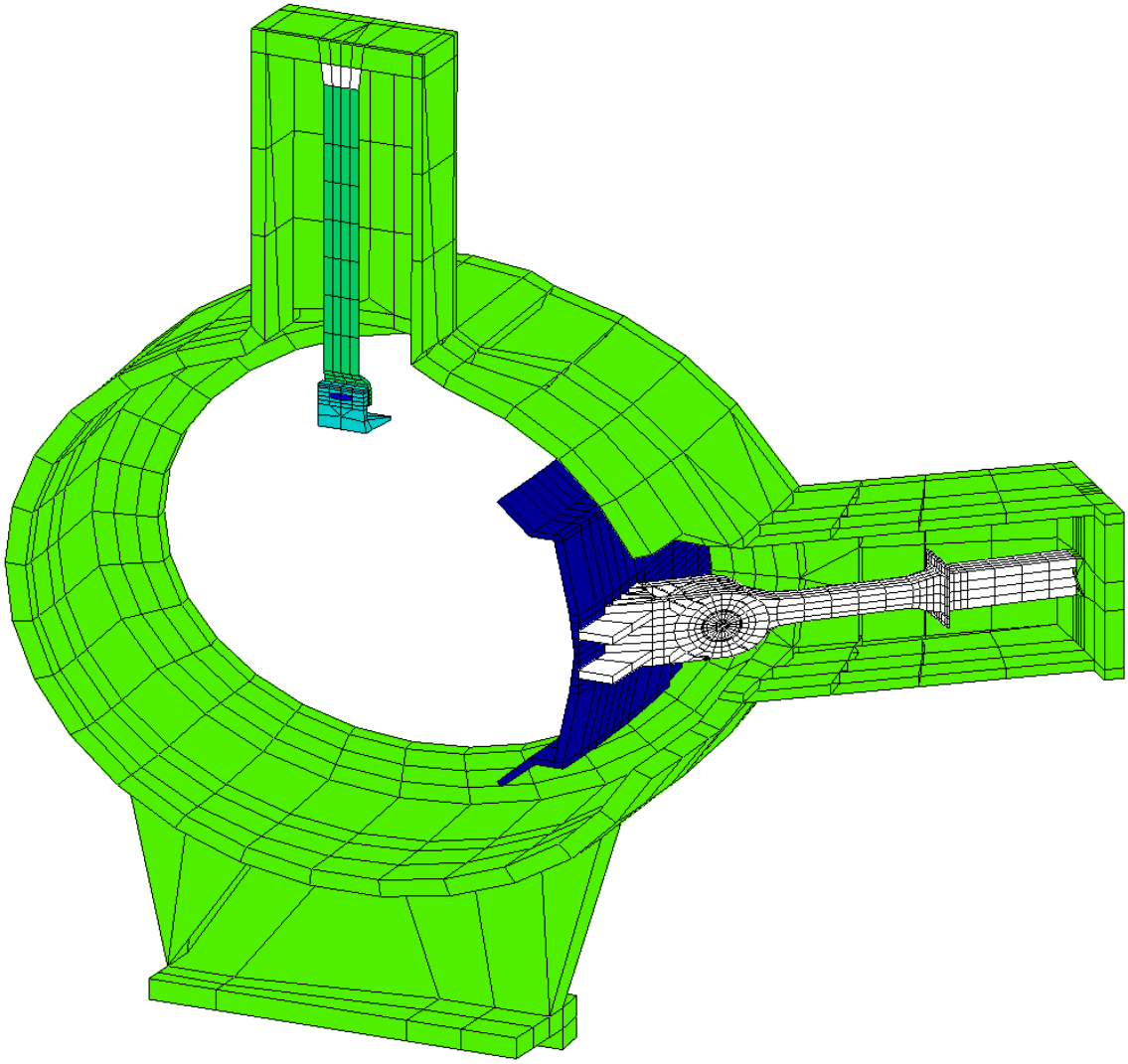

Figure 13.12 – Case and support rod model segment before reflection.

Table 13.4 – TS dimensions.

	Tube R_{outer} (mm)	Tube R_{inner} (mm)	Tube Length (mm)
Vac_Bore_Tube	275.0	250.0	1081.7
Vac_End_Flng	639.6	275.0	12.7
Vac_Out_Tube	665.0	639.6	1081.7
Shld_Bore_Tube	325.7	313.0	1049.9
Shld_End_Flng	601.4	325.7	6.4
Shld_Out_Tube	614.0	601.3	1049.9

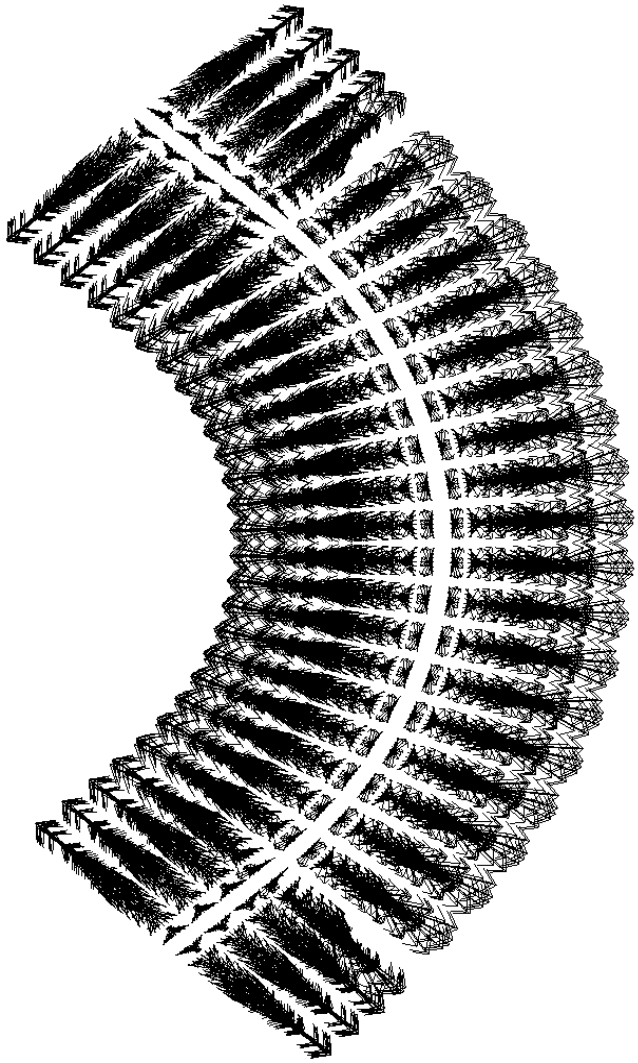

Figure 13.13 – Normal operating loads on the 3D model, looking down. Load vectors near the ends rotate toward the center of the elbow when the neighboring coil systems are turned off.

Table 13.5 – Run log for the large 3D model.

Run #	Date	Description
TS05	6-22-01	Includes Large Channel
TS06	7-18-01	Added Vertical Vee support where proton beam intersected radial strut box. Channel Omitted in this run
TS09	12-04-01	Mid Span radial Support , Omitted Vert Grav support at Vertical Vee
TS10	12-20-01	Put the Gravity support back at the Vertical Vee

Table 13.6 – Run log for the axisymmetric models.

Run #	Date	Description
acoi01	6-22-01	Single Interior coil
acoi02	12-26-01	Production Coil Straight Section
acoi03	12-26-01	Be Window Straight Sections

Table 13.7 – Axisymmetric model build and currents near the Be window.

Real	R (m)	Z(m)	DR(m)	DZ(m)	MAT
1	.4419	2.929	0698	.176	.51235
2	.42645	3.129	.0389	.176	.29761
3	.43345	3.329	.0529	.176	.39479
4	.4178	3.479	.0216	.076	.078886
5	.4609	3.579	.1078	.076	.34515
6	.43135	3.674	.0287	.046	-.062996
7	.49625	3.769	.1785	.076	.56331
8	.48465	4.039	.1553	.076	.4918
9	.4262	4.134	.0184	.046	-.043104
10	.45065	4.229	.0873	.08	.26934
11	.42385	4.329	.0337	.08	.10411
12	.43035	4.479	.0467	.18	.32427
13	.43085	4.679	.0477	.18	.33095
14	.43215	4.879	.0503	.18	.34929

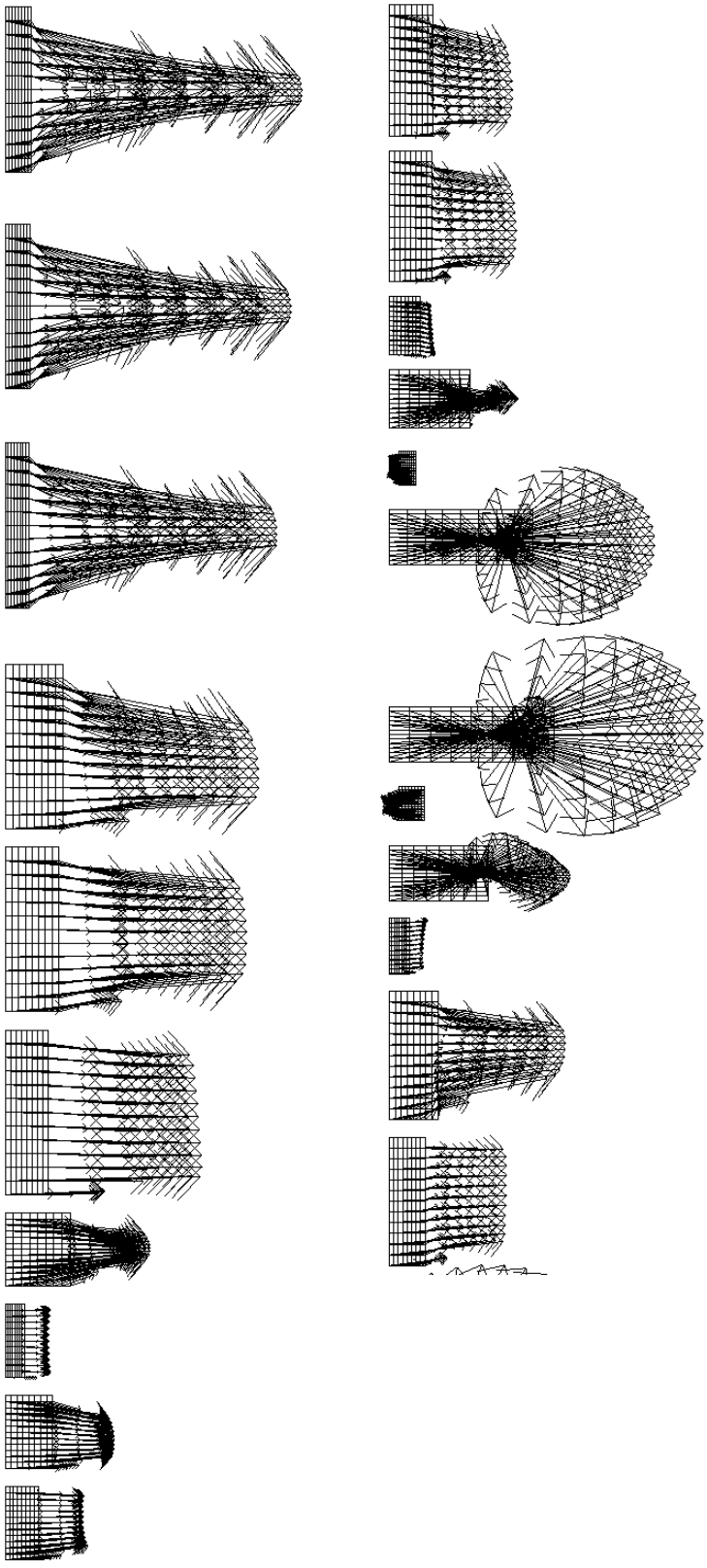

Figure 13.14 – TS Lorentz forces near Production Solenoid (left) and beryllium window (right).

Evolution of the Structural Concepts

Since a conceptual design is not a final design, it is useful to review some of the intermediate options considered to provide insight into the rational for the chosen solutions. Initial thoughts on the structural support of the transport solenoid anticipated the large net loads and global displacements of a large assembly of coils. An early concept placed each coil in its own individual cryostat (Figure 13.15). This would have been unworkable in terms of field ripple requirements, heat leak, and the necessity for a complicated superconducting buss - but global alignment would have been easier, and heavy load carrying members would not have been necessary. Instead, two large arrays of coils were chosen to make up the transport solenoid array. The mandrel and support designs have gone through a number of iterations. The first mandrel design used 1.0 cm thick flanges and 0.4 cm thick inner shell. The flanges were bolted at the outer perimeter only, without connection at the bore side of the flange. Compressive loads were carried well by this arrangement, but tensile loads (e.g., from centering) produced a prying action, that made the assembly weak in bending. Channels were added to help support tension, and to locally reinforce the support rod connection to the mandrel. The first cut at the channel design employed channels that were bent with a compound curvature (Figure 13.16), and would have been difficult to roll. These were replaced with a single large channel. The channel was modeled only on the outer radius of the elbow, and while it helped with the local attachment loads, a channel on the inner radius of the elbow was needed to support the bending stresses from the normal operating centering loads. Earlier over-constrained support schemes were less sensitive to this bending stress.

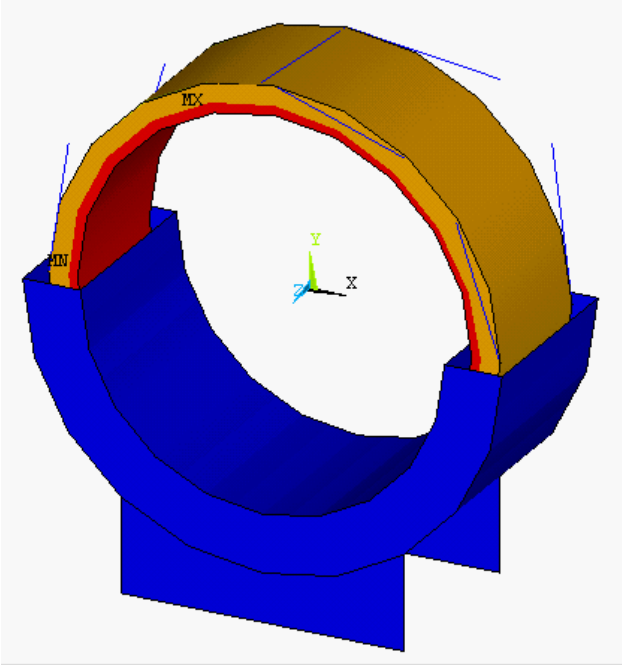

Figure 13.15 – Single coil module (cryostat section shown removed) radius rods are assumed as a cold mass support.

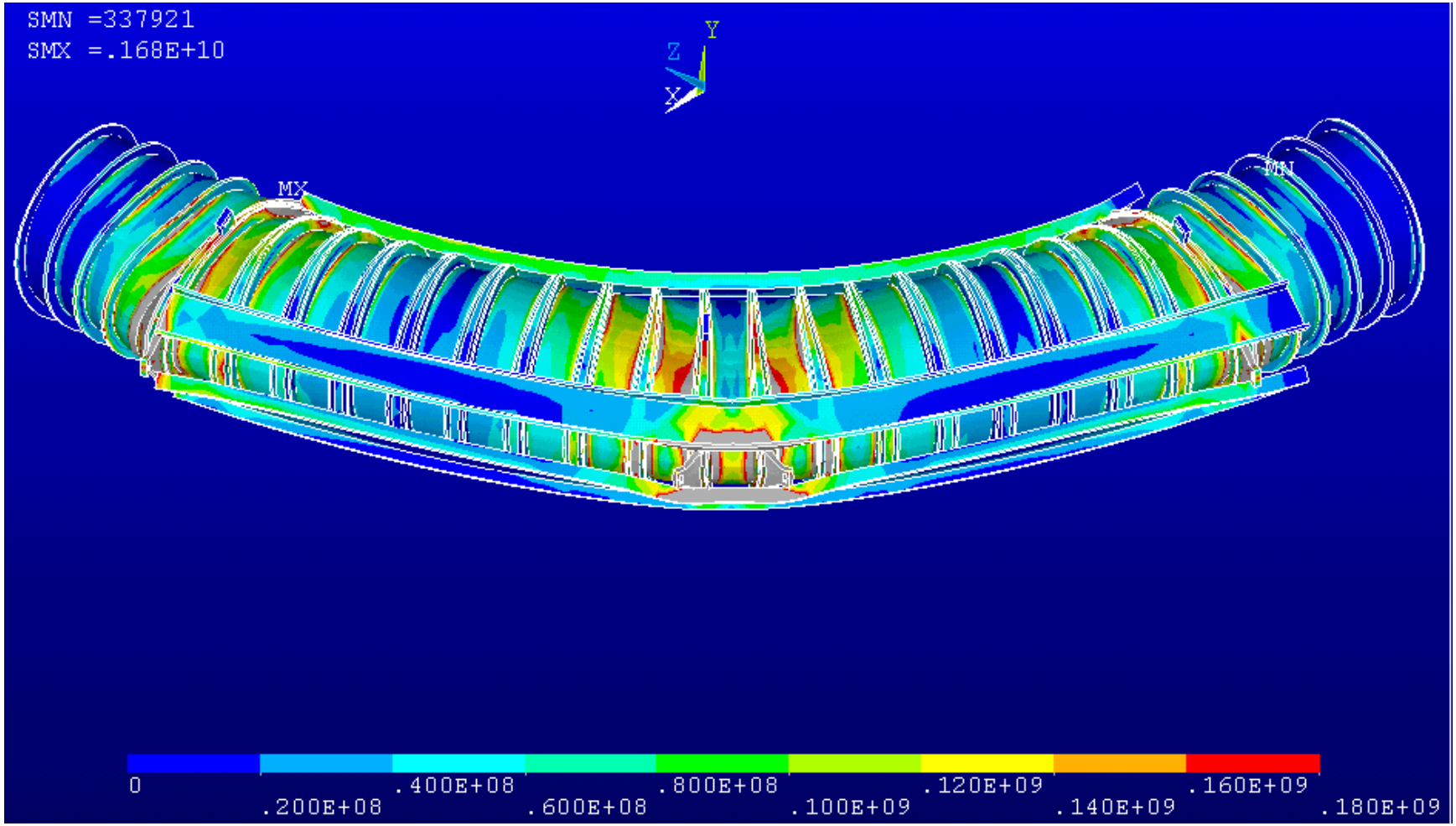

Figure 13.16 – Von Mises stresses, for normal operating loads, with the early "one-sided" flange bolting which allowed prying of the flanges, and the compound curvature channels.

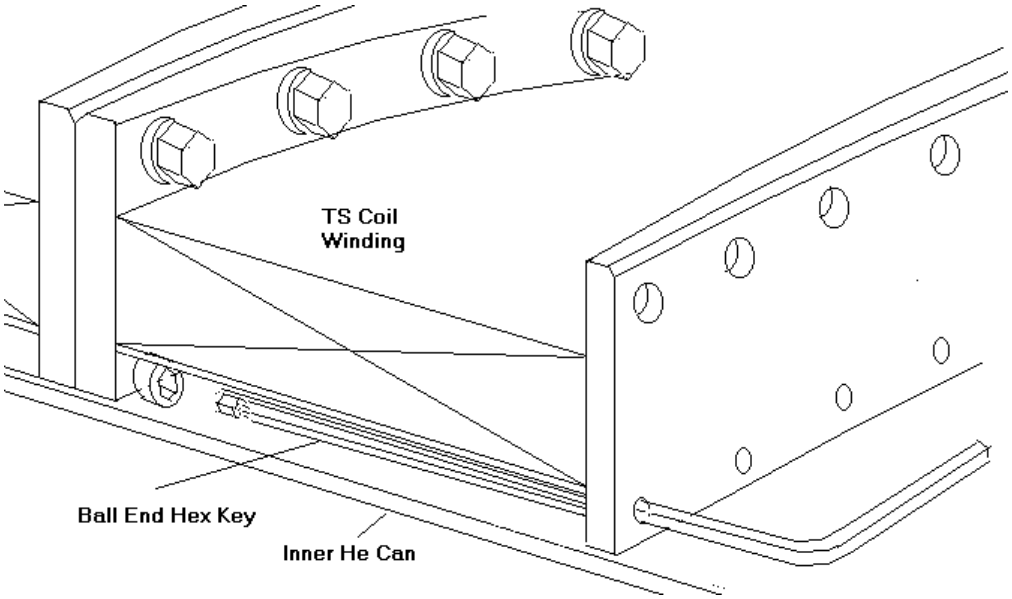

Figure 13.17 – A sequential bolted assembly scheme was required for a pool-cooled design. Access with a hex key through the neighboring flange was necessary. The present conduction-cooled design eliminates the tight fitting He can and allows for a much simpler assembly with full access to the bolting in the bore.

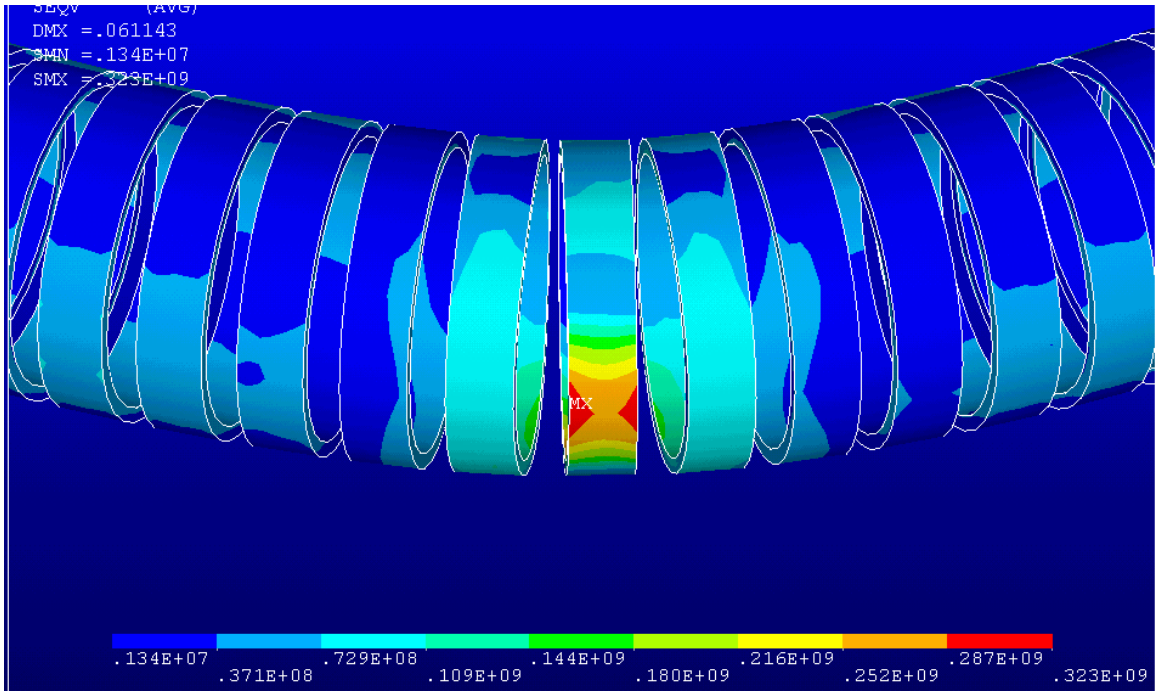

Figure 13.18 – Coil Von Mises stress with the early "one-sided" flange bolting that allowed prying of the flanges.

To make up the 90° bend of the elbow, wedge pieces (Figure 13.11) were bolted between the flanges. The first wedge design was a crescent, and not a full circle. This left the inner radius of the elbow without any axial load path and the tensile and compressive loads concentrated where the crescent began. Figure 13.17 shows an assembly scheme that allows inner bolting of flanges. Weld preps are shown that allowed for an additional structural weld that formed covers for the outer He can. This approach was abandoned when the cooling scheme was changed to a

conduction cooled design rather than a Helium bath cooled design. Access to the inner bolts is much facilitated by the removal of the Helium can, and conventional access to flange bolts is now possible.

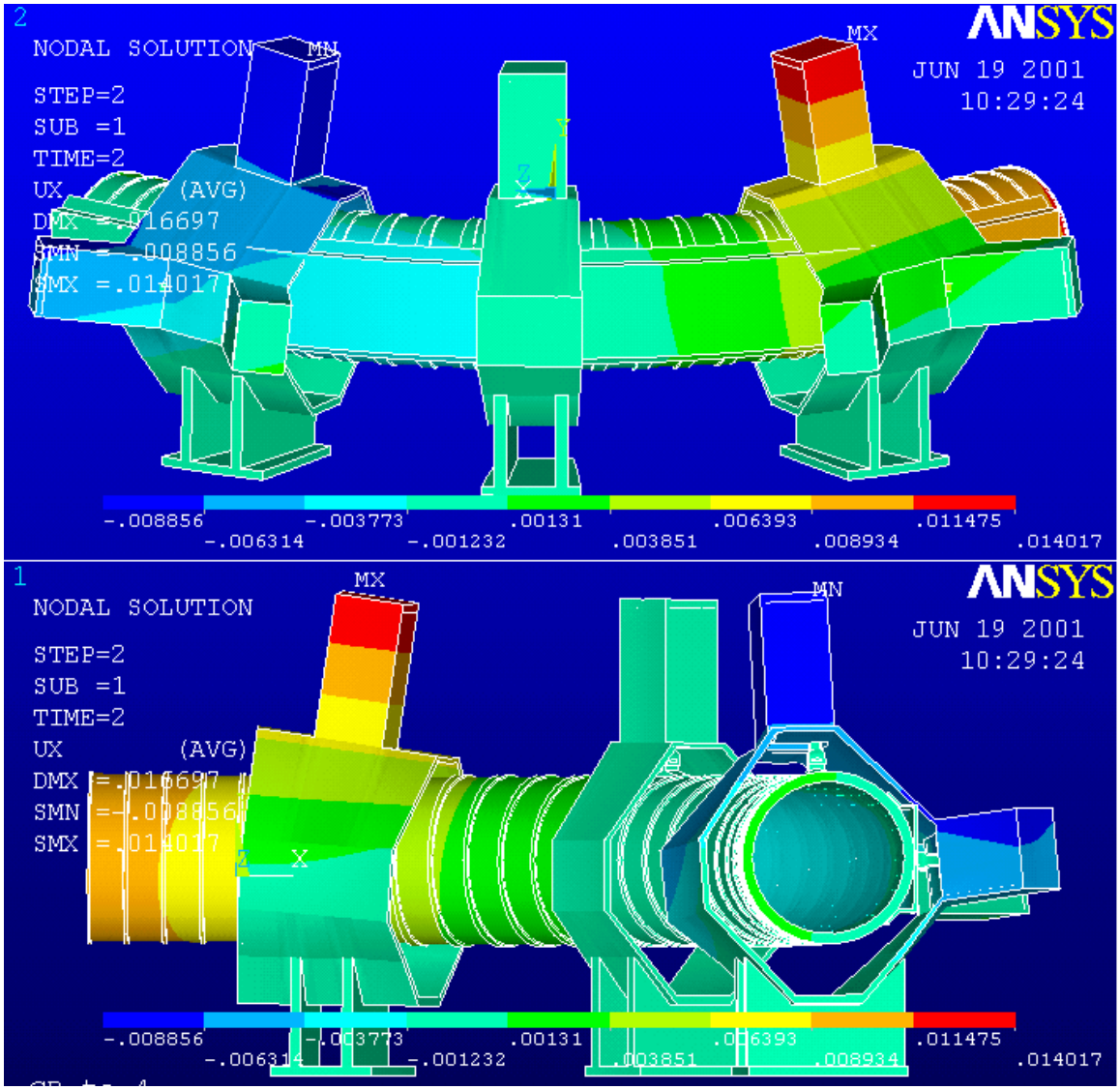

Figure 13.19 – Cooldown displacements of the "Over-Constrained" configuration with a rod pair at each end of the elbow - Note the vertical tower deflections indicating the coil contraction effects

Two over-constrained arrangements of support struts were investigated, but these put unnecessary cool-down stresses in the mandrel and the coils. It was thought that a stress free cool down was desirable. This reduced the number of supports. This coupled with the large assembly size of coils produced some large spans to be supported by the coil mandrel structure.

The present support arrangement (Figure 13.1) is a "sufficient constraint" system with heavy load carrying support struts that provide a statically determinant support scheme. It should be noted that the struts, under some of the loading conditions must support compression.

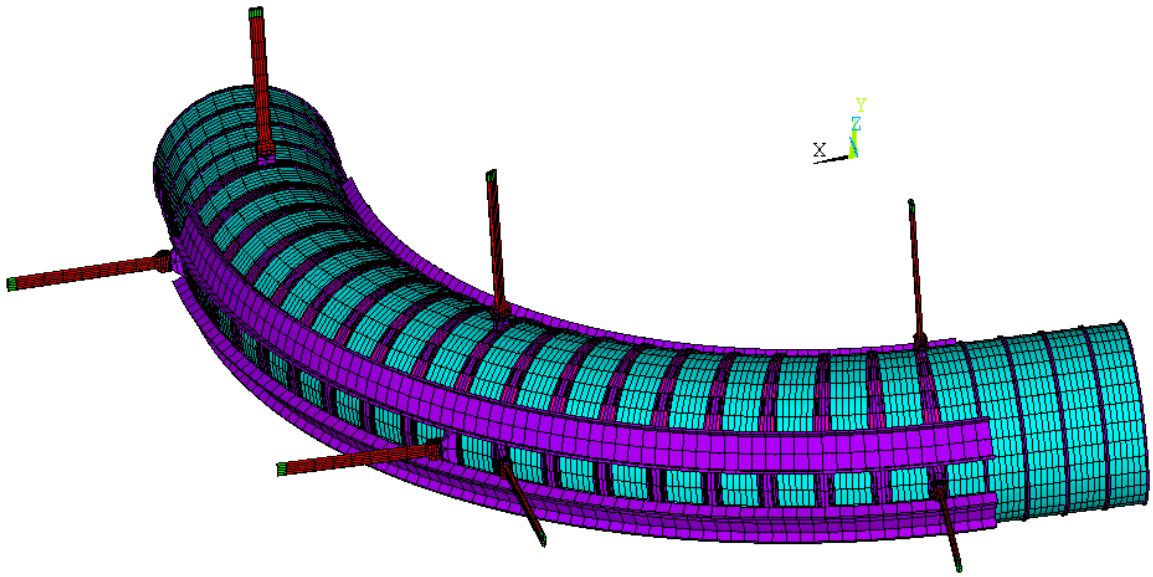

Figure 13.20 – An early "over-constrained" support concept, with a pair of angled support rods in the middle of the elbow and channels with compound curvature

Coil and Conductor Stress

Conductor configurations

Initial stress calculations were done on the preliminary conductor configuration shown in Figure 13.21, before the final conductor (Figure 13.22) was chosen. An approximate correction factor to be applied to the postprocess results is then: (1-0.286) / (1-0.484) = 1.38.

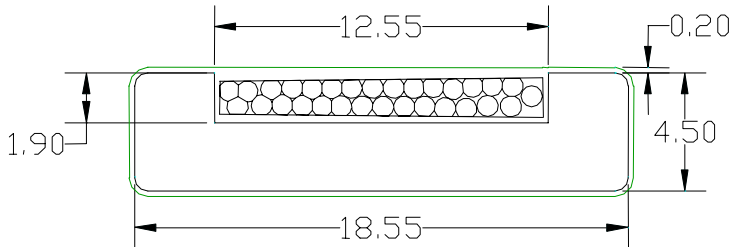

Figure 13.21 – The conductor cross-section used as a basis for stress calculations. The conductor is 28.6% of the volume.

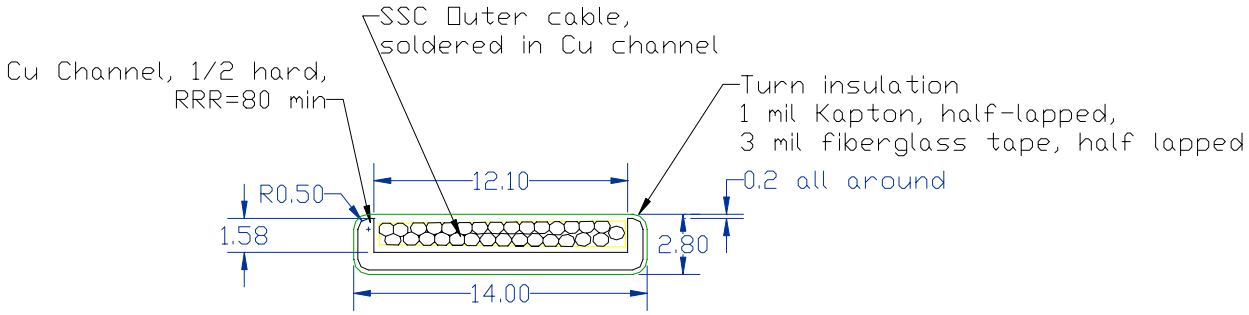

Figure 13.22 – Final TS conductor cross-section chosen. The conductor is 48.4 % of the volume.

Axisymmetric analyses

Results of three separate axisymmetric analyses are presented, and each are discussed in more detail below:

- Simplified analysis of a straightened string of solenoids
- TS coils in the straight section near the production solenoid
- Coils near the Be window

Straightened string

A simplified axisymmetric analysis was performed early, based on the straightened string of solenoids that make up the full array of the magnet system. An axisymmetric field and force calculation was done with a TS coil singled out with a more detailed mesh. Since the net axial loads are small for normal operating loading, half coil symmetry was used. For the axisymmetric analysis the "smeared" Von Mises stress was 39.2 MPa (Figure 13.23). The methods and the derivation of the stress multipliers are similar to those described in more detail in the PS stress analysis chapter. Recall that the multipliers enable calculation of the local stress from the "smeared" results of the model. With the appropriate multipliers, the copper stress is 47.1 MPa

(Figure 13.25), and 65 MPa with the final conductor correction. A better estimate of this stress, which more properly accounts for the effects of the bend and supports, is provided in the 3D model in the 3D model subsection.

Note the coil separation from the mandrel in Figure 13.24. In the 3D model discussed in the next subsection, the coil is preloaded to keep it in contact with the mandrel. The coil would "numerically spin" without this constraint. In the real coil, rotational motion should be anchored by some means such as a G-10 cleat. The torsional loads are small, but without the cleat, the coil might stick-slip-wander around the mandrel and end up loading the jumpers. The analysis discussed above is representative of the coils that are in the interior of the TS elbow array.

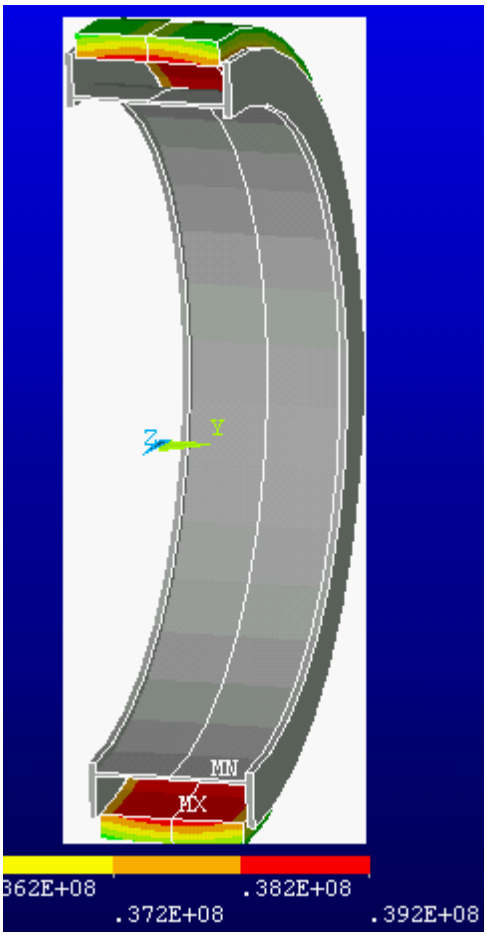

Figure 13.23 – Single coil axisymmetric analysis shown with axisymmetric and XZ plane reflection symmetry expansions. The maximum "smeared" Von Mises stress is 39.2 MPa.

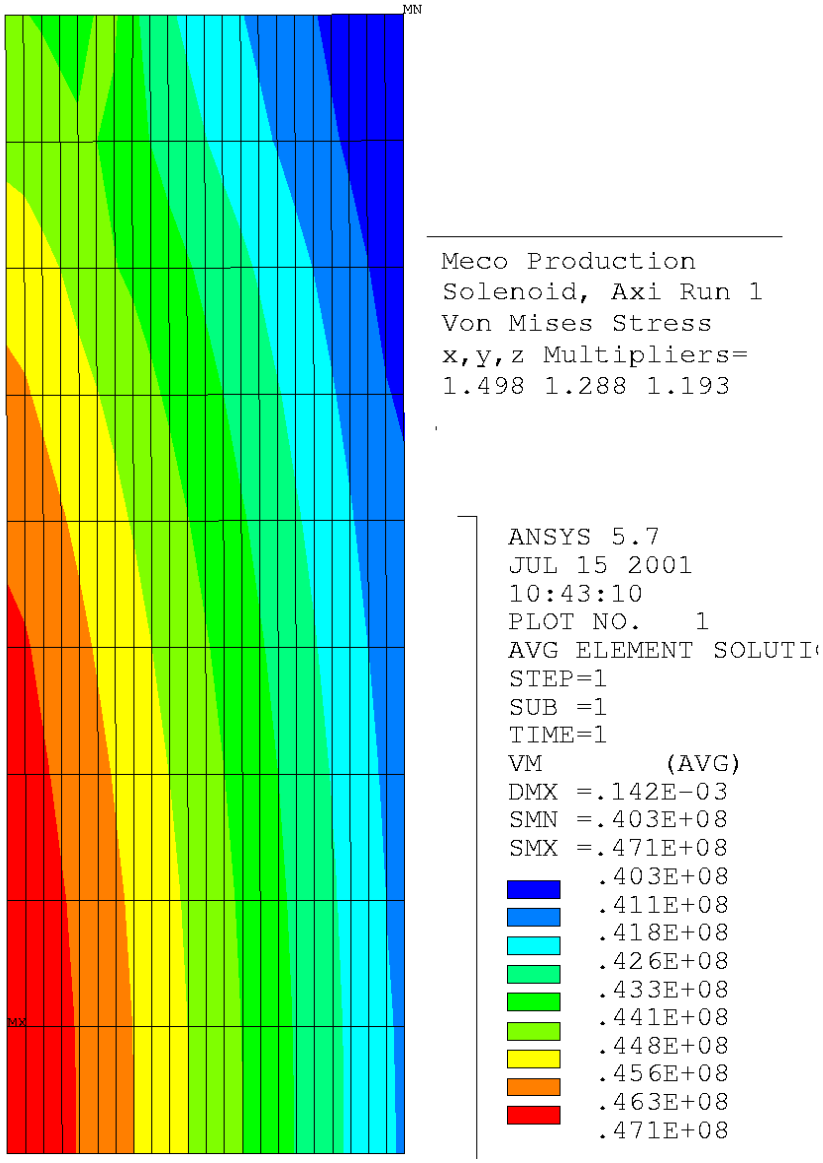

Figure 13.24 – Results of post-processing the axisymmetric model of a single coil based on multipliers from [3].

Straight section near PS

Coil geometries and currents are quite different at the end straight sections. An axisymmetric analysis of these coils was performed, this time without the mandrels modeled. Axial constraints were applied mid length of each coil to represent axial support by the mandrels. The model was analyzed based on currents in [5]. The post-processor that applies the individual conductor stress multipliers was run and the plot below resulted. The peak conductor VonMises stress was 71.6 MPa (Figure 13.25). With the final conductor cross section correction, these stresses rise to 98.8 MPa, still well below the 150 MPa allowable.

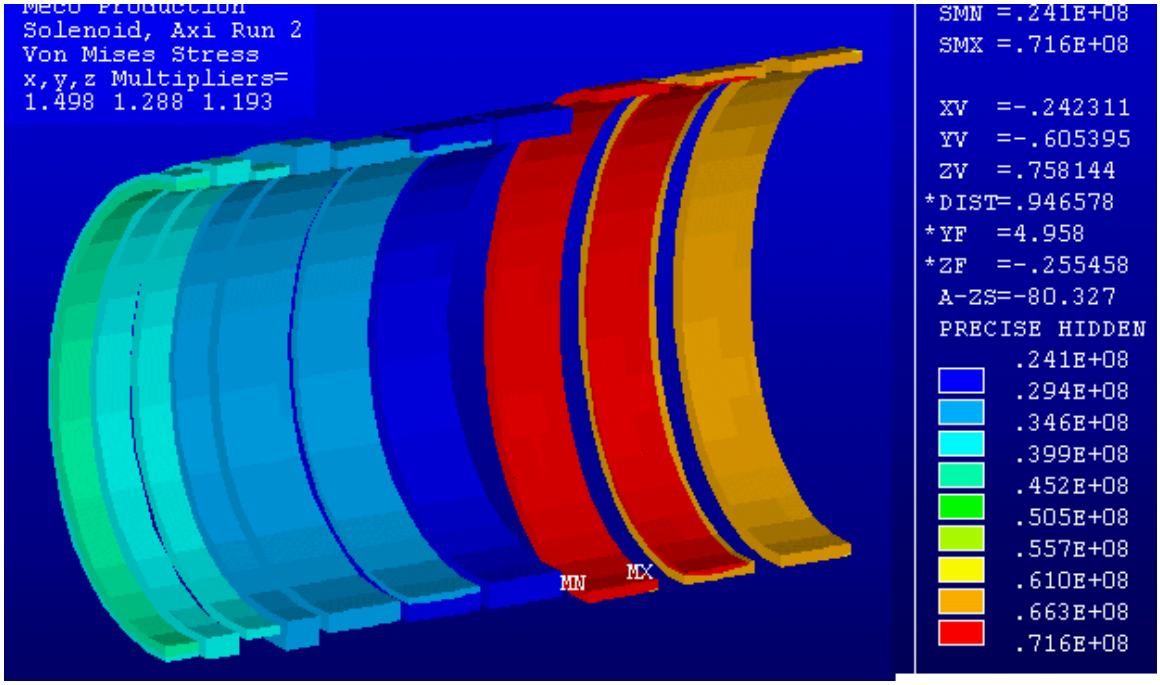

Figure 13.25 – TS coil stresses in straight section coils near the Production Solenoid - local conductor Von Mises stress.

Coils near the Be window

The other area of interest in the TS is the set of coils around the Be window. This is somewhat further from the high field end (near the production solenoid), but the coil geometry is quite different from the interior coils or the coils near the PS and DS. Again the evaluation is based on a simple axisymmetric analysis. There are some current reversals in these coils. The plot below is an exaggerated displacement plot with the small (red) coil, which is loaded in hoop compression translating radially inward. This coil has the maximum stress of 34.8 MPa (without the conductor multipliers), as shown in Figure 13.26, but this is quite low, and in actuality, it will be supported by its winding mandrel. This region of the TS is not expected to have any significant stress problems.

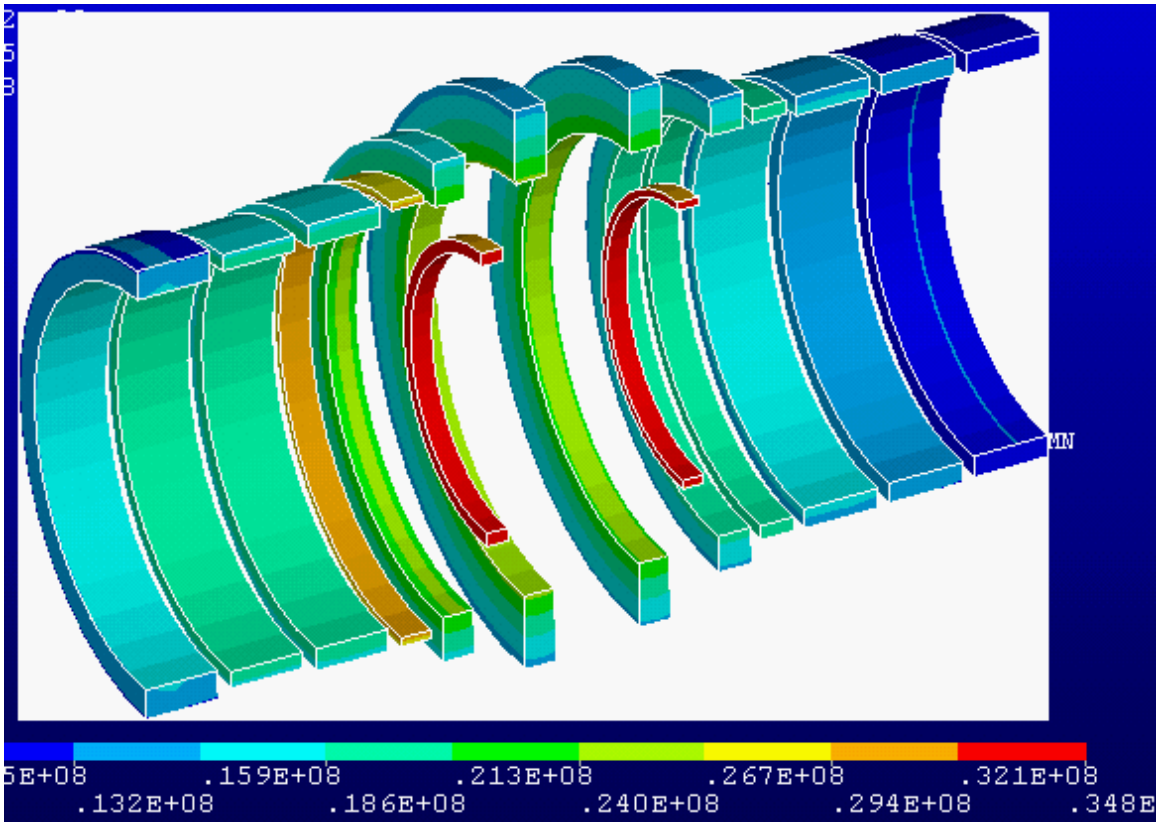

Figure 13.26 – Axisymmetric analysis of the coils near the Be Window. -"smeared" Von Mises stress (no conductor multipliers).

3D structural models

In the 3D model the coil "smeared" Von Mises stress under normal operating conditions (all coils energized) is up around 90 MPa (see Figure 13.27 and Figure 13.28) - exclusive of the local effects near the vertical “Vee” cold mass support, where the local attachment is modeled with less accuracy. The 90 MPa stress is actually present in the coil body near the mid-span support, in the center of Figure 13.28. Stresses elsewhere are actually lower. With the stress multipliers, the copper stress is estimated to be $90 \times 47.1 / 39.2 \times 90 = 108$ MPa. With the additional multiplier for the actual conductor cross-section finally chosen for the TS, the 108 MPa becomes 108×1.38 or 149 MPa (also tabulated in Table 13.1). The conductor Sm allowable is 150 MPa for a freestanding coil, not supported by an external case or mandrel as in the production solenoid. With the exception of the strut attachment locations, the transport solenoid windings have substantial margin.

The off-normal condition of one TS (u or d) on and one off was also evaluated with regard to the coil stress. Stresses for this load condition were found (Figure 13.29) to be somewhat less than normal operating load stresses.

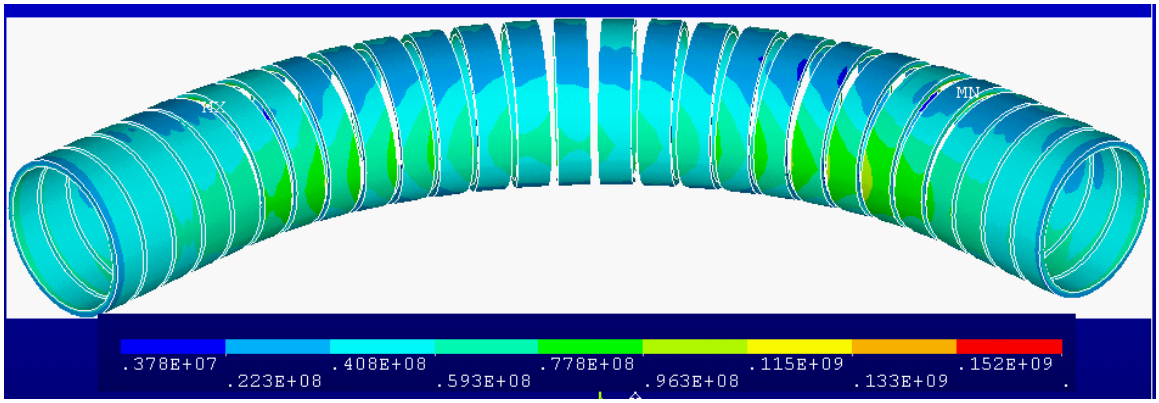

Figure 13.27 – Coil "smeared" Von Mises stress Run#6, no channel reinforcement.

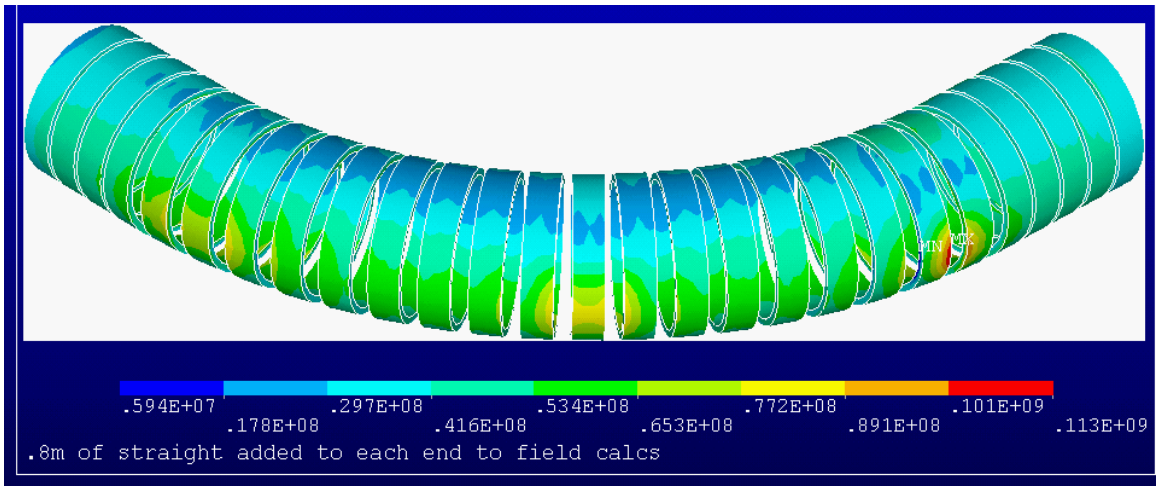

Figure 13.28 – Coil Von Mises stress with the tension-only mid span support. Local coil stresses are less than 113 MPa, peaking where the vertical pair of struts is connected to only one mandrel flange. Stresses are better than for the model below, which does not have the mid-span support.

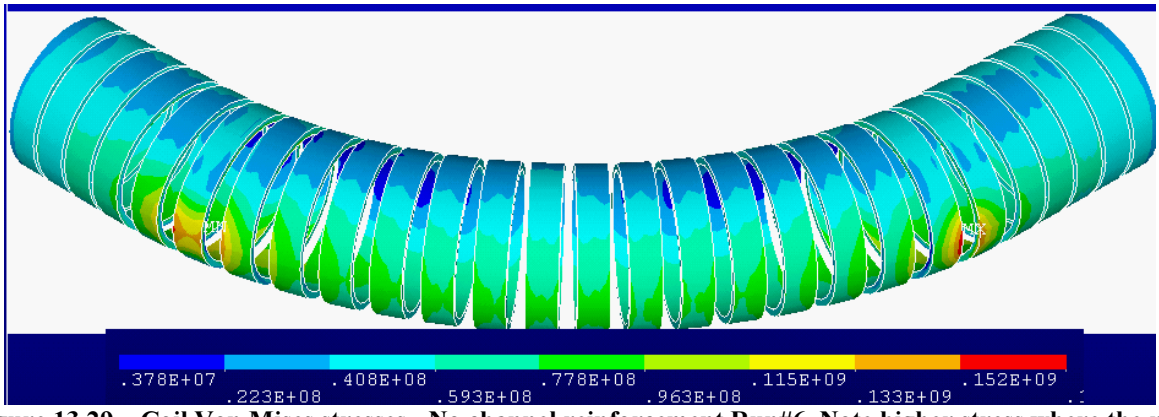

Figure 13.29 – Coil Von Mises stresses - No channel reinforcement Run#6. Note higher stress where the rod pair connects to the mandrel. The red contour ranges from 152 to 170 MPa. This local effect will have to be improved with local gussets, using the channel, or with an additional mid-span support as used in the model on top of the page.

Supports

The support rod arrangement has evolved, with a few different cold mass support concepts considered. The present basis of the design, shown in Figure 13.30, is intended as a minimum constraint strut design, similar in concept to that shown in Figure 13.31. The arrangement is one that has been used frequently for precise positioning of equipment in high energy physics experiments [4]. Two over-constrained arrangements, one involving a midspan “Vee” and another with two end supports, were also investigated, but these put unnecessary cool-down stresses in the mandrel and the coils. The present has one lateral "hard-point" represented by one pair of horizontal angled rods (Figure 13.32). This would be placed at the Beryllium window end of the elbow where axial contraction displacements (along the muon beam line) are to be minimized. A vertical "Vee" is employed to clear the proton beam (Figure 13.33). A midspan radial strut replaces the mid-span "Vee" used in the earlier design. Three smaller vertical gravity support rods are used as well. Figure 13.34 and Figure 13.35 show the rod design concepts that lead to the final conceptual design configuration shown in the drawings.

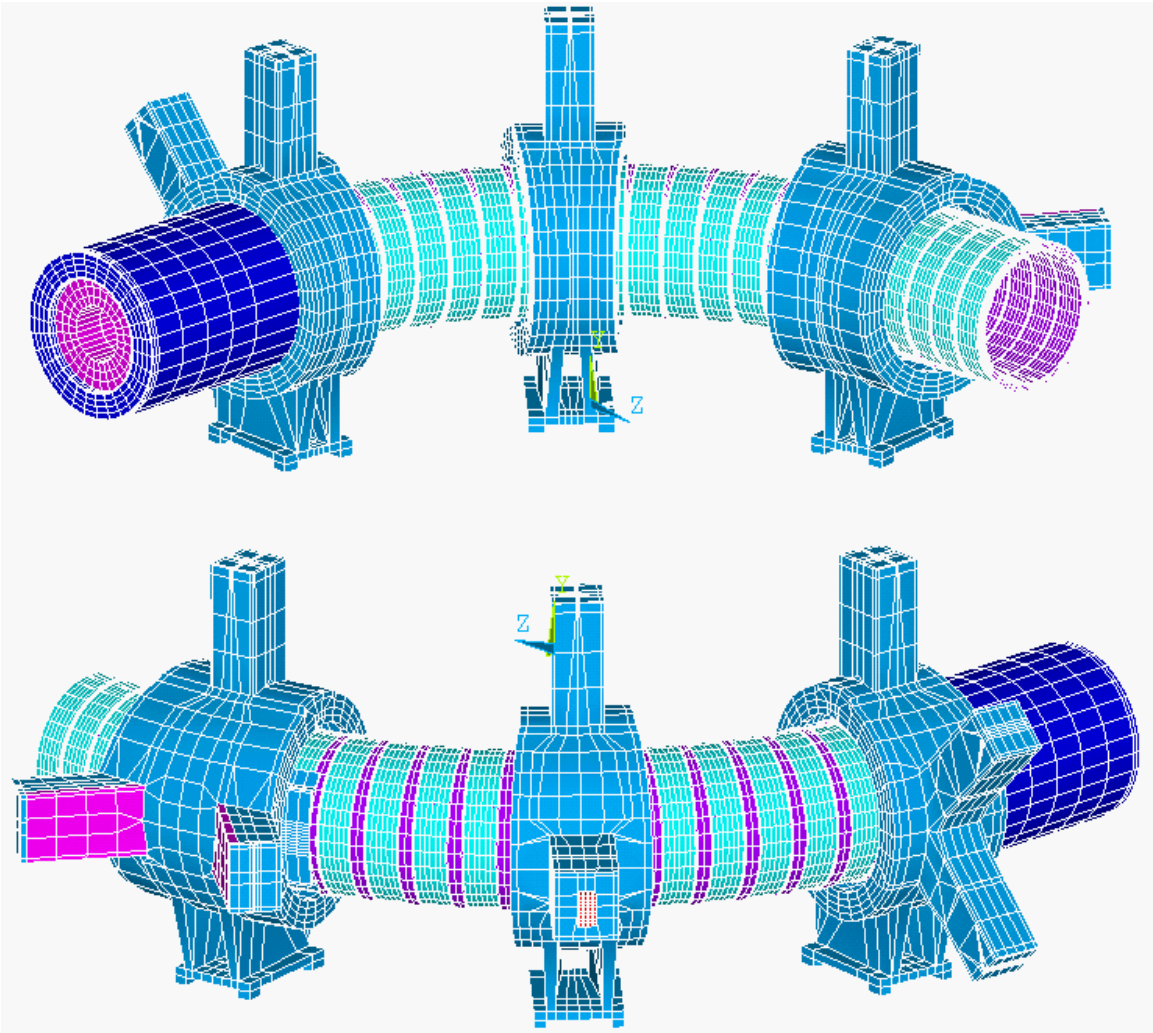

Figure 13.30 – Transport Solenoid structural model shown with some cryostat shells removed, and the "Final" conceptual design for the supports. The horizontal "Vee" is at the beryllium window end of the coil.

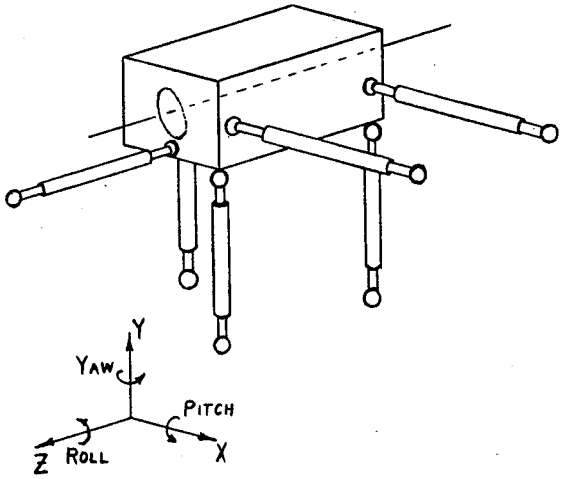

Figure 13.31 – Six struts restrain the six DOF of a rigid body [4]

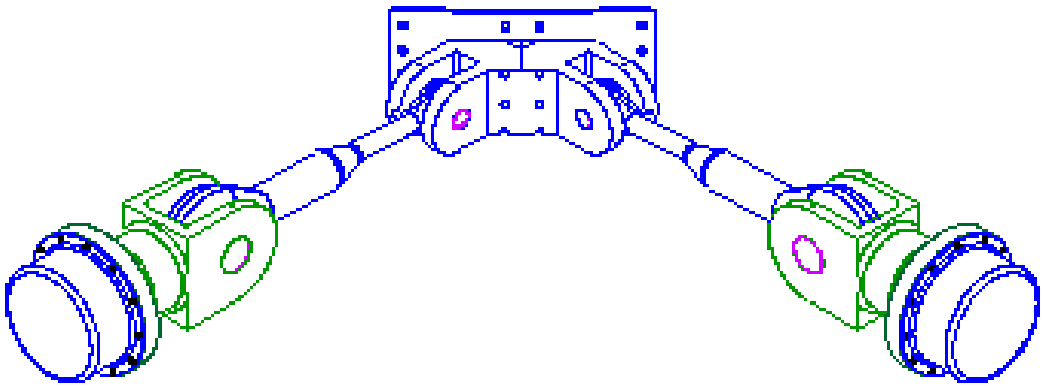

Figure 13.32 – Horizontal "Vee" and clevis support plate.

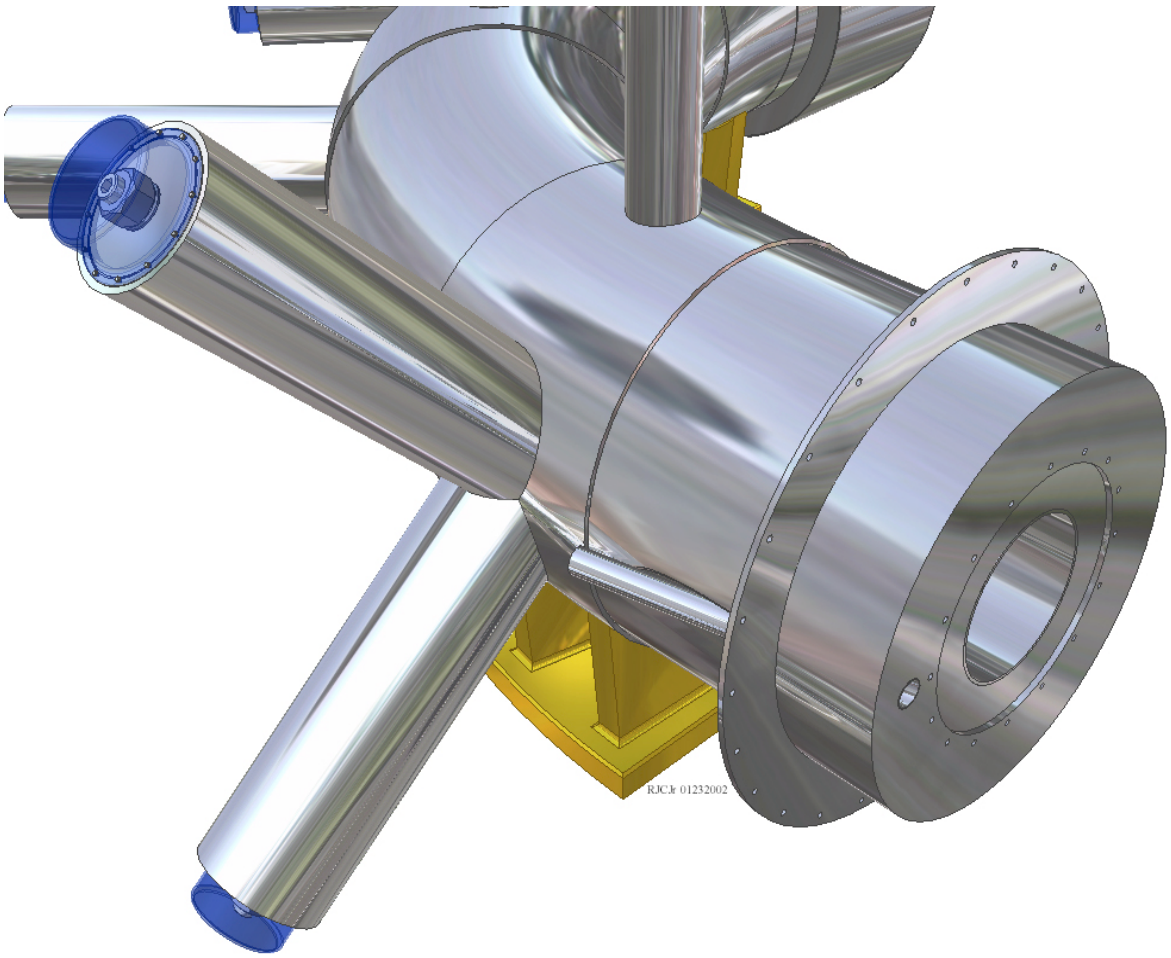

Figure 13.33 – A view of the vertical "vee" support that clears the proton beam. The structural model shown in Figure 13.30 does not include the cryostat outer shell.

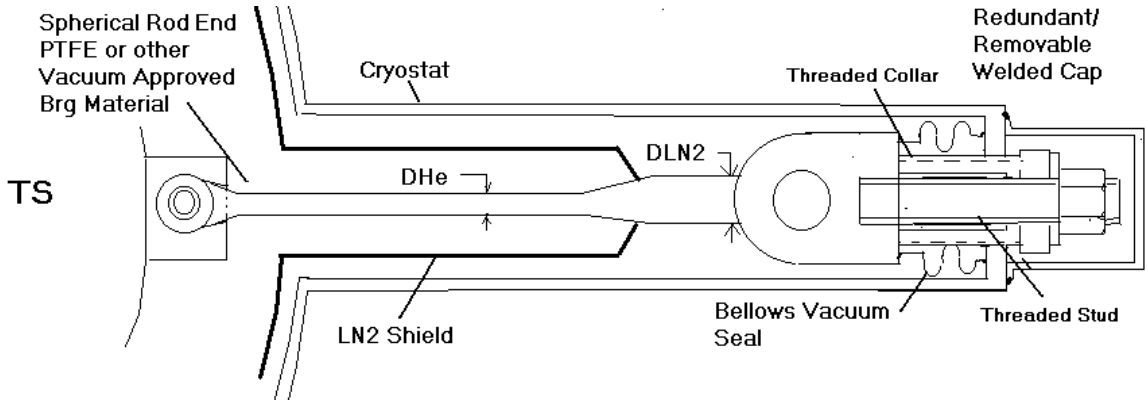

Figure 13.34 – Tension and compression strut concept used in horizontal and vertical "Vee" supports.

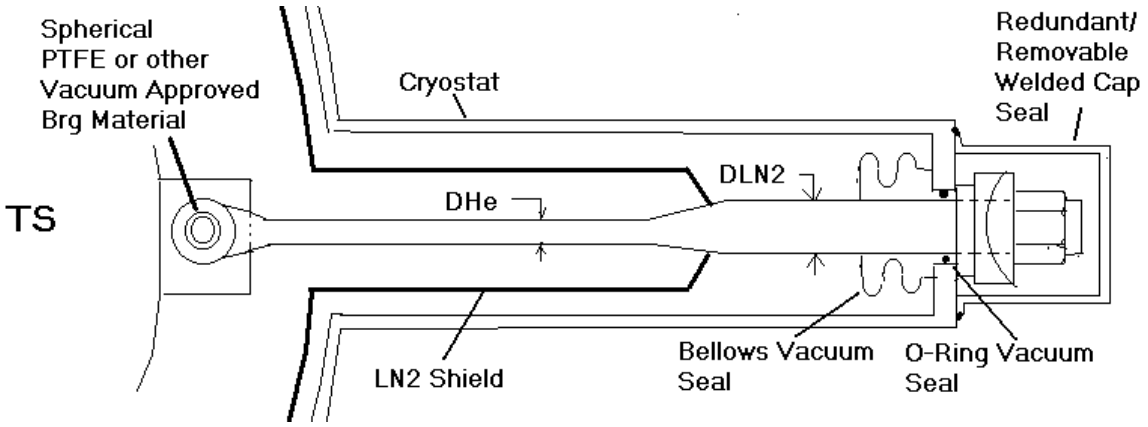

Figure 13.35 – Tension-Only Design - This is the concept proposed for the mid-span support.

Strut Stresses and Design

In the earlier large finite element model of the transport solenoid, the rods are modeled approximately with a strap-like cross section that could represent a rod or a pipe section. It has a cross section of .001197 m^2. The stresses in the rod are about 1.0 GPa, exclusive of the bending stresses. The rod load is then 10^9 (Pa) × 0.001197 (m^2) × 0.2248 (lb/N) = 269,085 lbs. The allowable for 316 at 4 K would be 594 MPa (0.6 × yield) = 86.3 ksi. The room temperature yield is only 275.8 MPa, which yields an allowable of only 24 ksi.

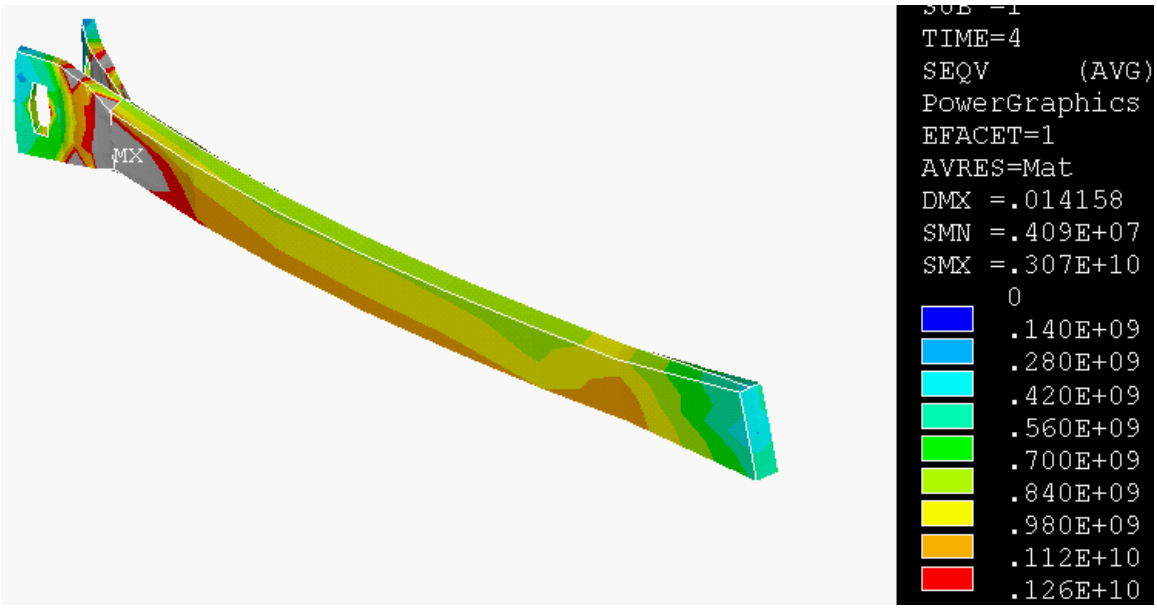

Figure 13.36 – Von Mises Stress in the early model of the strut. Note that the variations in the stress are due to bending. The design of the strut employs spherical rod ends and spherical washers to ensure only direct tension or compression is taken by the rods.

The rod cross section needs to be 269,085 / 86,300 = 3.12 in^2, which implies a diameter of 2.0 in at the 4 K end. The warm end needs to be 4 inches in diameter to satisfy the 24 ksi

allowable. For comparison, the 718 C-Mod drawbar (Figure 13.37) has a minimum rectangular cross section of 3.53×1.88, which for the 500,000 lbs gives a working stress of 75 ksi. The MECO TS strut will be sized assuming 316 SS material. Use of 718 would reduce the required cross sections. A finer model should be created during final design to better account for the full temperature profile along the chosen rod length and reconcile the cross-sections with the stress allowables accordingly.

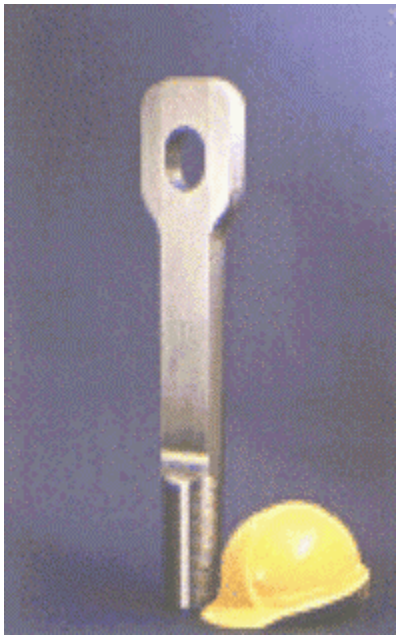

Figure 13.37 – For comparison, C-Mod's Drawbar holds 500,000 lbs - 2000 PSFC web photo.

The TS end supports are adjusted at assembly and after field mapping. The designs allow adjustment, under vacuum, cold, and partially energized. In order to keep the assembly bending stresses under control and allow a manageable number of mandrel bolts, the mid span radial support strut was added. On cool-down a small gap opens under the spherical washer at the warm end of the strut (Figure 13.38). The elbow structure of the TS shrinks to a slightly tighter radius of curvature. With the struts at the ends of the curve and the mid span strut shrinking about the same, the change in radius of curvature produces a slight gap which closes when the coil is energized. Stresses in the horizontal "Vee" are plotted in Figure 13.39 under the condition of normal operating loads. These stresses enabled sizing of the final rods. Note that these normal operating stresses are significantly less than the 1 GPa value discussed earlier for the case of one bent TS section energized and the other not. The horizontal rod attachment plate is bolted to the cold mass at the tapered flanges as shown in Figure 13.40. A copper cooling plate between the attachment plate and the coil flanges is traced with LHe tubing to intercept heat coming from the rods. A stress plot for the mid-span horizontal rod is shown in Figure 13.41. These stresses enabled sizing of the final rods.

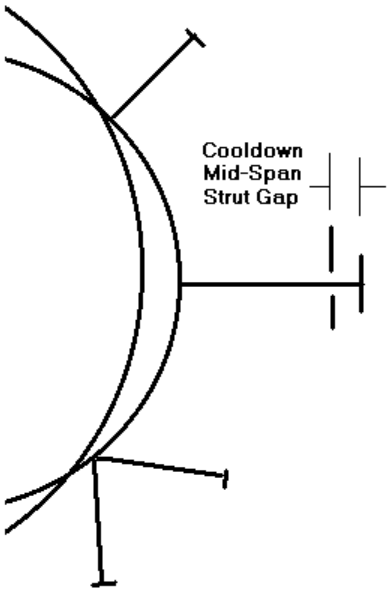

Figure 13.38 – Gap produced in mid-span support strut on cool-down.

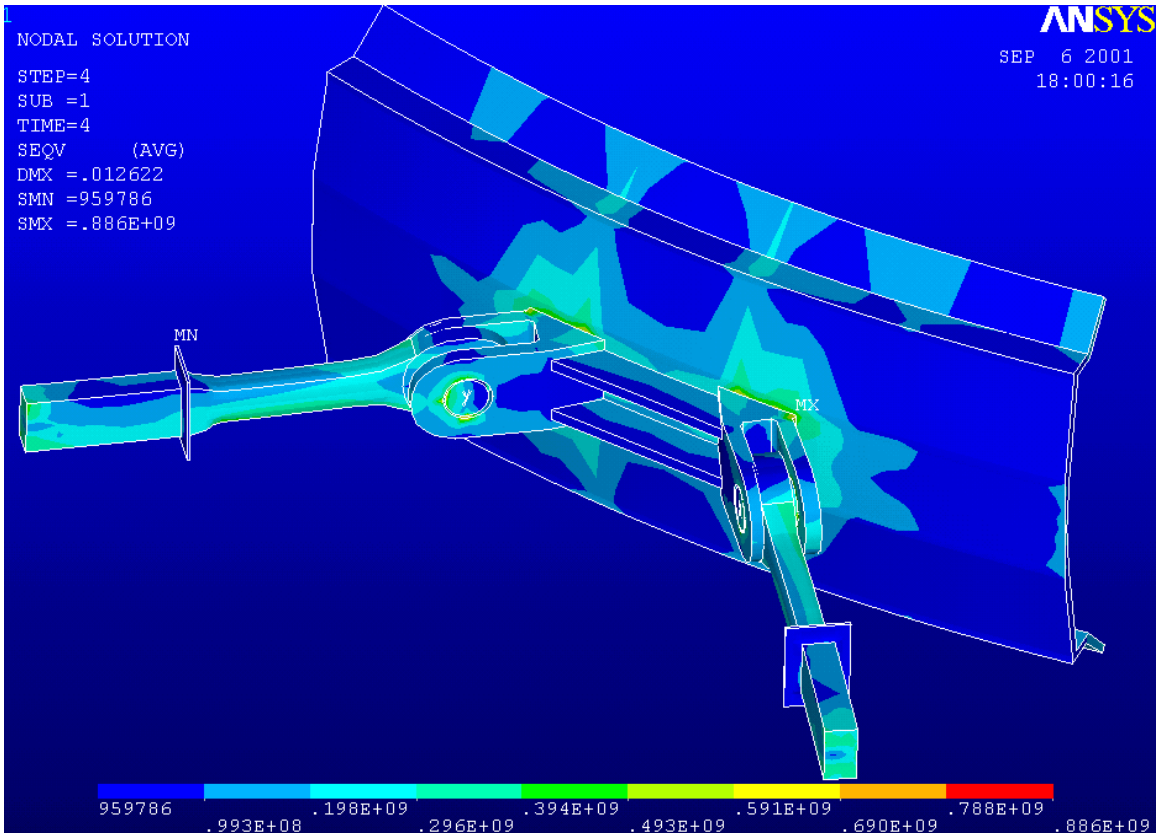

Figure 13.39 – Stresses in the "horizontal Vee" support during normal operating loads.

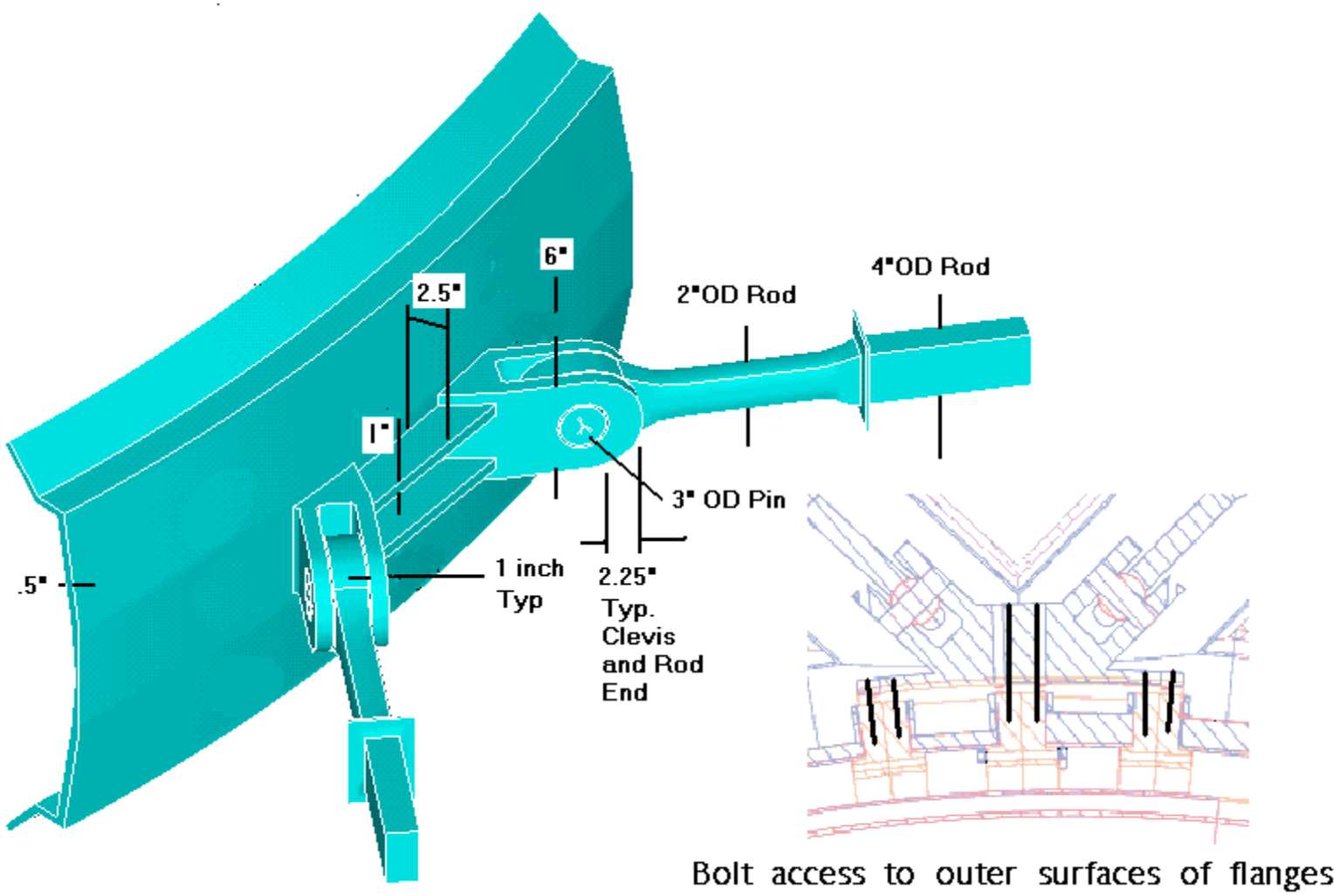

Figure 13.40 – Note that the centerline of the ¾" attachment bolts has been shifted ½ of a mandrel width to eliminate the bolt access problems under the clevis. Also under this plate is a copper plate that serves as the 4K shunt to the LHe piping on top of the coil assembly.

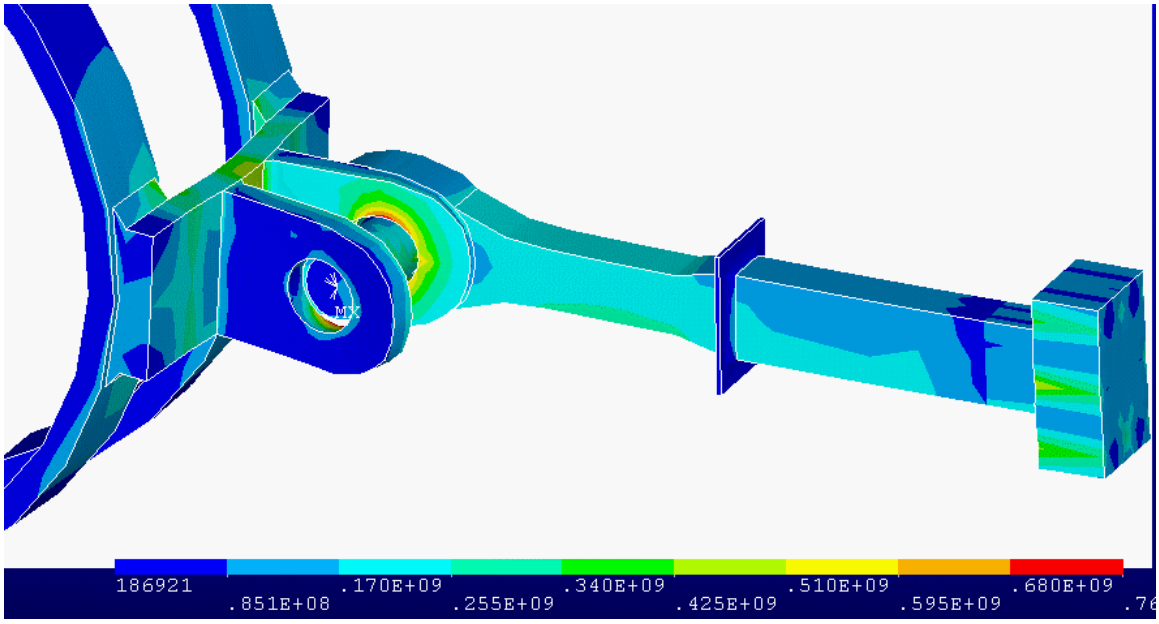

Figure 13.41 – Stresses in the mid-span support rod and clevis details.

There was some concern over the behavior of the LN2 thermal intercept on this large strut. The thickness of the rod is such that the nitrogen temperature might not get beyond the skin at the attachment of the interrupt, and the 2-inch diameter portion of the rod would have higher temperatures than 80K. This could be a problem with the stress allowable for the reduced cross section, or could represent an additional heat leak to the 4K end. A steady state conduction analysis was performed with a stress pass and the thermal differentials applied. An annular box containing LN2 with an immersed internal fin was shown to be a viable method of obtaining the required thermal connection. The diameter transition was made over a length of 2 inches. A load of 400,000 N, or 133% of the expected load, was applied to the strut. The load produces 200 MPa in the smaller diameter portion of the rod. The stress concentration at the diameter transition was small and the thermal stresses are very small. The LN2 temperature penetrates through the rod diameter well, as shown in the temperature plots of Figure 13.42 and Figure 13.43. The details of the optimum sizing and placement of the annulus as well as the coordinated rod diameter transition should be revisited during final design.

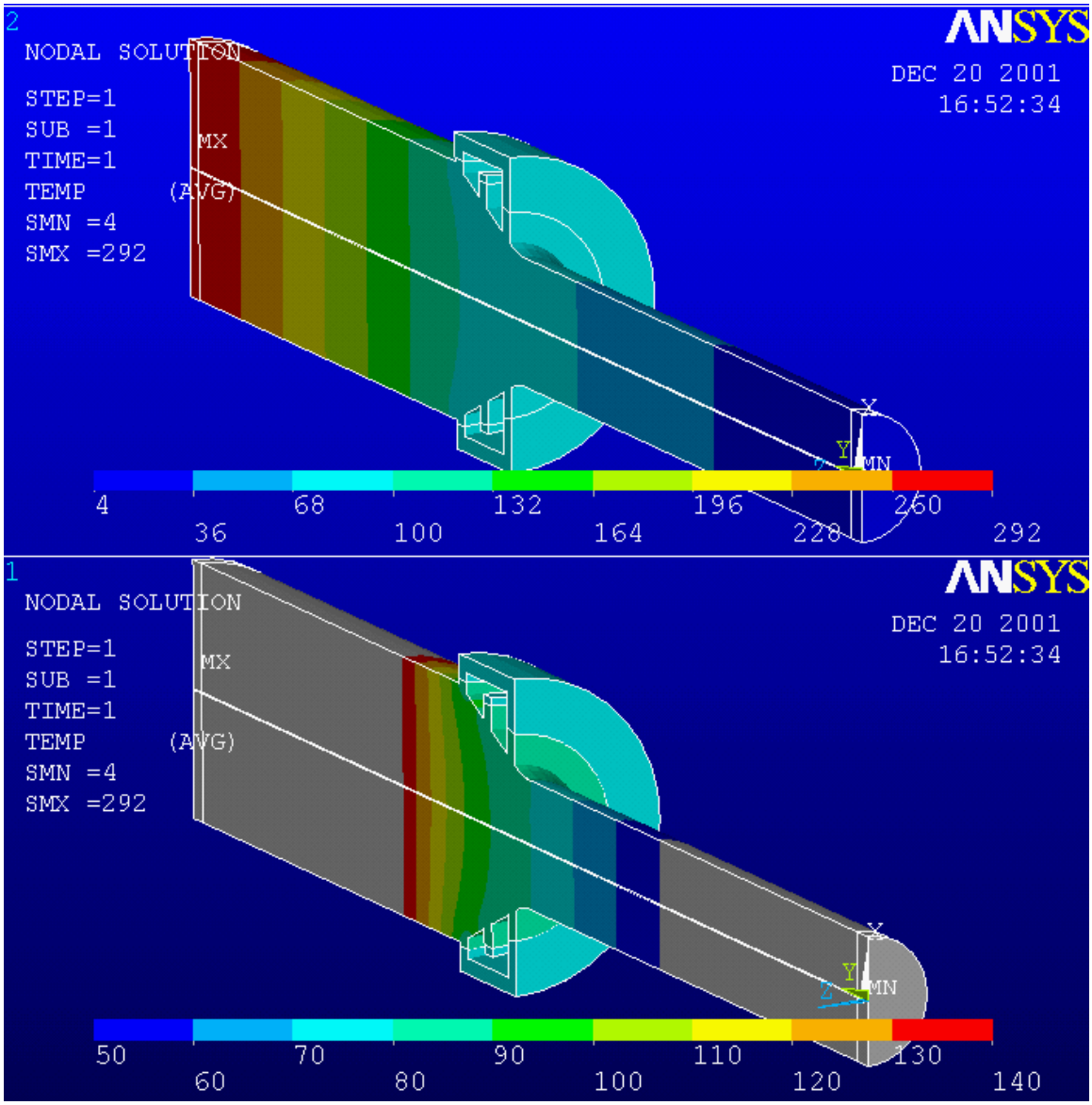

Figure 13.42 – Thermal conduction solution. The concern was that the thickness of the rod was such that the nitrogen temperature would not get beyond the skin and the 2-inch diameter portion of the rod would have higher temperatures than 80 K.

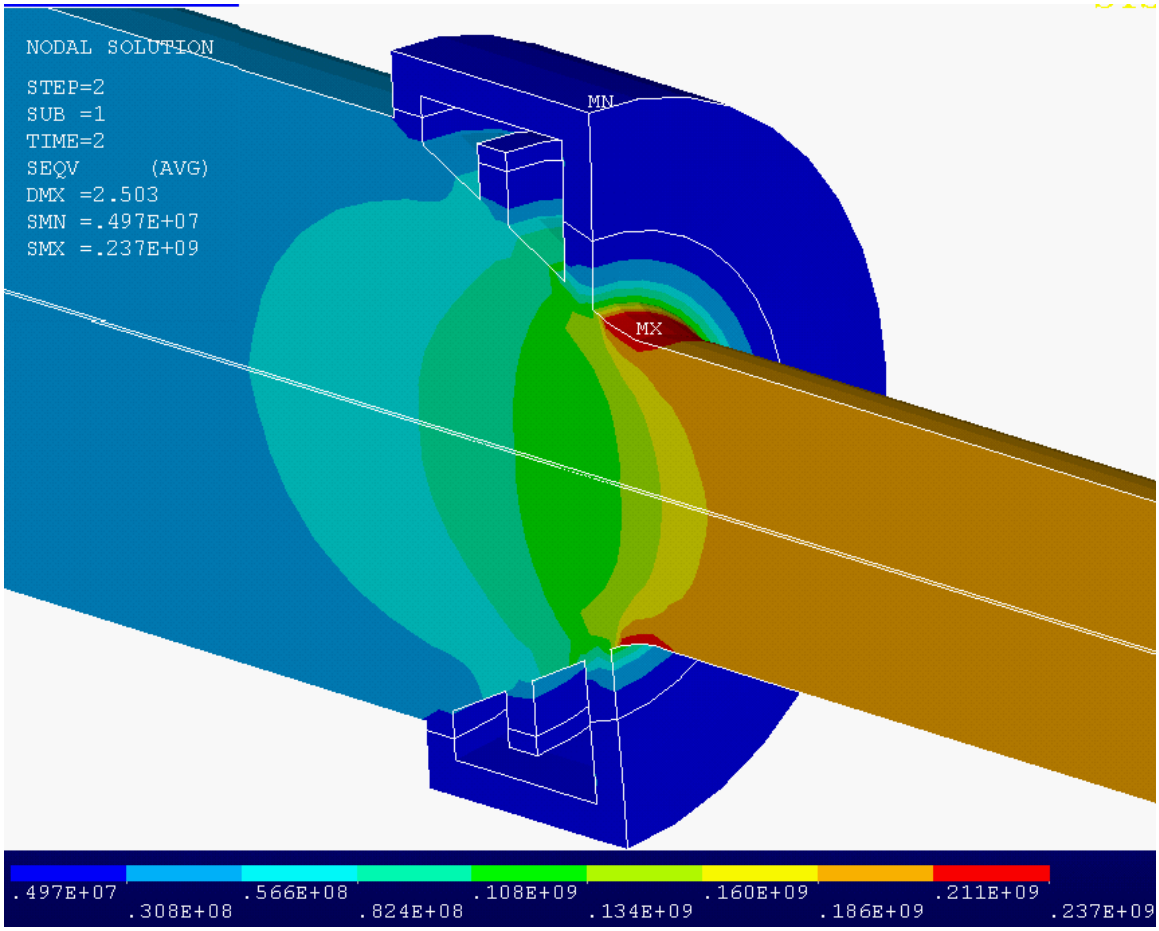

Figure 13.43 – Von Mises stress near the nitrogen intercept. This result includes the effects of the thermal gradient. The brown contour is 200 MPa.

Vertical Support Rods

Three vertical supports are used per TS elbow assembly (Figure 13.30). At the boundary between the production solenoid and the TS, a vertical "Vee" support system is used to allow passage of the proton beam. This "Vee" also supports the coil vertically. A model without a vertical rod at this end was tried with the expectation that the Vee would be sufficient, but because it connects to the TS on the OD of the large elbow formed by the TS magnet array, the “Vee” introduces a rotational moment. The "final" recommendation is to have the vertical "Vee" along with the vertical support rod that is centered on the magnet centerline.

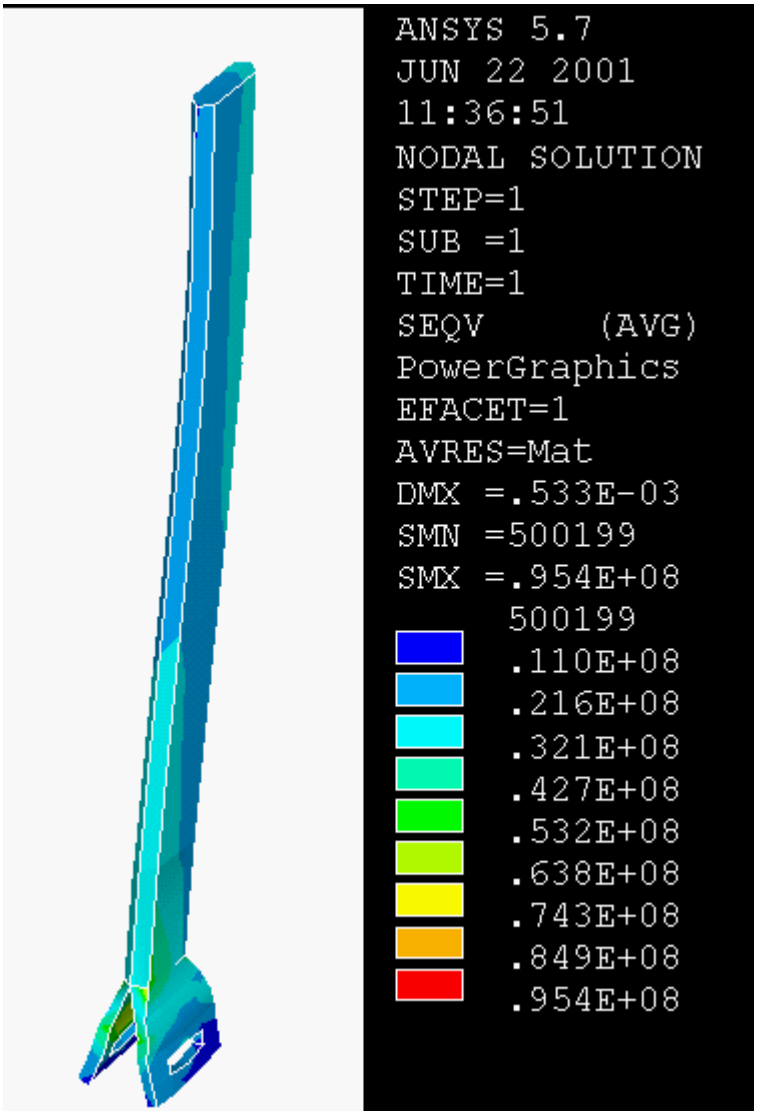

Figure 13.44 – The Vertical Rod is stressed to an average of no more that 40 MPa. The vertical rod load is then $40 \times 10^6 \times 0.001197 \times 0.2248 = 10780$ lbs

The rod cross section needs to be 10,780 / 24,000=0.448 in^2, which yields a diameter of 0.75 to 1.0 inch to satisfy the 24 ksi 316 room temperature allowable, and this is small enough that reducing the diameter for the 4 K portion isn't necessary.

Mandrels

Mandrel Assembly Bolting

Welded joints and combinations of welded and mechanical joints were considered for the assembly of the TS. Use of conduction cooling eliminated the need to integrate a He can with the mandrel structure and eliminated one of the attractions (added strength) of welding the mandrel sections together, a feature of the earlier design. Welding at final assembly, however, introduces a risk of distortion at a point when most of the cost and the critical part of the schedule is at risk. The final choice for the interconnections of the mandrel segments is bolted flanges as shown in Figure 13.45. Bolt loads were large for a configuration where radial support was only provided at the ends, and the final choice employs a horizontal mid-span support (Figure 13.30). This arrangement results in a global axial tensile bending load in the mandrels of 300 MPa, an improvement over the 500 MPa obtained in the earlier approach that employed only the end supports. The reduction of the bending tension improves the stresses related to the off-set loading of the flange in the final configuration (Figure 13.46). An assembly figure showing the integration of the conduction cooling copper shells and flanges is given in Figure 13.47.

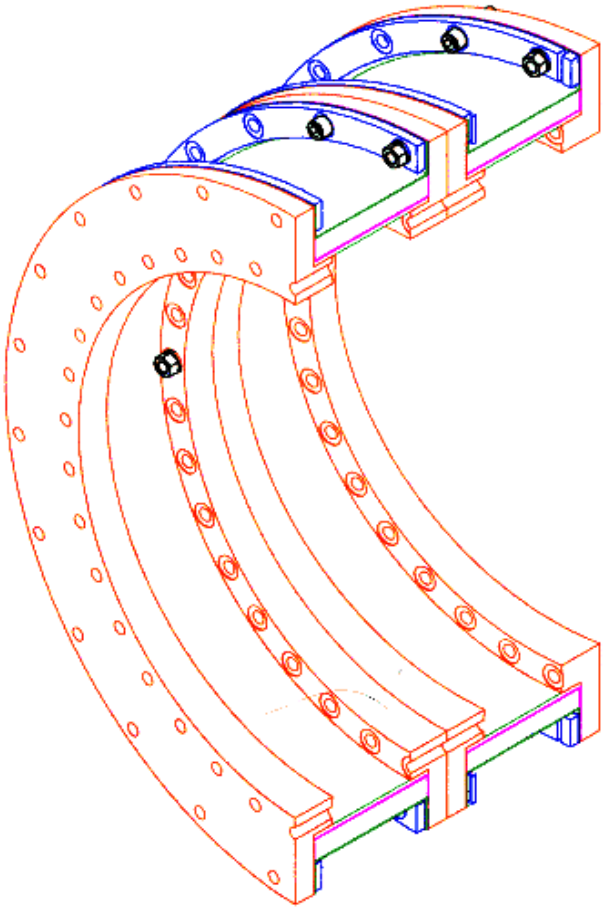

Figure 13.45 – Bolted mandrel design

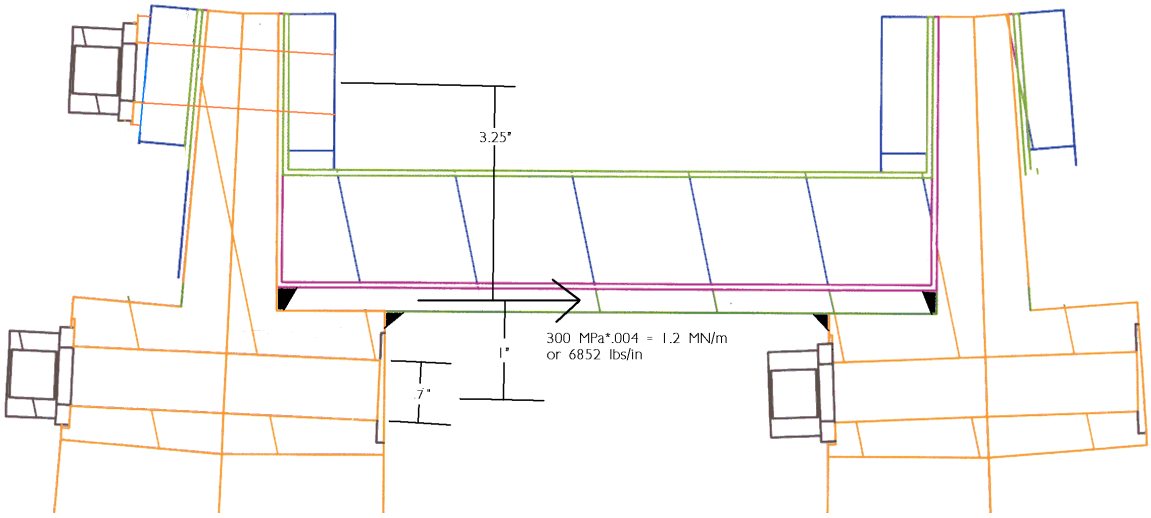

Figure 13.46 - For sizing the bolts, the direct mandrel tension resulting from bending of the TS is assumed to be transmitted directly into the lower flange bolt. For the bolts, this is conservative, The upper flange bolt will contribute some, and will carry the offset moment. This sketch shows the elbow inner radius equatorial plane tensile load.

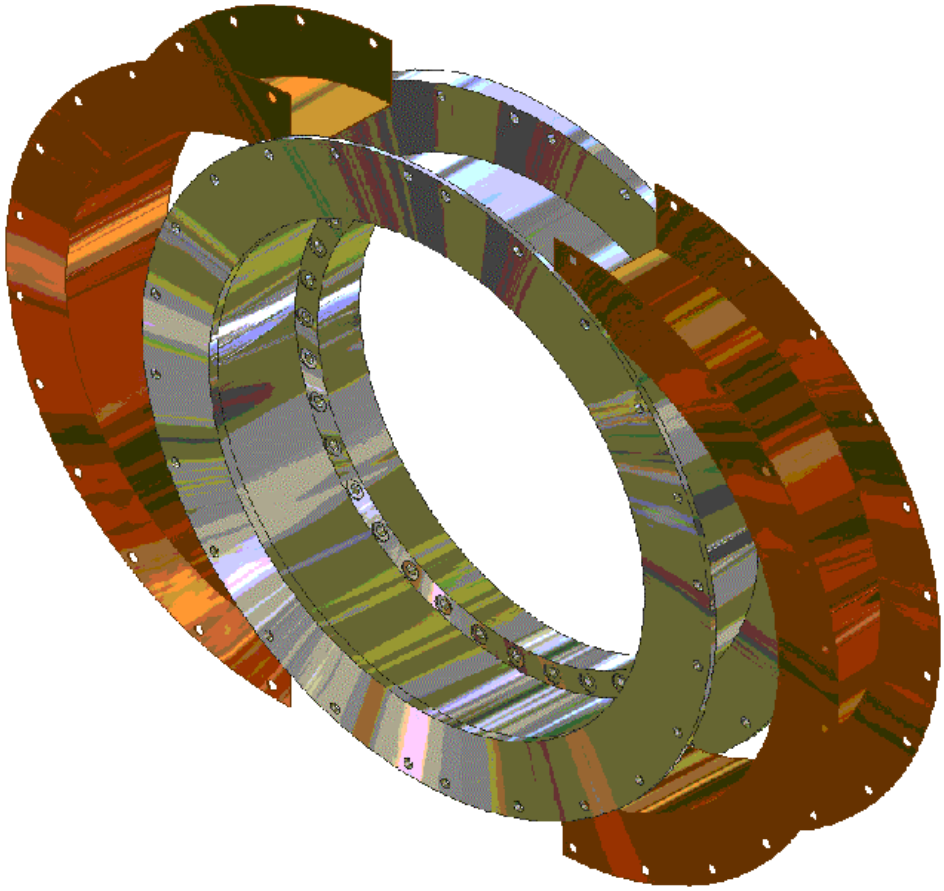

Figure 13.47 - Installing inner copper shells prior to winding. This is a mandrel at the curve/straight transition

The mandrel shell is 1/4 inch or 6.3mm thick, and the flanges are 10 mm. The black areas are the proposed welds. In order to obtain the full mechanical advantage of the rings, the bolts

should be as close to the mandrel shell as possible. Simple hand calculations indicated that the bolt off-set moment is unacceptable for the 1 cm thick side flange without reinforcement.

$$\sigma_b = 6852 \times 1.0" \times 6 / (0.01 \times 39.36)^2 = 265 \text{ ksi}$$

The 1 cm flange requires reinforcement at the bolting location. This was done by thickening the flange where the bolts pass through the flange (Figure 13.45). As implied above, the direct tension transferred from the mandrel inner shell to the bolted flanges is quite large. To make the spacing and bolt head diameter reasonable, high strength bolts with cryogenic working stress capabilities of 100 ksi are needed. INCONEL 718 is acceptable for cryogenic operation and would have the required strength.

Because of the lower bending stress for the final arrangement using the center support (300 MPa shell tension stress), 5/8 inch 718 bolts on 2.5 inch spacing are proposed, although other options (Table 13.8) are possible. The differential contraction of the TS support bolts for 718-316 is 1.75×10^{-6} which would cause a 3 inch long bolt to differentially "expand" 0.0015", corresponding to about 100 MPa or 15 ksi loss of bolt preload, which is acceptable. The larger load carrying capacity of 718 is recommended, but 316 is cheaper, and can be considered in the detailed design phase. The stress analyses leading to the final bolting arrangement of Figure 13.46 is given in Figure 13.48 and Figure 13.49.

Table 13.8 - Possible Bolting Options and Stresses

Bolt Diameter (in)	Stress Area (in^2)	Spacing (in)	Bolt Tensile Stress (ksi)
0.5	0.1416	1.5	120
0.625	0.2256	2	101
0.625	0.2256	1.75	88
0.75	0.334	2	68

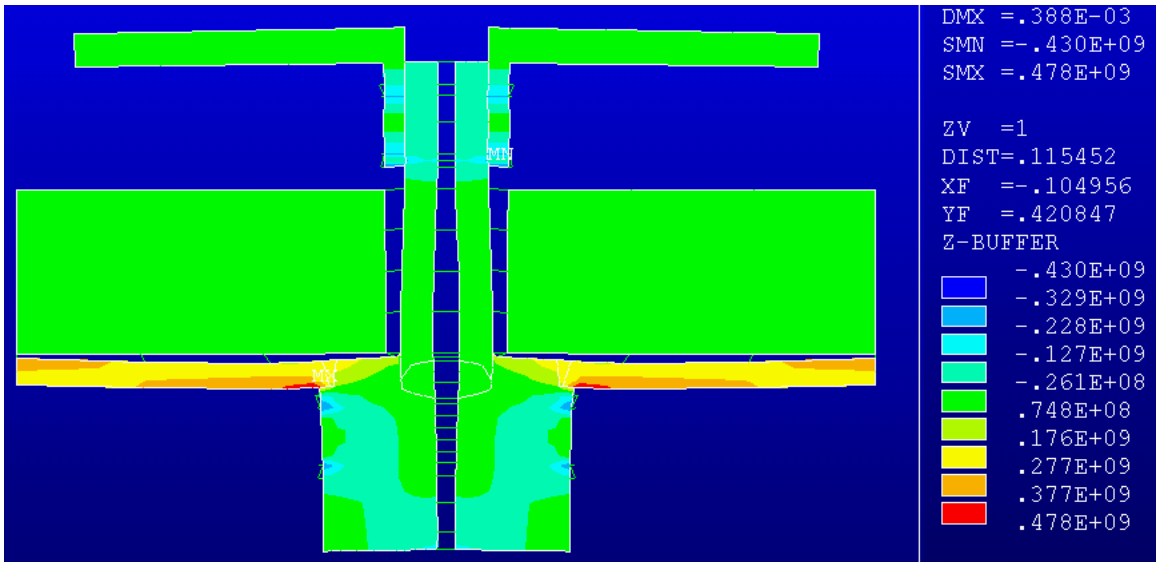

Figure 13.48 – The bolts have been removed from this model to show the prying action - the large gap in the flange-to-flange "contact" results from an interference used to preload the bolts.

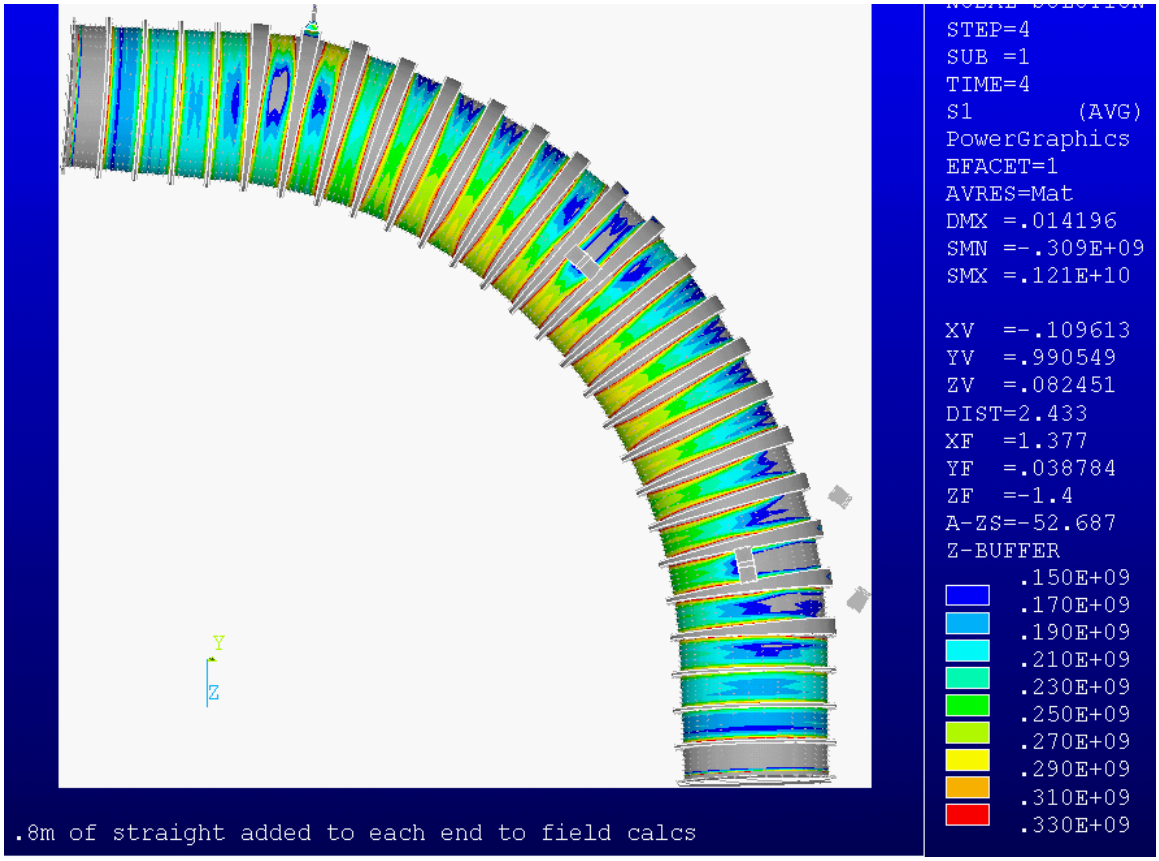

Figure 13.49 – Maximum principal tensile stress - Bolting on the "blue side" can have twice the spacing.

Other Analyses Using the Large 3D Model

This section briefly summarizes some of the other analyses and results from the 3D model. Although these are not design drivers, they are included for completeness.

Dead weight

Mandrel stresses resulting from deadweight alone were found to be small (Figure 13.50).

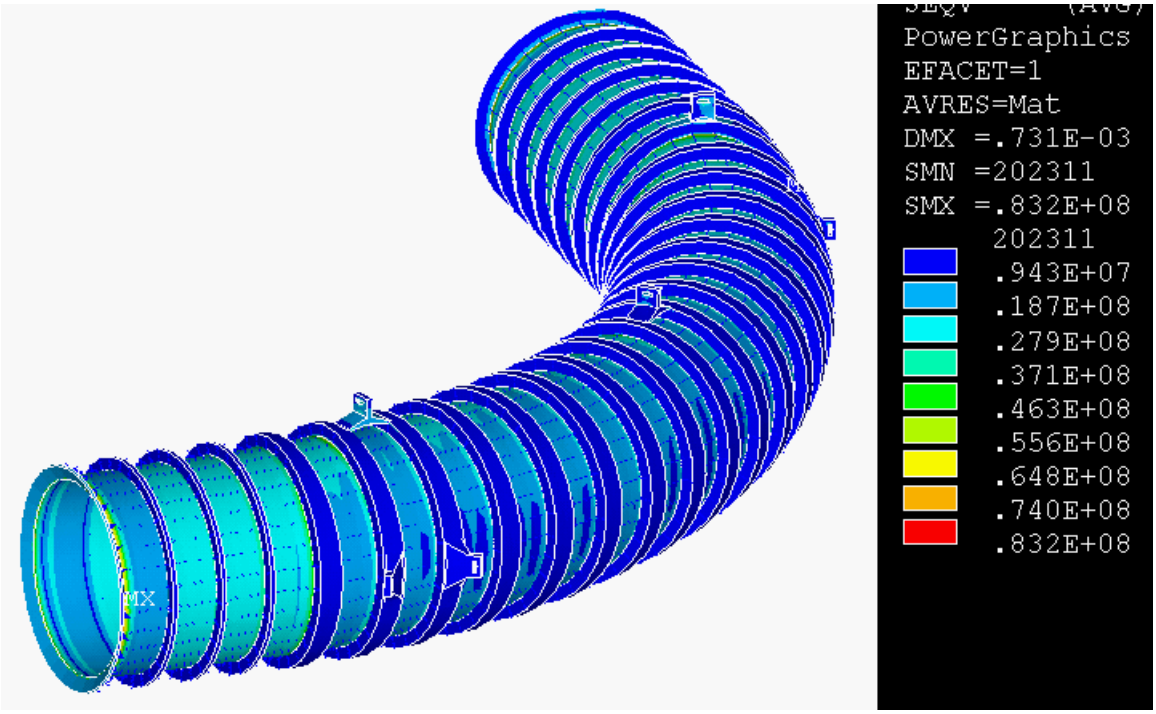

Figure 13.50 – Mandrel stresses, deadweight only

Cooldown

Mandrel stresses resulting from the combination of dead weight and cooldown are shown in Figure 13.51. These are also small.

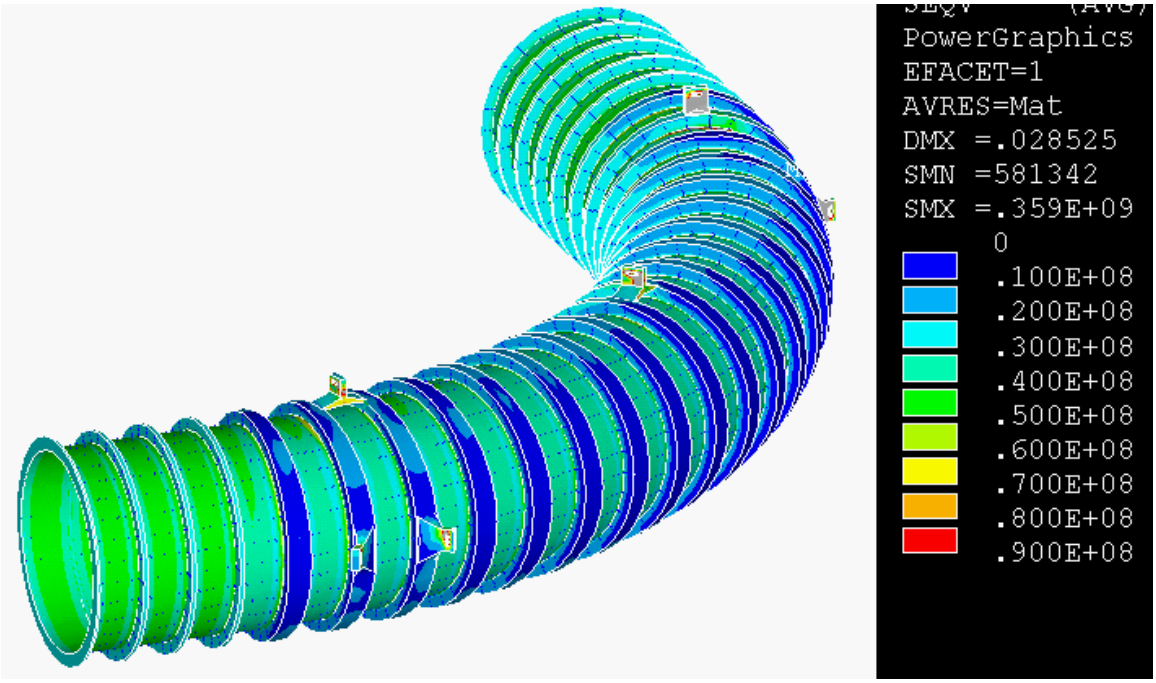

Figure 13.51 – Cooldown Von Mises Stresses in the Mandrel. Some of the mandrel stress shown here results from an interference artificially imposed between the coil and mandrel to numerically stabilize the model.

Support Cases/Cryostat and Collimator

The normal loading on the TS cryostat is a vacuum. The inner shell also provides the vacuum for the experimental volume, so, the inner shell's normal operating pressure differential is zero. Other pressure combinations are possible. The experimental volume can be brought to atmospheric pressure with the cryostat vacuum maintained. Based on operating experience with these types of systems, when the magnet is allowed to come up to room temperature, cold condensed gases evaporate and can pressurize the cryostat. This is expected to be no more than an atmosphere, making the pressure differential zero, except if the bore experimental volume is under vacuum, in which case the inner shell is loaded in compression.

The collimator and its dead load has been included in Run #6 of the large model of the magnet assembly, but no pressure loading was applied. In a new model the cantilevered portion of the cryostat is 1 cm thick, and the end ring is 5 cm thick (Figure 13.52). The vertical displacement is 0.3 mm at the end of the collimator under deadweight. The model does not include the full length of the inner cryostat wall, and the support from this will reduce the collimator displacement for the collimators at the PS and DS ends (The 1 cm thick cryostat end cap required at the Be window is discussed in the next paragraph). The peak von Mises stress in

the outer cryostat wall was solved (Figure 13.53) with strain compatibility with the frame (Figure 13.54) and found to be about 200 MPa, which is well within the allowable.

Spatial constraints at the Be window require that these cryostat end caps be only 1 cm thick. The constraint results from a combination of the simultaneous needs to preserve the 7.5 cm clearance between the TSu and TSd end caps and to meet field requirements in the region. The full cryostat bore tube was modeled to calculate the stresses in this 1 cm thick end cap (Figure 13.55 and Figure 13.56). The 1 cm thick annular diaphragm probably could not support the collimator as a cantilever, but with the bore tube acting as a beam and torque tube, the 1 cm thick end cap sees only about 54 MPa Von Mises stress (Figure 13.57). Displacements for this case are plotted in Figure 13.58, where the peak displacement of the bore tube is shown to be about 1.4 mm at mid-span.

To qualify the bore tube for the unlikely, but possible external pressure case, the model was run with 5 atmospheres external pressure and a large displacement solution, and the 1 cm diaphragm stress went up to 135 MPa, still below yield, and the model exhibited no tendency for instabilities. The model that gave these results is identical to the one shown in Figure 13.55, but with the increased pressure loading.

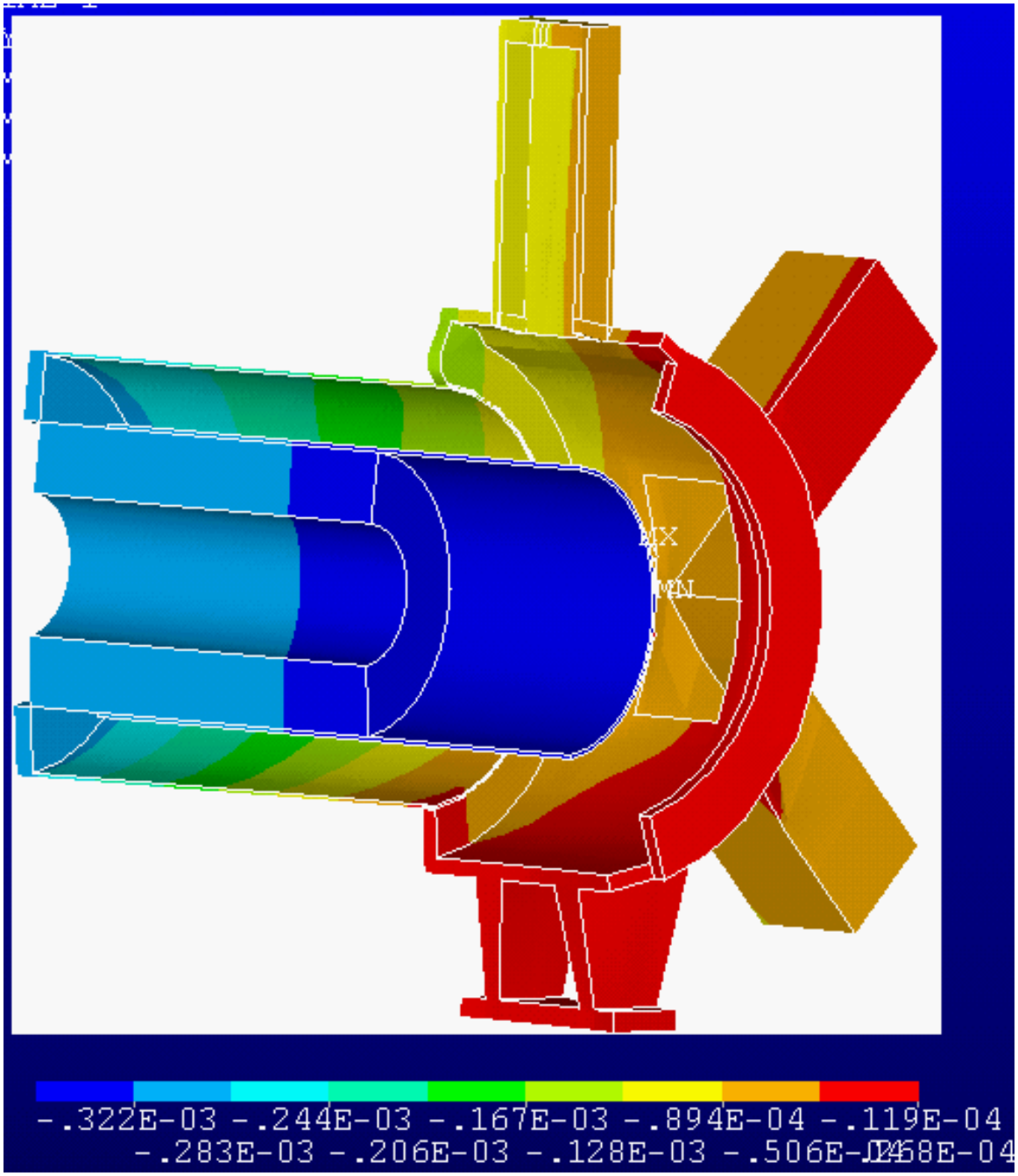

Figure 13.52 – Vertical displacements of the collimator. Sag at the collimator end is about 1/3 mm. This appears to be small but the inner cryostat shell will have to carry it's own deadweight and that of the collimator, with only support at it's ends. The model with the full bore tube and collimators at each end produced sag of 1.4 mm

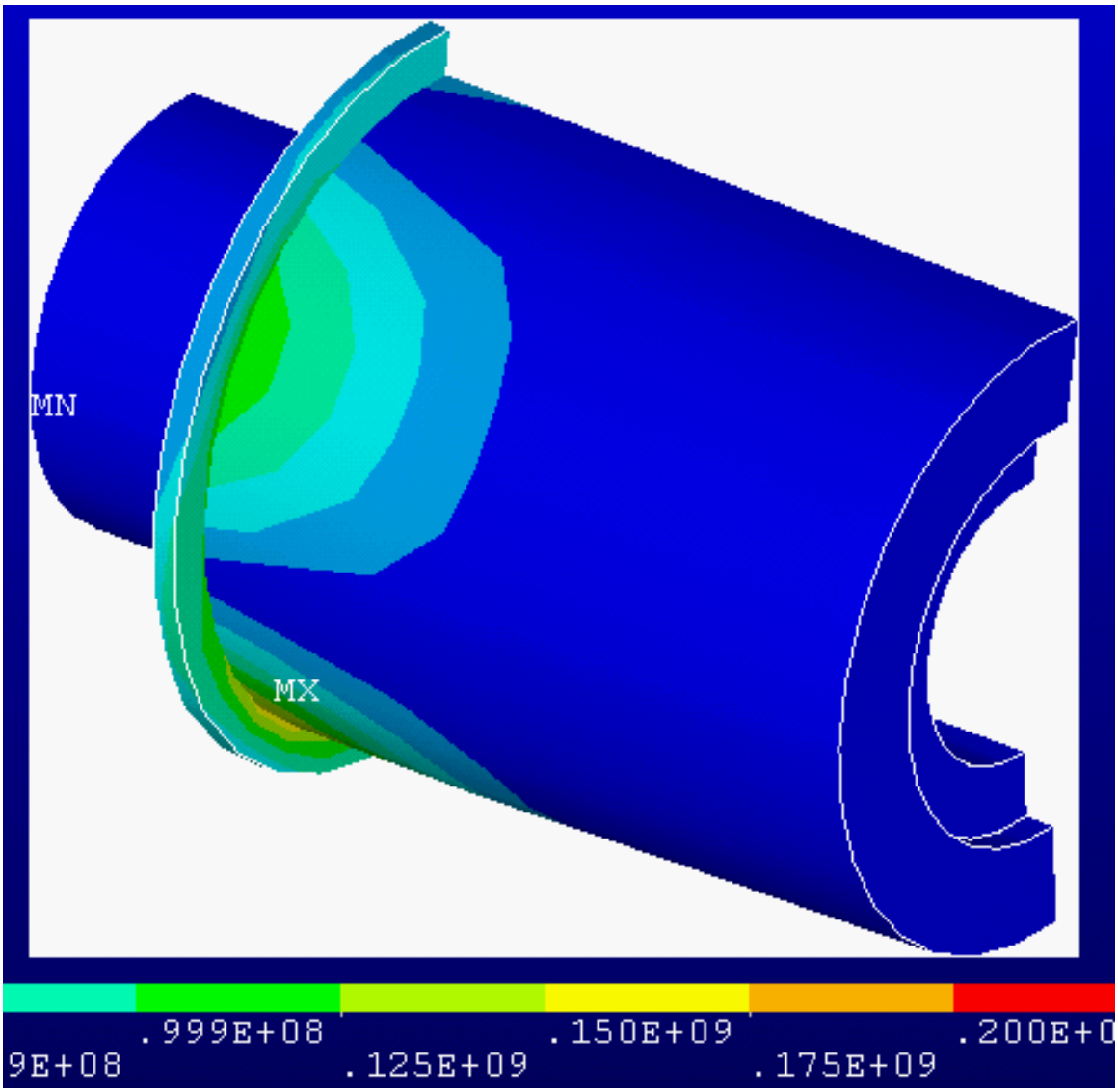

Figure 13.53 – Von Mises in the cryostat with the collimator loading ~200 MPa peak, and results from strain compatible stresses from the frame (Figure 13.54). The outer shell is modeled as 1 cm thick, or twice as thick as those sections of the outer cryostat that connect the support frames. The annular end plate at the right in this plot is 5 cm thick, and even though it is lightly stressed, it needs to be stiff to resist the collimator rotations.

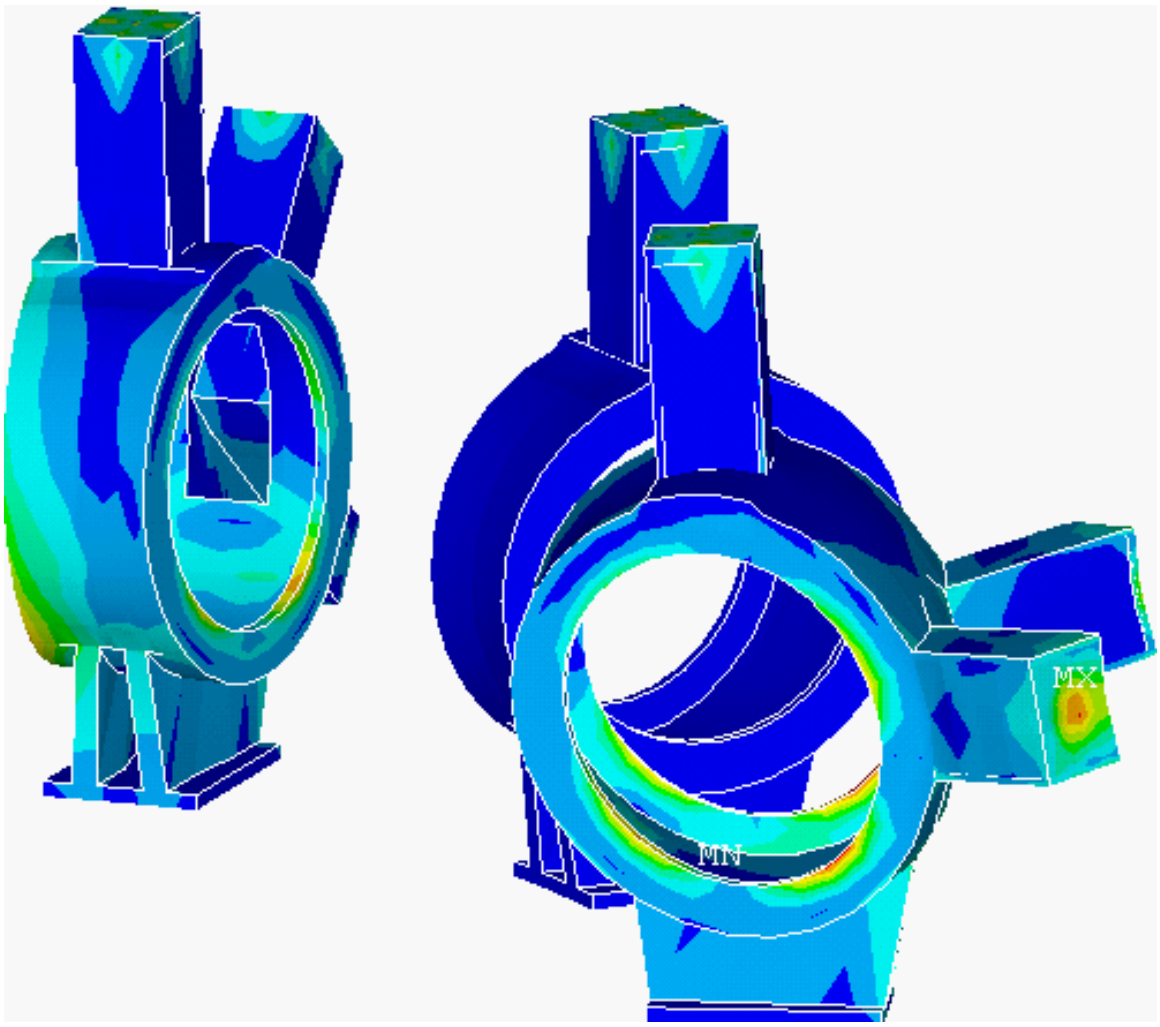

Figure 13.54 – TS support frame stress, normal operating loading. In this plot, the red contour is 360 MPa, the yellow contour is 240 MPa. The plate thickness used in this model is 2 cm. Rigidity is required of these frames as much as adequate stress. The lower support baseplate is 1 m below the beam centerline.

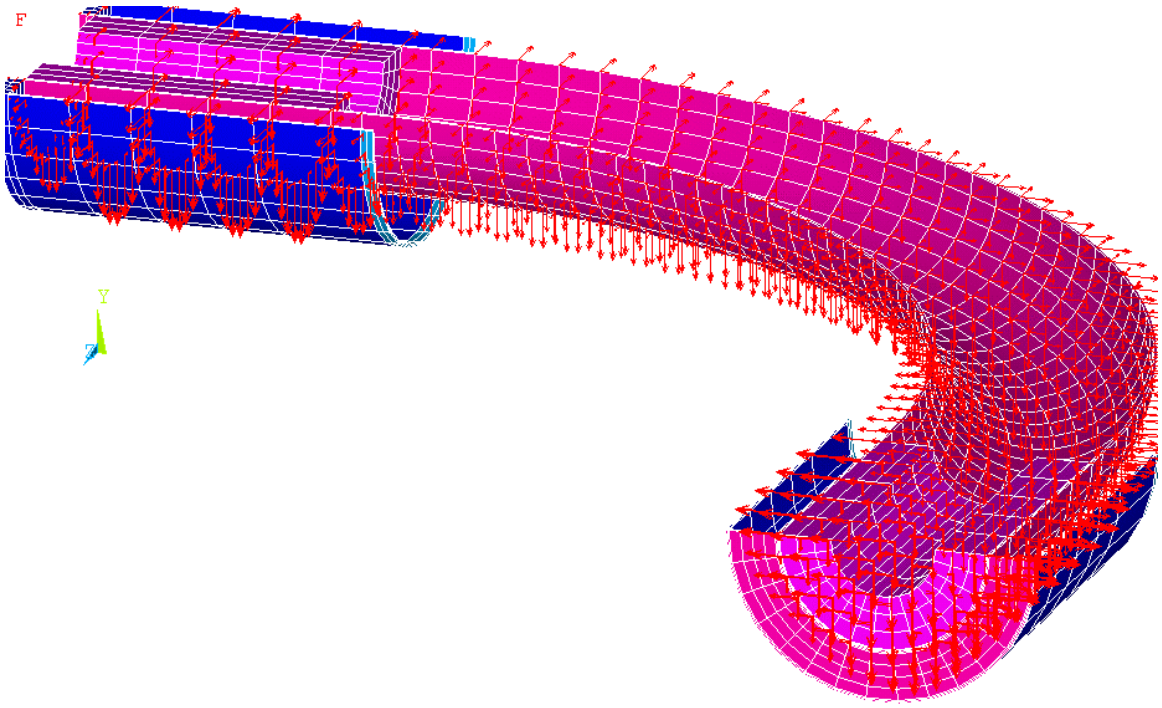

Figure 13.55 – Model of inner bore tube and collimators, supported by the outer cryostat extensions – lower half of model with pressure vectors.

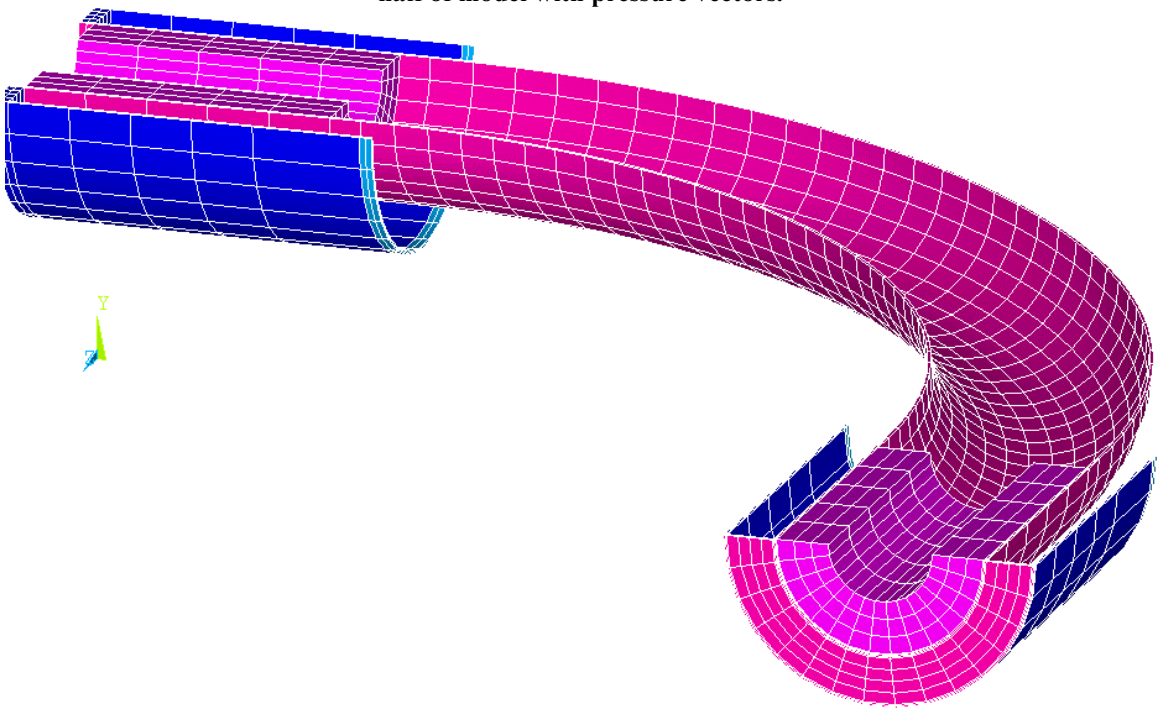

Figure 13.56 – Model of inner bore tube and collimators, supported by the outer cryostat extensions – lower half of model.

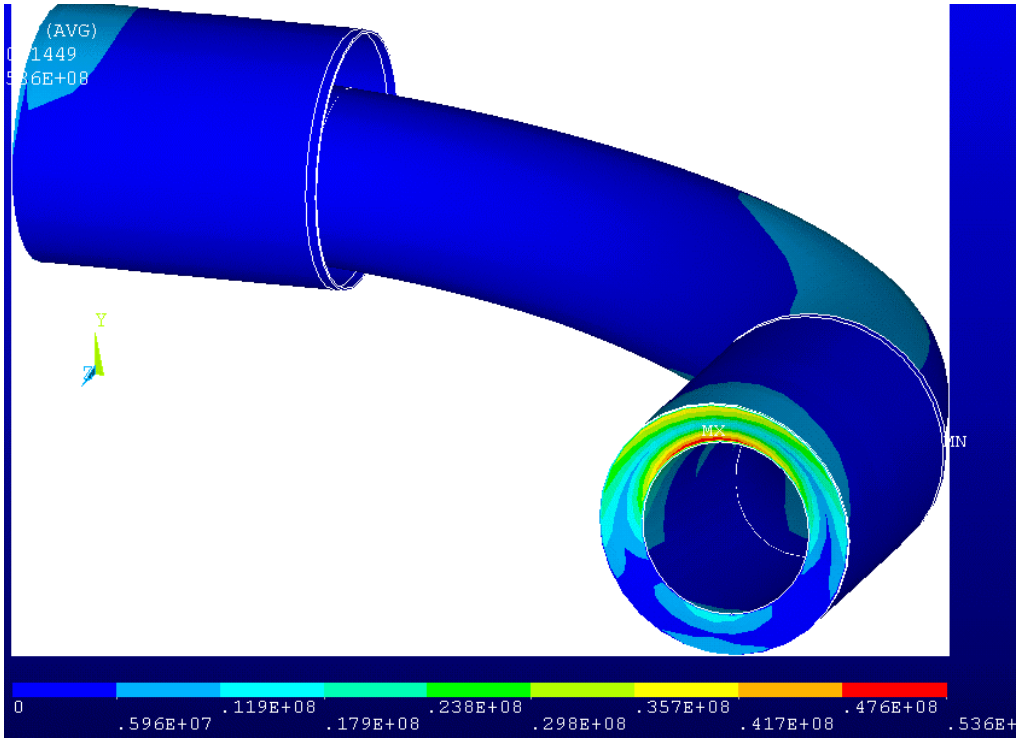

Figure 13.57 - Von Mises stress in the 1 cm thick cryostat end cap at the Be window end. The model is evaluating the impact of the collimator loads on the end cap with the effect of the curved bore tube included.

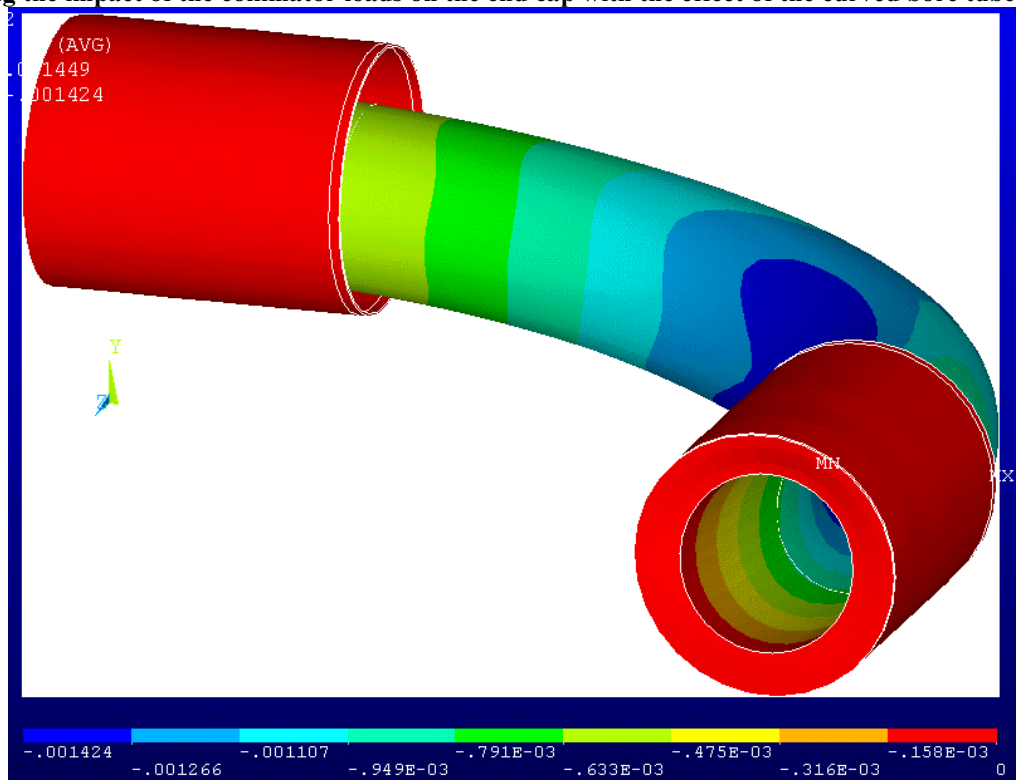

Figure 13.58 – Vertical displacements of the inner bore tube under its own deadweight and that of the collimators at each end. The collimators are shown removed for clarity.

The shell segments between the support frames were analyzed for buckling against external pressure. The eigenvalue solution for the 5 mm thick shell yielded load factors of 13 in order to produce the onset of buckling. In reality, 1/4 inch thick plate is probably a minimum for handling and welding to the heavy support frames. The first mode buckling shape is shown in Figure 13.59, and the large displacement analysis results for five atmospheres external pressure is shown in Figure 13.60. The solution was stable and stresses were only 58 MPa for this over-loaded case.

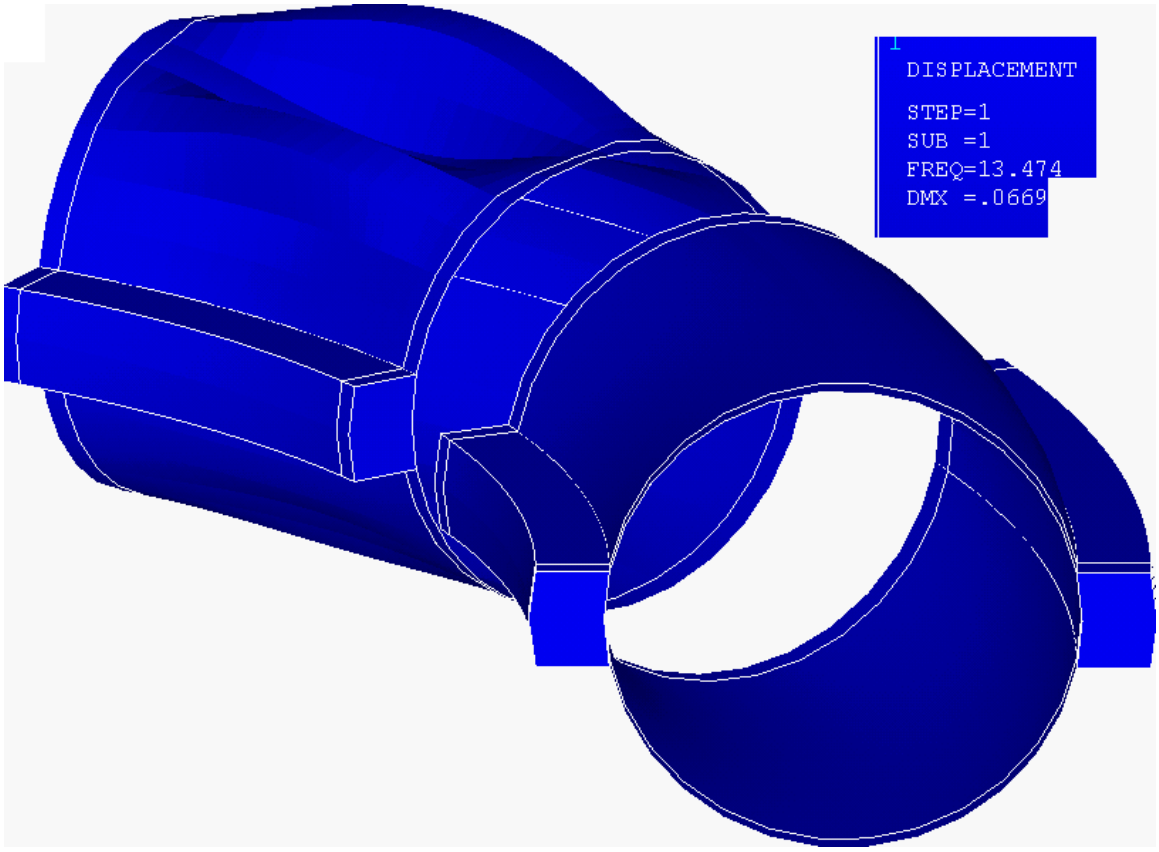

Figure 13.59 – The first buckling mode shape. TS outer cryostat sections.

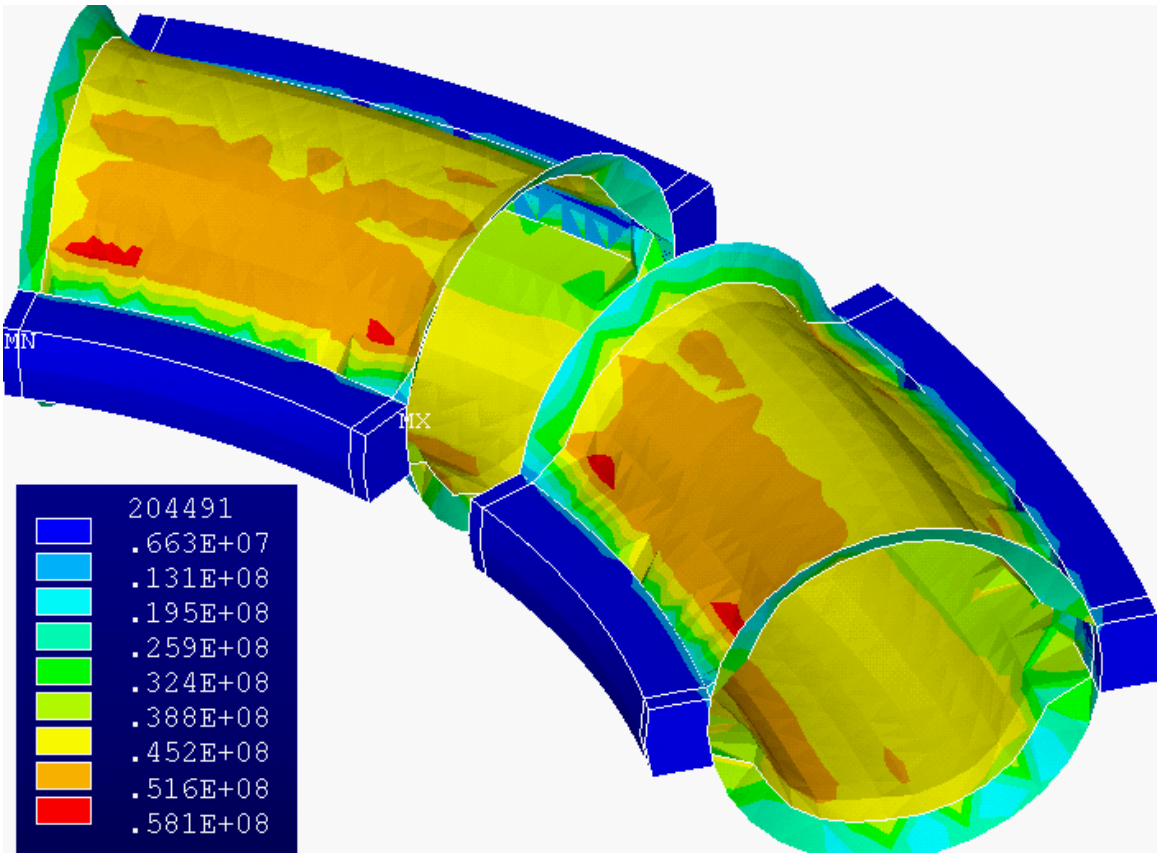

Figure 13.60 – Von Mises Stress, large displacement solution. Five atmospheres external pressure. 5mm shell.

References

[1] Coil Sizing Preliminary Results. A.L. Radovinsky MECO-MIT- A.L. Radovinsky-052501-01 May 25, 2001

[2] Email To: Bradford Smith From: W. Molzon, Monday, April 02, 2001 8:10 Subject: heat and radiation loading

[3] Production Solenoid Coil, Cryostat and Support Stress Analysis. July 12 2001 MECO-MIT-PHTitus-071201-02

[4] "Rigid, Adjustable Support of Aligned Elements Via Six Struts", W.Thur, et.al LBNL, Berkley Ca October 1997

[5] Coil builds from MECO-MIT. A.L. Radovinsky-101701-01

Section 14 - Analysis of the Detector Solenoid Mandrel, Winding and Supports

Introduction

The detector solenoid (DS) is the least loaded magnet of the MECO experiment. The full DS coil with its iron return frame, that forms part of the cosmic ray shield, is shown in Figure 14.1. The peak axial field (on axis) is 2 T vs. 5 T for the production solenoid. The coils are free standing with respect to hoop loading, and are restrained axially by the coil winding mandrels. 23 individual coils make up the detector solenoid. The winding mandrels have flanges that are bolted together to form the global structure. Figure 14.2 shows the Lorentz force distribution for a 22 coil set. Since these analyses, DS1, the coil at the left of the figure has been split into two coils to improve quench stress behavior. The straight solenoid used for the detector sees no large off axis loading like the centering force on the transport solenoid. There is a small net lateral load due to its interaction with the TS curved field, and there is a potential of a net side-load or vertical load if the iron shield that surrounds the coil is offset with respect to the centerline of the coil.

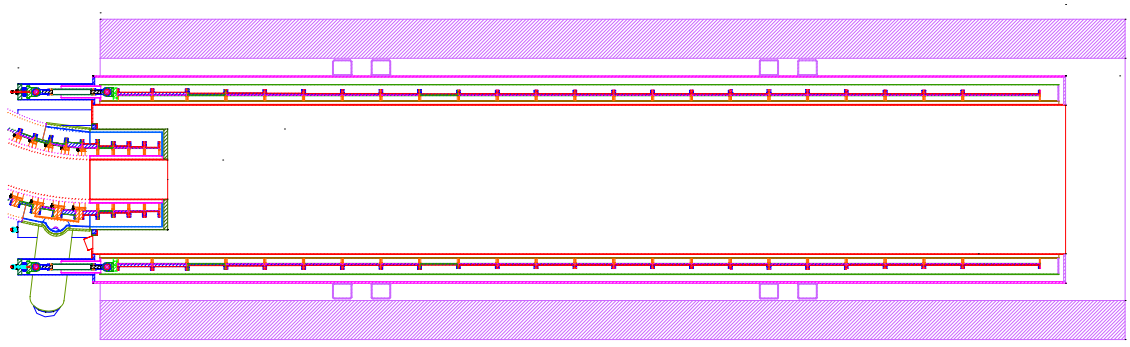

Figure 14.1 - Detector Solenoid in its Iron Return Frame

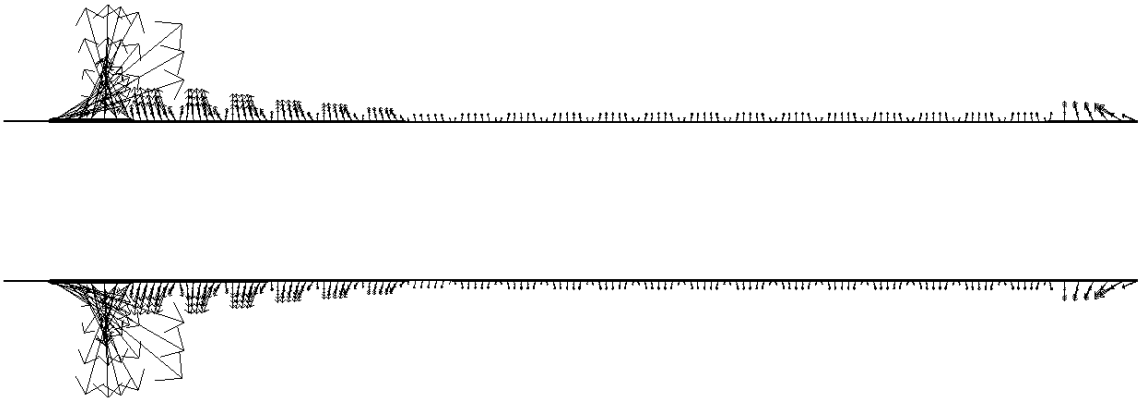

Figure 14.2 – Lorentz Forces from axisymmetric model, fields computed without iron.

Lorentz Forces are Not Strongly Effected by The Iron Shield

A steel radiation shield surrounds the detector solenoid. This is a rectangular box surrounding the circular solenoid, and there was a concern that it might cause non-axisymmetric loading. A thin slice model with the rectangular iron shield was analyzed (Figure 14.3). This analysis was intended to investigate only the structural concerns. In this model, the winding pack is 0.02m thick, centered at a radius of 1.08 m. The iron is 0.3 m away from the winding and the iron is 0.5m thick. The current density in the winding was adjusted to come close to 1.0 T. The resulting current density was 39.5×10^6 amps/m^2 (Figure 14.4). In the detector volume the field varied from 0.990 to 0.996 T. This same coarse model was run without the iron and the field was 0.89 T. The difference was 10%. The mesh was refined but was still fairly coarse by electromagnetic standards. With this refined mesh field without the iron was 0.96 without the iron (Figure 14.5). With a refined Mesh with iron , the field was .990 to .994. So the effect of the iron with the refined mesh, was about 3%. Field quality effects are addressed in the CDR chapter on Field Specification Matching (Section 3).

The Lorentz force plot (Figure 14.6) shows no apparent non-axisymmetry. The important conclusion for the structural analysis is that the iron can be ignored for computing the Lorentz force distribution - at least in the interior of the coil.

The larger 3D model with the end pole (discussed later) also showed the reduction when the iron was removed. The field went down from 0.997 with iron to 0.91, but there were some small indications of non-axisymmetry at the end of the solenoid.

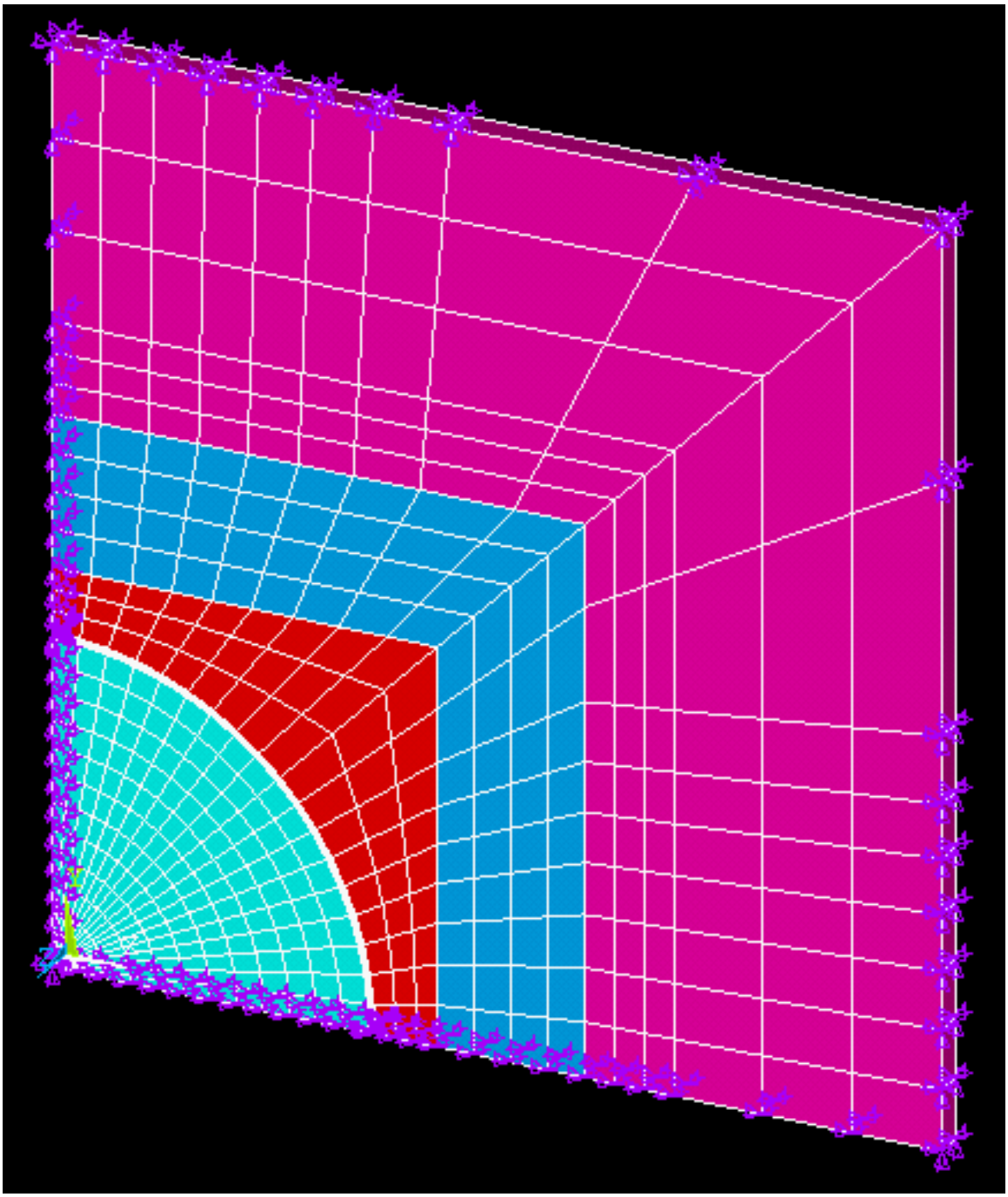

Figure 14.3 – Coarse mesh magnetic model

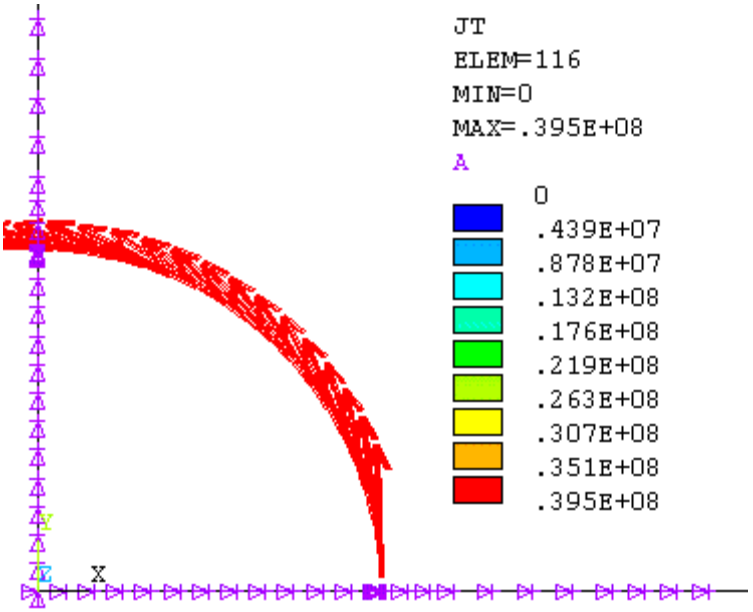

Figure 14.4 – Current density

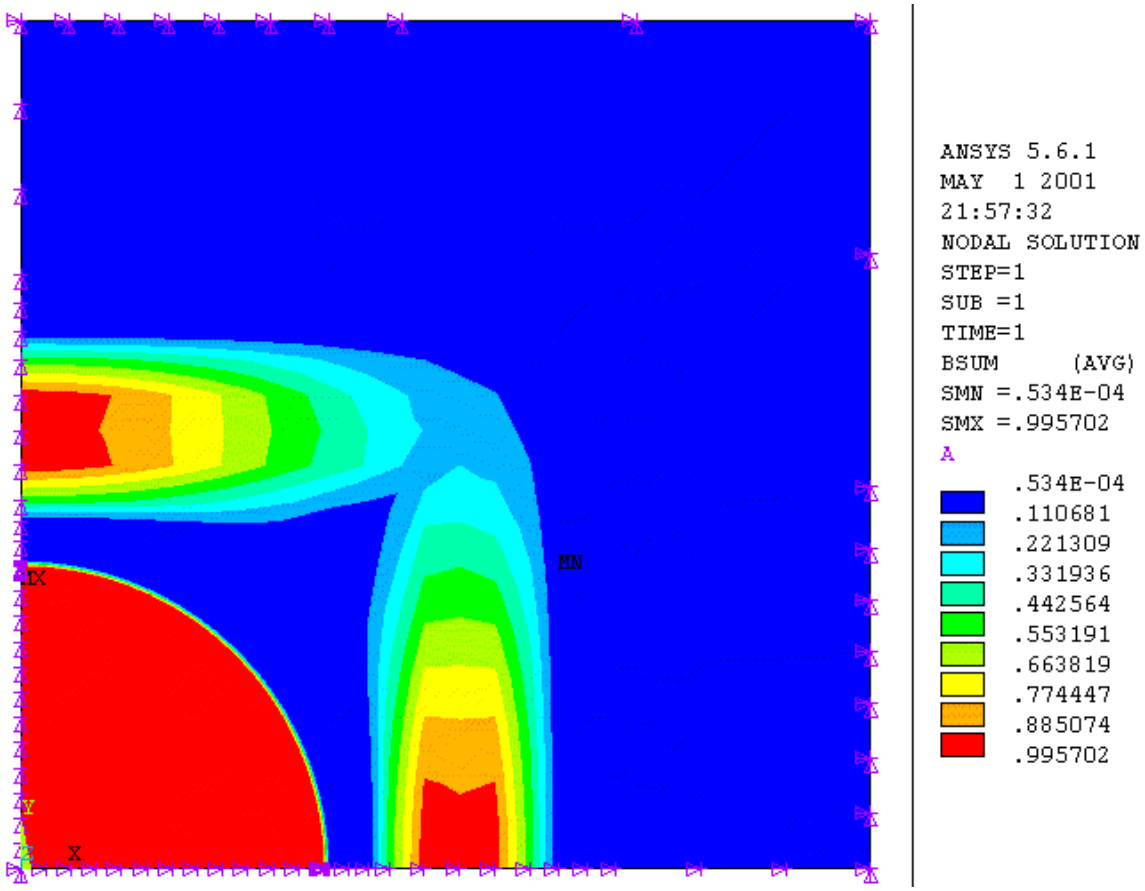

Figure 14.5 – Axisymmetric field plot

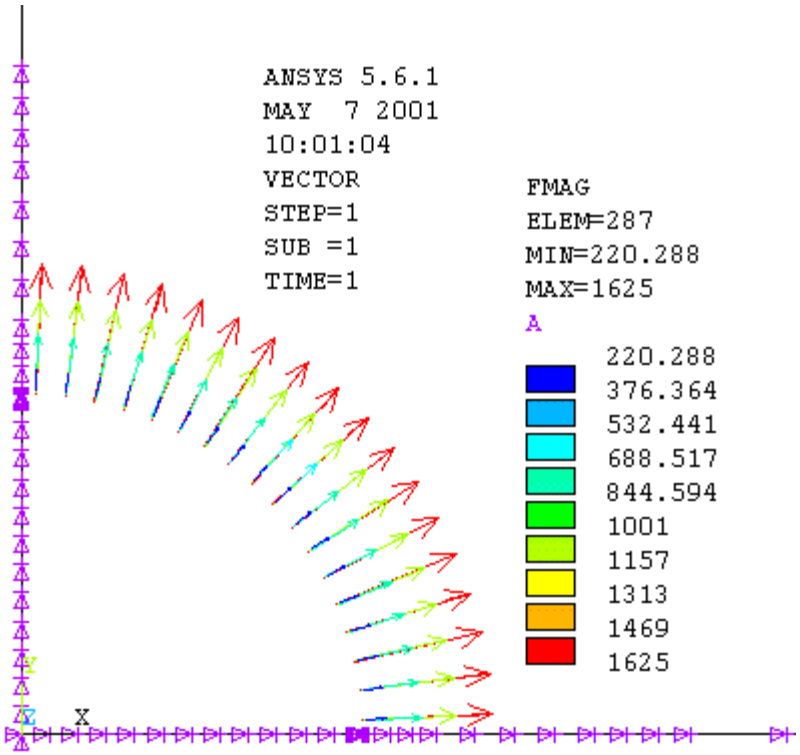

Figure 14.6 – Magnet Lorentz forces from the non-linear model with iron. Non-axisymetry is small and not evident in this plot, nor is it significant structurally.

Axisymmetric Model

The detector solenoid is a very long (11.25 m) thin sheet solenoid with a field gradient along the axis. A simplified axisymmetric analysis was performed based on the straightened string of solenoids that make up the full array of the magnet system. An axisymmetric field and force calculation was done. If the coil and mandrels were modeled in more detail, the coil would separate from the mandrel when it was energized. The coil could rotate without some constraint, a result similar to that already discussed in the TS structural chapter. Rotational motion should be anchored by some means such as a G-10 cleat. The torsional loads are small, but without the cleat, the coil might stick-slip-wander around the mandrel and end up loading the jumpers.

The axisymmetric model shows that axial stresses (Figure 14.7) and hoop stresses (Figure 14.8) are modest. The model is based on one of the coil builds/currents that preceded the final configuration, and some adjustments were made to approximate the changes in coil configurations and details that were made towards the end of the conceptual design. However, the changes are not significant structurally.

The size of the structure with respect to it's thin build raises special concerns. The builds from the coil/current set used were adjusted by 70 kA / 49 kA to model a later current density specified for the coils. As a convenience in the model generation, the full coil array is modeled as fully bonded. (i.e., the assembly of individual coils and mandrels is not modeled.). This approximation allows easier quantification of the hoop and axial stresses in the coil.

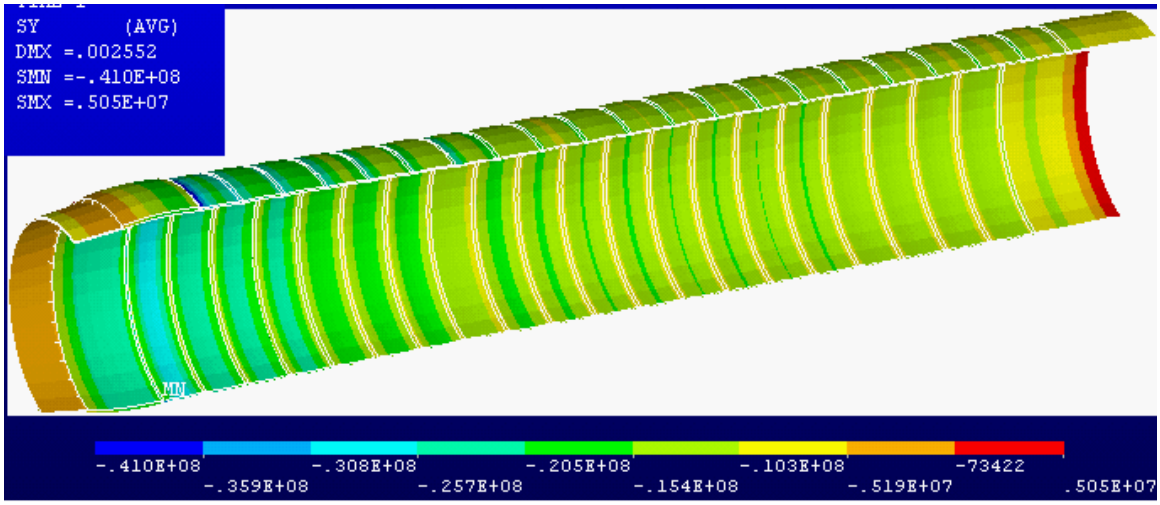

Figure 14.7 – Axial stress from the axisymmetric model - A symmetry expansion is used to visualize the half section of the coil. Maximum compression is 41 MPa.

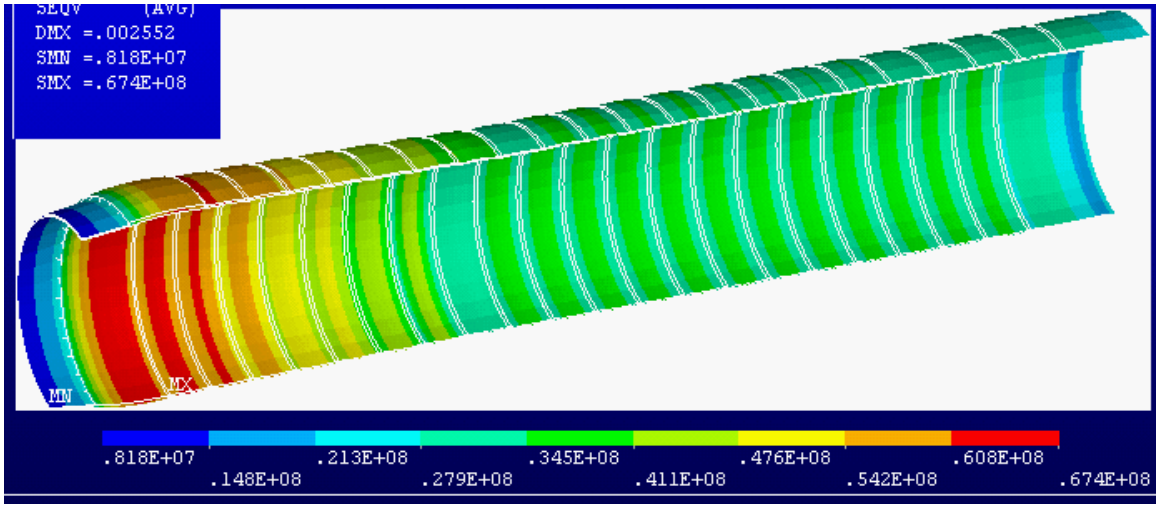

Figure 14.8 – Hoop stress in the axisymmetric model. The maximum value is 50.2 MPa.

Detector Solenoid Coil Stresses with Local Stress Multipliers Applied

As has already been discussed for the PS and TS coils, the structural analyses were done using the conductor cross section shown in Figure 14.9. The final DS conductor cross seciton is shown in Figure 14.10. The same post-processor used in the production and transport solenoids was applied to compute the local conductor stress state. This procedure applies stress multipliers to the "smeared" orthotropic properties employed in the axisymmetric analysis. The peak local conductor stress with the stress multipliers applied is only 80 MPa (Figure 14.11). In the final choice of conductor cross-section for the TS, the superconducting cable is almost twice the fractional area of the conductor. The change in stress is estimated by the copper area ratios, so the 80 MPa stress becomes 80 × (1-0.286) / (1-0.484) = 110 MPa. The conductor Sm Allowable = 150 MPa for a freestanding coil where the coil is not supported by an external case or mandrel. There is ample margin in the axisymmetric response of the coil.

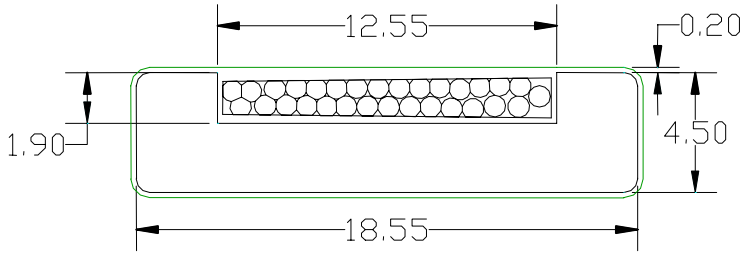

Figure 14.9 – Conductor cross-section used in the stress analysis. The final conductor cross section differs from this. The conductor is 28.6% of the volume.

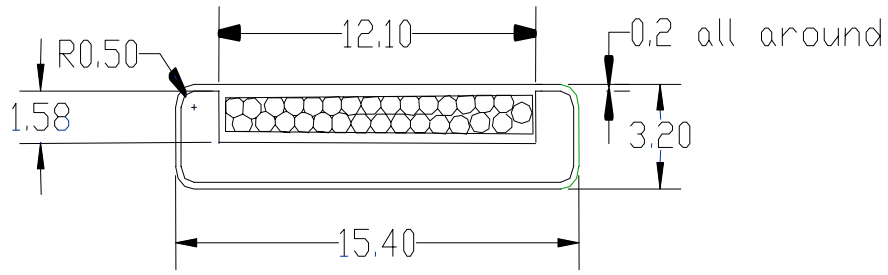

Figure 14.10 – Final DS conductor cross-section chosen. The conductor is 48.4% of the volume.

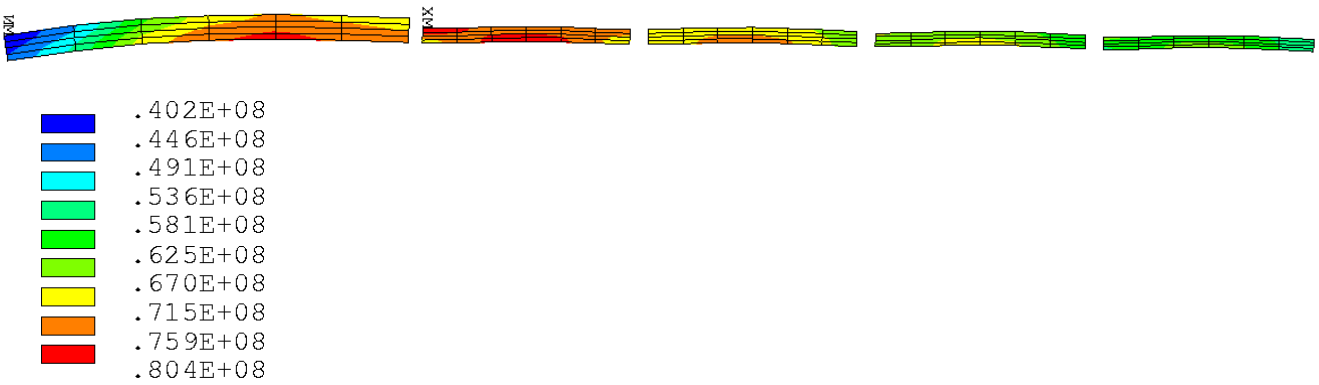

Figure 14.11 – Conductor stress with original multipliers, first five coils from the high field end. Note that the coil at left has been split into two coils to mitigate the quench behavior. A hot spot in the middle of this coil produced a non-uniform radial expansion that then caused axial bending stresses.

3D Gravity Load Model

In this analysis the mandrels are not modeled. The coils are bonded to model the epoxy impregnated winding pack. This approach is only an approximation of the interaction between the mandrels and the coils, but it should be conservative with respect to global behavior in that the main structural elements (the mandrels) are omitted. The mandrel shells are made up from 1/4 inch thick stock, and the flanges are 8 mm thick. Copper shells line the mandrels to form a thermal intercept, as in the TS. When the coil is energized, the mandrels and the flange connections see compression with the axial loading of the coils. Bending tension from the deadweight loading is very small and is only a concern with the coil turned de-energized. Vertical supports have been located to minimize this tension, but detailed analyses of the flange bolting similar to that done fore the TS should be a part of the final design effort. Bolt size and spacing is presently driven by thermal conduction requirements between the cooling tubes and the copper bars and copper shells. The bolts specified to connect copper chill bars, shells and mandrel flanges together are probably more than the deadweight tension stress would require. Coil deflections are calculated in Figure 14.12.

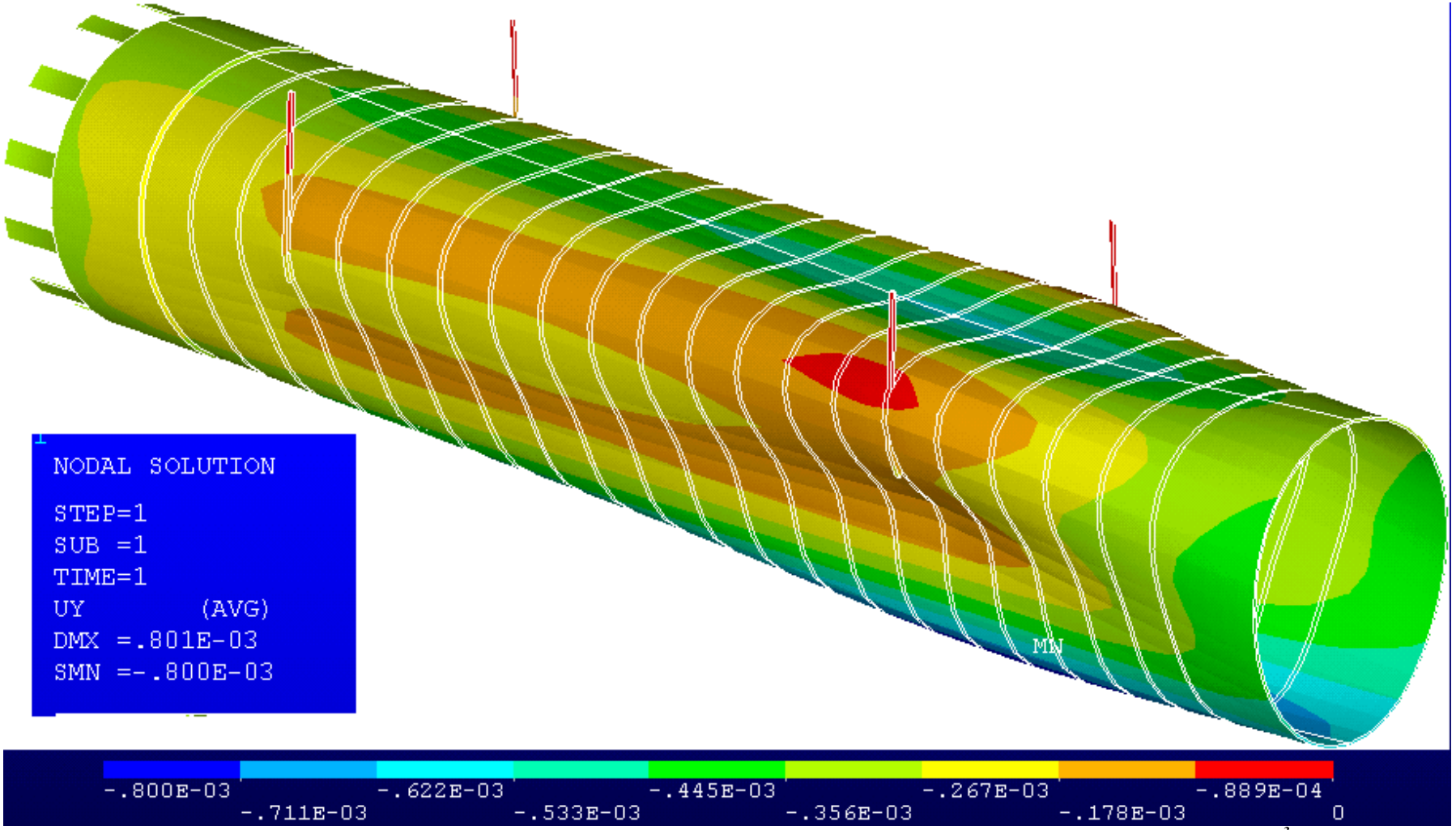

Figure 14.12 – Vertical displacement under gravity load. Maximum sag is at the bottom and is -0.8 mm. 1/2 Vol = 0.927 m^3

Force and Magnetic Stiffness Interactions with the Iron Box

Loads due to the interaction between the coil and the shield box that surrounds it were quantified by A. Radovinsky [7]. The results of this analysis are repeated in Figure 14.13 and in Table 14.1. The volume of the half symmetry coil structural model is 0.927 m^3. Using a density of 8900 kg/m^3 the total weight of the model is 16,500 kg or 161,705 N. This is comparable to the worst of the lateral or FZ loads for 8 cm assumed displacement. The displacement from the deadweight analysis is less than 1 cm, and mostly results from the shell flexure. The iron box interaction will produce roughly 10% higher downward loading related to gravity effects. It is conceivable that the shield box could be so poorly positioned outside the cryostat that the equivalent offset could be more like the 8 cm assumed. Lateral radius rods are needed to support this load, and the vertical support rods need to support the gravity loading and the lateral loading. The concept for these supports is shown in Figure 14.14, and their analysis is discussed in more detail in the next section.

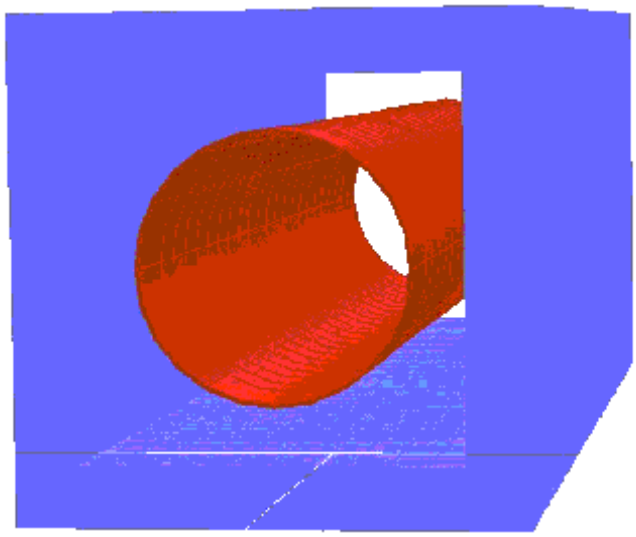

Figure 14.13 – In Radovinsky's model [7] X points down from the symmetry plane of the MECO magnet system, Y is along the axis of the DS, and Y complements XZ. dZ is the offset between the axis of the iron box, and the axis the coils of the DS in the equatorial plane.

Table 14.1 – Forces on the DS as a function of the lateral offset, dZ from [7]. Coordinates are defined in Figure 14.13 above.

dZ (cm)	FX (N)	FY (N)	FZ (N)
1	0	181511	16379
2	0	181291	38250
8	0	182124	169924

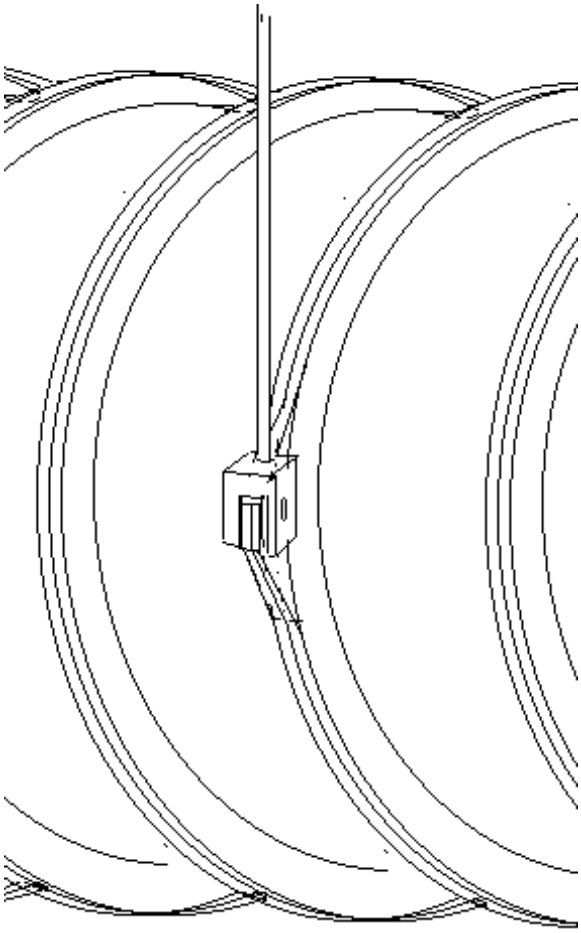

Figure 14.14 – Detector solenoid vertical hanger rod connected via a clevis to extensions of the mandrel flanges. The other end (not shown) is supported by a tower that is integral with the cryostat.

Axial Support Struts

The net axial load in the detector solenoid from the linear model is 0.5076 MN. Adding the effect of the iron shield, the net load is 0.5076 + 0.182 = 0.69 MN, or 155,112 Lbs. Eight compression struts are used which are similar in design to the PS axial supports. The load per strut is 19,400 lbs. 2.5 inch schedule 40 pipe is used. The margin against the AISC axial stress is about 6.6 for buckling based on 4K properties, and the factor of safety for the small region that is near room temperature is 26 ksi /11.4 = 2.3. These limits are plotted in Figure 14.15. The strut, as drawn in the CDR drawing package, is shown in Figure 14.16.

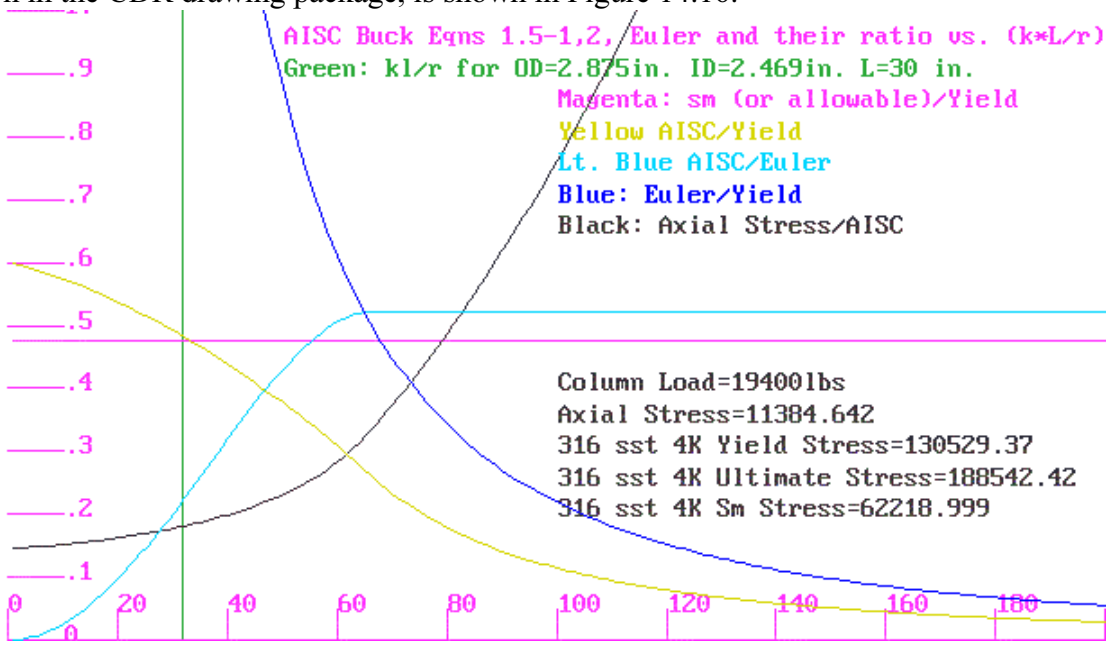

Figure 14.15 – Buckling evaluation of strut. Black curve shows the ratio of actual axial stress divided by AISC allowable, giving ~0.15, implying a factor of safety of 6.6.

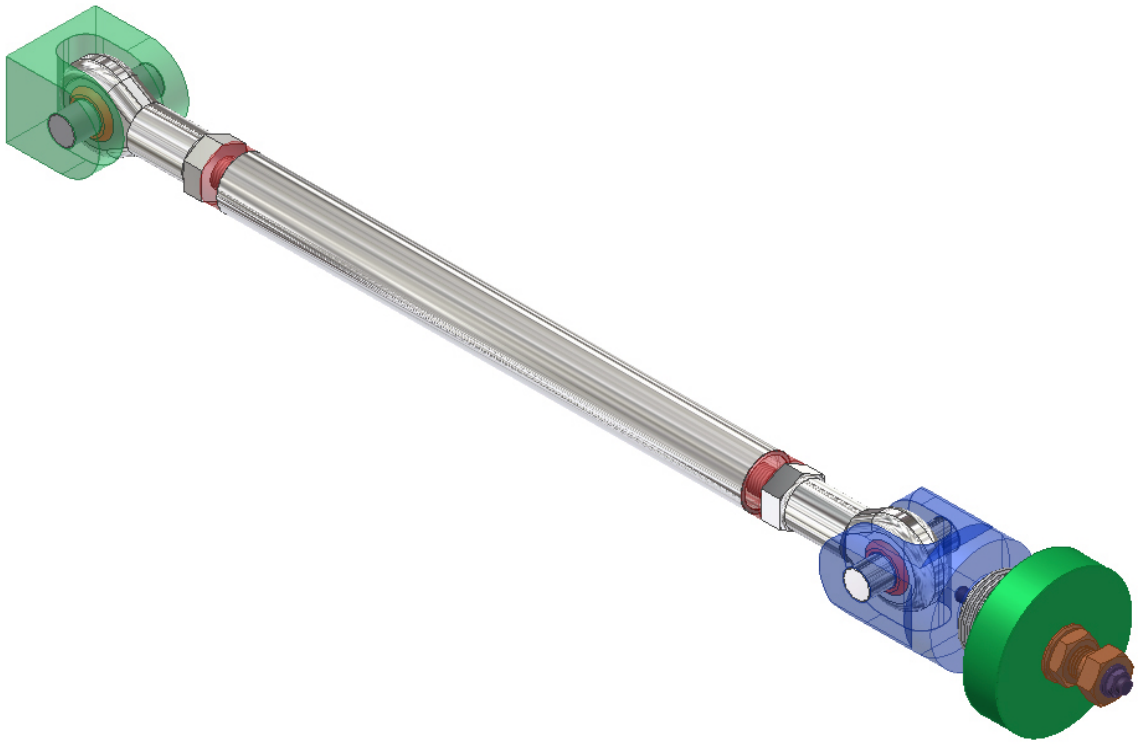

Figure 14.16 – Adjustable axial support strut used in both the production and detector solenoid.

Vertical and Horizontal Hanger Rods

The deadweight of just the coils was 16,500 kg or 161,705 N or 36,400 lbs at the time of this analysis. This was doubled to account for the mandrels, and conduction cooling copper bars and pipes. Referring back to Table 1.1 shows these early assumptions to be very conservative, since the conductor, mandrels, and copper for cooling sums to only 13,970 kg. Nevertheless, the analysis discussion proceeds with the conservative assumptions.

There are four vertical support rods. Each rod sees about 18,200 lbs. The rods are loaded about the same amount at room temperature and at cryogenic temperatures. The room temperature primary membrane allowable for 316 LN stainless is 183 MPa (26.6 ksi). A rod cross-section of 18,200 / 26,600 = 0.684 sq.in. This corresponds to something a bit smaller than a 1" diameter rod. To accommodate some concentrations around the LN2 intercept, and to allow for some shipping and seismic loading, 1.25 inch diameter rods are proposed. The lugs that the rod are attached to are made up from extensions of the mandrel plates which are only 8 mm thick each. Axial cooldown of the long coil will have to be accommodated by changes in inclination of the rods, thus the lug plates will either have to absorb a rotation, or a spherical bearing detail will have to be added. If a 3 inch bearing assembly is used, the bearing stress is 18,200 lbs / 3 / 0.016 × 39.37 = 9630 psi which is low for the 316 stainless used for the mandrel flanges. The lug net section should be 1.5 times the rod cross-section. This is due to bending in the minimum section of the clevis. It is also general practice in pin-connected plates for the head of the lug to be 1.5 times the pin diameter, to reduce the net section bending. The implementation of the hanger attachments to the DS mandrels as drawn in the CDR drawing package is shown in Figure 14.17.

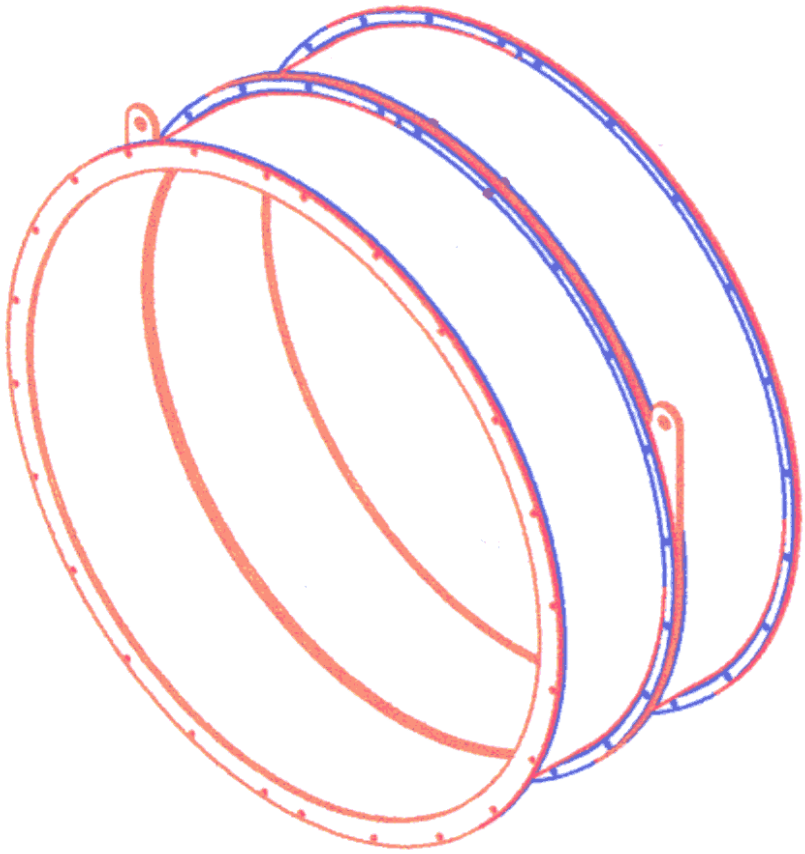

Figure 14.17 – Vertical support rod attachments to the DS mandrels from the CDR drawingsl.

End Pole Analysis

At the time of finalizing the Conceptual Design Report, the MECO project had not decided whether to implement a pole at the downstream end of the detector solenoid. Therefore, while this model does not represent the final design it does address the possibility of a non-axisymmetric loading at the end of the coil in the event a rectangular iron pole is implemented. For a thin sheet solenoid, small non-axisymmetric loads can cause bending of the winding pack. The solenoid is modeled with a constant current density along the length of the detector. No attempt is made to adjust the current density at the end to maintain the 1.0 T field.

In this analysis a 0.25 meter end plate is used that has a hole of radius 0.535 m (Figure 14.18). There is a 0.25 m space between the end of the winding and the inner surface of the pole piece. The model assumes symmetry at mid-length of the detector solenoid, and about horizontal and vertical planes. The iron radiation shielding is square and made up of flat plates that total 0.5m thickness. Shown in the field plot (Figure 14.19) is an up-down symmetry expansion with fields near the end pole. Figure 14.20 plots the field contours 1 meter upstream from the end of the DS windings. Figure 14.21 plots the field contours at the same location, but with a finer resolution, to show the non-axisymmetry of the field.

There is some "squareness" of about 1 contour variation, or only about 1%. This model represents the low field end. A 3D structural model was loaded with the appropriate Lorentz forces for the DS computed linearly. The resulting force distribution was scaled, along the whole length, by the 1% four “lobed” loading. The effect at the low field end is minimal because the axisymmetric loads are small. At the high field end the effect is superimposed on a higher stress, but is still only about one contour variation, or less than 15 MPa. The square shape that results from the “square” loading is evident in Figure 14.22, but the magnitude of the displacements is less than 2 mm.

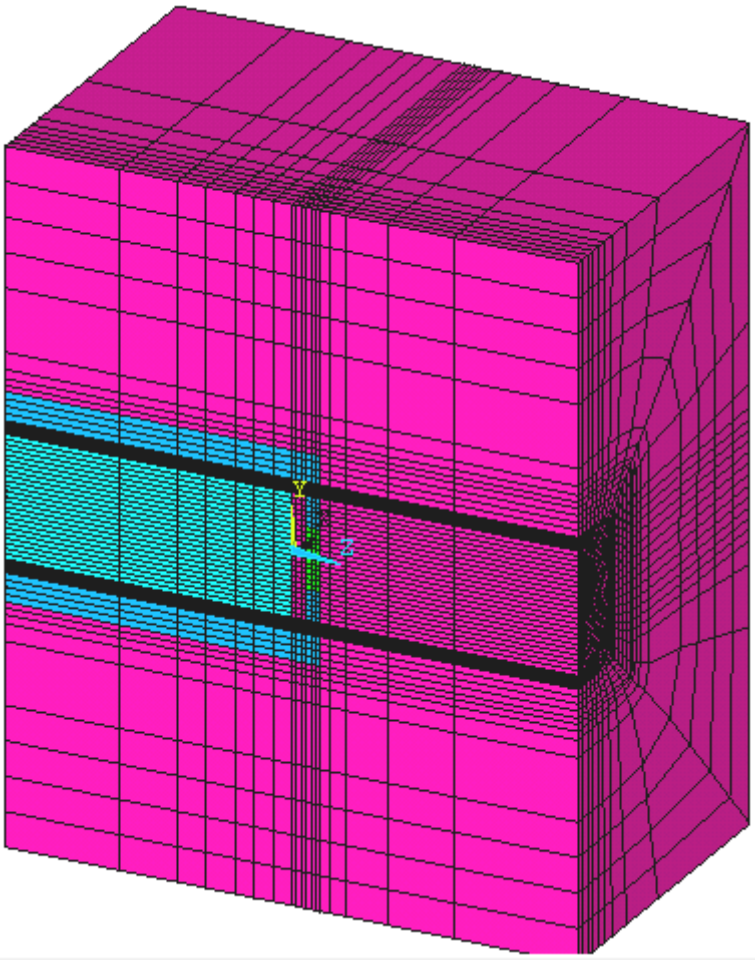

Figure 14.18 – Model end pole. The model assumes symmetry at mid-length of the detector solenoid, and about horizontal and vertical planes. Shown is an up-down symmetry expansion.

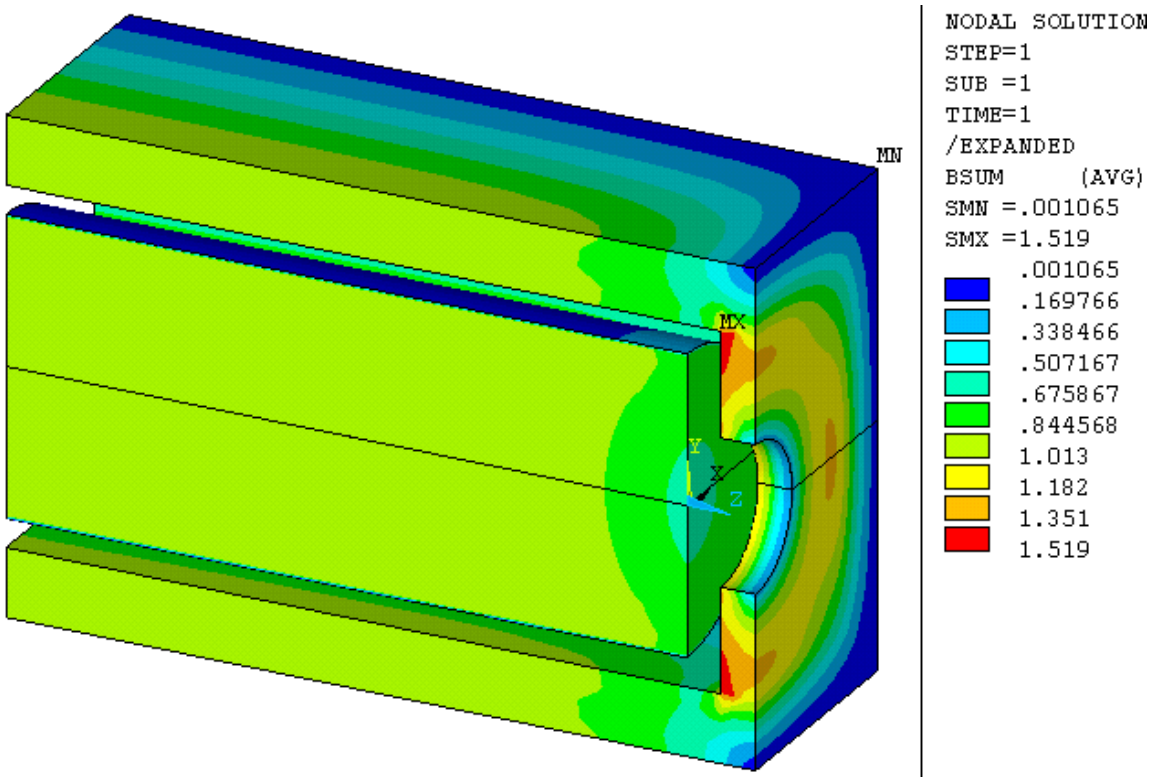

Figure 14.19 – End pole field. MECO has not decided if the addition of the end pole is needed.

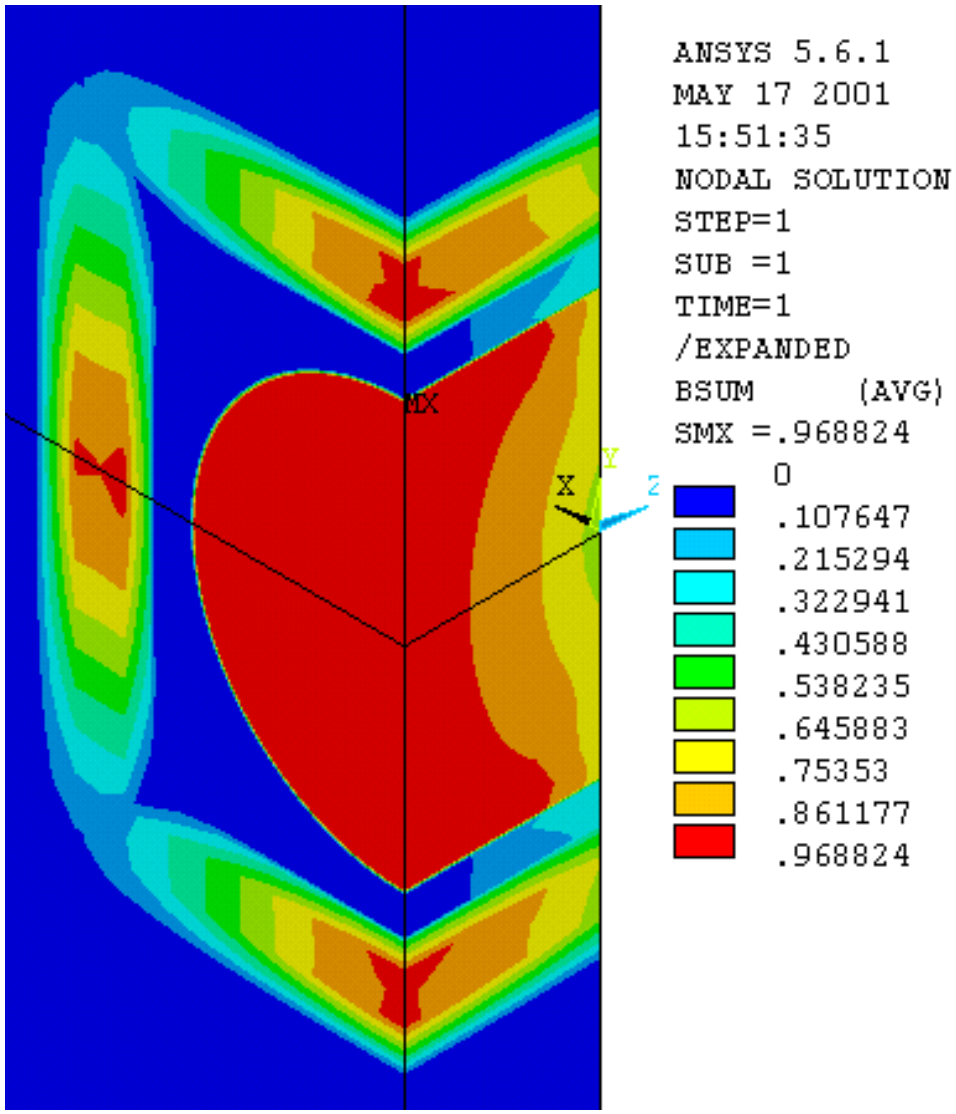

Figure 14.20 – Field Contours at 1 m upstream from the end of the bore of the solenoid. Without increasing the current in the end coils, the field drops off to 0.65 T at the end of the solenoid

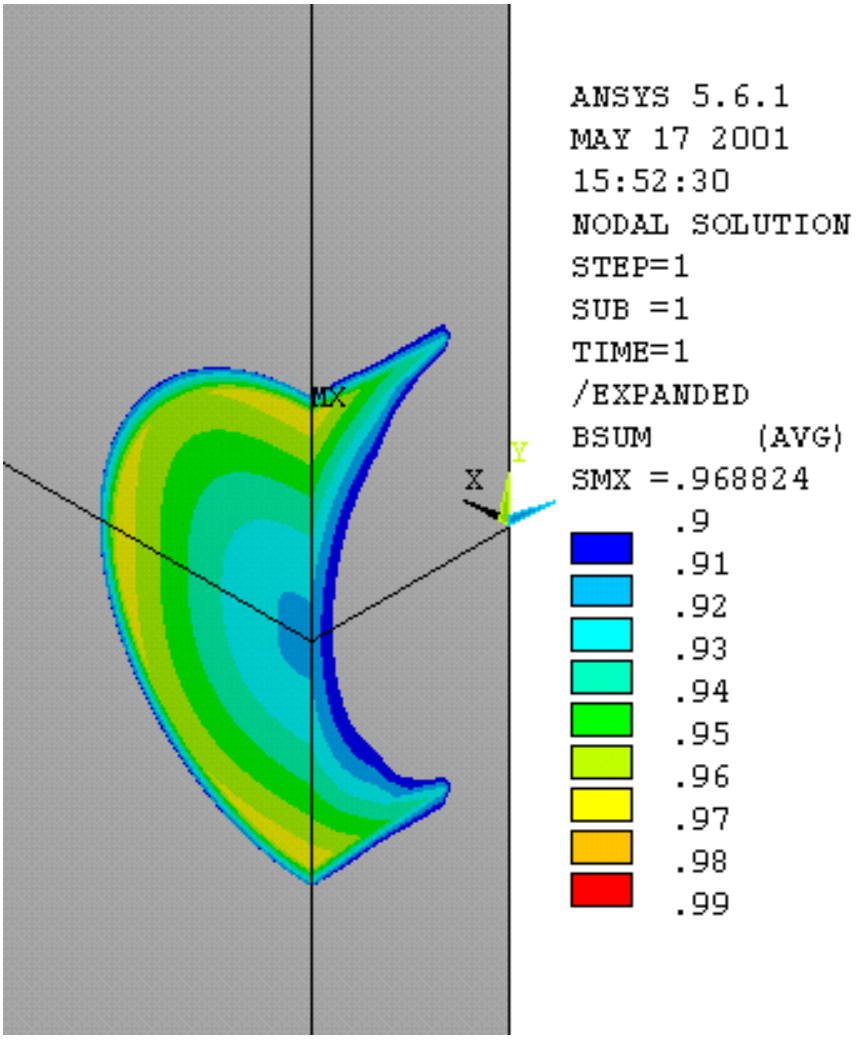

Figure 14.21 – Field contours at 1 m from the end of the bore of the solenoid.

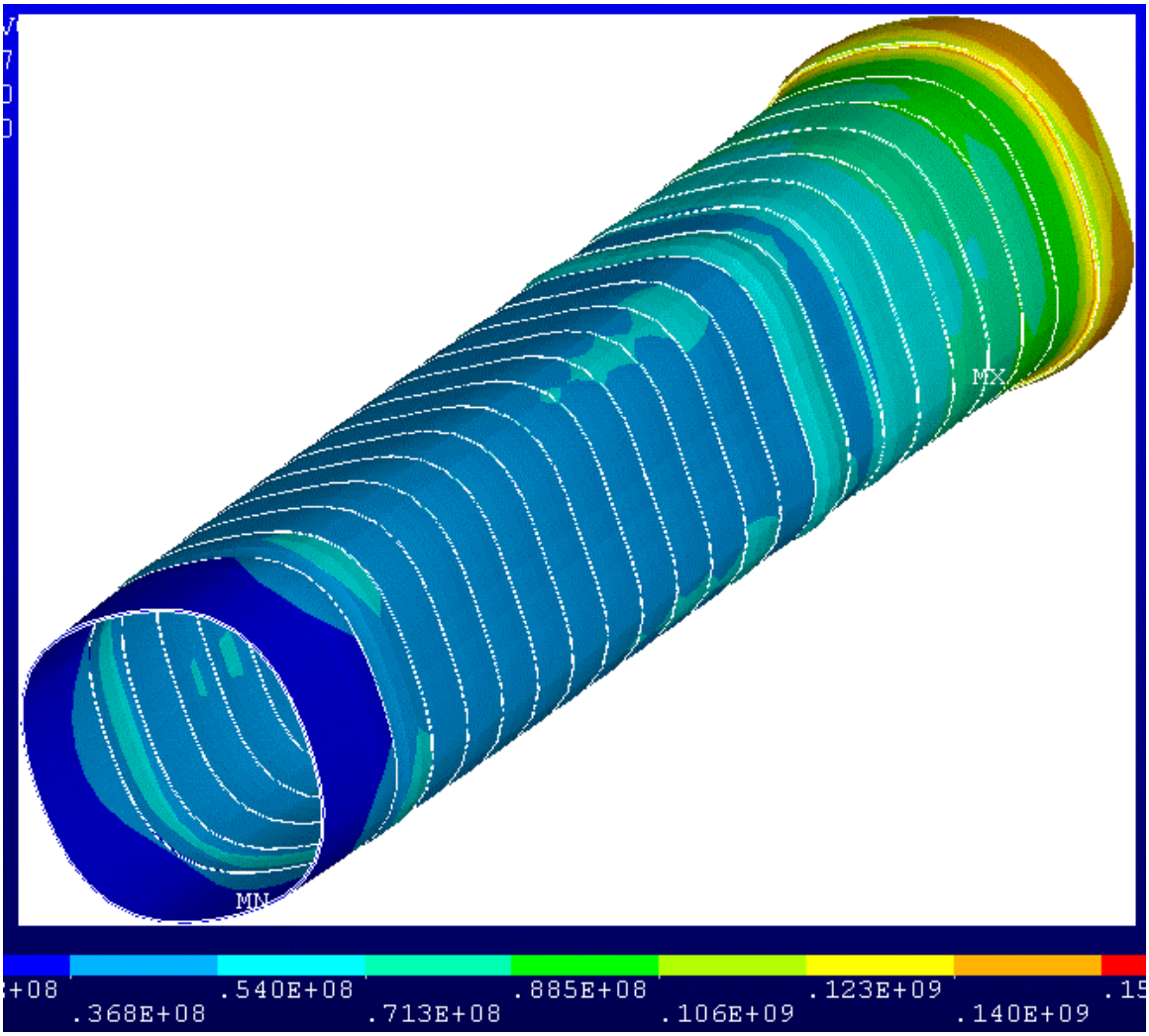

Figure 14.22 – Von Mises Stress in the DS with a 1% square lobed load variation

Field Decay on the Downstream End of the DS

The pole piece is not presently part of the design, and derives from an early requirement that the field drop quickly after the end of the DS. At the time of the CDR writing, the MECO project had not provided firm guidance regarding the fields in this area. Nevertheless, Figure 14.23 captures an early analysis to address this issue. The circular hole of this end pole may act to smooth out the "squareness" of the field distribution, and this effect should be re-visited during detailed design.

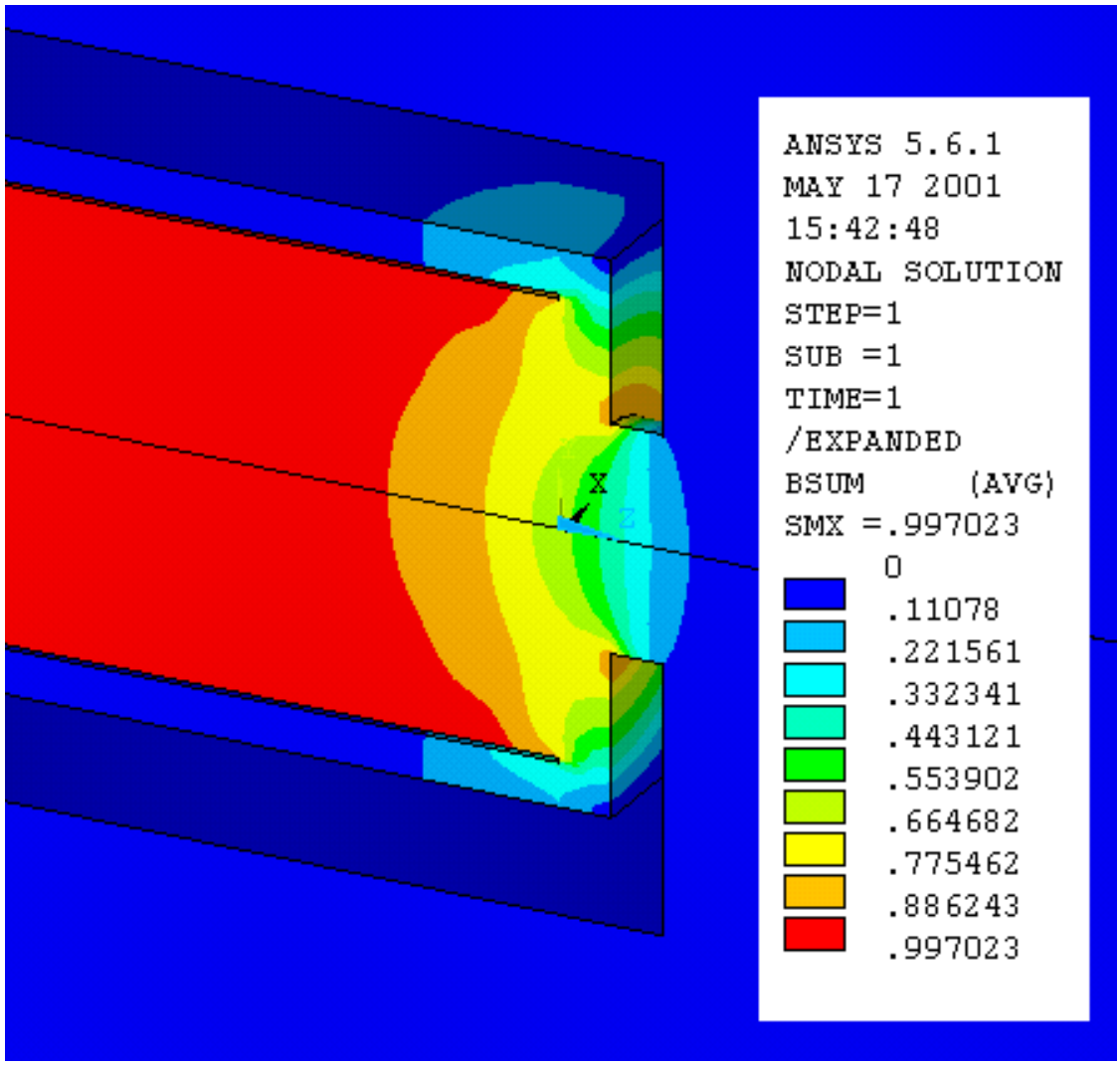

Figure 14.23 – Fields near the end pole piece/shield.

Cryostat

The primary function of the cryostat is to support the vacuum pressure loading. The crysotat is an annular vessel. The inner shell of the cryostat supports its own deadweight, and "internal" atmospheric pressure. The pressure load produces hoop tension, and has the tendency to stabilize the shell. Deadweight is non-axisymmetric and may be the limiting loading for the shell that is over 11 meters long, and only stabilized at its ends. The outer cryostat shell sees external pressure but it has no space limitations for the addition of stiffener rings. Because of the length of the vessel, differential Poisson effects resulting from the hoop tension in the inner annulus shell and hoop compression in the outer shell may produce axial compression in the outer shell, or difficult bending at the end caps.

Inner Shell Buckling

A linear buckling analysis of the inner shell loaded only with its own gravity loads and with the ends held fixed, was conducted (Figure 14.24). The inner shell was modeled with a 1 cm thickness, consistent with the final conceptual design. The analysis produced a factor of safety against buckling of greater than 387 for the shell at a 1.02 m radius, and 11.25 m long.

A non-linear large displacement solution was also done for the cryostat inner wall (Figure 14.25), and the collapse load was explored. Full restraint at the ends precluded buckling, but when the axial restraint was removed, the shell buckled somewhere between 150 and 200 times the gravity load. This analysis does not include the weights of the detector internals. These were considered in a model which included both inner and outer shells, and which is discussed after the next section.

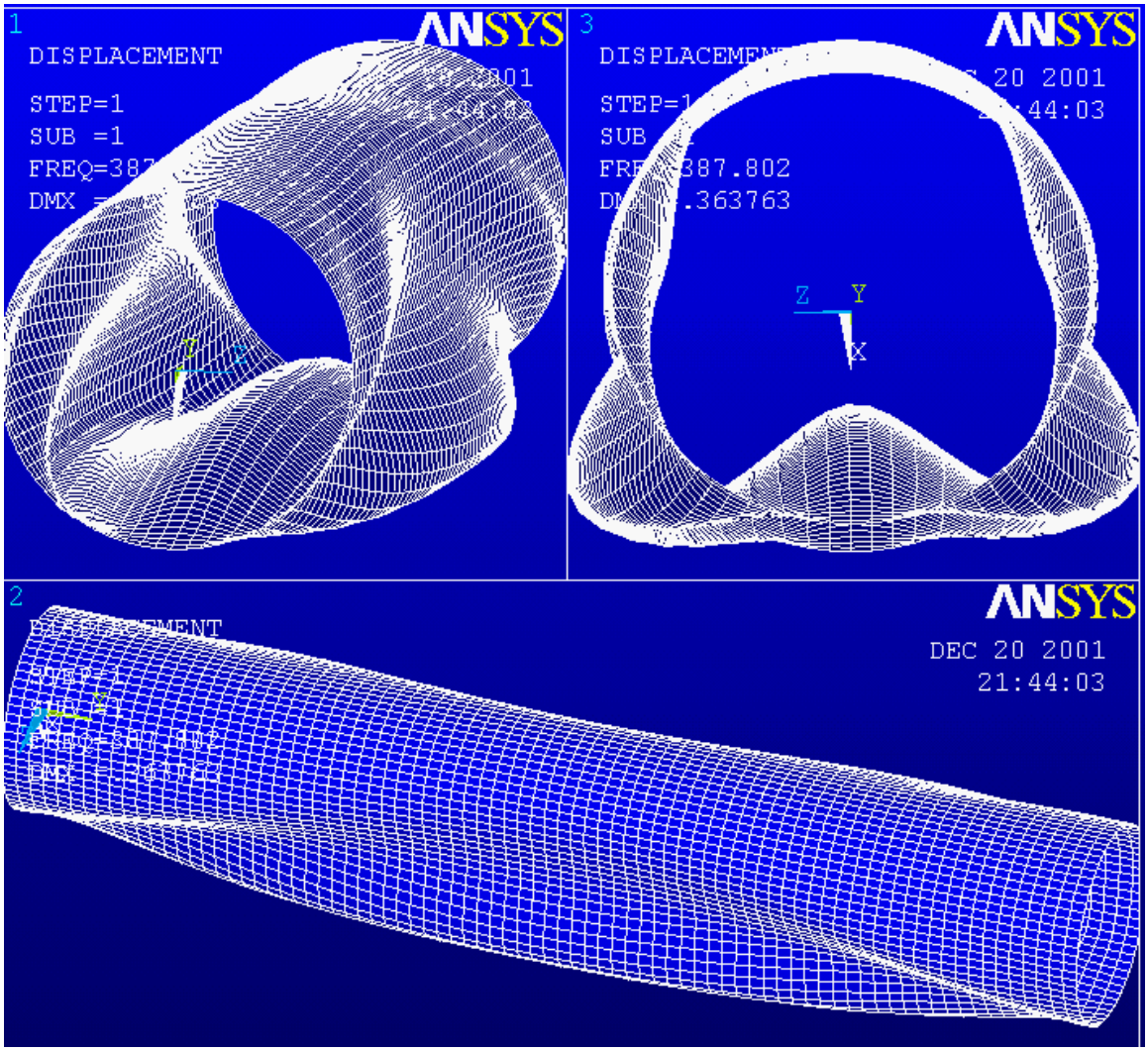

Figure 14.24 – Inner vessel wall, first mode buckling shape, deadweight load vector. The load multiplier in this linear Eigenvalue solution is 387. The second mode is similar, and has a similar multiplier. The third mode has a multiplier of 432. The linear analysis shows a large margin against buckling, but relies on end circular constraint.

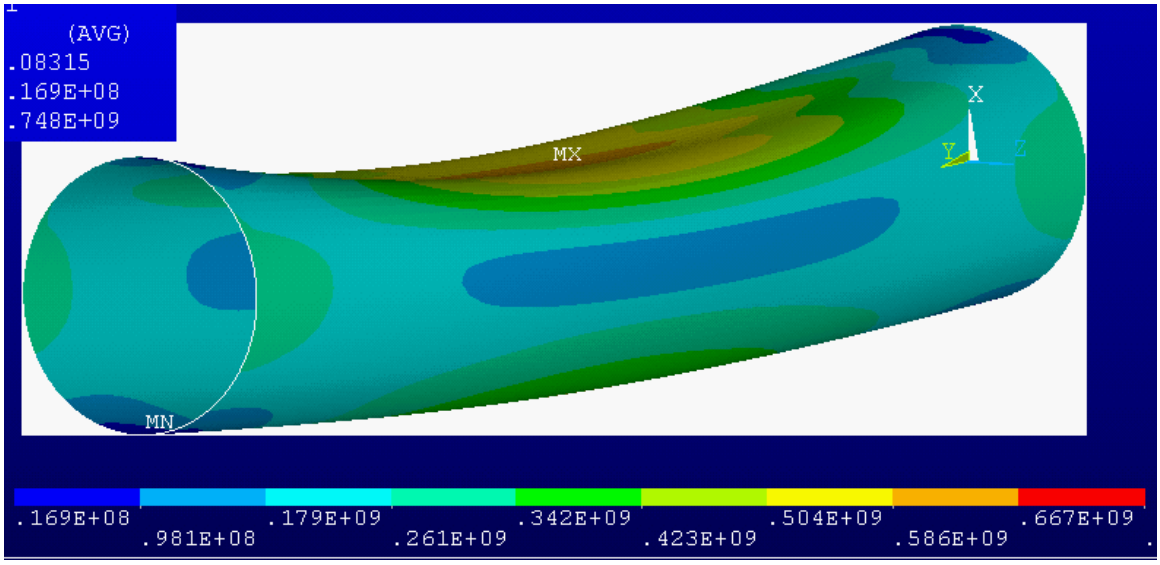

Figure 14.25 – Non-Converged Large displacement solution with ends held circular but free to displace axially. Greater than 150 times the gravity load.

Outer shell buckling

The outer shell is modeled with a 2 cm wall thickness, consistent with the final conceptual design. In the buckling analysis shown in Figure 14.26, the inner vessel, rail and target assemblies are omitted as are the cold mass support towers, and ring stiffeners that are integral with saddle supports. In these buckling results, the load multipliers are much smaller (Table 14.2) than those for the inner vessel wall. A large displacement solution is called for to ensure adequate margin against buckling, and should be pursued during final design.

Table 14.2 – Outer Shell Load Multipliers from the Linear Buckling Analysis

SHAPE NUMBER	LOAD MULTIPLIER
1	8.48
2	8.66
3	13.69

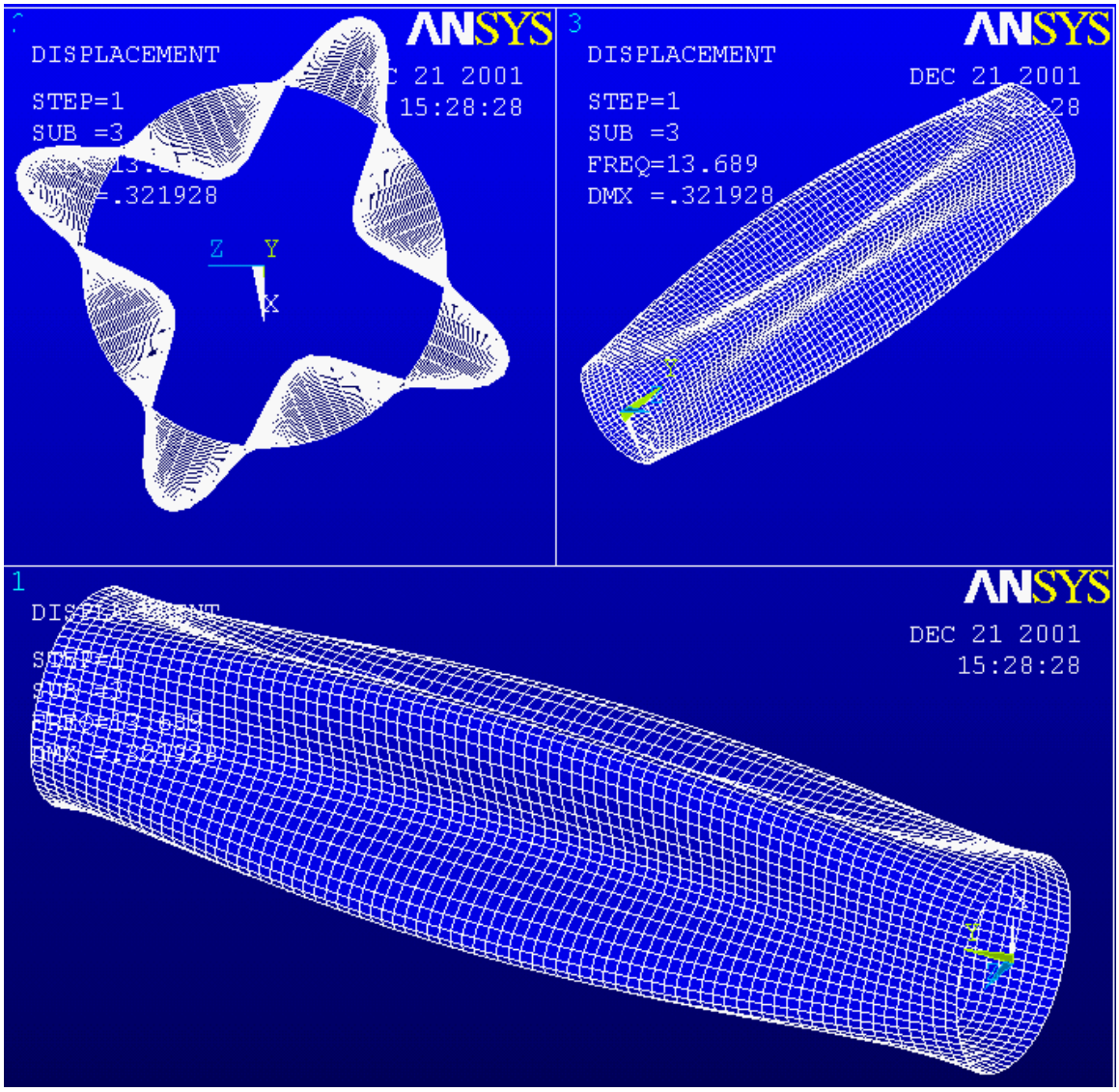

Figure 14.26 – Mode 3 Shape

Inner Shell Support of Detector Components Dead Weight

Aside from the deadweight of the cryostat, the internal components of the detector are supported off a set of rails mounted on the inner cryostat wall. The calorimeter cart, tracker cart, target cart, polyethylene shielding, rails, and miscellaneous produce a total local loading at various positions along the rail of 4250 kg and a distributed weight of 6800 kg to yield a total 11, 050 kg. For modeling purposes, these were all grouped into a plate with a fictitious thickness that represented a cubic meter of steel at the center of the long cryostat. A strip welded to the inner surface represented the rail. The resulting membrane Von Mises stresses are shown in Figure 14.27, and are small. The local details of the rail/wheel/shell interactions need to be addresses in the final design.

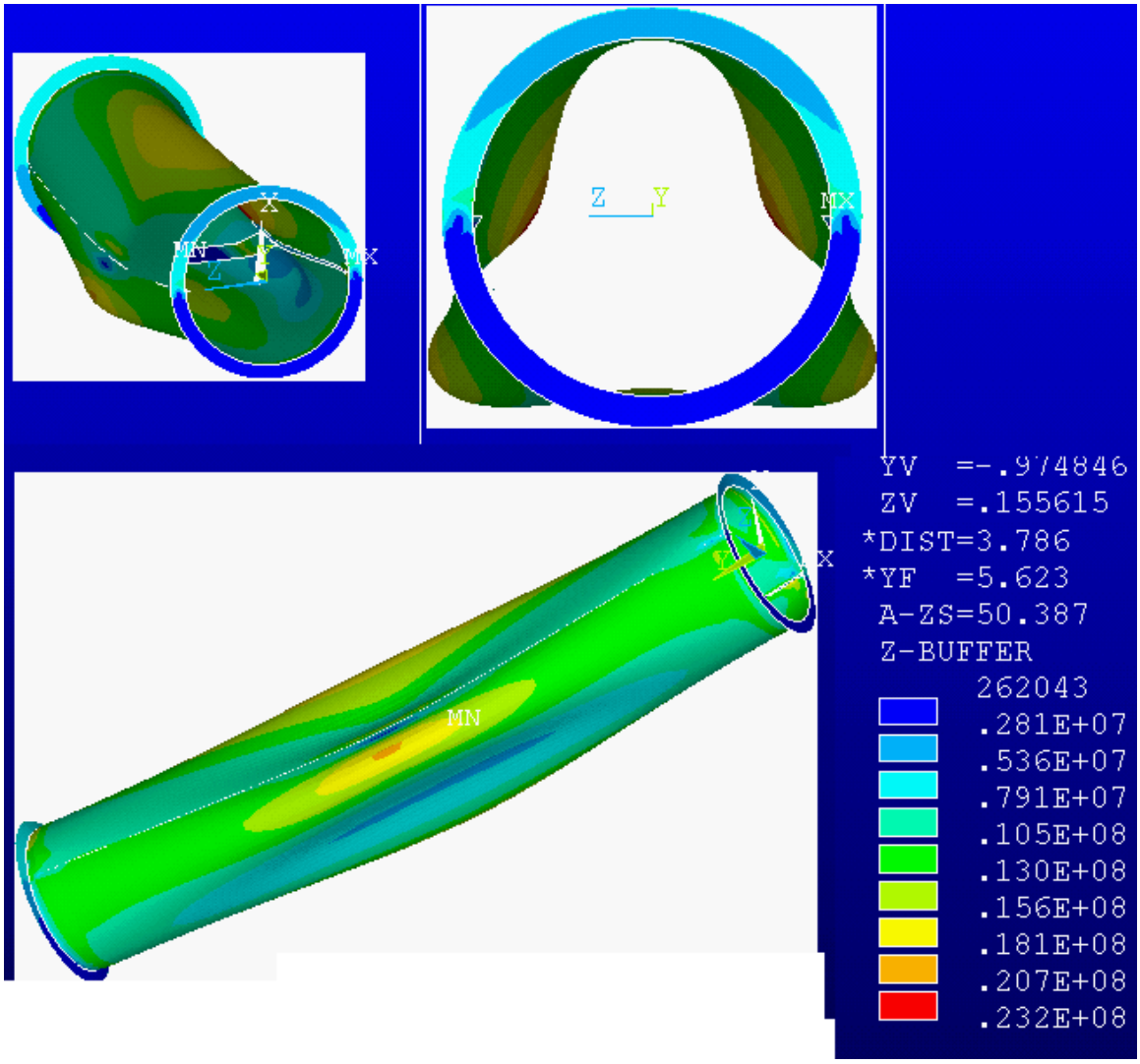

Figure 14.27 – Von Mises stress and deflected shape for the DS inner cryostat shell.

References

[1] Coil Sizing Preliminary Results A.L. Radovinsky MECO-MIT- ALRadovinsky-052501-01 May 25, 2001

[2] Email To: Bradford Smith From: w. Molzon, Monday, April 02, 2001 8:10 Subject: heat and radiation loading

[3] Production Solenoid Coil, Cryostat and Support Stress Analysis July 12 2001 MECO-MIT-PHTitus-071201-02

[4] "Rigid, Adjustable Support of Aligned Elements Via Six Struts", W.Thur, et.al LBNL, Berkley Ca October 1997

[5] "General Electric Design and Manufacture of a Test Coil for the LCP", 8th Symposium on Engineering Problems of Fusion Research, Vol III, Nov 1979

[6] Product Literature, Inco Alloys International, Inc Huntington West Virginia 25720, USA

[7] MECO-MIT- ALRadovinsky-111401-01 Forces in the DS Magnet with Iron

Section 15 - Cryogenic System Design

Overview

The cryogenic system consists of the cryogenic fluid supply for four 4.5 K cryostats enclosing the four solenoids, PS, TSu, TSd, and DS. The TSu cryostat contains the TS1, TS2 and TS3u coils, and the TSd cryostat contains the TS3u, TS4 and TS5 coils, consistent with the nomenclature used throughout this report. The cryogenic helium is supplied from a single refrigerator/liquefier. Liquid nitrogen is supplied from a liquid tank that is filled with trucked in liquid. The liquid helium is distributed from the liquefier through liquid nitrogen shielded vacuum insulated transfer ducts. The distribution to the DS and TS cryostats, is managed by the re-condensing control dewar. Distribution to the PS cryostat is managed by the PS storage dewar. Flow sheets in Figure 15.11 through Figure 15.14 show in schematic form the helium piping that interconnects the cryostats, the dewars and the refrigerator/liquefier. As shown on the flow sheets, the only components of the cryogenic system that are inside the nuclear radiation shielding walls are the magnets and cryostats. All active valves, gas cooled current leads and maintenance items are outside the shielding walls. This arrangement requires long superconducting current bus leads that pass through the shielding wall.

The interconnections and valves shown on the flow sheets have been arranged to provide very flexible operation of the system. The system can maintain all four solenoids in steady state operation with the magnets fully charged and the beam on. The system can cool all of the cryostats from room temperature to operating temperature using the liquefier/refrigerator, the liquefier compressors, and an auxiliary heat exchanger cooled with liquid nitrogen. The system can cool one or more of the cryostats while maintaining the other cryostats at operating temperature. The system can be protected during a quench event by the relief valves and burst disks shown on the flow sheets. Quick-closing the appropriate valves can minimize the disturbance of the system due to a quench. The system has the flexibility of operation to allow re-cooling after a quench without warming all parts of the system.

Helium system

Steady state 4.5 K cooling system

For normal steady state operation of the complete system the flow circuit is displayed on the flow sheets of Figure 15.15 through Figure 15.18. The circuit for steady operation is shown in red. As shown on the flow sheet of Figure 15.16, high-pressure helium ready for throttling through the J-T valve is passed from the liquefier to the valve box of the two-phase loop-control dewar. The high-pressure helium is throttled through the J-T valve and then passes through the re-condensing heat exchanger submerged in the liquid in the dewar. Here the flash vapor is re-condensed by heat transfer to the liquid in the dewar. The temperature difference for heat transfer is the saturation temperature decrease associated with the pressure drop through the remainder of the cooling loop through the TS and PS cryostats.

The very low vapor-fraction stream leaving the re-condenser flows through the shielding wall to the TSu cryostat and then through the single cooling tube that is thermally bonded to a series of cold plates for each coil. The TSu cold plate for a coil cools the conductor of the coil by

conduction through heat drains from a copper cooling-wrap surrounding the coil. The arrangements of the heat drains and the cooling wrap are discussed in a later section. The stream absorbs all heat leaking to or generated within the TSU coils by vaporization of liquid helium at essentially constant temperature. The stream leaves the TSu cryostat with a small vapor fraction and flows out through the shielding wall to the valve box for the TS cryostats. As shown in the flow sheet, the helium conduit from the cryostat to the valve box is thermally bonded to the superconducting current leads for the TSU cryostat. In the valve box a small portion of the helium stream is diverted to cool the gas cooled current leads from TSU. There are actually two pair of leads associated with the TSU cryostat, one for the TS13u coil set at 1500 A, and one for the TSd coil set at 4000A. A vacuum-to-helium lead-through is required where the superconducting leads pass into the gas-cooled leads. The warm helium leaving the gas-cooled leads flows back to the suction of the liquefier compressor. The current leads are described in more detail in the section on current leads.

The main stream of helium flows from the valve box through the shielding wall to the TSd cryostat. As the stream flows through the TSd cryostat, it absorbs all heat leaking to or generated within the TSd coils in the same manner as in the TSu cryostat. The stream leaves the TSd cryostat with an additional vapor fraction corresponding to the heat load of the TSd cryostat, and flows out through the shielding wall to the valve box. As shown in the flow sheet, the helium conduit from the cryostat to the valve box is thermally bonded to the superconducting current leads for TSd. In the valve box a small portion of the helium stream diverted to cool the gas cooled current leads from TSd. There are actually two pair of leads associated with the TSd cryostat, one for the TS3d5 coil set at 1500 A, and one for the TS4 coil set at 4000A. The main stream then flows from the valve box to the DS cryostat.

The helium stream cools the DS cryostat and current leads in the same manner as the TS cryostats. After cooling the TS and DS cryostats the stream flows from the valve box back to the control dewar with a substantial liquid fraction at 4.5K

The two-phase stream enters the control dewar, shown in the flow sheet of Figure 15.16, through a valve that can be throttled a small amount if necessary to maintain the temperature difference across the re-condensing heat exchanger in the control dewar. The returning two-phase stream enters the vapor space of the control dewar where the liquid fraction separates and collects in the liquid pool. The vapor fraction together with the vapor generated by the re-condenser flows from the vapor space of the dewar to the low-pressure passage of the liquefier/refrigerator. A constant liquid level is maintained in the control dewar by drawing liquid from the bottom of the liquid pool and passing it to the PS cryostat system. The flow to the PS is controlled by setting a small throttling of the vapor return valve in response to the liquid level in the control dewar.

The liquid from the TS-DS control dewar flows to the PS system, shown in the flow sheet of Figure 15.17, and joins the stream in the down-comer from the bottom of the PS dewar. The liquid stream in the down-comer is driven by natural convection between the PS dewar and the PS cryostat. The combined liquid stream flows down the down comer and into the bottom of the of the helium space in the PS cryostat. The PS cryostat operates flooded with liquid helium. Bubbles formed, as the liquid helium absorbs heat in the PS cryostat, rise to the top of the helium space in the PS cryostat and flow horizontally into the riser at the top of the cryostat. The riser carries the bubbles and a substantial amount of entrained liquid back to the PS dewar. The riser enters the bottom of the dewar and empties the riser stream into the dewar at the liquid level in the dewar. The large liquid surface area in the dewar allows the vapor bubbles to separate from

the liquid which then flows back to the down comer. The natural convection flow up the riser and down the down-comer is driven by the difference in the average density between the heavier all liquid in the down-comer and the lighter bubbly liquid in the cryostat and in the riser. The liquid level in the PS dewar is used as the signal to control the refrigeration output of the liquefier system. The vapor that separates from the liquid in the dewar flows out of the top of the vapor space in the dewar and then back to the TS-DS valve box where it joins the low-pressure flow back to the liquefier.

As shown on the flow sheets of Figure 15.12 and Figure 15.13, the PS cryostat can be cooled by a once through stream of liquid helium. High-pressure helium is throttled at the top of the PS dewar. The flash vapor is re-condensed in the internal heat exchanger. The liquid flows through the down comer into the helium space surrounding the coils. The vapor generated as the coils are cooled together with the vapor generated by the internal heat exchanger flows through the riser and into the dewar and them out the LP He line.

In contrast to the TS and DS. The current leads of the PS are in the helium space. The superconducting current bus leads pass through the shielding wall inside the helium down-comer conduit. At the bottom of the PS dewar, the superconducting current leads and the flow for the gas cooled leads branch off from the down-comer conduit and go to the cold end of the gas cooled current leads. The warm helium leaving the gas-cooled leads flows back to the suction of the liquefier compressor. The design of the current leads is discussed in more detail in the section on current leads.

The flow sheet of Figure 15.18 shows the connections to the helium liquefier and the connections to the cool-down heat exchanger. Shown in red are the flow of high-pressure helium from the liquefier to the valve box and the return flow of cold low-pressure helium. Also shown in red is the flow of warm low-pressure helium to the compressor suction.

States for steady-state operation with the beam on

Table 15.1 shows the proposed states for the heat loads shown in Table 15.2. These states are only representative states since the precise values depend on many details that will not be available until the detail design of the components are finalized. The states in Table 15.1 have been selected based on the design of the G-2 magnets that have been successfully operated at BNL. The basic parameter is the mass flow per unit area of the cooling tubes through the TS and DS. The range of values recommended by Green[9] is 10 to 40 kg/(s*m^2). The corresponding mass flow for the 0.625-in ID tube is 1.9 to 7.9 g/s for the helium flow. This range is within the range that is reasonable for a refrigerator with the capacity to cool the experiment. For example, the model 4000 liquefier refrigerator that is at Brookhaven has a J-T flow of 49 g/s for refrigerator mode and 15.1 g/s for liquefier mode. The corresponding ratings are 700 W in the refrigerator mode and 150 liter/hr in the liquefier mode.

[9] M. A. Green, W.A. Burnes, and J.D. Taylor, "Forced Two-phase Helium Cooling Large Superconducting Magnets, Advances in Cryogenic Engineering, Vol. 25, p. 420, Plenum Press, New York, 1980

Table 15.1 – State properties for steady operation of the cryogenic system.

State No	State description for Helium	Pressure (KPa)	Temperature (K)
1	After throttle into heat exchanger in control dewar	142	4.60
2	After heat exchanger in control dewar	140	4.58
3	Inlet to TSu cryostat	140	4.58
4	Exit from TSu cryostat	138	4.57
5	Inlet to TSd cryostat	138	4.57
6	Exit from TSd cryostat	136	4.58
6	Inlet to DS cryostat	136	4.58
7	Exit from DS cryostat	130	4.5
8	Two-phase return to control dewar	130	4.5
9	Vapor exiting control dewar	130	4.5
10	Liquid exiting control dewar	130	4.5
11	Liquid in the PS down comer	130	4.5
12	Two-phase in the PS riser	130	4.5
13	Vapor leaving the PS dewar	130	4.5

The heat loads shown in Table 15.2 are based as follows. The thermal conductance of stainless steel between 80 and 4.5 K is 3.5 W/cm. The loads for the mechanical supports for the coils are based on the geometry given in the section on forces and stresses. The loads for the helium valves are based on the conductance of the extended valve stems that have 80 K heat stations. The tubes of the stems are 18 inches long by 1-inch by 0.065 wall for the outer and 0.75 inch by .065 wall for the inner tube. The vacuum separator tubes are 18 inches long by 1-inch by .065 wall. The isolation for the vent tube for the PS is schedule 10S stainless steel pipe by 30 inches long.

The thermal radiation load is based on a surface emissivity of 0.02 and the total surface of the 4.5 K mass. The recommended insulation is MLI with the same conductance as that corresponding to the low emissivity surface and an open high vacuum. The MLI avoids the difficulties associated with the open vacuum.

The heat loads for the current leads are based on a required flow of helium from 4.5 K of 3.2 equivalent-liquid-liters per hour per 1000-amp pair. This value is for commercially available current leads

Table 15.2 – Heat loads for the 4.5 K system for steady state operation with the beam on

System component	Refrigeration at 4.5 K (W)	Liquid helium consumption (l/hr)
TS 1 totals	20.18	17.6
Supports	12.8	
Valves	1.37	
Vacuum separators	0.86	
Thermal radiation from 80 K	1.96	
Conductor electrical joints (qty 35)	3.19	
Current leads		17.6
TS 2 totals	20.13	17.6
Supports	12.8	
Valves	1.37	
Vacuum separators	0.86	
Thermal radiation from 80 K	1.96	
Conductor electrical joints (qty 33)	3.14	
Current leads		17.6
DS totals	20.63	12.8
Supports	6.04	
Valves	1.37	
Vacuum separators	0.86	
Thermal radiation from 80 K	8.26	
Conductor electrical joints (qty 24)	4.10	
Current leads		12.8
Control dewar		1.3
PS totals	208.37	11.2
Supports	8.0	
Valves	2.99	
Vacuum separators	0.86	
Thermal radiation from 80 K	3.28	
High energy radiation	192	
Conductor electrical joints (qty 10)	1.24	
Current leads		11.2
PS dewar		1.3
GRAND TOTALS	269.31	61.8

Thermal Design for the MECO Detector and Transport Solenoids

The detection and transport solenoids (DS and TS) are conduction cooled to 4.5 K using a two-phase flow design similar to the one used in the G-2 magnet program. The helium

temperature cooling tubes are soldered to cooling plates that span each individual coil and connect to 1.5 mm thick copper sheets that envelope the entire coil. A simplified cross sectional view of a coil is shown in Figure 15.1. The coil is encased in two 1.5 mm thick copper sheets. These sheets are bent at the ends to fit snugly into the mandrel as shown. Copper ribs are bolted over the upturned edges of the sheet to aid in the conducting heat to the thermal bridge mounted at or near the top of the coil. The bolts (not shown in Figure 15.1) pass through the rib, sheets, the coil mandrel, and through the next coil's mandrel, sheets and rib. The thermal bridge consists of a 1/4 inch (6.35 mm) thick copper plate with flanges that mate to the surfaces of the copper ribs. The width of the bridge is 16" (in the angular direction of the coil). The helium cooling tube (copper 5/8" ID) is laid out in a serpentine manner and brazed to the thermal bridge as shown in Figure 15.2. The copper ribs and the copper sheets extend around the entire solenoid. An analysis of the expected temperature distribution was performed for the thermally worst-case coil in the detection solenoid. The assumed dimensions for this case are summarized in Table 15.3.

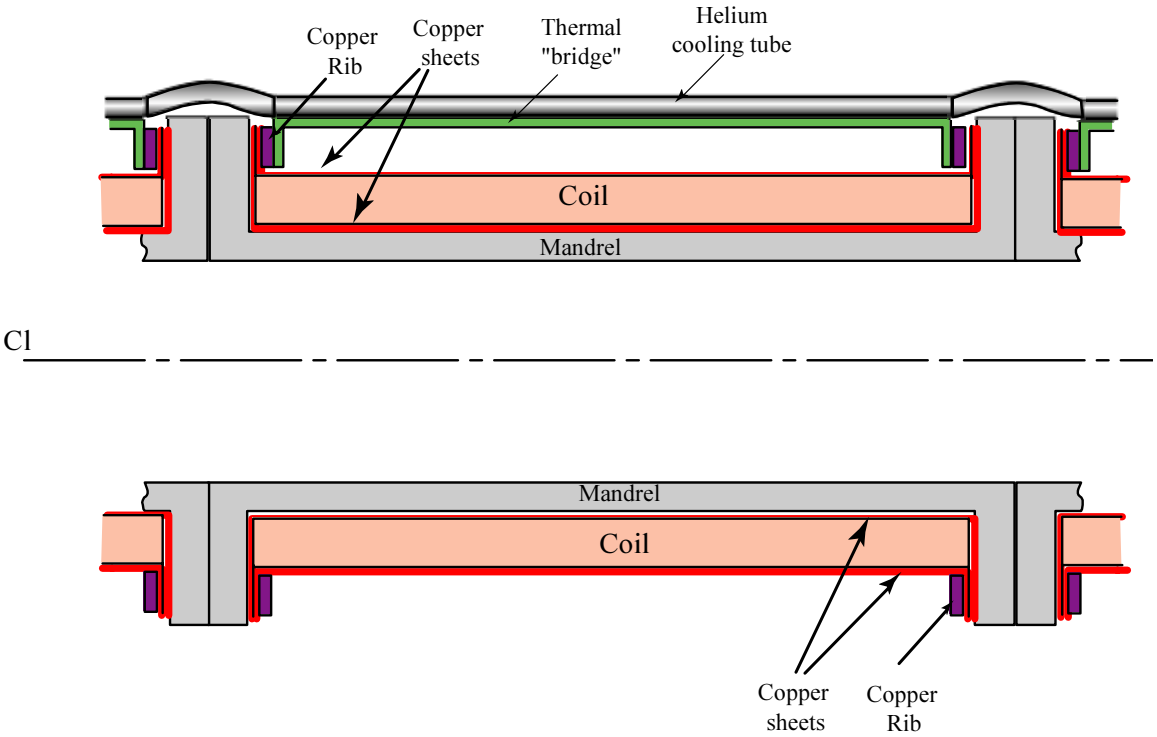

Figure 15.1 – A schematic cross section of the conduction cooling method proposed for the DS and TS. The drawing is not to scale.

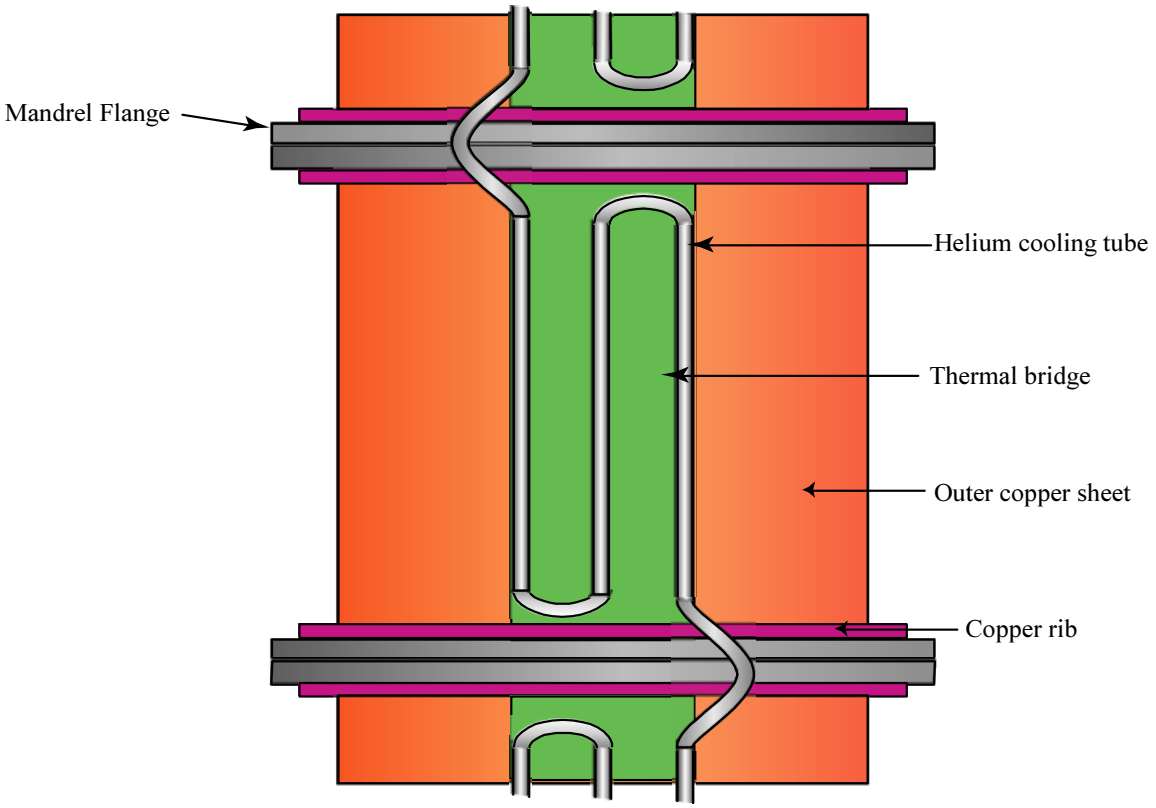

Figure 15.2 – A conceptual top view of a TS or DS coil segment. The 4 K cooling loop is shown brazed in position to the thermal bridge. The drawing is not to scale.

The thermal contact between the copper rib and the copper sheets are due to direct contact under the 5/8" diameter bolts that secure the copper ribs, copper sheets and the mandrel flanges together. The thermal conduction per bolt is calculated assuming that the apparent Cu-Cu contact area under the bolt is three times the cross sectional area of the bolt. The bolts are tightened to the point where the copper under the bolt is brought to one-third of its yield stress. The rms variation in the surface finish of the clean copper surfaces is assumed to be 0.002". Using the work Cooper, Mikic and Yavanovich ("Thermal Contact Conductance" Int. J. of Heat transfer v. 12, pp 279-300, year?) results in a thermal surface conductance of 6.45 W/K for each 5/8" diameter bolt. A similar conductance can be calculated for a 1/2" diameter bolt of 4.18 W/K. In reality, the contact conductance between the sheets and the ribs is concentrated around the bolts; however, in this model, we distribute the total conductance between the sheets and the ribs over the entire contact surfaces of the ribs and the sheets. Five 1/2” diameter bolts maintain the thermal contact between each copper rib and its thermal bridge. Once again, in the thermal model presented here, the concentrated conductance between the thermal bridge and the ribs around the 1/2" bolts is distributed over the contact area between the thermal bridge and the rib.

Table 15.3 – Worst case dimensions for conduction cooling in the DS and TS solenoids.

Diameter of solenoid	2.18 m
Distance between mandrel flanges	0.68 m
Copper sheet thickness	1.5 mm
Copper rib thickness	6 mm
Copper rib width	3.81 cm
Copper thermal conductivity	300 W/m-K
Diameter of main bolts	1.58 cm
Spacing of main bolts	30.48 cm
Thermal bridge width	40 cm
Thermal bridge thickness	6.35 mm
bolt diameter-thermal bridge	1.27 cm
Spacing of bolts-thermal bridge	7.6 cm
Heat load per unit surface area	4×10^{-2} W/m^2

The heat load is assumed to be a uniform heat load of 4×10^{-2} W/m^2 over the entire surface of the copper sheets. Superinsulated surfaces can have the thermal performance of vacuum insulated polished surfaces. The heat load was estimated by calculating the radiation interaction between two surfaces at 77 K and 4 K with an emissivity of 0.02. The cryostats are assumed to be superinsulated between 4 K and 77 K shield and from 77 K shield to 300 K.

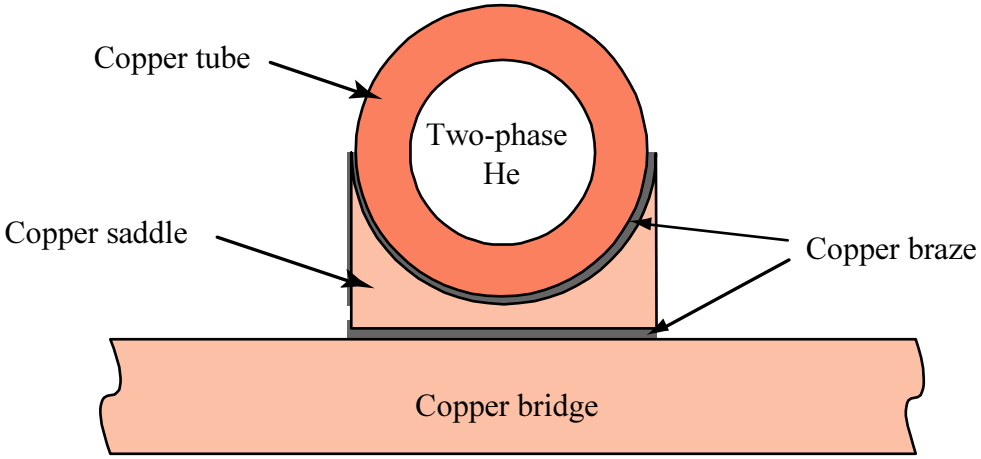

Figure 15.3 – Mounting scheme for the helium cooling tubes to the thermal bridge. The copper cooling tube is brazed to the copper saddle that is brazed to the copper bridge. (Not to scale.)

The thermal resistance due to the convection in the two-phase pipe is neglected. However the braze joints between the copper bridge and the He cooling tubes are assumed to have a thermal conductance per unit length of tube of 49 W/m-K. This is the thermal resistance of the structure shown in Figure 15.3. We have assumed that the copper braze has a thermal conductivity of 1 W/m-K and that each braze is 250 μm thick. The thermal contribution due to the thickness of the copper tube and the copper saddle are neglected.

Figure 15.4 shows the expected temperature distribution for the copper shield and bridge in "worst case" DS coil. The coordinates of the figure are the axial distance in the vertical direction and the circumferential distance in the horizontal direction. Since the temperature distribution will be symmetric over the axial centerline of the thermal bridge and the ring halfway between the coil ends, only part of the thermal bridge and the copper sheet is shown. The copper sheet is the rectangle in the upper half of the figure. The top edge of the figure is the centerline between the two ends of the coil. The lower edge of the Cu sheet area is the Cu rib. The right most edge of the figure is 180^{o} around the solenoid away from the thermal bridge. The left most edge of the figure is the axial centerline of the bridge. The figure shows one-quarter of the bridge section in violet on the lower left-hand side of the plot "folded away" from the copper sheet.

Figure 15.4 – Contour plot of the expected temperature distribution for the worst case coil in the DS.

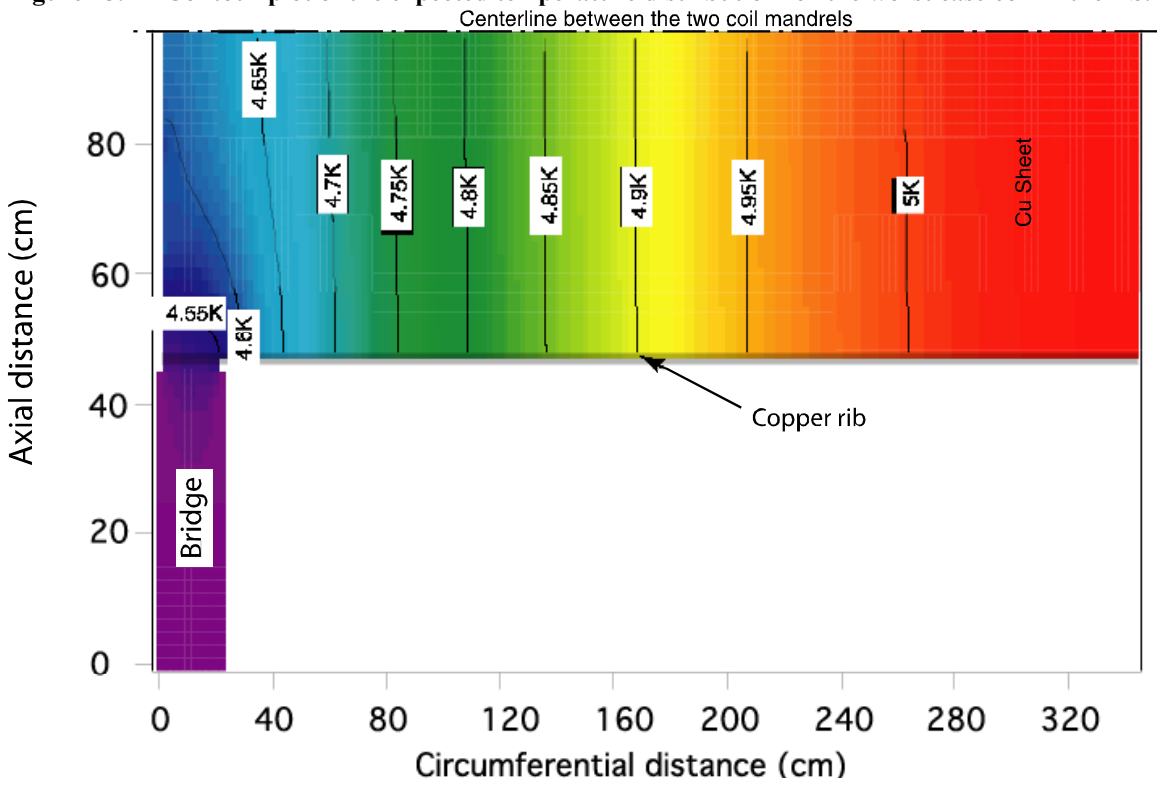

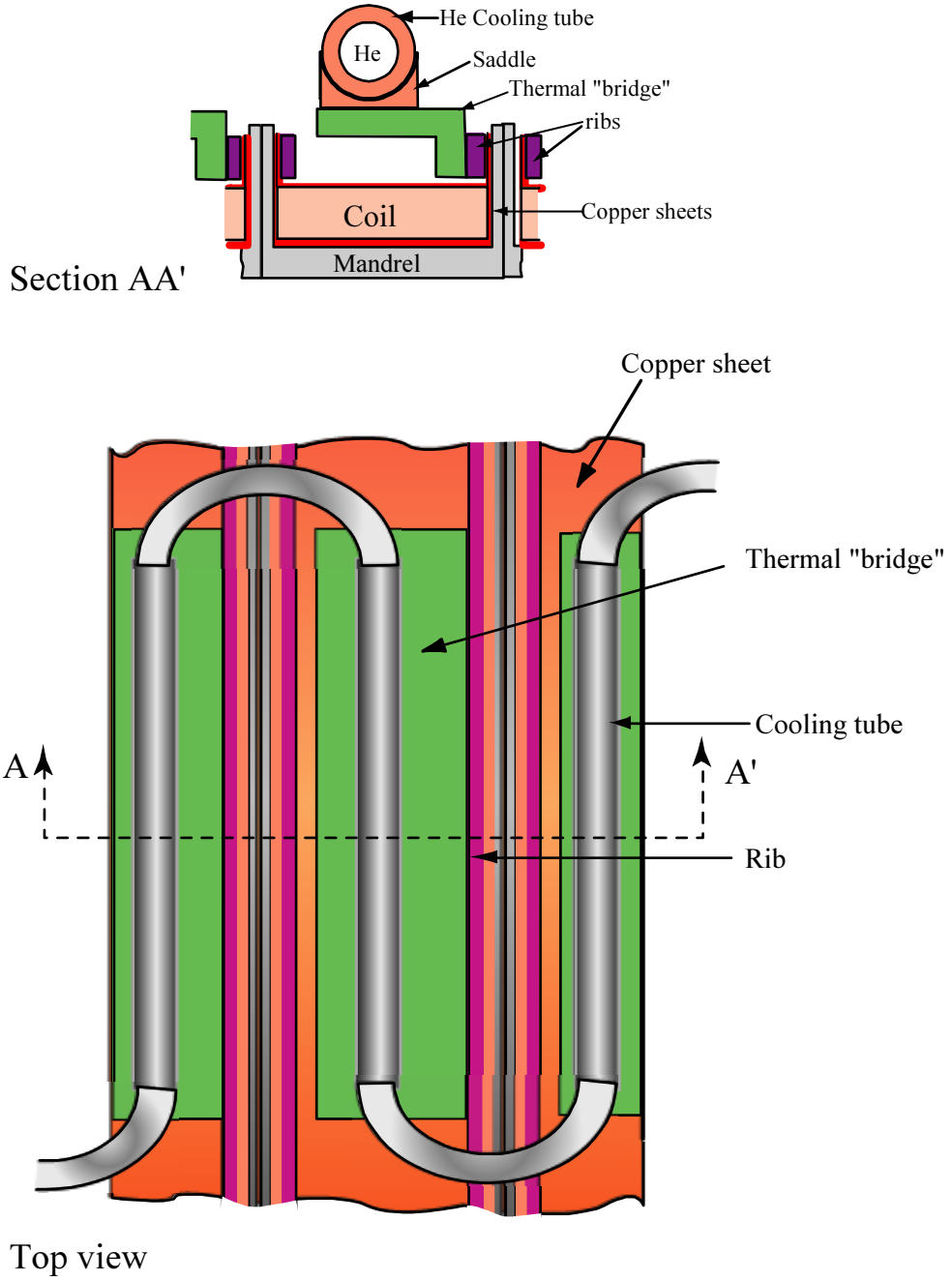

Figure 15.5 – Conceptual drawing for cooling of short sections of the TS coil. Do not scale.

The maximum temperature in the copper sheets is 5.04 K. Since the magnetic fields in the detection solenoid are relatively small, this temperature is within the margins set for the conductors in the coil. In this large coil, the conduction in the sheets dominates the conduction in the ribs. In the TS solenoids, the axial distance between the ends of the coil is not 68 cm as used above but rather ~5 cm. In this case, the cooling of the coil can be achieved using the configuration shown in the conceptual drawing of Figure 15.5. The thermal bridge dimension transverse to the centerline of the coil is still sixteen inches. The cooling tubes are now brazed in a single transverse pass across the thermal bridge. In this case, the thermal bridge is cantilevered

off one flange as shown. For the short coils, it is not necessary to connect the thermal bridge to both sides of the coil.

There are additional 4 K cooling stations for the support rods of the TS and DS solenoids (which are discussed further elsewhere in this report). These stations are directly cooled by the return trace of the helium cooling tube.

Please note that since the flow in the helium cooling tube is two-phase, frequent (and large) changes in the vertical elevation of the cooling tube should be avoided. Many large changes in elevation can lead to instabilities in the flow.

Thermal Design for the MECO Production Solenoid

Unlike the detector and transport solenoids, the production solenoid has a large nuclear heating load. The conduction cooling approach taken on the DS and TS coils does not work in the production solenoid. Here a pool boiling/natural convection approach was taken. The helium can for the PS coil system contains about 6700 liters of 2-phase helium at a saturation temperature of about 4.5 K. Using nuclear heating projections calculated by UC-Irvine, it was clear from the beginning that the very first PS coil at the 5 T end would have the lowest temperature margins for a coil design cooled at the ID and OD with bath helium. For this reason the thermal design focussed on this coil.

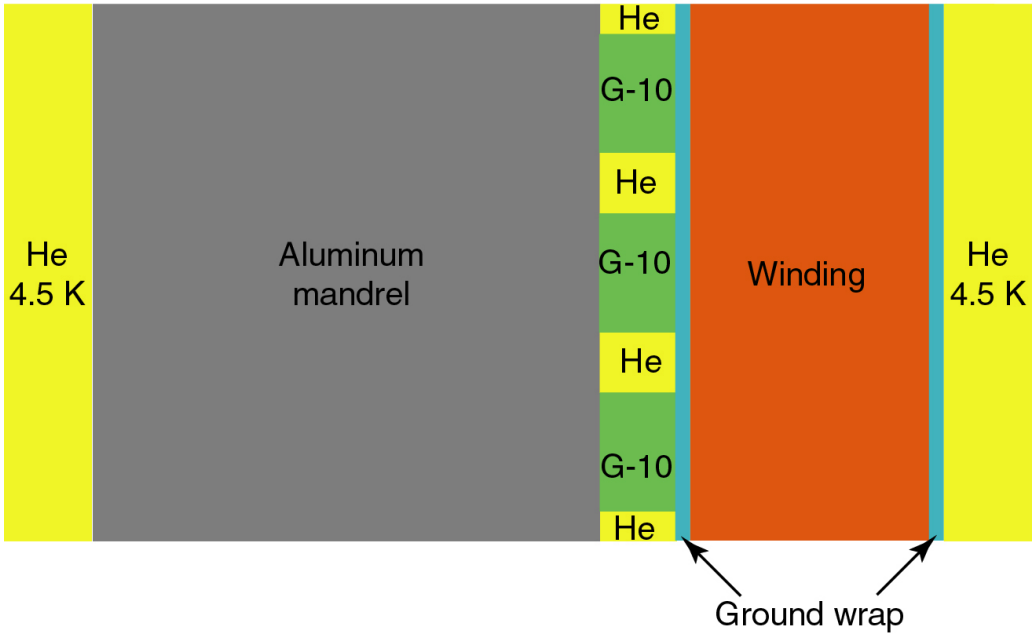

Figure 15.6 – Configuration of the 2D model used to calculate the temperature distribution in the coil windings and the aluminum mandrel. The vertical direction corresponds to the axial direction in the PS coil, the horizontal corresponds to the radial direction. The bore of the magnet is in the right hand direction. Do not scale.

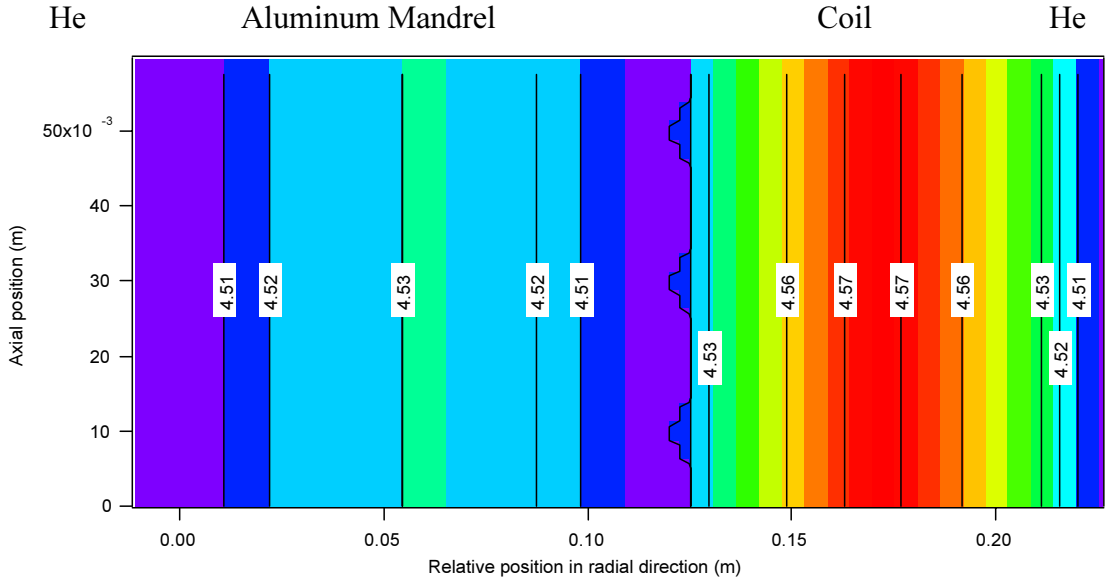

Figure 15.7 – Temperature distribution in the PS 1 coil with the radiation heat load. Violet corresponds to a temperature 4.5 K and red to 4.57 K. Labels on the temperature contours are in degrees Kelvin.

For a more detailed discussion of the thermal analysis please see MECO memos [mm038 and mm039].

The simplified thermal model of the design is shown in Figure 15.6. The outside surface of the aluminum mandrel is bathed in liquid helium at 4.5 K. The space between the winding and the aluminum is filled with 5 mm thick G-10 plastic interspersed with cooling channels. The cooling channels run in the coil's circumferential direction. They are 1 cm wide in the axial direction and 5 mm wide in the radial direction. The channel spacing is 2 cm on-center in the axial direction. The winding has a 1mm thick ground wrap on either side. Liquid helium bathes the inner surface of the winding through the ground wrap layer. The coils have a low effective radial thermal conductivity because of the low thermal conductivity of the electrical insulation around the conductor. An image of the expected temperature distribution with nuclear heating in the PS 1 coil is shown in Figure 15.7. The model shows that for a coil radial build of about 10 cm assumed in this model, the temperatures peak at 4.57 K near the middle of the coil. The proposed PS1 coil has a build of about 12.5 cm, which will result in slightly higher peak temperatures. The peak temperatures at the coil radial center are not so important, however, because, as discussed in [mm038], the minimum temperature margin in the PS coil is actually at the coil ID, immediately adjacent to the ground wrap. Nevertheless, this model was useful for setting the spacing of the helium channels at the coil OD, as discussed above.

One of the issues for cooling the PS coil using pool boiling is the concern that helium gas may be trapped on horizontal surfaces and insulate the coil from the liquid helium bath. This could result in a local hot spot on the coil that could induce a quench event. Care must be taken to insure against cup-like surfaces that could trap large gas bubbles on heat transfer surfaces. We do expect a helium gas bubble at the top part of the inner surface of the coils in the PS solenoid. Multiple open channels are placed vertically through every mandrel flange to allow the free flow of helium gas and liquid from the inner helium space to the outer helium space, as well as provide additional cooling contact area for the coils.

The deleterious insulating effect of a large bubble on the inner surface of the coil is mitigated by the large circumferential conductivity of the coil; and hence, the design can tolerate a large bubble. To show this, a model was developed to quantify the effect by assuming that there is no heat transfer from the coil to the gas in the bubble. Estimates of the bubble size in the inner bore of the PS 1 coil suggests the bubble would extend 14 cm in the circumferential direction for a 57 W load. Contour plots of the difference in temperature between the case with no bubble and for a bubble of 15 cm extent are shown in Figure 15.8. The model shows a local temperature increase of ~50 mK in the conductor at the center of the bubble over that of the no bubble case (4.564 K with the bubble versus 4.516 K without). The angular conduction in the coils spatially attenuates the disturbance in the temperature field in the radial direction.

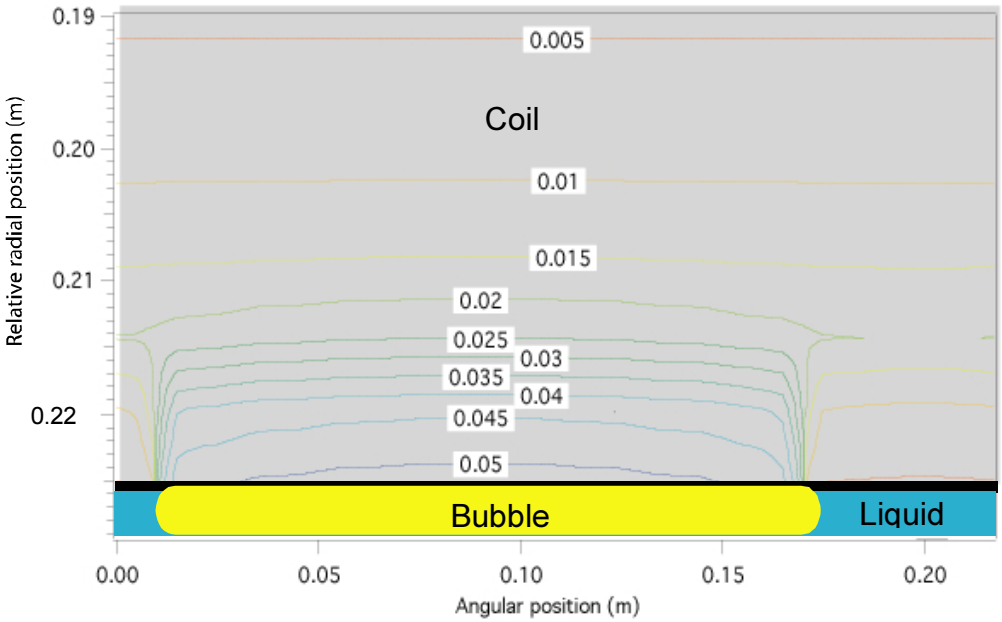

Figure 15.8 – Contour plot of the change in the temperature distribution in the PS 1 solenoid due to the presence of a 15 cm wide bubble on the inner surface of the coil. Temperature labels are in degrees Kelvin.

The boundary conditions imposed in this model require the heat transfer out the RHS of the graph above to enter on the LHS (a cyclic boundary condition). The bubble surface is assumed adiabatic and the liquid surface is held at 4.5 K. The boundary condition at the top of the graph requires that the surface where the cooling channels are (at relative radial position of 0.12 m is held at 4.5 K by the He flow there.

Flow in the channels between the Coil and the Mandrel

The flow in the He cooling channels that are between the mandrel and the coil is induced by the difference in the average density in the channel (due to the presence of bubbles) versus the liquid density in the outer helium bath of the dewar. To make sure that the channels do not become "gas bound" due to the heat flux of nuclear heating in the PS, a simple model to estimate of the flow velocities and the quality of the flow in the channel was made. Estimates of the heat load to the PS 1 coil vary from 50-70 Watts. This power will be carried away by the helium on the inner surface of the coil, the helium in the flow channels between the mandrel and the coil, and the helium on the outer surface of the coil. Using a worst case scenario, we assumed that 71 Watts of power is deposited into half of the vertical cooling channels in the PS 1 coil (62 channels 5mm x 1cm x 1.54 m long). The model suggests that the velocities in the channels will be of the order of 0.5 m/s with an average quality of 1.3 %. The low quality of the flow combined with the fact that the assumed heat flux is 4-5 times what will be realized in the real PS coils suggest that the flow channels will remain flooded with liquid, and hence, will operate as intended.

To be more specific about the model, the model assumes an entrance loss coefficient of 1 and an exit loss coefficient of 1 for each of the 1 cm diameter inlet and outlet holes into the flow channels. The viscous loss in the pipe is calculated using the viscosity of the liquid component, and an assumed quality at the mid-length point of the pipe. The velocity of the flow in the pipe is calculated using the assumed mid-length quality and requiring that the mass flow rate of the gas correspond to the total heat transfer rate divided by the heat of vaporization. The gas and liquid velocities are assumed to be the same. The gravitational head driving the flow is the difference in densities of the fluid in the channel and that of bulk liquid helium (the density of the helium in the outer He bath) multiplied by g and the diameter of the solenoid. The solution is arrived at by varying the mid-length quality until the head losses match the gravitational head.

The PS safety vent line

The sizing of the PS vent line and modeling of a quench event is discussed in detail in MECO memo #mm047. The proposed safety vent line is shown in Figure 15.9. The safety line is sized for a quench event where all coils in the PS simultaneously quench. The predicted internal pressure in the helium tank for various diameter safety lines is shown in Figure 15.10. The conceptual design has chosen the 10” diameter line. (The model uses an incompressible flow model for the flow in the pipe.)

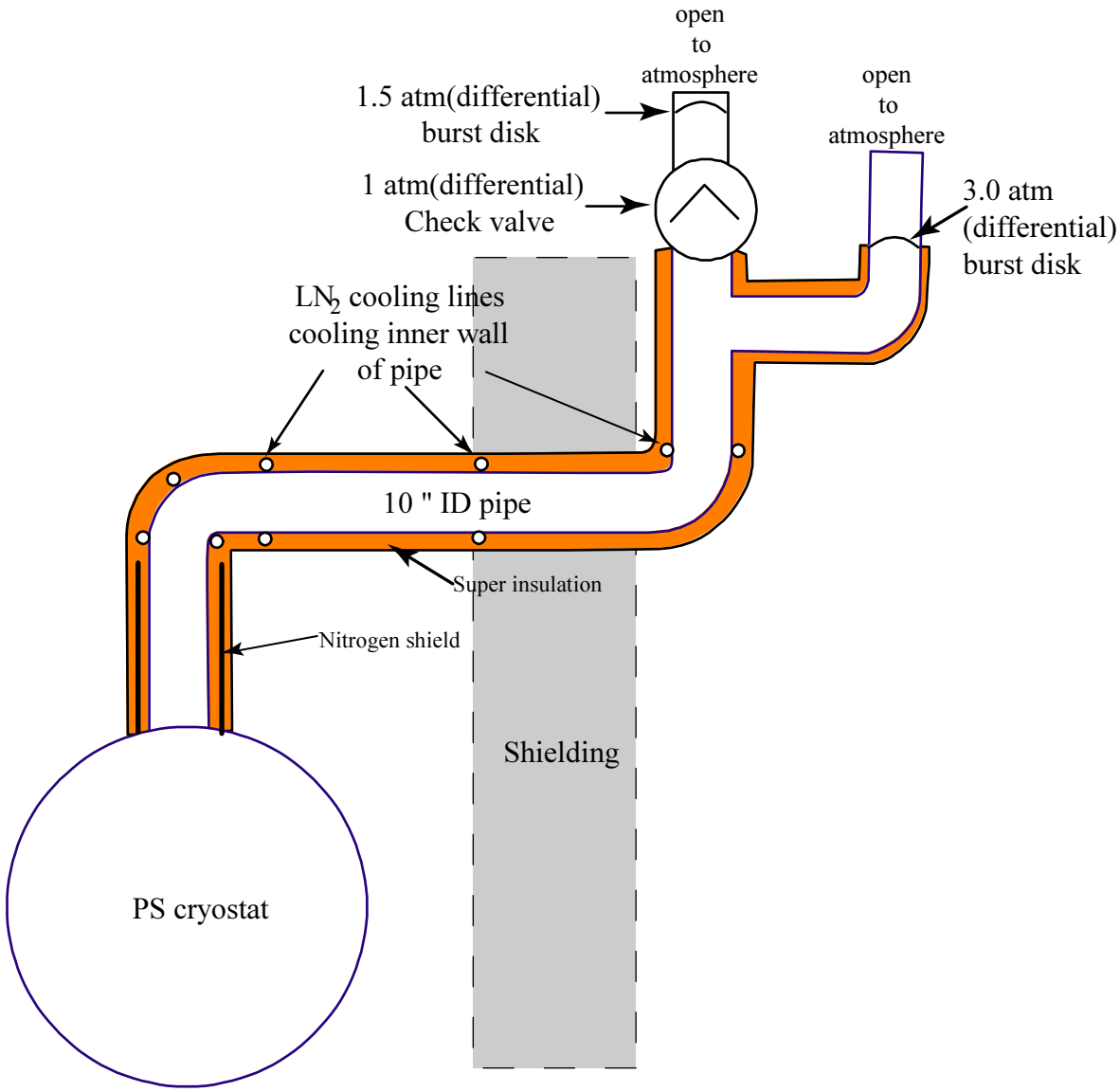

Figure 15.9 – The proposed vent line for the PS cryostat.

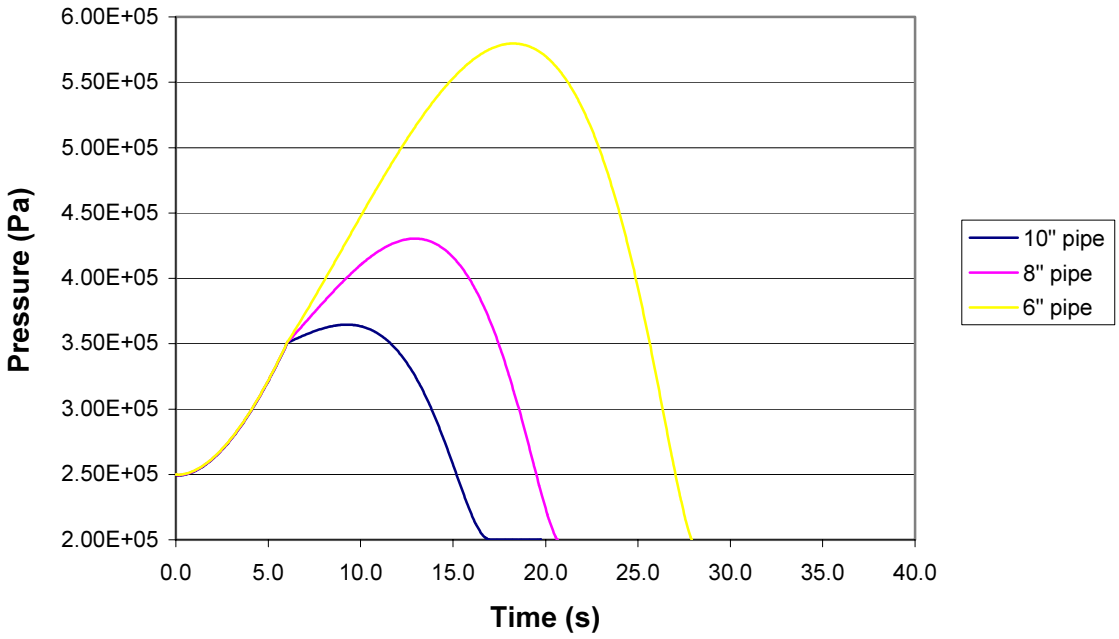

Figure 15.10 – Pressure versus time for an "all coil" quench in the PS solenoid for three different diameter safety pipes.

Liquid nitrogen system

Liquid nitrogen is utilized to reduce the refrigeration required at 4.5 K by intercepting heat flowing from room temperature. The liquid nitrogen is to be supplied by a commercial vendor. A large storage tank will be located at the site of the experiment. The regular delivery by transport trucks will keep an adequate supply in the storage tank. Permanently installed insulated piping will carry the liquid from the tank to the experiment, the liquefier refrigerator and to the cool-down heat exchanger.

Liquid nitrogen is transferred to the individual cryostats and dewars of the experiment through the same transfer conduits that carry the several 4.5 K lines. The liquid nitrogen lines in the conduit serve to cool the copper foil inter-layer heat station of the MLI insulation for the 4.5 K lines.

The liquid nitrogen lines in the conduits also serve to cool the heat stations on the thermal stand standoffs where the helium lines go through the walls separating the different vacuum systems in the cryostats and in the transfer conduits.

The heat stations for the valves in the valve box and for the valves in the PS dewar are also cooled by the liquid nitrogen lines.

The MLI insulation systems for the two dewars of the system are of the design used for commercial gas shielded helium storage and transport dewars.

In the individual cryostats (TS, DS and PS), the liquid nitrogen cools the mechanical support struts and the inter-layer heat station of the MLI (multi-layer insulation) insulation. One stream of nitrogen cools the heat stations on the support struts and a second stream cools the heat station in the MLI. The inter-layer heat station is formed from a copper sheet 1 mm thick. The nitrogen flows through 7 mm copper trace tubes that are thermally bonded to the copper sheet. The inter-layer heat station extends around the magnet coils of the TS and DS, covering the OD, ID and

ends. These circumferential sheets are slit to avoid eddy current loads during magnet quench. The heat station of the PS covers the helium volume in the same manner. The cooling trace tubes are spaced 1 m or less apart on the copper sheet of the heat station. The streams of nitrogen vapor leaving the cryostats are vented to the atmosphere. Other materials, e.g. aluminum, and configurations may be used for the liquid nitrogen cooled heat station.

Table 15.4 shows the heat loads for the liquid nitrogen system for steady state operation. The total liquid nitrogen consumption for these heat loads is 30 liters per hour. The liquid nitrogen consumption for the model 4000 liquefier refrigerator at BNL ranges from 7.4 g/s (33 liters/hr) for refrigeration mode to 109 g/s (109 liters/hr) for liquefaction mode.

Table 15.4 – Heat loads for the liquid nitrogen system for steady operation

Component	Heat station load (W)
PS cryostat	
Support stations	92
MLI stations	35
TS cryostat (both TS)	
Support stations	922
MLI stations	41
DS cryostat	
Support stations	64
MLI stations	89
Valve stations	58
Vacuum standoff stations	37
GRAND TOTAL	1338

Cool-down system

Cooling from room temperature to 80 K

Starting from room temperature, the system is cooled down to 80 K by a stream of helium gas that is supplied by compressor for the liquefier/refrigerator. The high-pressure helium from the compressor is cooled with liquid nitrogen to 80 K in an auxiliary heat exchanger. The liquid nitrogen is trucked in from a commercial source. From the heat exchanger shown in Figure 15.14, the 80 K helium gas is transferred through the connections shown in the flow sheet of Figure 15.12 to the TS-DS cryostats and the PS cryostat. The cool-down transfer piping is parallel to the 4.5 K piping in the schematic. As shown in Figure 15.11, valves can be set to direct the cool-down helium to the TSu, TSd and or DS cryostats and to close off the 4.5 K connections. The helium flows through the same cooling tubes in the cryostat that are used for steady state cooling. The flows through the cryostats are in parallel. As shown in Figure 15.12 valves can be set to direct the cool-down helium to the PS cryostat. The cool-down helium flows to the PS cryostat external dewar through the HP He line and or through the liquid He line. The cool-down helium returns through the LP He line. The cool-down helium flows from the HP He line through the internal heat exchanger in the dewar or from the liquid He line into the heat exchanger exit line. The cool down helium then flows through the down comer into the helium

space around the PS coils. The cool-down helium cools the PS coils by forced convection as it flows over the coils into the riser at the top of the helium space. The helium flows through the riser and into the dewar. The helium flows from the dewar through the LP He line and through the connections shown in Figure 15.12 to compressor suction on Figure 15.14.

Cooling from 80 K to 4.5 K

For cooling below 80 K, the refrigeration is from the expanders in the liquefier. In preparation for cooling below 80 K, the liquefier is cooled to operating temperature. During this stage of cooling the liquefier is operated in the 100 percent liquefier mode with the helium withdrawn for cooling the cryostats returned as warm helium to the compressor suction. A warm up heat exchanger may be required to prevent over cooling the compressor suction. Some of the wasted refrigeration may be recovered by utilizing internal cool-down by pass connections inside the liquefier. For minimum cool-down time the liquefier should be operated so that the expanders operate at their respective design points.

During the 80 K to 4.5 K cool down, high-pressure helium is passed from the liquefier to the individual cryostats through the HP He lines in the same way as for normal 4.5 K operation. The by-pass valves in the HP He lines between the TS and DS cryostats are opened to achieve parallel flows through the cryostats. The valves at the exits from the cryostats are set to direct the return gas from the cryostats to the cool-down helium return line. The return helium is returned to compressor suction or to internal by-pass lines within the liquefier.

When the cryostats and their coils have reached 4.5 K, the return gas is switched to the normal steady state configuration and the liquefier is adjusted for combined refrigeration and liquefaction operation. Near the end of the cool-down process the flows through the TS and DS cryostats can be switched to the steady-state series flow configuration. The final step of the cool down is to fill the control dewar to the normal liquid level. The PS cryostat is switched to the steady configuration after the PS dewar fills with liquid to the steady state level. The flow of HP He that is being throttled into the internal heat exchanger is turned off and the flow from the control dewar through the liquid line is turned on. The valve from the bottom of the PS dewar is opened into the down comer to establish the natural gravity driven circulation loop between the PS dewar and the helium space in the PS cryostat. When the beam is turned on, the additional vapor generated in cooling the PS coils will increase the flow rate in the convection loop and enhance the cooling of the PS coils.

Estimate of Cooldown Times

The estimated cooldown times are shown in Table 15.5. Three different limiting cases are given for the 300 to 80 K cooldown process as well as three limiting cases for the 80 to 5 K cooldown process.

The 300 to 80 K processes assumes that helium gas flowing at the full compressor flow rate (of 81 g/s) is cooled to 80 K using a liquid nitrogen heat exchanger and then passed through the cryostat to be cooled. The "Cooling Power limit" column contains the 1/e time to cool the solenoids assuming 100% heat exchange effectiveness between the solenoid and the He flow.

Table 15.5 – Estimate of cooldown times for three different cases.

	300 to 80 K cooldown			80 to 5 K cooldown		
	Cooling Power limit	**Thermal Resistance limit**	**Maximum ΔT of 10 K**	**Cooling Power limit**	**Thermal Resistance limit**	**Maximum ΔT of 10 K**
Coil	**hrs**	**hrs**	**hrs**	**hrs**	**hrs**	**hrs**
PS	8.77	34.58	58.89	20.331	26.66	50.04
TS	6.61	13.45	214.90	15.694	17.37	50.32
DS	3.09	7.21	121.37	7.672	8.91	29.19

The "Thermal Resistance Limit" column shows the results of models that attempt to account for the thermal resistances in the solenoid cryostats. In the PS, the heat transfer is assumed to occur only on the solenoid surface with largest radius (in the outer helium vessel). In this model, all the thermal energy stored in the solenoid and the mandrel is assumed to reside at the inner radius surface of the solenoid. The thermal flow path is assumed to be radially outward, through the coil (0.1 m thick), through the ground wrap, and into the helium ($h = 3$ W/m^2-K). The addition of these thermal resistances reduces the effectiveness of the heat transfer and increases the 1/e time for the 300 to 80 K process from 8.77 to 34.58 hrs in the PS solenoid.

The "Thermal Resistance Limit" models for the TS and DS systems place all the stored thermal energy at the radius corresponding to the center of the solenoid. The temperature at the center of the solenoid is assumed spatially uniform but temporally varying. The assumed conduction path from this thermal reservoir is radially through the coil winding to the copper sheets then through the copper sheets in the angular direction to the cooling platform. The Cu sheets are modeled as fins and no angular conduction is assumed in the windings. The thermal resistances in the cooling platforms (both convective and conductive) are neglected.

The "Maximum ΔT of 10 K" column shows the results of a model where the heat transfer rate is limited by requiring that the maximum temperature difference in the coil to be no more than 10 K. This is done to avoid excessive thermal strains in the magnet that might damage it. In this case, the maximum cooling rate is calculated by dividing the maximum temperature difference (10 K) by the resistances calculated in the Thermal Resistance Limit model discussed above. The total thermal energy stored in the solenoid is divided by this maximum cooling rate to determine the cooling time imposed by the 10 K restriction.

Three corresponding models were constructed for the 80 to 5 K cooldown case for each of the solenoids. The He mass flow in these cases (assumed to be coming from the liquefier) is 7.4 g/s. The results are shown in the table above.

The results indicate that the cooldown times for the TS and DS solenoids are substantial (5-10 days). These times could be shortened substantially by introducing additional "cooldown channels" that would reside on additional cooling platforms on the TS and DS coils. These channels would have flow in them only during the cooldown process. These models are rather crude and better estimates can be achieved by using both time and space dependent codes.

During the detailed design phase more detailed models will be used to determine the maximum ΔT which can be achieved for the PS, TS, and DS coils without exceeding thermal strain limits. A higher allowable ΔT will reduce the cool down times.

Quench of a solenoid

In the event of the quench of the coils of one of the solenoids, quick closing valves and by pass valves in the lines to the cryostat are actuated to minimize the effect of the rapid pressure rise on the associated dewar and the other parts of the system. The two-phase cooling loop that cools the coils of the TS and DS cryostats are vented by relief valves located in the valve box at each end of cooling loop. The PS coil requires a separate vent line to safely vent the overpressure resulting from the boil-off and blow-out of the inventory of liquid helium in the cryostat. The 10-inch vent line passes through the shield wall and the relief devices are placed outside the shield enclosure. The vent line is vacuum insulated up to the relief devices to avoid thermally driven oscillations within the vent line. Relief valves are in series with burst disks to avoid any long term freeze up of the vent lines as a result of relief valve leakage. Fast closing valves in the lines feeding the down comer and in the lines of the riser are closed in the event of a quench to prevent over pressuring the PS dewar. The helium vented because of a quench goes directly to atmosphere and is lost. The energy released during PS quench, about 33 MJ, is more than sufficient to boil-off the entire inventory of 6700 liters of helium in the PS cryostat.

Re-cooling after a quench

After the overpressure from the quench has dissipated, the cryostat is put in the configuration for cooling from 80 K to 4.5 K. The by-pass valves are set so that the other cryostats operate in the steady state mode. The warm cryostat is cooled by flowing 4.5 K helium into the cryostat and returning this helium through the cool-down lines leading back to compressor suction.

Component accessibility

All components that require maintenance are placed outside of the shield wall enclosure. This includes valves and gas cooled current leads. There are separate vacuum systems for the four magnet cryostats and the two dewars and the valve box. The multiple tube transfer conduits are vacuum insulated with LN2 shields that are cooled by the LN2 distribution lines that are also in the conduits, but are not shown on the flow sheets.

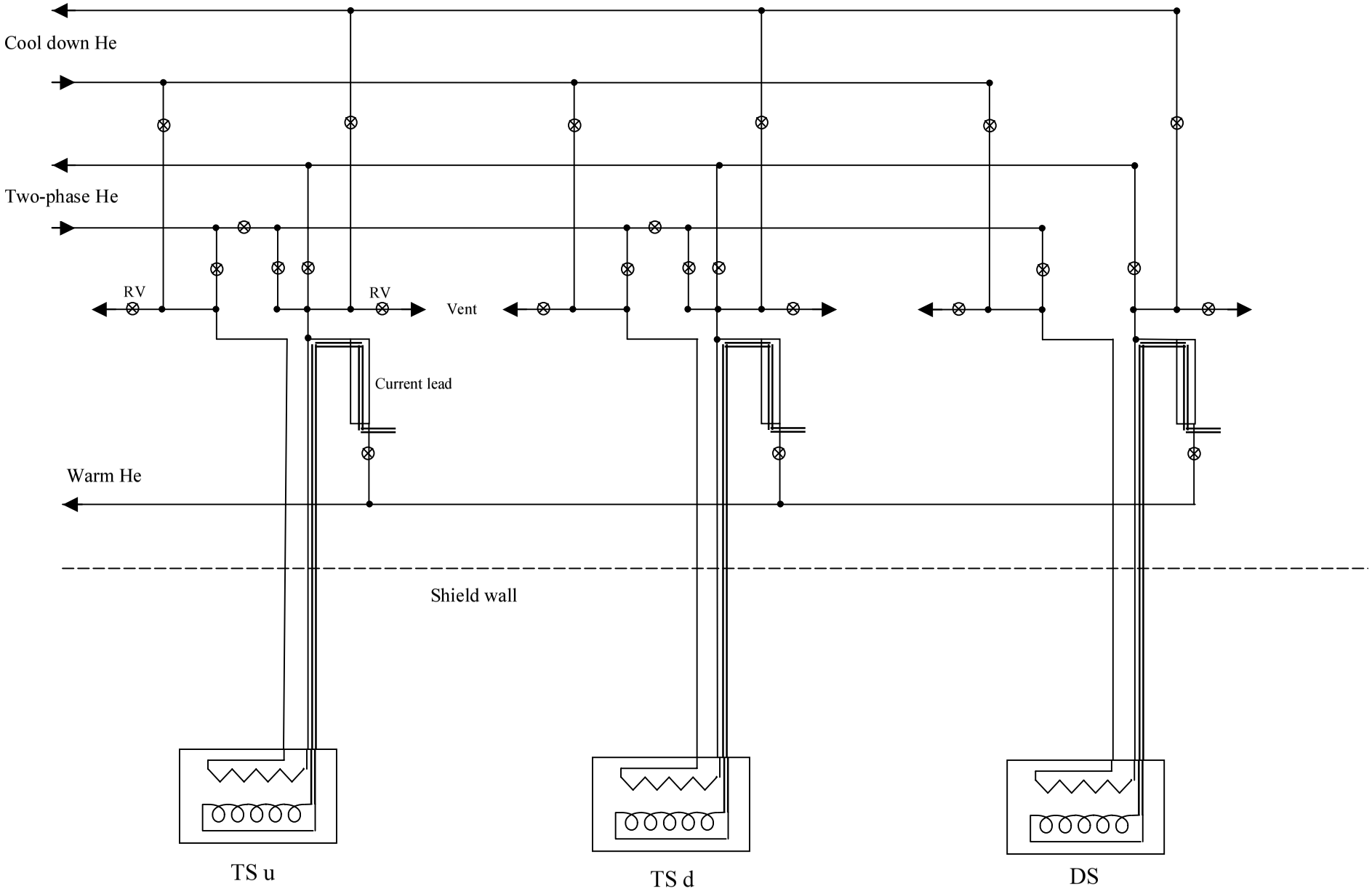

Figure 15.11 – Helium flow sheet for TSu, TSd, and DS cryostats and valve box

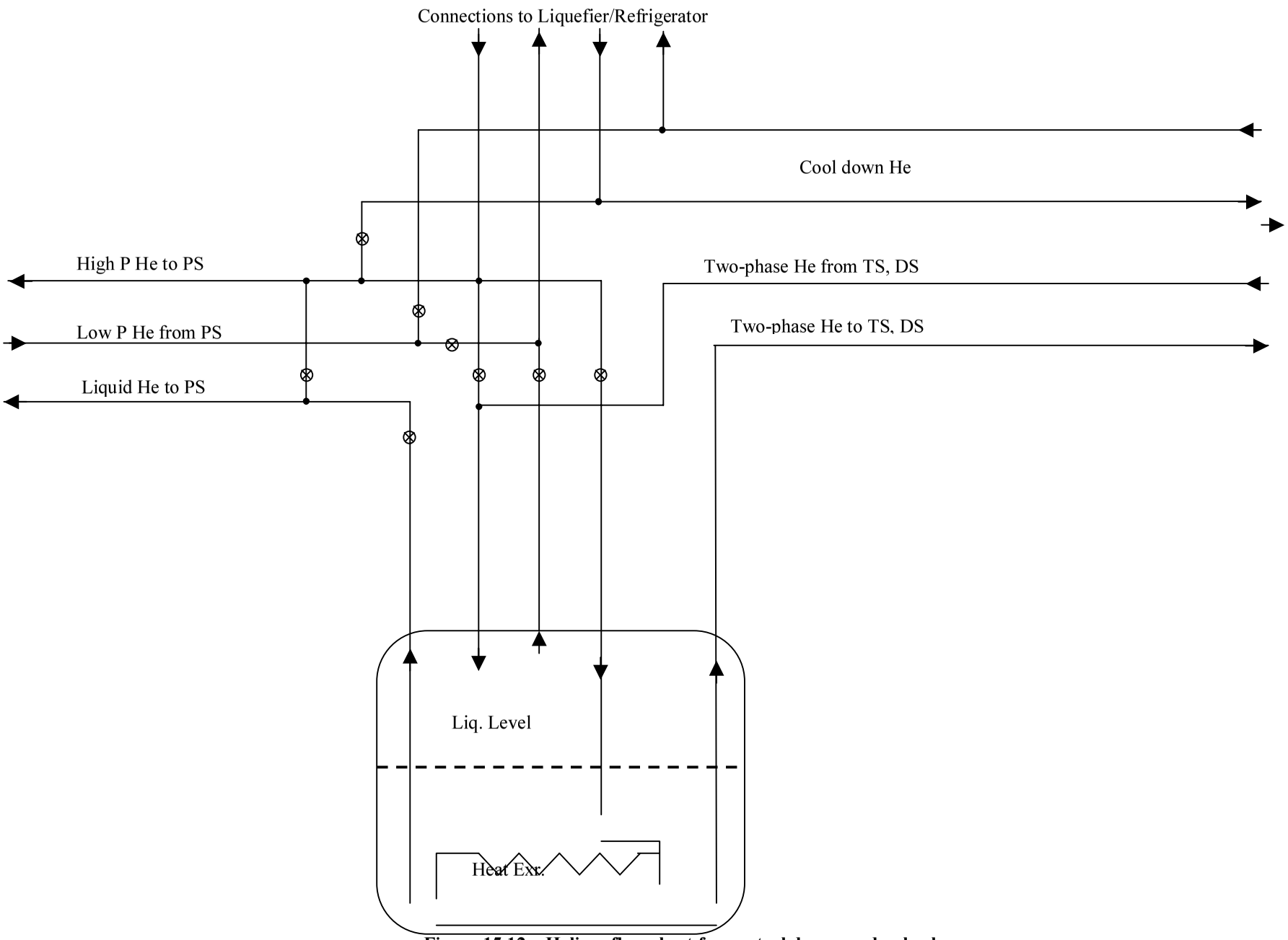

Figure 15.12 – Helium flow sheet for control dewar and valve box

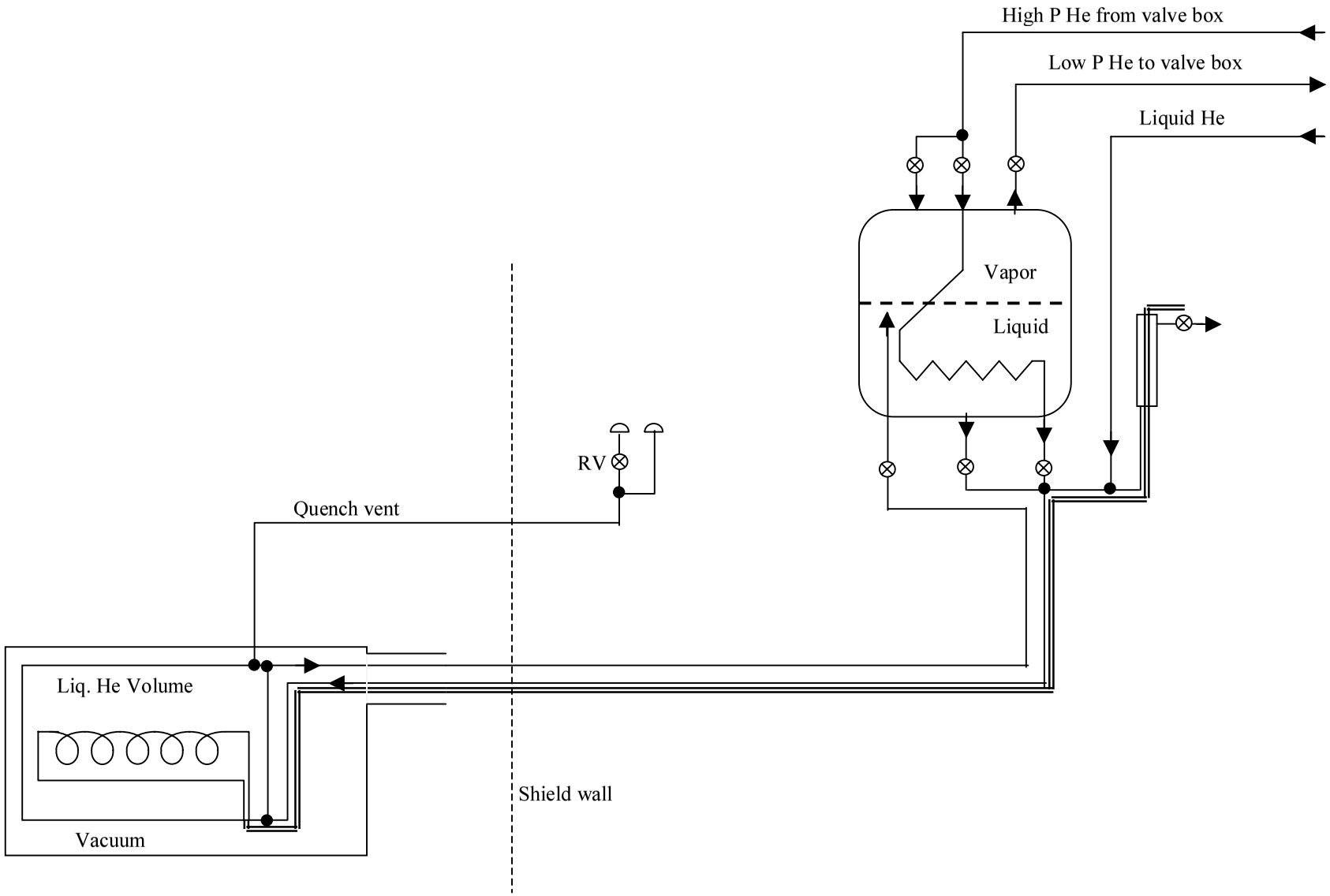

Figure 15.13 – Helium flow sheet for PS cryostat and dewar.

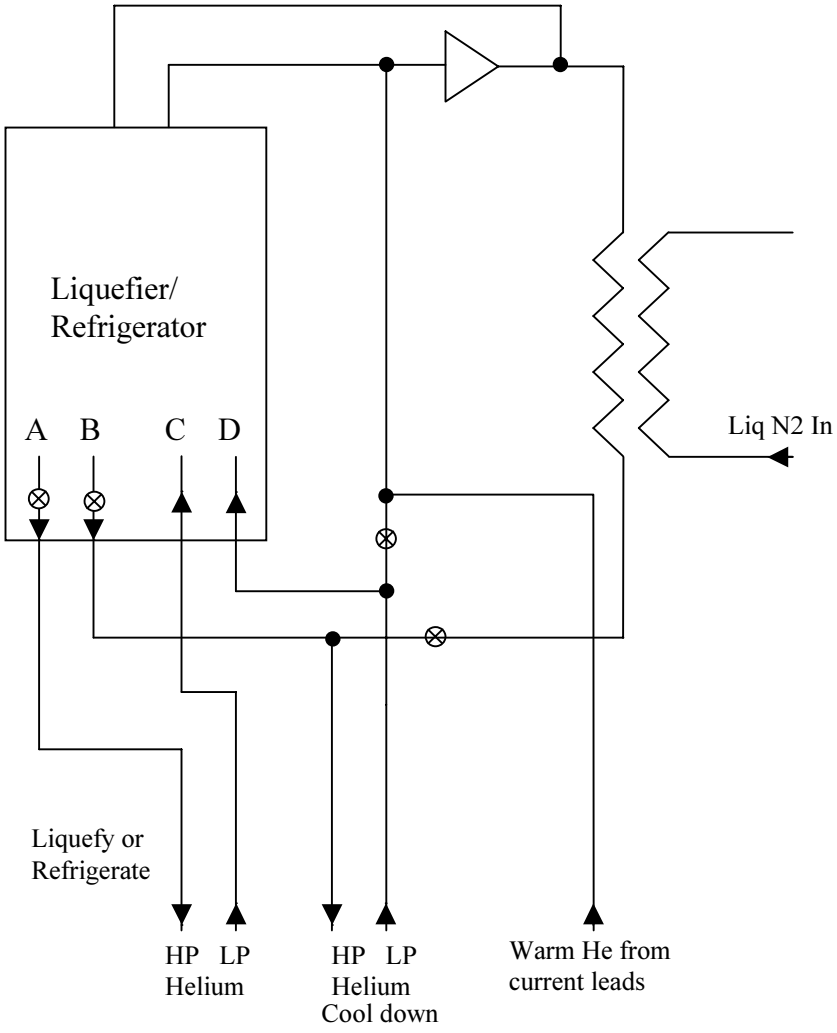

Figure 15.14 – Helium flow sheet for liquefier/Refrigerator and Cool-Down Heat Exchanger.

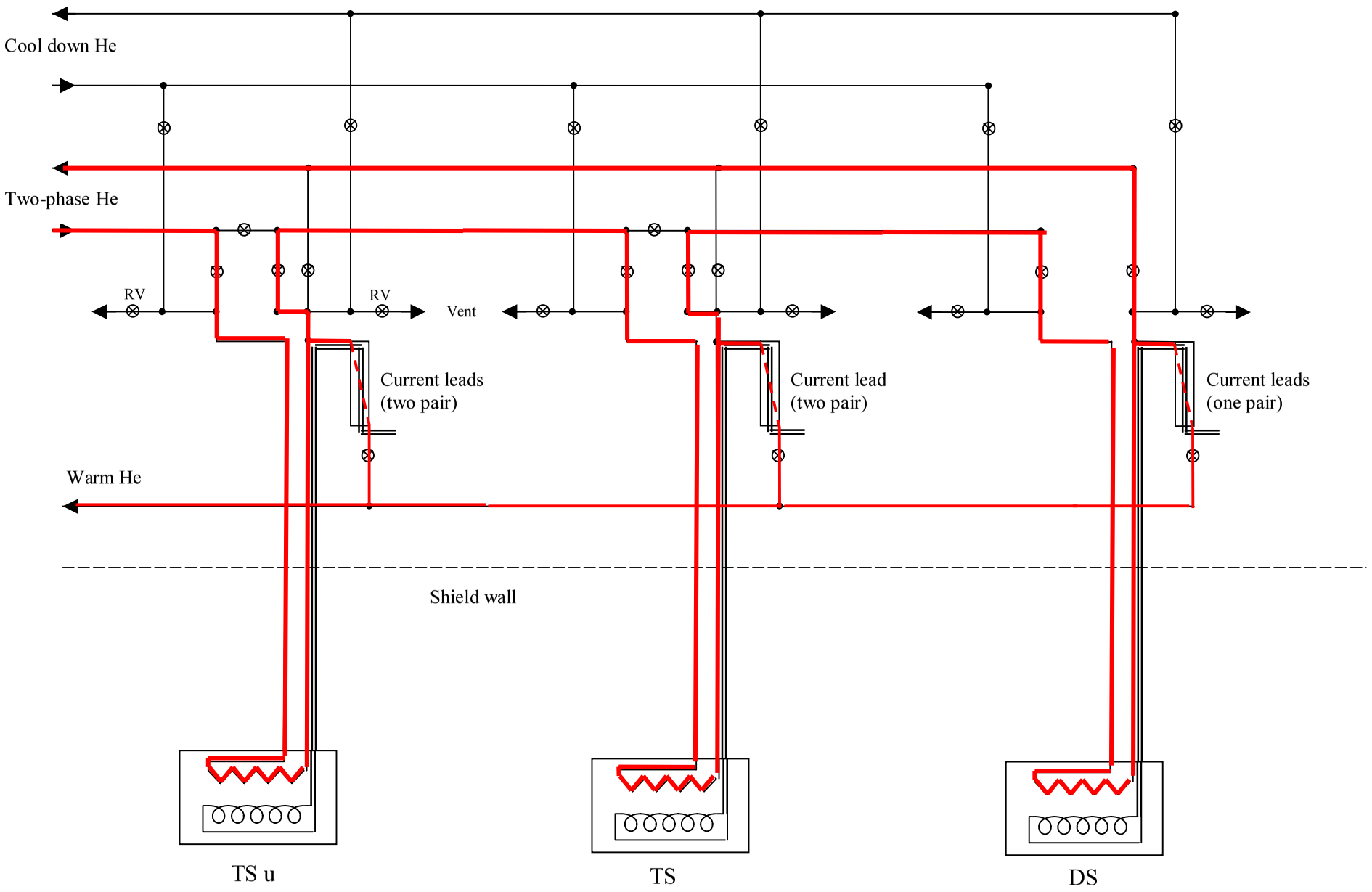

Figure 15.15 – Normal steady operation: Helium flow sheet for TSu, TSd, and DS cryostats and valve box.

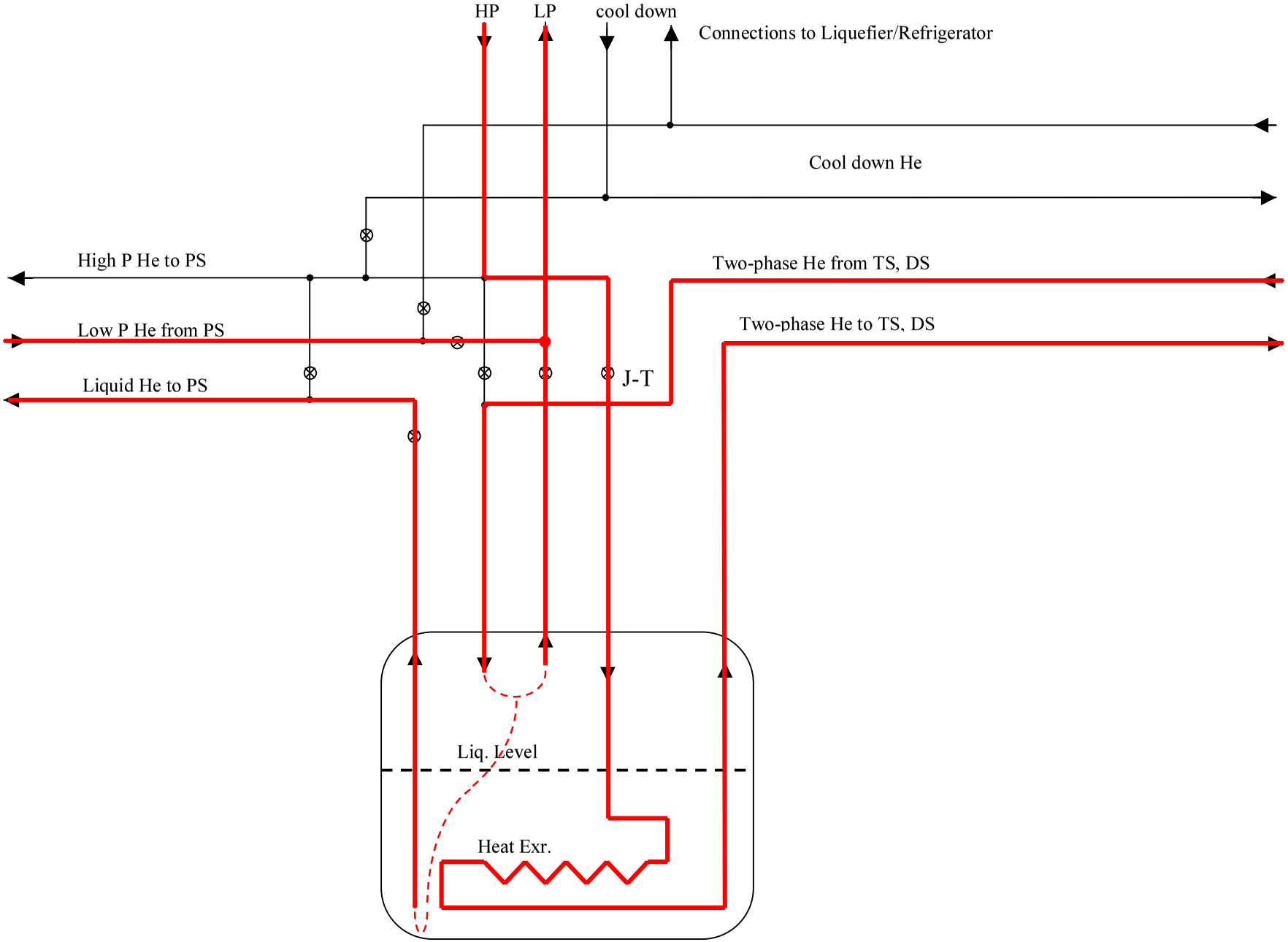

Figure 15.16 – Normal steady operation: Helium flow sheet for control dewar and valve box.

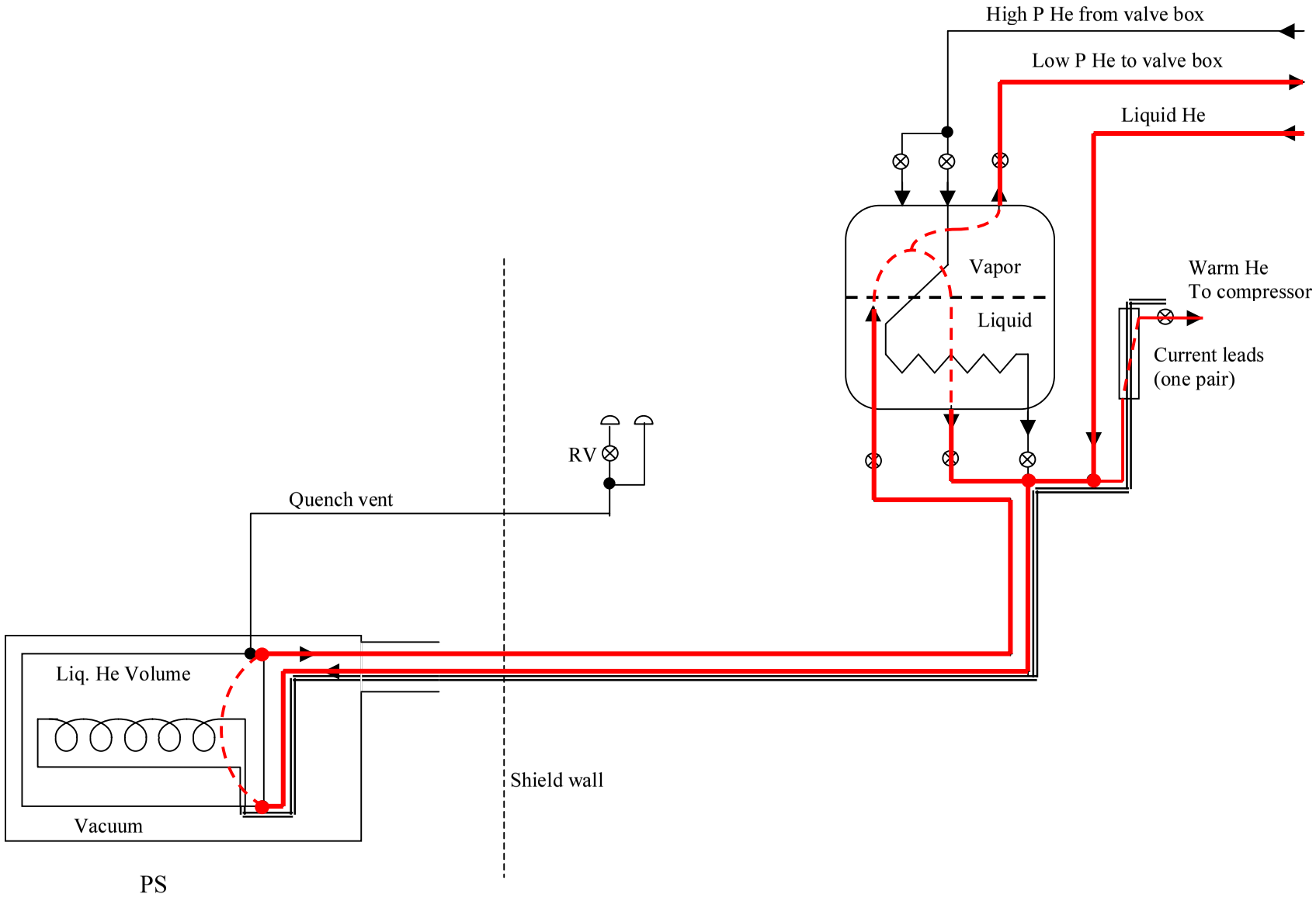

Figure 15.17 – Normal steady operation: Helium flow sheet for PS cryostat and dewar.

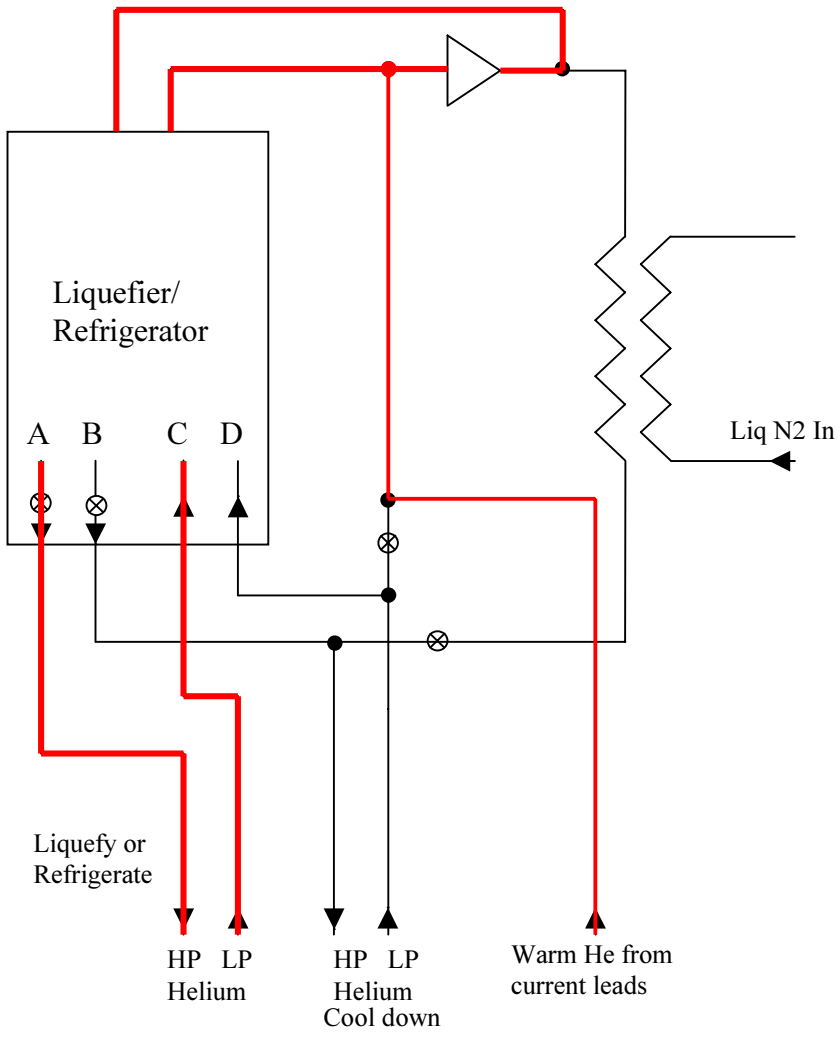

Figure 15.18 – Normal steady operation: Helium flow sheet for liquefier/Refrigerator and Cool-Down Heat Exchange.

Section 16 - Magnet Assembly

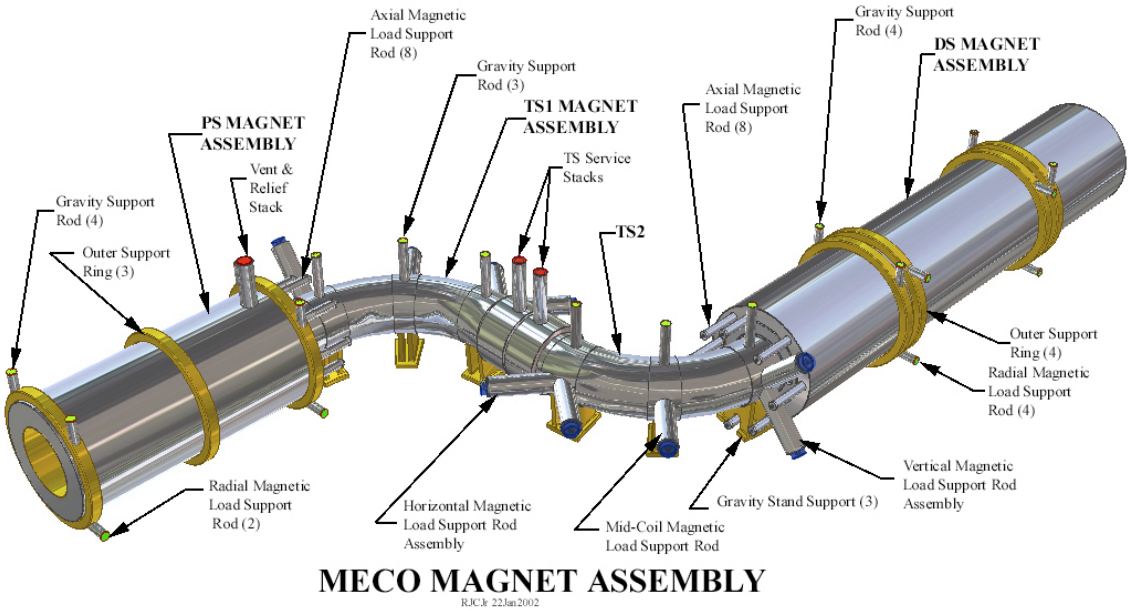

Figure 16.1 – Production Solenoid and it's cryostat; the transport solenoids - the break in the TS assemblies is in the middle of the "S", at the Berylium window, and the detector solenoid.

Introduction

The magnets for the experiment are in four major assemblies, using four cryostat vacuum boundaries, one for each magnet assembly. The four magnet assemblies are:

- The Production Solenoid (PS),
- One half of the Transport Solenoid (TSu), up to the Be window,
- A second Transport Solenoid assembly (TSd) nearest the detector solenoid,
- Detector Solenoid (DS).

It is intended that each of these assemblies would be completed in the factory ready to be connected to power, cryogenic and vacuum systems, and instrumentation. The bulk of the manufacturing process relates to manufacture of the mandrels and winding the coils within the mandrels. The conductor will come soldered into its copper stabilizer, on shipping spools. Modular winding of the many coil segments keeps the coil size manageable during the winding process. The build up of the large coil assemblies relies on machining tolerances of the coil mandrels. Bolted connections are used to assemble all the mandrels.

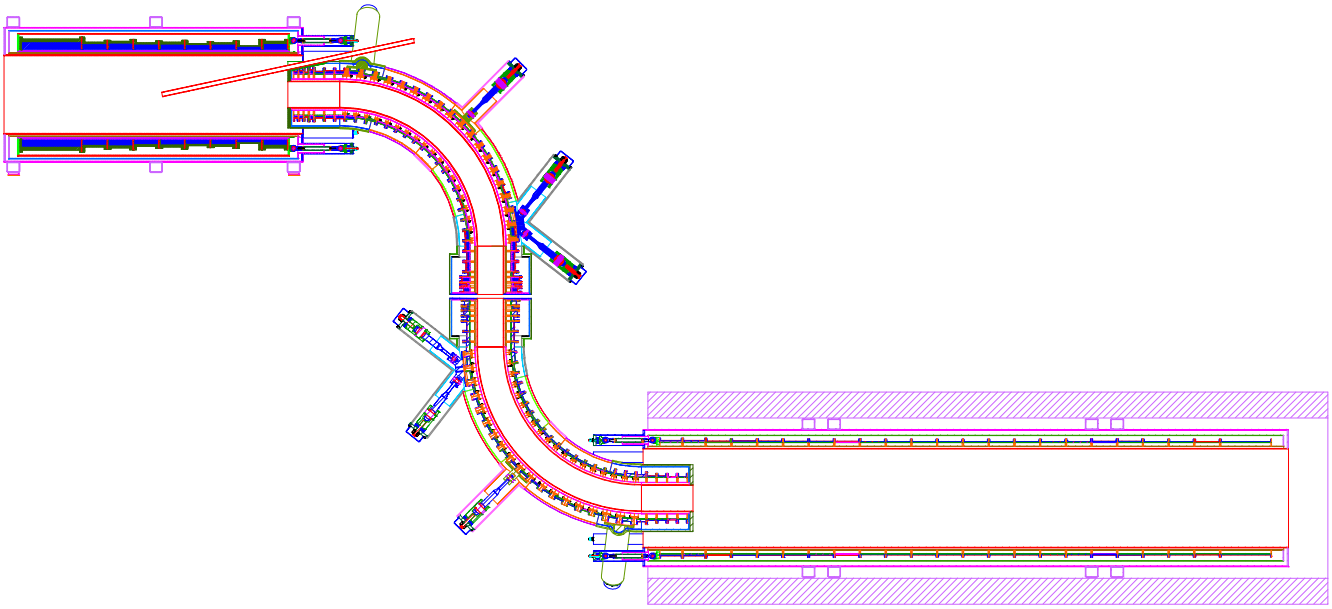

Figure 16.2 – Mid-plane section of the magnet assembly.

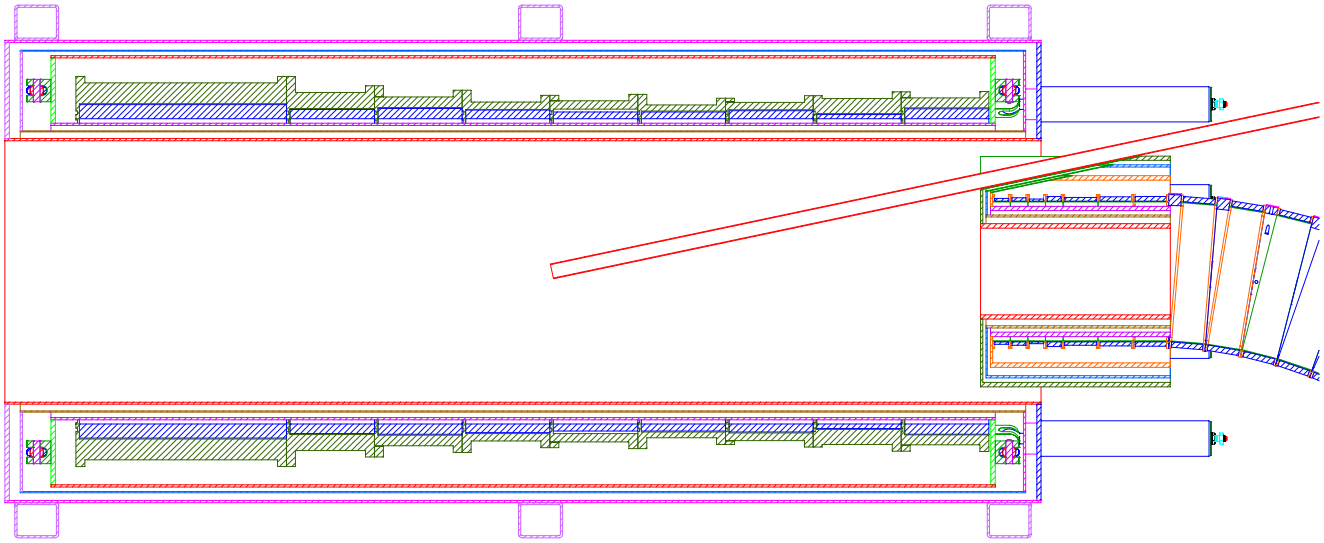

Figure 16.3 – The Production Solenoid assembly.

Production Solenoid Assembly

Coil Winding

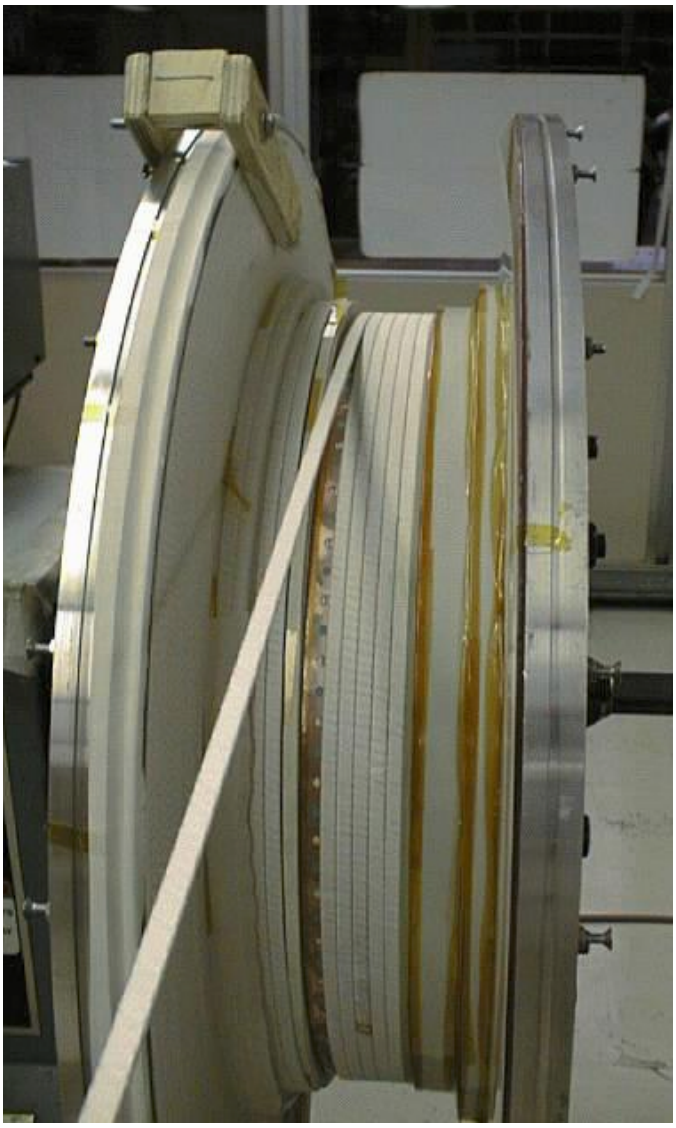

Figure 16.4 – Winding the LDX Floating Coil. The pancake on the left has been wound and is being held with the wooden clamp. This leaves both terminations at the coil OD. The remaining turns are layer wound.

The production solenoid consists of nine coil assemblies. Each consists of a coil and external aluminum mandrel. The external mandrel provides support of hoop stresses and an axial compressive preload which is intended to offset axial tensile stresses that occur during a quench. The winding must allow for the following:

- The design-intended fit with aluminum mandrels
- Obtaining the required helium volume between coil and mandrel with good thermal connection through the 1mm ground wrap
- Sequential bolted global assembly
- Fine position control and adjustment

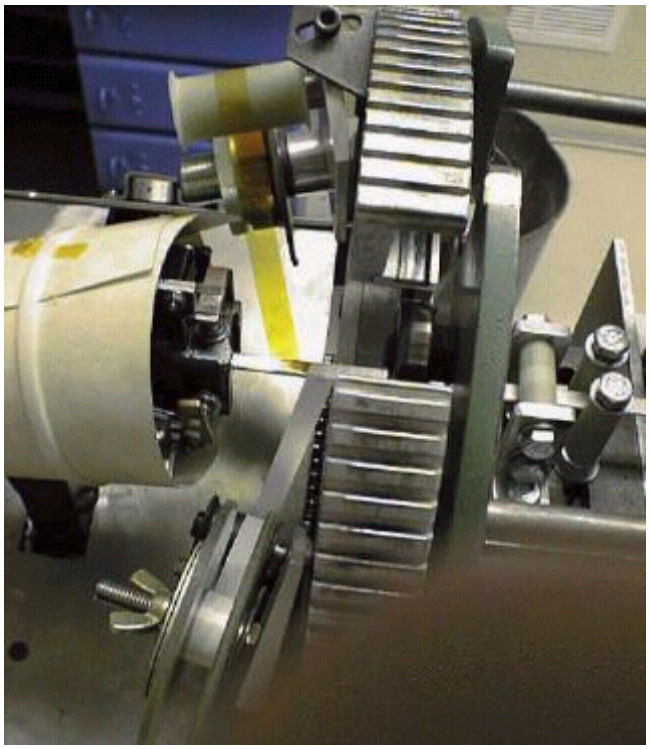

Figure 16.5 – The LDX floating coil taping head

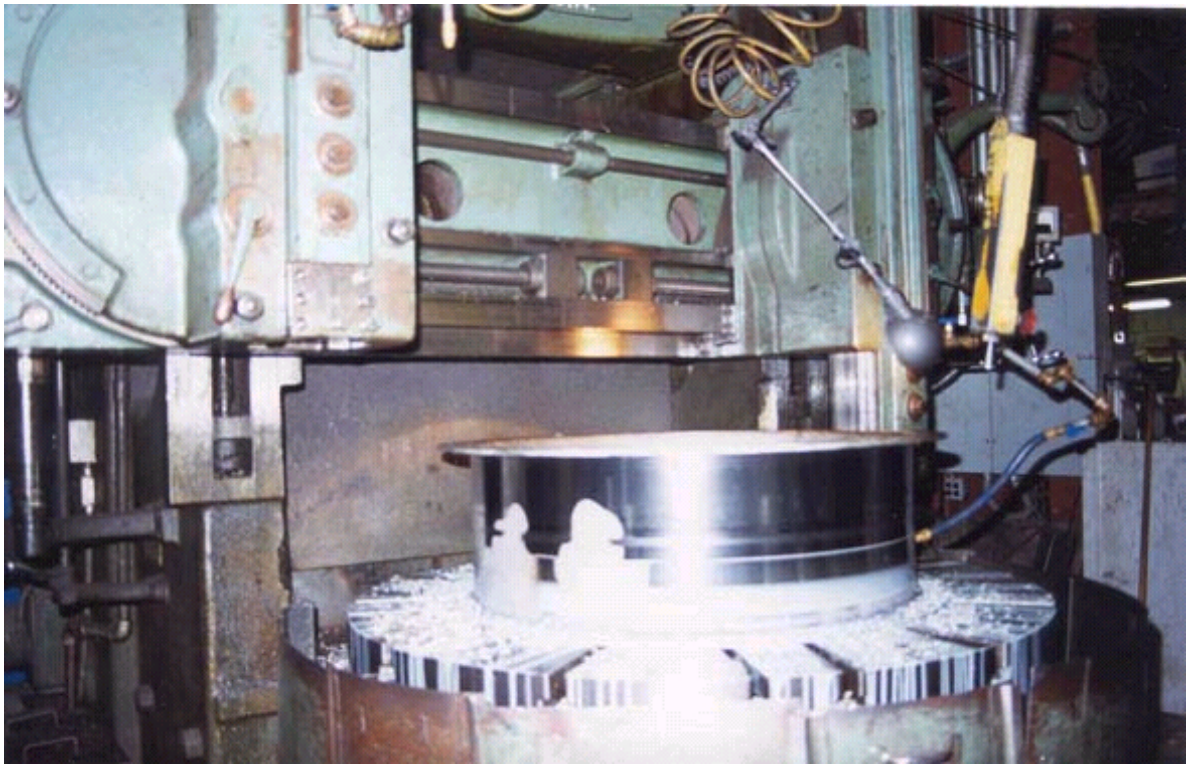

Figure 16.6 – Stainless steel coil form being machined on the King Vertical Boring Mill 62" Table (internet photo from an unknown project) http://www.metweld.com/machine.html

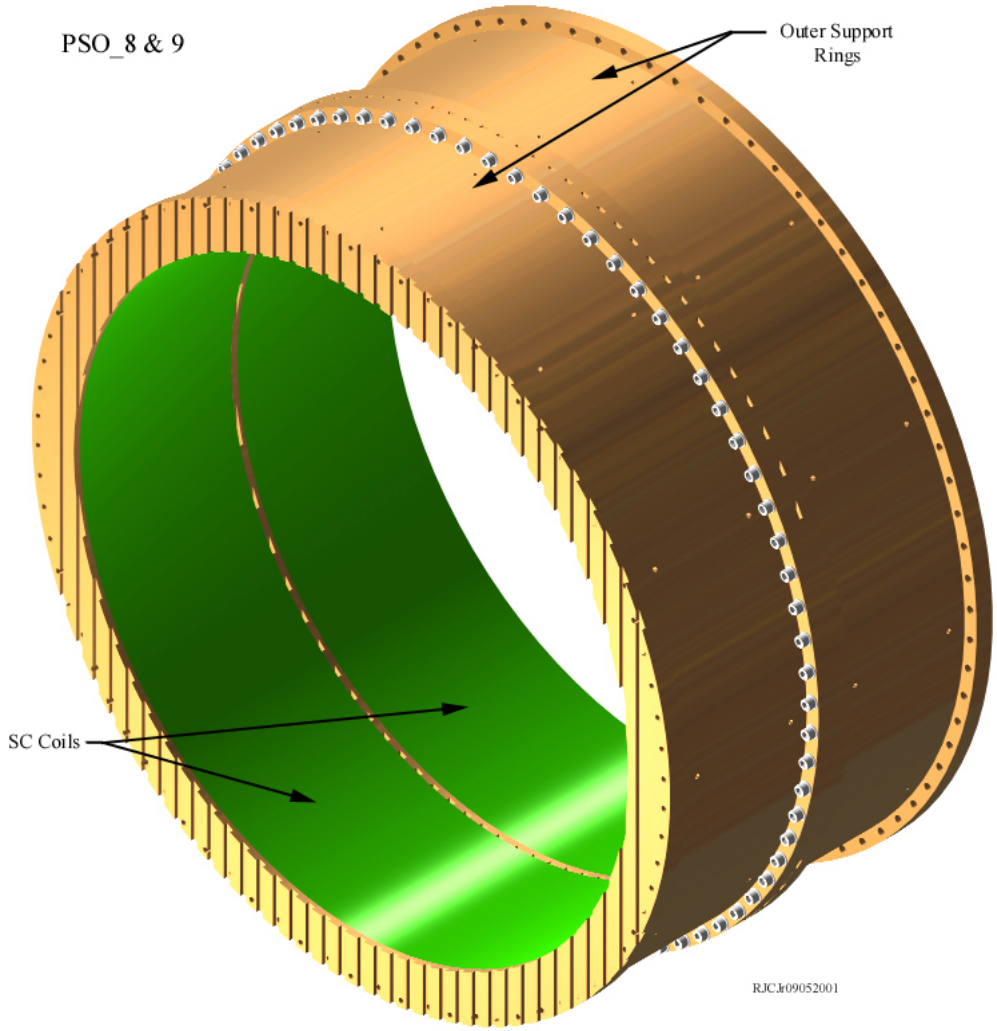

Figure 16.7 – Production Solenoid mandrel showing He bubble vent grooves, and flange bolting. This is an aluminum 6061T6 forging with all surfaces machined.

Wind on a removable inner mandrel. Turn insulation for all coils is specified as two half-laps of 1 mil Kapton tape (2 mils total), followed by 2 half laps of 3 mil fiberglass tape (6 mils total). Insulation is applied to the conductor using a dual taping head in the winding line between the pay off from the supply spool and the winding machine. Layout of the winding spools, roller, and tensioning rollers (if used) should be such that the insulation is applied after contact with the rollers, and the feed and roller layout should be such that the conductor bend curvature (whether from the supply spool winding or imposed by a set of feed rollers), prior to the tensioning stage is as close to it's final wound radius of curvature as possible. This is intended to reduce training due to plastic strain energy release when the coil is first energized. The taping head should be designed such that a tape jam automatically stops the taping process before the conductor is damaged or broken. Use G-10 ground plane sheets lining the ID and sides of the mandrel. The sheets on the sides of the mandrel should include a sheet of teflon to for a slip plane and allow differential radial "growth" of the coil on cooldown. The coil fit inside it's external mandrel will be a clearance fit for ease of insertion. The axial fit will be tight to develop the full axial

compression from the differential contraction of copper and aluminum, needed to offset quench stresses. A pancake is wound out to form a termination. This is done after unwinding the necessary length of conductor for the pancake from the supply spool then positioning the supply spool along the axis of the mandrel so that it can be rotated as the pancake is wound. This leaves a termination at the surface of the coil with the supply spool feeding the first layer of the layer wound portion of the coil. Next, apply 1mm outer ground wrap. Wrap silicon rubber bands about 1 cm wide on 2 cm pitch. These would be about .7 cm tall to yield a .5cm groove after machining. Clamp silicon rubber bands with tightly wrapped tape. Pack gaps with glass fiber roving. Vacuum Impregnate in a rubber mold

Preparation and Insertion in the Aluminum Mandrel

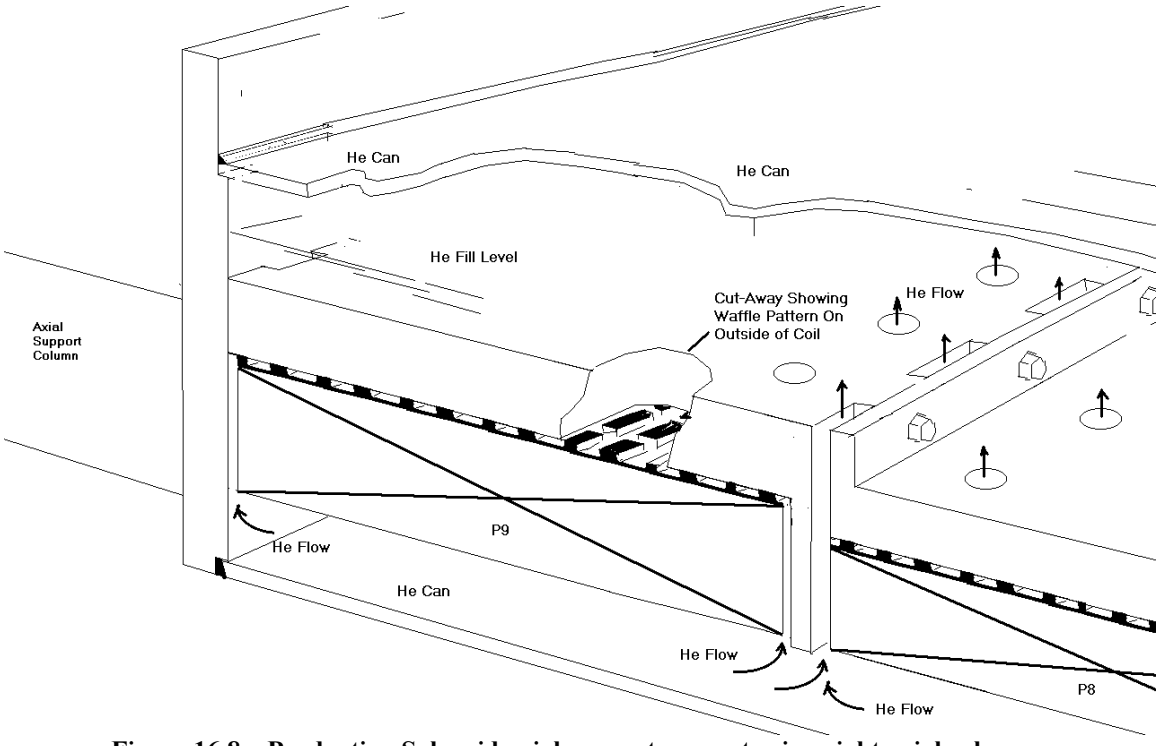

Figure 16.8 – Production Solenoid axial support concept using eight axial columns.

Peel away the mold, and cut the wrap on Silicon Rubber bands. Remove silicon rubber, Hi Pot, and perform turn-to-turn tests. Hand clean grooves, with care not to damage ground wrap. Remove winding mandrel. Machine the OD concentric with ID and 2 mm smaller than the aluminum mandrel ID. Machine helical grooves, about 3/4 the depth of the circumferential molded grooves to create a waffle pattern on the coil OD.

Alternate approaches to forming the OD cooling grooves, while keeping the ground insulation thickness between the coil and the He cooling channel were also considered. Both alternative approaches would vacuum impregnate the coil with the requisite 1 mm ground wrap in the impregnation. Then,

1. Strips of pre-formed G11-CR are epoxied to the outside of the coil with appropriate spacing. Machine the cross grooves to create the waffle pattern, or
2. Pre-form a molded silicon-rubber sheet that itself would form a mold for assembling the cooling channels. Pack fiber-glass into the silicon rubber mold, form the mold around the coil, and then impregnate the packing with epoxy. Machine the cross grooves to create the waffle pattern.

Forged Aluminum Mandrel Rings

Stress levels in the mandrels require a non-welded ring to be used. These are available. A prospective supplier may be found at http://www.forgedrings.com. Waffle pattern, and He vent holes puts Helium in contact with the coil ground wrap and mandrel. The slots in the flange allow Helium to pass into and out of the inner Helium volume. Helium channel depths (aluminum mandrel to outer surface of the 1mm thick ground insulation) should be at least 0.5 cm thick.

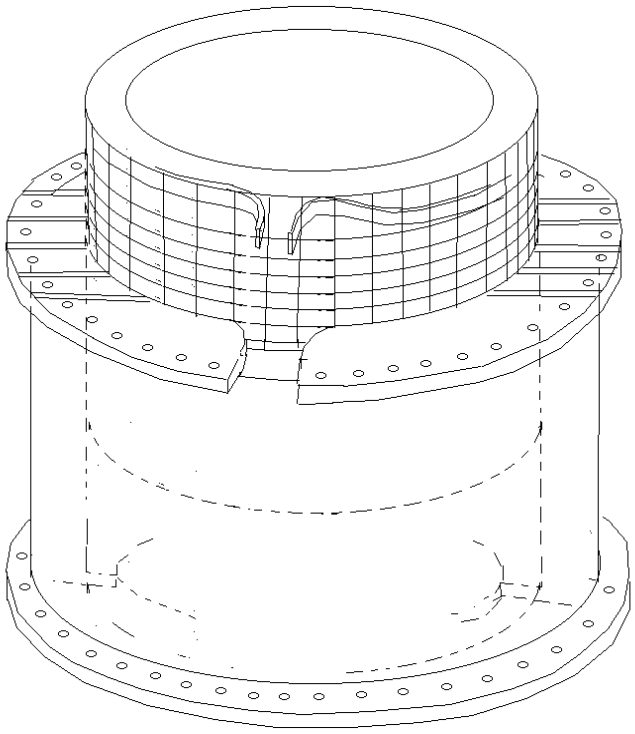

Figure 16.9 – The coil lead end break-outs fit a slot in the flanges, and allow access from the outer helium can volume.

At this point, the coil is ready to be inserted into the mandrel. Inspections and possibly a bucket test would be performed at this stage in the process. Originally, the coil was to be inserted in the mandrel by cooling the coil in LN2. With a 1mm allowed clearance, this is no longer necessary. Disassembly may still be difficult, and finding coil flaws before the tight and possibly

irreversible fit in the mandrel was considered essential. However, the 1mm radial gap allows room temperature insertion and later disassembly of the coil at room temperuature, if necessary. Even with a fully assembled coil array, disassembly to repair or replace a coil segment is possible.

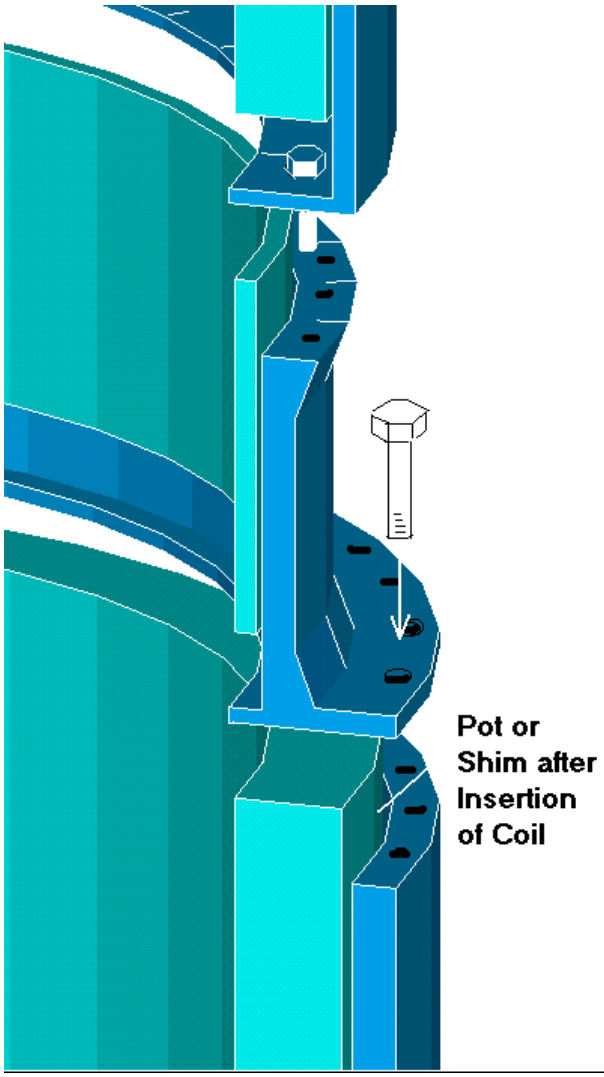

Figure 16.10 – Bolted mandrel assembly detail. Waffle cooling channels and helium vent grooves are not shown.

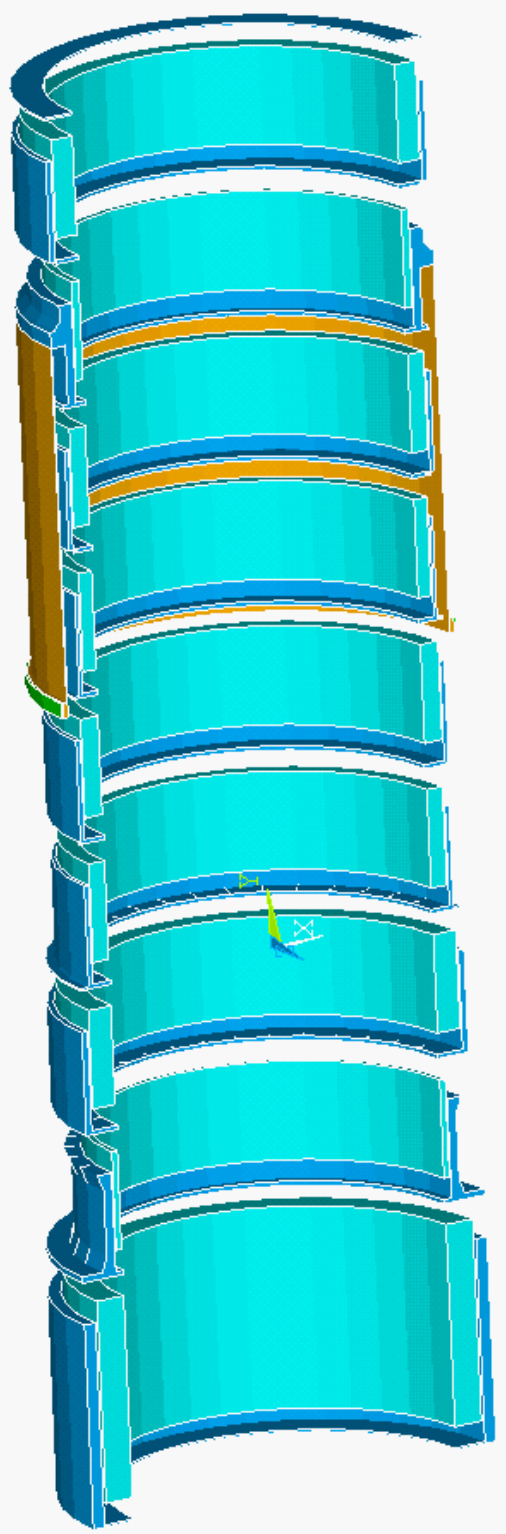

Figure 16.11 – Expanded Assembly View - Yellow "skirt" is an axisymmetric representation of flexure cold mass supports.

Perform Hi Pot and Turn-to-Turn Test

The coil lead end break-outs fit a slot in the flanges, and allow access from the outer helium can volume as shown in Figure 16.9. Jumpers are made up in outer He can volume, outside the aluminum mandrels.

Mandrel Assembly

Assembly of the full coil array may be vertical, as shown in Figure 16.10, or horizontal on the shop floor with blocking to support the coil segments and make up for the varying radial build of the different coils. P1 has the largest build, and floor assembly could start with that coil, with increasing heights of blocking as the assembly moves to the thinner coils at the other end of the production solenoid. Vertical assembly has the advantage of allowing simple vertical lifts to insert the inner cryostat shell and Helium can; and a vertical lift to slip on the outer Helium can, LN2 shield and outer cryostat shell. End cap closure welds are made at this point. There are some special procedures necessary for penetrations. These will be developed during detailed design. Bubble tests, and Helium sniff tests should be performed as volumes are closed, and can be pressurized. The helium can quench pressure relief system will be field connected as a module to the PS cryostat. Temporary blanks should be installed on the PS cryostat service tower to allow pressure tests and ensure cleanliness.

Tension/Compression Support Struts

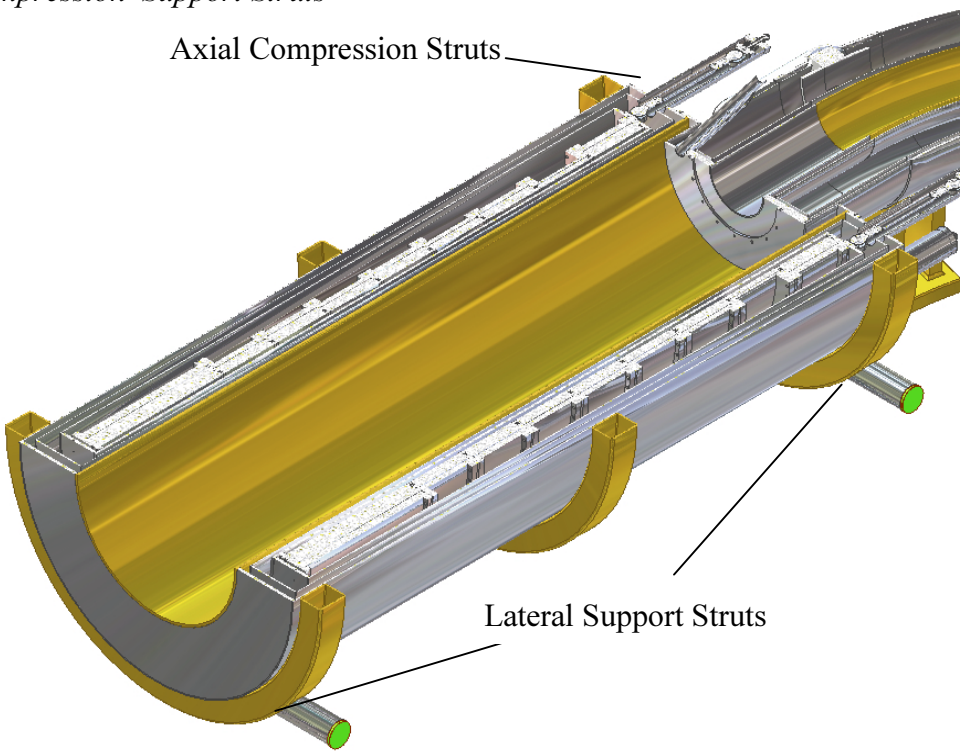

Figure 16.12 – Illustrates the support and compression struts for the PS.

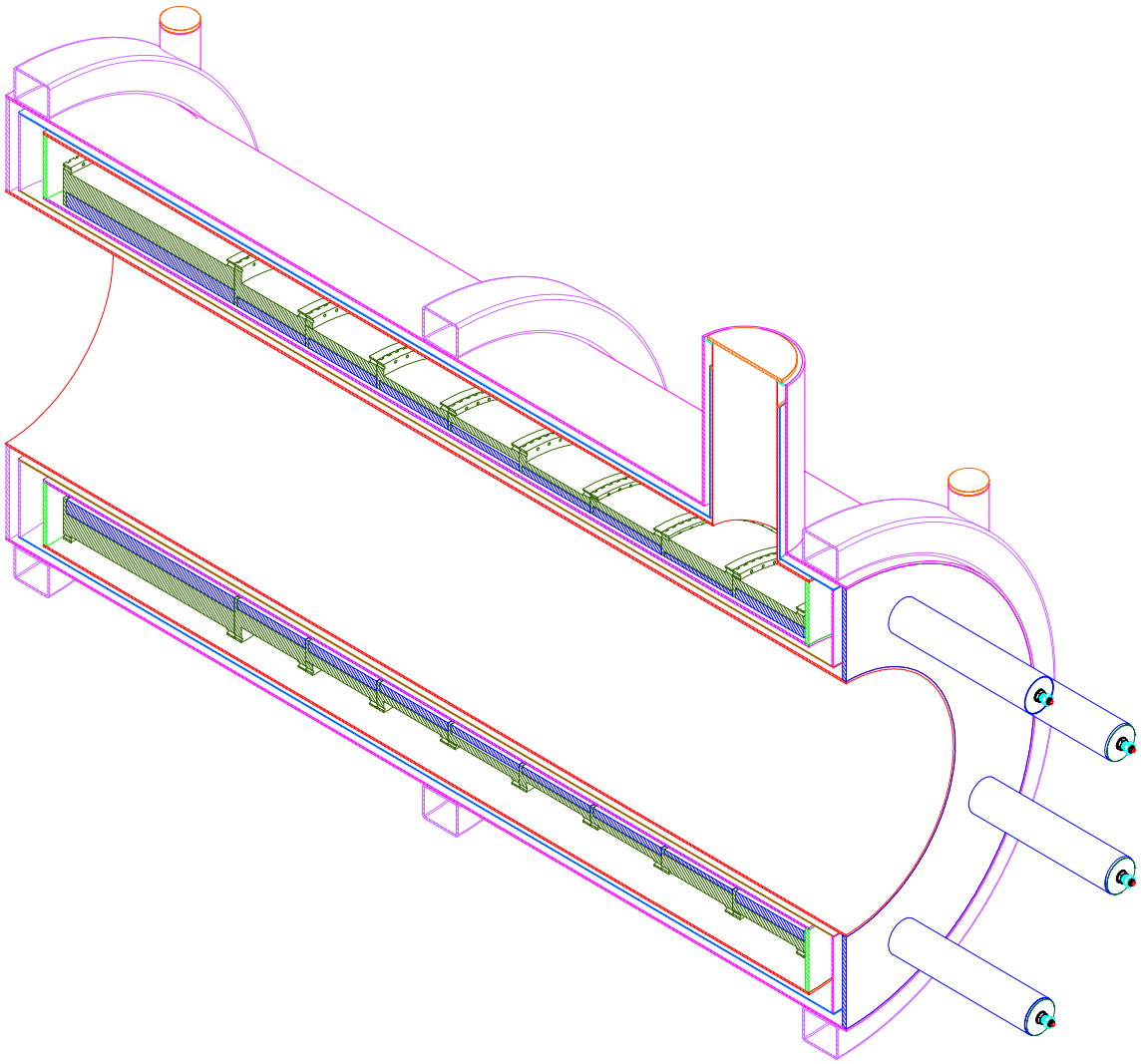

Figure 16.13 – Vertical section of the PS assembly.

The cold mass support rods and their towers must are then connected including the connections to the LN2 shield intercept points. The support rods are pipe sections intended for both tensile and compressive support. The LN2 shield intercept employs a short sleeve assembly seal welded to the outside of the strut to form a LN2 volume, which provides good heat transfer to the pipe section. The tower end cap weld or weld where the tower meets the cryostat annular end cap should be made after the struts and their LN2 shields are connected. Ends of the struts have special adjusting nuts, with bellows details that allow position adjustment under vacuum. These are not intended for factory fit-up. Whether at the factory or in the test cell, these nuts must be adjusted in small increments, especially those used in the axial support struts for which 8 rods act together, and will resist any single nut being turned. It is expected that fractional turns could be done sequentially. Simultaneous adjustment may be necessary. Attachment points on the stiffener box sections around the outer cryostat shell can be used for the upending operation. Horizontal assembly would require a long strongback lift beam to assemble the concentric cylindrical components.

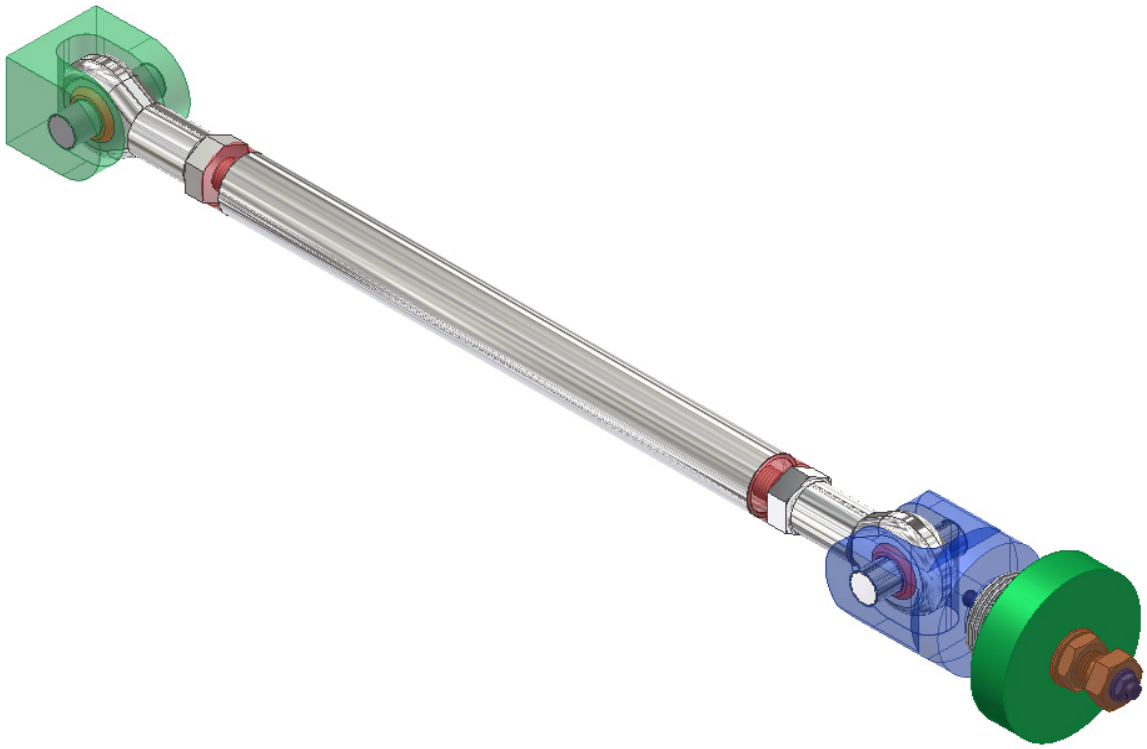

Figure 16.14 – Production Solenoid Support Strut

Spherical Ball Ends - Candidate Bearing Materials

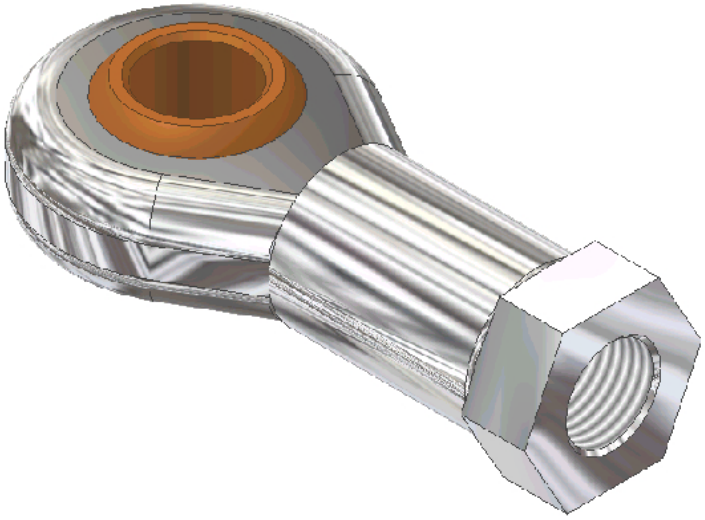

Figure 16.15 – Detail of the spherical ball-end connection.

The units used in the PS have an exposure to a small amount of radiation. The vacuum environment is the most significant non-standard condition that these units must survive.

Table 16.1 – Properties of candidate bearing materials.

Product	Material	Vacuum Qualified	Radiation Resistance	Compressive Strength	Magnetic?	OK for Cryogenics
C-Mod Drawbar	718-316	?	Yes	1 GPa	No	Yes
Dicronite	Tungsten Disulfide	Yes		2.4 GPa 350 ksi	No	-350°F
DU-Garlock	Moly Disulfide Bronze		$>10^9$ Rad	400 MPa		-328°F CIT Qual to 77°K
	Moly Disulfide			2.4 GPa 350 ksi		
Fiberslip	PTFE Fiberglass		$>10^9$ Rad (JET)	250 MPa (CIT)	No	ITER Qual to 4°K
JDB	Graphite/MoS2/PTFE		"Radiation Resistant"	250 MPa		

Figure 16.16 – JDB-1 strong brass bearing (http://www.sf-bearing.com/e-jdb.htm). Made in China.

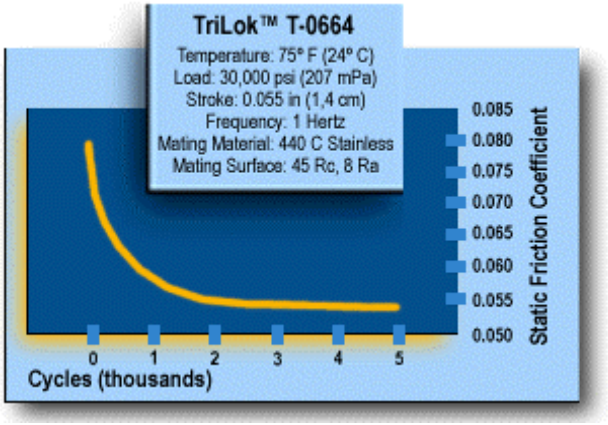

Figure 16.17 – DuPont TriLok™ metallic supported composites fiberglass PTFE cloth-lined metal.

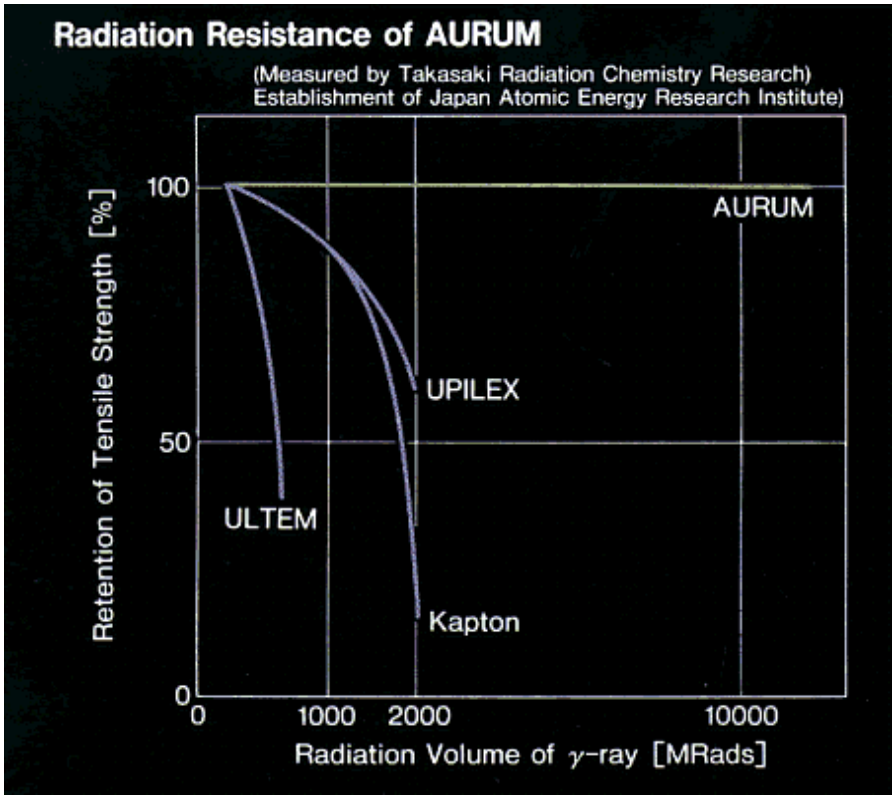

Figure 16.18 – Radiation resistance of Aurum (http://www.mitsuichemicals.com/spep/aurum/ch10.htm)

Transport Solenoid Assembly

Mandrel Manufacture

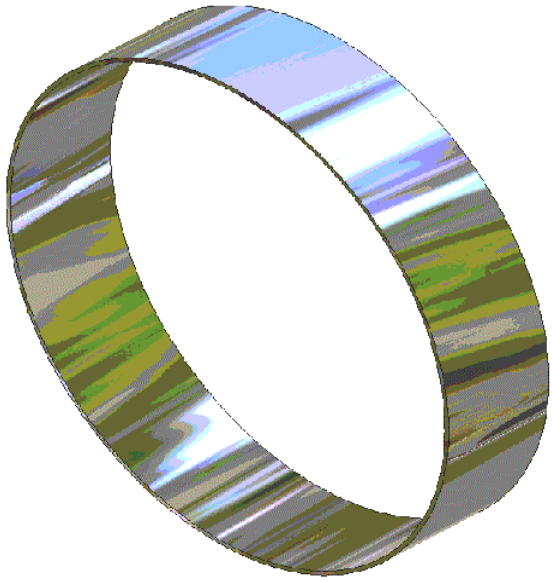

Figure 16.19 – TS mandrel inner shell - 1/4 inch plate.

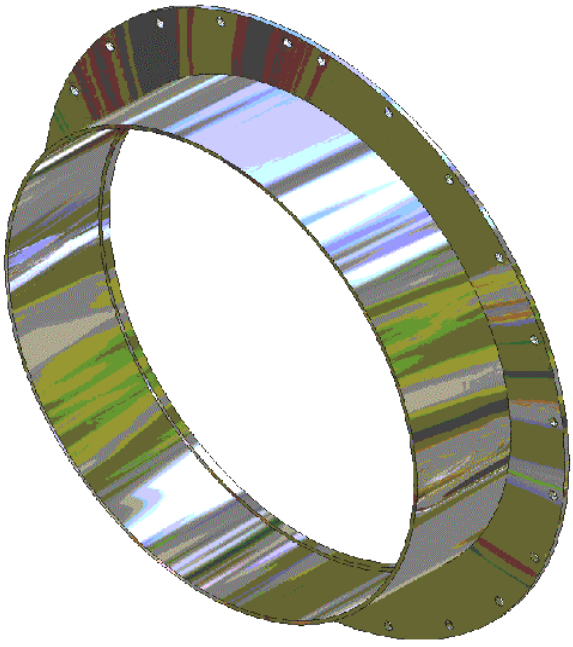

Figure 16.20 – Adding the flat flange that mates up with the straight section of coil segments.

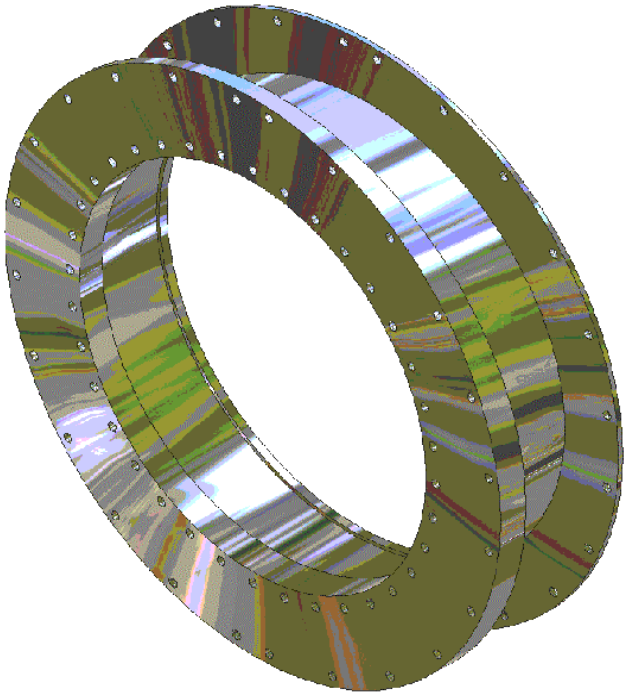

Figure 16.21 – Adding the wedge plate that begins the curved array of coils.

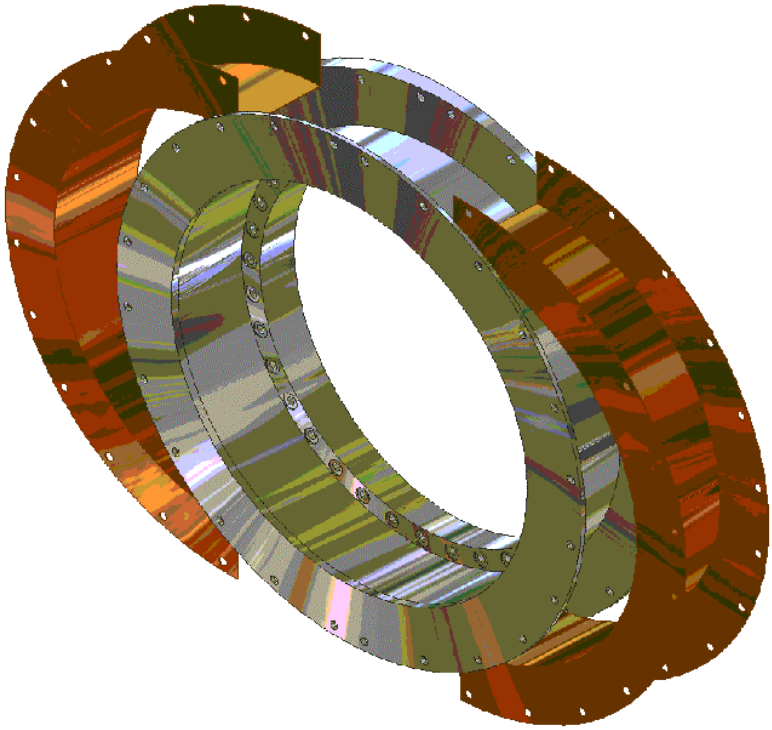

Figure 16.22 – Installing inner copper shells prior to winding

Coil Winding

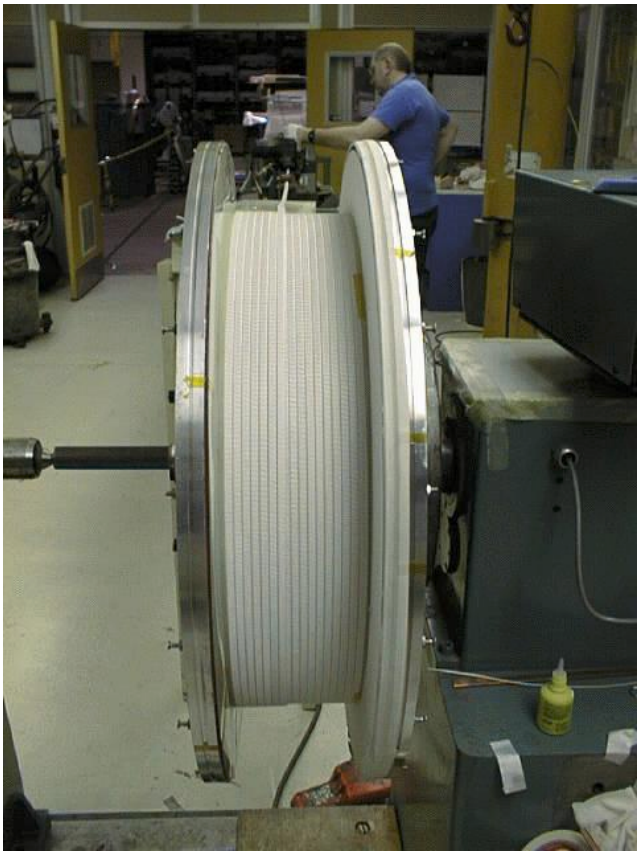

Figure 16.23 – Winding of the LDX Floating Coil. Very similar to winding the MECO TS coils. The winding mandrel becomes part of the TS structure.

The coil is wound on the structural mandrel, over copper thermal shields and a 1mm ground wrap. A pancake is wound out to form a termination. This is done after unwinding the necessary length of conductor for the pancake from the supply spool then positioning the supply spool along the axis of the mandrel so that it can be rotated as the pancake is wound. This leaves a termination at the surface of the coil with the supply spool feeding the first layer of the layer wound portion of the coil. Turn insulation for all coils is specified as two half-laps of 1 mil Kapton tape (2 mils total), followed by 2 half laps of 3 mil fiberglass tape (6 mils total). Insulation is applied to the conductor at some point between the pay off from the supply spool and adding the conductor to the winding. Layout of the winding spools, roller, and tensioning rollers should be such that the insulation is applied after contact with the rollers, and the feed and roller layout should be such that the conductor bend curvature (whether from the supply spool winding or imposed by a set of feed rollers), prior to the tensioning stage is as close to its final wound radius of curvature as possible. This is intended to reduce training due to plastic strain energy release when the coil is first energized. Cleats or locators must be provided. to allow radial growth, but limit circumferential motion when it is energized. Teflon sheets are needed between the ground wrap insulation and coil flanges as the coil contracts slightly on cooldown but expands under Lorentz loading. Following coil winding and ground wrapping, the coil is vacuum-impregnated with epoxy, cured in the mandrel, and then surface cleaned.

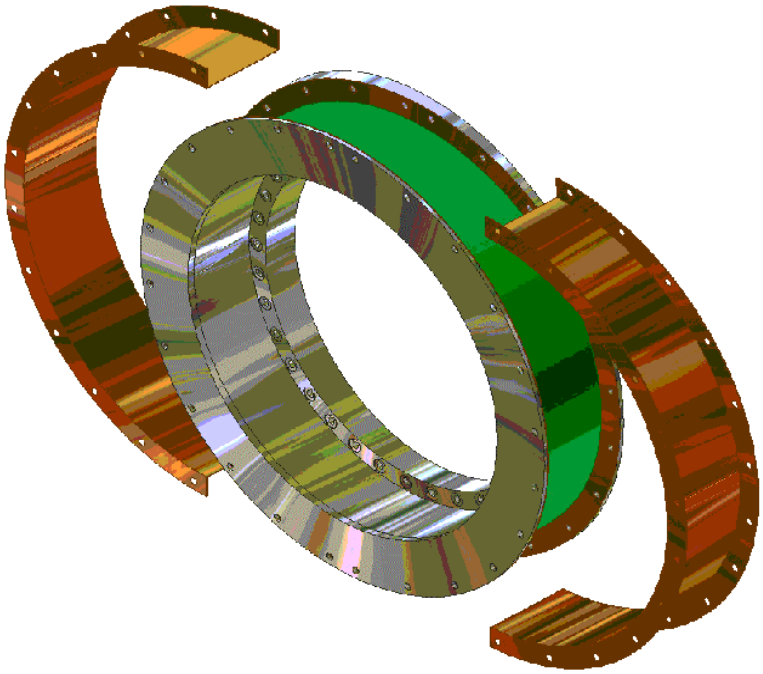

Figure 16.24 – Installing the outer copper shells.

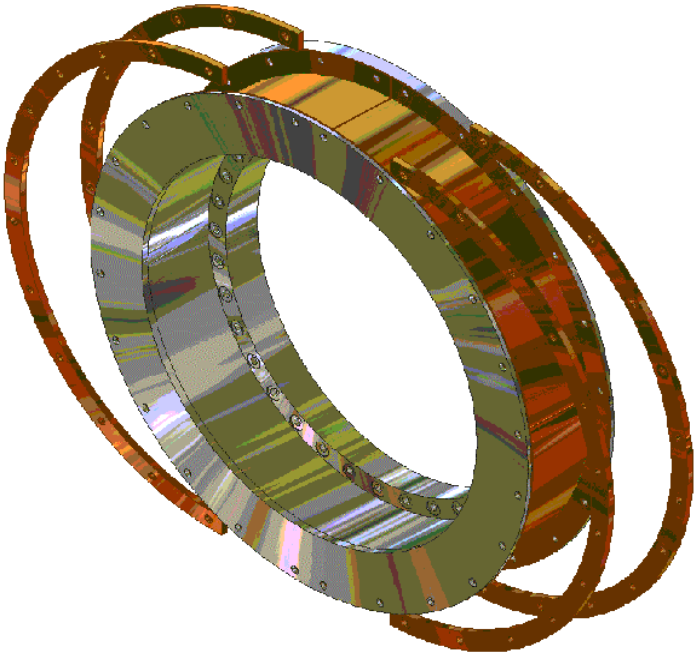

Figure 16.25 – Installing the copper conduction bars. These thermally connect the winding through the inner and outer shells with the closed loop Helium cooling pipes.

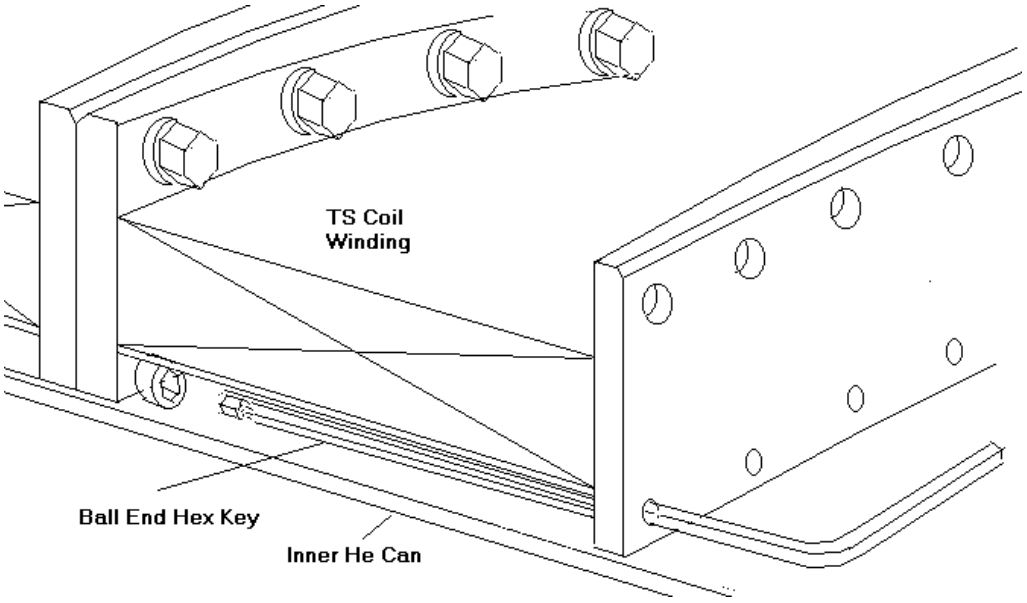

Figure 16.26 – TS bolted assembly scheme.

The outer copper shields are installed next. These are split shells that are thermal shields connected to the Helium conduction cooling system. During operation, these shell primarily work as radiation shields, but during cooldown, they function as conduction links to the coil, and must be in close thermal contact. A wrap of aluminum strap around the outer shells will shrink during cooldown and supply the required contact pressure. The outsides of these coils are radiating surfaces and must be polished or coated with a low emmissivity material. The 80 K to 4 K insulation system may include MLI in which case the low E material/polishing is not needed. The array of coils and mandrels that form the curved part of the TS are next bolted together. An earlier cooling scheme used an inner helium can that required sequential assembly of the mandrels over the bore tube/LN2 shield, and Helium can. The absence of the Helium can in the present design allows later insertion of the Bore tube/LN2 shield and assembly of the mandrel bolting in a clear bore of the array of mandrels. The machining tolerances of the mandrels should allow assembly on the shop floor supported with temporary blocking. Check alignment as the coils are assembled. With the curved array of TS coils completed, work can shift to insertion of the bore components. The intention is to have a smooth outer surface of the Cryostat/bore tube shell with a compound curvature. Inspect and leak check all vacuum welds. The bore tube is expected to be purchased as a one piece elbow from a piping supplier. The supplier may have used welds to form the elbow, and it is worth an inspection of all the shells prior to assembling them into the cryostat or experimental vacuum shells.

Availability of Elbows

Commercial availability of the 90-degree elbows required for the inner and outer helium and vacuum cans was explored with Shaw Group, who provided the budgetary estimate of Table 16.3, and other data of Table 16.2, against the preliminary requirements given by Figure 16.27and Table 16.2.

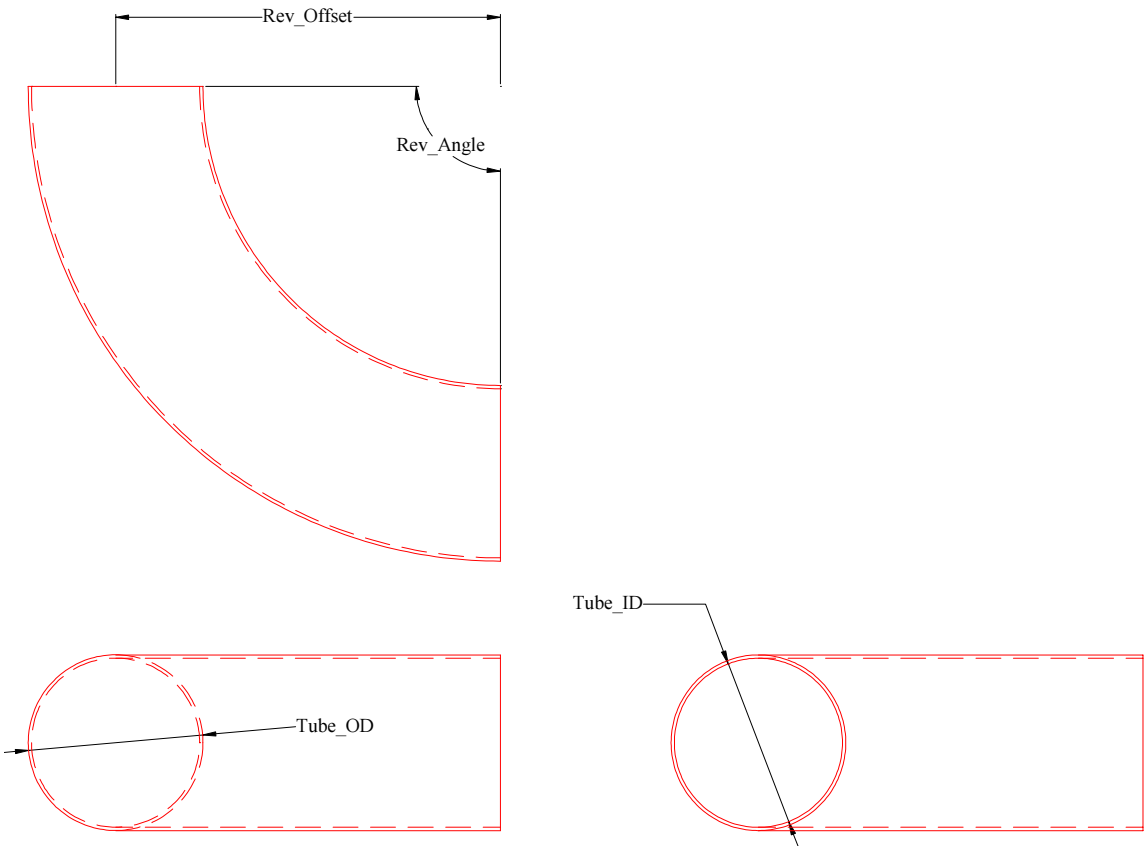

Figure 16.27 – Elbow dimensioning.

Table 16.2 – Elbow dimensions for each bend pipe section in the TS.

	Rev_Offset	Tube_OD	Rev_Angle	Tube_ID	Mat'l
90-LHe_Bore_Tube	2929	751.4	90	700.6	Ssteel
90_Lhe_Out_Tube	2929	1104	90	1053.2	Ssteel
90-Shld_Bore_Tube	2929	651.4	90	626.0	Al or Cu
90_Shld_Out_Tube	2929	1228	90	1202.6	Al or Cu
90-Vac_Bore_Tube	2929	550	90	499.2	Ssteel
90_Vac_Out_Tube	2929	1330	90	1279.2	Ssteel

Table 16.3 – Elbow pipe availability information from the Shaw Group Inc.

Pipe OD		Wall Thickness		Grade	Radius		Bend Angle	Budgetary Unit Price
(inches)	(mm)	(inches)	(mm)		(inches)	(mm)	(degrees)	
29.583	751.4	1.000	25.4	T304L	115.3150	2929	90.00	$22,357.00
43.465	1104.0	1.000	25.4	T304L	115.3150	2929	90.00	$32,886.00
21.654	550.0	1.000	25.4	T304L	115.3150	2929	90.00	$16,236.00
52.362	1330.0	1.500	38.1	T304L	115.3150	2929	90.00	$56,165.00

Table 16.4 – Additional pipe information from The Shaw Group, Inc.

Pipe OD (inches)	% Nominal Ovality	% Nominal Wall Thinning	Lbs. per Bend
29.583	2.4	11	5357
43.465	4.5	14	8097
21.654	1.4	8	3834
52.362	4.7	17	14683

Install multilayer insulation on the cryostat shell. Next, install the LN2 shield and tracing. This would be in segments with stand-offs so as not to compress the Multilayer insulation.

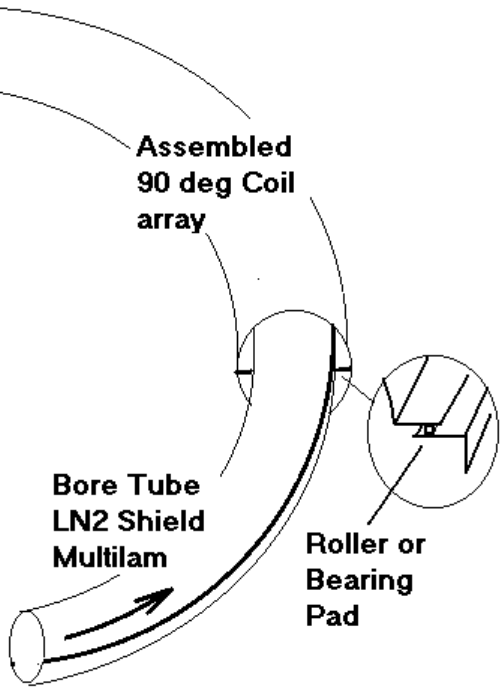

Figure 16.28 – Installation of the bore tube in the TS bend sections.

Next thread the curved bore tube/ LN2 shield assembly into the curved array of coils. It is expected that an off-center slide or cam follower track would be used for theis operation. Ultimately the support for the bore tube assembly will be supplied by connection of the ends to the cryostat end flanges.

The bore tube/LN2 shield straight sections at the ends of the TS are now added to the curved portion of the bore tube. Vacuum welds may be made from either the ID or OD and roots ground cleaned and inspected from the opposite side. Until the straight section mandrels are added, there is two-sided access to these joints.

Bolting of the straight section coil flanges is from the outside. The straight section mandrels are outside the support-rod attachments for the coil and are subjected to minimal side loading. The bolting sees minimal tensile loads, and the bore side bolting has been eliminated. This

allows simple access of assembly bolting without reaching in the annulus by the LN2 shields. Complete bolting of all coils and mandrels.

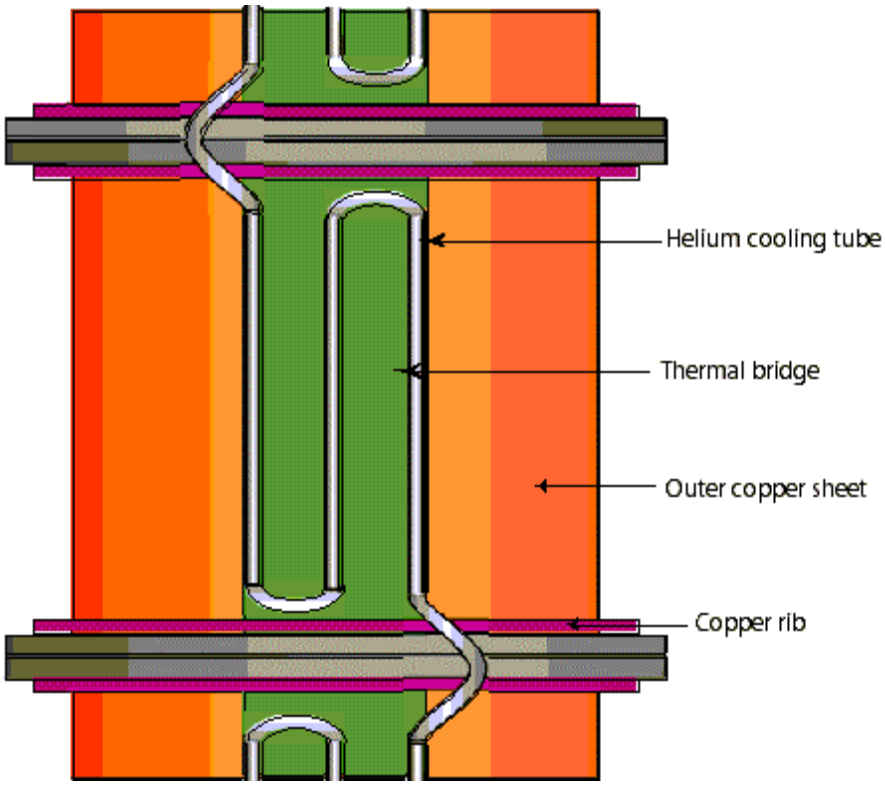

Figure 16.29 – A conceptual top view of a TS or DS coil segment. The 4 K cooling loop is shown brazed in position to the thermal bridge. The drawing is not to scale.

Installation of the He piping and conduction bars and thermal bridge plates is next. These components are also the structural support and cooling for the coil-to-coil joints. They are positioned off the vertical to allow the vertical supports to be positioned on the magnet centerline. Joints are made up by lap soldering the breakouts from each coil, insulating the joint, and clamping the joint to the copper cooling plates. Joints are visually inpsected and tested for voltage standoff of the insulation/clamping details.

Clevis plates for the horizontal cold mass support rods are now attached. These have heavy copper plates traced with helium tubing between the steel clevis plates and the coil mandrels. These are connected with an array of bolts that must be torqued. After the coil array is complete, a test of the magnetic alignment using low current at room temperature may be appropriate. The coil assembly is now ready to be transferred to the lower half of the TS outer cryostat shell.

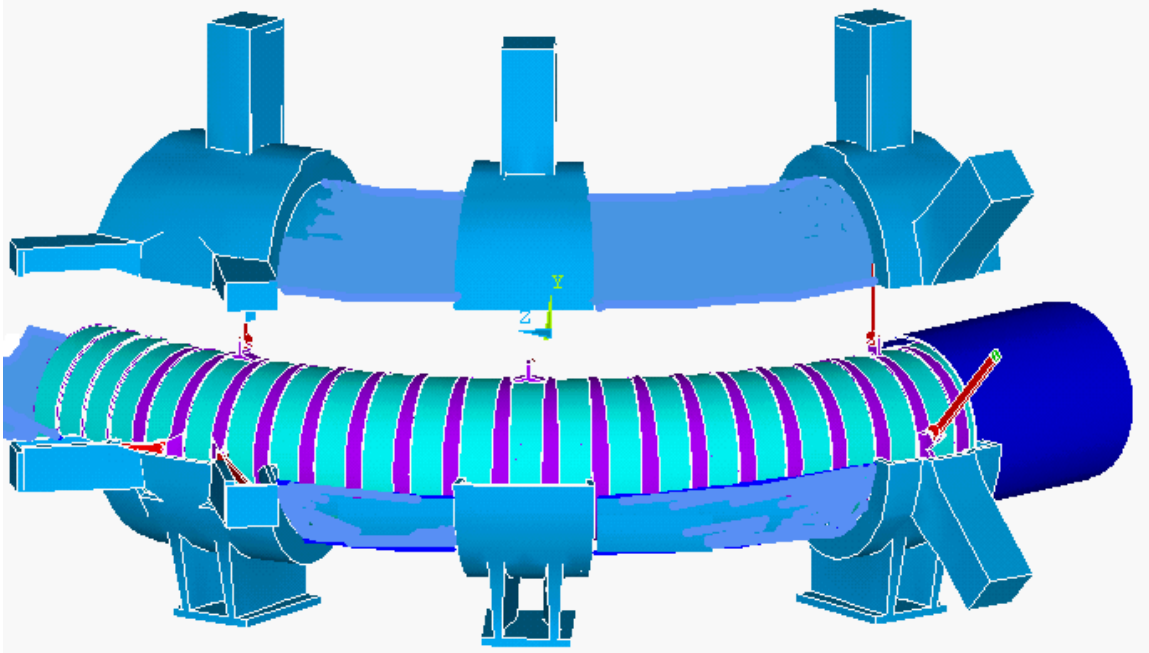

Figure 16.30 – Split cryostat concept.

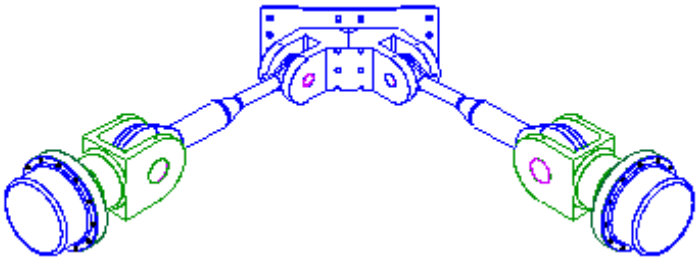

Figure 16.31 – Horizontal "Vee" and Clevis support plate

The horizontal "Vee" rod boxes should be split in such a way that the cryostat-shell locator pins should not be loaded by the strut loads, i.e. the split should be above the mid-plane to keep the attachment points of the struts all within the lower case half. The Upper strut load on the vertical "vee" will have to be transferred to the lower structure via heavier shear pins. The downward force component of the upper strut in the "vee" will help hold the cryostat casing down.

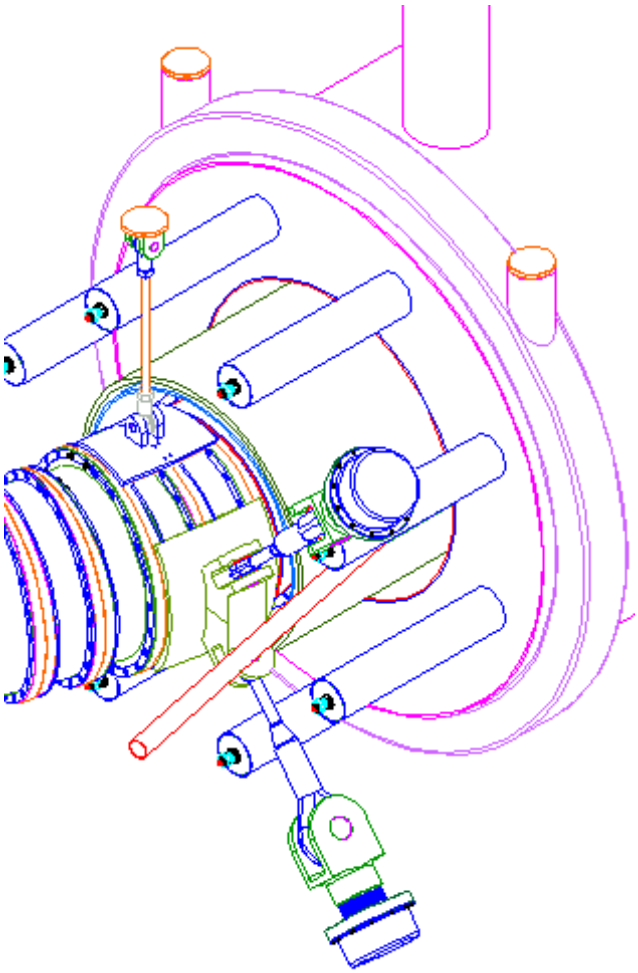

Figure 16.32 – Vertical "Vee" near PS.

The lower half of the LN2 shields has been assembled in the cryostat. This forms a cradle for assembly of the magnet and insulation. Bumpers support the coil in the "cradle". When the vertical cold mass support rods are installed, they will be used to lift the coil off the bumpers. The large horizontal support rods are now attached to the clevis plates mounted on the mandrels. The upper halves of the LN2 shields are now installed, then the multilayer insulation. Instrumentation and cryogenic lines are connected. LN2 interrupts on the support rods are connected to the LN2 shields.

The horizontal "Vee" rods are easily laid into their horizontal "Vee" "cradle". The vertical Vee support rods may need some special temporary rigging to pass them into the upper section of the cryostat. The vertical Vee is used where the proton beam passes out of the production solenoid. A single radial support is used at the detector end. Lift and place the assembled coil in the lower half cryostat assembly in which the lower half of the LN2 shield and multilaminate have been inserted.

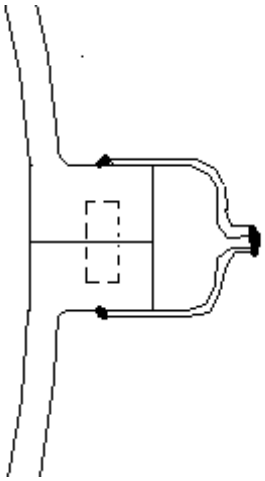

Figure 16.33 – Split casing with pins and lip seal. This can be nibbled or sheared off for disassembly.

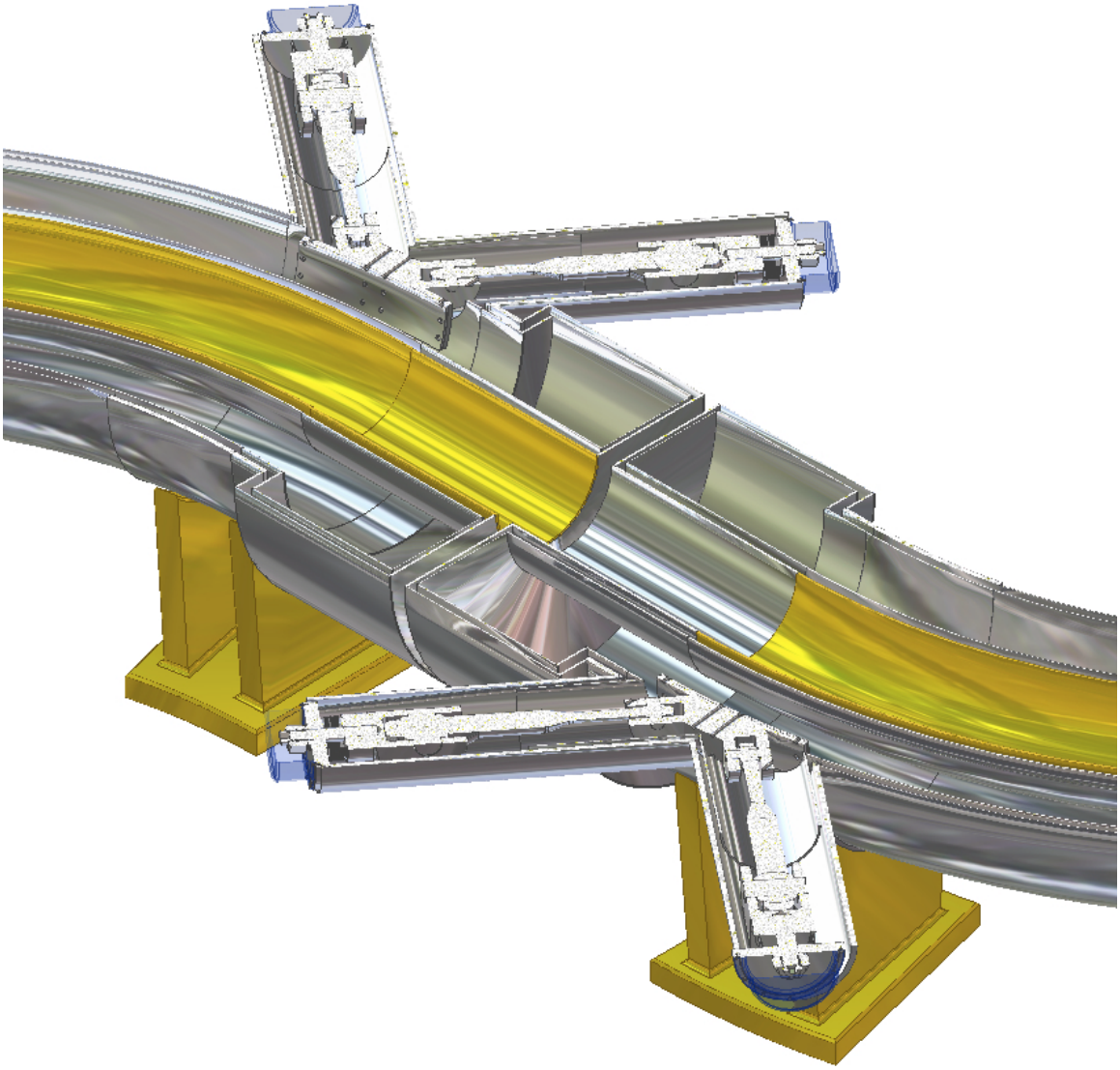

Figure 16.34 – TS interface at the Be Window. The magnets are not shown.

Make up fluid and electrical connections. Lower the upper half of the cryostat section onto the assembled coil. Make up gravity support rods. Tension gravity support rods, lifting magnet assembly off bumper supports. Level/align with cold mass support adjustment nuts. The split casings have flanges with locator pins. The joint could be sealed with a sheet metal lip seal weld. weld (see Figure 16.33). It appears at this time that the straight sections of the TS cryostats do *not* need to be split at the equator for coil installation.

Final Transport Solenoid Support Adjustment

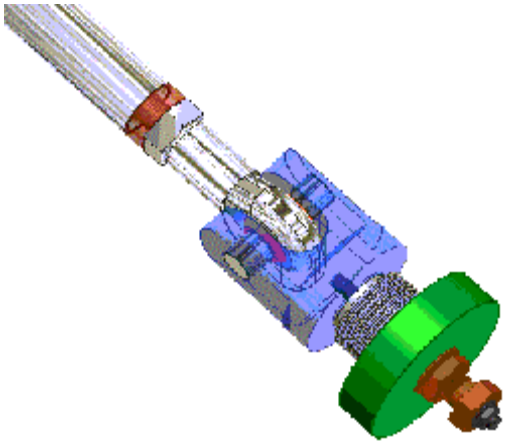

Figure 16.35 – Support strut end.

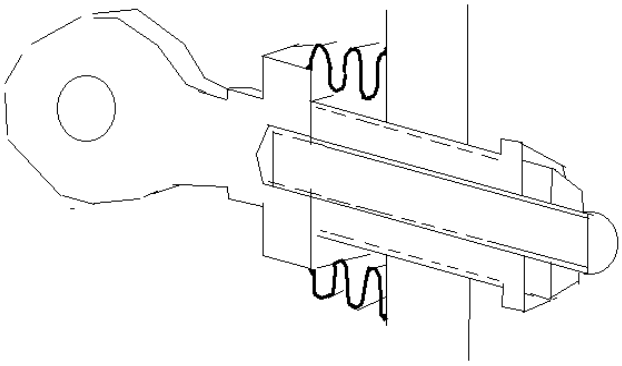

Figure 16.36 – Adjustment detail at the end of the strut. Bellows maintains vacuum during adjustment.

The transport solenoid assemblies have collimators at each end of the coil - four total. These should be trial fit at the factory, but since they are cantelevered from the end flange, they should probably be removed for shipping. A handling frame should be provided for factory fit-up and site assembly

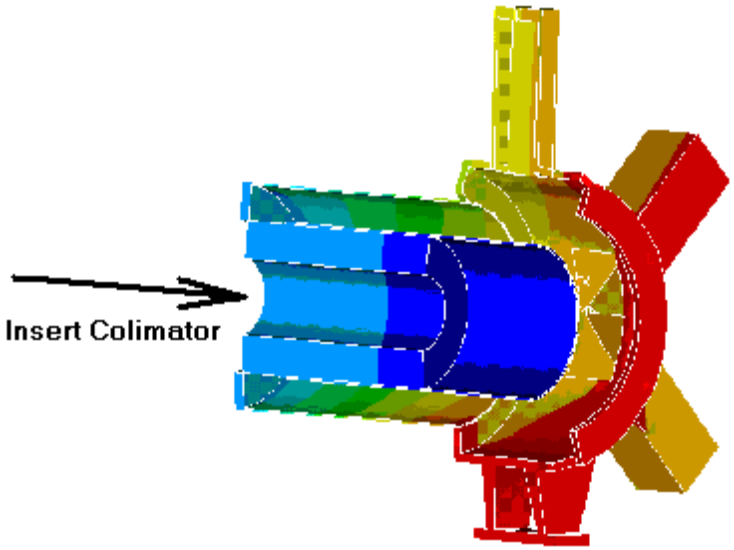

Figure 16.37 – Inserting the collimator into the TS straight sections.

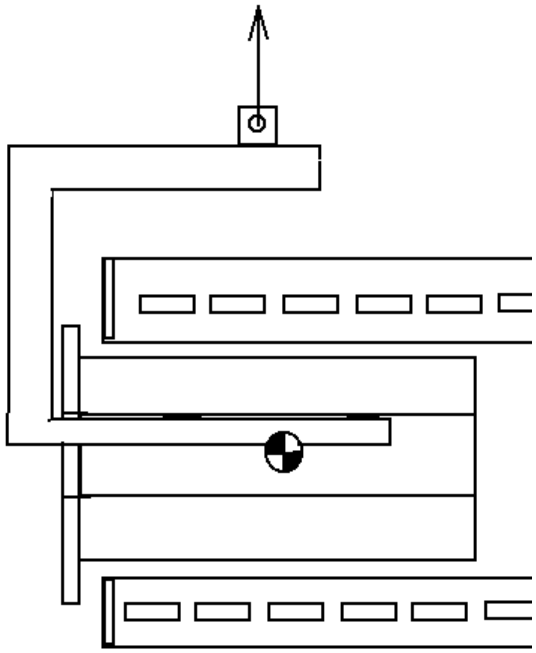

Figure 16.38 – Sketch of a handling frame to support the collimator during rigging.

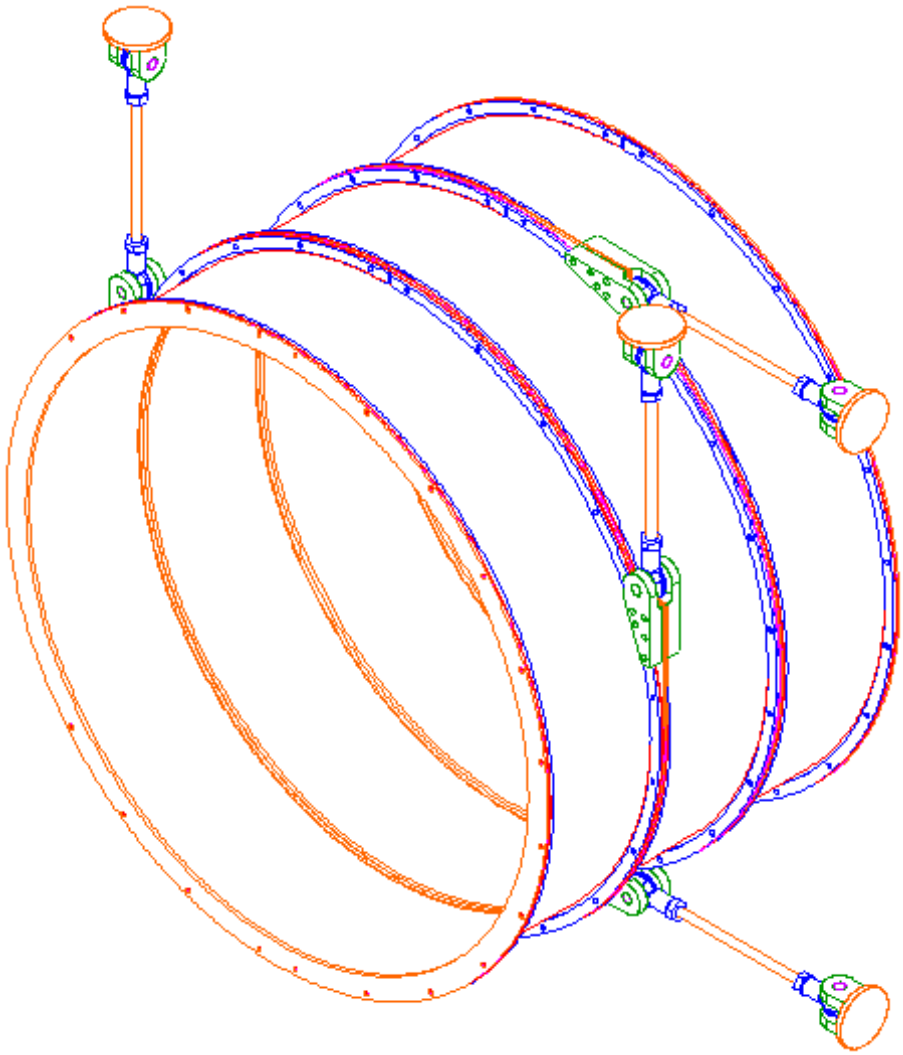

Figure 16.39 – Arrangement of Detector Solenoid support rods.

Detector Solenoid Assembly

The detector solenoid coil winding follows the same procedure as the transport solenoid. The cooling system used for the DS is the same as that for the TS and so the copper thermal radiation shields, and thermal conduction base and bridge plates are conceptually the same, but are at a much larger radius than the TS. The larger size of the coil however should make winding and handling operations different than the TS. A 0.25 inch thickness has been specified for the mandrel shell, primarily for ease of handling. Sidewalls of the mandrel are 0.8 cm. This will still be relatively flexible at the DS diameter. The winding machine layout will probably require internal stiffeners for the mandrel. The mandrel flanges should be machined after welding. The accuracy of the long assembly of coils relies on the precision of the flange-to-flange face parallelism. As for the production solenoid, vertical or horizontal assembly is possible, however because of the size of the assembled coil, and the relatively thin shells that make up the coil, special care is needed in an up-ending operation. The coil is over 11 meters long and crane headroom may make vertical assembly difficult. Even under gravity loads, the inner and outer

cryostat shells need the stabilizing effects of the outer annular cryostat end plates. Temporary spiders should be used until the shells are welded to the end caps.

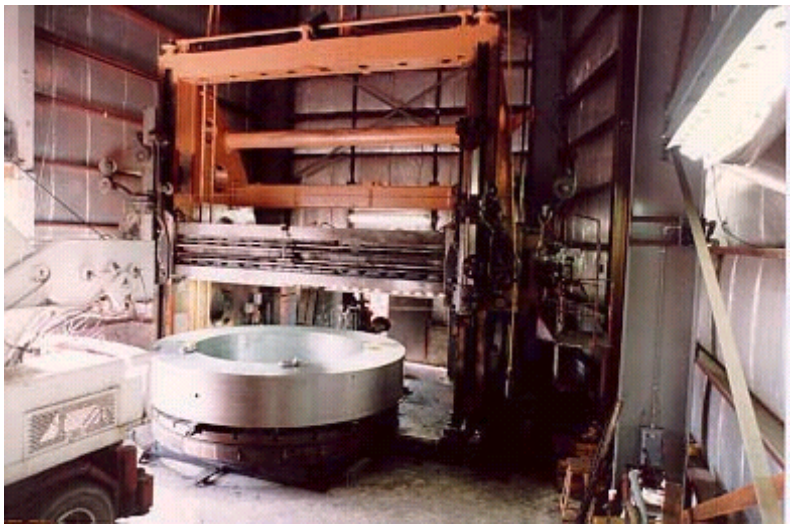

Figure 16.40 – Niles Vertical Lathe 240" dia x 198"
(http://www.demmercorp.com/equpment/evt0001.htm)

Axial support rods are similar in design to the PS and the assembly of these should progress in the same manner as for the PS. The lateral and vertical support rods have towers away from the ends of the cryostat and the assembly of the cryostat shells must clear these penetrations. The clevis extension is bolted to the mandrel flanges, allowing these to be added through the tower openings if this is needed to clear the cryostat shell as it is slipped onto the magnet assembly.

Figure 16.41 – Vertical support attachment detail.

Section 17 - Installation

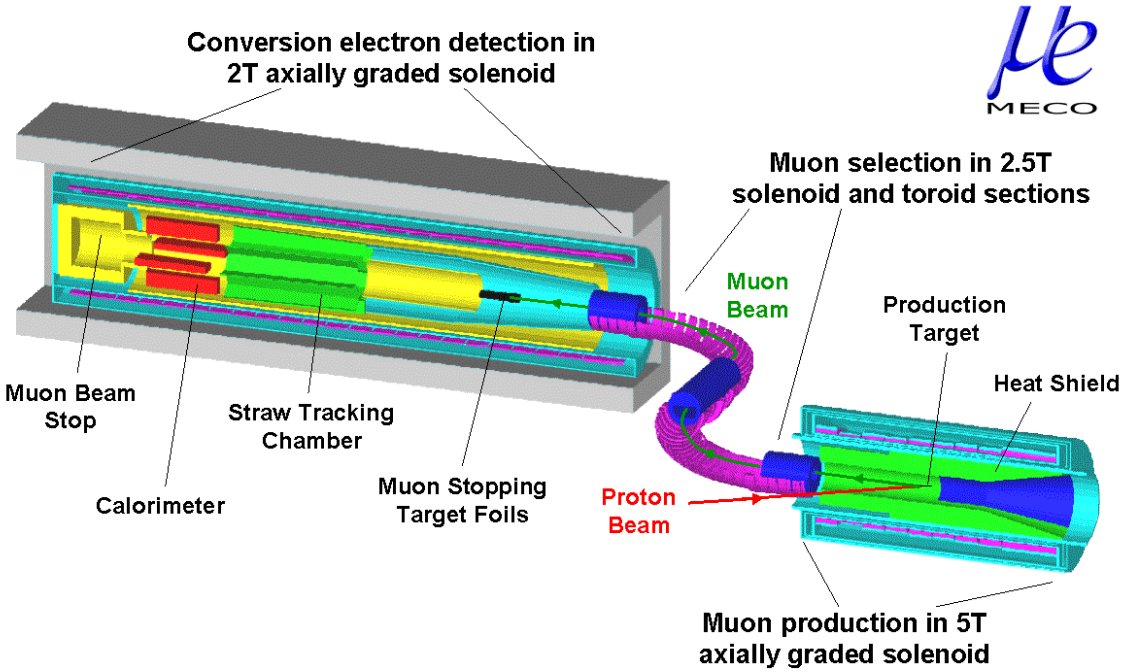

Figure 17.1 – An overview of the MECO experiment.

Introduction

The MECO experiment will be installed in the Alternating Gradient Synchrotron experimental hall at Brookhaven National Laboratory. The magnets for the experiment are in four major assemblies, using four cryostat vacuum boundaries, one for each magnet assembly. The four magnet assemblies are:

- The Production Solenoid (PS),
- One half of the Transport Solenoid (TS), up to the Be window,
- A second Transport Solenoid assembly nearest the detector solenoid,
- Detector Solenoid (DS).

It is intended that each of these assemblies would be shipped from the factory ready to be connected to power, cryogenic systems, and instrumentation. Other Components are logically grouped on skid assemblies for ease of shipment, installation, and start-up testing. It is suggested that the experiment be mounted on a steel and concrete frame that is built off the floor of the test hall. The frame, which is not designed at this point in the project, allows integration of lower iron and concrete shields.

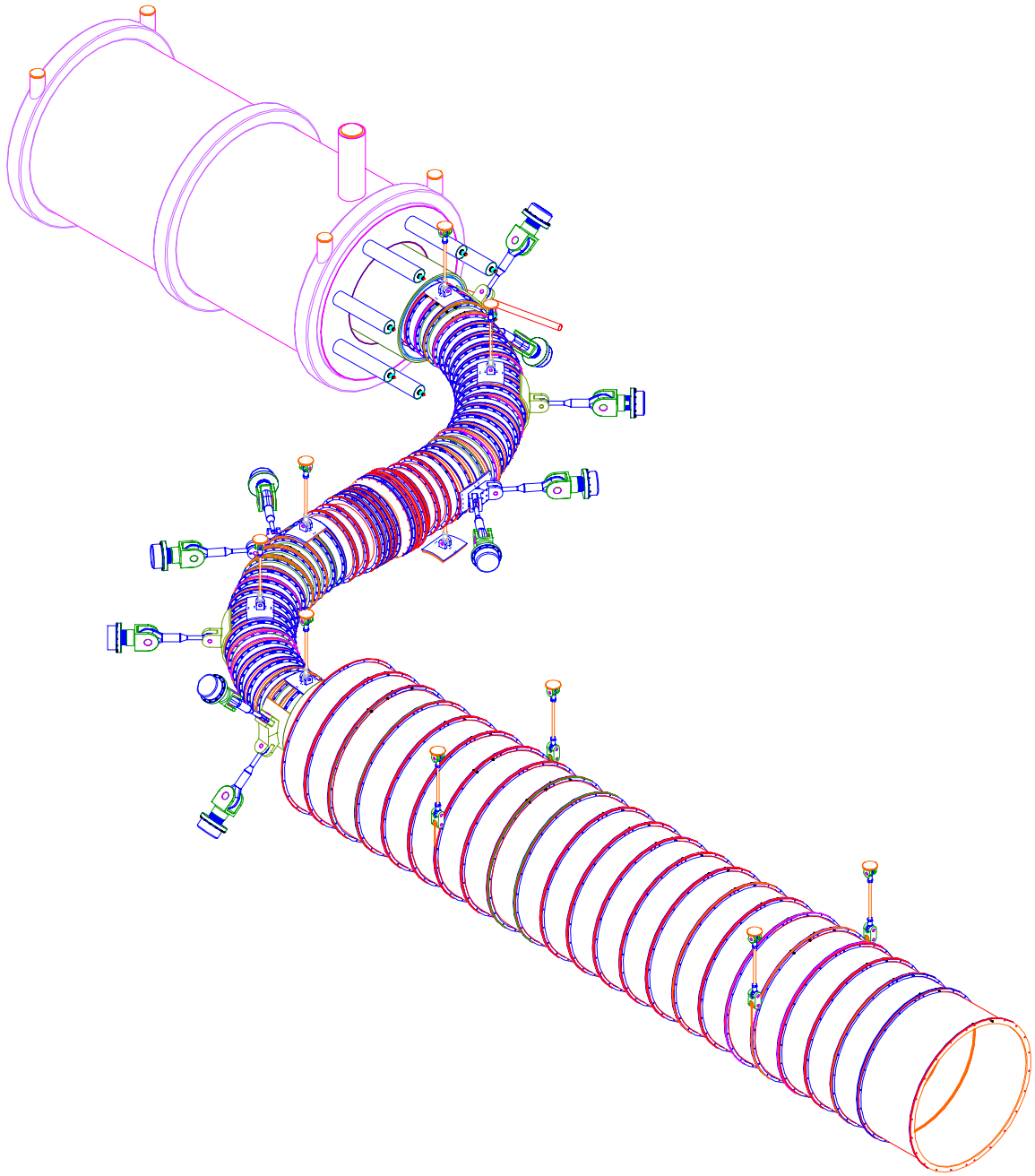

Figure 17.2 – Production Solenoid and it's cryostat, the transport solenoids (the break in the TS assemblies is in the middle of the "S", at the Berylium window), and the detector solenoid. The TS and DS are shown without their cryostats.

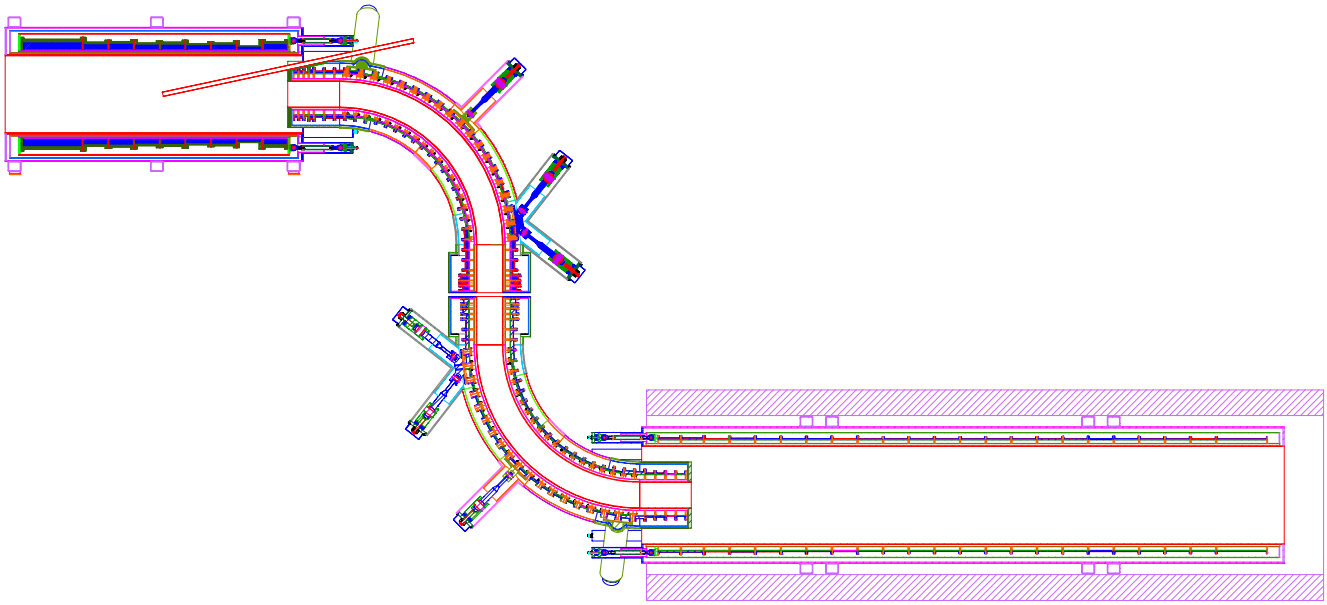

Figure 17.3 – Mid-plane section of the magnet assembly.

Other large skid mounted assemblies include the major cryostat components:

- Five skid-mounted Cold Box/Control Box/Vacuum Pump assemblies
- Transfer lines
- PS power lead/ Helium feed pipe assembly
- Two TS power-lead, helium-line-traced, vacuum-jacketed assemblies
- One DS power-lead, helium-line-traced, vacuum-jacketed assembly
- Copper/Tungsten Shield Assembly
- Pedestal frame
- DS Iron Shield Slabs
- Quench Detection System Electronics
- Power Supplies and Quench Protection Equipment

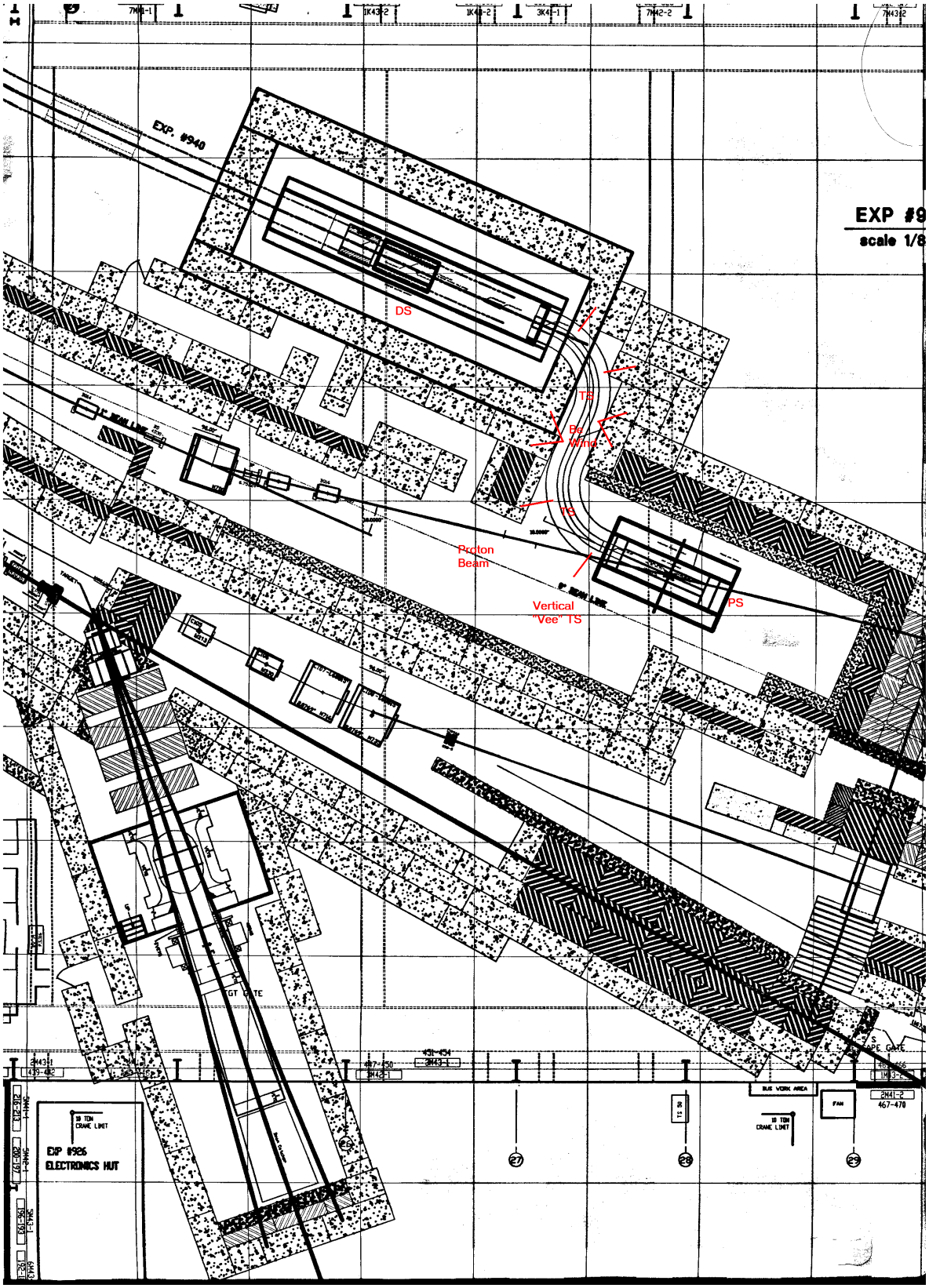

Figure 17.4 – General Arrangement of the MECO Experimental area. Grid lines are on 200-inch centers. Receipt overhead doors are at the right.

Receipt/Laydown Space Requirements

The overhead door that provides access to the test cell is at the PS end of the cell, and a receipt order of DS TS2, TS1, and PS would allow magnet assemblies to be positioned at their final location as they are received. The cell is large enough, however, that laydown/storage space would be available for almost any receipt sequence. The capability for this flexibility in the coil installation order may be useful, since a preliminary evaluation showed that the overall schedule is minimized with a TS1-TS2-DS-PS delivery sequence, in that order. Also, each assembly is sufficiently large and complex that unexpected schedule delays in any one are possible and might result in a delivery sequence that would differ from the baseline plan. The overhead door to the test cell is estimated to be large enough to pass the largest magnet assembly, but it could, with minimal cost, be widened.

Table 17.1 – Approximate dimensions of installation assemblies. Figure 17.5 shows the dimensions to which the tabulations correspond.)

Component	Weight (kg)	Length (m)	Width (m)	Height (m)
PS	53,000	6.9	3.1	3.8
TS1	31,000	5.9	5.7	3.5
TS2	30,000	5.9	5.7	3.5
DS	52,000	13.6	3.1	3.1
Cold Box (each)				
Cu/W Shield	40 ton			

The facility crane capacity is 40 ton and has full floor access. The PS and DS are heavier than the crane capacity and will need to be moved with equipment additional to the existing crane. Rollers, chain hoist, and/or come-alongs are a possibility. These components should be handled on cribbing at the assembly pedestal elevation. There are a number of other rigging and handling options. A portable rubber tired gantry crane might be rented and used in concert with the overhead crane.

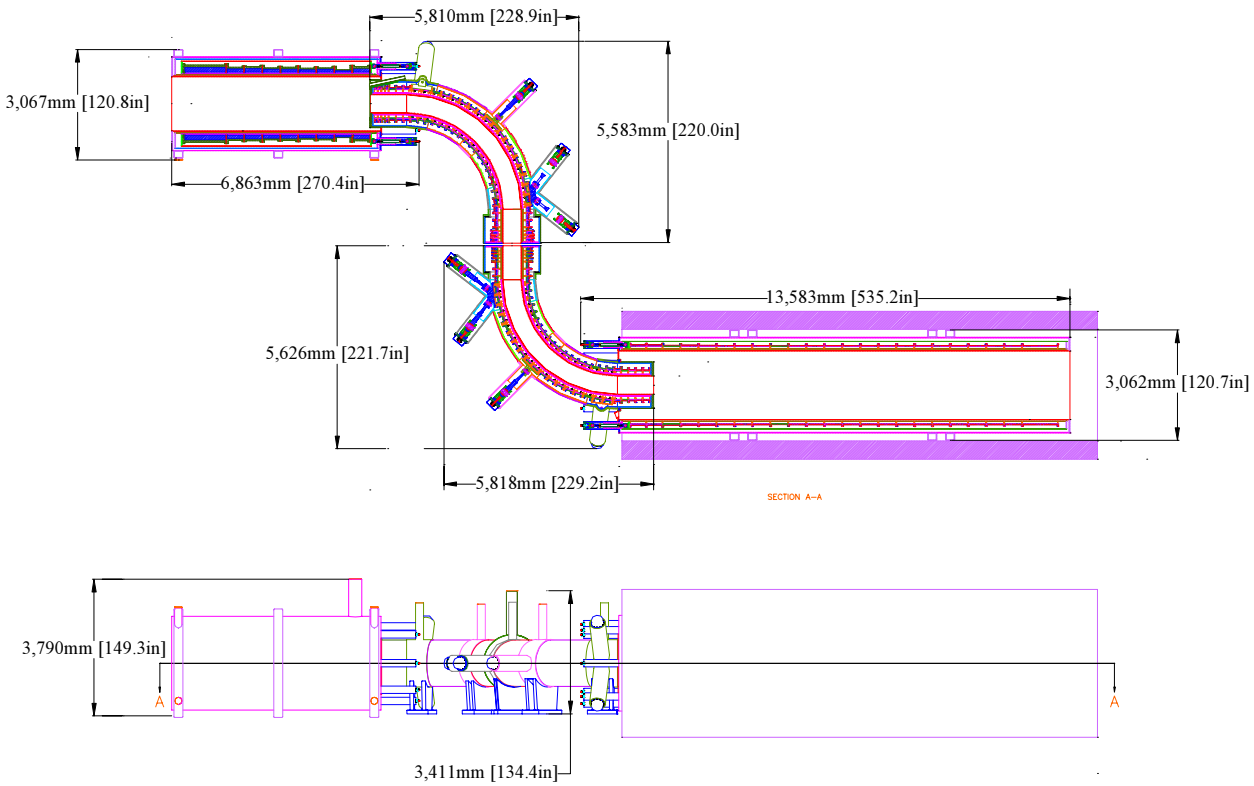

Figure 17.5 - Envelope dimensions of the individual cryostats

Lift Points, Rigging Guidelines

Cold mass support towers may be loaded in-line with the axis of the tower. Tower ends will have lift lugs provided. Upstream ends of the coil systems tend to be heavier than downstream ends. Centers of Gravity shall be provided at the detailed design phase.

Receipt Inspection, Testing

The magnets are fully assembled and tested at the factory, and should not require anything other than a thorough visual inspection. Cryogenic and electrical connections should be inspected for indications of rough handling. Magnet cold mass supports are designed to allow adjustment outside the cryostat, and there is provision during manufacture to have coil assemblies rest on vertical bumpers/rails during assembly. The vertical gravity support rods are then used to lift the cold mass off these supports. These features could be used to provide support during shipment, in which case, the vertical cold mass support rods may need to be tensioned, and the magnets may need an initial alignment. Field mapping and the adjustable cold mass supports will be used later for final alignment. The present design drawings do not provide adjustment features in all locations in the PS and DS. Alignment procedures need to be re-visited during the detailed design phase of the project.

Base Pedestal

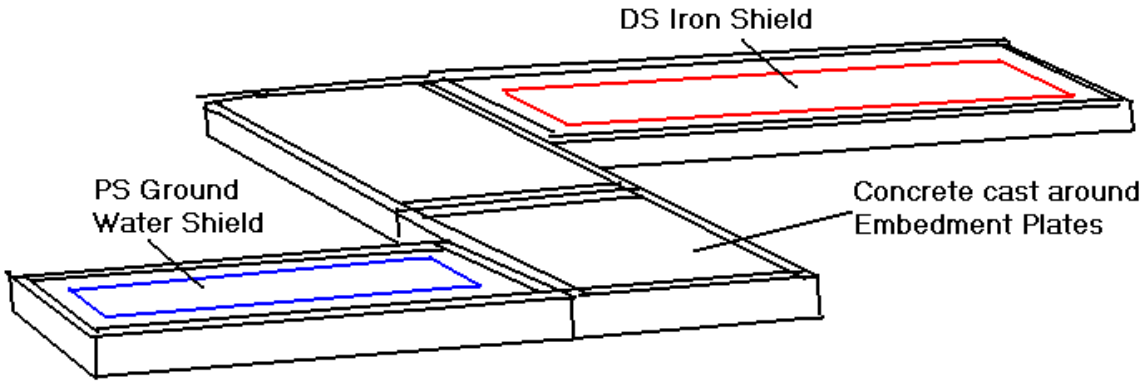

Figure 17.6 – The base pedestal for the magnet system.

Assembly begins with the base pedestal assembly. This is a series of frame and shield components that lays on the cell floor. Magnet sub assembly loads are large, and are reacted through this base. Magnet loads sum to zero and when reacted by the base impose only deadweight loads on the cell floor. The base/pedestal was chosen over loading floor embedments because of the need to provide heavy shielding under the experiment as well as on the side and top. Integrating the shields with the pedestal framing allowed both the force control and shielding requirements to be satisfied with the same structure. The pedestal framing has not been designed as a part of the conceptual design phase, but is envisioned as framing-steel boxes, one each for the four major coil sub-assemblies, that can be filled with steel and/or concrete shielding material. Embedment plates can be integral with the steel shielding and frame structure and interconnected with cast concrete via Nelson studs. The four base assembly interconnections should be adequate to transmit the magnet subassembly loads. The base forms a rugged structure to interact loads. However, consideration should be made to allow feasible disassembly during the decommissioning of the experiment. Embedments have not been sized, but to facilitate positioning of especially the PS and DS which are above the crane capacity, embedment plates should be threaded, rather than having protruding studs.

Assembly Pedestal Load Management

The system is separated into four magnet assemblies. It is not practical to react cold mass loads without going through warm structure due to thermal contraction and Lorentz load displacements. The philosophy at this point in the conceptual design effort is to react loads through individual magnet assembly supports, each connected to floor embedments. The assembly floor pedestal reacts attractive and repulsive loads between the magnets. Structure could be added between the magnet assemblies to reduce the loading in the pedestal, but the details of the boundaries between magnets makes the addition of structure unattractive. Access to the Be window and it's vacuum boundary would be restricted if structure were added to bridge this gap. The area at the end of the PS and the beginning of the TS includes shielding, and a vacuum seal and proton beam tube that must be accessed. This area would be made more congested by the addition of interconnecting structure. This installation description assumes conventional saddle/baseplate supports that are shimmed and grouted in place. Coil installation will be described from the detector solenoid end.

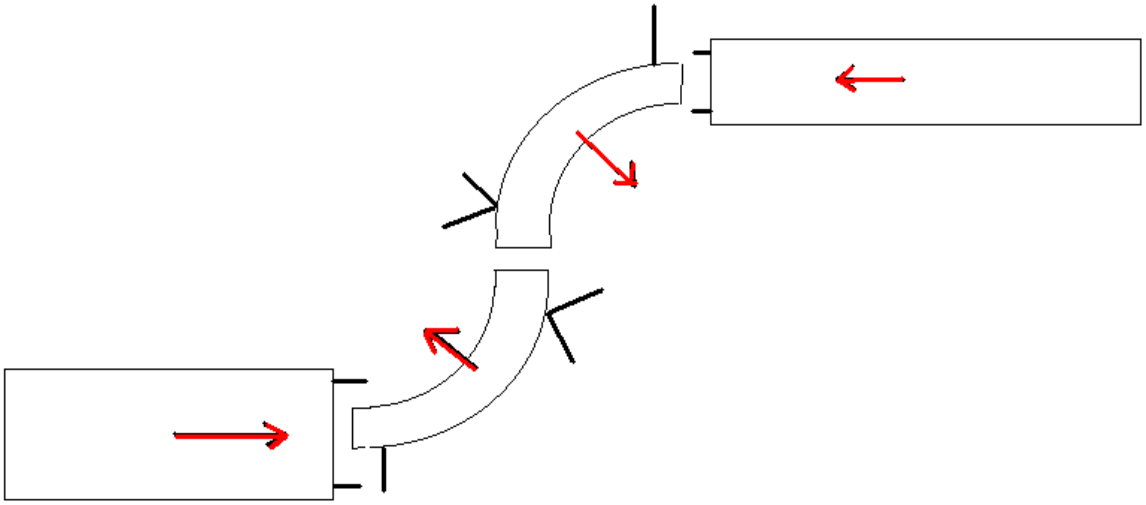

Figure 17.7 – Forces and Moments Sum to Zero
Production Solenoid Net Axial Load is 1.49 MN, or 334,755.8 Lbs
Detector Solenoid Net Axial Load .5076 MN, or 114,120 Lbs

Installation of the Detector Solenoid

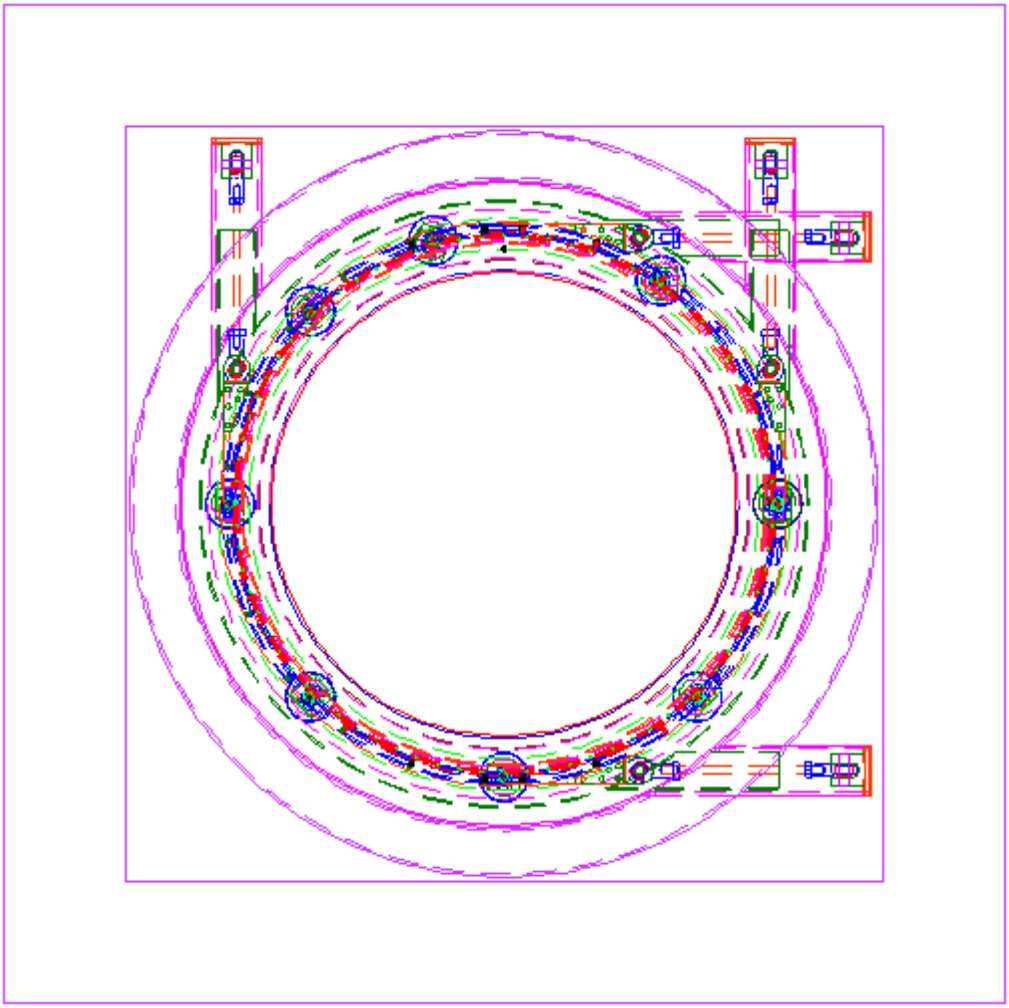

Figure 17.8 – Axial view of the Detector Solenoid, its cryostat, and the iron cosmic ray shielding.

This installation is a rigging problem due to the weight and size. Installation of the DS simply involves its placement and positioning on the support pedestal. There is a net axial load directed towards the TS. Because of the length of the coil, the axial load will produce mainly shear loading on the embedments. The detector solenoid has a support frame with a shear panel to react axial loads. The details of this design may be similar to the support for the production solenoid.

Installation of the Transport Solenoid

Embedment Loads

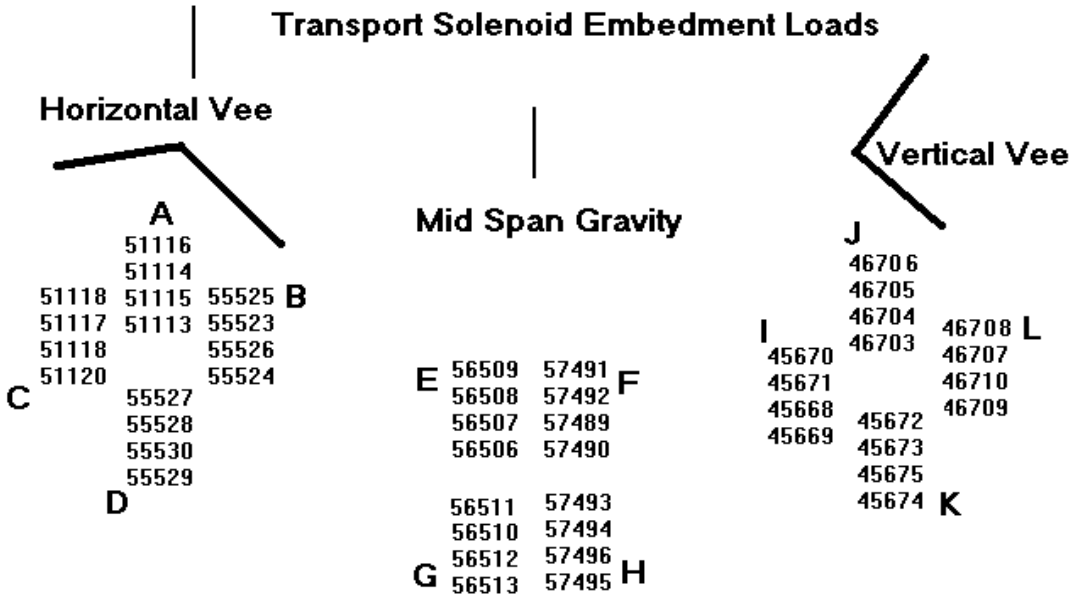

Figure 17.9 – Transport Solenoid embedment loads.

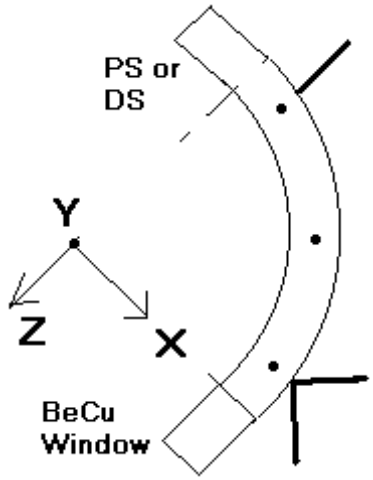

Figure 17.10 – Coordinate system used for the TS bend sections.

The base of each of the TS support structures has four pads modeling embedments. These are 1.05 m below the beamline. Embedment loads would be greatly reduced if the TS support base plates were widened. This should be investigated during the design phase.

Table 17.2 – Normal operating reaction forces. The coordinate system is shown in Figure 17.10, and the pad arrangement is illustrated in Figure 17.11.

Pad	FX (lbs)	FY (lbs)	FZ (lbs)
A	62096.7	223910.02	-100664.3
B	94370.8	228624.52	74329.2
C	67492.4	-225885.78	75617.3
D	40208.4	-220769.34	-91469.7
E	-1751.4	9926.606	-3346.12
F	3240.2	10227.478	2008.9
G	975.5	-1183.4488	-244.6
H	317.65	-881.81397	-901.3
I	-72948.0	196954.47	-84227.1
J	90473.2	221507.8	-62717.8
K	84591.5	-205183.95	-43931.4
L	-71073.8	-204941.17	-60796.4

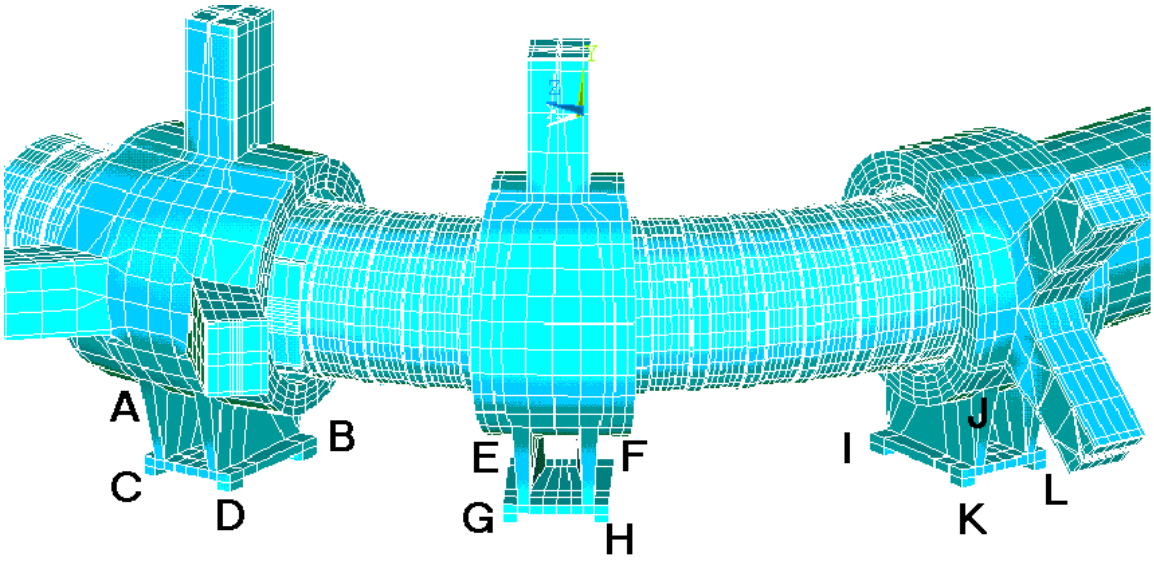

Figure 17.11 – Arrangement of the support pads for the TS bend sections.

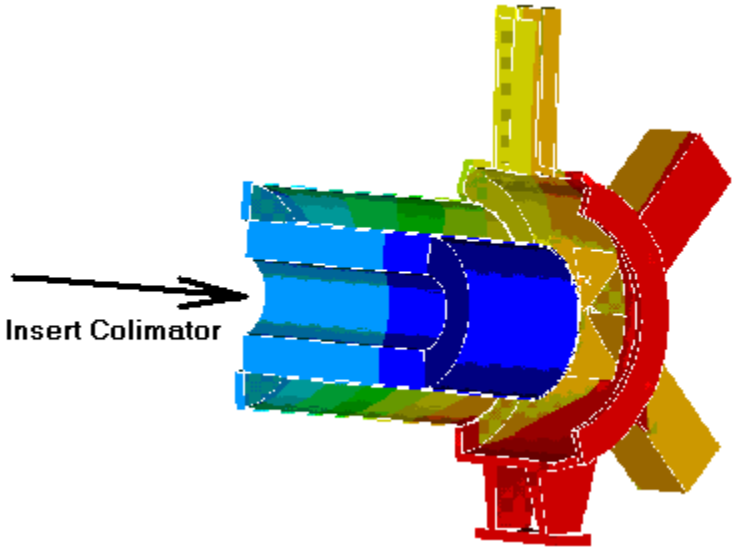

Figure 17.12 – Collimators are slid in the TS bore at each end of each TS, at the Be window ends.

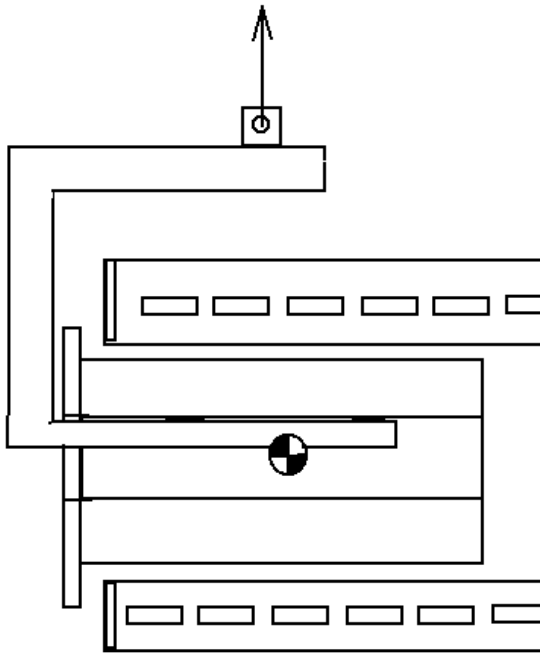

Figure 17.13 – Collimator handling frame.

The collimators can be shipped integral with the TS assembly, but ideally it will be shipped separately. It is readily slipped in to the end of the TS with the help of a frame that allows a lift over the CG. Since the inner bore of the TS cryostat is the vacuum boundary for the magnet cryostat and for the experiment, the mounting flange for the collimator must not violate either boundary

Production Solenoid Installation

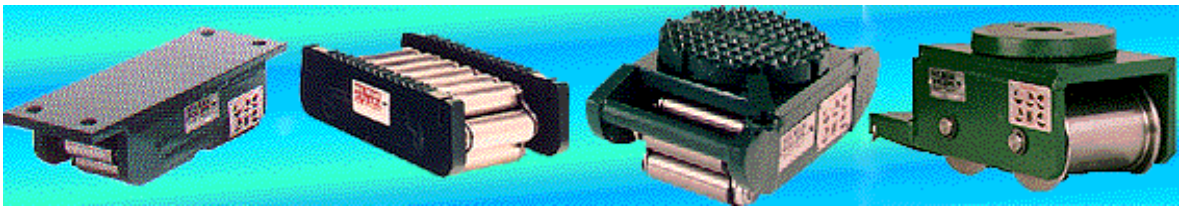

Figure 17.14 – Use of Hillman rollers is one way of solving the 40 Ton crane limit. These rollers are for moving from 1 to 200 tons on hard level floor surfaces without a track (http://www.hilmanrollers.com/C1.htm).

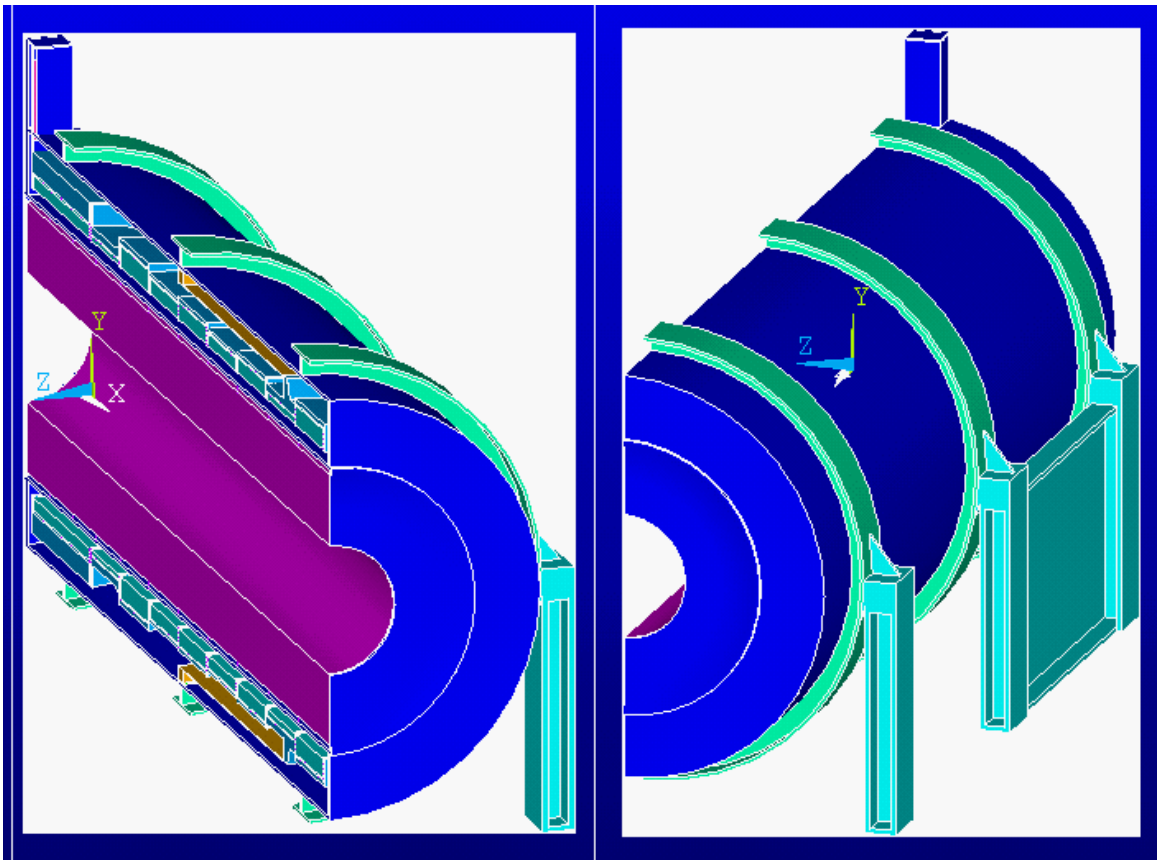

Figure 17.15 – PS external support structure.

The production solenoid is one of two assemblies that are too heavy for the overhead crane system available in the experimental cell. Use of rollers on tracks laid on cribbing is one solution. As previously mentioned the 40-ton overhead crane used in concert with a rental gantry or yard crane could handle the weight of the DS and PS. The cell is large enough that a yard crane can be brought into the cell. Installation of the PS simply involves its placement and positioning on the support pedestal. There is a net axial load directed towards the TS. Because of the length of the coil, the axial load will produce mainly shear loading on the embedments. The production solenoid model at left shows the frame with a shear panel to react axial loads

Field Mapping and Final Positioning

The coil structural analyses will probably not be precise enough to predict accurate coil positions after cooldown and under load, because of the bolted connection tolerances and compliance, uncertainty in the coil moduli, interactions with the aluminum mandrels in the PS, and fabrication tolerances. The support struts are designed with adjustments that can be made at cryogenic temperature and under vacuum. There are bellows details, and nested thread details to allow this. With this detail, an estimate has been made regarding how large the adjustment capability needs to be. At the end of detailed final design, the displacements should be predictable within millimeters, and strut adjustments can be provided to accommodate a few centimeters. There is a substantial ability to accept certain of the misalignments, and the struts can be used to make final adjustments to magnetic fields as well as geometry. It will be difficult to make the adjustments in the TS supports with the coils energized. Field mapping may be conducted at full field, and the current backed off to allow turning the TS adjustment nuts. Supports for the PS and DS and all the vertical support rods can be adjusted with the coils energized.

Insertion of the Production Target/Heat and Radiation Shield Assembly

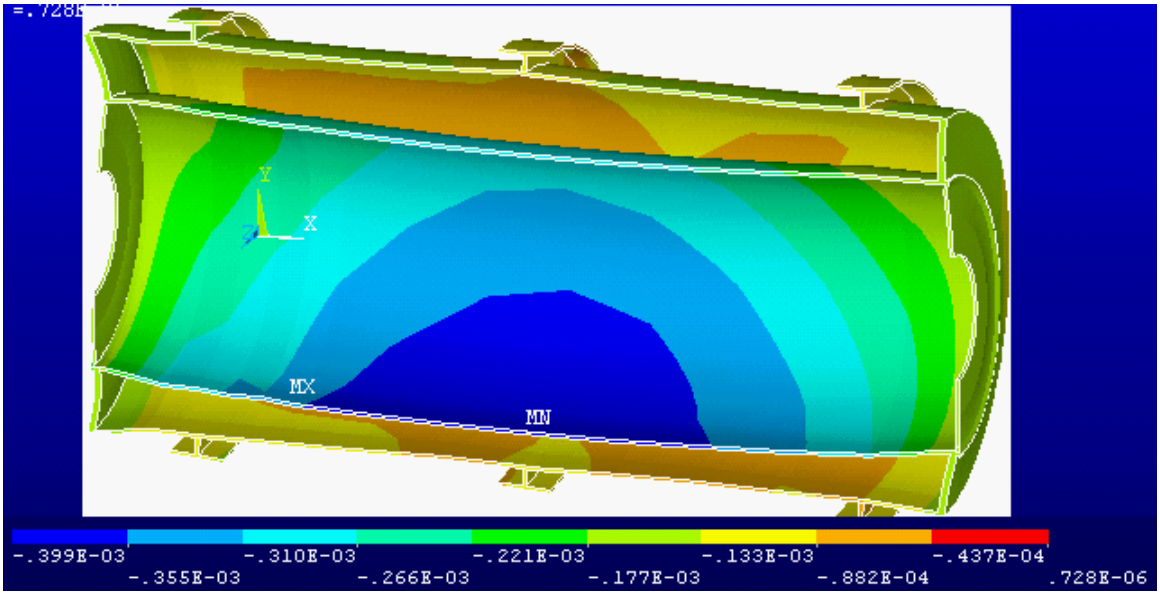

Figure 17.16 – Vertical Displacement of the cryostat shells under pressure and shield deadweight. The maximum displacement is mid span on the inner shell which supports the deadweight of the shield. Run#grav01

The assembly sequence proposed by the project is to use a strongback that extends the target/shield assembly and allows multiple support points. The PS coil and cryostat are slipped onto the cantilevered end of the strongback/target/shield, and slid halfway on. The supports are then repositioned outside the PS and the PS is translated the rest of the way towards the TS.

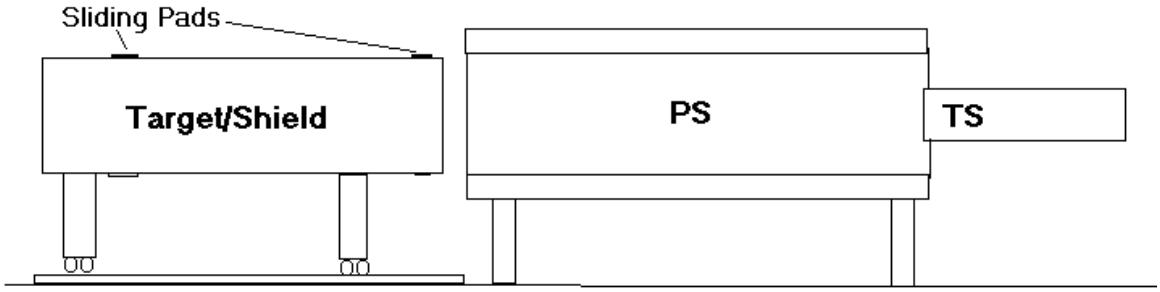

Figure 17.17 – Alternative Target/Shield installation procedure.

An alternate assembly procedure would utilize the inner bore of the PS cryostat. The target/shield assembly can be supported outside of the PS which has been fully erected, and power, cryogenic and instrumentation connections either made-up or in process of being made up. This can be slid in using the support of the inner cryostat wall. Sliding pads can be the same bearing material qualified for the spherical ball ends, or use cam followers. The inner shell of the PS cryostat has been qualified for the deadweight of the target/shield assembly. The frame for the target/shield would need to provide support for the cryostat shell to maintain circularity and develop the shell strength as a beam. The overhead crane can provide some relief of the Target/Shield dead load as the assembly is inserted, reducing the insertion force and reducing the cryostat shell stresses. As the target/shield assembly is inserted in the PS, the temporary roller supports would be removed.

Connecting the Vacuum Boundary between TS and the PS Experimental Volume

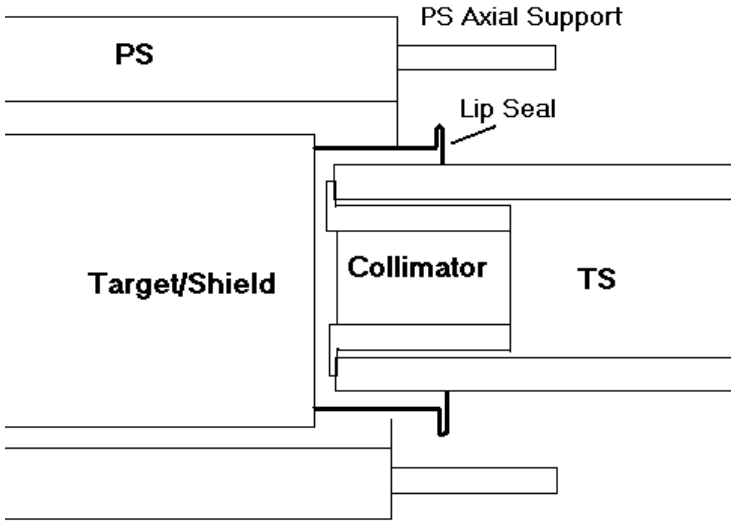

Figure 17.18 – Vacuum boundary between PS bore and TS bore.

Cryogenic System Installation

The cryogenic system is divided into modular subassemblies connected by field assembled lines. All the 4 K lines are vacuum insulated. Room temperature power leads are made up at the vapor cooled leads, which are expected to be a part of the Dewar/Valve Box assemblies for each coil assembly. Welds of field run vacuum and Helium lines should have visual, penetrant, and Helium spectrometer inspections.

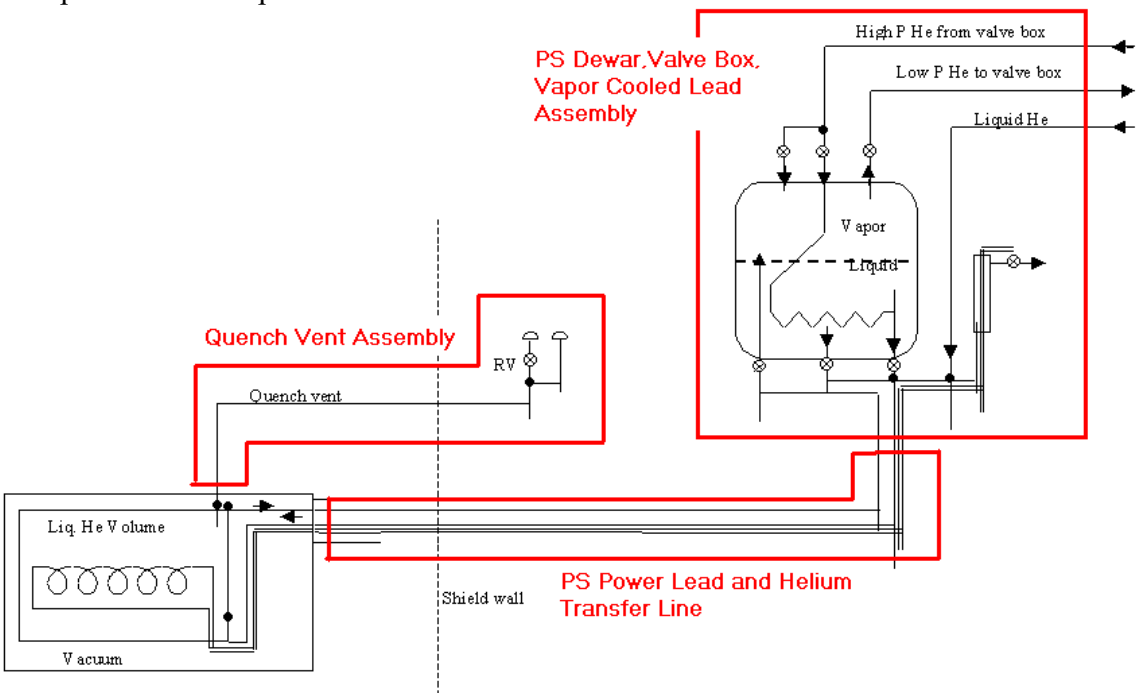

Figure 17.19 – PS power lead and helium transfer line assembly, dewar, and valve box.

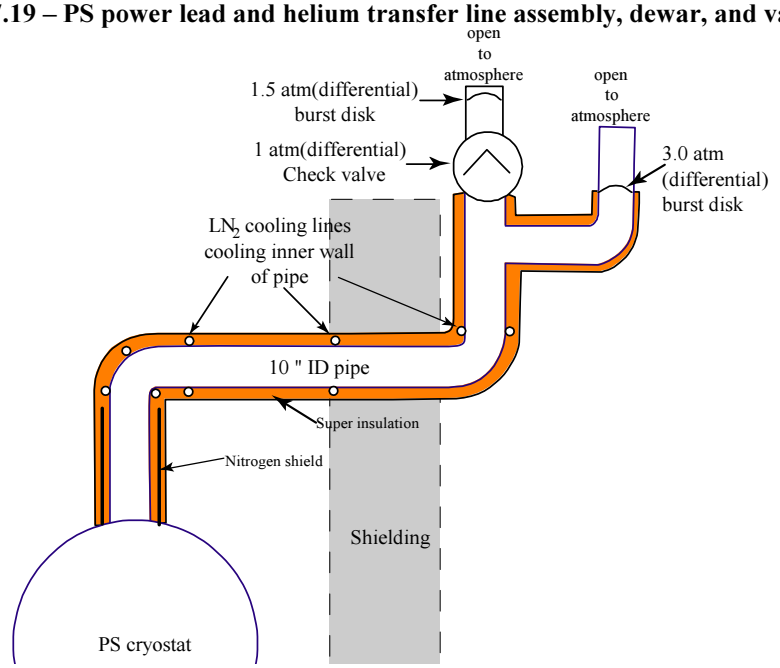

Figure 17.20 – PS quench vent assembly.

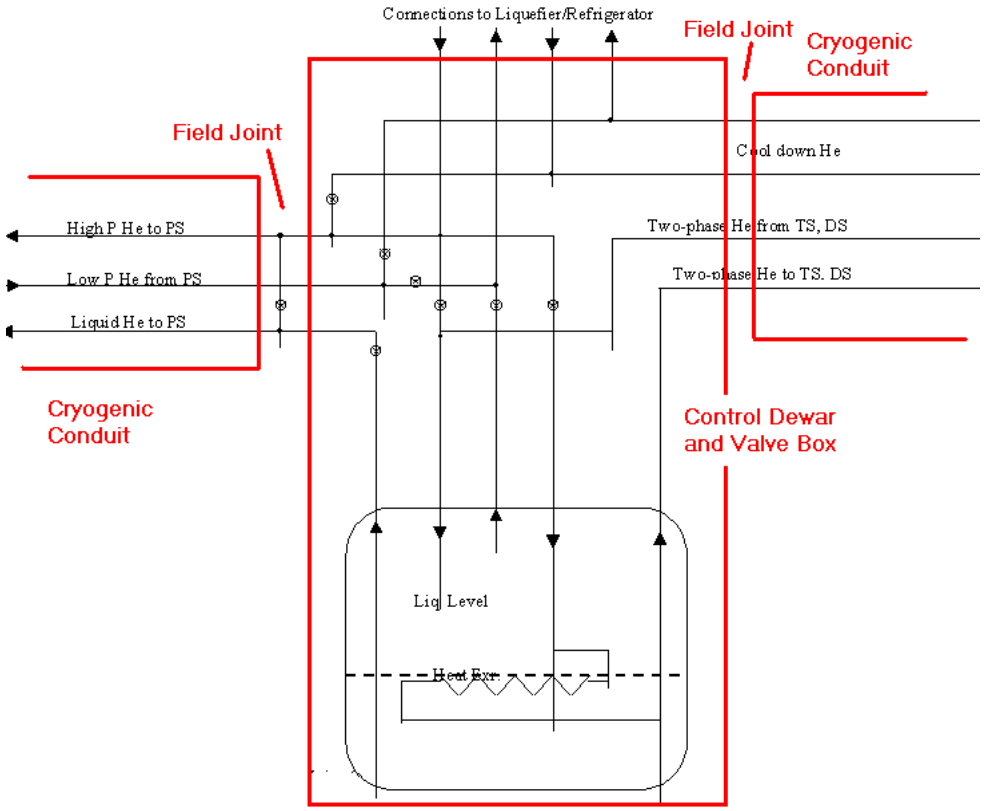

Figure 17.21 – Cryogenic control dewar and valve box.

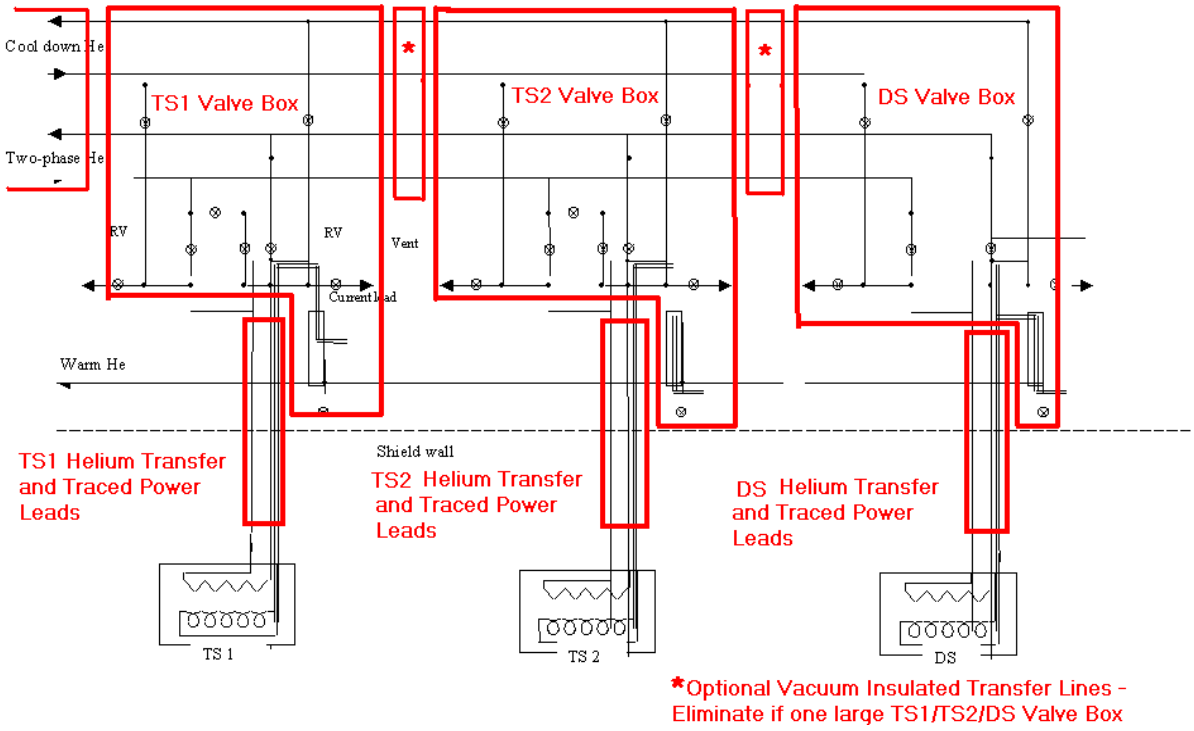

Figure 17.22 – TS cryogenic system components.

Installation of cryogenic conduits

The cryogenic system is divided into modular sub assemblies that are interconnected in the field. Cryogenic conduits are connected between the sub assemblies after the sub assemblies are in place. The cryogenic conduits enclose and vacuum insulate all cryogenic lines between the modules. The vacuum for insulation is divided so that each cryostat and the associated cryogenic conduit that penetrates the shield wall have a common vacuum. This allows the vacuum to be pumped from outside the shield wall. The control dewar and the PS dewar have separate vacuums. The dewars and the valve boxes are connected by cryogenic conduits with the appropriate helium and LN2 tubes. The separate vacuums are maintained by vacuum isolation barriers incorporated in the helium conduits at appropriate locations. The heat leak from the vacuum isolation barriers is minimized by thin-walled tubular pant-legs that have heat stations cooled by the LN2 flow. As shown in the sketch, a field assembled connection is made between the cryogenic conduit and the associated valve box or cryostat. First, each of the internal tubes is joined by TIG welding with an orbiting tube welder. Then the 4 K MLI is applied, followed by the radiation shield that is wrapped over the 4.5 K tubes. The 80 K MLI is then applied over the radiation shield. The field joint is completed by TIG welding a longitudinally split tube over the joint thus completing the vacuum wall.

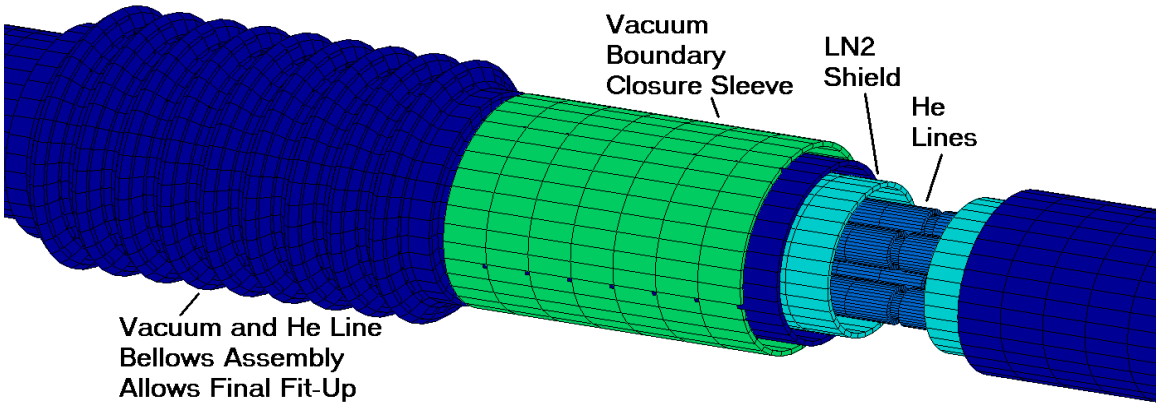

Figure 17.23 – Typical cryogenic conduit joint. The LN2 shield includes a supply line (not shown).

The superconducting current leads are installed within the conduit between the cryostat and the associated valve box. The leads are cooled by a helium flow within the conduit. The electrically insulated TS and DS leads are thermally clamped to a helium tube while the PS leads are within a helium tube. The superconducting leads within the conduit are connected to the coil terminal leads with joints that are the same as the coil-module to coil-module joints with in the cryostat. The low resistance electrical joint is made first and then the tube joints are welded. The tubes have offset bends to allow room for the electrical joint and clearance of the orbit welder. These joints will require larger diameter vacuum wall over the joint. Similar joints will be required outside the shield wall where the superconducting leads are connected to the cold end of the gas cooled current leads.

The superconductor and the tubes are bent to the required radius then assembled and insulated. Welding together short lengths of elbow and or longitudinally split lengths of pipe completes the vacuum wall.

PS Power Lead and Helium Transfer line Assembly

The PS lead / busbars serve as the helium transfer tube from the external PS control dewar to the PS magnet cryostat. Since the bus bars will be contained within the equivalent of a liquid helium transfer tube the bus bars must be contained inside the helium space, and the transfer line thermally shielded and vacuum insulated. The size and complexity of the run between the PS service tower, and the PS control dewar will determine the feasibility of having a field fabricated vs. a factory assembled unit.

Shield Block Assembly

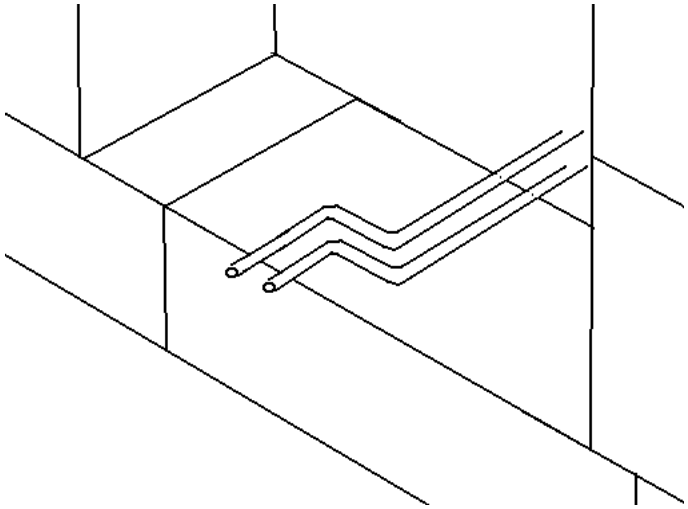

Figure 17.24 – 1/2 in Helium line with 2 inch vacuum jacket can be factory fabricated with 6 inch bends. Smaller radii are achieved with a mitered cut on the vacuum jacket.

Shield blocks will have to accommodate doglegs for all the vacuum, cryogenic, and instrumentation penetrations. The cryogenic conduits will have offset dogleg bends within the shielding wall to prevent radiation leaks. Special shielding blocks will be cast with a split at the level of the penetrating conduit. The conduit will fit one half in the lower block and one half in the upper block. With the lower block in place, the conduit is completely installed and then the upper block is fit over the conduit in the lower block. Long radius bends will be required for the cryogenic conduits. The sequence of placement of the blocks should allow passage of the field run lines with a minimum of relocation of the blocks.

Vacuum System

An attractive arrangement is to have dedicated vacuum pumps for each major skid mounted assembly. The cryogenic conduits can serve as vacuum connects to the coil vacuum.

Connections of the Power Supplies

Six lead connections are required; one for the PS, two for each of the two TS assemblies, and one for the DS.

Section 18 - Draft MECO Test Plan

Introduction

This section describes the testing to be accomplished on the Superconducting Magnet System for the MECO Experiment. Acceptance of the Magnet System by the MECO Project is predicated on satisfactory completion of all tests identified herein. The Contractor may perform other tests preliminary to the formal acceptance tests, but these are not included here.

The Contractor and MECO Project Staff (or other designated MECO Subsystem Manager) will perform three test segments prior to Magnet System delivery:

1. Superconductor Tests
2. Warm Coil Tests
3. Warm Magnet Subsystem Alignment Verification.

Although testing of some magnet sub-system coils could be performed at the contractor's factory, the very large size and complexity of the entire magnet and cryogenic systems, combined with the substantial amount of time required for cool-down, start-up, testing, warm-up and shipping to BNL would not be acceptable from a schedule standpoint. It would also require the use of a large helium liquefier at the magnet Contractor’s site. Thus, cold magnet system testing will only be performed at the BNL.

The sequence of test segments is designed to evaluate system functions in the order needed for a safe progression from basic, passive functions to those that impose maximum stress on magnet components.

The Contractor is responsible for assembly and installation of the Magnet System and performance of the specified tests. MECO Project Staff or designated Sub-System manager will participate in the planning and execution of the tests, as appropriate, and certify the acceptance criteria have been met

Certain tests can only be performed, however, with support services or equipment provided by the MECO Project or BNL. These services and equipment items are summarized as follows:

MECO Staff and/or designated Subsystem Manager will witness the following acceptance tests, which will occur at the indicated location. In some cases, MECO project personnel will participate in the planning and execution of the tests as appropriate. A Master Fabrication and Test Sequence Document is included in a separate section below.

Table 18.1 -MECO furnished services

Item	Location
1. Testing of superconducting wire	TBD
2. Approve coil warm dimensions	Contractor
3. Witness coil warm measurement	Contractor
4. Witness & approve coil HiPot & turn-to-turn voltage tests	Contractor
5. Magnetic verification (warm)	Contractor
6. Site services at BNL	BNL
7. Witness & approve leak tests	Contractor/BNL
8. Magnetic verification (cold)	BNL

Table 18.2 – MECO furnished hardware

Item	Location
1. Superconducting cable for PS, TS and DS coils	Contractor
2. Site services & equipment	BNL
3. PS Coil radiation shielding	BNL
4. DS Coil iron shield and other detector components	BNL
5a. TS coil collimators-trial fit	Contractor
5b. TS coil collimators-final installation	BNL
6. Main helium liquefier	BNL

.

1 — SUPERCONDUCTOR ACCEPTANCE

The MECO Project provides SSC inner cable and SSC outer cable. Although this superconducting strand and cable is well characterized, some limited measurements should be made on the supplied material to verify the performance of the delivered stock. The exact number of samples to be tested is to be determined in cooperation with the MECO Project. Wire verification tests will be performed on samples extracted from the supplied cable. Further limited conductor tests will be performed on samples of the various grades of PS, TS, and DS cable-soldered-in-copper channel conductors.

1.1 — SSC Strand Data Review

The Contractor will analyze test results of wire and cable provided with the SSC cables for compatibility with the MECO magnet specifications and planned operating environment.

1.2 — Strand I_c

Based upon the results of this analysis, the Contractor, in collaboration with the MECO Project, will select a representative number (TBD) of cables, from which a number (TBD) of individual wires will be extracted. The Contractor will perform short sample tests to verify the manufacturers' test results and as support of the database. Tests will be in a magnetic field range of 2 T – 6 T and a temperature range of 4.2 K – 6 K.

1.3 — Integrated Conductor Tests

The integrated conductors for the MECO magnets will be made from SSC cable soldered into a monolithic copper stabilizer channel. Tests and measurements of representative samples of each finished conductor type for the PS, TS and DS magnets will be performed.

1.3.1 — Dimensional Verification

Dimensional readings will be made to verify that the conductors have been fabricated within tolerances.

1.3.2 — RRR

Residual Resistivity Ratio (RRR) will be determined over the temperature range 273K – 15K on final soldered cable-in-channel conductor samples. Number of samples is TBD. These tests may be performed in conjunction with conductor Ic tests performed at TBD.

1.3.3 — Insulation

The insulation integrity will be continuously checked with a spark curtain just after the wrapping head and prior to winding. The spark tester settings are TBD. Indications of current leakage should cause the insulating machine to stop for pinhole investigation, repair and retest. Appropriate safety measures must be taken to set current limits on any discharges, to ensure that the coil winding and other personnel are not subjected to excessive body current in the event of an insulation breakdown.

1.4 — Conductor Ic

Samples from the production of the various grades of PS, TS, and DS cable-soldered-in-copper channel conductors will be taken at a frequency TBD. Critical current tests of these conductor samples will be performed by TBD in a large conductor test facility. Measurement of RRR will be made in conjunction with this test during sample cool-down.

2 — COIL VERIFICATION AND ACCEPTANCE

2.1 — Completed Coil Electrical Tests

2.1.1 — Requirements

The completed coil electrical detailed test requirements will be defined during the design phase. Primary tests to be performed include HiPot tests, turn-to-turn voltage tests, electrical resistance and inductance measurements.

2.1.2 — HiPot Testing

HiPot testing of the PS, TS, and DS coil systems must be performed. Since these coils are comprised of many sub-coils connected in series, each individual coil module must be individually HiPot tested before making the lead splices between coil modules. HiPot testing will then be repeated on major coil assemblies for each independent set of electrical circuits.

2.1.3 — Turn-To-Turn Voltage Tests

Each individual coil shall be subjected to turn-to-turn voltage tests. The exact method for this test is TBD. The main objective of this test, however, is to detect turn-to-turn shorts prior to coil Vacuum Pressure Impregnation (VPI). Turn-to-turn voltage will be set at some (TBD) multiple of the maximum turn-to-turn voltage that exists with 2 kV across the coil terminals. Note that if no additional layer-to-layer insulation is provided by the final design (consistent with the conceptual design), then the layer–to-layer voltage must be used as the turn-to-turn voltage for the purpose of these tests

2.1.4 — Inductance Tests

Inductance of all sub-coils will be measured to compare with the theoretical values, and to determine if there are internal shorts.

2.1.5 — Other Coil Electrical Testing

Electrical testing will also be performed during the coil winding activity. The conductor payout spools will be made of non-conducting materials, and will be mounted such that the spooled conductor remains electrically isolated from the payout platen. The hidden spooled conductor lead will be mounted on the spool in such a way as to afford an electrical connection during winding. The coil winding table and the coil case base plate will be held at earth ground by direct connection to the building AC earth ground. These actions permit HiPot and voltage drop testing during the coil winding activity.

2.1.5.1 — HiPot Tests During Coil Winding

A series of HiPot tests will be performed during coil winding, and the results recorded in the coil traveler. Detailed specifications are TBD.

2.1.5.2 — Voltage Drop Testing During Coil Winding

During coil winding, the warm conductor will be periodically (TBD) energized at low current (~10 A) and the voltage drop measured versus turn number and recorded in the coil traveler winding record. Detailed specifications for these tests will be determined during the engineering design phase.

2.2 — Warm Measurement and Fiducialization

2.2.1 — Requirements

The completed coil warm measurement and fiducialization test requirements will be determined during the engineering design phase. The warm measurement of the magnetic profile will determine that the coil systems have been manufactured to the electrical and geometric design specifications. This will involve detailed magnetic mapping. It should be carried out at the fabrication site, so that major corrections can be made, if necessary under factory-controlled conditions and with major fabrication tools available. These measurements will be made with the collaboration of the MECO Project, and subject to their acceptance. For these tests, the coils will be energized warm to a reasonable current level to provide a significant field-mapping signature, but not so high as to cause damage to the coil system.

3 — LOW POWER SYSTEM TEST

The Low Power System Test (LPST) is primarily intended for verification of the system integrity prior to or after shipping and handling or after disassembly. It may also be appropriate when the magnet has been warm or un-powered for extended periods.

The following instrumentation and control components must be verified for correct operation of the magnet system power supplies, Quench Detection System (QDS), Quench Protection System (QPS), data acquisition and control functions, and cryogenic system components. A detailed test plan for startup must be established for these systems.

3.1 — Instrumentation and Control

- External Cabling and Interconnections
- Control Computer
- Quench Detection Systems
- Quench Protection System
- PLCs
- UPS
- External Ethernet Connections
- Instrumentation
- Voltage Taps
- Interlocks
- Motor Drives and Actuators (for cryogenic valves)

3.2 — Power Supplies

- Utilities and Water
- Internal Interlocks
- Warm Buses
- Fast Dump Systems
- Charging Circuit Operation

4 — SYSTEM ACCEPTANCE TEST

The MECO Superconducting Magnet System Acceptance Tests (SMSAT) are defined in this section. The PS, TS (u&d), and DS magnet systems have been designed to be modular and capable to be independently operated including vacuum, power, and cryogenic systems. It is very likely that fabrication of individual magnet subsystems will be completed and delivered to the experimental hall at BNL in a staged delivery. In order to minimize the total duration of system acceptance and start-up, it is envisaged that each subsystem would be started up and accepted in order of delivery. There would be a final total system acceptance including all interface assembly issues after all sub-systems are in place. It is expected, however, that the systems will be located in their final assembly positions upon arrival at BNL. This installation and assembly sequence would then dictate the acceptance test sequence.

The site of the acceptance tests will be in the experimental hall provided by BNL. All site services will be provided by BNL. Start-up and Acceptance Tests will be accomplished with a collaborative time comprised of Contractor, MECO Project, and BNL personnel. A Memorandum of Understanding (MOU) or similar document will define the individual roles and responsibilities of the three parties. A top-level series of acceptance tests is described in this section.

General Conditions

1. The magnet system contractor, or his designated alternative technical representative, shall provide a single point of contact for technical considerations and evaluations related to this acceptance test. The technical representative shall be on site for all acceptance test procedures and witness tests. This technical representative shall interact with the MECO Project technical representative and the BNL technical representative.

2. The basis for conducting the SMSAT shall be a signed and accepted final issue of the Acceptance Test Plan (ATP) and the Technical Specification (TS), which are TBD. Test procedures not specifically covered by the ATP, but which are otherwise necessary for the SMSAT, shall be as mutually agreed to by the Contractor, the MECO Project technical representative and the BNL technical representative.

3. A detailed list of responsibilities of the representatives of the Contractor, the MECO Project, and BNL will be mutually agreed early in the design phase of the project.

4.1 — Full System Vacuum Acceptance

Each magnet subsystem contains it's own integral vacuum boundary. Each subsystem will be independently verified and accepted. The type and order of tests include:

4.1.1 — Calibration of Helium Mass Spectrometer Leak Detectors

4.1.2 — Vessel Pressure and Leak Tests

- Define Vessel Test Pressure based on maximum allowable pressure
- Define Vessel Pressure Test Procedure
- Perform Vessel Final Leak Test
- Perform Vessel Final Pressure Test

4.1.3 — Cryogenic Sub-systems Pressure and Leak Tests

- Perform Nitrogen Gas Purge of Helium Cryogen System
    - Remove air, water, and water vapor by flowing dry nitrogen gas
- Perform Nitrogen Gas Purge of LN2 Cryogen System
    - Remove air, water, and water vapor by flowing dry nitrogen gas
- Define Cryogenic Sub-system Test Pressure For Magnetic Acceptance Testing
- Define Helium Cryogenic Sub-system Pressure Test Procedure
- Perform Helium Cryogenic Sub-system Pressure Test
- Perform Nitrogen Cryogenic Sub-system Pressure Test

4.2 — Instrumentation and Controls

A test procedure for the instrumentation and controls will be developed and specified. For this test segment the control system and instrumentation wiring shall be complete for the particular magnet sub-system and fully powered. The data acquisition system should be fully functional and logging control and test data from the start-up and acceptance tests. The test procedure for the Quench Detection System (QDS) is especially critical.

4.3 — Initial Cool Down

Specific test requirements are TBD. A detailed test procedure will be developed. A number of critical systems issues must be addressed in the initial cool-down of the Superconducting Magnet System including: operation of all of the cryogenic valving and control loops. In particular, the anticipated sensitivity and response rates of most elements are unknown. The operation of the BNL helium refrigerator/refrigerator with the magnet system will be tested for the first time. All cryogenic sensors (temperature, level, pressure) are new and need verification. The low temperature thermometer calibrations need to be verified and checked against the calibrations during cool-down. The superconducting current buses cryogenic operation needs to be verified.

4.4 — Magnet Energized Interlocks

The instrumentation test requirements are TBD. For this test segment, the Magnet System shall be in the COLD state. The charging circuit shall be complete. The power supply and bus water-cooling circuits shall be operational and interlocked. The voltage taps shall be complete.

All magnet, power supply and cryogenic system interlocks need to be tested and verified. The quench dump circuit should be operational in this system check.

4.5 — Ramp and Quench

This test segment validates the performance of the Superconducting Magnet System (SMS), charging circuit and Quench Protection System (QPS) at levels up to 105% of the design nominal maximum operating current. Specific test requirements are TBD. Up to this time the stage of commissioning the SMS has had only minimal excitation levels. Ramp rate dependent behavior of the system is unknown. The VCL and superconducting bus response to excitation are also unknown.

The ramp and quench tests are divided into two stages. In the first stage each magnet sub-system (PS, TS (u&d), DS) is independently operated with ramp tests at stored energy levels to approximately 10, 40, 70, 100 and 110% of the design maximum level, as shown in Table 4-1. A maximum current ramp will be established for each test scenario, with the fastest ramp rates used at the lowest nominal current levels. An especially slow current ramp rate value will be established for the over-current Test #5.

Table 18.3 - SMS Ramp and Quench Test Currents and other parameters.

Test #	E/E_{max}	I/I_{max}	$\dot{I}_{max}$ (A/s)
1	0.1	0.3	TBD
2	0.4	0.6	TBD
3	0.7	0.8	TBD
4	1.0	1.0	TBD
5	1.1	1.05	TBD

The nominal operating current for each coil set is shown in Table 4-2. The test series will require an independent test sequence for each of the PS, TSu, TSd, and DS magnets. Magnet sets TSu and TSd each contain two independent electrical circuits within each cryostat, respectively. But each shall have both circuits energized simultaneously. Thus, for example, when testing TSu, current charge rates for TS13u and TS2 will be set to achieve the same fraction of nominal operating current, respectively, at the same time.

All magnet subsystems shall be capable of ramping to full nominal operating current in 1 hour. Ramp rates at lower currents may be higher, and higher ramp rates at lower currents may be used to evaluate the stability of the system. The SMS is required to operate one time at full nominal operating current, stably, for a period of 1 hour.

During the ramp and quench tests, a full-complement of current, voltage and cryogenic (pressure, temperature, mass flow) data should be continuously recorded. If the instrumentation is properly configured, this data can be later analyzed, taking into account static heat loads, to determine the approximate AC losses dissipated in the magnet system. Although this information is not required for acceptance purposes, it could be particularly useful as diagnostic information should there be any difficulty in achieving full nominal operating current levels.

Table 18.4 – Nominal operating currents for each coil set.

Coil Set	Location	Operating Current (A)
1	PS	3500
2	TS13u	1500
3	TS2	4000
4	TS3d5	1500
5	TS4	4000
6	DS	4000

Following successful completion of these test steps the magnet subsystems will be energized to full operating current resulting in the complete MECO superconducting magnet system operating at full nominal current rating. The proposed energization sequence is, PS to full operating current, then DS to full operating current, and finally TSu and TSd to full operating current simultaneously. This sequence is proposed because the TS coils have the strongest magnetic coupling to the PS and DS, and they alone have the possibility of reaching an unacceptable over-current condition if either the PS or DS quenches and the PS or DS QPS is activated without simultaneously activating the TS QPS.

4.5.1 — Required Test Preparations

The SMSAT shall be complete through Section 4.4. At all times during the course of the tests described in this Test Segment a minimum level of test personnel will be present to adequately monitor and operate all control systems for the power supplies, QDS and QPS, cryogenic system, and DAS. In addition, safety monitors shall be required. Since the complete test sequence duration could be one or more months, a detailed test schedule and schedule for manning shifts for this phase of the testing shall be proposed and agreed upon by the Contractor, MECO project and BNL representatives.

1. The SMS state shall be Cold, and the Energize mode enabled.
2. All activities other than test activities should be terminated in the immediate area of the SMS under test. If other assembly work is to be continued, for example, installation of another magnet subsystem, the SMS under test must have a gated and interlocked, limited access perimeter established.
3. Verify that all safety equipment is functioning, e.g., pressure relief valves and burst disks, electrical emergency dump switches, etc. A safety officer in charge of the test must verify that other activities outside the test area will not interfere with the functioning or safety of the test. Independent testing of the calibration functionality and integrity of each QDS and QPS circuit shall have already been completed to the greatest extent possible.
4. Sweep the area around the SMS for tool, hardware, fixtures, and any other loose magnetic materials. Secure the area around the SMS against personnel access. Gate and interlock the access area to the SMS.
5. Carryout and log all other safety and preparatory procedures as required by the detailed test plan.

4.5.2 — Ramp Test #1

1. Program and initiate a linear ramp to 30% of the nominal operating current at the slowest ramp rate (TBD). Monitor lead flow and voltage drop, cryogen levels, strain gauges (if any), bus water-cooling parameters, and voltage taps. Pause the ramp as necessary to evaluate and stabilize the system. Should a quench occur during this ramp, evaluate the system response, taking direct action if the system does not do so automatically. An automatic response to a quench from any valid cause shall constitute a validation of the QPS at this excitation. Examine the QDS signal data to ascertain that it is performing as designed and issuing a legitimate and not false quench detection signal. Note that the quench detection bridge balance circuits might require adjustment during this early stage testing to minimize inductive coupling. If the magnet being tested is either the PS or DS, confirm that the QDS of the quenching coil also activates the QPS of both the TSu and TSd coil circuits. If a quench occurs, start over from step 1. If quenches persist and training is not evident, halt all testing until the cause can be ascertained and mitigated. During this initial test the quench balancing circuits should be used to cause a simulated quench at 10 % of nominal current. The operation of the QDS and QPS should be monitored and evaluated before proceeding to other parts of this test. A second test of the quench protection system should be made using the manual safety trigger system.

2. Maintain the 30% current excitation level for a period sufficient to evaluate cryogen system stability. Adjust system parameters as required. Record the required lead flows for nominal voltage drop. Vary the lead flows over an interval and evaluate voltage drop sensitivity. Record the voltage tap values.

3. Slow Discharge the current

4. Ramp up to 30% of nominal operating current and initiate a fast dump after equilibrium is reached at that current level

5. Repeat steps 1-3 at increasing ramp rates, with ramp rate sequence TBD. Halt testing and adjust the system as required if any necessary sub-system performance is insufficient at any of these ramp rates.

4.5.3 — Ramp Test #2

1. Program and initiate a linear ramp to 60% of the nominal operating current at the slowest ramp rate TBD. Monitor lead flow and voltage drop, cryogen levels, strain gauges (if any), bus water-cooling parameters, and voltage taps. Pause the ramp as necessary to evaluate and stabilize the system. Should a quench occur during this ramp, evaluate the system response, taking direct action if the system does not do so automatically. An automatic response to a quench from any valid cause shall constitute a validation of the QPS at this excitation. If a quench occurs, start over from step 1. If the magnet being tested is either the PS or DS, confirm that the QDS of the quenching coil also activates the QPS of both the TSu and TSd coil circuits. If quenches persist and training is not evident, halt all testing until the cause can be ascertained and mitigated. Verify correct operation of the QDS as above.

2. Maintain the 60% current excitation level for a period sufficient to evaluate cryogen system stability. Adjust system parameters as required. Record the required lead flows for nominal voltage drop. Vary the lead flows over an interval and evaluate voltage drop sensitivity. Record the voltage tap values.

3. Slow Discharge the current.

4. Ramp up to 30% of nominal operating current and initiate a fast dump after equilibrium is reached at that current level.

5. Repeat steps 1-3 at increasing ramp rates, with ramp rate sequence TBD. Halt testing and adjust the system as required if any necessary sub-system performance is insufficient at any of these ramp rates.

4.5.4 — Ramp Test #3

1. Program and initiate a linear ramp to 80% of the nominal operating current at the slowest ramp rate TBD. Monitor lead flow and voltage drop, cryogen levels, strain gauges (if any), bus water-cooling parameters, and voltage taps. Pause the ramp as necessary to evaluate and stabilize the system. Should a quench occur during this ramp, evaluate the system response, taking direct action if the system does not do so automatically. An automatic response to a quench from any valid cause shall constitute a validation of the QPS at this excitation. If the magnet being tested is either the PS or DS, confirm that the QDS of the quenching coil also activates the QPS of both the TSu and TSd coil circuits. If a quench occurs, start over from step 1. If quenches persist and training is not evident, halt all testing until the cause can be ascertained and mitigated. Verify correct operation of the QDS as above.

2. Maintain the 80% current excitation level for a period sufficient to evaluate cryogen system stability. Adjust system parameters as required. Record the required lead flows for nominal voltage drop. Vary the lead flows over an interval and evaluate voltage drop sensitivity. Record the voltage tap values.

3. Slow Discharge the current.

4. Ramp up to 30% of nominal operating current and initiate a fast dump after equilibrium is reached at that current level.

5. Repeat steps 1-3 at increasing ramp rates, with ramp rate sequence TBD. Halt testing and adjust the system as required if any necessary sub-system performance is insufficient at any of these ramp rates.

4.5.5 — Ramp Test #4

1. Program and initiate a linear ramp to 100% of the nominal operating current at the slowest ramp rate TBD. Monitor lead flow and voltage drop, cryogen levels, strain gauges, bus water-cooling parameters, and voltage taps. Pause the ramp as necessary to evaluate and stabilize the system. Should a quench occur during this ramp, evaluate the system response, taking direct action if the system does not do so automatically. An automatic response to a quench from any valid cause shall constitute a validation of the QPS at this excitation. If the magnet being tested is either the PS or DS, confirm that the QDS of the quenching coil also activates the QPS of both the TSu and TSd coil circuits. If a quench occurs, start over from step 1. If quenches persist and training is not evident, halt all testing until the cause can be ascertained and mitigated. Verify correct operation of the QDS as above.

2. Maintain the 100% current excitation level for a period sufficient to evaluate cryogen system stability. Adjust system parameters as required. Record the required lead flows for nominal voltage drop. Vary the lead flows over an interval and evaluate voltage drop sensitivity. Record the voltage tap values.

3. Slow Discharge the current.

4. Ramp up to 30% of nominal operating current and initiate a fast dump after equilibrium is reached at that current level.

5. Repeat steps 1-3 at increasing ramp rates, with ramp rate sequence TBD. Halt testing and adjust the system as required if any necessary sub-system performance is insufficient at any of these ramp rates.

4.5.6 — Ramp Test #5

1. Program and initiate a linear ramp to 100% of full nominal operating current at the slowest ramp rate TBD. Pause at this level for a sufficient time to reach equilibrium values in all subsystems

2. Program and initiate a linear ramp from 100% to 105% of full nominal operating current at the slowest pre-determined ramp rate. Pause the ramp as necessary. When 110% nominal operating current is reached, hold for 1 hour. . An automatic response to a quench from any cause shall constitute a validation of the QPS for full current excitation. If the magnet being tested is either the PS or DS, confirm that the QDS of the quenching coil also activates the QPS of both the TSu and TSd coil circuits. If a quench occurs, start over from step 1. If quenches persist and training is not evident, halt all testing until the cause can be ascertained and mitigated. Verify correct operation of the QDS as above.

3. Program and initiate a linear down-ramp from 105% to 100% of full nominal operating current at the slowest pre-determined ramp rate. Pause at this level for a sufficient time to reach equilibrium values in all subsystems.

4. Visually verify the condition and operation of all sub-systems. When satisfied that all systems are in order, manually initiate a fast dump from this current level. Verify correct execution of the QPS.

4.5.7 — Continuation of Ramp Tests

Once this test sequence is completed for the first Magnet Subsystem, maintain the magnet in the cold state at zero operating current. Begin testing the remaining, untested Magnet Subsystems following the same 5-step test procedure established above. During this period, the Heat Load Verification Tests (Tests 4.6.2-3) can be carried out without transport current to establish long-term, background static heat loads.

4.6 — Heat Loads

Specific test requirements are TBD. Specifically, the each SMS shall have a helium heat leak at full nominal current not to exceed TBD W with a lead consumption of TBD l/hr, and the nitrogen heat leak shall not exceed TBD W. The heat leak and lead flow requirements are related. To get accurate heat loads in general the system must be at temperature for an extended period, and this is why the heat load measurements have been left to the end of the SMSAT.

The following tests should be performed independently for the PS, TSu, TSd, and DS magnet sub-systems. These tests, except for 4.6.1, can be performed on the magnet sub-system which has already been completed the ramp and quench tests.

4.6.1 — Heat Load Verification

Ramp the magnet to full nominal operating current. Demonstrate that stable cryogen reservoir levels can be maintained. With cryogen supplies interrupted, demonstrate that the magnet can operate at full nominal current for TBD hours.

4.6.2 — LHe Static Boil Off Test

Perform a LHe static boil off test by measuring liquid levels in the cryogenic supply cold-box or by other means of monitoring net helium mass flow, as appropriate for the given cryogenic sub-system. Exact test procedures are TBD.

4.6.3 — LN2 Static Boil Off Test

Perform a LN2 static boil off test by measuring liquid levels in the liquid nitrogen supply system- or by other means of monitoring net nitrogen mass flow, as appropriate for the given cryogenic sub-system. Exact test procedures are TBD.

4.7 — Full SMS Operation

When each magnet subsystem has independently achieved full nominal operating conditions, the entire magnet ensemble will be energized to nominal operating conditions, according to the following sequence.

1. With all systems cryogenically stable, energize the DS to 100% nominal operating current at a ramp-rate TBD, but not exceeding 1-hour duration.

2. Wait for cryogenic system stabilization for all magnet systems.

3. Energize the PS to 100% nominal operating current at a ramp-rate TBD, but not exceeding 1-hour duration.

4. Wait for cryogenic system stabilization for all magnet systems

5. Energize the TSu to 100% nominal operating current at a ramp-rate TBD, but not exceeding 1-hour duration.

6. Wait for cryogenic system stabilization for all magnet systems
7. Energize the TSd to 100% nominal operating current at a ramp-rate TBD, but not exceeding 1-hour duration.

8. Establish that the complete SMS and supporting cryogenic systems are in stable equilibrium.

9. Perform the Final Acceptance Magnetic Verification Methods (Test 5)

5 — FINAL ACCEPTANCE MAGNETIC VERIFICATION TEST

5.1 — Test Requirements

The system acceptance test – cold alignment verification test requirements are to be defined in a test requirements document, based on the Field Specification Section 3 of the CDR, and additional input from the MECO Project.

5.1.1 — Summary

The purpose of the Final Acceptance Magnetic Verification Test ("Verification") is to verify that the MECO Superconducting Magnet System (SMS), when energized to the nominal operating current levels for each coil sub-system achieves the required field distribution along the beam-line and within a specified radius from the beam-line as a function of axial location.

This task involves two principal activities:

1. Accurate measurement of the field distribution at specified locations.
2. Adjustment of the coil support system to achieve the required field distribution.

The actual field distribution can only be determined with the SMS in the cold and fully energized condition. The field mapping equipment therefore, must be remotely operable within the beam-line tube from the upstream end of the PS to the downstream end of the DS. This will require a substantial design of the field mapping equipment, including a method for calibrating the sensors, and an accurate and precise method for determining the field sensing probe location.

Once a field-mapping sweep has been completed, the data will analyzed to determine if the specified field profile has been achieved. If not, an analysis must be performed to determine how the coil supports must be adjusted for better field quality. The warm alignment and magnetic verification steps should be performed as accurately as possible, and take into account final coil displacements due to Lorentz forces, and thermal strains due to cool-down. A sophisticated fiducial mapping system is envisaged for accurate coil placement.

Master Fabrication and Test Sequence

This integrated fabrication and test sequence has been prepared to serve as a road map for the in process subsystem tests, and acceptance tests, and their relationship to assembly stages.

Table 18.5 – List of tests to perform during subsystem fabrication and assembly.

Tests during Subsystem Fabrication and Assembly	Tester	Test Location	Test Conditions
1. Conductor			
Strand	Contractor	Contractor	
Cable	Contractor	Contractor	
Stabilizer	Contractor	Contractor	
Integration Dimensions	Contractor	Contractor	
Integrated Conductor	MECO Project/BNL	BNL	
Insulation Integrity	Contractor	Contractor	
2. Coil Components			
Bobbin dimensions	Contractor	Contractor	
Vacuum tests	Contractor	Contractor	
3. Coils			
In process electrical and dimensional	Contractor	Contractor	Warm
Warm magnetic verification	Contractor	Contractor	Warm
Final electrical	Contractor	Contractor	Warm
4. Vessel			
Vessel shell material	Contractor	Contractor	
Vessel dimensions	Contractor	Contractor	
Vessel final vacuum test	Contractor	Contractor	Warm
5. Cold Mass			
Dimensions and alignment	Contractor	Contractor	Warm
Sensors and wiring	Contractor	Contractor	Warm
Cold bus electrical	Contractor	Contractor	Warm
Vacuum tests	Contractor	Contractor	Warm
6. Cryo-distribution Box			
Sensors and wiring	Contractor	Contractor	Warm
Safety devices	Contractor	Contractor	Warm
Electrical tests	Contractor	Contractor	Warm
Vacuum	Contractor	Contractor	Warm
7. Power Supply and Charging Circuit			
Operational test	Contractor	Contractor	Dummy Load
Dump switch and resistor test	Contractor	Contractor	Dummy switch signals and programmed power supply waveshape.

Table 18.6 – List of tests to conduct during system assembly.

Tests during Assembly	Tester	Test Location	Test Conditions
8. Low Power System Test	Contractor	Contractor	Warm
SHIP TO BNL			
9. Integration/Final Assembly			
Final system leak test	Contractor	BNL	Warm
Warm alignment verification	Contractor	BNL	Warm
10. Magnetic Verification	MECO Project	BNL	LN2 Temp.
11. Low Power System Test	Contractor	BNL	Warm
12. System Acceptance Test	Contractor	BNL	Cold
13. Magnetic Verification	MECO Project	BNL	Cold